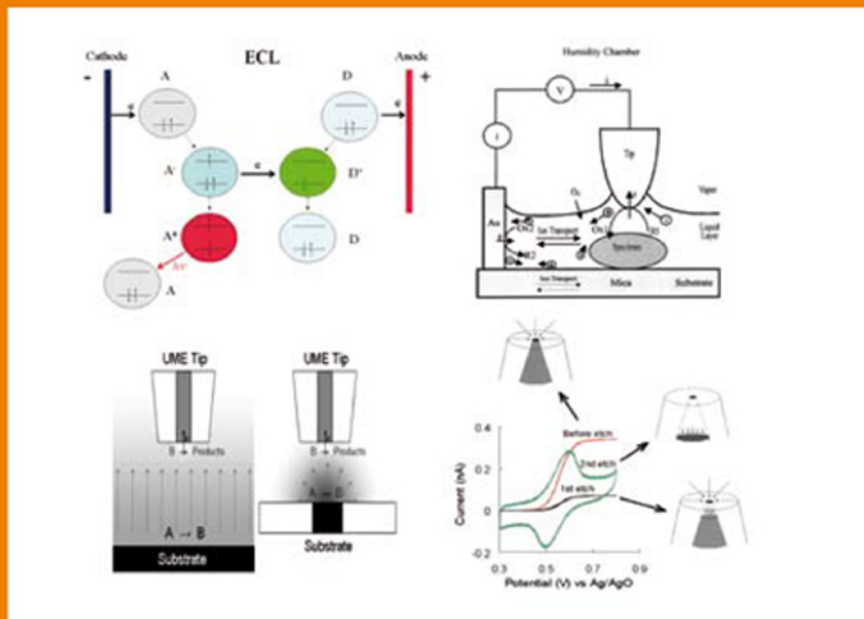# Handbook of Electrochemistry

Edited by
Cynthia G. Zoski

Handbook of Electrochemistry

This page intentionally left blank

Handbook of Electrochemistry

Cynthia G. Zoski

New Mexico State University
Department of Chemistry and Biochemistry
Las Cruces, New Mexico, USA

Notice
No responsibility is assumed by the publisher for any injury and/or damage to persons or property as a matter of products liability, negligence or otherwise, or from any use or operation of any methods, products, instructions or ideas contained in the material herein. Because of rapid advances in the medical sciences, in particular, independent verification of diagnoses and drug dosages should be made

For information on all Elsevier publications
visit our website at books.elsevier.com

Working together to grow
libraries in developing countries
www.elsevier.com | www.bookaid.org | www.sabre.org

ELSEVIER   BOOK AID International   Sabre Foundation

Preface

Electrochemistry now plays an important role in a vast number of fundamental research and applied areas. These include, but are not limited to, the exploration of new inorganic and organic compounds, biochemical and biological systems, corrosion, energy applications involving fuel cells and solar cells, and nanoscale investigations. There are many excellent textbooks and monographs, which explain the fundamentals and theory of electrochemistry. This handbook is not a textbook, however, but rather a source of electrochemical information, details of experimental considerations, representative calculations, and illustrations of the possibilities available in electrochemical experimentation. It is most closely allied with the textbook *Electrochemical Methods: Fundamentals and Applications* by Allen J. Bard and Larry R. Faulkner, second edition.

The *Handbook of Electrochemistry* is divided into five parts: Fundamentals (Chapter 1), Laboratory Practical (Chapters 2–10), Techniques (Chapters 11–14), Applications (Chapters 15–17), and Data (Chapters 18–20). Chapter 1 covers the fundamentals of electrochemistry that are essential for everyone working in this field and sets the stage for the following 19 chapters. Thus, Chapter 1 presents an overview of electrochemical conventions, terminology, fundamental equations, electrochemical cells, experiments, literature, textbooks, and specialized books. Laboratory aspects of electrochemistry are emphasized in the following nine chapters that include *Practical Electrochemical Cells* (Chapter 2), *Solvents and Supporting Electrolytes* (Chapter 3), *Reference Electrodes* (Chapter 4), *Solid Electrode Materials: Pretreatment and Activation* (Chapter 5), *Ultramicroelectrodes* (Chapter 6), *Potentiometric Ion-Selective Electrodes* (Chapter 7), *Chemically Modified Electrodes* (Chapter 8), *Semiconductor Electrodes* (Chapter 9), and *Microelectrode Arrays* (Chapter 10). Electrochemical techniques covered in this handbook range from classical experiments (Chapter 11) to *Scanning Electrochemical Microscopy* (SECM) (Chapter 12), *Electrogenerated Chemiluminesence* (Chapter 13), and *Spectroelectrochemistry* (Chapter 14). These four chapters also include representative applications based on the method described. Specific electrochemical applications based on the preceding chapters illustrate the impact of electrochemistry in exploring diverse topics ranging from electrode kinetic determinations (Chapter 15), unique aspects of metal deposition (Chapter 16) including micro- and nanostructures, template deposition, and single particle deposition, and electrochemistry in small places and at novel interfaces (Chapter 17) including biological cells, single molecule electrochemistry, and electrochemistry at liquid/liquid interfaces. The remaining three chapters provide useful electrochemical data and information involving electrode potentials (Chapter 18), diffusion coefficients (Chapter 19), and methods used in measuring liquid-junction potentials (Chapter 20). The majority of the chapters were supervised by a single corresponding author. Exceptions to this are Chapters 6, *Ultramicroelectrodes*; Chapter 16, *Metal Deposition*; and Chapter 17, *Electrochemistry in Small Places and at Novel Interfaces*, where several authors contributed to different sections in a specific chapter.

I would like to thank the contributors of this handbook, colleagues in the electrochemical community, and the authors of the many papers, textbooks, and specialized books whose work is cited in this handbook and has led to the development of electrochemistry, its expansion into diverse areas, and much of the information presented in this handbook. I especially want to thank Allen J. Bard, a pioneer in electrochemistry, for his helpful comments, suggestions, advice, and unwavering encouragement during the editing of this handbook.

Cynthia G. Zoski

Contents

Colour Section to be found at the end of the book

This page intentionally left blank

Corresponding Authors

Shigeru Amemiya University of Pittsburgh, Pittsburgh, PA, USA

Melisa D. Arning Saint Louis University, St. Louis, MO, USA

John E. Baur Illinois State University, Normal, IL, USA

Adam J. Bergren Iowa State University, Ames, IA, USA (present address: The University of Alberta, Edmonton, Alberta, Canada)

Shaowei Chen University of California, Santa Cruz, CA, USA

Madalina Ciobanu Vanderbilt University, Nashville, TN, USA

David E. Cliffel Vanderbilt University, Nashville, TN, USA

Stephen Creager Clemson University, Clemson, SC, USA

Christophe Demaille Université Paris 7-UMR CNRS 7591, France

Guy Denuault University of Southampton, UK

Robert A.W. Dryfe University of Manchester, Manchester, UK

Grant A. Edwards Iowa State University, Ames, IA, USA (present address: Northern Kentucky University, Highland Heights, KY, USA)

Andrew G. Ewing Pennsylvania State University, PA, USA

Fu-Ren F. Fan The University of Texas at Austin, Austin, TX, USA

José Fernandez The University of Texas at Austin, Austin, TX, USA

Robert J. Forster Dublin City University, Ireland

Santosh K. Haram University of Pune, Ganeshkhind, Pune, India

Katherine B. Holt The University of Texas at Austin, Austin, TX, USA (present address: University College London, London, UK)

Tia E. Keyes Dublin City University, Ireland

Anthony Kucernak Imperial College London, London, UK

Youngmi Lee University of Tennessee, Knoxville, TN, USA

Biao Liu The University of Texas at Austin, Austin, TX, USA

Janine Mauzeroll Université Paris 7-UMR CNRS 7591, France (present address: Université du Québec à Montréal, Montréal, Québec, Canada)

Wujian Miao   The University of Southern Mississippi, Hattiesburg, MS, USA

Shelley D. Minteer   Saint Louis University, St. Louis, MO, USA

Michael V. Mirkin   Queens College – CUNY, Flushing, NY, USA

Reginald M. Penner   University of California, Irvine, CA, USA

Marc D. Porter   Iowa State University, Ames, IA, USA (present address: Arizona State University, Tempe, AZ, USA)

Yuanhua Shao   Peking University, Beijing, China

Timothy J. Smith   The University of Texas at Austin, Austin, TX, USA

Keith J. Stevenson   The University of Texas at Austin, Austin, TX, USA

Greg M. Swain   Michigan State University, East Lansing, MI, USA

Sabine Szunerits   Institut National Polytechnique de Grenoble, Domaine Universitaire, France

Paolo Ugo   University of Venice, Venice, Italy

Ran Tel-Vered   University of Texas at Austin, Austin, TX, USA

Henry S. White   University of Utah, Salt Lake City, UT, USA

Nathan J. Wittenberg   Pennsylvania State University, PA, USA

Cynthia G. Zoski   New Mexico State University, Las Cruces, NM, USA

Part One

FUNDAMENTALS

This page intentionally left blank

– 1 –

Fundamentals

**Madalina Ciobanu, Jeremy P. Wilburn,
Morgan L. Krim, and David E. Cliffel**

Department of Chemistry, Vanderbilt University,
Nashville, TN 37235, USA

1.1 CONVENTIONS IN ELECTROCHEMISTRY

The science of electrochemistry is concerned with electron transfer at the solution/electrode interface. Most of the basic principles and relationships, however, were described prior to the discovery of the electron by J. J. Thompson in 1893. In 1800, Alessandro Volta invented the first battery, then known as a voltaic pile, by alternating stacks of copper and zinc disks separated by paper soaked in acid solutions. With the discovery of a sustainable source of electrical current, the stage was set for the rapid development of the area of science now known as electrochemistry. By 1835, Michael Faraday had already defined the anode, cathode, electrode, electrolyte, and ion: concepts without which any definitive description of electrochemistry is virtually impossible.

The positive and negative mathematical convention for electrical charge is attributed to Benjamin Franklin (1). Charles-François de Cisternay du Fay had earlier theorized the existence of only two types of electrical charge. Du Fay had named the charge generated by rubbing a glass rod as "vitreous," while the equivalent charge generated by rubbing amber, or resin, as "resinous." Franklin, however, envisioned electrical charge as being attributed to the level of a single invisible fluid present inside objects (i.e., a negatively charged object had a lesser amount of this fluid and a positively charged one had an excess amount). Franklin accordingly renamed resinous charge as negative and vitreous charge positive, thereby establishing the convention that would eventually demand the electron to be defined as a negative charge.

1.1.1 Potential conventions

Although the work of Faraday had established early on the relationship between the current generated during electrolysis and the amount of generated species, the dependence of cell

potential on the concentration of electroactive species remained theoretically elusive until the advent of thermodynamics. Let us consider the following reduction reaction:

$$O + ne^- \rightleftharpoons R \qquad (1.1.1)$$

where O is the oxidized species, R is the reduced species, and n is the number of electrons exchanged between O and R. The relationship between the concentration of oxidized species [O], concentration of reduced species [R], and free energy (ΔG [J mol^{-1}]) is given as

$$\Delta G = \Delta G^0 + RT \ln \frac{[R]}{[O]} \qquad (1.1.2)$$

where R is the gas constant (8.3145 J mol^{-1} K^{-1}) and T [K] is the temperature. The critical aspect of this equation is that the ratio of reduced to oxidized species can be related to the Gibbs free energy change (ΔG), from which we can then derive the potential (E [V]):

$$\Delta G = -nFE \qquad (1.1.3)$$

Here E is the maximum potential between two electrodes, also known as the open-circuit potential (OCP) or the equilibrium potential, which is present when no current is flowing through the cell, and F is Faraday's constant ($1F = 96{,}485.3$ C mol^{-1}). If the reactant and product have unit activity, and E is for the reaction in the direction of reduction (left to right in equation (1.1.1)), then equation (1.1.3) can be written as

$$\Delta G^0 = -nFE^0 \qquad (1.1.4)$$

In this case, the potential is known as the *standard electrode potential* (E^0 [V]) or the *standard potential* and it relates to the *standard Gibbs free energy change* (ΔG^0 [J mol^{-1}]). It should be noted here that due to the minus sign in equation (1.1.4), all spontaneous reactions (i.e., with $\Delta G^0 < 0$) will have a positive standard electrode potential ($E^0 > 0$).

The mathematical expression describing the correlation between potential and concentration for a cell reaction is a central tenant of electrochemistry and is known as the *Nernst equation* (obtained by combining equations (1.1.2)–(1.1.4)):

$$E = E^0 + \frac{RT}{nF} \ln \frac{[O]}{[R]} \qquad (1.1.5)$$

In addition to the use of the *standard potential* (E^0), reaction potentials may also be reported with the convention of *electromotive force* (*emf or $\mathscr{E}$* [V]). The convention of *emf* was adopted to make the calculation of cell potentials, from the combination of two half-reactions, more straightforward. For a reduction reaction, the *standard potential* and the *emf* have the same value, while for the same reaction written in the direction of oxidation (e.g., the reverse reaction), their signs are opposite. Using the example of a silver iodide cell, consider the complete cell schematic:

$$(anode)\, Ag^0 \rightarrow Ag^+ + e^- / electrolyte / AgI + e^- \rightarrow Ag^0\, (cathode) \qquad (1.1.6)$$

The calculation of cell potential for *emf* requires only the addition of the *emf* values for each half-reaction, while the same cell potential calculation using *standard potentials* requires the usage of the following convention:

$$E^0_{cell} = E^0_{cathode} - E^0_{anode} \tag{1.1.7}$$

The anode half-reaction can be written either as a reduction (equation (1.1.8)) or as an oxidation (equation (1.1.9)):

$$Ag^+ + e^- \rightleftharpoons Ag^0 \quad E^0 = +0.799 \text{ V}, \mathscr{E} = +0.799 \text{ V} \tag{1.1.8}$$

$$Ag^0 \rightleftharpoons Ag^+ + e^- \quad E^0 = +0.799 \text{ V}, \mathscr{E} = -0.799 \text{ V} \tag{1.1.9}$$

The *standard potential* of the anodic oxidation reaction is given in equation (1.1.9), and the *standard potential* of the cathodic reduction reaction is

$$AgI + e^- \rightleftharpoons Ag^0 + I^- \quad E^0 = -0.152 \text{ V} = \mathscr{E} \tag{1.1.10}$$
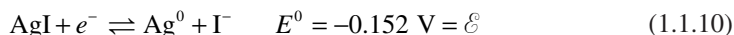
First, we will use the *emf* convention. The anodic reaction is an oxidation, and therefore the sign of the *standard potential* must be reversed to give the *emf*. For the cathodic reaction, however, the reaction is a reduction, and therefore the *emf* is the same as the *standard potential*. The cell *emf* would be given as

$$\mathscr{E}_{cell} = \mathscr{E}_{cathode} + \mathscr{E}_{anode} = -0.152 \text{ V} + (-0.799 \text{ V}) = -0.951 \text{ V} \tag{1.1.11}$$

The same calculation for the *standard potential* convention would be

$$E^0_{cell} = E^0_{cathode} - E^0_{anode} = -0.152 \text{ V} - 0.799 \text{ V} = -0.951 \text{ V} \tag{1.1.12}$$

Therefore, the result is the same regardless of the convention used. We can also calculate the standard free energy change for the net reaction by using equation (1.1.4):

$$\Delta G^0 = -(1)F(-0.951 \text{ V}) = +91.76 \text{ kJ mol}^{-1} \tag{1.1.13}$$

The results from equations (1.1.12) and (1.1.13) indicate that this net reaction is not spontaneous; therefore it requires energy input in order to occur.

Each half-cell reaction has a specific standard potential reported as the potential of the reduction reaction vs. the normal hydrogen electrode (NHE). In an electrochemical cell, there is a half-cell corresponding to the working electrode (WE), where the reactions under study take place, and a reference half-cell. Experimentally the cell potential is measured as the difference between the potentials of the WE half-cell and the reference electrode/reference half-cell (see Chapter 4). The archetypal reference electrode is the NHE, also known as the standard hydrogen electrode (SHE) and is defined, by convention, as 0.000 V for any temperature. Although the NHE is not typically encountered due to difficulty of operation, all conventional electrodes are in turn referenced to this standard to define their absolute potential (i.e., the Ag/AgCl, 3 M KCl reference has a potential of 203 mV vs. the NHE). In practice, experimental results are either stated as being obtained vs. a specific reference electrode, or converted to potentials vs. NHE.

Numerous tables exist referencing E^0 values for the most typically encountered redox reactions (see Chapter 18). Initially these tables were derived from thermodynamic data,
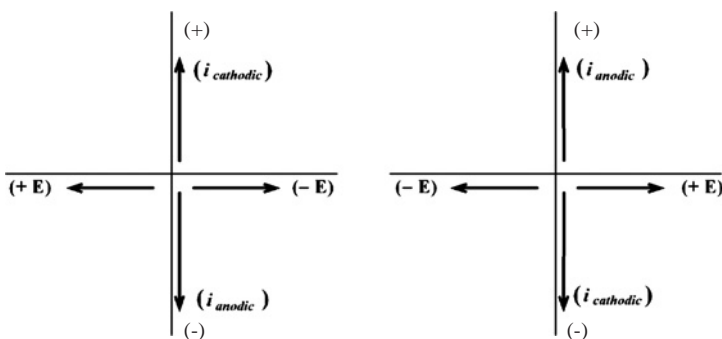
Figure 1.1   American (left) and IUPAC (right) voltammogram conventions.

and as the science has progressed these values have been confirmed in most cases via electrochemical experimentation.

1.1.2   Current conventions

As previously mentioned, Faraday initially coined the expressions ion, anode, and cathode. Faraday called the active species in his electrolysis experiments ions, using a Greek word loosely translated as wanderer. Therefore, anodic currents are generated by species (anions) diffusing (wandering) toward the anode and cathodic currents by those (cations) diffusing toward the cathode. The anode and cathode are defined by convention, with the anode always being the site of oxidation and the cathode the site of reduction. The mathematical signs of currents and potentials measured at the anode and cathode depend on the type of electrochemical cell being investigated. There are two basic classifications: cells are either galvanic, where reactions are spontaneous (such as batteries), or electrolytic where a current or potential is applied to drive a chemical reaction (see Section 1.6).

Additionally, there are two conflicting conventions dictating the graphical depiction of combined voltage/current plots, known as voltammograms (see Figure 1.1); both conventions are currently found in the literature. In both conventions, the potential is plotted on the x-axis and the current on the y-axis. In the older convention, known as the polarographic or American convention, positive potentials lie to the left of the origin and cathodic current is positive, while the International Union of Pure and Applied Chemistry (IUPAC) has adopted the opposite convention, also known as the European convention, where positive potentials are to the right of the origin, and anodic currents are positive. The American convention (positive cathodic currents and negative potentials to the right) will be used throughout this book, unless otherwise indicated.

1.2   TERMINOLOGY

The definitions provided here tend to follow the IUPAC instructions (2), where possible. Additional explanations are present, as some terms have specific meanings in electrochemistry (3).

Anode: *electrode* where the *oxidation* takes place.

Auxiliary (Counter) Electrode (CE): *electrode* that helps pass the current flowing through the cell; the current travels between the *WE* and *CE*; typically no processes of interest (under study) occur at the surface of *CE*; example: Pt wire.

Battery: one or more *galvanic cells*.

Cathode: *electrode* where the *reduction* takes place.

Cell Potential (E [V]): the sum of electrical potentials within an *electrochemical cell* that also accounts for all *redox processes* occurring at the *electrodes*.

Chronoamperometry: electrochemical methods that utilize a potential step and have the output current readings vs. time.

Electrochemical Cell: device that involves the presence of faradaic currents as a result of *redox* chemical reactions; it can be either a *galvanic cell*, when the reactions are spontaneous, or an *electrolytic cell*, when the reactions are non-spontaneous.

Electrochemical Mediator: the electrochemically active species with fast kinetics that will undergo a *reduction* or an *oxidation* reaction at the *electrode*, thus yielding a *faradaic current* that can give information about a kinetically slow process.

Electrode: it represents an electrical conductor/semiconductor in an *electrochemical cell*; in electrochemistry, it is the conductive phase where the electron transfer occurs; it can be an *anode* or a *cathode*.

Electrolytic Cell: energy-consuming device that converts electrical energy into chemical energy; it consists of at least two *electrodes* and an *electrolyte* solution; *cathode* is negative as compared to the *anode*; example: electrolysis cell.

Equilibrium Potential (E_{eq} [V]): the potential associated with an electrode when all redox processes are in equilibrium; the net current is zero under these conditions and the electrode potential is given by the *Nernst* equation.

Faradaic: the multitude of processes involving *redox* chemical reactions.

Fuel Cell: device similar to a *galvanic cell* used for the conversion of chemical energy into electricity, sustained by a continuous supply of chemical reactants from outside the cell; example: H_2–O_2 cell.

Galvanic (Voltaic) Cell: self-powered device that produces electricity by means of chemical energy; it is limited by the supply of the chemicals contained inside the device; it consists of two *electrodes* (*anode* and *cathode*) and an *electrolyte* solution; the *cathode* is positive as compared to the *anode*.

Half-cell: the *anode* or the *cathode* compartment of an *electrochemical cell*, including all reactions that occur at that particular electrode.

Half-reaction: the redox reaction that occurs in one *half-cell*, either at the *anode* or at the *cathode*.

Ideal Non-polarizable (Depolarized) Electrode: it is a type of electrode that does not change its potential upon passage of current; example: *reference electrode*.

Ideal Polarizable (Polarized) Electrode (IPE): it is a type of electrode that exhibits a large change in potential for an infinitesimal change in current; example: *WE*.

Interface (Junction): in an *electrochemical cell*, it represents the location where two distinct phases come in contact with each other: solid–liquid (*electrode*–solution), two liquids of different concentrations and/or compositions (*reference electrode*–solution), etc.

Nernstian: a *reversible redox* process that follows equilibria equations.

Non-faradaic: processes that follow Ohm's law; they are comprised of all processes that occur at the *electrode* (excluding chemical reactions) and account for solution conductivity and capacitive charging.

Normal/Standard Hydrogen Electrode (**NHE/SHE**): it is the standard *reference electrode*; all *standard potentials* are referred to *NHE*; its potential is by definition 0.000 V.

Oxidation: refers to the process in which a chemical species loses one or more electrons; it is the reverse of the *reduction*.

Oxidized Species/Oxidizing Agent/Oxidant (**O**): the chemical species that undergoes the *reduction*, enabling the *oxidation* of a different species.

Overpotential (***η* [V]**): deviation of the *electrode/cell potential* from its *equilibrium* value, $\eta = E - E_{eq}$; it can be either positive or negative.

Potentiometry: electrochemical methods that utilize near zero currents and have the output potential readings vs. time, using the *Nernst* equation to find analyte concentrations.

Redox: a *process* that involves both a *reduction* and an *oxidation*.

Redox Couple: the chemical species that has at least two oxidation states, and thus can act either as the *reduced* or the *oxidized species* (depending on the oxidation state); example: Fe^{3+}/Fe^{2+}.

Reduced Species/Reducing Agent/Reductant (**R**): the chemical species that undergoes the *oxidation*, enabling the *reduction* of a different species.

Reduction: refers to the process in which a chemical species gains one or more electrons; it is the reverse of the *oxidation*.

Reference Electrode (**RE**): *electrode* that can maintain a constant potential under changing experimental conditions; the *WE* potential is referenced vs. the *RE* potential; *REs* are typically *anodes* in *electrochemical cells*; example: *NHE*.

Standard Reduction Potential (***E*⁰ [V vs. *NHE*]**): is defined as the potential of the *reduction half-reaction* at the *electrode*, with respect to the *NHE*; each redox couple has a fixed *standard reduction potential*.

Supporting Electrolyte: an ionic substance (typically a salt) that is present in a solution to ensure its conductivity; example: KCl. The *supporting electrolyte* reduces the migration effects in the solution; it does not undergo redox chemistry, and thus its ions are called *spectator ions*. Sometimes the *supporting electrolyte* is referred to simply as the *electrolyte*.

Voltammetry: electrochemical methods that utilize a potential ramp (e.g., increase or decrease with time) and have the output current vs. potential.

Working Electrode (**WE**)/***Indicator Electrode***: *electrode* where the *redox processes* under study occur; *WEs* are typically *cathodes*; example: ion-selective electrode or noble metal.

1.3   FUNDAMENTAL EQUATIONS

The ability to predict how a system will behave under certain conditions is very important for practicing electrochemists. In this regard, the fundamental equations described in this section can be quite useful. Let us consider the case of a simple redox process:

$$O + ne^- \rightleftharpoons R \tag{1.3.1}$$

1.3.1 Nernst equation

The Nernst equation solves the potential of an electrochemical cell containing a reversible system with fast kinetics and it is valid only at equilibrium and at the surface of the electrode:

$$E = E^{0\prime} + \frac{RT}{nF} \ln \frac{C_O^*}{C_R^*} \tag{1.3.2}$$

$$E = E^0 + \frac{RT}{nF} \ln \frac{a_O}{a_R} \tag{1.3.3}$$

where $E^{0\prime}$ [V] is the formal potential, E^0 [V] is the standard potential, C^* [mol L^{-1}] is the bulk concentration for the considered species, and a [mol L^{-1}] is the activity. A common assumption is to ignore the activity coefficients resulting in $E^0 = E^{0\prime}$. The formal potential in equation (1.3.2) accounts for the activity coefficients for the species O and R. The values for the formal potential (see Chapter 18) are dependent upon the nature of both the solvent and the supporting electrolyte. If we consider the reduction reaction for a platinum solution (Pt^{2+}) with a concentration of 1 mM at a solid platinum electrode:

$$Pt^{2+} + 2e^- \rightleftharpoons Pt \tag{1.3.4}$$

then we are able to apply the Nernst equation to calculate the voltage drop across this system; since the reduced form is a solid, it has unity activity; the activity for very dilute solutions (1 mM) is the same as the concentration, so we can write

$$E = 1.188V + \frac{RT}{2F} \ln \frac{0.001}{1} = 1.099 \text{ V} \tag{1.3.5}$$

The standard electrode potential for platinum is 1.188 V and the temperature is 25 °C. The voltage of this half-reaction is 1.1 V.

1.3.2 Equilibrium constant

The free energy change in the form of equation (1.1.4) can be related to the equilibrium constant (K), assuming unit activity for electrons:

$$\Delta G^0 = -RT \ln K \tag{1.3.6}$$

This relationship is an example of the power of electrochemistry. A single experimental measurement, such as E^0, can be used to directly calculate K. For example, a cell consisting of a silver electrode and a silver electrode coated with solid silver iodide can be used to determine the solubility product (K_{sp}) of silver iodide. For the net chemical reaction of the cell:

$$AgI_{(s)} \rightleftharpoons Ag^+ + I^- \tag{1.3.7}$$
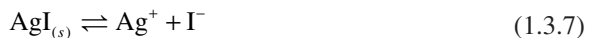
since AgI is a solid, K becomes K_{sp}. Given that the cell potential is -0.951 V, that it is a one electron reaction, and from equation (1.1.4):

$$\Delta G^0 = -(1)F(-0.951 \text{ V}) = (0.951 \text{ V})F \tag{1.3.8}$$

The value obtained for the change in free energy can be then substituted into equation (1.3.6) and K_{sp} calculated for 25 °C as follows:

$$K_{sp} = e^{-(0.951 \text{ V})F/RT} = 8.3 \times 10^{-17} \tag{1.3.9}$$

1.3.3 Mass-transfer limited current

The expression for the mass-transfer limited current i_l [A] is given by

$$i_l = nFAmC \tag{1.3.10}$$

where C [mol cm^{-3}] represents the concentration of the electrochemically active species that gets converted at the electrode; if the entire analyte gets converted, then C is equal to the initial bulk concentration of the analyte, C^*. If in equation (1.3.10) we know that the analyte ($C^* = 20$ mM) reacts completely at an electrode that has the area $A = 0.1$ cm^2 in a process that involves the transfer of $n = 2$ electrons, and that the solution is stirred in such a manner that the mass-transfer coefficient $m = 0.01$ cm sec^{-1}, we can then calculate the value for the mass-transfer limiting current $i_l = 4$ mA.

1.3.4 Cottrell equation

The Cottrell equation is derived from Fick's second law of diffusion (Section 1.5) and predicts the variation of the current in time, when a potential step is applied under conditions of large overpotential. For this equation to be valid the current must be limited by diffusion of the analyte to the electrode surface, and thus the solution has to be unstirred. The overpotential at which the reaction is driven must be large enough to ensure the rapid depletion of the electroactive species (O) at the electrode surface, such that the process would be controlled by the diffusion to the electrode. This equation is most often applied to potential step methods (e.g., chronoamperometry; see Chapter 11):

$$i(t) = \frac{nFAD_O^{1/2}C_O^*}{\pi^{1/2}t^{1/2}} \tag{1.3.11}$$

where D_O [cm^2 sec^{-1}] is the diffusion coefficient for the species O, and A [cm^2] is the electrode area.

   In an unperturbed solution, when a potential step is applied that causes a surface reaction to occur, the current decays according to the Cottrell equation. One application is the determination of the diffusion coefficient for an electrochemically active species O, with the initial concentration of 0.1 M, that undergoes a single electron reduction at a 1 mm diameter electrode. The current decays to a diffusion limited current of 68 µA after 2 sec. When applying the Cottrell equation it is important to note that the concentration has to be converted to mol cm^{-3} (in our case 0.1 M corresponds to 10^{-4} mol cm^{-3}). The electrode area is 7.85×10^{-3} cm^2, and the value for the diffusion coefficient can be calculated as 5×10^{-6} cm^2 sec^{-1}.

1.3.5 Faraday's law

Faraday's law correlates the total charge, Q [C], passed through a cell to the amount of product, N [mol]:

$$Q = nFN \tag{1.3.12}$$

where F is Faraday's constant, $F = 96{,}485.3$ C mol^{-1}, and n is the number of electrons transferred per mole of product. Faraday's law can be used in many applications, such as electrogravimetry (to find the amount of substance deposited at an electrode) and coulometry (to find the total amount of electricity required for complete electrolysis of a compound); it can also be used for finding the number of electrons implicated in an electrolytic process. In order to reduce one mole of a generic reactant according to equation (1.3.1) ($n = 1$), we need to pass through the cell a total charge equal to 9.65×10^4 C.

When we pass a 2 A current for 3 h through a solution containing copper ions, we are able to collect 7.11 g of pure copper. We can now find what was the oxidation state of the copper ions in the initial solution. The total charge passed through the solution is 21,600 C. Upon converting the mass of copper into moles (0.11 moles), we can use equation (1.3.12) to find $n = 2$. Thus our starting solution contained Cu^{2+} ions.

1.4 FACTORS AFFECTING REACTION RATE AND CURRENT

1.4.1 Current, current density, and rate

In order to grasp what is taking place in an electrochemical reaction, the concept of current and how the current changes when a stimulus is applied must be understood. The current is equal to the change in charge with time, or

$$i = \frac{dQ}{dt} \tag{1.4.1}$$

where i [A] is the faradaic current, t [sec] is the time, and Q [C] is the charge given by Faraday's law (equation (1.3.12)).

Chemical reactions can be either *homogeneous* or *heterogeneous*. The first type occurs in a single phase, and its rate is uniform everywhere in the volume where it occurs:

$$\text{Rate [mol sec}^{-1}] = \frac{dN}{dt} \tag{1.4.2}$$

Heterogeneous reactions occur at the electrode-solution interface, and they are characteristic of electrochemistry. While the expression for the reaction rate is similar to equation (1.4.2), it depends upon the area of the electrode, A [cm^2], or the area of the phase boundary where the reaction occurs:

$$\text{Rate [mol sec}^{-1} \text{ cm}^{-2}] = \frac{i}{nFA} = \frac{j}{nF} \tag{1.4.3}$$

where j [A cm^{-2}] is the current density. In order to compare processes that take place at electrodes of varying size, the rate of reaction has to be normalized for the area of the electrode (equation (1.4.3)). The size of the electrode is crucial to the amount of product created in a bulk electrolysis experiment, for example. For a one electron reaction, with 0.1 moles of reactant that gets converted into product for 1 h at an electrode of 1 cm^2 area, we can calculate the charge $Q = 9.6 \times 10^3$ C, the current $i = 2.7$ A, and the current density $j = 2.7$ A cm^{-2}. From equation (1.4.3) we can then obtain the reaction rate: 28 µmol sec^{-1} cm^{-2}.

There are four major factors that govern the reaction rate and current at electrodes: (i) mass transfer to the electrode surface; (ii) kinetics of electron transfer; (iii) preceding and ensuing reactions; (iv) surface reactions (adsorption). The slowest process will be the rate-determining step. Let us consider the case of the simple reaction:

$$O + ne^- \rightleftharpoons R \tag{1.4.4}$$

This reaction may be considered as a set of equilibria involved in the migration of the reactant to the electrode, the reaction at the electrode, and the migration of the product away from the electrode surface into the bulk of the solution (Figure 1.2).

For this reaction to proceed, O is required to move from the bulk solution near the electrode surface. This aspect of the mechanism is related to mass transfer and is governed by equations such as Fick's laws of diffusion and Nernst–Planck. Mass transfer from the bulk solution towards the electrode surface could limit the rate of the reaction (Section 1.5).

When all of the processes leading to the reaction are fast, this leaves the electron transfer reaction as the limiting factor. The measurement of fast electron transfer rates is still limited by the non-faradaic time constant for the electrode, τ [sec]:

$$\tau = R_s C_d \tag{1.4.5}$$

where R_s [Ω] is the solution resistance and C_d [F] is the double layer capacitance. In a potential step experiment, if $R_s = 1000$ Ω and $C_d = 10$ µF, we can calculate the time constant $\tau = 10$ msec. The double layer charging will be complete (95%) in a time frame equal to 3τ (30 msec for our example) (3). For the same type of potential step experiment, the variation of the non-faradaic current, i_{nf} [A], in time, t [sec], is given by

$$i_{nf} = \frac{E}{R_s} e^{-t/R_s C_d} \tag{1.4.6}$$
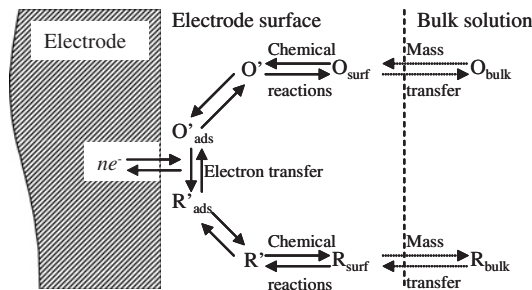
Figure 1.2   Processes involved in an electrode reaction (adapted from reference (3), with permission).

where E [V] is the magnitude of the potential step. The expression of the current from equation (1.4.6) indicates that the reaction cannot proceed faster than τ. One way to measure faster electron transfer kinetics is to increase the solution conductivity by lowering R_s. In voltammetry/amperometry this is accomplished by using a three-electrode cell instead of a two-electrode cell (Section 1.7).

In a potential sweep experiment (see Chapter 11) the output is the current, which accounts for both the faradaic and non-faradaic processes. Since the scan rate, v [V sec^{-1}] is known, it is possible to calculate the non-faradaic current, i_{nf} [A]:

$$i_{nf} = vC_d \qquad (1.4.7)$$

For an electrode with $A = 0.2$ cm^2 and a capacitance of 15 μF cm^{-2}, we can calculate $C_d = 3$ μF. If this electrode is employed in a potential sweep experiment where the scan rate is 10 mV sec^{-1}, then the corresponding non-faradaic current (equation (1.4.7)) is 30 nA.

The oxidized species from Figure 1.2 might undergo a chemical reaction preceding the reaction at the electrode surface. The coupled preceding chemical equilibrium can have a dramatic effect and is critical to understanding the system. If the electron transfer at the electrode is fast while the preceding chemical equilibrium is slow, then the slow chemical reaction is the *rate-determining step* and has the largest influence on the faradaic current. Also, a similar examination of reactions that occur after a fast electron transfer may provide information about the system under study (see Chapter 15).

Reactions involving changes in the electrode surface also affect the rate of the reaction. These reactions include adsorption, desorption, and crystallization. They are able to affect the system by changing the electrolyte-electrode interface, and thereby changing the electrochemical behavior of the electrode. When the electroactive species is directly adsorbed onto the surface of an electrode, the effect of "pre-concentrating" the reactant species makes them instantly available at the electrode. In a voltammetry experiment, this would lead to a curve whose shape is not affected by diffusion (Chapter 11).

1.4.2 Reversibility

Reversibility is a key concept when dealing with electrochemical reaction mechanisms. An electrochemical cell is considered *chemically reversible* if reversing the current through the cell reverses the cell reaction and no new reactions or side products appear:

$$Sn^{2+} + 2Fe^{3+} \rightleftharpoons 2Fe^{2+} + Sn^{4+} \qquad (1.4.8)$$

An electrochemical cell is considered *chemically irreversible* if reversing the current leads to different electrode reactions and new side products. This is often the case if a solid falls out of solution or a gas is produced, as the solid or gaseous product may not be available to participate in the reverse reaction. When a solid zinc electrode is oxidized in an acidic system with a platinum electrode the following two reactions take place:

$$Zn_{(s)} \rightarrow Zn^{2+} + 2e^- \qquad (1.4.9)$$

$$2H^+ + 2e^- \rightarrow H_{2(g)} \text{ (Pt electrode)} \qquad (1.4.10)$$

When this system is reversed, by the application of a potential with a greater magnitude than the cell potential with the opposite bias, a different set of reactions occur, rendering this system chemically irreversible:

$$2H^+ + 2e^- \rightarrow H_{2(g)} \text{ (Zn electrode)} \tag{1.4.11}$$

$$2H_2O \rightarrow O_{2(g)} + 4H^+ + 4e^- \text{ (Pt electrode)} \tag{1.4.12}$$
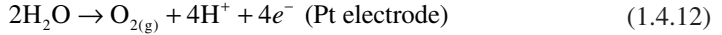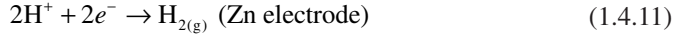
The concept of *thermodynamic reversibility* is theoretical. It applies to adiabatic changes, where the system is always at equilibrium. An infinitesimal change causes the system to move in one particular direction, resulting in an infinitesimal response; the analogy in electrochemistry is that a small change in potential could result in the reversal of the electrochemical process. In electrochemistry, the researcher is concerned with *practical reversibility*. In reality electrochemical processes occur at finite rates, and as long as the experimental parameters are set in a manner that allows for the reversal of the reaction to regenerate the original species, the processes are deemed *practically reversible*. For these systems the Nernst equation (equation (1.3.2)) holds true at all times.

1.4.3 Kinetics

1.4.3.1 Overpotential

For a non-spontaneous cell reaction to occur, an overpotential, η [V], must be applied. The extent to which the reaction is driven beyond the equilibrium potential, E_{eq} [V], is

$$\eta = E - E_{eq} \tag{1.4.13}$$

In order to deposit a metal ion, such as Pt^{2+}, from a solution at a certain rate, without consideration of ion concentration and the surface effects at which the deposition occurs, an application of a potential, i.e., $E = 2$ V, greater than the $E_{eq} = 1.2$ V, is necessary. In this case $\eta = 0.8$ V.

1.4.3.2 Butler–Volmer Equation

The Butler–Volmer equation can be used to predict the current that results from an overpotential when mass-transfer limitations are eliminated. Let us consider the case of a simple reduction reaction (Butler–Volmer always assumes that $n = 1$):

$$O + e^- \underset{k_b}{\overset{k_f}{\rightleftharpoons}} R \tag{1.4.14}$$

where k_f [cm sec^{-1}] and k_b [cm sec^{-1}] are the heterogeneous rate constants for the forward reduction and backward oxidation electrode reactions, respectively. The final form of the Butler–Volmer equation (equation (1.4.25)) predicts the current of a system as a function of the overpotential in a well-stirred cell. The overall current, i [A], can be viewed as the difference of the cathodic (reduction) current, i_c [A], and the anodic (oxidation) current, i_a [A]:

$$i = i_c - i_a \tag{1.4.15}$$

Each of the currents is proportional to their corresponding heterogeneous rate constant:

$$i_c = FAk_f C_O(0,t) \tag{1.4.16}$$

$$i_a = FAk_b C_R(0,t) \tag{1.4.17}$$

where F is Faraday's constant, A [cm^2] is the area of the electrode, and $C_j(x,t)$ [mol cm^{-3}] is the concentration of species j at the distance x [cm] from the electrode at the time t [sec]. Here we are considering reactions at the electrode surface, therefore $x = 0$. The forward and reverse rate constants can be written as a function of the standard heterogeneous rate constant, k^0 [cm sec^{-1}]:

$$k_f = k^0 e^{-\alpha f(E-E^{0'})} \tag{1.4.18}$$

$$k_b = k^0 e^{(1-\alpha)f(E-E^{0'})} \tag{1.4.19}$$

where the coefficient $f = F/(RT)$ and the transfer coefficient, α, is a dimensionless parameter with values between 0 and 1, and is often estimated to be 0.5.

By dividing the expressions for the rate constants from equations (1.4.18) and (1.4.19) we obtain a relation that governs all models of electrode kinetics, not only for equilibrium cases (3):

$$\frac{k_b}{k_f} = e^{f(E-E^{0'})} = e^{-(E-E^{0'})/kT} \tag{1.4.20}$$

where k [J K^{-1}] is Boltzmann's constant.

By combining equations (1.4.15) – (1.4.19), the current of the reaction may be described by the complete *current–potential characteristic*:

$$i = FAk^0[C_O(0,t)e^{-\alpha f(E-E^{0'})} - C_R(0,t)e^{(1-\alpha)f(E-E^{0'})} \tag{1.4.21}$$

This equation is the basis for all accounts of heterogeneous electrode kinetics, including the expression for the *Butler–Volmer equation*.

When an electrochemical cell is at equilibrium there is no net current, because the system contains a cathodic current balanced by an equal and opposite anodic current:

$$i_0 = i_a = i_c \tag{1.4.22}$$

where i_0 [A] is the exchange current and can be written as

$$i_0 = FAk^0 C_O^{*(1-\alpha)} C_R^{*\alpha} \tag{1.4.23}$$

where C_j^* [mol cm^{-3}] is the bulk concentration for the j species. The exchange current can be derived experimentally from Tafel plots (Figure 1.3). Equation (1.4.23) can be used for calculating the standard heterogeneous rate constant. If the exchange current is determined to be 15 μA at a 1 mm^2 electrode in a solution where the concentrations of both the oxidized and reduced forms are 0.1 M, then $k^0 = 1.6 \times 10^{-4}$ cm sec^{-1}.
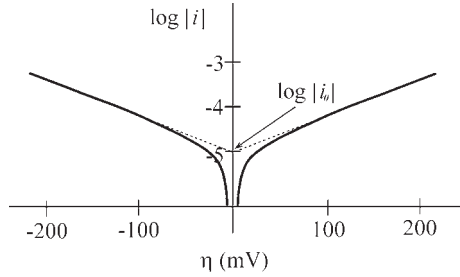
Figure 1.3   Tafel plot (adapted from reference (3), with permission).

From equations (1.4.21) and (1.4.23) we can obtain the *current–overpotential equation*:

$$i = i_0 \left[\frac{C_O(0,t)}{C_O^*} e^{-\alpha f \eta} - \frac{C_R(0,t)}{C_R^*} e^{(1-\alpha) f \eta} \right] \tag{1.4.24}$$

where η [V] is the overpotential. With efficient mass transfer the concentrations of the bulk solution and the solution at the electrode surface ($x = 0$) are equal and the *current–overpotential equation* (equation (1.4.24)) reduces to the *Butler–Volmer equation*:

$$i = i_0 \left[e^{-\alpha f \eta} - e^{(1-\alpha) f \eta} \right] \tag{1.4.25}$$

This equation can be used to predict the current when the mass-transfer limitation is eliminated. In a well-stirred solution diffusion to the electrode is no longer the limiting factor in the experiment. In a cell at 25 °C, if $\alpha = 0.5$ and $i_0 = 10$ µA, for an overpotential of 200 mV the resultant current calculated with equation (1.4.25) is 0.49 mA.

1.4.3.3   Tafel equation

The Tafel equation links the applied overpotential to the current, i [A], that passes through the circuit:

$$\eta = \frac{RT}{\alpha F} \ln i_0 - \frac{RT}{\alpha F} \log i \tag{1.4.26}$$

In equation (1.4.26), the *y*-axis intercept at no overpotential can be used to calculate the exchange current, i_0 [A]. Tafel equation can be written in a very simple form as

$$\eta = a + b \log i \tag{1.4.27}$$

where a and b are constants that can be easily inferred from equation (1.4.26). A graphic representation of log |i| vs. η is known as a *Tafel plot*. The utility of equation (1.4.27) is limited by the reverse reaction and diffusion. When the overpotentials are small ($<$50 mV), the slope increases because the backward reaction becomes greater than 1% of the forward reaction, changing the relative concentrations at the electrode surface (equation (1.4.24)). When very large overpotentials ($>$few hundred mV) are applied, the slope of the line can deviate below the prediction of the Tafel equation because of mass-transfer limitations.

Tafel plots are composed of an anodic branch for positive overpotentials and a cathodic branch for negative overpotentials. The slope of the linear region on the Tafel plot (between 50 mV and very large overpotentials) can be used to calculate α, the transfer coefficient:

$$\text{reduction slope} = \frac{-\alpha F}{2.3RT} \tag{1.4.28}$$

$$\text{oxidation slope} = \frac{(1-\alpha)F}{2.3RT} \tag{1.4.29}$$

If the slope is 8.46, then at 25 °C the transfer coefficient $\alpha = 0.5$. Tafel plots can also be used to calculate exchange current from the y-intercept of the Tafel regions. From Figure 1.3, $\log |i_0| = -5$, and thus $i_0 = 10\ \mu A$.

1.5   EQUATIONS GOVERNING MODES OF MASS TRANSFER

Mass transfer can be accomplished in three different ways and/or a combination of these modes: (a) *migration*—movement of charged particles in an electric field; (b) *diffusion*—movement of species against a concentration gradient; (c) *convection*—movement of species induced by stirring or density gradients. The more modes of mass transfer are present concurrently, the more complicated the equations that describe them are.

1.5.1   Nernst–Planck equation

The Nernst–Planck equation below relates the unidirectional (x) flux of a species j to diffusion, migration, and convection:

$$J_j(x) = -D_j \underset{\text{1st term}}{\underbrace{\frac{\partial C_j(x)}{\partial x}}} - \underset{\text{2nd term}}{\underbrace{\frac{z_j F}{RT} D_j C_j \frac{\partial \phi(x)}{\partial x}}} + \underset{\text{3rd term}}{\underbrace{C_j v(x)}} \tag{1.5.1}$$

where $J_j(x)$ [mol cm^{-2} sec^{-1}] is a one-dimensional flux for species j at distance x [cm] from the electrode; D_j [cm^2 sec^{-1}], z_j, and C_j [mol cm^{-3}] are the diffusion coefficient, the charge, and the concentration for the species j, respectively; $v(x)$ [cm sec^{-1}] is the rate with which a volume element moves in solution; $\partial C_j(x)/\partial x$ is the concentration gradient; and $\partial \phi(x)/\partial x$ is the potential gradient along the x-axis. In equation (1.5.1), the first term is concerned with the diffusion and is, in fact, Fick's first law (equation (1.5.2)), the second term accounts for the migration of the species in the solution, and the last term represents the convection of the solution.

1.5.2   Fick's laws of diffusion

Fick proposed two laws of diffusion in solution. These equations describe the relation between the flux of a substance and its concentration as a function of both time and position.

The first law describes the flux of a species, O, as a function of the change in its concentration, C_O [mol cm^{-3}], with distance, x [cm], from an electrode, at a time t [sec]:

$$-J_O(x,t) = D_O \frac{\partial C_O(x,t)}{\partial x} \tag{1.5.2}$$

where $J_O(x,t)$ [mol cm^{-2} sec^{-1}] is the flux of species O, and D_O [cm^2 sec^{-1}] is the diffusion coefficient. The second law relates the change in concentration with time to the change in flux with position:

$$\frac{\partial C_O(x,t)}{\partial t} = D_O \left(\frac{\partial^2 C_O(x,t)}{\partial x^2} \right) \tag{1.5.3}$$

From the point of view of an experimentalist that has to interpret data, it is desirable to reduce the complexity of the equations that govern the mass transfer. This can be accomplished by minimizing the effects of convection, for example, by using quiescent conditions (not stirring). Migration can be reduced by adding a supporting electrolyte to the solution to carry the current and to minimize R_s and $(\partial \phi / \partial x)$; the appropriate supporting electrolyte should be inert and present in high concentration (ca. 100 times greater than the concentration of the analyte).

Alternatively, the solution can be stirred so fast that the flux J becomes a function of convection only. Under constant stirring,

$$v(x) = m \tag{1.5.4}$$

where m [cm sec^{-1}] is the mass-transfer coefficient, and it represents the speed with which the species j gets at the surface of the electrode. Thus,

$$J = mC_j \tag{1.5.5}$$

The flux can also be written as

$$J = \frac{1}{A} \frac{dN}{dt} \tag{1.5.6}$$

where A is the area of the electrode. Since

$$\frac{dN}{dt} = \frac{i}{nF} \tag{1.5.7}$$

we can combine equations (1.5.5)–(1.5.7) to get the expression for the mass-transfer limiting current i_l [A],

$$i_l = nFAmC \tag{1.5.8}$$

The mass-transfer coefficient can be quantified for particular applications, such as the rotating disk electrode (see Chapters 11 and 19):

$$m = 0.62 D^{2/3} \omega^{1/2} \upsilon^{-1/6} \tag{1.5.9}$$

where ω [sec^{-1}] is the angular frequency of rotation and υ[cm^2 sec^{-1}] is the kinematic viscosity; and for an ultramicroelectrode of radius r_0, at steady state,

$$m = \frac{4D}{\pi r_0} \qquad (1.5.10)$$

Mass transfer occurs before charge transfer (Figure 1.2), and we always have both processes occurring. The slower of the two processes is the rate-limiting step. If the applied potential has small values, then the charge transfer is going to be slow and will become the limiting factor; in this case we can often totally neglect the contribution of the mass transport. However, if the applied potential is high, then the charge transfer is very fast, and the mass transfer is the rate-limiting step. At low potentials, we can write the following expression for the current:

$$i = FAk_f C_O \qquad (1.5.11)$$

where the reaction rate k (Section 1.4) has the same units as m. Whichever of the two is the smallest governs the reaction. If $k < m$, we are kinetically limited and apply equation (1.5.11); if $k > m$, then we are mass-transfer limited and apply equation (1.5.8).

The mass-transfer limiting current, which is by definition independent of potential, can be also written as

$$i_l = \frac{nFADC^*}{\delta} \qquad (1.5.12)$$

where δ [cm] is the thickness of the Nernst diffusion layer. The values for δ are in the range 10^{-3}–10^{-1} cm (4). Equations (1.5.8) and (1.5.12) are practically the same because $m = D/\delta$.

If the mass transfer is governed by diffusion, then

$$\delta = \sqrt{\pi Dt} \qquad (1.5.13)$$

From equations (1.5.12) and (1.5.13), for a diffusion-controlled unidirectional process, the current i will decrease with time, as shown by *Cottrell equation*:

$$i(t) = \frac{nFAD^{1/2}C^*}{\pi^{1/2}t^{1/2}} \qquad (1.5.14)$$

Equation (1.5.13) enables the calculation of the period that takes for a molecule of analyte to wander a certain distance. If the diffusion coefficient for the analyte is 5×10^{-6} cm^2 sec^{-1}, then it will take 6.4 sec to wander 0.01 cm.

If in equation (1.5.14) we know that $i = 1$ mA, $n = 1$, $D = 5 \times 10^{-6}$ cm^2 sec^{-1}, $A = 0.1$ cm^2, and $\delta = 10$ μm, then we are able to calculate $C = 21$ mM. Cottrell equation enables many electrochemical techniques by relating the current in a directly proportional manner to the concentration of the electrochemically active species.

1.6   ELECTROCHEMICAL CELLS

Electrochemical cells (see Chapter 2) are divided into two sub-types, galvanic and electrolytic. Galvanic cells are those whose reactions are spontaneous ($\Delta G < 0$) when the electrodes are connected via a conductor (i.e., a copper wire), while an electrolytic cell requires a potential in excess of its OCP to be applied in order to drive an electrochemical process (e.g., non-spontaneous, $\Delta G \geq 0$). In order to better describe the composition of an electrochemical cell, a notation system has been devised to represent both the individual components of the cell and the phases in which they reside. A comma separates components that exist within the same phase in this system, and phase boundaries are represented by a single slash mark. Phase boundaries that possess a potential that is considered to be a negligible component of the overall cell potential (i.e., a salt bridge) are depicted with a double slash. The activities or concentrations of all species should also be specified, and the cell is always written from the anode (at left) to the cathode (at right). For example, a copper plating *electrolytic cell* comprised from copper and platinum electrodes immersed in an aqueous solution containing H_2SO_4 and $CuSO_4$ (Figure 1.4) would be written as

$$Cu\,/\,Cu^{2+}, H^+, SO_4^{2-}\,/Pt \tag{1.6.1}$$

If the cell contained two divided chambers linked by a KCl salt bridge, with the first containing the platinum electrode in $CuCl_2$ and the second containing the copper electrode in HCl, it would then be written as

$$Cu/H^+/\!/Cu^{2+}/Pt \tag{1.6.2}$$

Electrolytic processes are used by the pharmaceutical industry (electrochemical synthesis) and heavily by the metal-refining industry where they represent the only currently utilized means of production of aluminum from alumina ore. These industrial electrolytic processes, by some estimates, use a significant fraction of the electricity produced worldwide today (5).
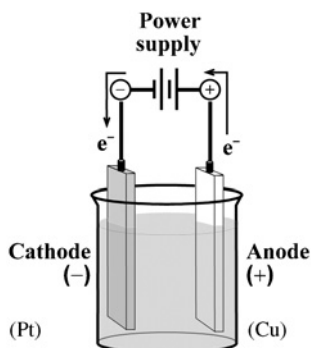
Figure 1.4   An electrolytic electrochemical cell. (for colour version: see colour section at the end of the book).
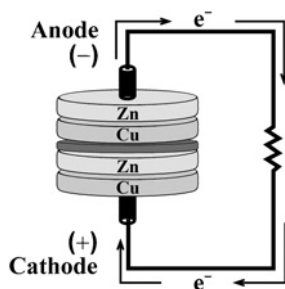
Figure 1.5 A galvanic electrochemical cell. (for colour version: see colour section at the end of the book).

The schematic depiction of Volta's battery (Section 1.1), which is composed of stacked copper and zinc disks separated by paper soaked in an acidic solution (Figure 1.5), could be represented as

$$Zn/Zn^{2+} /\!/ Cu^{2+}/Cu \qquad (1.6.3)$$

This is an example of a *primary* (*non-rechargeable*) *cell*. Other types of important galvanic cells include *secondary* (*rechargeable*) *cells* and *fuel cells*. It should be noted that when a *secondary galvanic cell* is being recharged, it becomes an *electrolytic cell*, because a potential is being applied in order to reverse the direction of the spontaneous electrochemical reaction.

While it may suffice to describe the electrodes of a galvanic cell as simply an anode or cathode, electrodes in electrolytic cells are called on to perform more specialized roles. In order to differentiate the electrodes, they are labeled according to their specific role in the cell: the working electrode (WE), the reference electrode (RE), and the counter electrode (CE), also known as the auxiliary electrode. The use of these labels helps to avoid confusion since in some experiments, where the direction of current flow reverses periodically, the WE and CE alternate between acting as anode and cathode.

The WE, typically a cathode, is generally where the reaction of interest occurs. Typical WEs (see Chapters 5 and 6) include the noble metals (especially gold and platinum), carbon (including pyrolytic carbon, glassy carbon, carbon paste, nanotubes, and vapor-deposited diamond), liquid metals (mercury and its amalgams), and semiconductors (indium-tin oxide, Si, see Chapter 9). WEs can be chemically modified (see Chapter 8) in order to increase their sensitivities toward specific species (i.e., become chemical sensors) or to decrease the potential required to drive a particular reaction (i.e., catalysis).

Regardless of whether an electrolytic cell is of the two-electrode or three-electrode configuration, it must contain a reference electrode, typically classified as an anode. The RE (see Chapter 4) is composed of a system of phases, which retain an essentially constant composition, and therefore provides a stable potential by which the WE potential can be monitored. The phases present in REs undergo reversible redox processes at a very high rate, enabling them to rapidly adjust to changes in the solution's ionic activity, but leaving them sensitive to the passage of large current densities. For some systems, where there are no major fluctuations of ionic activity, a noble metal electrode (e.g., a platinum wire) may

be substituted for the reference electrode. In this case, the substitute is referred to as a quasi-reference electrode.

Since REs can be damaged by the presence of large current densities and may lose their ideal non-polarizable behavior, a three-electrode configuration is often used. The third electrode, called the CE/auxiliary electrode, is provided as a current sink to shunt excess current away from the RE. The CE is generally chosen to be inert under the reaction conditions (i.e., a large-area noble metal electrode such as platinum is common), and may be placed in a separate cell joined by a sintered glass frit for experiments where very large currents are generated.

1.7   CELL RESISTANCE; CAPACITANCE; UNCOMPENSATED RESISTANCE

Two types of current may flow in an electrochemical cell, faradaic and non-faradaic. All currents that are created by the reduction and/or oxidation of chemical species in the cell are termed faradaic currents. Faradaic currents may be described by the following equation:

$$\frac{dQ}{dt} = \frac{d}{dt}(nFN) = nF\frac{dN}{dt} \tag{1.7.1}$$

where Q [C] is the charge, t [sec] is the time, n is the number of electrons transferred, F is Faraday's constant, and N is the number of moles reacted. All other current is deemed non-faradaic in nature, and is directly related to Ohm's law:

$$i = \frac{V}{R} = \frac{V}{Z} \tag{1.7.2}$$

where i [A] is the current, V [V] is the potential, R [Ω] is the resistance, and Z [Ω] is the impedance. While the resistance is applicable when considering Ohm's law in an electrical circuit, the application to an electrochemical cell requires the usage of impedance, which includes elements of resistance and capacitance.

In order to describe the effects of resistance and electrode capacitance in electrochemical cells, it is useful to introduce the concept of the ideal polarizable electrode (IPE). The IPE (Figure 1.6) is one that will not pass any charge across the solution/metal interface when the potential across it is changed. The behavior of the IPE then mimics that of a capacitor in an electrical circuit, with the one difference being that the capacitance of an
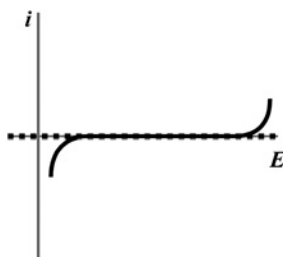
Figure 1.6   The ideal polarizable electrode in theory (dashed line) and in practice (solid line).

IPE will be dependent on the potential placed across it, while for a normal capacitor it will not. In Figure 1.6 the dashed line depicts how close a real electrode can come to behaving as an IPE over a limited potential range. Above and below that range, the real electrode will begin to pass a charge. Therefore within that specific potential range, the real electrode will mimic the IPE and behave as a capacitor.

The electrode/solution interface itself is thought of as an *electrical double layer* composed of the electrical charge at the surface of the electrode itself and the charge of the ions disbursed in the solution at a small distance from the electrode surface. This double layer is formed when a potential is applied to the electrode and causes a *charging current* (non-faradaic current) to pass through the cell. The solution half of the double layer can be thought of as being made up of distinct sub-layers (Figure 1.7). The first layer consists of solvent molecules and specifically adsorbed (desolvated) ions. The locus of the electrical centers of this layer is termed the boundary of the *inner Helmholtz plane* (IHP) and lies at a distance of χ_1 from the electrode surface. The second layer consists of solvated ions. Since these ions are completely surrounded by solvent molecules, they may approach no closer than χ_2 and the locus of the electrical charges from these ions is known as the *outer Helmholtz plane* (OHP). Ions that remain solvated are termed non-specifically adsorbed, and may only approach up to the OHP. The interactions of non-specifically adsorbed ions with the electrode surface only involve long-range electrostatics and are independent of chemical properties. The ionic species in this plane are less compact than the IHP and are disbursed in a three-dimensional region called the *diffuse layer*, which extends well into the bulk of the solution.

During most electrochemical experiments, only the reaction occurring at one electrode, usually the WE, is of interest. In these cases, an IPE is paired with an electrode whose behavior approaches that of an ideal non-polarizable electrode (e.g., an RE). When the potential is measured between the WE (IPE) and the RE, there will be a voltage drop observed that is equivalent to iR_s, as given by Ohm's law:

$$V = iR = iR_s \qquad (1.7.3)$$
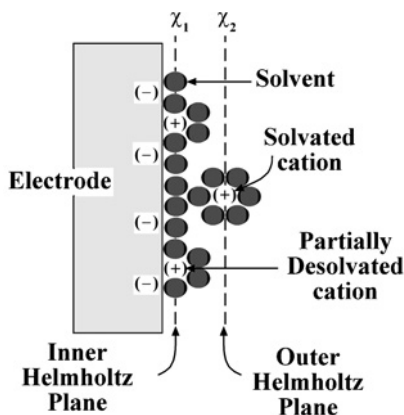
Figure 1.7   The electrical double layer (adapted from reference (3), with permission). (for colour version: see colour section at the end of the book).

where i [A] is the current passing through the cell and R_s [Ω] is the solution resistance. For systems where iR_s is small ($<$ 1–2 mV) a two-electrode system may be used. If iR_s is larger, a two-electrode cell may still be used, but it will require a smaller current. The usage of an ultramicroelectrode (UME, Chapter 6), with diameter $<$50 µm, will result in a drastic decrease in current. Currents measured in systems with UMEs are typically in the nA–pA (10^{-9}–10^{-12} A) range. Therefore, with a UME even non-polar solvents can be utilized without breaking the 2 mV barrier (R_s of 2 MΩ and i of 1 nA give 2 mV of potential drop).

For cases where iR_s cannot be kept below 2 mV, a three-electrode cell must be used. Usually potentiometric applications employ two-electrode cells, whereas three-electrode cells improve results for voltammetry and amperometry. The third electrode is a CE and is used as a current sink for the cell (Figure 1.8). In the three-electrode cell, the majority of the current passes between the WE and the CE, which lowers the potential drop resulting from iR_s measured between the RE and the WE, but does not completely eliminate it. If the cell is pictured as a potentiometer (Figure 1.9), the solution resistance (R_s) can be split into two components, termed the *compensated resistance* (R_c) and the *uncompensated resistance* (R_u), one of which (R_c) can be eliminated from the measurement based on the positioning of the RE. By positioning the RE as close as possible to the WE, a majority of R_s can be eliminated. In some cases (e.g., where an organic solvent is used) the total resistivity of the solution cannot be minimized sufficiently through the placement of the RE, due to the low conductivity (i.e., higher R_s) of the solvent itself. In these cases ultramicroelectrodes are generally required, since their very much smaller area greatly reduces the current, which reduces the overall value of iR_s.
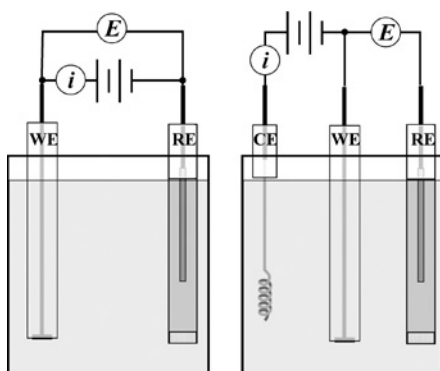
Figure 1.8 Schematic representation of two-electrode (left) and three-electrode (right) electrochemical cells. (for colour version: see colour section at the end of the book).
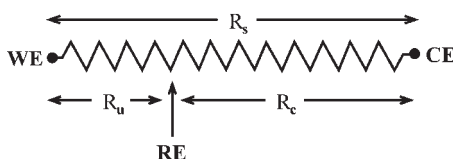
Figure 1.9 Schematic representation of an electrochemical cell as a potentiostat.

1.8   OVERVIEW OF ELECTROCHEMICAL EXPERIMENTS

The electrochemical techniques can be divided into two major groups: *static* ($i = 0$) and *dynamic* ($i \neq 0$) (6). *Potentiometry* is a *static* method, and it measures the rest potential vs. time; the most common applications in *potentiometry* are the use of ion-selective electrodes and pH meters. The *dynamic* methods comprise mostly all the other electrochemical techniques (3). Table 1.1 lists the most commonly used methods among this group.

1.9   ELECTROCHEMISTRY LITERATURE; TEXTBOOKS; SPECIALIZED BOOKS

The scope of this book is to outline the basic theories and concepts that may be encountered by a researcher in the course of basic electrochemical experimentation. This section

TABLE 1.1

General classification of electrochemical dynamic methods

Controlled Potential	Potential Step	Amperometry	Chronoamperometry; Double Potential Step Chronoamperometry	
		Chronocoulometry; Double Potential Step Chronocoulometry		
		Sampled Current Voltammetry; Differential Pulse Voltammetry; Square Wave Voltammetry		
	Potential Sweep	Voltammetry	Stationary	Linear Scan Voltammetry
				Cyclic Voltammetry
			Hydro-dynamic	Stirred Solution/Flow Cell
				Rotating Disk Electrode; Rotating Ring-Disk Electrode
			Anodic Stripping Voltammetry (Stationary/Hydrodynamic)	
	Constant Potential	Bulk Electrolysis	Stirred Solution	
			Flow Electrolysis	
Controlled Current	Chronopotentiometry		Constant-Current	
			Linearly Increasing Current	
			Current Reversal	
			Cyclic	
	Coulometry		Coulometric Titrations	
	Electrolysis			
Controlled Charge	Charge Step	Coulostatic Methods		
Impedance Techniques	ac Voltammetry (ac Polarography)			
	Electrochemical Impedance Spectroscopy			

aims to serve as an introduction to a few of the types of literature (published in English) that may be relied upon to provide additional assistance to those researchers. There are a few key scientific journals that focus exclusively on electrochemistry, and those will be listed here along with their publishers. Also included are publications that, while not exclusively focusing on electrochemistry, often include significant articles on the science. Additionally, there is a well-established pool of review series and more specialized texts that give a far more in-depth consideration of specific electrochemical principles than is the goal of this book. The lists here are intended as a starting place, and as always should supplement, rather than replace, a search of current scientific literature.

1.9.1   Electrochemical journals

Analytical Chemistry (1947-), ACS Publications.
Bioelectrochemistry (1974-), Elsevier.
Electroanalysis (1989-), Wiley.
Electrochemical and Solid State Letters (1998-), The Electrochemical Society.
Electrochemistry Communications (1999-), Elsevier.
Electrochimica Acta (1959-), Elsevier.
Journal of the American Chemical Society (1879-), ACS Publications.
Journal of Applied Electrochemistry (1971-), Kluwer Academic Publishers.
Journal of Electroanalytical Chemistry and Interfacial Chemistry (1959–1992), Journal of Electroanalytical Chemistry (1992-), Elsevier.
Journal of the Electrochemical Society (1902-), The Electrochemical Society.
Journal of Physical Chemistry (1896–1996, after 1997 Journal of Physical Chemistry B), ACS Publications.
Journal of Solid State Electrochemistry (1997-), Springer-Verlag.
Langmuir (1985-), ACS Publications.
Solid State Ionics (1980-), Elsevier.

1.9.2   Specialized texts

1.9.2.1   General

W. J. Albery, *Electrode Kinetics*, Clarendon Press, Oxford, 1975.

A. J. Bard, L. R. Faulkner, Eds., *Electrochemical Methods: Fundamentals and Applications*, 2nd ed., John Wiley and Sons: New York, 2001.

J. O'M. Bockris, S. U. M. Khan, *Surface Electrochemistry: A Molecular Level Approach*, Plenum Press: New York, 1993.

J. O'M. Bockris, A. K. N. Reddy, *Modern Electrochemistry*, 2nd ed., Plenum Press: New York, 1998, 2 volumes

J. O'M. Bockris, S. U. M. Khan, *Quantum Electrochemistry*, Plenum Press: New York, 1979.

P. A. Christensen, A. Hamnett, *Techniques and Mechanisms in Electrochemistry*, Blackie Academic and Professional: New York, 1994.

B. E. Conway, *Theory and Principles of Electrode Processes*, Ronald Press: New York, 1965.

E. Gileadi, *Electrode Kinetics for Chemists, Chemical Engineers, and Materials Scientists*, VCH: New York, 1993.

H. H. Girault, *Analytical Electrochemistry,* EPFL-Press: Lausanne, Switzerland, 2004.

J. Goodisman, *Electrochemistry: Theoretical Foundations, Quantum and Statistical Mechanics, Thermodynamics, the Solid State*, Wiley: New York, 1987.

C. H. Hamann, A. Hamnett, W. Vielstich, *Electrochemistry*, Wiley-VCH: Weinheim, Germany, 1997.

G. Hodes, *Electrochemistry of Nanomaterials*, Wiley-VCH: Weinheim, Germany, 2001.

D. J. G. Ives, G. J. Janz, *Reference Electrodes: Theory and Practice*, Academic Press: New York, 1961.

K. Izutsu, *Electrochemistry in Nonaqueous Solutions*, Wiley-VCH: Weinheim, Germany, 2002.

J. Koryta, J. Dvorak, L. Kavan, *Principles of Electrochemistry*, 2nd ed., Wiley: New York, 1993.

H. Lund, O. Hammerich, *Organic Electrochemistry*, Marcel Dekker: New York, 2001.

D. A. MacInnes, *The Principles of Electrochemistry*, Dover: New York, 1961.

R. Memming, *Semiconductor Electrochemistry*, Wiley-VCH: Weinheim, Germany, 2001.

P. M. S. Monk, *Fundamentals of Electroanalytical Chemistry*, Wiley: New York, 2001.

J. S. Newman, *Electrochemical Systems*, 2nd ed., Prentice-Hall: Englewood Cliffs, NJ, 1991.

K. B. Oldham, J. C. Myland, *Fundamentals of Electrochemical Science*, Academic Press: San Diego, 1994.

A. J. L. Pombeiro, C. Amatore, Eds., *New Trends in Molecular Electrochemistry*, Marcel Dekker: New York, 2004.

P. H. Rieger, *Electrochemistry*, 2nd ed., Chapman and Hall: New York, 1994.

I. Rubinstein, Ed., *Physical Electrochemistry: Principles, Methods, and Applications*, Marcel Dekker: New York, 1995.

W. Schmickler, *Interfacial Electrochemistry*, Oxford University Press: New York, 1996.

J. Wang, *Analytical Electrochemistry*, 2nd ed., John Wiley and Sons: New York, 2000.

P. Zanello, *Inorganic Electrochemistry: Theory, Practice, and Applications*, Royal Society of Chemistry: Cambridge, England, 2003.

1.9.2.2 *Methodology*

R. N. Adams, *Electrochemistry at Solid Electrodes*, Marcel Dekker: New York, 1969.

A. J. Bard, *Electrogenerated Chemiluminescence*, Marcel Dekker: New York, 2004.

C. M. A. Brett, A. M. O. Brett, , *Electrochemistry: Principles, Methods, and Applications*, Oxford University Press: UK, 1993.

P. Delahay, *New Instrumental Methods in Electrochemistry*, Interscience: New York, 1954.

Z. Galus, *Fundamentals of Electrochemical Analysis*, 2nd ed., Wiley: New York, 1994.

E. Gileadi, E. Kirowa-Eisner, J. Penciner, *Interfacial Electrochemistry: An Experimental Approach*, Addison-Wesley: Reading, MA, 1975.

P. T. Kissinger, W. R. Heineman, Eds., *Laboratory Techniques in Electroanalytical Chemistry*, 2nd ed., Marcel Dekker: New York, 1996.

J. J. Lingane, *Electroanalytical Chemistry*, 2nd ed., Interscience: New York, 1958.

D. D. Macdonald, *Transient Techniques in Electrochemistry*, Plenum Press: New York, 1977.

C. K. Mann, K. K. Barnes, *Electrochemical Reactions in Nonaqueous Systems*, Marcel Dekker: New York, 1970.

D. T. Sawyer, A. Sobkowiak, J. L. Roberts, Jr., *Electrochemistry for Chemists*, 2nd ed., John Wiley and Sons: New York, 1995.

F. Scholz, Ed., *Electroanalytical Methods: Guide to Experiments and Applications*, Springer: New York, 2002.

F. Scholz, U. Schroeder, R. Gulaboski, *The Electrochemistry of Particles and Droplets Immobilized on Electrode Surfaces*, Springer: New York, 2004.

Southampton Electrochemistry Group, *Instrumental Methods in Electrochemistry*, Ellis Horwood: Chichester, UK, 1985.

P. Vanysek, Ed., *Modern Techniques in Electroanalysis*, Wiley: New York, 1996.

1.9.2.3   Data

A. J. Bard, R. Parsons, J. Jordan, Eds., *Standard Potentials in Aqueous Solution*, Marcel Dekker: New York, 1985.

B. E. Conway, *Electrochemical Data*, Elsevier: Amsterdam, 1952.

A. L. Horvath, *Handbook of Aqueous Electrolyte Solutions: Physical Properties, Estimation, and Correlation Methods*, Ellis Horwood: Chichester, UK, 1985.

G. J. Janz, R. P. T. Tomkins, *Nonaqueous Electrolytes Handbook*, Academic Press: New York, 1972, 2 volumes.

L. Meites, P. Zuman, *Electrochemical Data*, Wiley: New York, 1974.

L. Meites, P. Zuman, et al., *CRC Handbook Series in Organic Electrochemistry*, CRC Press: Boca Raton, FL, 1977–1983, 6 volumes.

L. Meites, P. Zuman, et al., *CRC Handbook Series in Inorganic Electrochemistry*, CRC Press: Boca Raton, FL, 1980–1988, 8 volumes.

R. Parsons, *Handbook of Electrochemical Data*, Butterworths: London, 1959.

J. F. Zemaitis, D. M. Clark, M. Rafal, N. C. Scrivner, *Handbook of Aqueous Electrolyte Thermodynamics: Theory and Applications*, Design Institute for Physical Property Data: New York, 1986.

1.9.3   Review series

A. J. Bard (from Vol. 19 with I. Rubinstein), Eds., *Electroanalytical Chemistry*, Marcel Dekker: New York, 1966–2004, 22 volumes.

A. J. Bard et al., Eds., *Encyclopedia of Electrochemistry*, Wiley-VCH: Germany, 2002–2007, 11 volumes.

A. J. Bard, H. Lund, Eds., *Encyclopedia of the Electrochemistry of the Elements*, Marcel Dekker: New York, 1973–1986, 16 volumes.

B. E. Conway et al., Eds., *Modern Aspects of Electrochemistry*, Plenum Press: New York, 1954–2004, 38 volumes

P. Delahay, C. W. Tobias (from Vol. 10, H. Gerischer, C. W. Tobias), Eds., *Advances in Electrochemistry and Electrochemical Engineering*, Wiley: New York, 1961–1984, 13 volumes.

H. Gerischer, C. W. Tobias, Eds., *Advances in Electrochemistry and Electrochemical Engineering*, Wiley-VCH: Weinheim, Germany, 1990–1997, 5 volumes.

Specialist Periodical Reports, *Electrochemistry*, G. J. Hills (Vols. 1–3), H. R. Thirsk (Vols. 4–7), and D. Pletcher (Vols. 8–10) Senior Reporters, The Chemical Society: London, 1968–1985, 10 volumes.

E. Steckhan, Ed., *Electrochemistry* (*Topics in Current Chemistry*), Springer: New York, 1987–1997, 6 volumes.

E. Yeager, J. O'M. Bockris, B. E. Conway et al., Eds., *Comprehensive Treatise of Electrochemistry*, Plenum Press: New York, 1984, 10 volumes.

E. Yeager, A. J. Salkind, Eds., *Techniques of Electrochemistry*, Wiley-Interscience: New York, 1972–1978, 3 volumes.

REFERENCES

1. D. E. Roller, R. Blum, *Physics: Electricity Magnetism and Light*, Holden-Day: San Francisco, 1982, Vol. 2.

2. A. D. McNaught, A. Wilkinson, IUPAC, *Compendium of Chemical Terminology: IUPAC Recommendations*, Blackwell Science: Oxford, England; Malden, MA, USA, 1997.

3. A. J. Bard, L. R. Faulkner, *Electrochemical Methods: Fundamentals and Applications*, Wiley: New York, 2001.

4. E. Gileadi, *Electrode Kinetics for Chemists, Chemical Engineers, and Materials Scientists*, VCH: New York, 1993.

5. United States Energy Information Administration, Office of Energy Markets, EIA-846, *1998 Manufacturing Energy Consumption Survey*, 1998.

6. P. T. Kissinger, W. R. Heineman, *Laboratory Techniques in Electroanalytical Chemistry*, Marcel Dekker: New York, 1984.

This page intentionally left blank

Part Two

LABORATORY PRACTICAL

This page intentionally left blank

– 2 –

Practical Electrochemical Cells

Shaowei Chen

Department of Chemistry and Biochemistry, University of California,
Santa Cruz, CA 95064, USA

2.1 MATERIALS

There are a variety of materials that can be used to make electrochemical cells. The most common ones include glass (Pyrex and quartz), Teflon, Kel-F, and Nylon. A practical consideration in selecting these materials is that the materials should be easily processable, inert to the electrochemical reactions, and cost-effective. For most electrochemical reactions, a Pyrex glass cell is used because it is easy to make and glass is generally a very low cost material. However, when the reaction involves media that are corrosive to glass (e.g., high pH, hydrofluoride, etc.), Teflon, Kel-F, Nylon or other plastic materials should be used instead. In the presence of some organic solvents, however, the plastic materials might decompose leading to contamination and hence interference in sensitive measurements. It should also be noted that in the presence of some strong acids, sometimes Nylon may not be stable and therefore glass should be the material of choice.

2.2 GENERAL CELL DESIGNS

The exact design of an electrochemical cell varies with the specific needs of an experiment. On the laboratory scale, typically if the amount of analytes is not a concern, a 25–50 mL cell (or even larger) can be used for the sake of convenience. With limited quantities of samples, a solution volume of a few mL is reasonable. Even smaller volumes of sample solutions (say, $<\mu L$) are also possible. However, in these cases, electrodes of ultrasmall dimensions (UMES, see Chapter 6) will have to be used and aligned properly. Complication in the current/potential measurements might occur as a result from solution resistance (see Chapters 1 and 3) and heterogeneity of the electrolyte solutions. These may render data analysis difficult and sometimes ambiguous.

In this chapter, we will describe several examples of electrochemical cell designs for a variety of systems and applications in a research laboratory. It should be noted that the

overview is not intended to be exhaustive. Rather, it provides some illustrating examples where one may adapt or modify the fundamental principles for their specific needs. The readers may refer to other reviews for more information (1).

2.2.1   Two-electrode cells

Two-electrode cells (see Chapter 1) consist of a working electrode and a reference electrode. Since the potential of the working electrode is monitored relative to the reference electrode, the potential of the reference electrode must be maintained at a constant value. In other words, the reference electrode must behave as an ideal nonpolarized electrode with current passing between working and reference electrodes. Classically, two-electrode cells have been used in polarographic studies with a dropping mercury electrode (DME) as the working electrode and a large mercury pool as the reference (Figure 2.1). These two electrodes are aligned concentrically. Since the area of the pool is substantially large compared to that of the DME electrode, the pool is considered unpolarized and hence a reasonably good reference for potential control (though of an unknown potential). Another issue that one has to bear in mind is the solution resistance (R_s) and consequently the iR_s drop. Typically in these polarograhic measurements, $i < 10$ μA and $R_s < 100$ Ω and hence $iR_s < 1$ mV, which is negligible. For more resistive systems such as nonaqueous media, one can use a very small electrode (for instance, an ultramicroelectrode, see Chapter 6) to keep a very low current profile, on the order of nA. With such a current scale, solution resistance within the range of kΩ to MΩ can still be acceptable.

Two-electrode cells have also been used in measurements of the solid-state electronic conductivity of nanoparticles and other materials. A typical cell is a concentric tubular structure with an inner dimension on the order of a few mm where a pair of disk-shaped electrodes can be plugged in and sandwich the electrolyte confined within a tubular interior (Figure 2.2). To maintain good contact between the electrode and the electrolyte, the two electrodes have to be pressed in where the interelectrode distance can be accurately
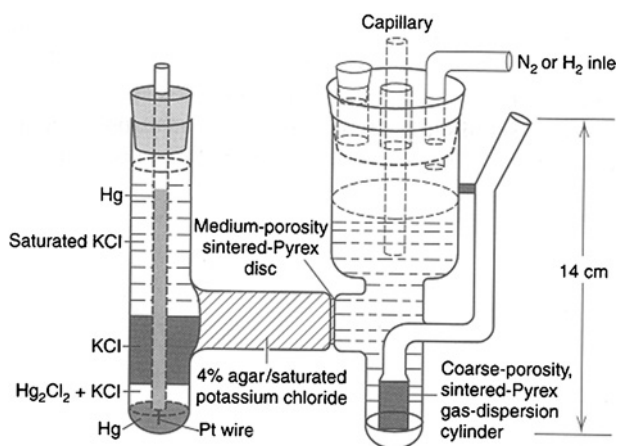
Figure 2.1   Two-electrode cell for polarography (2, 3).

Figure 2.2   Two-electrode cell for solid-state conductivity measurements. (for colour version: see colour section at the end of the book).

measured by a micrometer scale. Therefore, the cell materials should be able to sustain a relatively high mechanical pressure. Materials with good mechanical toughness such as Kel-F are generally a good choice; glass is generally too brittle, while Nylon and Telfon are too soft. To maintain the electrode positions during experimental measurements, some screw threads can be machined onto the electrodes and the interior of the electrochemical cell such that hand tightening may be good enough to achieve a satisfactory contact between the electrode and the electrolyte.

2.2.2   Three-electrode cells

Three-electrode cells (see Chapter 1) are the most commonly used setup in electrochemical studies, especially when the cell resistance is relatively high. In this configuration, the potential of the working electrode is still monitored relative to the reference potential; however, the current passes between the working electrode and a separate auxiliary (counter) electrode. Since no (or little) current passes to the reference electrode (see Chapter 4), it approaches ideal nonpolarizability and is hence a reliable reference for potential control. Experimentally, the tip of the reference electrode is placed as close as possible to the working electrode in order to minimize (uncompensated) solution resistance where control of the voltammetric current scale will also be critical, as mentioned above. The position of the reference tip should not interfere with the mass transfer of electrolyte species. Two typical configurations are shown in Figure 2.3. Generally the cell constitutes three compartments that can be separated by a glass frit with medium porosity (top panel). The glass frits are used to reduce the interference of electrochemical reactions at the counter electrode and yet allow electrical conductivity. Generally, the center compartment contains the supporting electrolyte and the redox molecules, whereas in the two side compartments only the supporting electrolyte is added. An additional opening can be added for degassing purposes (details below). In cases where no substance is produced at the counter electrode via electrolysis that can reach the working electrode, a frit separator is not necessary (bottom panel).

2.3   ELECTROCHEMICAL CELLS FOR SPECIFIC APPLICATONS

2.3.1   Flow-through cells

Flow-through cells involve a continuous feeding of sample solution and hence can be used for real-time detection and monitoring. The exact configuration varies with the specific needs of an experiment. Figure 2.4 shows some typical cell arrangements (e.g., thin-layer cell (TLC) and wall-jet cell) and electrode geometries including tubular electrodes, planar
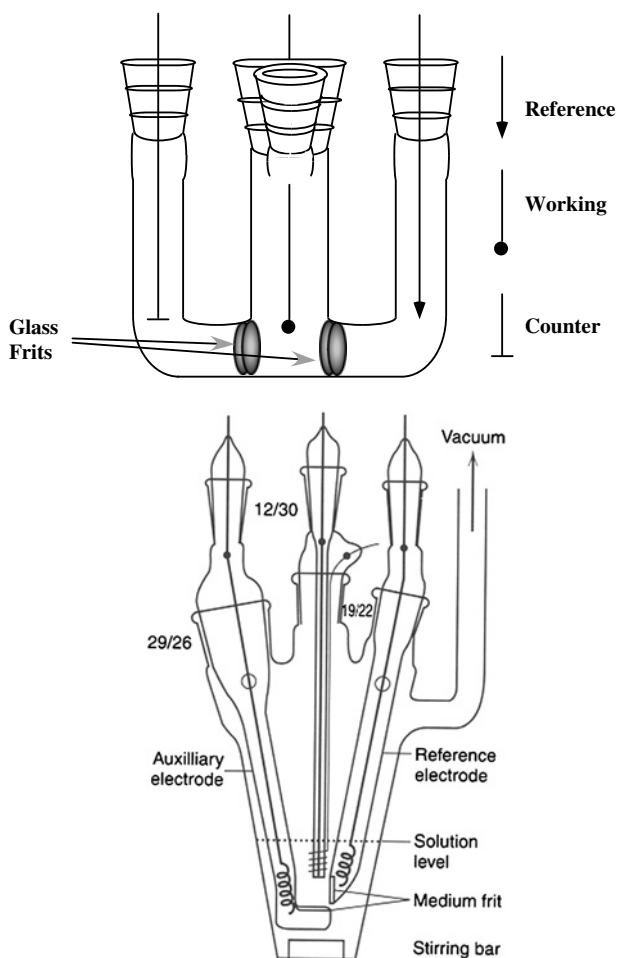
Figure 2.3   Three-electrode electrochemical cells. Three-compartment cell with (top panel) and without (bottom panel) glass frits (3, 4). (for colour version: see colour section at the end of the book).

electrodes with parallel flow, planar electrodes with perpendicular flow, and wall-jet electrodes. Flow cells can be in two- or three-electrode configurations.

Figure 2.5 shows a two-electrode flow cell with reticulated vitreous carbon (RVC) as the working electrode. There are a wide variety of electrode materials for flow cell applications ranging from microconical platinum, to platinum grid, to gold micromesh, to graphite packing, etc. In this configuration, the sample solution is fed through the cell under a constant flow and a steady-state current is measured. It should be noted that here the reference electrode is isolated from the sample solution by a cation-exchange membrane and the internal filling solution is also replaced continually. The immediate advantage of such a design is drastic simplification of instrumentation and accurate and precise measurements of low concentrations of analytes.
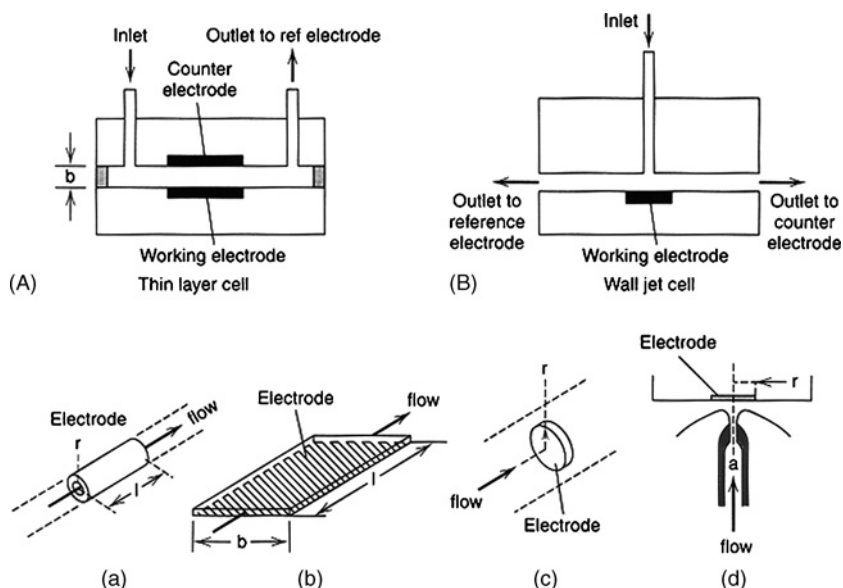
Figure 2.4   Typical cell arrangements and electrode geometries for electrochemical flow cells. Top: (A) thin-layer cell, (B) wall-jet cell. Bottom: Various electrode geometries: (a) tubular electrode, (b) planar electrode with parallel flow, (c) planar electrode with perpendicular flow, (d) wall-jet electrode (5, 6).
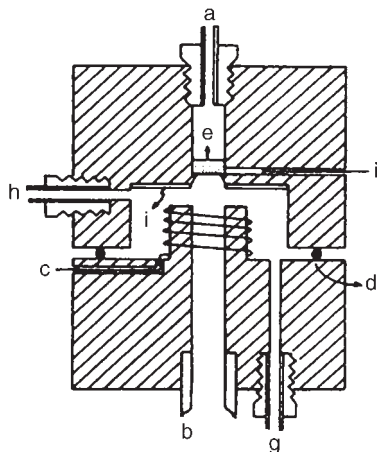
Figure 2.5   Flow-through cell with RVC electrode and reference electrode. a, sample solution inlet; b, sample solution outlet (Tygon); c, lead to reference electrode; d, O-ring; e, RVC electrode, one disk shown; f, cation exchange membranes; g, reference solution inlet; h, reference solution outlet; i, lead to working electrode (7).

In a three-electrode configuration, the flow direction is typically parallel to the working electrode surface; the working electrode is placed opposite to the auxiliary electrode in the walls of the thin flow channel. Thus, the current density across the electrode is not significantly influenced by iR drop due to the low impedance between the electrodes. The performance can be further enhanced by using parallel or series working electrodes, as shown in Figure 2.6. Such flow cells can be used as detector cells in liquid chromatography (Figure 2.7), where there can be at least two configurations: (a) the auxiliary and reference electrodes can be placed downstream from the working electrode; (b) the working and auxiliary electrodes are facing each other across the flow channel and the reference electrode is placed downstream.

In other systems, the flow is perpendicular to and centered on the electrode surface. The main advantage is to reduce the dead volume and enhance the mass transfer to the working electrode surface. An example is shown in Figure 2.8 and such a configuration has been used as a detector in microbore chromatography. For bulk electrolysis, perpendicular flow cells have also been used with a working electrode of large surface area (Figure 2.9).

Flow cells can also be equipped with dual working electrodes that serve as the generator and collector electrodes. The working principle is similar to that of a rotating ring-disk
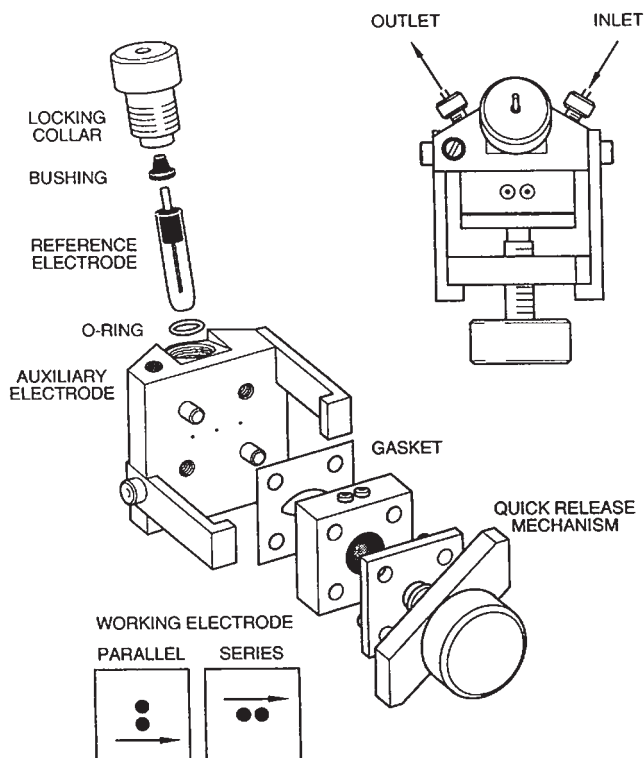
Figure 2.6   Cross-flow cell design with parallel or series working electrodes (8).
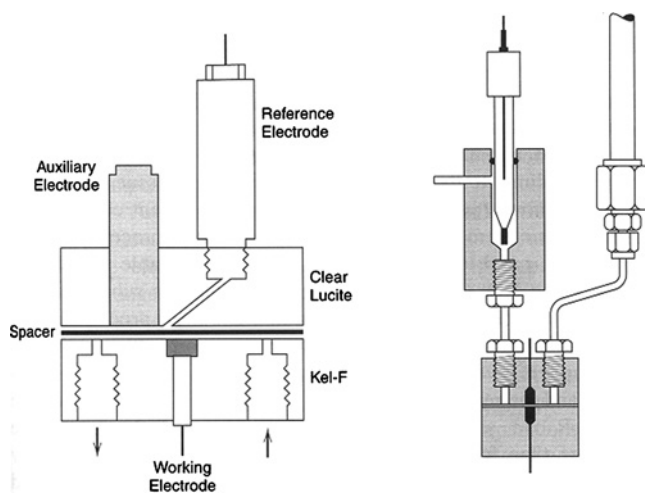
Figure 2.7   Thin-layer LC detector cells. *Left*: Cell with auxiliary and reference electrodes in thin-layer portion downstream from working electrode (9). *Right*: Cell with working and auxiliary electrodes facing each other and reference electrode downstream in flow channel (10, 11).
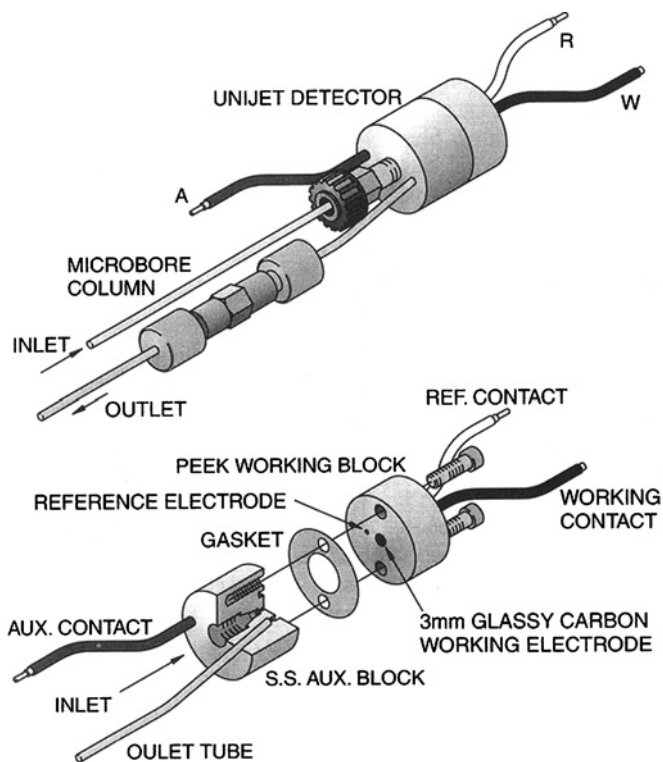
Figure 2.8   Radial flow thin-layer electrochemical cell for microbore chromatography (8).
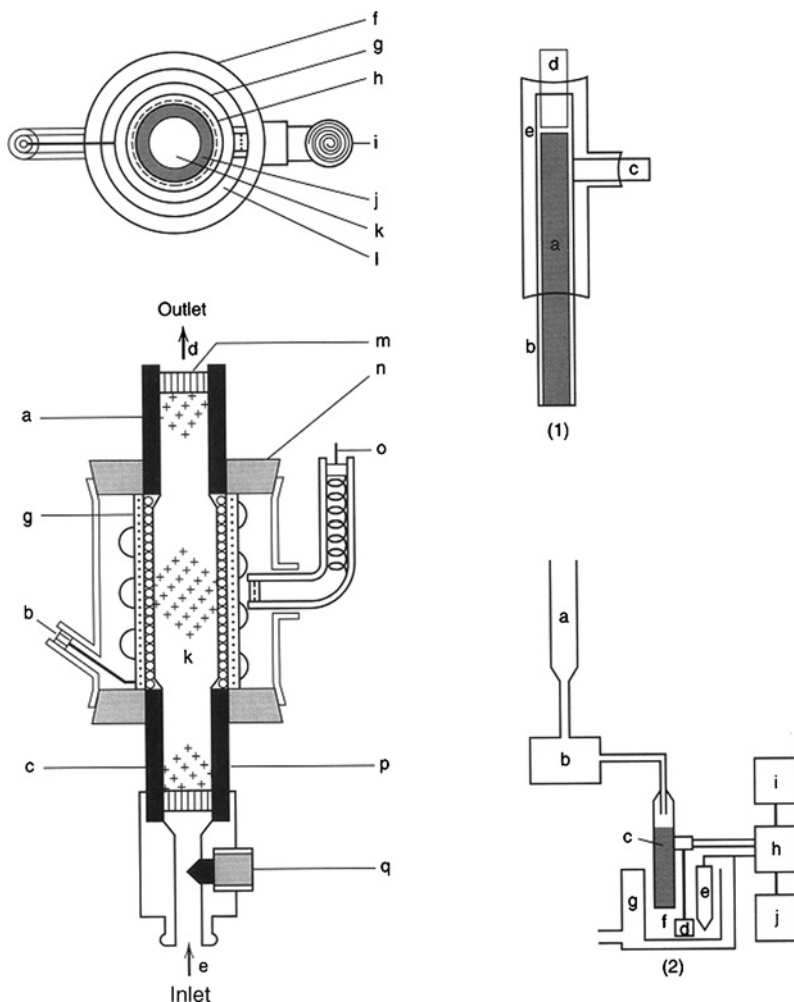
Figure 2.9   Flow electrolytic cells. *Left*: cell utilizing glassy carbon granule working elect-rode (k), silver auxiliary electrode (g), Ag/AgCl reference electrode (o, i) with porous glass separator (h). Other components are (a, c) lead for working electrode; (b) lead to auxiliary electrode; (d) solution outlet; (e) solution inlet; (f) glass or plastic tube; (j, p) porous carbon tube; (l) saturared KCl solution; (m) silicon rubber (12). *Right*: cells with reticulated vitreous carbon (RVC). (l): (a) RVC cylinder, (b) heat shrink tube, (c) graphite rid sidearm, (d) glass tube, (e) glass and epoxy support. (2) Schematic diagram of complete apparatus. (a) Solution reservoir, (b) pump, (c) RVC electrode, (d) platinum electrode, (e) saturated calomel electrode (SCE) reference electrode, (f) downstream reservoir, (g) run-over collector, (h) potentiostat, (i) recorder, and (j) digital voltmeter (13, 14).
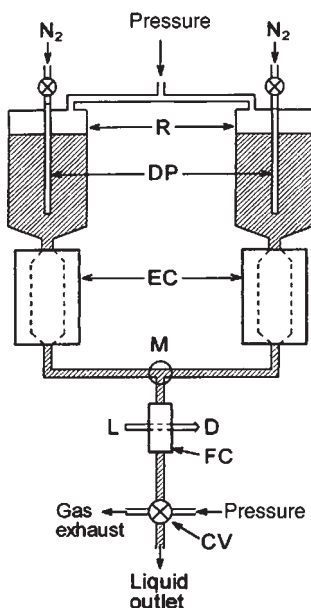
Figure 2.10   (a) Schematic representation of a dual-electrode flow cell. (b) Actual complete dual electrode flow assembly. Solution flows by gravity from upper reservoir. For greater clarity, the "O-ring joint" portion of the cell with the dual working electrodes is shown in exploded form. A close-up view of this portion with the porous silver electrodes is shown in (c) (15, 16).

electrode. A setup is shown in Figure 2.10 where the two electrodes are large beds of glassy carbon particles.

It is anticipated that, in comparison with the two-electrode counterpart, the three-electrode design will provide better control of electrode potential and voltammetric detection in reaction media of high resistance and high currents.

2.3.2   Thin-layer cells (TLCs)

Thin-layer cells (TLCs) typically involve a micrometer-thick (2–100 μm) layer of electrolyte solution that is confined at the electrode surface (the above-mentioned thin-layer flow cell is one example). This confinement can be created by two working electrodes that face each other (twin-electrode mode) or a working electrode facing a flat barrier (single-electrode mode), as shown in Figure 2.11. Since the cell thickness is generally smaller than the diffusion layer thickness, mass transfer within the layer can be ignored. Therefore, the reaction is akin to bulk electrolysis, but within a confined interfacial environment. The thickness of the solution layer can be accurately adjusted and measured by a micrometer scale. For the twin-electrode (generator–collector) configuration, ideally, the two working
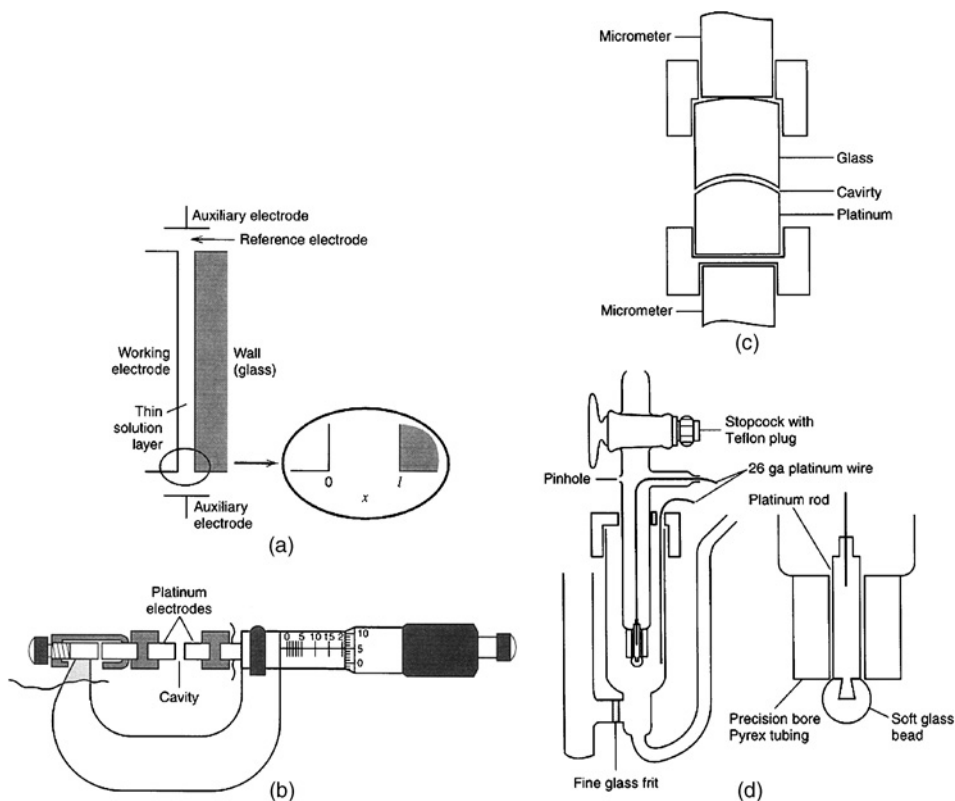
Figure 2.11   (a) Schematic diagram of a single-electrode thin-layer cell. (b) Micrometer, twin-electrode thin-layer cell with adjustable solution layer thickness. (c) Close-up of electrode portion for single-electrode configuration of (b). (d) Capillary-wire single electrode thin-layer electrode (17, 18).

electrodes are of the same geometric area and positioned concentrically facing each other. The bottom electrode is embedded in the cell housing with the electrode surface at the same level as the compartment bottom. The entire housing can be attached to the stationary end of a micrometer scale (by a set screw, for instance). The top electrode is attached to the moving piston of the micrometer scale. A lid can be put on the cell chamber for enclosure purpose. In the center there is an opening for the top working electrode and two small holes are drilled for electrical contacts for the reference and counter electrodes (an additional one can be made for deaerating purpose). It is important that the electrode surfaces are flat and ideally should parallel to each other. In addition, the thin-layer area is generally kept much larger than that of the working electrodes to minimize mass transfer effect from the edge. Since the counter electrode is generally placed outside the thin-layer portion, a rather significant resistive drop may occur between the working electrode and the counter electrode which may complicate the distributions of electrode potential and current density.

The cell can be made of Teflon, Kel-F, or Nylon with electrical contacts to the electrodes achieved by set screws. This type of setup generally works very well for aqueous electrochemical systems. For volatile organic media, leaking and evaporation of solvents will be an issue. One possible solution is to put the entire cell setup inside a housing container that is saturated with the respective solvent.

2.3.3   Spectroelectrochemical cells

Spectroscopic measurements can be carried out concurrently with electrochemical control (see Chapter 14), with each technique providing complementary information about the chemical systems of interest. These studies mainly involve two modes, transmission and reflection, and the measurements can be *in situ* or *ex situ*. In transmission experiments, the typical setup involves a light beam passing through the working electrode. One can then, for example, measure the optical absorbance as a function of electrochemical potentials. Figure 2.12 shows one of these cells used in UV–vis measurements. One can also use a quartz cuvette as the electrochemical cell inside which the three electrodes are placed. Here the (quasi)reference and counter electrodes are placed at the corners of the cuvette while the working electrode is typically made of materials of optical transparency so that it will not interfere with the optical pathway. There are a variety of electrodes that are optically transparent, including indium-tin oxide (ITO), gold or platinum minigrids, and ultrathin gold films (e.g., <50 nm) deposited onto a glass substrate. Figure 2.13 shows
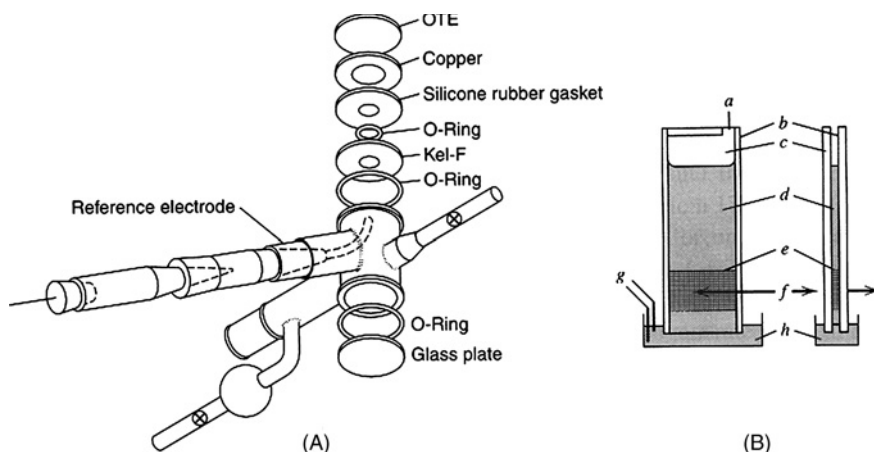
Figure 2.12   (A) Cell for transmission spectroelectrochemistry involving semi-infinite linear diffusion. Light beam passes along vertical axis (19). (B) Optically transparent thin-layer system: front and side views. (a) Point of suction application in changing solutions; (b) Teflon tape spacers; (c) 1×3 in. microscope slides; (d) test solution; (e) gold minigrid, 1 cm height; (f) optical beam axis; (g) reference and auxiliary electrodes; and (h) cup containing test solution (20, 21).
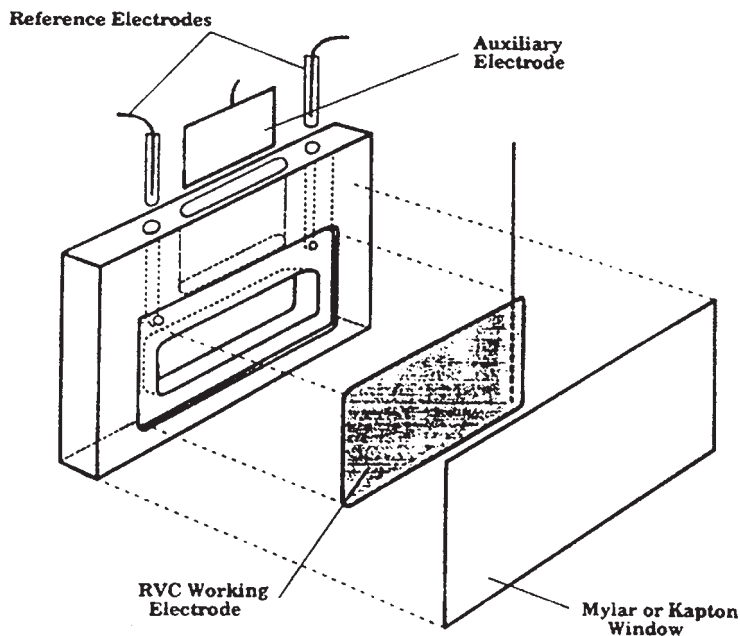
Figure 2.13 Assembly of sandwich-type optically transparent electrochemical cell for EXAFS spectroelectrochemistry (22).

a sandwich-type electrochemical cell for extended X-ray absorbance fine structure (EXAFS) spectroelectrochemistry where the cell body is of MACOR and the working electrode is RVC.

One may recognize that there exists a concentration gradient of the reaction product at the electrode surface. This might complicate the quantitative spectroscopic evaluation. In combination with the flow cells described above, one can design a spectroelectrochemical flow cell for continuous monitoring of the sample solutions, where the concentration of the electrogenerated species can be maintained uniform in the solution. The feeding of the solution is through a thin channel between a working electrode and a counter electrode and is controlled by an outside pump. Figure 2.14 depicts a representative stop-flow spectro-electrochemical setup.

In the reflection mode, typically specular reflectance is measured on the electrode surface. It is anticipated that the variation of the surface structure (e.g., surface adsorption, phase transitions, etc.) will result in appreciable changes in the reflectivity properties. One can thus correlate the structural characteristics gleaned from spectroscopic measurements with electrochemical results. Figure 2.15 shows a cell assembly for internal reflection spectroelectrochemistry. Several spectroscopic techniques have been used, such as infrared, surface plasmon resonance, and X-ray based techniques (reflectivity, standing wave, etc.). Figure 2.16 depicts a cell setup for (A) infrared spectroelectrochemistry (IR-SEC) and (B) surface X-ray diffraction.
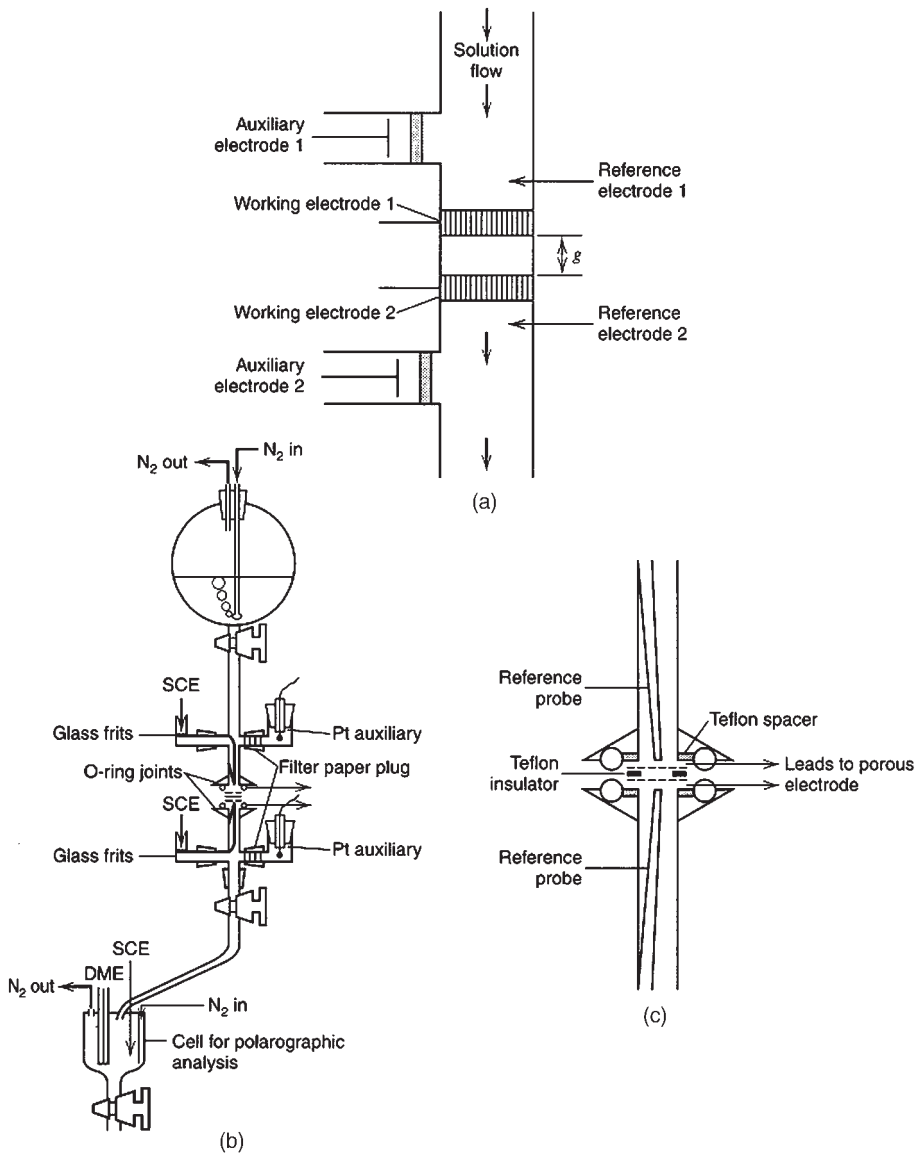
Figure 2.14   A stopped-flow optical absorption cell equipped with two column-type cells for rapid electrolysis. R, solution reservoir; DP, N_2 gas bubbling; EC, electrochemical cell for flow electrolysis; M, mixer; FC, flow-type optical absorption cell; L, light beam; D, photodetector, CV, control valve (23, 24).
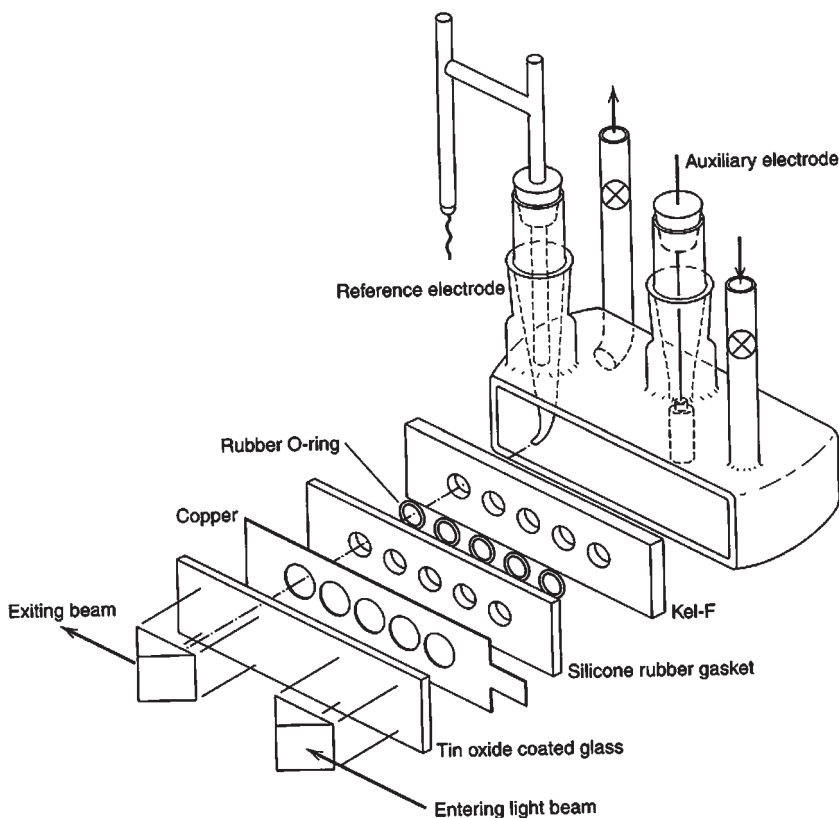
Figure 2.15   Cell assembly for internal reflection spectroelectrochemistry (25, 26).

In these studies, generally a very thin layer of solution is used to cover the electrode surface in order to minimize the reflective effect of the solvent and to make electrical contacts. On top of this solution layer, a Mylar film is used to enclose the solution to prevent solvent vaporization. The general principle of cell design is quite similar to that of TLCs described above except that the top cover of the cells must be spectroscopically transparent (for instance, replaced by a Mylar film here).

Electrochemical measurements can also be coupled with mass spectrometry. Figure 2.17 shows a schematic diagram of the apparatus for differential electrochemical mass spectrometry (DEMS). Here the chamber connected directly to the electrochemical cell and the mass spectrometer (MS) is pumped differentially by turbo pumps PA and PB. Electrolysis products are passed into the ionization chamber (i), analyzed in the quadrupole mass filter (ii), and detected with either a Faraday cup (iii) or electron multiplier (iv). Such DEMS measurements can be used *in situ* to identify electrolysis products. This may lead to an understanding of the electron-transfer reaction mechanism and optimization of the reaction process.
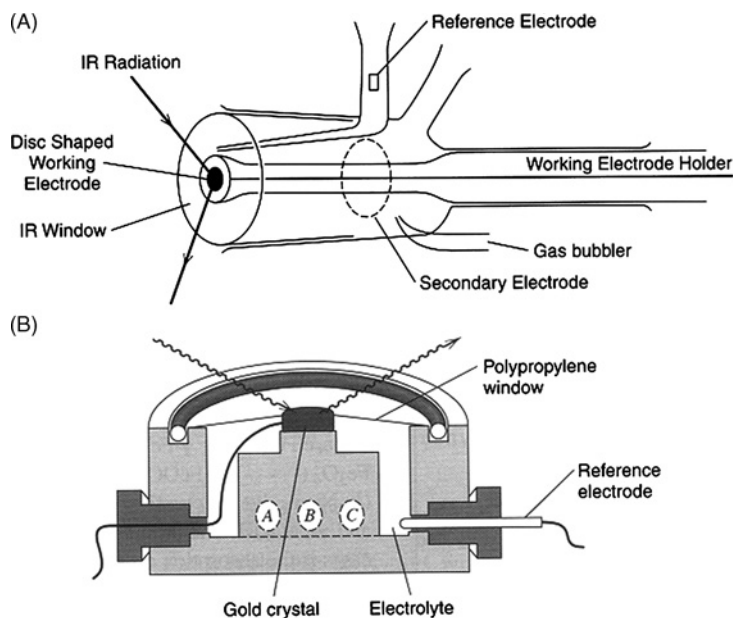
Figure 2.16   Spectroelectrochemical cells for (A) IR-SEC (27) and (B) X-ray diffraction experiments. In (B) a single-crystal gold electrode is used with a thin layer of solution held between the polypropylene window and the electrode. The window is held in place by an O-ring that clamps it to the Kel-F cell body. A and C are electrolyte ports and B is the counter electrode (28).

Electron paramagnetic resonance (EPR) spectroscopy has also been coupled with electrochemical measurements where radical species are involved in the electrochemical reactions. Figure 2.18 shows a cell for simultaneous electrochemical-EPR studies. The EPR measurements can be *ex situ* where the radicals are formed outside of the spectrometer (Figure 2.19). In addition, in combination with the flow cell design described above, one can also use electrochemical-EPR technique to monitor the generation of free radicals in a continuous stream of solutions (Figure 2.20).

2.3.4   Electrochemical cells for molten salts

Molten salts (or ionic liquids) represent a unique class of electrochemical systems. These materials may be corrosive, moisture- or oxygen-sensitive, and/or with a high melting temperature. All these factors must be taken into account in the design of electrochemical cells for molten salt research. Figure 2.21 depicts two gas-tight Pyrex glass electrochemical cells for use with moderate-melting molten salts. Figure 2.22 demonstrates a setup for high-melting molten salts. Typically, in these cell setups, additional provision must be made for temperature measurements and control (through a thermocouple or thermistor). More comprehensive reviews regarding cell designs for molten salts can be found in the literature (37, 38).
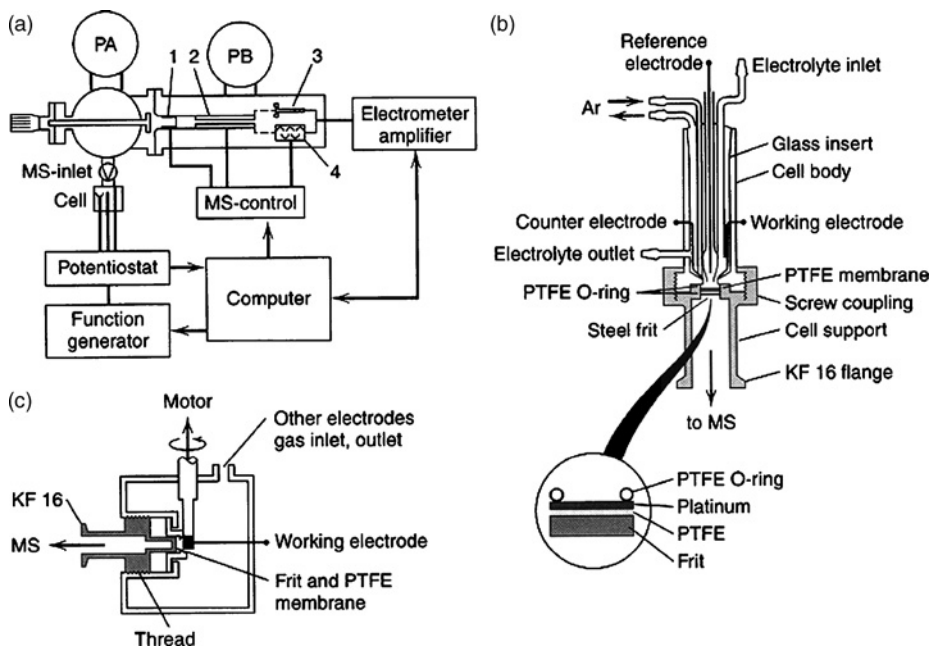
Figure 2.17   *Top left*: (a) schematic diagram of apparatus for DEMS. *Right*: (b) electrochemical cell for on-line mass spectrometry with a porous electrode. Electrode show is Pt with Teflon (PTFE)-treated glass frit (29). *Bottom left*: (c) electrochemical cell with a rotating cylinder electrode and sampling with separate inlet to MS (30, 31).
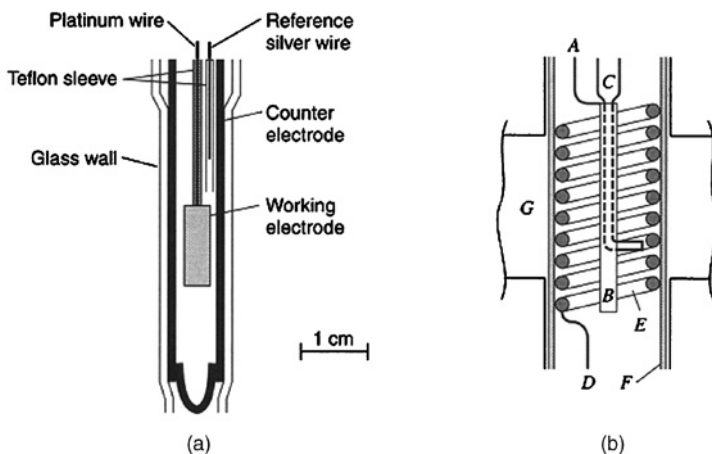
Figure 2.18   Cells for simultaneous electrochemical-EPR experiments. (a) Flat cell with platinum working and tungsten auxiliary electrodes for use in a rectangular cavity (32). (b) Cell with a helical gold working electrode (E) that forms the center conductor of a coaxial cylindrical microwave cavity (G). A, auxiliary electrode lead; B, central platinum auxiliary electrode; C, Luggin capillary for reference electrode; D, working electrode lead; F, quartz tube (33).
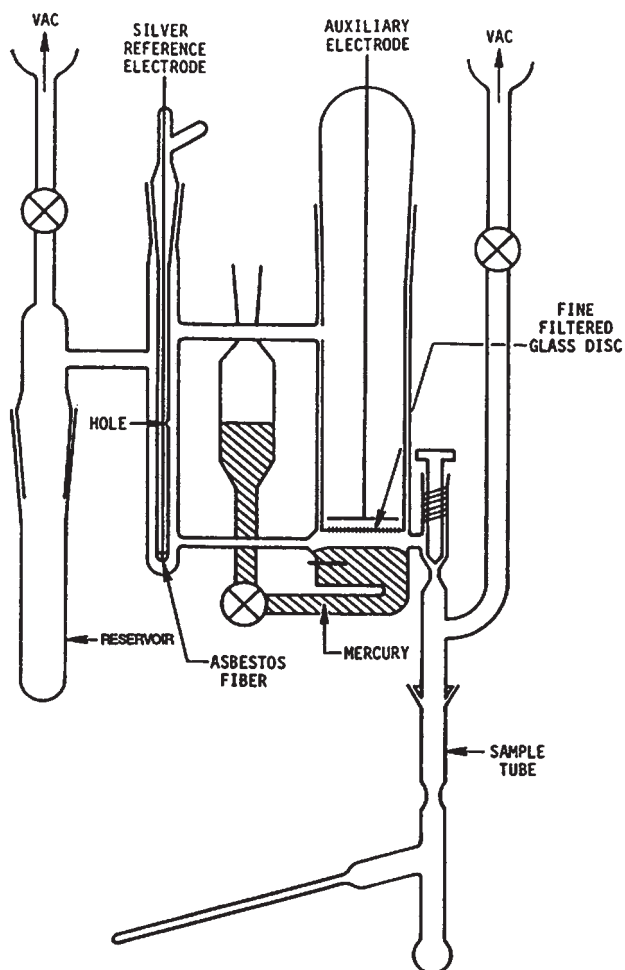
Figure 2.19   Cell used for generation of radicals outside the spectrometer for EPR detection (34).

2.3.5   Attachment to a vacuum line

For electrochemical systems that are sensitive to air and/or moisture, the cells are typically attached to a vacuum line. Here the solution is bubbled with a dry inert gas of ultrahigh purity (e.g., Ar, N_2, etc.) to remove dissolved oxygen. The cell is then attached to a vacuum line or introduced into a glove box to prevent back-contamination. Figure 2.23A shows a simple vacuum cell that consists of two glass units with a three-electrode configuration, which have been used extensively in preliminary work and for elevated-temperature studies with molten scintillator dyes as solvents (39). Figure 2.23B depicts a similar vacuum cell but with several additional features including an attached sidearm chamber for
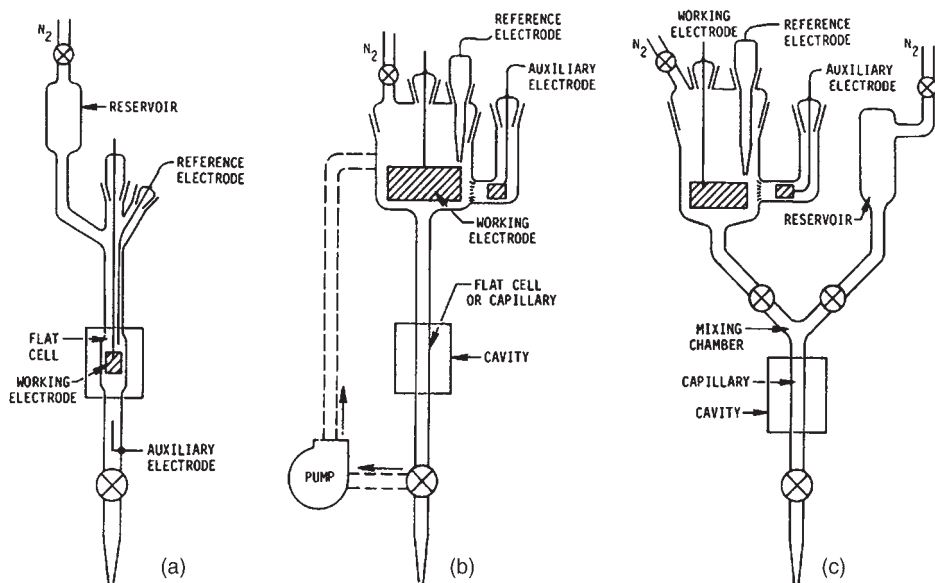
Figure 2.20   EPR-electrochemical cells for flowing electrolysis: (a) gravity-flow system with internal generation; (b) recirculating electrolyte with external generation; (c) flow-mixing cell to study kinetics of reactions with electrochemically generated radicals (35).

freeze-pump-thaw cycles, a microelectrode as the working electrode and a macroeletrode for bulk electrolysis (4, 42). For extremely air-sensitive compounds, one can add an internal Al_2O_3 drying column into the vacuum electrochemical cell.

For quantitative electrochemical studies, one would like to be able to adjust the solution concentration. This can be achieved by using a cell shown in Figure 2.24 where one can control the addition of a certain amount of solution by attaching to the electrochemical cell a buret or a graduated ampule, for example.

Vacuum cells have also found use in spectroelectrochemical studies. Here, optically transparent electrodes may have to be used. Figure 2.25 shows a schematic setup of a vacuum spectroelectrochemcial cell that can be used in UV–vis spectral measurements, for example. Attachments to a main vacuum line and a solution ampule can also be accommodated.

2.4   ESTABLISHING AND MAINTAINING AN INERT ATMOSPHERE

In many electrochemical studies, an inert atmosphere is needed to prevent the interference of the oxygen reaction at the electrode surface. Typically ultra-high-purity (UHP) nitrogen or argon is used. Nitrogen is less expensive, whereas the density of argon is greater than that of air and hence provides a better protection layer over the electrochemical solution. The inert gas must be saturated with the pure solvent used in preparing the reaction solution

Sealed under vacuum

Side arms for solute addition

Tungsten wire sealed in glass

Al(III)/Al Reference electrode

Working electrode spot welded to tungsten wire

(Side view)

a. Al reference electrode

b. Pt—foil auxiliary electrode

c. Pt—wire working electrode

d. Pt—foil quasi—reference electrode

e. W—wire or GC rod working electrode

(Top view)

(A)

M

Gas Inlet

Kovar Seal

Hg

5 cm

Hole for Pressure Equilibra- -tion

Divider

Gas Outlet or Vacuum

Matched Flange

Pt Liner

Pt Foil

Glass

Brass

Cork

Teflon

O-Ring

Disk Electrode

Thermistor

Thermostating Jacket

(B)

Figure 2.21 Gas-tight Pyrex glass electrochemical cell for use with (A) moderate-melting molten salts (35) and (B) gas-tight cell with a magnetically coupled drive for rotating-disk electrode voltammetry in moderate-melting salts (36).
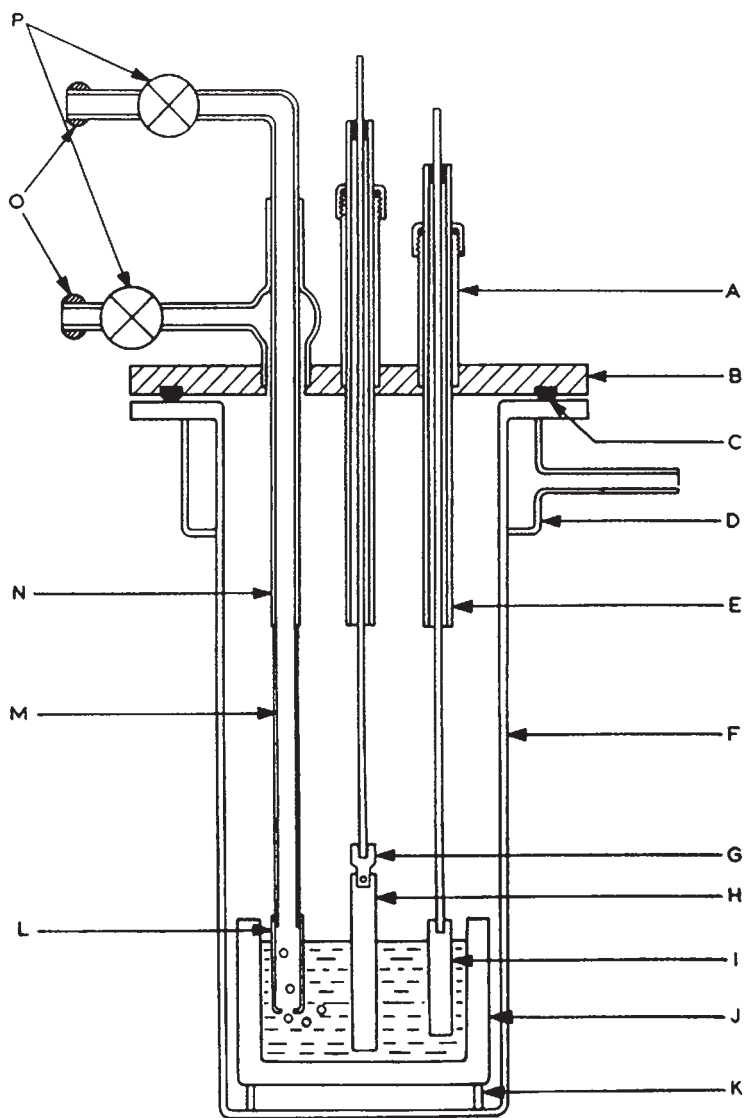
Figure 2.22   Cell used for high-melting alkali metal fluorides: (A) tube with screw cap, (B) brass head, (C) Viton O-ring, (D) cooling jacket, (E) Pyrex glass support tube, (F) cell body made from nickel or Inconel, (G) stainless-steel conductor block, (H) graphite or tungsten cathode, (I) graphite anode, (M) stainless steel tube, (N) Pyrex glass gas inlet tube, (O) ball joint, (P) vacuum valves (37).

such that the loss of solvent during degassing can be minimized. This is particularly impor-
tant when dealing with volatile organic media. In practice, the solution is bubbled with the
inert gas for at least 20 min by inserting the tubing into the solution. Then the tubing is
withdrawn from the solution with a separation of a few mm above the solution surface. In
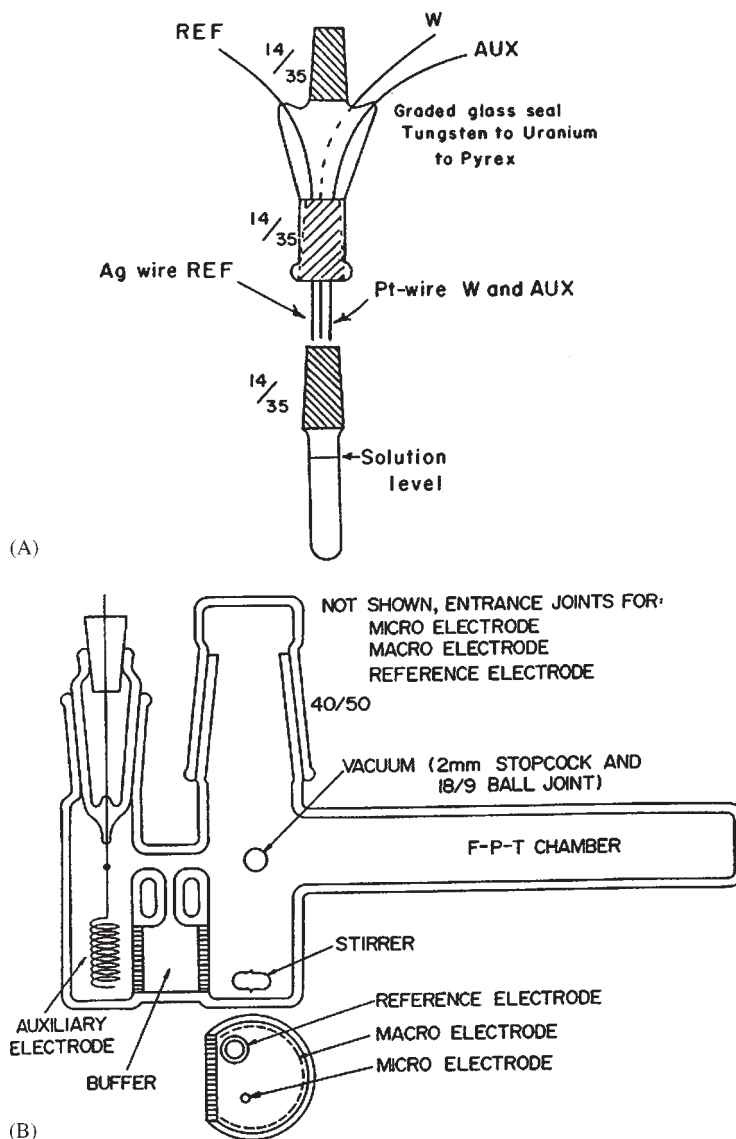
Figure 2.23   (A) Simple vacuum electrochemical cell that is suitable for direct freeze-pump-thaw of the solution. It is very useful for rapid exploratory experiments under vacuum (40). (B) Vacuum electrochemical cell with freeze-pump-thaw chamber (41).

so doing, an inert atmosphere is maintained within the reaction compartment. One can increase the efficiency of protection by reducing the exposure of the reaction compartment to the outside atmosphere, for instance, by sealing the opening with parafilm or Teflon tapes (but make sure to have a small leak so that pressure will not be built up inside the
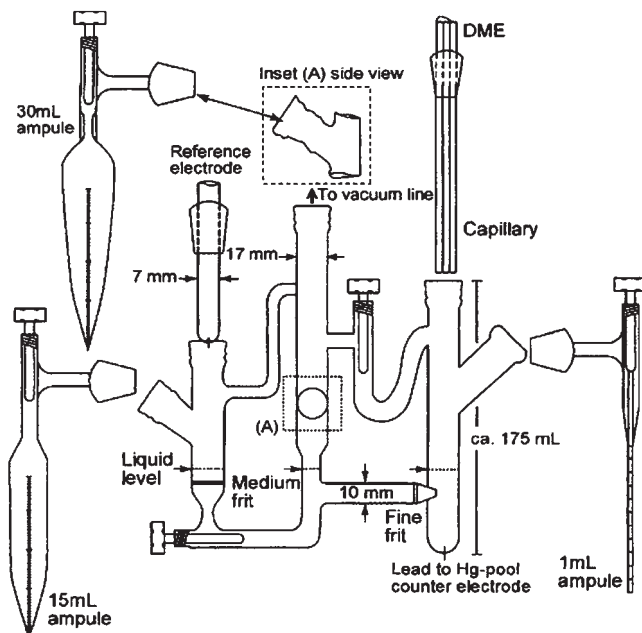
Figure 2.24 Vacuum electrochemical cell and assorted glassware that allows for concentration-dependent electrochemical studies using a dropping mercury electrode (43).
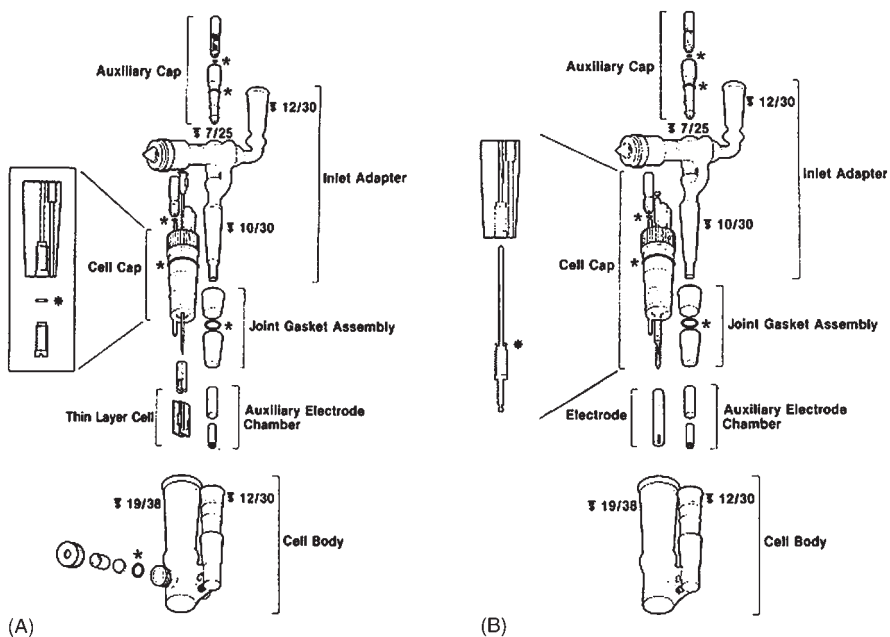
Figure 2.25 Vacuum electrochemical cells (A) vacuum spectroelectrochemical cell that contains an optically transparent thin-layer electrode (OTTLE) and (B) electrochemical cell assembly (44).

reaction chamber). Another concern is the choice of tubing used in the setup. For aqueous solutions, generally most synthetic tubings (Nylon, Teflon, etc.) are acceptable. For organic solutions, care must be taken to make sure that the tubing is inert in the solvent to prevent the interference in electrode reactions. This is particularly important in *in situ* spectroscopic studies such as fluorescence or infrared measurements. Therefore, it is always helpful if one can do a control experiment prior to any new setup.

REFERENCES

1. F. M. Hawkridge, in *Laboratory Techniques in Electroanalytical Chemistry*, 2nd ed., P. T. Kissinger, W. R. Heineman, Eds., Marcel Dekker: New York, 1996.
2. L. Meites, *Polarographic Techniques*, 2nd ed., Wiley-Interscience: New York, 1965.
3. A. J. Bard, L. R. Faulkner, *Electrochemical Methods*, 2nd ed., John Wiley & Sons: New York, 2001, p. 26.
4. A. Demortier, A. J. Bard, *J. Am. Chem. Soc.* **95**, 3495 (1973).
5. H. Gunasingham, B. Fleet, *Electroanal. Chem.* **16**, 89 (1989).
6. A. J. Bard, L. R. Faulkner, *Electrochemical Methods*, 2nd ed., John Wiley & Sons: New York, 2001, p. 448.
7. W. J. Blaedel, J. Wang, *Anal. Chem.* **51**, 799 (1979).
8. S. M. Lunte, C. E. Lunte, P. T. Kissinger, in *Laboratory Techniques in Electroanalytical Chemistry*, 2nd ed., P. T. Kissinger, W. R. Heineman, Eds., Marcel Dekker: New York, 1996.
9. J. A. Wise, W. R. Heineman, P. T. Kissinger, *Anal. Chim. Acta* **172**, 1 (1985).
10. Bioanalytical Systems, Inc.
11. A. J. Bard, L. R. Faulkner, *Electrochemical Methods*, 2nd ed., John Wiley & Sons: New York, 2001, p. 449.
12. T. Fujinaga, S. Kihara, *CRC Crit. Rev. Anal. Chem.* **6**, 223 (1977).
13. A. N. Strohl, D. J. Curran, *Anal. Chem.* **51**, 353 (1979).
14. A. J. Bard, L. R. Faulkner, *Electrochemical Methods*, 2nd ed., John Wiley & Sons: New York, 2001, p. 442.
15. J. V. Kenkel, A. J. Bard, *J. Electroanal. Chem.* **54**, 47 (1974).
16. A. J. Bard, L. R. Faulkner, *Electrochemical Methods*, 2nd ed., John Wiley & Sons: New York, 2001, p. 447.
17. A. T. Hubbard, F. C. Anson, *Electroanal. Chem.* **4**, 129 (1970).
18. A. J. Bard, L. R. Faulkner, *Electrochemical Methods*, 2nd ed., John Wiley & Sons: New York, 2001, p. 453.
19. N. Winograd, T. Kuwana, *Electroanal. Chem.* **7**, 1 (1974).
20. W. R. Heinman, B. J. Norris, J. F. Goelz, *Anal. Chem.* **47**, 79 (1975).
21. A. J. Bard, L. R. Faulkner, *Electrochemical Methods*, 2nd ed., John Wiley & Sons: New York, 2001, p. 681.
22. L. R. Sharp, W. R. Heineman, R. C. Elder, *Chem. Rev.* **19**, 705 (1990).
23. M. Oyama, K. Nozaki, T. Nagaoka, S. Okazaki, *Bull. Chem. Soc. Jpn.* **63**, 33 (1990).
24. M. Oyama, K. Nozaki, S. Okazaki, *Anal. Chem.* **63**, 1387 (1991).
25. N. Winograd, T. Kuwana, *J. Electroanal. Chem.* **23**, 333 (1969).
26. A. J. Bard, L. R. Faulkner, *Electrochemical Methods*, 2nd ed., John Wiley & Sons: New York, 2001, p. 694.
27. A. Bewick, K. Kunimatsu, B. S. Pons, J. W. Russel, *J. Electroanal. Chem.* **160**, 47 (1984).
28. J. McBreen, in *Physical Electrochemistry*, I. Rubinstein, Ed., Marcel Dekker: New York, 1995, Chap. 8.

29. B. Bittins-Cattaneo, E. Cattaneo, P. Konigshoven, W. Vielstich, *Electroanal. Chem*. **17**, 181 (1991).
30. S. Wasmus, E. Cattaneo, W. Vielstich, *Electrochim. Acta* **35**, 771 (1990).
31. A. J. Bard, L. R. Faulkner, *Electrochemical Methods*, 2nd ed., John Wiley & Sons: New York, 2001, p. 721.
32. I. B. Goldberg, A. J. Bard, *J. Phys. Chem*. **75**, 3281 (1971).
33. R. D. Allendoerfer, G. A. Martinchek, S. Bruckenstein, *Anal. Chem*. **47**, 890 (1975).
34. I. B. Goldberg, T. M. McKinney, in *Laboratory Techniques in Electroanalytical Chemistry*, 2nd ed., P. T. Kissinger, W. R. Heineman, Eds., Marcel Dekker: New York, 1996.
35. C. L. Hussey, in *Laboratory Techniques in Electroanalytical Chemistry*, 2nd ed., P. T. Kissinger, W. R. Heineman, Eds., Marcel Dekker: New York, 1996.
36. P. G. Zambonin, *Anal. Chem*. **41**, 868 (1969).
37. S. H. White, in *Molten Salt Techniques*, D. G. Lovering, R. J. Gale, Eds., Plenum: New York, 1983, Vol. 1, Chap. 2.
38. F. Lantelme, D. Inman, D. G. Lovering, in *Molten Salt Techniques*, R. J. Gale, D. G. Lovering, Eds., Plenum: New York, 1984, Vol. 2, Chap. 5.
39. C. P. Keszthelyi, A. J. Bard, *J. Electrochem. Soc*. **95**, 2395 (1973).
40. N. E. Tokel, C. P. Keszthelyi, A. J. Bard, *J. Am. Chem. Soc.* **94**, 4872 (1972).
41. V. Katovic, M. A. May, C. P. Keszthelyi, in *Laboratory Techniques in Electroanalytical Chemistry*, 2nd ed., P. T. Kissinger, W. R. Heineman, Eds., Marcel Dekker: New York, 1996.
42. A. J. Bard, *Pure. Appl. Chem*. **25**, 379 (1971).
43. J. L. Mills, R. Nelson, S. G. Shore, L. B. Anderson, *Anal. Chem*. **43**, 157 (1971).
44. E. A. Blubaugh, L. M. Doane, *Anal. Chem*. **54**, 329 (1982).

– 3 –

Solvents and Supporting Electrolytes

Stephen Creager

Department of Chemistry, Clemson University, Clemson,
SC 29634, USA

3.1 INTRODUCTION

All electrochemical reactions and phenomena occur in a medium, usually a solvent containing dissolved ions (often called the supporting electrolyte or just the electrolyte) which are mobile and able to support current flow. The properties of this medium (which we will call the solvent–electrolyte combination, or sometimes the electrolyte for short) are critically important to any electrochemical experiment. A medium containing mobile ions must exist between the electrodes in an electrochemical cell to allow for control and/or measurement of the electrode potential in the cell, which is required in nearly all electrochemical experiments. A medium with good solvating power is needed to dissolve reactants and products from the electrode reaction, and one with reasonably low viscosity is often needed to allow for rapid transport of reactants and products to and from electrodes. Finally, a medium with low reactivity, or at least with a specific desired reactivity, is needed that will be compatible with oxidizing and reducing electrodes and with reactive species which might be created at electrodes, for any of a wide variety of reasons including analysis, synthesis, energy conversion, or simply the novelty of making a new species for the first time and studying its properties.

This chapter will focus on the properties of some solvent–electrolyte combinations that are commonly used in electrochemical science. Many excellent reviews exist on the properties of solvents and solvent–electrolyte combinations for use as media for performing electrochemical experiments (1–5) and we will not attempt to present a comprehensive review of this material. Rather, we present a discussion focusing on some critical aspects of solvent and electrolyte properties as they relate to electrochemical science, along with some select data on particular solvent and electrolyte combinations that are commonly used. We also include some suggested methods for purifying commonly used solvents and electrolytes. Our purpose is to present a chapter that will provide the reader with some intuition regarding the factors that can be important in selecting a suitable solvent–electrolyte combination for a particular application or experiment, and some practical guidance for preparing and using selected solvents and electrolytes.

Handbook of Electrochemistry
Edited by C.G. Zoski

3.2 ELECTROLYTE CONDUCTIVITY

One of the most important qualities that a medium must possess to be useful in electro-chemical science is an ability to support current flow. Electrochemical reactions always produce or consume ions at electrodes, and the electrolyte provides the pathway for ions to flow between and among electrodes in the cell to maintain charge balance. The ability of a phase to support current flow by motion of charged particles (ions in an electrolyte) when an electric field exists within the phase is called the conductivity, usually abbreviated as κ. Conductivity has units of ohm^{-1} cm^{-1}, sometimes called siemens cm^{-1}. Conductivity is a property of a phase or material; for an electrolyte phase of uniform cross-section of area A and length L, whose electrical resistance is R, the ionic conductivity is given by $\kappa = (1/R)(L/A)$. Conductivity is the inverse of resistivity, usually abbreviated as ρ, with units of ohm cm. Representative values for ionic conductivity for some commonly used solvent–electrolyte combinations in electrochemistry are presented in Table 3.1.

A full consideration of all the factors affecting ionic conductivity in electrolytes is beyond the scope of this chapter. Even so, it is worthwhile to consider, in a simplified way, the factors affecting ionic conductivity to gain an understanding of how the conductivity of various solvent–electrolyte combinations depends on the solvent and electrolyte properties.

Ionic conductivity in electrolytes depends on two main factors: (i) the concentration of free charge carriers (ions) and (ii) the ability of the charge carriers (ions) to move in an electric field. Obviously, charge carriers tend to be present at high concentration when the concentration of dissolved salt in an electrolyte phase is high, and in general more concentrated salt solutions are expected to exhibit higher conductivities. This expectation is generally true, and fails only at very high salt concentrations near the solubility limit where the properties of electrolyte phases change drastically mainly due to the limited availability of solvent. For example, the room-temperature ionic conductivity of an aqueous lithium chloride solution increases monotonically with concentration to reach a peak value of 0.17 ohm^{-1} cm^{-1} for a 20 wt.% solution (approximately 5.3 M) but then decreases to a value of 0.15 ohm^{-1} cm^{-1} for a 30 wt.% solution (approximately 8.3 M) (7). This fact may be understood by noting that in a 30 wt.% aqueous lithium chloride solution there are only 2.7 water molecules present for each ion which is not enough to form a proper salvation shell for each ion. Also the viscosity of highly concentrated salt solutions can be large, which can limit ion mobility and yield diminished conductivity.

Electrolytes may be broadly considered in two groups: the strong electrolytes and the weak electrolytes. Strong electrolytes are electrolytes that are normally fully dissociated into ions when dissolved. A good example is sodium chloride in water. Weak electrolytes are electrolytes that normally exist in a partially dissociated state such that some portion, often a large portion, of the dissolved electrolyte exists in an uncharged form, usually a neutral molecule. A good example of a weak electrolyte is acetic acid in water. A 0.1 M solution of acetic acid in water is only about 1% dissociated into protons and acetate ions, with approximately 99% of the acetic acid being present as neutral molecules. This fact makes the conductivity of an acetic acid solution much less than would be expected if one assumed full dissociation of the acid into free protons and acetate ions. Normally, the electrolytes chosen for making solvent–electrolyte combinations for use in electrochemical experiments are strong electrolytes. All the electrolytes in Table 3.1 are strong electrolytes.

Table 3.1

Selected ionic conductivity values for solvent–electrolyte combinations

Solvent	Electrolyte	Electrolyte concentration (M)	Temperature (°C)	Conductivity (ohm^{-1} cm^{-1})	Reference
Water	HCl	6.0	25	0.84	(6)
Water	HCl	1.0	25	0.33	(6)
Water	HCl	0.1	25	0.039	(6)
Water	H_2SO_4	0.53	25	0.21	(7)
Water	H_2SO_4	0.10	25	0.048	(7)
Water	KCl	1.05	25	0.11	(7)
Water	KCl	0.1	25	0.013	(6)
Water	$LiClO_4$	0.1	25	0.0089	(6)
Acetonitrile	$TEAClO_4$	1.0	25	0.050	(8)
Acetonitrile	$TEAClO_4$	1.0	22	0.026	(9)
Acetonitrile	$TEAClO_4$	0.1	22	0.0084	(9)
Acetonitrile	$TEABF_4$	1.0	25	0.056	(8)
Acetonitrile	$TEAPF_6$	1.0	25	0.055	(8)
Acetonitrile	$TEACF_3SO_3$	1.0	25	0.042	(8)
Acetonitrile	$TBAClO_4$	1.0	22	0.023	(9)
Acetonitrile	$TBAPF_6$	1.0	25	0.031	(8)
Acetonitrile	$LiPF_6$	1.0	25	0.050	(8)
Acetonitrile	$LiCF_3SO_3$	1.0	25	0.0097	(8)
Dimethyl-formamide	$TBABF_4$	1.0	25	0.0145	(10)
Propylene carbonate	$TBABF_4$	1.0	25	0.0074	(8)
Propylene carbonate	$TBAPF_6$	1.0	25	0.0061	(8)
Dichloro-methane	$TBAClO_4$	1.0	22	0.0064	(9)
Dimethoxy-ethane	$TBABF_4$	1.0	25	0.0044	(10)
Tetrahydro-furan	$TBABF_4$	1.0	25	0.0027	(10)
Butyronitrile	$TBAPF_6$	0.3	25	0.0079	(11)
Dichloro-methane	$TBAPF_6$	0.1	Ambient	0.0014	(12)
Trifluoro-toluene	$TBAB(C_6F_5)_4$	0.1	Ambient	0.0013	(12)
Tetrahydro-furan	$TBAPF_6$	0.1	Ambient	0.0005	(12)

One factor that can limit the free ion concentration in a strong electrolyte solution is ion pairing, whereby free ions associate with ions of opposite charge to make electrically neutral ion pairs that do not contribute to the conductivity. Ion pairing differs from the process described above for weak electrolytes because the bonding in an ion pair is entirely electrostatic, whereas that in most weak electrolytes involves formation of covalent molecular bonds. Ion pairing may be understood as a competition between the energy of electrostatic

attraction of two oppositely charged ions toward each other, which serves to keep the ion pair together, and the thermal energy in the medium, which serves to break the ion pair apart. A full consideration of the theory of ion pairing is beyond the scope of this chapter and the reader is referred to some excellent references for a more thorough treatment (13, 14). Even so, it is useful to consider some predictions from theory regarding how ion pairing should depend upon solvent and electrolyte properties. The Bjerrum theory of ion pairing, which is the earliest and simplest such theory, predicts that ion pairing will be greatest when the salt concentration is high, the salt ions are small and have high charge, the temperature is low, and the solvent permittivity (dielectric constant) is low. These predictions are generally borne out in experiments. For example, in a potassium chloride solution in water (dielectric constant = 78) at ambient temperature the extent of ion pairing is reported to be so low as to be undetectable, whereas in a 0.1 M solution of KCl in methanol solvent (dielectric constant = 32.6) approximately 32% of the KCl is reported to exist as K^+Cl^- ion pairs, and for a similar solution in acetic acid solvent (dielectric constant = 6.2) over 99.9% of the dissolved KCl is reported to exist in an ion-paired state (14). In solvents of low dielectric constant the effect can be particularly strong; for example, Koryta reports that a 3×10^{-5} M solution of tetraisopentylammonium nitrate in water shows no evidence of ion pairing whereas in a similar solution of dioxane, which has a dielectric constant of 2.2, the concentration of free nitrate ions is reduced to the very low value of 8×10^{-12} M (14). In general, ion pairing may be considered to occur to only a small extent in most aqueous electrolyte solutions, but it can be quite substantial for electrolyte solutions in organic solvents with low dielectric constants, e.g. free ions are thought to be nearly absent in electrolyte solutions in solvents with dielectric constants below approximately 5 (14).

The ability of free ions to move in an electric field is described in terms of the ion mobility, abbreviated u_i for an ion i. Ion mobility is the velocity that an ion attains per unit of electric field. Considering an ion as a charged sphere and the solvent as a continuum fluid, the ion mobility for an ion i is given by the equation $u_i = |z_i|e/(6\pi\eta r_i)$ where z is the ion charge, e the electronic charge, η the solvent viscosity, and r the ion radius. We see from this equation that ion mobilities (and therefore electrolyte conductivities) are expected to be highest for highly charged small ions in solvents of low viscosity. This is generally true, and solvents of very high viscosity (e.g., dimethylsulfoxide (DMSO) and benzonitrile) tend to be less widely used when rapid mass transfer is important.

An interesting trade-off arises when considering the effect of ion size on electrolyte conductivity. Large ions would appear to be disfavored due to their low mobility. However, large ions can sometimes be more easily solvated than small ions, especially in low-polarity solvents for which ion solvation energies are likely to be low and salts of small, highly charged ions are often insoluble. Salts of large ions are also less prone to undergo ion-pairing interactions in such solvents. Thus, especially in low-polarity solvents, it is often necessary to use salts of very large ions despite their low ion mobility.

3.3   CELLS, ELECTRODES, AND ELECTROLYTES

Current flow between electrodes in electrochemical cells occurs through the electrolyte phase and is described in terms of a solution resistance for the electrolyte between the electrodes. The magnitude of this resistance depends on the ionic conductivity of the electrolyte, as
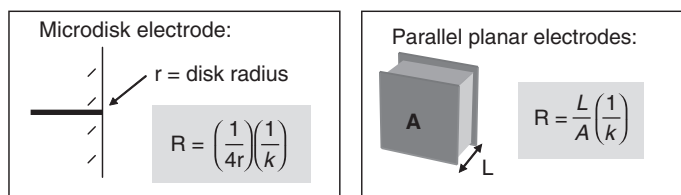
Figure 3.1 Relationships between solution resistance and cell geometry for two limiting cases of electrodes in contact with electrolytes. (for colour version: see colour section at the end of the book).

Table 3.2

Calculated solution resistance values for microdisk and planar electrodes in contact with electrolytes

Microdisk configuration		Parallel plane configuration	
r_{disk} (cm)	R_{sol} (ohm)[a]	d_{space} (cm)	R_{sol} (ohm)[a]
1	5	10	200
0.1	50	1	20
0.01	500	0.1	2
0.001	5000	0.01	0.2

[a]Solution resistances were calculated assuming an electrolyte conductivity of 0.05 ohm^{-1} cm^{-1}.

described above, and also on the geometric arrangement of electrodes in the cell. We consider here the effect of electrode and cell geometry on the solution resistance in the cell.

The dependence of solution resistance on cell and electrode geometry is complicated for the general case and requires integration over the full three-dimensional geometry of the cell for a rigorous solution. Although such treatments are beyond the scope of this chapter, it is useful to consider some limiting cases. Figure 3.1 presents two such cases: one for a disk electrode embedded in an insulator and immersed in an electrolyte phase, and the other for a pair of parallel planar electrodes with an electrolyte phase interposed between them. The figure includes equations for estimating the solution resistance using only the electrolyte conductivity and parameters relating to electrode size and spacing for the calculation.

Table 3.2 presents some calculated values of solution resistance for various combinations of electrode size and spacing with reasonable assumptions for electrolyte conductivity. We see that for the microdisk configuration solution, resistance increases with decreasing electrode size, and that for the parallel planar electrode configuration, resistance decreases with decreasing spacing. Calculations of this sort can be useful when trying to evaluate ohmic losses associated with uncompensated solution resistance in cells in which a net current flows. Ohmic losses are of approximate magnitude $I \times R$ where I is the cell current and R the solution resistance. A more thorough treatment must consider how current depends on electrode geometry, which is a rich subject that is considered in more depth in Chapters 6, 11, and 19 of this handbook. For the present, we note only that ohmic losses usually represent a source of error in attempts to control and/or measure the potential of a working electrode relative to a reference electrode while current is flowing. It is usually desirable to keep such losses as low as possible, and one way to achieve this is to use electrolytes having conductivity as high as possible.

3.4   CELL TIME CONSTANTS

Simple electrochemical cells have characteristic time constants associated with them. The cell time constant may be thought of as the time it takes for the electrical double layer at a polarizable working electrode to be charged or discharged. A simple cell may be considered as a series combination of the solution resistance and a double-layer capacitance, and the time constant for such a combination is simply the product of the resistance and the capacitance. It is instructive to consider the magnitudes of cell time constants for some simple cells in common electrolytes. Using the resistance values in Table 3.2 for microdisk electrodes, and making the reasonable assumption that the specific capacitance of a working electrode is approximately 20 μF cm^{-2}, we readily calculate that the time constant for a 1 mm radius disk electrode in contact with a 0.05 ohm^{-1} cm^{-1} electrolyte is approximately 30 μsec, and that for a 10 μm radius disk electrode is approximately 0.3 μsec. These values represent lower limits on the timescale over which methods involving current flow at electrodes may be used to study dynamics associated with electrode reactions.

The use of solvent–electrolyte combinations having low ionic conductivity will result in substantial increases in cell time constant. Thus, another reason for using electrolytes with high conductivity is that doing so allows for more rapid control of applied potential at electrodes, which allows for study of more rapid chemical dynamics in cell reactions.

3.5   SOLVENTS

Many organic liquids (in addition to water) have been used as solvents for electrochemical experiments, and many excellent reviews exist on the properties of solvents and solvent–electrolyte combinations for use as media for performing electrochemical experiments (1–5). We will not attempt a comprehensive review of this collected material here. Rather, we present a brief discussion of the solvent properties that are especially relevant for the use of solvents in electrochemical experiments, followed by a discussion focusing on a few solvents that are commonly used in electrochemistry.

There is no such thing as a "universal solvent" for electrochemistry, any more than there is a universal solvent for any other type of chemistry. The solvent properties that are most important are dictated by the application and can vary widely. Even so, it is possible to focus on a few groups of solvent properties that are particularly important for applications in electrochemistry. One important property is the ability of a solvent to dissolve and dissociate salts to achieve a reasonably high ionic conductivity. We have seen that there are problems associated with the use of solvents that do not have adequate ionic conductivity. The ability of a solvent to dissolve and dissociate salt is in fact a special case of a more general solvent property, which is the solvating power of the solvent. Except in special cases such as electrodeposition or electrochemically induced precipitation, it is usually desired that solvents solvate the reactants and products in electrochemical reactions. Solvents are often chosen for their ability to do this.

The other general solvent property category that is often especially important in electrochemistry is reactivity, including acidity/basicity, nucleophilicity/electrophilicity, redox, polarity, and many other types of reactivities which are limited only by the chemistry one
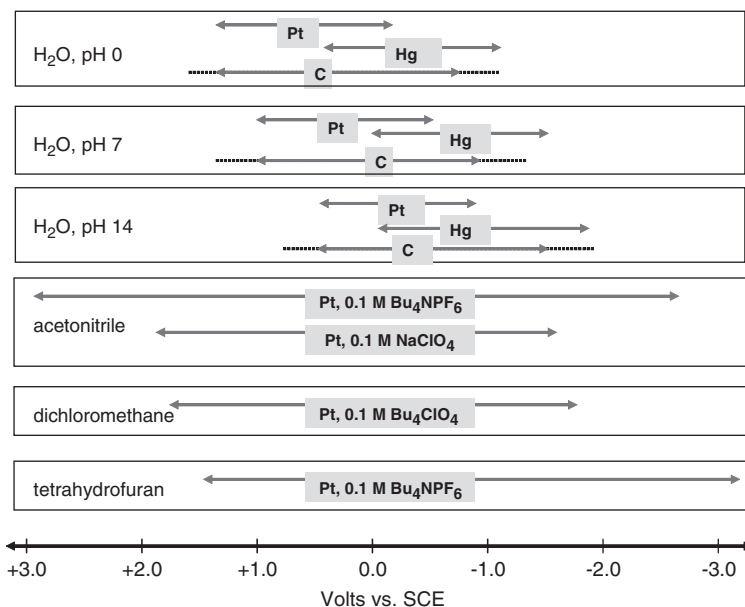
Figure 3.2   Potential limits for some selected combinations of solvent, electrolyte, and working electrode. Data compiled from Rieger, Electrochemistry, 2nd edition, Chapman & Hall, New York, 1994; Bard and Faulkner, "Electrochemical Methods", Wiley, New York, 1980; and Rocklin, in "A Practical Guide to HPLC Detection", D. Parriott, Ed., Academic Press, San Diego, 1993, Chapter 6. (for colour version: see colour section at the end of the book).

is attempting to perform on the solvent. Susceptibility to oxidation or reduction is especially important in electrochemistry since the solvent is often in contact with electrodes that are held at very oxidizing and/or reducing potentials, and at which highly oxidized and/or reduced species are produced. Figure 3.2 presents a summary of selected potential limits for some common combinations of solvent, electrolytes, and electrode. Other factors that can be important include liquid range, optical properties, volatility, toxicity, and cost. Table 3.3 presents a summary of selected properties of a few commonly used solvents in electrochemistry, and Figure 3.3 presents the structures of some of these solvents, grouped so as to highlight the structural similarities between and among various solvents.

3.5.1   Protic solvents

The common protic solvents for electrochemistry are water and the lower alcohols such as methanol and ethanol. All protic solvents are prone to proton reduction to yield hydrogen gas, and they are used for reductive electrochemistry only with electrodes such as mercury or carbon for which proton reduction is kinetically slow, or in circumstances where a species of interest is added with the intent that it be protonated or that it reacts with solvent in a desired way. Of course, much electrochemistry is performed in water due to its ubiquity in the natural world and its excellence as a solvent for salts.

Table 3.3

Properties of some commonly used solvents in electrochemistry (6)

Common name	Molecular weight (g mol^{-1})	Freezing point (°C)	Boiling point (°C)	Density (g cm^{-3})	Viscosity (centipoise)	Dielectric constant (DC)	Dipole moment
Water	18.02	0.0	100.0	0.997	0.890	80.1	1.85
Methanol (MeOH)	32.04	−97.5	64.6	0.791[20]	0.544	33.0	1.70
Acetone	58.08	−94.7	56.1	0.785[25]	0.306	21.0	2.88
Acetonitrile (AN)	41.05	−43.8	81.7	0.786[20]	0.369	36.6	3.92
Butyronitrile	69.11	−111.9	117.6	0.794[20]	0.553	24.8	3.9
Benzonitrile	103.12	−14.0	191.1	1.009[15]	1.267	25.9	4.18
Dichloromethane	84.93	−97.2	40.0	1.327[20]	0.413	8.93	1.6
N,N′-dimethyl-formamide (DMF)	73.09	−60.5	153	0.945[25]	0.794	38.3	3.82
N-methyl-pyrrolidinone (NMP)	99.13	−23.1	202	1.023[25]	–	32.6	4.1
γ-Butyrolactone	86.09	−43.6	204	1.130[20]	–	39.0	4.27
1,2-dimethoxy-ethane (glyme)	90.12	−69.2	84.5	0.864[25]	0.455	7.3	–
Tetrahydrofuran (THF)	72.11	−108.44	65	0.883[25]	0.456	7.52	1.75
Dimethylsulfoxide (DMSO)	78.13	17.89	189	1.101[25]	1.987	47.2	3.96
Sulfolane	120.17	27.6	287.3	1.272[18]	–	43.3	4.8
Propylene carbonate (PC)	102.09	−48.8	242	1.205[20]	–	66.14	4.9
Trifluoro-toluene	146.11	−29.0	102.1	1.188[20]	–	9.22	2.86

Note: Superscript numbers represents the temperature, in degree celsius, at which the density was measured.
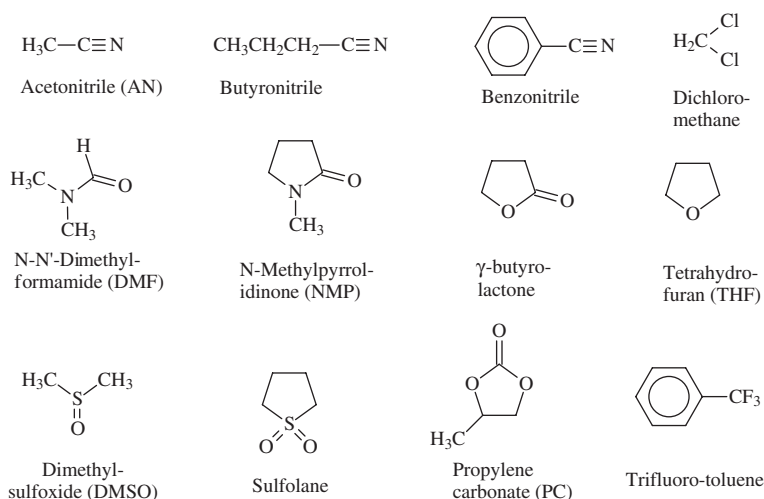
Figure 3.3   Structures of organic solvents commonly used in electrochemistry.

3.5.2 Nitriles

The organic nitriles acetonitrile, butyronitrile, and benzonitrile are widely used in electrochemistry. They offer a quite favorable combination of good organic solvating power from their hydrocarbon character, and high polarity from the polar nitrile group. The nitrile group is not easily oxidized or reduced and nitriles are not strongly acidic or basic, which gives them excellent stability under both oxidizing and reducing conductions in electrochemical cells. They are good general-purpose aprotic organic solvents for electrochemistry. Acetonitrile is also fully miscible with water, and can be useful for studies in which a mixed solvent system is desired for solubility and/or reactivity reasons.

3.5.3 Halogenated organics

Halogenated organic solvents such as dichloromethane and dichloroethane, and in some cases *ortho*-dichlorobenzene (e.g., fullerenes) and trifluorotoluene, have excellent solvating power for a wide range of organic and organometallic compounds and, as such, they have been widely used as electrochemical solvents. Their use has declined in recent years due to concerns about their toxicity and the disposal of halogenated solvents, which certainly limits their use in any large-scale application. Still, for research applications they present a good compromise between polarity and organic solvating power and they are still widely used. Halogenated solvents will in general be subject to electroreduction, which can limit their use in situations involving generation of powerful reducing agents or application of highly reducing potentials. They are good choices for oxidative electrochemistry.

3.5.4 Amides

Organic amide solvents such as dimethylformamide (DMF) and *N*-methylpyrrolidinone (NMP) are good choices when a polar, high-boiling solvent is desired. These solvents are often useful for dissolving polar organic molecules that do not dissolve in water or in conventional organic solvents. They are also often used to dissolve polar polymers, in part because they can be heated to quite high temperatures before boiling. DMF can be difficult to purify since it decomposes slightly at its normal boiling point to produce small amounts of dimethylamine. NMP is a cyclic analog of DMF that is a good all-purpose polar organic solvent.

3.5.5 Sulfoxides and sulfones

Dimethylsulfoxide (DMSO) and sulfolane are also good choices when a polar, high-boiling solvent is desired. DMSO has a quite high viscosity that limits transport rates and ionic conductivities, but it is also quite polar and dissolves many salts and organic compounds easily. Sulfolane is among the highest boiling organic solvents that can be used for electrochemical studies, and is therefore useful for high-temperature electrochemical studies.

3.5.6   Ethers, carbonates, lactone

Tetrahydrofuran (THF) and 1,2-dimethoxyethane (glyme) are the most commonly used ether solvents in electrochemistry. They are very inert, especially toward reducing conditions. They are fairly non-polar (low dielectric constants), which can make dissolving electrolytes and achieving high conductivity in salt solutions in these solvents difficult. Organic carbonates such as propylene carbonate (PC) and ethylene carbonate (EC), and lactones such as γ-butyrolactone are especially good choices for lithium salts such as $LiPF_6$, LiTriflate, and LiTFSI, which are all widely used in lithium battery technology. They have not been widely used for other applications in electrochemistry but they should be well suited for such applications.

3.6   SALTS

The number of salts that are widely used as supporting electrolytes in electrochemical experiments is surprisingly small, considering how many salts are known. This is particularly true of organic solvents, which are not normally considered as good solvents for salts and for which salts must usually have substantial organic characteristics to be soluble. To a certain extent, the anions and cations in such salts may be considered separately since both species are generally stable and in most cases the anions and cations may be "mixed and matched" to produce the desired salt.

Figure 3.4 presents structures of some cations and anions that are the components of commonly used salts for preparing organic electrolytes. By far, the most commonly used cations
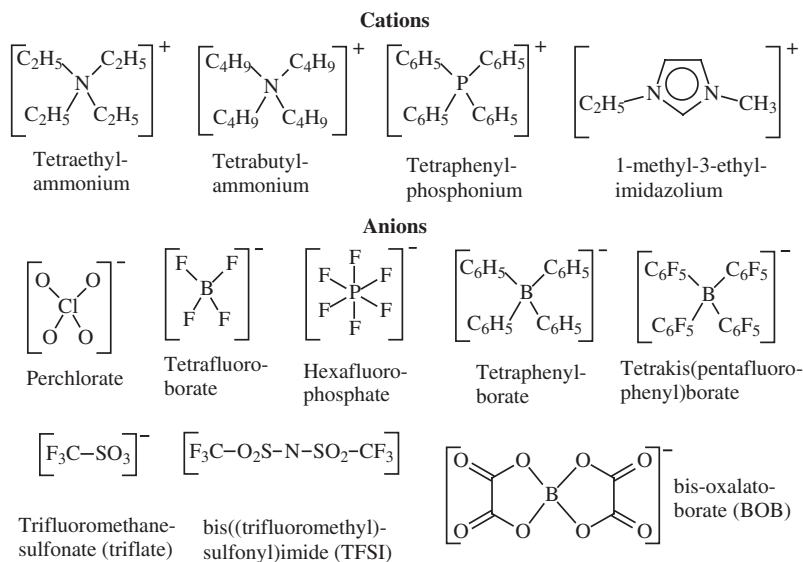
Figure 3.4   Anions and cations of salts commonly used in electrochemistry.

are the tetra-alkylammonium ions; their organic character combined with their relatively low electroreductive reactivity makes them well suited for use in electrochemical experiments. Tetraethylammonium (TEA) and tetrabutylammonium (TBA) ions are the most widely used. There is more diversity among the anions. Perchlorates have been widely used in the past but their use is discouraged today due to explosion hazard concerns. Tetrafluoroborate and hexafluorophosphate salts are excellent replacements for perchlorates and are widely used. Tetraphenylborate salts are also suitable, as are salts based on the tetrakis-(pentafluorophenyl)borate anion which is an extremely unreactive, non-coordinating anion with good solubility in low-reactivity solvents such as trifluorotoluene (12). Finally, lithium salts of fluorosulfonates such as triflate, fluorosulfonimides such as bis[(trifluoromethyl)sulfonyl]imide (TFSI), and borates such as bis-oxaloborate (BOB) are being developed for use in lithium battery technology. These anions are attractive because they are resistant to electro-oxidation and reduction and they dissolve in organic solvents to produce electrolytes with high conductivity, which should make them useful in a variety of electrochemical experiments.

3.7 "EXOTIC" ELECTROLYTES

It is useful to compare the properties of the solvent–electrolyte systems we have considered so far with those of some more "exotic" electrolytes, meaning electrolytes with unusual properties not found in conventional electrolytes. Table 3.4 presents a compilation of ionic conductivities of some electrolytes that are extreme in some ways. The first four entries illustrate that an otherwise conventional electrolyte, $TBAPF_6$ in butyronitrile, can

Table 3.4

Ionic conductivity values for some "exotic" electrolytes

Medium	Electrolyte	Electrolyte concentration (M)	Temperature (°C)	Conductivity (ohm^{-1} cm^{-1})	Reference
Butyronitrile	$TBAPF_6$	0.2	0	0.0033	(15)
Butyronitrile	$TBAPF_6$	0.2	−40	0.0016	(15)
Butyronitrile	$TBAPF_6$	0.2	−80	0.0004	(15)
Butyronitrile	$TBAPF_6$	0.2	−120	0.00002	(15)
Nafion 1100 EW	Fluorosulfonate	1 (approx.)	25	0.06–0.08	(16, 17)
PC/EC/polyacrylonitrile gel	LiTFSI, LiTriflate, $LiPF_6$	5–15 wt.%	30	0.001–0.005	(18)
Polyethyleneglycol-dimethylether (350 MW) with fumed silica additive	LiTFSI	1 (approx.)	30	0.0025	(19)
Polyethylene oxide	LiTFSI, LiTriflate, $LiClO_4$	8–15 wt.%	50	0.0001–0.0002	(20)
Imidazolium BF_4/PF_6/TFSI/ionic liquids		3–6	Ambient	0.010–0.001	(21)

be used at ultralow temperatures. Combinations of butyronitrile with various halogenated organic solvents have been used to produce liquid electrolytes that can be used at temperatures as low as $-160\ ^{\circ}C$ (or 113 K) (15). Low-temperature electrochemistry can be useful for a variety of purposes including slowing down very fast reactions to capture reactive intermediates, measuring activation energies as part of a mechanistic study, or even for studying phenomena such as magnetism or superconductivity that are manifested only at very low temperature.

The next entry is for Nafion, a proton-conducting fluorosulfonic acid ionomer material which in membrane form is widely used in PEM fuel-cell technology. The conductivity value quoted is for a fully hydrated membrane at an ambient temperature. Note that the conductivity is less than that of a comparable aqueous acid solution, for example 0.5 M sulfuric acid, but by a factor of only 3–4. Heavily hydrated Nafion membranes contain a lot of water, and consequently they behave a lot like aqueous acid solutions. The next three entries are for various gel and solid-polymer electrolytes containing lithium salts. All these material are membranes; some contain some potentially volatile solvents, while others do not. Conductivities for these materials are low relative to true liquid solvents but they are still well within the range of usable values for electrochemical experiments. The semi-solid character of these materials, combined with their near-zero volatility (for solid-polymer electrolytes which do not contain volatile solvents), makes them suitable for use under high-vacuum conditions which makes them potentially useful for fabrication of electrochemical devices which are targeted for use in vacuum or under conditions which could otherwise result in solvent loss by evaporation.

The last entry in Table 3.4 is for a series of room-temperature ionic liquids based on combinations of imidazolium cations with hexafluorophosphate, tetrafluoroborate, and fluorosulfonimide anions. These materials are interesting because they contain only ions (e.g., no volatile or uncharged components). Room-temperature ionic liquids based on chloroaluminate anions with various organic cations have also been described (22). Conductivity values are perhaps surprisingly low for these materials considering that they contain only ions at relatively high concentrations. This fact probably reflects the relatively large size of the ions, the still somewhat high viscosity of the ionic liquids, and some degree of ion association/pairing. Still, the low volatility, low reactivity, low water solubility, and relatively high ionic conductivity of these ionic liquids make them attractive for use in electrochemical studies where the complete absence of a volatile and/or reactive solvent is desired.

3.8   PURIFICATION PROCEDURES FOR SOME COMMONLY USED SOLVENTS IN ELECTROCHEMISTRY

It is difficult to generalize about the need for solvent and electrolyte purification or the best procedures to follow in a particular application. Common impurities in nearly all organic solvents and electrolytes are water and oxygen, which can be present in commercial materials in concentrations ranging from zero to a few millimolar depending on the source of the material. The nature and amounts of other impurities are highly dependent on the particular material in question. In general, care should be taken to ensure that solvent and

electrolytes are free from impurities when highly reactive species are being used or generated at electrodes which could react with impurities and/or when impurities in the solvent/ electrolyte could contaminate an electrogenerated product that is being collected. Problems can be particularly acute when concentrations of electroactive species are low (e.g., less than millimolar) since under such conditions, solvent and electrolyte impurities can be present at concentrations greater than that of the component being studied. Whenever possible, the best policy is often to use solvents and electrolytes from commercial sources in the best purity available, and to adopt additional purification procedures if initial experiments suggest that the materials in as-received form are not adequate for the task in hand.

Many procedures for purifying solvents and electrolytes have been described in the original literature. Some excellent compilations have also appeared; one that this author has found to be particularly useful is "Purification of Laboratory Chemicals", in the fifth edition, by Armarego and Chai (23). This volume is an update of the volume of the same name, originally authored by Perrin and Armarego (24). Many of the procedures described below are summaries of the procedures that appear in this volume. The interested reader is encouraged to consult the book by Armarego and Chai for further details and references to the original literature.

3.8.1   Acetonitrile

Acetonitrile is available commercially in sufficiently high purity for routine applications. Common contaminants in commercial acetonitrile are water, acetamide, ammonia, and ammonium acetate. Removal of water by shaking with silica gel or 4 Å molecule sieves, or with activated alumina (activated by heating at 250 °C for 4 h) is effective. Subsequent treatment with calcium hydride until hydrogen evolution stops, followed by fractional distillation over calcium hydride, provides an acceptably pure solvent. Calcium sulfate and calcium chloride are reported to be ineffective as drying agents for acetonitrile, and distillation using phosphorous oxide (P_2O_5) as drying agent is discouraged because use of excess P_2O_5 can cause formation of an orange polymer. Storage over activated 3 Å molecular sieves is recommended to keep water levels low following purification.

3.8.2   Butyronitrile

Treatment with concentrated HCl is recommended to remove isonitriles, followed by drying over potassium carbonate and fractional distillation. Further drying over activated alumina is effective for removing water.

3.8.3   Benzonitrile

The same treatment described above for butyronitrile is also effective for benzonitrile, with the single difference that the fractional distillation is recommended to be performed under reduced pressure (boiling point 69 °C/10 torr).

3.8.4   Propylene carbonate

Common contaminants in commercial PC include propylene oxide, carbon dioxide, propanediols, allyl alcohol, ethylene carbonate, and water. Purification may be accomplished by percolation through 5 Å molecular sieves (activated by treatment at 350 °C for 14 h under argon), followed by distillation under vacuum and storage under molecular sieves.

3.8.5   Dichloromethane

A rapid treatment involves reflux over solid calcium hydride followed by fractional distillation and storage over 4 Å molecular sieves. A more comprehensive and effective procedure involves treatment with concentrated H_2SO_4 until the acid layer remains colorless, followed by washing with water, aqueous base (carbonate, bicarbonate, or hydroxide solution), and water again, followed by drying over $CaCl_2$ and distillation over $CaSO_4$, CaH_2, or P_2O_5, gives material of acceptable purity. Storage over 4 Å molecular sieves helps keep water levels down. Dichloromethane should be stored in brown bottles to prevent photolysis by ambient light.

3.8.6   Dimethylformamide

Dimethylformamide (DMF) decomposes slightly via a process which is catalyzed by strong acids or bases, so such materials should be avoided during purification. A recommended procedure is to use a preliminary drying step with $CaSO_4$, $MgSO_4$, silica gel, or type 4 Å molecular sieves, followed by vacuum distillation and storage over 3 or 4 Å molecular sieves.

3.9   PURIFICATION PROCEDURES FOR SOME COMMONLY USED SALTS IN ELECTROCHEMISTRY

Most of the following salts are available from commercial sources in the indicated form and may be used as received for routine applications. The following purification procedures are recommended when very pure materials, free from all undesirable impurities including water, are needed.

3.9.1   Tetraethylammonium tetrafluoroborate

Recrystallization from a 5:1 mixture of ethyl acetate/hexane, or from methanol/diethyl ether, followed by storage under vacuum at 95 °C for 48 h.

3.9.2   Tetraethylammonium tetraphenylborate

Recrystallization from aqueous acetone followed by drying at 60 °C under vacuum for several days.

3.9.3   Tetraethylammonium hexafluorophosphate

Recrystallization from hot water.

3.9.4   Tetrabutylammonium tetrafluoroborate

Recrystallization from water or aqueous ethanol, or ethyl acetate/pentane, or pure ethyl acetate with cooling in dry ice to induce precipitation, followed by drying at 80 °C under vacuum.

3.9.5   Tetrabutylammonium hexafluorophosphate

Recrystallization from aqueous ethanol, or from absolute ethanol, followed by drying in vacuum at 70 °C for 10 h.

3.9.6   Lithium perchlorate

Recrystallization from water or aqueous methanol, followed by heating at 170–180 °C in an air oven (vacuum is also suitable) to remove waters of hydration. Subsequent crystallization from acetonitrile is also suggested to improve purity.

REFERENCES

1. A. J. Fry, in *Laboratory Techniques in Electroanalytical Chemistry*, 2nd ed., P. T. Kissinger, W. R. Heineman, Eds., Marcel Dekker: New York, 1996.
2. D. T. Sawyer, A. Sobkowiak, J. L. Roberts, in *Electrochemistry for Chemists*, 2nd ed., Wiley: New York, 1995.
3. C. J. Janz, R. P. T. Tompkins, *Nonaqueous Electrolytes*, Academic Press: New York, 1972 and 1974, Vols. I and II.
4. C. K. Mann, in *Electroanalytical Chemistry*, A. J. Bard, Ed., Marcel Dekker: New York, 1969, Vol. 3, p. 57.
5. H. Lund, in *Organic Electrochemistry*, 3rd ed., H. Lund, M. M. Baizer, Eds., Marcel Dekker: New York, 1991.
6. D. R. Lide, Ed., *CRC Handbook of Chemistry and Physics*, 85th ed., CRC Press: Boca Raton, FL, 2004.
7. R. C. Weast, Ed., *CRC Handbook of Chemistry and Physics*, 60th ed., CRC Press: Boca Raton, FL, 1980.
8. M. Ue, K. Ida, S. Mori, *J. Electrochem. Soc.* **141**, 2989 (1994).
9. K. M. Kadish, J. Q. Ding, T. Malinski, *Anal. Chem.* **56**, 1741 (1984).
10. H. O. House, E. Feng, N. P. Peet, *J. Org. Chem.* **36**, 2371 (1971).
11. L. K. Safford, M. J. Weaver, *J. Electroanal. Chem.* **331**, 857 (1992).
12. R. J. Lesuer, C. Buttolph, W. E. Geiger, *Anal. Chem.* **76**, 6395 (2004).
13. J. O. M. Bockris, A. K. N. Reddy, *Modern Electrochemistry*, Plenum: New York, 1970, Vol. 1, p. 251.

14. J. Koryta, J. Dvorak, L. Kavan, *Principles of Electrochemistry*, 2nd ed., John Wiley & Sons: Chichester, 1993, p. 23.
15. S. Ching, J. T. Mcdevitt, S. P. Peck, R. W. Murray, *J. Electrochem. Soc.* **138**, 2308 (1991).
16. G. Pourcelly, C. Gavach, in *Proton Conductors. Solids, Membranes, and Gels-materials and Devices*, P. Colomban, Ed., Cambridge University Press: Cambridge, UK, 1992.
17. Y. Stone, P. Ekdunge, K. Simonsson, *J. Electrochem. Soc.* **143**, 1254 (1996).
18. H. S. Choe, B. G. Carrol, D. M. Pasquariello, K. M. Abraham, *Chem. Mater.* **9**, 369 (1997).
19. H. J. Walls, P. S. Fedkiw, T. A. Zawodzinski, S. A. Khan, *J. Electrochem. Soc.* **150**, E165 (2003).
20. A. Vallee, S. Besner, J. Prud'homme, *Electrochim. Acta* **37**, 1579 (1992).
21. A. B. Mcewen, H. L. Ngo, K. Lecompte, J. L. Goldman, *J. Electrochem. Soc.* **146**, 1687 (1999).
22. T. A. Zawodzinski, R. A. Osteryoung, *Inorg. Chem.* **27**, 4383 (1988).
23. W. L. F. Armarego, C. L. L. Chai, *Purification of Laboratory Chemicals*, 5th ed., Butterworth Heinemann: Amsterdam, 2003.
24. D. D. Perrin, W. L. F. Armarego, *Purification of Laboratory Chemicals*, 3rd ed., Pergamon Press: Oxford, UK, 1988.

– 4 –

Reference Electrodes

Timothy J. Smith and Keith J. Stevenson

The University of Texas at Austin, USA

4.1 INTRODUCTION

The composition of a good reference electrode (RE) must remain effectively constant, unvarying for the duration of an experiment, in order to provide a stable potential for controlled regulation of the working electrode (WE) potential. The chosen RE should be an ideal nonpolarizable electrode (1), i.e., its potential does not change regardless of current flow through the RE. The reaction at the RE should be reversible, permitting a potential to be calculated from the Nernst equation, as well as have the capability to recover its potential after a current stress. This requires that the RE act as a source or a sink for small currents due to imperfections in potentiostat or galvanostat design without displaying a change in its potential throughout the duration of the experiment.

4.1.1 Selecting a reference electrode

Many considerations must be weighed in choosing a suitable RE for an experiment. Proper experimental design must prevent incompatible species present in the electrolyte from reacting with the RE materials. For instance, an ionic species with poor solubility can precipitate in the frit, clogging the RE, and thus increasing the junction potential. Additionally, species that are in the electrochemical cell can interfere with the performance of an RE by poisoning the controlling redox process (i.e., H_2 catalysis), or increase the solubility of the reference couple (i.e., Ag|AgCl). Cell conditions such as pressure and temperature must also be considered in choosing the appropriate RE for a particular experiment as the equilibrium of the redox couple is dependent on these parameters. Time requirements can allow the use of a less robust RE, permitted that the RE is stable over the duration of the measurement. One option that allows for flexibility in the selection of an RE is the incorporation of a double junction, or a salt bridge, to separate the RE from the WE. Nonetheless, several different RE varieties are available for use in electrochemical experiments. In the following, we describe common elements for the construction of a stable RE and provide tips for their calibration and maintenance.

4.1.2   Converting between aqueous potential scales

It is often useful to compare experimentally measured cell potentials. A useful conversion chart is provided in Table 4.1 for conversions between reference scales.

4.2   BASIC COMPONENTS OF A REFERENCE ELECTRODE

All REs consist of four essential parts: body, top seal, junction, and active component of the electrode. Many of these elements are interchangeable and can be tailored to meet a variety of experimental conditions. However, the active component is what defines the reference potential.

4.2.1   Body material

The material selected for the tube or body of the RE must withstand the usage requirements for the electrode as well as the fabrication process. This typically precludes the use of plastics for most hydrogen electrodes as well as the use of glass (and Vycor) for extreme alkaline or hydrofluoric acid (HF) solutions. Table 4.2 lists the general chemical stability of some commonly used materials.

4.2.2   Top seal

The presence of a seal at the top of an RE will affect the performance of the RE in several ways. An air-tight, leak-proof seal is used to retain H_2 in some varieties of hydrogen electrodes and can both reduce the flow of filling solution through the junction at the base of an RE and eliminate filling solution evaporation. A leaky seal will have the opposite effect and should only be used with saturated filling solutions.

(a) *Platinum–glass seal*. A platinum–glass seal (3) can be made using flint (soft) glass and a propane torch. Borosilicate glass (i.e., Pyrex) used with platinum requires a hotter flame and produces a poor seal. If required, this type of seal should be made with assistance from an experienced glass blower. The platinum glass seal should be leak proof. Two examples of this type of seal are shown in Figure 4.1A.

(b) *Polymer cap*. A polymer cap can be made using a metal wire that is force fit into a machined piece of Teflon or other polymer where it can be fit to the inside diameter (male cap) or outside diameter (female cap) of a glass or polymer body as shown in Figure 4.1B. This type of seal can be made leak proof with the addition of an o-ring to the Teflon end piece. Care must be taken so that high forces are not placed on the inside diameter of a glass tube, due to the stresses that can be created from the cutting of the tube. Fire polishing can create a poorly toleranced hole that is difficult to make leak proof. For electrodes where a vent is required to produce a "leaky reference" electrode, this type of seal can be made to meet these requirements. This type of seal simplifies refilling the RE by functioning as a filling port.

Table 4.1

Aqueous RE potential scale conversions

Electrode description			Hydrogen	Mercury						Silver chloride	
				Calomel				Sulfate	Oxide		
To convert		*From→To*	NHE *or* SHE	SCE	SSCE	NCE	MSRE	1M NaOH	Saturated KCl/NaCl	3M KCl/NaCl
Hydrogen		NHE *or* SHE	0	−0.241	−0.236	−0.280	−0.640	−0.098	−0.197	−0.209
Mercury	Calomel	SCE	+0.241	0	+0.005	−0.039	−0.399	+0.143	+0.044	+0.032
		SSCE	+0.236	−0.005	0	−0.044	−0.404	+0.138	+0.039	+0.027
		NCE	+0.280	+0.039	+0.044	0	−0.360	+0.182	+0.083	+0.071
	Sulfate	MSRE	+0.640	+0.399	+0.404	+0.360	0	+0.542	+0.443	+0.431
	Oxide	1M NaOH	+0.098	−0.143	−0.138	−0.182	−0.542	0	−0.099	−0.111
Silver chloride		Saturated KCl/NaCl	+0.197	−0.044	−0.039	−0.083	−0.443	+0.099	0	−0.012
		3M KCl/NaCl	+0.209	−0.032	−0.027	−0.071	−0.431	+0.111	+0.012	0

NHE: Normal Hydrogen Electrode ($a_{H^+} = 1$); SHE: Standard Hydrogen Electrode ($a_{H^+} = 1$); SCE: Saturated Calomel Electrode (saturated KCl); SSCE: Saturated Salt Calomel Electrode (saturated NaCl); NCE: Normal Calomel Electrode (1 M KCl); MSRE: Mercury(I) Sulfate Reference Electrode (saturated K_2SO_4).

Table 4.2

Solvent compatibility chart (2)

Body material		Acids		Bases	Organics						
		Organic	Inorganic		Aromatics	Ketones	Aldehydes	Ethers	Amines	Halogenated	Aliphatic
Halogenated											
Polytetrafluoro-ethylene	PTFE Teflon®	A	A	A	A	A	A	A	A	A	A
Perfluoro (ethylene-propylene) copolymer	FEP Teflon®	A	A	A	A	A	A	A	A	A	A
Polychlorotri-fluoroethylene	PCTFE Kel-F®	A	A	A	A	A	A	B	A	B	A
Fluoroelestomer	Viton®	B	B	B	A	C	B	C	B	B	A
Polyolefins											
Polypropylene	PP	B	B	A	C	B	B	C	A	B	B
Polyethylene	LDPE	B	B	B	C	B	B	B	B	B	B
	HDPE	B	B	B	C	B	B	B	B	B	B
Polyacetal	Delrin®	C	C	C	A	A	A	A	B	B	A

A: acceptable; B: not all members of class acceptable; C: not acceptable.
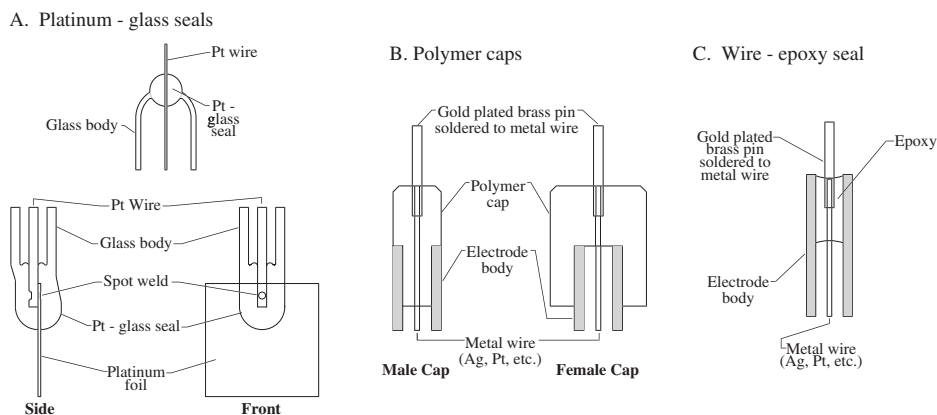
Figure 4.1   Reference electrode top seal types: (A) platinum–glass seals; (B) polymer caps; (C) wire–epoxy seal.

(c) *Wire–epoxy seal.* The wire–epoxy seal, shown in Figure 4.1C, is a simple, quick, and inexpensive seal for REs. This type of seal is leak proof, but concerns should be raised about any volatiles emitted or leached from the epoxy that could be electro-active or coat the active surface of the electrode. This seal can make changing the filling solution difficult, requiring removal of the junction unless a filling port is built into the RE.

4.2.3 Junction (4)

The junction separates the internal filling solution of the RE from the external electrolyte of the electrochemical cell. In some instances, no junction is used due to the similarity between filling solution and the electrolyte in the electrochemical cell. In others, a double junction is used to prevent mixing of incompatible species between the RE and electro-chemical cell. Junctions are covered in more detail in Section 4.4.

(a) *Vycor, polyethylene, or Teflon frit.* The frit material can be sealed to the body material with heat shrink tubing. The recovery temperature of the heat shrink must be low enough that no damage is done to the frit material during the sealing process. This type of junction is shown in Figure 4.2A.
(b) *Ceramic junction.* A ceramic frit can be sealed into a glass RE body using standard glass blowing techniques. The ceramic must be held tightly in the glass with no spaces on the sides of the ceramic, otherwise solutions will bypass the ceramic. This type of junction, shown in Figure 4.2B, typically has a very low leak rate.
(c) *Glass wool, cellulose pulp, or agar.* Glass wool or other junction material can be filled or wedged into a restricted end of the RE body as shown in Figure 4.2C. The leak rate can be adjusted by changing both the type and the density of the material.

A. Vycor, polyethylene, or teflon frit

RE body

Heat shrink
tubing

Frit

B. Ceramic junction

Glass RE
body

Ceramic
Frit

C. Glass wool, cellulose pulp, or agar

RE
body

Glass
wool,
cellulose
pulp, or Agar

D. Platinum, quartz, or asbestos fiber

Glass RE
body

Wire or
fiber

E. Cracked glass bead

Glass RE
body

Glass
bead

F. Luggin capillary

Glass RE
body

Ultra fine
capillary
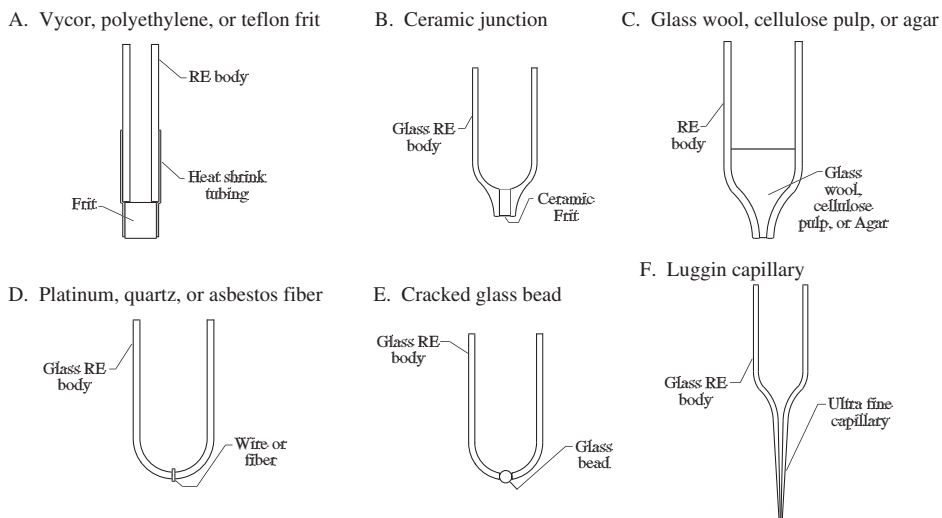
Figure 4.2   Reference electrode junction types: (A) Vycor, polyethylene, or Teflon frit; (B) ceramic junction; (C) glass wool, cellulose oulp, or agar; (D) platinum, quartz, or asbestos fiber; (E) cracked glass bead; (F) Luggin capillary.

A. Heat gun with concentrator adapter

CAUTION:
EXTREME HEAT

Hot air

Rotate electrode

B. Nichrome resistance wire (powered with a variac)

Coiled Nichrome resistance wire

Components
centered in coil

Frit

Heat
shrink
tubing

Electrode Body
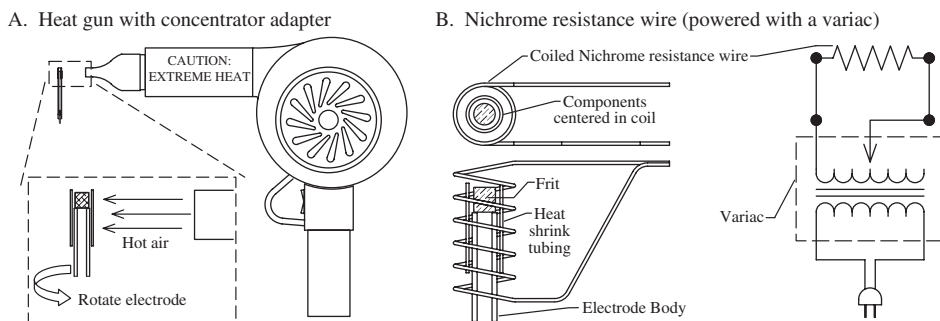
Variac

Figure 4.3   Suggested methods to shrink heat shrink tubing: (A) heat gun with concentrator adapter; (B) nichrome resistance wire (powered with a variac).

(d)   *Platinum wire, quartz, or asbestos fiber.* An imperfect seal (5) can be created between the fiber or wire and the glass body of the RE. This serves as a leak through which the filling solution can interact with the electrolyte of the electrochemical cell. This type of junction is shown in Figure 4.3D.

(e)   *Cracked glass bead.* Fusing a glass bead to a hole in a glass RE body using a torch, and then initiating a crack at the interface, will create a cracked glass bead junction. This type of junction is shown in Figure 4.2E.

(f)   *Luggin capillary.* A Luggin capillary, shown in Figure 4.2F, can be constructed by pulling a fine capillary at the end of a glass electrode body. The diameter of the capillary will determine how fast the filling solution leaks out of the RE.

4.2.3.1   Sealing junctions to the RE body with heat shrink tubing

Heat shrink tubing can be recovered to its minimum diameter through the careful exposure to heat. This can be accomplished with an oven, hot air gun, or a coil of nichrome wire. Care must be taken so that the filling solution is not heated excessively as localized boiling could occur, creating high pressure inside the electrode. Excessive heat can also cause the heat shrink to become brittle, or melt the frit, closing the pores and destroying its functionality. Several types of heat shrink tubing that are commercially available are listed in Table 4.3, and methods to apply heat to shrink the tubing are shown in Figure 4.3.

4.2.4   Active component of RE

The active component of an RE defines the baseline potential that is developed by the RE. The details of this RE component are illustrated in Figure 4.4 and are discussed in the following sections of this chapter.

Table 4.3

Heat shrink recovery data

Heat shrink polymer		Recovery temperature ± 5% (°C)
Teflon® (6)	PTFE	340
	FEP	190
Fluoroelastomer (7)	Viton®	175
Polyolefin (6)	Polyolefin	100
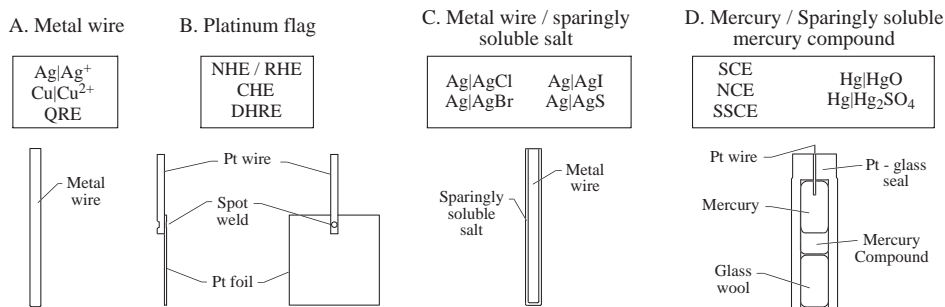
Figure 4.4   Reference electrode active component: (A) metal wire; (B) platinum flag; (C) metal wire/sparingly soluble salt; (D) mercury/sparingly soluble mercury compound.

4.3 ELECTRODE DETAILS AND FABRICATION

4.3.1 Hydrogen electrodes

Controlling redox process:

$$2H^+ + 2e^- \rightleftharpoons H_2, \quad E^\circ_{Pt|H_2,H^+} = 0.0000V$$
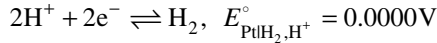
The Normal Hydrogen Electrode (NHE) or Standard Hydrogen Electrode (SHE) is the standard reference point for standard electrochemical reduction potentials, with its potential, E°, assigned as 0.0000 volts (V) at all temperatures by convention. By definition, the hydrogen must be at 1 atm pressure and the activity of hydronium ions equal to 1. These requirements are difficult to attain experimentally, and lower concentrations of acid are often used, as well as a slightly higher pressure of hydrogen gas, due to experimental necessity. As such, the hydrogen RE deviates from the defined potential of 0.0000 V, but is calculable using the Nernst equation, expressed in the following form:

$$E_{Pt|H_2,H^+} = E^\circ_{Pt|H_2,H^+} + \frac{RT}{F} \ln \frac{a_H}{\sqrt{p_{H_2}}} \qquad (4.1)$$

$$p_{H_2} = P_{barometric} - P_{H_2O} + (4.2 \times 10^{-5})h \qquad (8) \qquad (4.2)$$

where h is the depth of delivery of the H_2 supply to solution (in mm), $P_{barometric}$ the barometric (atmospheric) pressure (in atm), and P_{H_2O} the partial pressure of water vapor that can be estimated for dilute solutions as the same as pure water. Values are listed in Table 4.4.

4.3.1.1 *Active component for hydrogen electrodes*

The active body of an NHE is typically a platinized platinum foil, but it can be any material that catalyzes hydrogen. Other alternatives include platinized gold foil, palladized gold, or platinum foils. Palladium is sometimes used for the catalyst due to the increased ability of hydrogen to permeate into bulk palladium compared with platinum. This can be advantageous since palladium can be presaturated with hydrogen prior to measurement, removing the need for a hydrogen gas supply. Unplatinized platinum surfaces can be used, but they remain active only for a short duration, typically a few hours. The platinum deposit should not be too heavy, otherwise a sluggish electrode will result (10).

Table 4.4

Partial pressure of water vapor from 0 to 100 °C (9)

t (°C)	P_{H_2O} (atm)	t (°C)	P_{H_2O} (atm)	t (°C)	P_{H_2O} (atm)
0	6.0330×10^{-3}	30	4.1900×10^{-2}	70	0.30768
10	1.2120×10^{-2}	40	7.2849×10^{-2}	80	0.46754
20	2.3082×10^{-2}	50	0.12183	90	0.69200
25	3.1276×10^{-2}	60	0.19671	100	1

$P_{H_2O} = (1 \times 10^{-8})t^4 - (3 \times 10^{-7})t^3 + (4 \times 10^{-5})t^2 + (1 \times 10^{-4})t + 7 \times 10^{-3}$.

Table 4.5

Platinization recipes

	I	II	III
Chloroplatinic acid	0.072 M (3.5%)	0.072 M (3.5%)	0.042 M (2%)
Lead acetate trihydrate	1.3×10^{-4} M (0.005%)	1.3×10^{-4} M (0.005%)	–
Hydrochloric acid	–	2 M	2 M
Current density (mA/cm^2)	30	30	10–20
Deposition time (min)	5	5	10–20
Deposit color	Very black	Very black	Light gray to golden
Reference	Bates (13)	Feltham and Spiro (14)	Hill and Ives (15)

Note: Stirring is required for all recipes.

(a) Electrode preparation

Cleaning a platinum substrate (11). The platinum substrate is soaked in 50% aqua regia (1:3 concentrated HNO_3 + HCl) for several minutes, and then rinsed in distilled water. Next, it is placed in concentrated nitric acid for several minutes, and then again washed in distilled water. Just prior to platinization, the platinum substrate is cycled between -1.0 and 0 V (vs. NHE) in dilute sulfuric acid (~0.1 M).

   Platinizing substrate. Several methods are available for platinization of electrodes. The first two include lead in the recipe, the addition of which serves as an additive that leads to a blacker deposit, and allows for good adhesion to the substrate. If lead in the deposit is a problem, it can be removed (12) by soaking in an aerated 1 M perchloric acid solution for 24 h. The last method does not contain lead, and results in a gray to golden deposit. Any of the three methods listed in Table 4.5 are acceptable for hydrogen electrode fabrication.

(b) Storage

Platinized electrodes should be stored in distilled water and not left to sit in air as this quickly destroys the catalytic activity and necessitates replatinization.

(c) Renewal

Platinized electrodes can be renewed by removal of previous platinization with 50% aqua regia, followed by cleaning and fresh platinization as described above.

4.3.1.2   *H₂ purification and presaturation (16)*

The purity of the hydrogen supply will affect the potential of the electrode by poisoning the catalyst sites (CO and CO_2) or changing the reactions taking place at the catalyst (O_2). Purification of an H_2 supply can be accomplished with a series of filters, including O_2 and CO_2 removal. A particle filter should also be included in the purification train.

(a) O_2 removal

Recombination catalyst. A recombination catalyst is used to recombine O_2 impurities with H_2 to form H_2O. One example is the platinum catalyst that operates at room temperature and is available commercially.

A. Sacrificial reduced metal (16)

C. Presaturation
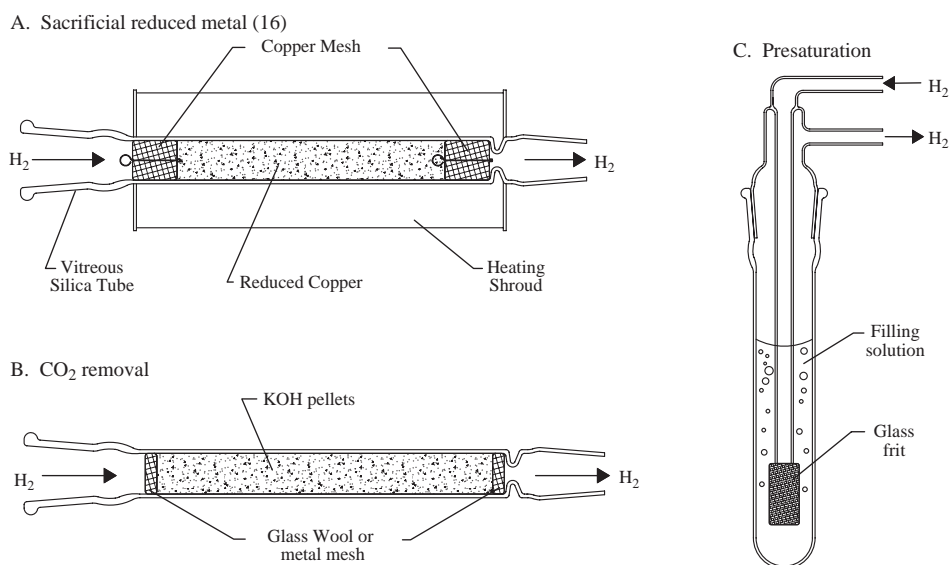
B. CO_2 removal

Figure 4.5 H_2 purification and presaturation: (A) sacrificial reduced metal (16); (B) CO_2 removal; (C) presaturation.

Sacrificial reduced metal. A sacrificial metal filler is oxidized in the presence of oxygen, trapping the O_2 as a solid metal oxide. Typically, these must be operated at higher temperatures to promote faster kinetics, such as reduced copper that requires an operating temperature of between 450 and 700 °C. An example configuration is shown in Figure 4.5A.

(b) CO_2 removal

The removal of CO_2 from an H_2 gas stream can be accomplished with a glass tube packed with KOH pellets, as shown in Figure 4.5B. This works best if used after a recombination-type O_2 removal system because the H_2O present in the effluent increases the solubility of CO_2 into the thin layer of water on the KOH pellets.

(c)   Presaturation

If dry H_2 is used for an RE, the bubbling gas will slowly increase the concentration of the electrolyte due to the H_2O that is dissolved in the exiting H_2 stream. To minimize this, the H_2 gas stream can be presaturated prior to introduction into the RE by bubbling it through a chamber filled with the same electrolyte as that in the electrode, as shown in Figure 4.5C.

4.3.1.3   *Normal Hydrogen Electrode (NHE) and Reversible Hydrogen Electrode (RHE)*

(a)   Filling solutions

NHE. By definition, the NHE should have a hydronium ion activity of unity, and a partial pressure of hydrogen gas of 1 atm. Being experimentally difficult to attain, other concentrations and pressures are typically used, and the potential is corrected for these conditions using the equations listed above. Table 4.6 lists the activity of H^+ for dilute HCl solutions at 25 ºC.

Table 4.6

Mean molal activity coefficients of $HCl_{(aq)}$ at 25 ºC (20)

m_{HCl} (mol/kg)	$\gamma_{\pm}$	a_{H^+}	b_{HCl} (mol/kg)	$\gamma_{\pm}$	a_{H^+}
0.001	0.9650	9.650×10^{-4}	0.005	0.9280	4.640×10^{-3}
0.002	0.9519	1.904×10^{-3}	0.010	0.9040	9.040×10^{-3}
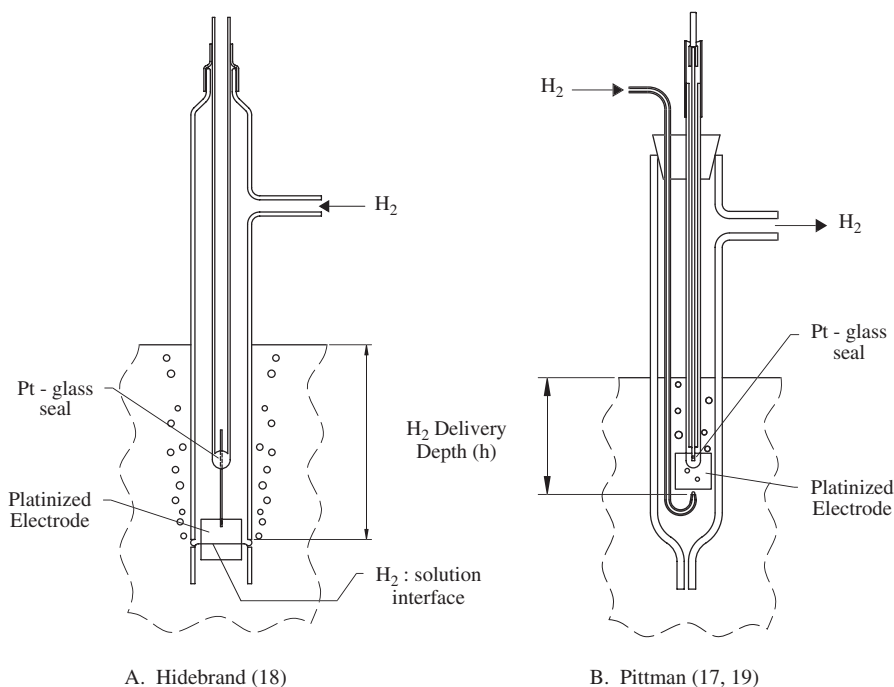
Figure 4.6 Normal Hydrogen Electrode and Reversible Hydrogen Electrode designs (17): (A) Hildebrand (18); (B) Pittman (17, 19).

RHE. The RHE is assembled directly in an electrochemical cell, with the electrolyte in the cell as the RE filling solution. This necessitates the calculation of the potential from the Nernst equation using the pH of the cell solution and the applied H_2 partial pressure (Figure 4.6).

4.3.1.4   *Convenient Hydrogen (CHE)/Self-Contained Hydrogen (SCHE) Electrodes*

The Convenient Hydrogen Electrode (21) (CHE) or the Self-Contained Hydrogen Electrode (22) (SCHE) is an RE with a hydrogen bubble contained within the electrode body that replaces the hydrogen gas supply required for typical hydrogen REs. The thin layer of solution drawn by capillary action onto the platinized electrode surface quickly
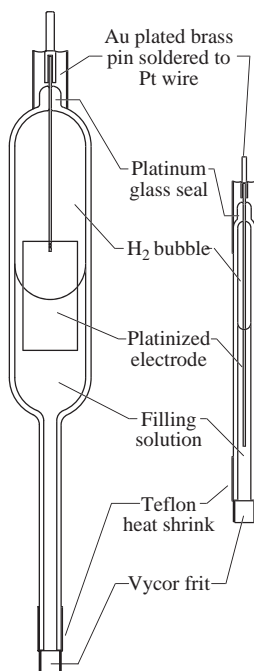
Figure 4.7   Convenient Hydrogen Electrode.

saturates the active surface of the electrode with H_2, mimicking the action of bubbling gas near an electrode in the NHE. This electrode is stable for several weeks and is easily refilled with hydrogen. This electrode makes no effort to exclude oxygen, so the potential will deviate several millivolts from the NHE, requiring calibration with another RE. This electrode is very useful for studies in acids, especially fuel cell studies, where counter ions such as chloride can poison the catalyst being studied. One key advantage of a CHE is that its size can be tailored to meet experimental requirements. The H_2 can either be electrolytically generated within the electrode or filled from an external H_2 gas supply. Two different CHE electrodes are shown in Figure 4.7.

(a) Electrode preparation
     Platinization. Platinization should be carried out as described for the NHE, producing a light gray platinized surface.
(b) Filling solution (other filling solutions possible)
         0.05–0.5 M H_2SO_4.
         0.1–1 M NaOH.
         Works best between pH 0–2 and 12–14; other pHs may need to be buffered to increase the current sink/source capability of the RE.
(c) H_2 filling
     Hydrogen can be bubbled into the electrode with a Teflon or glass tube connected to an H_2 gas supply. Alternatively, making the CHE negative with respect to an

inert counter electrode (CE) can generate H_2, taking care that the CE is sufficiently separated from the CHE so as to prevent excess O_2 from entering the electrode body. During electrolytic hydrogen generation, any restrictive junction must be removed from the electrode, due to the possibility of dangerous pressures being created by the generation of gas in a confined space.

(d) Junction exceptions

In some experimental situations, no junction is used, especially with microscale REs (μREs). When using the CHE in alkaline solutions of pH $>$ 8, a VYCOR® frit cannot be used, as it will dissolve.

4.3.1.5 Dynamic Hydrogen Reference Electrode (DHRE)

The Dynamic Hydrogen Reference Electrode (23) (DHRE) functions by producing H_2 and O_2 at a pair of electrodes, using the H_2-producing electrode as a reference potential. This potential will deviate from the NHE due to the overpotential applied for the H_2 generation. The electrode pair is vertically separated (1 cm) with the upper electrode producing O_2 (positive) with respect to the lower H_2-producing electrode. The H_2-producing electrode is typically platinized, to reduce the overpotential required to produce a stable potential. The electrodes can be microfabricated so long as the electrodes are separated sufficiently to prevent diffusion of O_2 from one electrode to the H_2-producing electrode within the experimental time frame. One type of DHRE is shown in Figure 4.8.
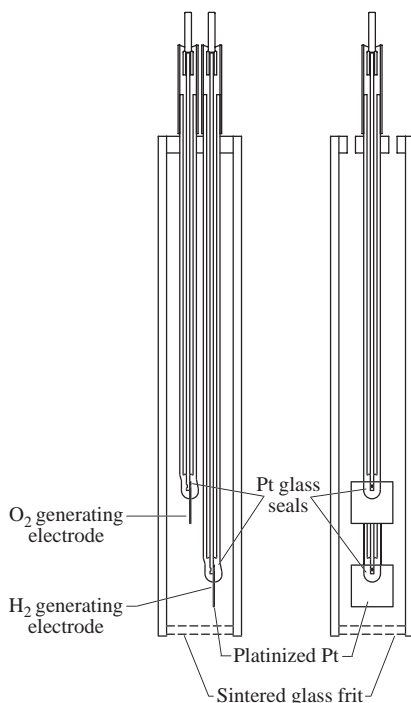
Figure 4.8 Dynamic Hydrogen Electrode.

A. Power supply I   B. Power supply II
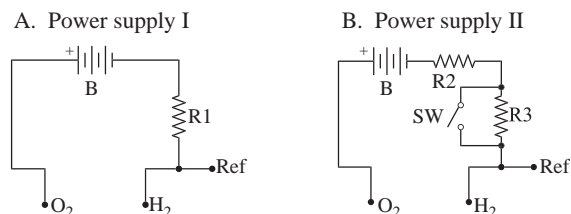
Example values for a 1cm^2 surface area electrode:
B=45V, R1=45kΩ, R2=5kΩ, R3=40kΩ

Figure 4.9   DHRE power supply circuits: (A) power supply I; (B) power supply II.

(a)   *Active components.* Two electrodes are required for this RE. The H_2-generating elec-
      trode should be platinized platinum, and the O_2 can be any inert electrode, but is
      often platinum. These electrodes can be reduced in size from the macroscale 1 cm^2
      platinum flag electrodes to UMEs. Care must be taken so that the O_2 generated does
      not readily diffuse to the H_2 electrode, otherwise the potential will change.
(b)   *Platinization.* Platinization should be carried out as with the NHE to produce either
      a thin light gray coating or a thick black coating.
(c)   *Power circuit.* The DHRE requires a constant-current power supply to support the
      electrolysis of both O_2 and H_2. Care should be taken that the current does not devi-
      ate during the experiment, otherwise the reference potential will drift. A stable DC
      power supply capable of delivering 1–10 mA/cm^2 of constant current (see below)
      should be used to prevent drift. With a 1 mA/cm^2 current source (Figure 4.9A), the
      potential should stabilize after approximately 20 min to the H_2 reference potential.
      To reduce the time required for stabilization, a switch can be used (Figure 4.9B) that
      first supplies 10 mA/cm^2 current for 10 min, and then can be switched to 1 mA/cm^2
      current for constant operation during the electrochemical experiment.

4.3.2   Mercury electrodes (24)

Mercury REs are formed with mercury in its purified, liquid form, along with a spar-
ingly soluble mercury salt (i.e., mercury(I) chloride, mercury(I) sulfate, or mercury(II)
oxide). Because mercury is easy to purify through distillation, it is easy to reuse and
forms a consistent surface, adding to the ability to create REs repeatedly. Due to envi-
ronmental concerns, mercury electrodes are less favored today. Two modern styles of
mercury REs are shown in Figure 4.10.

(a)   Hg purification
      Mercury is available in >99.9999% purity levels commercially, removing the need
      for purification in the laboratory as was required in the past.
(b)   Glass considerations
      The glass in the mercury-containing portion of the RE should be made hydrophobic,
      thus eliminating solvent entrapment on the sides of the mercury and the possibility of

A. Larger volume mercury pool; must be rigidly held for stable potential

B. Smaller volume mercury pool; less sensitive to electrode movement

Filling ports with caps

Teflon cap/ active electrode holder

Excess electrolyte crystals (e.g. KCl)

Filling solution

Filling port with cap

Mercury Compound (e.g. calomel)

Active Electrode (described below)

Hg

Glass body

Pt-glass seal

Filling solution

Vycor frit with Teflon heat shrink (shown) or Ceramic frit sealed into glass

Glass body

Ceramic frit sealed into glass (shown) or Vycor frit with Teflon heat shrink

Figure 4.10   Basic Mercury Reference Electrode designs: (A) larger volume mercury pool, must be rigidly held for subtle potential; (B) smaller volume mercury pool, less sensitive to electrode movement.

producing a sluggish or erratic RE. This treatment can cause problems with a platinum glass seal requiring an alternate electrode design or in the least care should be taken so that the glass in the vicinity of the platinum wire or at a Pt/glass seal is not treated.

Hydrophobic glass treatment. Clean dry glass should be heated to 100 °C, before being filled with 1% Dow-Corning Silicone Fluid No. 200 in CCl_4. The glass should then be emptied, drained, and baked at 300 °C for 2 h, before being thoroughly extracted with CCl_4 to remove any unbonded silicone (25). Other commercial treatment procedures are available.

4.3.2.1   Saturated Calomel Electrode (SCE)

Controlling redox process:

$$Hg_2Cl_2 + 2e^- \rightleftharpoons 2Hg + Cl^-, \quad E^\circ_{Hg|Hg_2Cl_2} = 0.268V \text{ versus NHE (25°C)}$$

Mercury|mercury(I) chloride (*also mercurous chloride or calomel*), abbreviated as Saturated Calomel Electrode (SCE), is the most widely used mercury RE (26). The preparation of this electrode, especially the purity of the mercury and the method of addition of mercury(I) chloride to the mercury, strongly affects the performance and potential exhibited. This RE can be very reproducible if produced and handled carefully. The potential of

the mercury(I) chloride RE is defined by the chloride concentration in the filling solution, and can be calculated as shown below:

$$E_{Hg|Hg_2Cl_2} = E^{\circ}_{Hg|Hg_2Cl_2} - \frac{RT}{F} \ln a_{Cl^-} \tag{4.3}$$

This electrode displays hysteresis upon heating and cooling (27), and it is not recommended that the electrode be used above 70 °C. Temperature effects are discussed in Section 4.8.1.3.

(a) Electrode preparation
Mercury preparation. No special preparative steps are required if mercury of sufficient purity is used.

Hg_2Cl_2 preparation. High-purity Hg_2Cl_2 is available commercially, or it can be produced by chemical precipitation as described below. The Hg_2Cl_2 must be a finely divided powder (0.1–5 μm) to produce a well-behaved RE.

Hg|Hg_2Cl_2 electrode preparation (see Figure 4.11). Method I (28). On adding the Hg_2Cl_2 to the dry mercury; it will rapidly form a pearly skin on the surface. Once the surface is completely covered, the addition of Hg_2Cl_2 is stopped, otherwise the electrode will be sluggish. This interface must be prepared prior to the introduction of filling solution for a stable potential to develop.

Method II (29). Hg and Hg_2Cl_2 should be ground together with a few drops of KCl filling solution using a mortar and pestle to form a paste. The paste should be placed in the tube, in direct contact with the Pt wire. About 1 cm thick paste should be used.

(b) Filling solution
SCE—saturated KCl.
SSCE—saturated NaCl.
NCE—1N KCl.
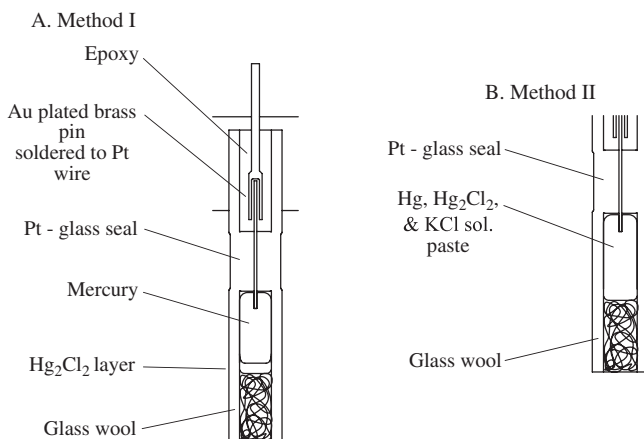
Figure 4.11   SCE active electrode body: (A) method I; (B) method II.

(c) Hg$_2$Cl$_2$ preparation

Chemical precipitation (30). About 1 g of reagent-grade mercury(I) nitrate dihydrate, Hg$_2$(NO$_3$)$_2$ 2H$_2$O, should be mixed with 200 µl of concentrated nitric acid and ~20 ml of water. Add this solution dropwise for 2 min into a covered beaker containing approximately 100 ml of 0.1 M HCl, using a magnetic stir bar to continuously stir the solution. After the addition is completed, stir the suspension for an additional hour. Allow the precipitate to settle, decant the supernatant solution, and repeat this twice to completely rinse the precipitate. Filter the precipitated mercury(I) chloride with a sintered glass crucible, rinsing quickly with four portions of cold distilled water, and then transfer it to a vacuum desiccator. It is important that the HCl used be free from traces of other halogens, otherwise the mercury(I) chloride produced will be contaminated with other mercury(I) halides, resulting in an RE with a mixed potential.

Electrochemical production. Electrochemically prepared Hg$_2$Cl$_2$ can be produced (30) in a similar fashion as HgSO$_4$ described in the next section, but it is less stable than chemically precipitated material and therefore its preparation is not discussed further.

4.3.2.2 Mercury Sulfate Reference Electrode (MSRE)

Controlling redox process:

$$Hg_2SO_4 + 2e^- \rightleftharpoons 2Hg + SO_4^{2-}, \quad E^\circ_{Hg|HgSO_4} = 0.615V \text{ versus NHE } (25°C)$$

Mercury|mercury(I) sulfate (*also mercurous sulfate*), abbreviated as Mercury Sulfate Reference Electrode (MSRE), is the second (26) most used mercury RE after SCE. The construction of the MSRE is similar to that of the SCE, although it is less sensitive to the purity of the mercury. The reproducibility (31) of the MSRE is second only to the NHE, and given the absence of chloride ion in the construction of the MSRE, it has found use in systems with sensitivity to chloride content. The reference potential of the MSRE is calculated as follows:

$$E_{Hg|HgSO_4} = E^\circ_{Hg|HgSO_4} - \frac{RT}{F} \ln a_{SO_4^{2-}} \tag{4.4}$$

(a) Electrode preparation

Mercury preparation. No special preparative steps are required if mercury of sufficient purity is used (31).

Hg$_2$SO$_4$ preparation. High-purity Hg$_2$SO$_4$ is available commercially, can be produced electrochemically, or by chemical precipitation as described below.

Hg|Hg$_2$SO$_4$ electrode preparation (32) (Figures 4.12 and 4.13). Approximately 2.5 mm thick layer of Hg$_2$SO$_4$ should be coated on the mercury before flushing out the assembly five times with the filling solution. To equilibrate, the RE should sit overnight in fresh filling solution.

(b) Filling solution.

Saturated K$_2$SO$_4$ or $\geq$1 M H$_2$SO$_4$—dilute solutions exhibit poor reversibility (33).

(c) Mercury(I) sulfate production (32, 34)

Mercury(I) sulfate must be prepared, washed, and stored in acid as hydrolysis occurs in neutral solutions. The details for its preparation are described below.
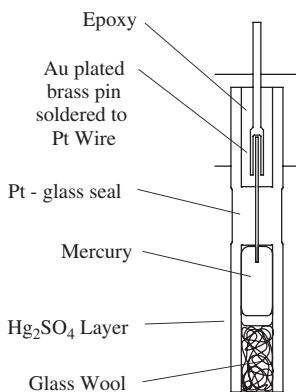
Figure 4.12   MSRE active electrode body.
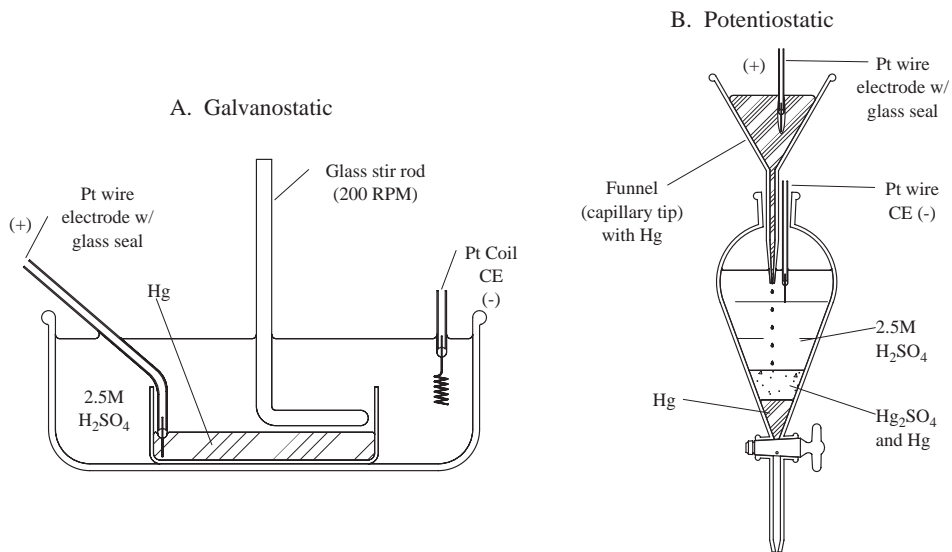
Figure 4.13   Electrochemical Hg_2SO_4 preparation: (A) galvanostatic; (B) potentiostatic.

Electrochemical preparation. Galvanostatic (see Figure 4.13A). Mercury can be oxidized in 2.5 M H_2SO_4 by applying a current density of 40 mA/cm^2 between an Hg pool electrode and a platinum coil CE. The setup, depicted in Figure 4.13A, consists of a glass stirrer that is positioned so as to not agitate the Hg pool electrode, but to keep the Hg_2SO_4 in suspension and allow for mixing. This method will produce 1–1.2 g of Hg_2SO_4 per cm^3 Hg. The Hg_2SO_4 is gray and contains finely divided mercury.

Potentiostatic (see Figure 4.13B). Mercury can also be oxidized using a dropping Hg electrode created by employing a funnel filled with Hg. As shown in Figure 4.13B, the Hg is dropped into 2.5 M H_2SO_4 at an applied potential of 2 V. The Hg_2SO_4 produced is gray and contains finely divided mercury as above.

Chemical precipitation. Mercury(I) sulfate can be prepared in a similar fashion as mercury(I) chloride (31). First, about 1 g of reagent-grade mercury(I) nitrate dihydrate, $Hg_2(NO_3)_2$ $2H_2O$, is moistened with 200 μl of concentrated nitric acid and dissolved in 20 ml of water. This solution is then added dropwise for 2 min into a covered beaker containing approximately 100 ml of 1 M H_2SO_4 while using a magnetic stir bar to continuously stir the solution. After addition, the suspension should be stirred for an hour. The precipitated mercury(I) sulfate is rinsed in a sintered glass crucible with ample cold 1 M H_2SO_4, and then stored in ≥1 M H_2SO_4, protected from light. Chemically precipitated mercury(I) sulfate can be recrystallized (35) by first dissolving the Hg_2SO_4 in concentrated sulfuric acid in the presence of Hg. This solution is then added dropwise to an excess of absolute methanol causing the mercury(I) sulfate to precipitate. The mercury(I) sulfate that is precipitated is white. The precipitate is washed 20 times employing decantation. Again, the Hg_2SO_4 should be stored in ≥1 M H_2SO_4 and protected from light.

4.3.2.3 *Mercury(II) oxide reference electrode (Hg|HgO)*

Controlling redox process (36):

$$HgO + 2e^- + H_2O \rightleftharpoons Hg + 2OH^-, \quad E^\circ_{Hg|HgO} = 0.098V \text{ versus NHE (25°C)}$$

The mercury(II) oxide (mercuric oxide) RE is limited to use in highly alkaline solutions due to the stability of the oxide. While mercury(II) oxide is the only stable oxide, it can exist as either red or yellow powders that differ in solubility (37). The potential of the mercury(II) oxide RE is independent of the electrolyte, but depends on the activities of both OH^- and H_2O (36). The potential can be calculated as follows (36):

$$E_{Hg|HgO} = E^\circ_{Hg|HgO} - \frac{RT}{F} \ln \frac{a_{OH^-}}{\sqrt{a_{H_2O}}} \tag{4.5}$$

This electrode is stable for several days and reproducible to ±0.1 mV (38).

(a) Electrode Preparation
    Mercury Preparation. No special preparative steps are required if mercury of sufficient purity is used.
        HgO preparation. Method I. Either high-purity mercury(II) oxide (available to 99.999% purity commercially) or reagent-grade mercury(II) oxide that is thoroughly extracted with water on a steam bath (39) can be used. *Note*: Yellow oxide will equilibrate more slowly than red oxide.
        Method II (39). The mercury(II) oxide can also be produced by the ignition of mercury(II) nitrate that has been carefully crystallized. The mercury(II) oxide must be washed before use.
        Hg|HgO electrode preparation (39) (see Figure 4.14). The RE is assembled similarly to the SCE but with an alkaline solution, typically saturated $Ca(OH)_2$, as the filling solution.
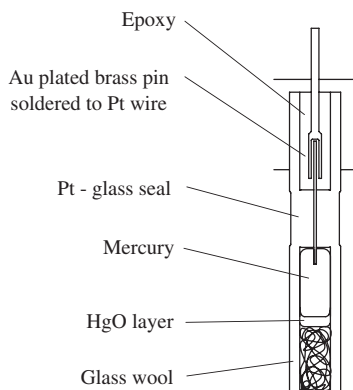
Figure 4.14   Hg|HgO active electrode body.

(b)   Filling solution
      Saturated Ca(OH)$_2$.

4.3.3   Silver electrodes

4.3.3.1   Silver/silver chloride reference electrode (Ag|AgCl)

Controlling redox process:

$$AgCl + e^- \rightleftharpoons Ag + Cl^-, \quad E^\circ_{Ag|AgCl} = 0.222\,V \text{ versus NHE } (25\,°C)$$

The silver–silver chloride RE is the most regularly used RE due to its simplicity, inexpensive design, and nontoxic components (40). The simplicity of the Ag|AgCl RE lends itself to microfabrication as well as incorporation into sensors. The potential is calculated as follows:

$$E_{Ag|AgCl} = E^\circ_{Ag|AgCl} - \frac{RT}{F} \ln a_{Cl^-} \tag{4.6}$$

(a)   Electrode preparation (Figure 4.15)
      High-purity silver wire (>99.999% Ag) preparation. High-purity silver wire will have an oxide on its surface that must be removed before use. This can be accomplished by dipping (41) the wire in 0.1 M HNO$_3$ for a few seconds. The wire should be rinsed with 18 MΩ cm water prior to use in subsequent steps.
      Anodic AgCl coating (42). The freshly cleaned silver wire can be chloridized by placing it in a compartmentalized cell containing 0.1–1 M HCl or KCl and applying 0.4 mA/cm^2 current for 30 min. The coated wire should be washed with 18 MΩ cm water and soaked for 1–2 days in 18 MΩ cm water. The color of the AgCl should be sepia (dark brown with a reddish tint) if chloridized in the absence of light or pale tan to brown if chloridized while exposed to a light source. After washing, the coating color will range from pink to a shade of plum.
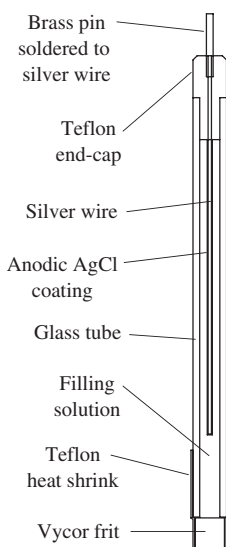
Figure 4.15   Ag|AgCl electrode.

(b)   Filling solution
      KCl—saturated, 3.5 M, 3 M.
      NaCl—saturated, 3.5 M, 3 M HCl—dilute.
      Saturated KCl should be presaturated with AgCl due to higher solubility of AgCl (43).

4.3.3.2   *Silver/silver cation reference electrode (Ag|Ag$^+$)*

Controlling redox process:

$$\text{Ag}^+ + \text{e}^- \rightleftharpoons \text{Ag}, \quad E^{\circ}_{\text{Ag|Ag}^+} = 0.799\text{V versus NHE (25°C)}$$
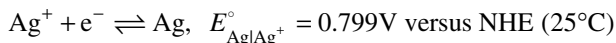
This RE is typically used as a nonaqueous RE with AgNO$_3$ and a supporting electrolyte dissolved in MeCN or other organic solvents as the filling solution. The potential can be calculated as follows (44):

$$E_{\text{Ag|Ag}^+} = E^{\circ}_{\text{Ag|Ag}^+} + \frac{RT}{F} \ln \alpha_{\text{Ag}^+,\text{solv}} m_{\text{Ag}^+} \gamma_{\text{Ag|Ag}^+,\text{solv}} \tag{4.7}$$

where $\alpha_{\text{Ag}^+,\text{solv}}$ is the degree of ionization of Ag in the solvent, m_{Ag^+} the molality of Ag$^+$, and $\gamma_{\text{Ag|Ag}^+,\text{solv}}$ the molal ionic activity coefficient of Ag$^+$ in the solvent.
There may be variability in the potential of the RE prepared with different solvents due to differences in the degree of ionization of the silver ion in each solvent. The potential of a 10 mM AgNO$_3$ in MeCN is reported (45) as 0.3 V versus SCE$_{\text{aq}}$. This RE cannot be used in solvents that are readily oxidized by Ag$^+$ (46).
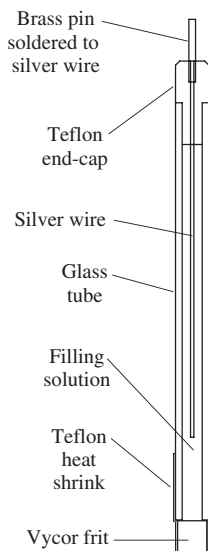
Figure 4.16   Ag|Ag$^+$ electrode.

(a)   Electrode preparation (Figure 4.16)
      High-purity silver wire (>99.999% Ag) preparation. See Ag|AgCl preparation
      procedure.
(b)   Filling solution
      A range of filling solutions is used with the Ag|Ag$^+$ RE. Typical solutions are listed
      below:
          Silver ion source: 10 mM or 0.1 M AgNO$_3$.
          Solvents: acetonitrile, propylene carbonate, dimethyl formamide, or dimethyl
          sulfoxide.
          Supporting electrolyte: 0.1 M tetrabutylammonium perchlorate (TBAP), or same
          as that used in electrochemical cell.

4.3.4   Quasi-reference electrodes (QRE)

A quasi-reference electrode (QRE) is a general phrase for any poorly defined or unpoised
RE. A QRE typically consists of an inert metal wire such as platinum or gold. A silver
wire can also be used, so long as silver ions do not interfere with the measurements. The
potential should ideally be steady, but the actual potential is not predictable if it is
unpoised. Some methods to circumvent the ill-defined potential are to compare the
potential to a conventional RE, or to include an electrochemical couple as an internal
standard (see Section 4.6.2). A QRE is a low-impedance RE, but is also a polarizable
electrode.

4.4   JUNCTIONS

As previously mentioned, the primary task of the junction on an RE is to separate the filling solution of the RE from the electrolyte of the electrochemical cell. If the two solutions being separated contain either electrolytes with different mobilities, or the same electrolyte in different solvents, a junction potential will develop. The potential drop (ΔV) that is developed across the junction is the product of the impedance (Z) of the junction and the ion flux (or current, i) that flows through it, according to Ohms Law ($\Delta V = iZ$). Experimentally, it is best to minimize the junction potential, and to ensure that it remains constant during any experiment. The current that the RE experiences is typically limited by the potentiostat input impedance in its electrometer and is typically beyond the control of the experimenter. Additionally, the impedance of the junction is controlled by the pore size and density of the material as well as the nature of the electrolytes on either side of the junction. To minimize the potential drop for any given junction, the electrolytes on either side should have similar ionic mobilities, which are listed in Table 4.7.

When using a high-flow rate junction, the impedance is effectively decreased, but the amount of filling solution that can interact with the sample increases, requiring careful design, and sometimes a compromise. Some data on common frit materials are shown in Table 4.8.

4.4.1   Filling solutions

When choosing (54) a filling solution for an RE, several factors must be considered. The filling solution should not react with any species in the electrochemical cell, or interfere with the measurement in any way. While difficult to do in highly acidic or basic solution due to the high mobilities of hydroxyl and hydronium ions, it is best to match the

Table 4.7

Ionic mobilities of various ions calculated for infinite dilution at 25 °C (47)

Cations	Mobility ($cm^2/(V\ sec)$)	Anions	Mobility ($cm^2/(V\ sec)$)
H^+	3.625×10^{-3}	OH^-	2.05×10^{-3}
K^+	7.619×10^{-4}	Cl^-	7.912×10^{-4}
Na^+	5.193×10^{-4}	Br^-	8.13×10^{-4}
Li^+	4.010×10^{-4}	I^-	7.96×10^{-4}
NH_4^+	7.61×10^{-4}	NO_3^-	7.404×10^{-4}
$1/2\ Ca^{2+}$	6.166×10^{-4}	OAc^-	4.24×10^{-4}
		ClO_4^-	7.05×10^{-4}
		$1/2\ SO_4^{2-}$	8.27×10^{-4}
		HCO_3^-	4.610×10^{-4}
		$1/3\ Fe(CN)_6^{3-}$	1.047×10^{-3}
		$1/4\ Fe(CN)_6^{4-}$	1.145×10^{-3}

Note: The mobility is the limiting velocity of the ion in an electric field of unit strength (48).

Table 4.8

Common frit materials

Type	Pore size	Impedance (saturated KCl)	Leak rate[a] (μl/h)	Compatibility issues
Vycor (49, 50)	4 nm	500 Ω	Modest	Not compatible with strong bases, HF
Polyethylene (51)	–	–	–	Used in strongly basic solutions
Ceramic (52)	–	1000 Ω	3–30	Can be used in strong bases; avoid precipitates and colloids
Ceramic/ conductive polymer (53) composite	Pores filled with conductive polymer	500 Ω– 2.7 kΩ	7.4×10^{-4} to 5.7×10^{-5}	Resistant to strong acids, alkalis, and organic solvents

[a]The leak rate is dependent on several factors in addition to the porosity of the junction, including the height of solution over the frit, the pressure on this solution, as well as the depth that the junction is immersed and the pressure on that solution.

mobilities of anionic and cationic species, minimizing the junction potential. Due to the difficulty in balancing all these parameters, it is sometimes necessary to use a salt bridge or a double-junction RE, minimizing both electrolyte interactions and the potential across the junctions.

4.4.2   Salt bridges

Salt bridges are used to both minimize and stabilize the junction potential between solutions of different compositions as well as minimizing any cross-contamination between solutions. One vital consideration in setting up a salt bridge between different solvents is ensuring that the electrolyte in the bridge is soluble in both and interferes with species in neither. Typical electrolytes (55) for salt bridges include KNO_3, KCl, $NaSO_4$, and NH_4NO_3. In some cases, the electrolyte in a salt bridge is gelled to reduce cross-contamination while maintaining a high conductivity. This is described in more detail below.

(a)   Gelling an electrolyte (56)

   Aqueous. A 4% agar solution can be used to gel an electrolyte by first dissolving the agar in hot water and adding the electrolyte salt. The hot agar solution is then transferred to the target vessel by pouring it, drawing it in with a vacuum, forcing it in with slight backpressure such as with a syringe, or by using pipette. It is extremely important that bubbles are not trapped in the gelled material, creating breaks in the ion flow path. The agar solution is then permitted to cool to room temperature, forming a gel. This procedure is equally useful to gel the electrolyte in an RE, salt bridge, or double-junction RE, but is not recommended for bridging from an aqueous to an organic solution.

   Organic. Methylcellulose can be used as a gelation agent in pyridine and possibly other organic solutions. This is done by adding 5 g of methylcellulose to 100 ml of a 0.5 M solution of $LiClO_4$ in pyridine. This will produce a colorless, transparent, and conductive electrolyte gel.
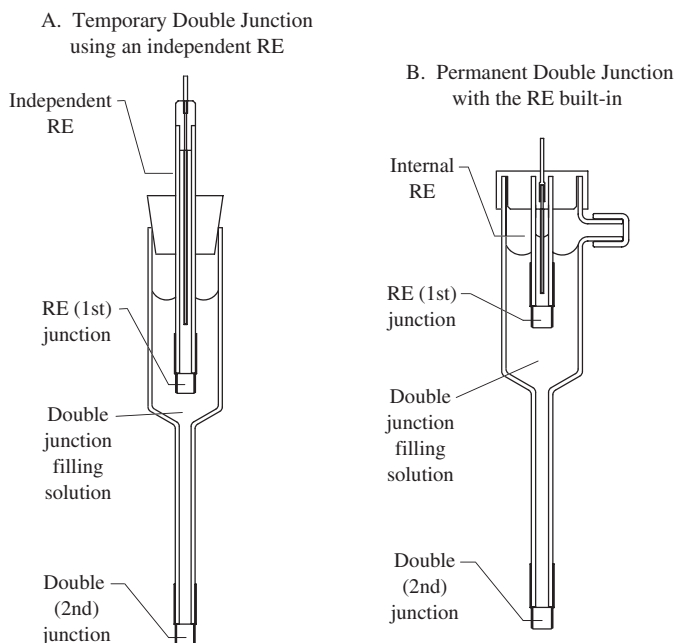
Figure 4.17 Double junctions: (A) temporary double junction using an independent RE; (B) permanent double junction with the RE built-in.

4.4.3 Double-junction reference electrodes

A double-junction RE incorporates a salt bridge into the RE design, typically to improve the compatibility of the electrolytes in the filling solution with those in the electrochemical cell. Chloride-containing electrodes are often isolated from an electrochemical cell due to the contamination and catalyst-poisoning potential of chloride ions. This is easily done using a K_2SO_4 solution between the two junctions. Two types of double junctions are shown in Figure 4.17.

4.4.4 Reference electrode impedance

The impedance of an RE can be measured with any potentiostat with built-in electrochemical impedance spectroscopy (EIS) capabilities or with the addition of a separate frequency response analyzer (FRA). One method is described below.

(a) Measuring the impedance of an RE (57)

   The RE and an inert CE of sufficient size are placed in a beaker containing electrolyte. The RE is connected to the WE terminal of the potentiostat, and the CE is connected to both the RE and the CE terminals. An impedance scan is set up from at least 10 kHz down to 1 Hz, with no DC potential (V_{DC}) applied ($V_{DC} = V_{OCP}$, where V_{OCP} is open circuit potential) and an AC waveform (V_{AC}) of 5–10 mV amplitude.
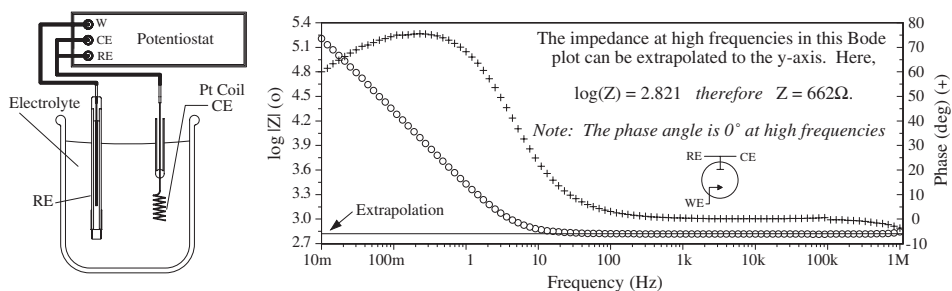
Figure 4.18   Measuring the impedance of a reference electrode.

Caution: If V_{DC} is set to any potential other than the open circuit potential, appreciable current can flow, possibly destroying the RE! The impedance at high frequencies is the impedance of the RE. At these frequencies, there should only be a real component to the impedance, and no imaginary components (the phase angle should be at or near 0°). The interpretation of sample data is shown in Figure 4.18 with a diagram of setup required for this measurement.

4.5 REFERENCE ELECTRODES: NONAQUEOUS SOLVENTS

Nonaqueous solvent systems introduce additional considerations into the process of selecting an RE for electrochemical measurements. There are relatively few REs designed for these systems, with most based on exotic formulations specific to the electrochemical system of study. Due to space constraints, only the Ag|Ag$^+$ RE is described here. In certain circumstances, aqueous REs can be used, but the electrolyte must be soluble in the nonaqueous solvent. In some cases, alternative filling solutions (58) for aqueous Ag|AgCl or SCE REs can be used, such as aqueous lithium chloride or quaternary ammonium chloride. Another possible solution for using an aqueous RE in a nonaqueous solution is through the use of a salt bridge or a double-junction RE. Both tetraethylammonium picrate and tetra-*n*-butylammonium tetraphenylborate ($NBu_4^+BPh_4^-$) are nearly equitransferent in many organic solvents (59) and either can be used within a salt bridge.

One caveat to using aqueous REs in nonaqueous solvents is that the potential measurements carried out cannot be related (59) from solvent to solvent even though the same RE is used. This is due to the difference in junction potentials that exist between systems. The acceptability of various REs in different solvents is summarized in Table 4.9.

As described in Section 4.3.3.2, the Ag|Ag$^+$ RE can be used with a variety of organic solvents. Using the same solvent in the RE filling solution as in the electrochemical cell will minimize the junction potential of the RE. The limitations of this electrode are that only solvents in which a silver salt is soluble and not oxidized by the Ag$^+$ can be used. Similar to the difficulty in comparing potentials between different solvents using aqueous

Table 4.9

Reference electrodes for use in dipolar aprotic solvents (58, 60)

RE	Acetonitrile	Propylene carbonate	Dimethyl formamide	Dimethyl sulfoxide
$Pt\vert H_3O^+, H_2$	S	S	S	NR
$Ag\vert Ag_{solv}^+$	S	S	S	S
$Ag\vert AgCl$	NR	NR	NR	NR
$Ag\vert AgCl\Vert$	S	S	S	S
$Hg\vert Hg_2Cl_2$	NR	NR	NR	NR
$Hg\vert Hg_2Cl_2\Vert$	S	S	S	S
$Li\vert Li(OH_2)_4^+$		S	S	S

S: satisfactory stability and reproducibility; NR: not recommended (unstable and/or not reproducible); the symbol '‖' denotes a salt bridge.
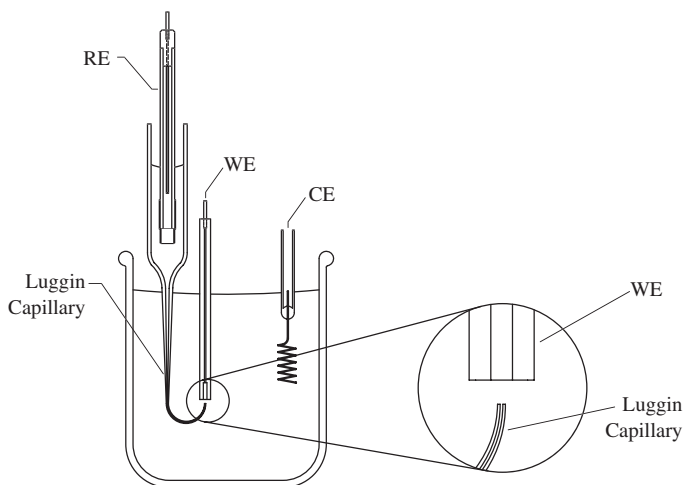
Figure 4.19   Luggin capillary placement.

REs, this RE suffers the same limitation. One solution to this problem is calibration of the RE using internal standards as described in Section 4.6.2. In some cases with nonaqueous solvents, solubility limitations provide reduced conductivity in the electrochemical cell resulting in large uncompensated resistances between the RE and WE. One way to reduce the uncompensated resistance is to use a Luggin capillary to sample the electrochemical cell in the vicinity of the WE by placing the outlet of the Luggin capillary in close proximity to the WE. To prevent shielding of the WE, the minimum distance between the Luggin capillary and the WE should be no closer than two times (61) the diameter of the WE. The placement of the capillary with respect to a WE is shown in Figure 4.19.

4.6 REFERENCE ELECTRODE CALIBRATION

4.6.1 Versus a second reference electrode

The potential of all REs should be checked periodically. This is easily accomplished by using a high-impedance voltmeter and a second RE that is held as a laboratory standard (62), shown in Figure 4.20. This laboratory-standard RE should be a well-behaved RE, such as Ag|AgCl (saturated KCl), and maintained in the laboratory solely for the purpose of calibration. This will prevent any questions as to fouling, clogging, or contamination and will give confidence in the calibrations conducted. To calibrate an RE or check its potential, both the RE in question and the laboratory-standard RE are placed in a common electrolyte of high conductivity (e.g., saturated KCl) that is maintained at a constant temperature. The standard RE is connected to a common meter, and the voltage of the RE in question is read. If the potential takes a long time to settle, the RE must be evaluated and possibly rebuilt, as the junction is likely clogged. An RE evaluated in this way is considered acceptable if its potential is within a few mV of the accepted standard potential. The two electrodes should not be left connected to the voltmeter or the potentiostat, as described below, for any extended duration since to measure the potential, a small, nonzero current must flow.

4.6.2 Using a well-defined redox couple

A well-defined redox couple can be used to calibrate an RE or as an internal standard in electrochemical experiments. The reference redox couple must be stable for the duration of the measurement, and must exhibit a repeatable potential in the system used. A good reference redox couple (63) for nonaqueous, and some carefully controlled aqueous systems, is the ferrocene/ferrocenium (Fc|Fc$^+$) couple at 0.5–10.0 mM concentration. Standard reduction potentials, $E°$, for various solvents (64) are listed in Table 4.10. Other couples can be found in References (64–66).
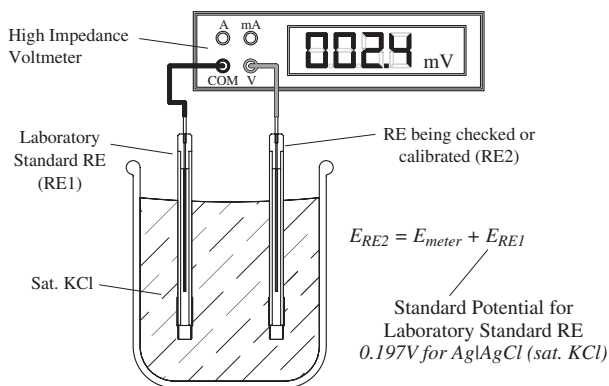
Figure 4.20   Calibration of a reference electrode with a second reference electrode.

Table 4.10

Suggested reference redox systems (65)

Solvent[a]	$E^{\circ}_{Fc|Fc^+,solvent}$ (V versus NHE) (66)
Ferrocene|ferrocenium	
H₂O	0.40
MeCN	0.69
DMF	0.72
Py	0.76
Me₂SO	0.68

Note: Other reference redox systems include: Rb/Rb^+ and $Fe(bpy)_3^{2+}/$ $Fe(bpy)_3^{3+}$ (where bpy: 2,2′-bipyridine).
[a]Unstable in some organics due to decomposition.
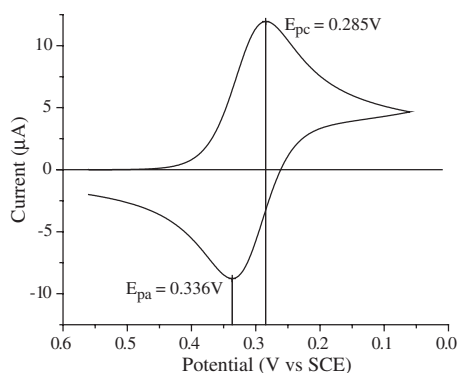
$$E_{1/2} = \frac{E_{pc} + E_{pa}}{2}$$

$$E_{1/2} = \frac{0.285V + 0.336V}{2} = 0.311V$$

Literature Value:

$$Fc^+ + e^- \rightleftharpoons Fc \qquad E^0 = +0.31V \text{ vs } SCE_{aq} \text{ (66)}$$
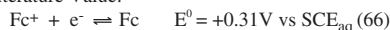
Experimental value is the same as the literature value.

Figure 4.21   Calibration of an RE using a well-defined redox couple (67).

4.6.2.1   Verifying the potential of an RE with a well-defined redox couple

In addition to checking the reference potential with a second RE, an RE can be checked using a well-defined redox couple. This is done by running a cyclic voltammogram (CV) and comparing the $E_{1/2}$ value to that which is expected of the redox couple, as shown in Figure 4.21. As when checking an RE versus a laboratory-standard RE, agreement between calculated and experimental $E_{1/2}$ within a few mV for the reference couple indicates an acceptable RE.

4.6.2.2   Defining potentials with a well-defined redox couple as an internal standard (68)

Internal standards are routinely used in analytical measurements to aid in the quantification of analyte signals in chromatography, or as reference energy standards in NMR. An internal standard can be used in electrochemistry as a reference potential standard in circumstances that an RE alone does not provide an adequately known reference potential in a particular system. This may be the case if a QRE (Section 4.3.4) is used or if large junction potentials are encountered within an electrochemical cell, as with an aqueous RE in a

A

I

add ferrocene

II

-1.6 -1.2 -0.8 -0.4 0.0 0.4 0.8 1.2 1.6
Potential (V vs. Ag|Ag$^+$ *)

* Ag|Ag$^+$ RE (10mM AgNO$_3$
in CH$_3$CN with 0.1M TBAP)

B

$E_{1/2}$=0.089V

II

-1.6 -1.2 -0.8 -0.4 0.0 0.4 0.8 1.2 1.6
Potential (V vs Ag|Ag$^+$ *)

$E_{1/2}$=0.399V

III

-1.6 -1.2 -0.8 -0.4 0.0 0.4 0.8 1.2 1.6
Potential (V vs. SCE)

$E_{1/2}$=0.698V

IV

-1.6 -1.2 -0.8 -0.4 0.0 0.4 0.8 1.2 1.6
Potential (V vs. Cu QRE)

C

II

III

IV

-2.4 -2.0 -1.6 -1.2 -0.8 -0.4 0.0 0.4 0.8 1.2 1.6
Potential (V vs $E_{1/2}$ (Fc/Fc$^+$))
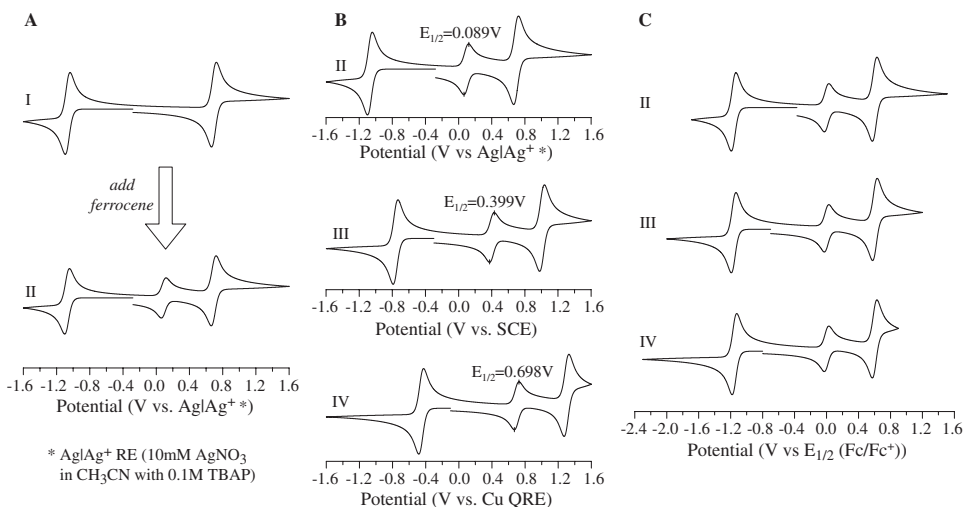
Figure 4.22   (A–C) Calculating a potential scale with an internal standard.

nonaqueous system (Section 4.5). In either case, a well-defined redox couple can be used as an internal standard. The redox potential ($E_{1/2}$) of the internal standard should be well separated from the electrochemical system under study, and should not chemically inter-fere. Care must also be taken that no electrode fouling or inactivation occurs from the use of the internal standard.

Figure 4.22 demonstrates how to calculate a potential scale with an internal standard using a sample system of 5 mM Ru(acac)$_3$ in CH$_3$CN with 0.1 M TBAP as a supporting electrolyte. Initially (Figure 4.22A), a CV is acquired without internal standard (plot I), and then a measured amount of ferrocene is added and an additional CV is collected (plot II). This verifies the sufficient separation between analyte and internal standard peaks, as well as provides a simple way to distinguish which peak belongs to the internal standard. The half-wave potential ($E_{1/2}$) can be calculated for the internal standard as demonstrated in Figure 4.21. This is shown in Figure 4.22B for the same system with ferrocene added as an internal standard versus three different REs. The experimental potential scale can then be adjusted such that the $E_{1/2}$ of the reference couple is used as a 0 V reference point on the potential axis. Figure 4.22C shows the potential scales of each CV normalized to the experimentally determined $E_{1/2}$ value of the ferrocene internal standard, demonstrating that with this technique, the peaks line up regardless of the RE used, so long as the RE is sta-ble for the duration of the experiment.

4.7   MAINTENANCE

All REs need to be rebuilt or regenerated several times during their life, but with care-ful handling and proper storage conditions, the time between rebuilding cycles can be maximized. Even with the utmost care, junctions will clog, current will pass, and filling

solution will become contaminated. This section provides information on proper storage and maintenance of REs.

4.7.1   Storage

The majority of REs should be stored in solutions that are the same as the filling solution (e.g., SCE in saturated KCl). The manufacturers of some specialty REs provide directions with the RE. Storage solutions for REs with nonsaturated filling solutions should be protected from evaporative losses, otherwise the concentration of the filling solution will increase through diffusion with the storage solution. An RE should never be permitted to dry out. Certain REs are light sensitive (Ag|AgCl and MSRE) and should be shielded from light sources for maximum life.

4.7.2   Cleaning junctions

Junctions can become clogged through several means including precipitation within the junction, plugging the pores with colloids from sample solutions, proteins binding within the pores, and organic contamination. Using an RE in an incompatible electrolyte such as K^+ with ClO_4^- will form an insoluble salt, clogging the junction. Due to the colorless nature of Vycor, it will typically change color when contaminated, turning yellowish when contaminated with organics and even brown with severe organic contamination followed by heating. In many cases, it is possible to renew a clogged junction, whereas for others, it must be replaced. In the simplest cases, a precipitated salt can be dissolved out, otherwise the contamination must be digested. When cleaning a junction, attention must be paid to both the junction material and the contaminant, otherwise the junction may be dissolved along with the contamination. Several junction cleaning methods are described in Table 4.11.

4.7.3   Replacing filling solutions

Through normal use of an RE, the filling solution and the electrolyte of the electrochemical cells with which it is used will diffuse together, diluting and contaminating each other. This requires that the filling solution of any RE be changed periodically, the frequency of which is dependent on the actual usage of each RE. When changing the filling solution, the replacement solution should have the proper concentration for the RE (i.e., Ag|AgCl (saturated KCl) the filling solution should be saturated with KCl and AgCl.) The introduction of air bubbles upon introducing the new filling solution should be avoided, and removed if inadvertently introduced.

4.7.4   Regenerating the reference electrode

When required, most REs can easily be refreshed with new filling solution or a new frit, but in some cases, the entire electrode must be rebuilt. The possible actions for each RE are summarized in Table 4.12.

Table 4.11

Junction cleaning procedures

Before cleaning	Before the washing procedure, the RE filling solution must be removed, and if possible, the active portion of the RE should be removed from the electrode body or the frit removed from the electrode body and cleaned alone, to prevent any contamination or reactions from destroying the RE	
Cleaning	Contaminant	Procedure
	Proteins (69)	Soak in a 0.1 M HCl and 1 wt% pepsin solution followed by thorough rinsing with deionized water
	Silver sulfide (70)	Soak in a 0.1 M HCl and 7.5 wt% thiourea solution followed by thorough rinsing with deionized water
	Organic (49) (i.e., yellowed Vycor)	Soak the frit in a strong oxidizing solution (e.g., 30% H_2O_2 or concentrated HNO_3 with a few crystals of $KClO_3$ or $NaClO_3$) heated to 100 °C until any color disappears. The frit should then be washed thoroughly with deionized water
After cleaning	After cleaning, the junction and/or RE body should be rinsed with filling solution to remove all traces of the cleaning solutions, and the RE rebuilt and refilled	

Table 4.12

Renewal and regeneration possibilities for reference electrodes

Electrode	Possible actions for regeneration
NHE *or* SHE	Replace filling solution; if H_2 supply is bad, replace; replatinize electrode
CHE	Replace filling solution and/or junction; refill with H_2; replatinize electrode
DHRE	Replace filling solution; if no bubbles or low current, replace power supply and/or replatinize H_2 electrode
SCE, MSRE, Hg|HgO	If new filling solution and/or new junction do not work, electrode must be rebuilt using new or repurified mercury and the appropriate mercury salt. See appropriate section above
Ag|AgCl	If new filling solution and/or new junction do not work, rechloridize the silver wire. This is accomplished by first removing the old AgCl by soaking in concentrated NH_4OH, and then following the same procedure as building an new RE, outlined in Section 4.3.3.1
Ag|Ag$^+$	Replace filling solution and/or junction; clean Ag wire

4.8   TROUBLESHOOTING

4.8.1   Special notes

4.8.1.1   High-frequency effects

The impedance of an RE, particularly if large, can have undesired effects in electrochemical experiments (Table 4.13). This is especially true for high-frequency or high-speed

Table 4.13

Troubleshooting reference electrodes

Problem	Cause	Solution
Incorrect potential	Filling solution is not at the correct concentration, or species that diffused into the RE are interfering with the redox couple in the RE	Replace filling solution
	Clogged frit	Clean or replace frit as it may be clogged with insoluble salts Do not polish the junction of an RE. You will only embed polishing media and ground pieces of frit material in the frit
	Sparingly soluble salt is completely dissolved (i.e., silver wire in Ag|AgCl looks like silver)	Replate if Ag|AgCl RE. Rebuild if Hg-based RE
Sluggish (potential appears to change or settle over time of experiment)	Clogged frit	Clean or replace frit
	Platinization too thick	Remove old platinization; replatinize the electrode
	Mercury salt too thick	Rebuild RE with new or repurified Hg and new mercury salt
Erratic and/or sluggish	Bubble on frit	Tap or flick RE to remove bubbles
Noisy voltammetry Discontinuity in EIS	RE impedance too high	Use a double RE (high-frequency shunt)

measurements. This can show itself as a noise in most methods, and as a discontinuity in EIS measurements at high frequency. Figure 4.23A shows a bode plot of an EIS measurement displaying this characteristic discontinuity between frequencies of 100 kHz and 1 MHz.

The discontinuity occurs even with an RE with very low impedance (~600 Ω). Problems of this type can be addressed using a double RE, or a high-frequency shunt. This is created using a typical RE connected in parallel with a capacitor and a platinum wire that is placed directly in the electrochemical cell, as shown in Figure 4.24. Its purpose is to pass high frequencies directly into the cell solution, effectively bypassing the RE with a high-pass filter. This double RE used in the same experiment described above in place of the solitary RE is shown in Figure 4.23B. Notice that the discontinuity at high frequencies disappears when the shunt is incorporated.

In fast-sweep rate cyclic voltammetry, an RE with high impedance can cause noise to be superimposed onto the CV due to a slowed potentiostat response, as well as contributions from environmental noise sources (71). This effect is shown in Figure 4.25 with CVs at 10 V/sec in a solution of 0.59 mM Co(III)(Salen)$^+$ in DMF with 0.1 M NBu$_4$PF$_6$ as a supporting electrolyte. Potentiostat sensitivity settings of both 10^{-4} A/V (Figure 4.25A)

A. EIS with Single Reference Electrode

B. EIS with Double Reference Electrode (high frequency shunt)
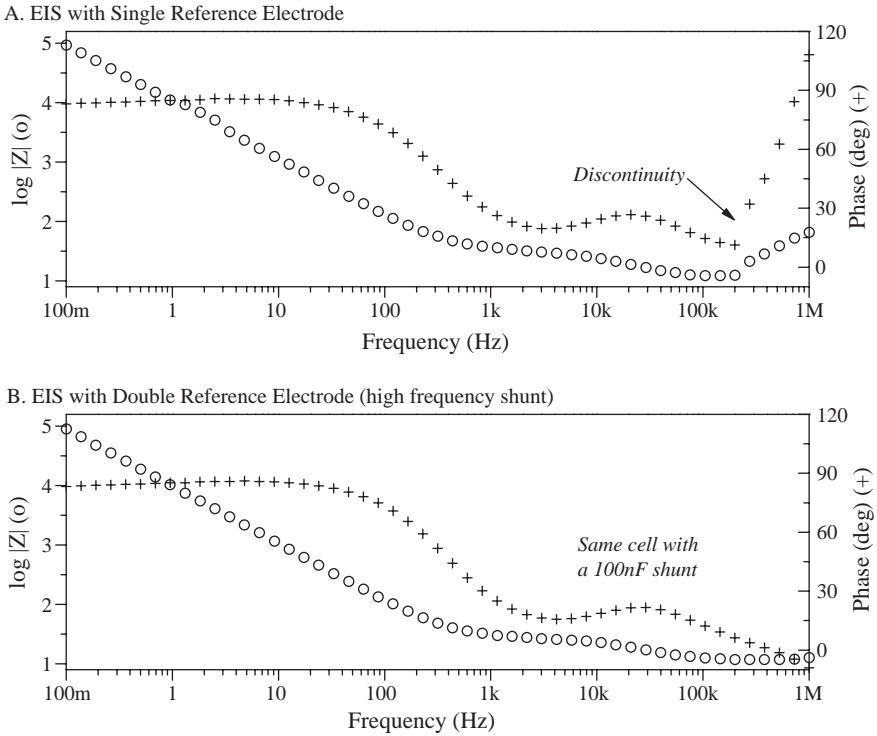
Figure 4.23   High-frequency reference electrode impedance problems in electrochemical imped-
ance spectroscopy. EIS with (A) single reference electrode and (B) double reference electrode (high-
frequency shunt).
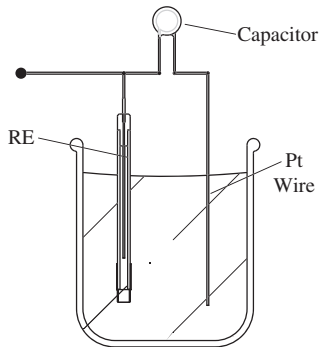
Figure 4.24   Double reference electrode.
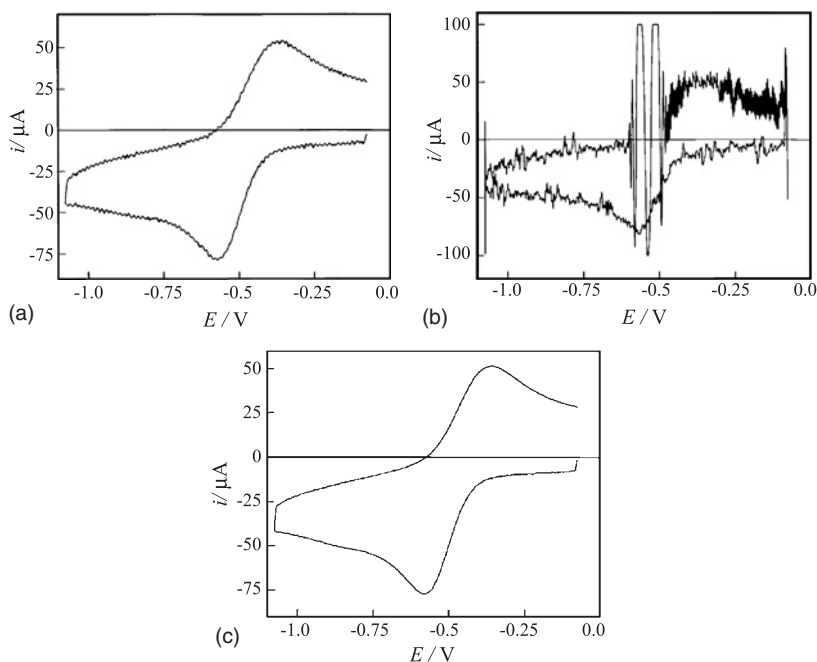
Figure 4.25   (A–C) Effect of high RE impedance on fast-scan rate CV. [Reprinted with permission from reference (71). Copyright 1994, Bioanalytical Systems, Inc.]

and 10^{-5} A/V (Figure 4.25B) result in noisy data. The incorporation of a double RE, as described above, produces a less noisy CV, shown in Figure 4.25C.

4.8.1.2   Microscale reference electrodes

In many cases, modern electrochemists are probing systems where classical REs are much too large. Microscale reference electrodes (µREs) are now being used, such as with solid-state REs incorporated into biosensors. These µREs are typically miniaturized versions of the classical electrodes that utilize novel solutions to attain the size required, usually using polymer films for both the electrolyte and the junction material. The most popular in the literature is the Ag|AgCl µRE using either thick- or thin-film polymer methods to create a mixed polymer–electrolyte and an additional polymer layer that serves as a membrane junction. Simonis *et al.* (72) recently compared thin- versus thick-film techniques for the Ag|AgCl µRE. In addition to the Ag|AgCl µRE, Ag|Ag$^+$ µREs have been described (73), and general methods for the miniaturization of REs through the use of micromachining techniques are presented by Suzuki (74). The DHRE could also be miniaturized using standard microfabrication techniques.

4.8.1.3   Temperature effects on reference electrode potentials

Using an RE at a temperature other than standard temperature (25 °C) requires a correction to be made to the potential due to differences in solubility and activity of the components

Table 4.14

Temperature-dependent potentials

RE	Equation (valid for 0–100 °C for calomel; 0–95 °C for Ag|AgCl; 0–60 °C MSRE)
SCE (75)	$E = 0.2412 - 6.61 \times 10^{-4}(t-25) - 1.75 \times 10^{-6}(t-25)^2 - 9.0 \times 10^{-10}(t-25)^3$
NCE (75)	$E = 0.2801 - 2.75 \times 10^{-4}(t-25) - 2.50 \times 10^{-6}(t-25)^2 - 4 \times 10^{-9}(t-25)^3$
Ag|AgCl (76)	$E = 0.23659 - 4.8564 \times 10^{-4} t - 3.4205 \times 10^{-6} t^2 - 5.869 \times 10^{-9} t^3$
MSRE (33)	$E = 0.63495 - 7.8144 \times 10^{-8} t - 4.2689 \times 10^{-11} t^2$

of the RE. The SHE is defined as 0.0000 V at all temperatures, so no correction is required. Listed in Table 4.14 are temperature correction formulas for Ag|AgCl, NCE, SCE, and MSRE REs. It has been recommended (29) that calomel-based electrodes should not be used above 70 °C for long durations.

REFERENCES

1. A. J. Bard, L. R. Faulkner, *Electrochemical Methods*, 2nd ed., John Wiley & Sons: New York, 2001, p. 22.
2. Compiled with data obtained from: Chemical Resistance Data. [Online]. Available at: http://www.tank-depot.com/engineerdata/chemicalres.pdf. Accessed 7 Sept. 2004. Quick Reference Polymer Solvent Compatibility Chart. [Online]. Available at: http://www.upchurch.com/TechInfo/polymerInfo.asp. Accessed 7 Sept. 2004. Spill Prevention Guidance Document, Appendix E: Chemical/Material Compatibility Matrix. [Online]. Available at: http://enviro.nfesc.navy.mil/ps/spillprev/appx_e_chem.pdf. Accessed 7 Sept. 2004. Dupont Dow Elstomers. Viton Brochure. [Online]. Available at: http://www.dupont-dow.com/literature/viton/090017a28008d688.pdf. Accessed 10 Sept. 2004. Cole-Parmer: Chemical Resistance Database. [Online]. Available at: http://www.coleparmer.com/techinfo/ChemComp.asp. Accessed 12 Sept. 2004.
3. R. Barbour, *Glassblowing for Laboratory Technicians*, Pergamon Press: Oxford, 1978, pp. 122–131.
4. E. P. Serjeant, in *Potentiometry*, E. P. Serjeant, Ed., John Wiley & Sons: New York, 1984, p. 111.
5. D. T. Sawyer, A. Sobkowiak, J. L. Roberts Jr., *Electrochemistry for Chemists*, 2nd ed., John Wiley & Sons: New York, 1995, p. 179.
6. Zeus Industrial Products, Heat Shrink Tubing—Recovery Information. [Online]. Available at: http://www.zeusinc.com/heatshrink.asp. Accessed 4 Oct. 2004.
7. 3M™ Heat Shrink Tubing Selection Guide. [Online]. Available at: http://www.3m.com/market/electrical/elpd/oem/pdf/heat_shrink_tubing_guide.pdf. Accessed 29 Sept. 2004.
8. H. Galster, *pH Measurement Fundamentals, Methods, Applications, Instrumentation*, VCH: Weinheim, 1991, p. 68.
9. L. Haar, J. S. Gallagher, G. S. Kell, *NBS/NRC Steam Tables*, Hemisphere Publishing: New York, 1984.
10. G. J. Hills, D. J. G. Ives, in *Reference Electrodes*, D. J. G. Ives, G. J. Janz, Eds., Academic Press: New York, 1961, p. 107.
11. *Ibid.*, p. 106.

12. A. M. Feltham, M. Spiro, *Chem. Rev.* **71**, 177 (1971). R. G. Bates, *Determination of pH Theory and Practice*, 2nd ed., John Wiley & Sons: New York, 1973, p. 292.
13. R. G. Bates, *ibid.*, p. 291.
14. A. M. Feltham, M. Spiro, *op. cit.*, p. 193.
15. G. J. Hills, D. J. G. Ives, *op. cit.*, pp. 106–108.
16. G. J. Hills, D. J. G. Ives, *op. cit.*, pp. 93.
17. G. J. Hills, D. J. G. Ives, *op. cit.*, p. 99.
18. J. H. Hildebrand, *J. Am. Chem. Soc.* **35**, 847 (1913).
19. R. W. Pittman, unpublished, 1959.
20. G. J. Hills, D. J. G. Ives, *J. Chem. Soc.* 318 (1951).
21. S. Gong, J. Lu, Y. Heqing, *J. Electroanal. Chem.* **436**, 291 (1997).
22. F. G. Will, *J. Electrochem. Soc.* **133**, 454 (1986).
23. J. Giner, *J. Electrochem. Soc.* **111**, 376 (1964).
24. G. J. Hills, D. J. G. Ives, in D. J. G. Ives, G. J. Janz, Eds., *op. cit.*, Chapter 3. J. Newman, K. E. Thomas-Alyea, *Electrochemical Systems*, 3rd ed., John Wiley & Sons: New York, 2004, p. 137.
25. G. J. Hills, D. J. G. Ives, in D. J. G. Ives, G. J. Janz, Eds., *op. cit.*, p. 136.
26. J. Newman, K. E. Thomas-Alyea, *op. cit.*, p. 139.
27. H. Kahlert, in *Electroanalytical Methods*, F. Scholz, Ed., Springer-Verlag: Berlin, 2002, p. 266.
28. G. J. Hills, D. J. G. Ives, in D. J. G. Ives, G. J. Janz, Eds., *op. cit.*, p. 132.
29. E. P. Serjeant, *op. cit.*, p. 99.
30. G. J. Hills, D. J. G. Ives, in D. J. G. Ives, G. J. Janz, Eds., *op. cit.*, p. 135.
31. D. J. G. Ives, F. R. Smith, in D. J. G. Ives, G. J. Janz, Eds., *op. cit.*, p. 403.
32. *Ibid.*, p. 405.
33. *Ibid.*, p. 404.
34. G. A. Hulett, *Phys. Rev.* **32**, 257 (1911).
35. D. J. G. Ives, F. R. Smith, in D. J. G. Ives, G. J. Janz, Eds., *op. cit.*, p. 406.
36. Research Solutions and Resources. Hg/HgO Reference Electrode. [Online]. Available at: http://www.consultrsr.com/resources/ref/hgopotl.htm. Accessed 15 Oct. 2004.
37. D. J. G. Ives, in D. J. G. Ives, G. J. Janz, Eds., *op. cit.*, p. 335.
38. J. Newman, K. E. Thomas-Alyea, *op. cit.*, p. 140.
39. D. J. G. Ives, in D. J. G. Ives, G. J. Janz, Eds., *op. cit.*, p. 336.
40. H. Kahlert, *op. cit.*, p. 268.
41. J. M. Thomas, *J. Chem. Ed.* **76**, 97 (1999).
42. D. T. Sawyer, A. Sobkowiak, J. L. Roberts Jr., *op. cit.*, p. 189. G. J. Janz, in D. J. G. Ives, G. J. Janz, Eds., *op. cit.*, p. 205.
43. D. T. Sawyer, A. Sobkowiak, J. L. Roberts Jr., *op. cit.*, p. 190.
44. G. J. Hills, in D. J. G. Ives, G. J. Janz, Eds., *op. cit.*, p. 438.
45. L. Meites, Ed., *Handbook of Analytical Chemistry*, McGraw Hill: New York, 1963, Section 5.
46. D. T. Sawyer, A. Sobkowiak, J. L. Roberts Jr., *op. cit.*, p. 201.
47. A. J. Bard, L. R. Faulkner, *op. cit.*, p. 68, and references cited therein.
48. *Ibid.*, p. 66.
49. Corning, VYCOR® Brand Porous Glass 7930 Data Sheet. [Online]. Available at: http://www.corning.com/lightingmaterials/images/Vycor_7930.pdf. Accessed 8 Sept. 2004.
50. Koslow Scientific. Porous Vycor. [Online]. Available at: http://www.koslow.com/vycor.html. Accessed 8 Sept. 2004.
51. Princeton Applied Research, http://www.princetonappliedresearch.com.
52. D. T. Sawyer, A. Sobkowiak, J. L. Roberts Jr., *op. cit.*, p. 180.
53. WPI. Dri-Ref Reference Electrodes. [Online]. Available at: http://www.wpiinc.com/WPI_Web/Biosensing/Dri-Ref.html. Accessed 18 Oct. 2004.

54. D. T. Sawyer, A. Sobkowiak, J. L. Roberts Jr., *op. cit.*, p. 181.
55. H. Kahlert, *op. cit.*, p. 274.
56. D. T. Sawyer, A. Sobkowiak, J. L. Roberts Jr., *op. cit.*, pp. 182–184.
57. Gamry Instruments. Reference Electrode Impedance Check. [Online]. Available at: http://www.gamry.com/App_Notes/ReferenceElectrodes/Reference_Impedance_Check.htm. Accessed 28 Oct. 2004.
58. D. T. Sawyer, A. Sobkowiak, J. L. Roberts Jr., *op. cit.*, p. 200.
59. *Ibid.*, p. 182.
60. J. N. Butler, Advances in Electrochemistry and Electrochemical Engineering, in *Electrochemistry*, P. Delahay, Ed., John Wiley & Sons: New York, Vol. 7, 1970.
61. A. J. Bard, L. R. Faulkner, *op. cit.*, p. 27.
62. H. Kahlert, *op. cit.*, pp. 276–277.
63. *Ibid.*, pp. 270–271.
64. A. Tagni, T. Hayashi, *Ferrocenes*, VCH: Weinheim, 1995.
65. A. J. Bard, L. R. Faulkner, *op. cit.*, p. 812, and references cited therein.
66. D. T. Sawyer, A. Sobkowiak, J. L. Roberts Jr., *op. cit.*, p. 203, and references cited therein.
67. R. D. Williams, University of Texas at Austin, simulated data.
68. R. R. Gagné, C. A. Koval, G. C. Lisensky, *Inorg. Chem.* **19**, 2854 (1980).
69. H. Kahlert, *op. cit.*, p. 276.
70. H. Galster, *op. cit.*, p. 114.
71. B. Gollas, B. Krauss, B. Speiser, H. Stahl, *Curr. Seps.*,**13**, 42 (1994). A. W. Bott, *Curr. Seps.* **14**, 64 (1994).
72. A. Simonis, H. Luth, J. Wang, M. J. Schoning, *Sens. Acuators B* **103**, 429 (2004).
73. M. Ciobanu, J. P. Wilburn, I. Nicholas, P. Ditavong, D. A. Lowy, *Electroanalysis* **14**, 989 (2002).
74. H. Suzuki, *Chem. Sens.* **13**, 55 (1997).
75. G. J. Hills, D. J. G. Ives, in D. J. G. Ives, G. J. Janz, Eds., *op. cit.*, p. 161.
76. G. J. Janz, in D. J. G. Ives, G. J. Janz, Eds., *op. cit.*, p. 189.

– 5 –

Solid Electrode Materials: Pretreatment and Activation

Greg M. Swain

Department of Chemistry, Michigan State University,
East Lansing, MI 48824-1322, USA

5.1 INTRODUCTION

Solid electrodes have been a mainstay in electroanalytical chemistry for nearly five decades now (1). For a solid material to function as an electrochemical electrode, it must possess several characteristics: electrical conductivity, chemical and electrochemical stability over a wide range of conditions, rapid electron transfer for a wide variety of redox systems, and reproducible electrical, microstructural, and chemical properties. Table 5.1 lists some desirable electrode properties for materials used in electroanalytical measurements. A challenge with making high-quality electroanalytical measurements is reproducibly controlling the electrode's physicochemical properties in such a way as to achieve a low background current and a rapid rate of electron transfer for the target analyte. Electrodes exhibiting these properties are referred to as being "active" or in an "activated state". Activation is accomplished by a process known as electrode pretreatment, which involves conditioning the surface morphology, microstructure, and chemistry in a manner that promotes low background current and rapid reaction kinetics (both electron and proton transfer) with a redox analyte dissolved in solution or confined to the surface.

Electrochemical reactions are heterogeneous in nature with the reaction kinetics being controlled by the properties of the electrode–electrolyte interface and the concentration of reactant available at this interface. Therefore, the physical, chemical, and electronic properties of the electrode surface are of paramount importance. Several factors will influence the electron-transfer kinetics for a redox system: (i) type of electrode material, (ii) surface cleanliness, (iii) surface microstructure, (iv) surface chemistry, and (v) electronic properties (e.g., charge carrier mobility and concentration, which can be potential dependent for some semiconducting electrodes). Of course, if the solid is not a good electrical conductor (low charge carrier mobility and/or carrier concentration), then the current flow will be limited and the material will have drawbacks for electrochemical measurements. With the exception

Handbook of Electrochemistry
Edited by C.G. Zoski

Table 5.1

Material and electrochemical properties of an ideal electrode

---

High electrical conductivity
Hard and durable
Homogeneous microstructure throughout the bulk
Reproducible physical, chemical, and electronic properties
Good chemical inertness
Low and stable background current
Morphological and microstructural stability over a wide potential range
Rapid electron-transfer kinetics for a wide range of redox systems
Easily fabricated, shaped, and inexpensive in cost

---

of the electronic properties, the extent to which any one of the above-listed factors influences the electrochemical reaction kinetics very much depends on the particular redox system (2–8). The effectiveness of the pretreatment for a particular redox system also depends on the electrode material. For example, the same pretreatment applied to two different electrode materials often results in different levels of activation for each toward the same redox system. Surface cleanliness is a critical property for every electrode and all redox systems. For example, it is highly unusual for a researcher to simply take an electrode out of laboratory storage and use it as it is to make a high-quality measurement. This is because contaminants from the air adsorb onto the surface, particularly carbon materials, and block sites for electron transfer. This leads to complete electrode blocking and, at the very least, an increased electron-tunneling distance and/or alteration in the local double-layer structure. Air oxidation of the surface can also occur producing a change in the surface chemistry, wettability, and microstructure. Furthermore, every electrode has a past history of use that affects its performance. Therefore, every electrode needs to be first pretreated in order to make it ready for the electrochemical measurement. Pretreatments activate the electrode by some combination of surface cleaning, alteration of the exposed microstructure (i.e., edge plane exposure), and manipulation of the surface chemistry (i.e., introduction of surface carbon–oxygen functionalities).

Every pretreatment protocol should have some sort of surface cleaning as its first step, although it should be pointed out that the apparent heterogeneous electron-transfer rate constant, k°_{app}, for some redox systems is more strongly influenced by surface cleanliness than other factors. For instance, k°_{app} for $Fe(CN)_6^{3-/4-}$ can decrease by orders of magnitude $(10^{-2}–10^{-5}$ cm sec$^{-1})$ for an unclean compared to a clean electrode surface (2–8). In contrast, k°_{app} for $Ru(NH_3)_6^{3+/2+}$ might decrease by only a factor of 5–10 for the same unclean surface (2–8). The rate constants are referred to as "apparent (app)" because they are often not corrected for electric double-layer effects (so-called Frumkin effects). As I have already mentioned, oxidation reactions can occur, particularly with carbon electrodes, that will alter the electrode surface chemistry and even the microstructure if severe enough. These oxidation reactions occur during exposure to the ambient air or can be potential-induced. Depending on the redox system, surface oxidation can accelerate or decelerate the rate of electron transfer. Incorporating oxygen makes electrode surfaces more polar and hydrophilic and, consequently, more wettable with water. It also makes them more susceptible to molecular adsorption involving polar adsorbates whether the molecule be a contaminant or the redox analyte under study. When reaction intermediates or products adsorb, active sites on the electrode may be blocked. At the very least, molecular adsorption creates a prior

Table 5.2

Common redox analytes: relative effect of factors on the heterogeneous electron-transfer rate constant

Redox analyte	Cleanliness	Microstructure	Surface chemistry
$Ru(NH_3)_6^{3+/2+}$	Weak	Weak	Weak
Chlorpromazine	Weak	Weak	Weak
Methyl viologen	Weak	Weak	Weak
$IrCl_6^{2-/3-}$	Weak	Weak	Weak
Ferrocene	Weak	Weak	Weak
Ferrocene carboxylic acid	Weak	Weak	Weak
$Fe(CN)_6^{3-/4-}$	Strong	Strong	Strong
Ascorbic acid	Strong	Strong	Minor
Catechol	Strong	Strong	Strong
$Fe^{3+/2+}$	Strong	Strong	Strong
$Eu^{3+/2+}$	Strong	Strong	Strong

history that can be carried over to the next measurement if the electrode is not properly cleaned. Table 5.2 shows some of the common redox systems used to probe the electrochemical activity of electrode materials, along with a listing of the relative influence of surface cleanliness, microstructure, and chemistry on k_{app}° for each. In summary, factors, such as the surface microstructure, surface oxides, adsorption strength, and surface cleanliness, influence k_{app}° for all redox systems to varying extents. The challenge is to reproducibly pretreat an electrode in a manner that activates it for the particular redox system under study.

Extensive research has been conducted over the years within the electroanalytical community in an effort to understand how solid electrodes are "activated" by pretreatment. Many pretreatment protocols have been established that can reproducibly activate various electrode materials. These include mechanical polishing, vacuum heat treatment, laser-based thermal treatment, electrochemical polarization, radio-frequency plasma treatment, and microwave plasma treatment. The ability to reproducibly activate macrosized electrodes results, to a large degree, because the surface can be polished prior to treatment. Polishing removes the effects of the electrode's past history and allows a particular pretreatment to be performed on a fresh surface. Thus, polishing is often the first step in any pretreatment protocol. A prerequisite for performing high-quality electrochemical measurements is the preparation of an electrode with reproducible physical, chemical, and electronic properties. It is very easy, even for the novice, to pretreat an electrode and improve k_{app}° from say 10^{-5} to 10^{-3} cm sec^{-1}, but difficult to achieve large rate constants of $>10^{-2}$ cm sec^{-1}. Great care and attention must be given to how an electrode is pretreated if one intends to use it in a high-quality electroanalytical measurement.

The commonly used pretreatment protocols for activating solid electrodes are reviewed in this chapter. Specifically, the pretreatment of carbon, metal, and semiconductor electrodes (thin conducting oxides) is discussed. Details of how the different electrode materials are produced, how the particular pretreatment works, and what effect it has on electron-transfer kinetics and voltammetric background current are given, since these factors determine the electroanalytical utility of an electrode. Issues associated with cell design and electrode placement (Chapter 2), solvent and electrolyte purity (Chapter 3), and uncompensated ohmic resistance (Chapter 1) are discussed elsewhere in this book. This

chapter is divided into three main sections: carbon electrodes (highly oriented pyrolytic graphite (HOPG), glassy carbon, pyrolyzed photoresist films, fibers, nanotubes, diamond films, and tetrahedral amorphous carbon (Ta-C) films), metal electrodes (Pt and Au), and semiconductor electrodes (indium tin oxide (ITO)). Since carbon is widely employed in electroanalysis, a significant portion of this chapter is devoted to it. The various types of high-surface-area carbon powders used as catalyst support materials, for example, are not discussed as these materials typically are not used in electroanalysis.

5.2   CARBON ELECTRODES

Carbon is the most commonly used electrode material in electroanalytical chemistry and it is available in a variety of microstructures: graphite, glassy carbon, carbon fiber, nanotube, amorphous powders, and diamond. The electrochemical properties of many of these carbon types are discussed in the seminal book by Kinoshita (9). Some carbon electrode types (e.g., glassy carbon) have been studied and used extensively for ~40 years now. Even so, there are still incompletely understood points about the structure–performance relationship and how this relationship affects electrochemical activity. Details of this research history are given in monographs by McCreery (10–12). Carbon exists in two distinct crystalline structures: diamond and graphite. The diamond crystal is cubic and the carbon atoms are arranged in a tetrahedral configuration with sp^3-hybridized bonding between them. This strong covalent bonding makes diamond the hardest known substance. For this reason, two commercial applications of diamond are as a grit for abrading and polishing metals and as a coating for cutting tools. Graphite consists of a hexagonal structure with the carbon atoms arranged in a trigonal configuration of sp^2-hybridized bonding. This atomic arrangement leads to the formation of layer planes or graphene sheets with a spacing of 3.354 Å. Strong covalent bonding exists between the atoms within the graphene sheet (*a*-axis). Unlike diamond though, weak van der Waals forces exist between the layer planes to hold them together (*c*-axis). It is because of these weak interactions that the graphene sheets can slide across one another, making the material a good lubricant. There are permutations of the graphitic microstructure that characterize other types of sp^2 carbon electrode materials. For instance, when the in-plane dimension of the graphene sheets is small (i.e., high fraction of crystallite edges) and the spacing between them is large, this carbon is categorized as amorphous (e.g., powders, glassy carbon, etc.). Amorphous films of diamond also exist with mixtures of sp^3- and sp^2-bonded carbon, such as Ta-C. There is also a more exotic form of carbon known as the "buckyball" or fullerene that was discovered in 1985. The "buckyball" resembles a soccer ball in shape and contains 60 carbon atoms (C_{60}) in a spherical structure consisting of 20 hexagons and 12 pentagons arranged on the surface. The discovery has led to an expansion of research on C_{60} and variations of this structure (e.g., nanotubes) (13). The important take-home message is that carbon electrode materials possess different microstructures and surface chemistries depending on the type and how each was processed. As a consequence, the electrochemical properties can vary from material to material. Of all the solid electrodes utilized in electroanalytical chemistry, carbon materials are probably the most challenging and problematic from this perspective.

5.2.1   Highly oriented pyrolytic graphite

Highly oriented pyrolytic graphite (HOPG) is a special type of carbon that is analogous to a single-crystal metal (1, 9–12). It is prepared by exposing pyrolytic graphite, a material formed from the decomposition of hydrocarbon gases on a heated surface, to high pressure and temperature. It is composed of a lamellar arrangement of condensed polyaromatic planes (i.e., graphene sheets) stacked in a slightly staggered fashion. The material is turbostratic, which means that the graphene sheets are rotationally disordered (i.e., random angular orientations to one another) and the alternating ABAB…stacking pattern of single-crystal graphite (that is produced naturally) is observed only over short distances along the c-axis. The interplanar spacing generally ranges from 3.35 to 3.39 Å. Organized arrangements of these graphene sheets are termed crystallites with the dimensional parameters L_c (stacking height), L_a (layer plane width), and d (interplanar distance). L_a is the mean size of the graphitic microcrystallite along the a-axis that always lies in the plane of the hexagonal lattice. L_c refers to the coherence length of the graphene sheet stacking in a direction perpendicular to L_a. Knowledge of these parameters, obtained from X-ray diffraction measurements, is usually sufficient to predict many of the material properties. An exposed hexagonal surface that is perpendicular to the c-axis is referred to as a basal plane whereas a cut surface parallel to the c-axis is called an edge plane. Raman spectroscopy is a useful tool for characterizing the microstructure of carbon materials, in particular, for examining the edge/basal plane ratio (14–16). The spectrum for the low-defect material (i.e., primarily basal plane exposed) has a single sharp peak at 1582 cm^{-1} (so-called G band), which has been assigned to an E_{2g} or a lattice "ring breathing" mode. Such a spectrum is seen for materials with large L_a and L_c parameters. The E_{2g} peak broadens and shifts to a higher frequency with decreasing L_a and L_c. If the graphene sheets are separated by intercalants (e.g., staging), a shoulder can develop on the 1582 cm^{-1} peak that is upshifted to ca. 1620 cm^{-1}. When L_a is decreased (i.e., significant edge plane is exposed), a new peak develops at 1360 cm^{-1} (the so-called D band). This peak correlates with the presence of edge plane density and the 1360/1580 cm^{-1} relative peak intensity ratio scales proportionally with $1/L_a$ (i.e., decreasing microcrystallite size) (14–16). The 1360 cm^{-1} band has been assigned to an A_{1g} mode and arises from a breakdown of the selection rules for optical excitation of phonons in the graphite lattice caused by the termination of the extended graphene sheets. As a consequence, new vibrational modes, including A_{1g}, become active. The important take-home message is that the 1360 cm^{-1} band correlates with microstructural disorder.

The reason HOPG is analogous to a single-crystal metal is because of the ordered arrangement of the carbon atoms within a graphene sheet. Each carbon atom is bonded to three others in the layer plane. The distance between neighboring carbon atoms is 1.42 Å, which is very close to the C−C bond distance in benzene. In addition to being well ordered, the surface is atomically smooth over relatively large dimensions (micrometers), making the material quite useful for studying electrochemical reactions, molecular adsorption, and potential-induced microstructural degradation at the atomic level. Physically, its stiffness along the a-axis is due to the strong σ bonds between the carbon atoms. However, the material is held together along the c-axis by weak van der Waals forces acting on the layer planes. Electronically, the material is also anisotropic because of the extended π-electron system. The material has metallic conductivity along the a-axis and semiconducting to

semimetallic conductivity along the *c*-axis. For example, the electrical conductivity is on the order of 10^5 $(\Omega \text{ cm})^{-1}$ along the *a*-axis and 10^3 $(\Omega \text{ cm})^{-1}$ along the *c*-axis, producing an anisotropy factor about 100, or so (10–12, and references therein).

The background current for the relatively defect-free basal plane is typically low within the working potential window with values <5 μA cm^{-2} (8, 10–12). This is because of the characteristically low double-layer capacitance, C_{dl}, of 1–5 μF cm^{-2} (8, 10–12). The more defective the basal plane is, the greater the 1360/1580 cm^{-1} Raman peak intensity ratio and the background current are. The magnitude of the peak ratio correlates with the fraction of edge plane exposed, hence the microstructural disorder. Gewirth and Bard used STM to characterize the types of defects native to the basal plane (17). The adsorption of polar molecules is generally weak on the basal plane with the adsorption enthalpy and coverage scaling with the amount of exposed edge plane and the increased carbon–oxygen functionality that exists there. Molecular adsorption tends to be much stronger on this surface for both chemical and electronic reasons (10–12, 18–20). HOPG has some very well-established electrochemical characteristics with the activity of the edge plane sites differing greatly from the basal plane sites (1, 8, 10–12). Microstructurally, chemically, and electronically, the edge plane sites are unique. Therefore, depending on the exposed microstructure and the particular redox system under study, the electrochemical properties of HOPG can be quite varied.

5.2.1.1   Layer plane cleavage

Since HOPG is a soft, microstructurally ordered material, some conventional pretreatment methods are typically not employed. For instance, one does not usually mechanically polish the electrode because of the microstructural damage this would introduce. The microstructural changes and the corresponding alterations of surface chemistry would have a significant impact on the magnitude of the background current, the extent of molecular adsorption, and k°_{app} for those redox systems that are "surface sensitive". A very good way to achieve a clean basal plane, without microstructural damage, is to carefully cleave the layer planes. The scotch tape method is one of the means to accomplish this. In this method, one simply presses a piece of Scotch^{TM} tape across the surface of HOPG and then carefully lifts the tape, peeling away graphene sheets. Another cleavage method involves the use of a sharp knife blade to remove the graphene sheets. For this and all pretreatments, gloves should be worn and the electrode should be handled with tweezers to avoid contamination. As long as either of these methods is performed carefully, minimal damage to the basal plane will result. The basal plane surface is fragile and also susceptible to damage during physical manipulation and mounting in the electrochemical cell. In order to conduct electrochemical measurements on a low-defect basal plane, an o-ring is often used with gentle pressure to define the area exposed to the solution. Care should be taken to avoid damaging the surface during handling and mounting. The two AFM images in Figure 5.1 show a surface after a careful cleavage (left) with no evident damage over a 5 $\times$ 5 μm^2 area and a surface (right) with some layer plane damage (i.e., cleavage plane). This is a useful first step in any pretreatment protocol for this electrode material.

5.2.1.2   Solvent cleaning

Exposure to clean organic solvents is another useful method for cleaning the HOPG surface without introducing alterations in the surface microstructure and chemistry. It is often
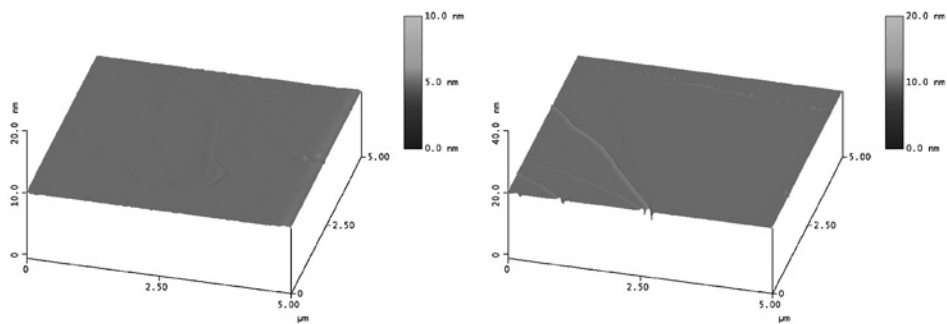
Figure 5.1 Atomic force micrographs of the basal plane of HOPG after (left) careful layer plane cleavage and (right) damaging cleavage leaving a fracture plane. (for colour version: see colour section at the end of the book).

applied in conjunction with layer plane cleavage. In fact, all the pretreatments for HOPG discussed here are often performed with layer plane cleavage as the first step. This pretreatment method works by dissolving and/or desorbing adsorbed contaminants from the surface (21). An exposure time of 20–30 min is usually sufficient. Solvent cleaning can be performed on the entire electrode or on the electrode surface when mounted in the electrochemical cell. Several different solvents can and should be used including acetonitrile, isopropanol, dichloromethane, and toluene. The type of solvent required for activation ultimately depends on the molecular structure of the admolecule or contaminant on the surface. In other words, the solvent should be selected for its solubilizing power of the admolecule(s). The solvent should also be purified by distillation and stored over activated carbon (AC) prior to use because reagent-grade solvents often contain impurities that may adsorb on and contaminate the electrode surface (21). The large surface area of suspended AC particles provides numerous sites for the preferential adsorption of solvent and/or impurities, thereby removing the latter from the solvent. Effective solvent clean-up can usually be achieved after exposing the distilled solvent to AC for 2 days. The use of "clean" organic solvents is critical for the success of this activation method. Care should be taken to avoid transferring the AC in the solvent to the electrochemical cell containing the HOPG, or any other electrode for that matter. This is usually accomplished by filtering. If the particle transfer occurs, the carbon will contact the surface and change the electrode's behavior. No new active sites are created by this pretreatment. Existing ones are simply cleaned and made ready for electron transfer. This is a general pretreatment applicable for all electrodes and for all redox systems.

5.2.1.3 *Laser activation*

This pretreatment can be used to activate HOPG for electron transfer and it can be damaging or non-damaging to the surface microstructure, depending on the conditions (10, 11, 22). Through a combination of active site generation and surface cleaning, short intense laser pulses *in situ* can increase k_{app}° for several redox systems (e.g., $Fe(CN)_6^{3-/4-}$, dopamine, and ascorbic acid) by several orders of magnitude. In this treatment, short (ca. 10 nsec) and intense (ca. 10–100 MW cm^{-2}) pulses of light from a Nd:YAG or N_2 laser are applied to

the HOPG surface immersed in a supporting electrolyte solution. If the incident power density is low ($<$50 MW cm^{-2}), then microstructural alterations of the basal plane do not occur and the pretreatment simply heats the electrode surface. This "heat treatment" activates the electrode by desorbing contaminants and exposing "clean" existing edge plane. However, at power densities $>$50 MW cm^{-2}, the basal plane microstructure is altered, leading to the formation of new edge plane sites. These microstructural changes are manifested in an increase in the 1360/1580 cm^{-1} Raman peak intensity ratio. Increased surface roughening, background current, and molecular adsorption also occur as a consequence of increased microstructural disorder. If this pretreatment is performed *in situ*, then a clean edge plane is exposed and k°_{app} for Fe(CN)$_6^{3-/4-}$ can increase from $<$10^{-5} to ca. 10^{-1} cm sec^{-1} (10, 11, 22). In solution, limited surface oxide formation occurs at these newly exposed edge plane sites if the applied potential is maintained below about +1.0 V vs. SCE. However, once exposed to the laboratory atmosphere, the laser-activated surface tends to be quite reactive and surface oxygen is incorporated at the newly formed edge plane. This pretreatment can both clean existing active sites and create new ones, depending on the conditions. As stated, the most active regions on HOPG for electron transfer, and other sp^2 carbons, are generally associated with the graphitic edge plane.

5.2.1.4 Heat treatment

Heat treatment activates HOPG by desorbing contaminants and/or removing chemisorbed oxygen from the exposed edge plane sites, depending on the temperature. This pretreatment is effective at cleaning and producing low-oxide carbon surfaces. For best results, the pretreatment should be performed under the clean conditions of high vacuum ($<$10^{-6} Torr); however, activation can also be achieved if the treatment is conducted under a thorough inert gas purge. Surface carbon–oxygen functional groups will populate any exposed edge plane and defect sites. Contaminant adsorption, particularly polar molecules, will be strongest near these sites. Heating the electrode to about 500 °C in the absence of oxygen is effective at desorbing contaminants and exposing a clean surface. The electrode will still retain much of the surface oxygen as these functional groups do not decompose at a significant rate until temperatures $>$500 °C (23). A treatment time of 10–30 min is usually sufficient for cleaning. If higher temperatures are employed, the carbon–oxygen functional groups will decompose (CO and CO$_2$ evolution) and this can lead to pitting and exposure of new edge planes. The pretreatment needs to be performed under vacuum or an inert gas atmosphere if a clean, low-oxygen surface is desired. If significant levels of oxygen are present in the gas phase during heat treatment, then surface oxidation and corrosion (gasification) will occur. The morphological and microstructural changes associated with gas-phase oxidation of HOPG have been reported by Beebe and coworkers (24). The heat-treated HOPG surface will be deactivated by contaminant adsorption and reaction with the atmosphere after short-term exposure to the air, so electrochemical measurements should be made immediately after treatment for best results.

5.2.1.5 Electrochemical polarization

Although altering both the surface microstructure and the chemistry, electrochemical polarization can be used to activate HOPG. Anodic polarization, depending on the severity,

can clean the surface, create new edge plane, and introduce surface oxygen. The 1360/1580 cm^{-1} Raman peak intensity ratio is a useful indicator of the microstructural disorder and XPS can be used to quantify the level of surface oxygen. Of all the pretreatments used to activate HOPG, electrochemical polarization has the most dramatic effect on surface microstructure and chemistry (10–12). Generally, the background current and the extent of molecular adsorption track the fraction of edge plane exposed. k_{app}° for some redox systems (e.g., ascorbic acid and Fe(CN)$_6^{3-/4-}$) increases by several orders of magnitude after electrochemical polarization. For example, the surface-sensitive Fe(CN)$_6^{3-/4-}$ has a k_{app}° value of ca. 10^{-5} cm sec^{-1} on a low-defect basal plane surface and a value of ca. 10^{-2} cm sec^{-1} on the same surface after anodic polarization (8, 10–12, 25). The extent of microstructural damage depends on the charge passed at the particular applied potential. Exposure of edge plane increases both the density of electronic states in the vicinity of the site and the surface oxygen content (8, 10–12, 25). The increased density of electronic states necessarily means that a different double-layer structure exists at these sites. This may lead to a greater potential drop locally, hence faster electron-transfer kinetics. Increasing the surface oxygen content can result in the acceleration of electron-transfer rates if specific functional groups are involved in the redox reaction mechanism (26). An important point to remember about pretreatment methods such as electrochemical polarization is that they can affect more than one electrode property (e.g., electronic structure, surface oxides, wettability, etc.) and this makes it difficult to elucidate structure–function relationships.

The mechanism of edge plane formation during anodic polarization in mild acid has been studied by McCreery and coworkers (25, 27) using *in situ* Raman spectroscopy. They found that the first step is separation of the graphene sheets due to the interlayer incursion of solvent molecules and/or intercalated anions. The extent of anion intercalation depends on the electrolyte composition, specifically the anion type, ionic strength, existing defect density on the basal plane surface, and the applied potential. The important potential is actually the applied potential relative to the point of zero charge. The second step involves fracturing of the graphene sheets, a process by which the new edge plane is exposed. Solvent and/or anion intercalation, driven by the positive potentials used for polarization, produces microstructural strain. Eventually, the strain gets large enough to fracture the layer planes because they can no longer bend and flex. This fracturing exposes the new edge plane and increases the local density of electronic states and the surface oxygen content.

There are many electrochemical pretreatment protocols reported in the literature. Potentiostatic, potentiodynamic, and galvanostatic methods have been used. An excellent method for electrochemically pretreating HOPG is potential cycling between −0.5 and 1.5 V vs. SCE in 0.1–1 M KNO$_3$ at 50 mV sec^{-1}. Anodic potential limits below ~1.0 V produce "minor" microstructural alterations and minimal surface oxidation, whereas potential limits >1.5 V lead to "severe" damage and extensive oxygen incorporation (25–28). In general, one needs to balance the need for active site generation (e.g., edge plane formation) with the consequential effects listed above that can have a limiting effect on the electroanalytical utility of the electrode.

The severity of the polarization depends on the anodic potential limit. The electrochemical oxidation of HOPG at positive potentials (>1.5 V) has been studied by numerous groups. For example, Gewirth and Bard used *in situ* scanning tunneling microscopy to

study the basal plane of HOPG during potentiodynamic polarization in 0.1 M H_2SO_4 (17). They proposed that a graphite oxide layer forms following a nucleation and growth process. The early stages of potential cycling between 0 and 1.8 V vs. AgQRE produced roughened and apparently oxidized regions of the surface with lower barrier height than the untreated surface. Continued potential cycling caused further roughening and expansion of the oxidized regions to completely cover the surface. Similar observations were made by Zhang and Wang (29). Goss *et al.* studied the oxidation of HOPG in 1.0 M KNO_3 using *in situ* atomic force microscopy, and found that potential cycling to potentials between 1.5 and 2.0 V SSCE produced isolated surface blisters (30). The outermost layer of the blister was found to be the top-most graphene sheet, whereas the interior of the blister contained graphite oxide. The authors proposed that following potential-dependent intercalation of electrolyte anions and solvent, blisters form as a result of electrolytic gas evolution at subsurface active sites with accompanying graphite oxide formation. The initially formed graphite intercalation compound subsequently oxidizes water or carbon to form graphite oxides. The surface oxides can be problematic in some electrochemical measurements. For example, the voltammetric background current increases and peaks develop in the 0–0.5 V vs. SCE range at acidic pH when redox-active surface carbon–oxygen functional groups are present. The redox-active functional groups are of the quinone/hydroquinone type (20, 31, 32). Their presence can interfere with the electrochemical measurement of the redox analytes at low concentration by causing a reduction in the signal-to-background (S/B) ratio for the measurement. The background voltammetric peaks associated with the redox-active oxygen functional groups shift with pH (-59 mV dec^{-1}) (20, 31, 32).

The increased carbon–oxygen functional group content produced by electrochemical polarization has been correlated with increased rates of electron transfer for some redox systems. For example, Kepley and Bard showed that the k_{app}° value for the quinone/hydroquinone redox couple tracked the thickness of the oxide layer formed by severe anodic polarization (33). McCreery and coworkers reported that k_{app}° for the $Fe^{3+/2+}$ redox system can be increased by orders of magnitude when surface oxygen is incorporated at the edge plane sites on the HOPG surface, particularly carbonyl functional groups (26). These authors, as well as others, have proposed that the electrochemical polarization mechanism involves the creation of oxygen functional groups that act as electron- and/or proton-transfer mediators. Oxygen functional groups can impact upon electrochemical reactions directly or indirectly. They can directly affect the reaction kinetics and mechanism by providing (i) specific reaction or adsorption sites for a particular redox system and (ii) sites that facilitate proton exchange with those redox systems that undergo proton transfer. The functional groups can indirectly affect the reaction kinetics by providing sites for contaminant adsorption from the solution. Furthermore, the increased electrode reaction kinetics might not be due to the oxygen functional groups at all, but rather due to the increased density of electronic states that accompanies the edge plane formation, sites at which the oxides form (2–5, 22). The carbon–oxygen functional groups can impact the structure of the electric double layer. The nature of water interaction with a hydrophobic basal plane and a hydrophilic, oxygen-containing edge plane site will be different. Some of the functional groups that can form are not electroactive but are acidic in nature and undergo deprotonation. This ionization alters the charge on the surface of the electrode and leads to pH-dependent k_{app}° for some redox

systems. For example, carboxylic acid functional groups can form during polarization with a pK_a of ca. 4.5. Deprotonation of these groups occurs at pH values above the pK_a, creating increased negative surface charge. For electrochemically treated glassy carbon, and the same should hold true for HOPG, Deakin *et al.* observed that the k^o for anionic redox systems (Fe(CN)$_6^{3-/4-}$ and IrCl$_6^{2-/3-}$) decreased with increasing solution pH (i.e., increasing negative surface charge) (31). The opposite behavior was seen for the cationic redox systems (Ru(NH$_3$)$_6^{3+/2+}$). Blurton looked at the surface chemistry changes of low-porosity graphite during potentiodynamic polarization in H$_2$SO$_4$ (34). It was observed that multiple anodic and associated cathodic peaks develop in the 0–1.5 V vs. SHE window, which were attributed to redox-active quinone/hydroquinone functional groups. Panzer and Elving also studied the surface chemistry of pyrolytic graphite during potentiodynamic polarization in aqueous and non-aqueous media (35). Generally speaking, from all the published work with HOPG, applied potentials of 1.5 V or greater are needed to expose new edge plane sites. The formation of these sites leads to an increase in k_{app}° for some surface-sensitive probes such as Fe(CN)$_6^{3-/4-}$. Rate constant increases from 10^{-5} to 10^{-2} cm sec^{-1} should accompany new edge plane formation.

5.2.2   Glassy carbon

Glassy carbon (GC), also referred to as vitreous carbon, is the most commonly used carbon electrode for electroanalysis (10–12). It is available in variety of architectures including rods, disks and plates. Unlike HOPG and other graphites, GC is hard and microstructurally isotropic (the same in all directions). It is impermeable to gases and liquids and has slightly lower electrical and thermal conductivity (9–12, 36, 37). The material is prepared by heat treating polyacrylonitrile (PAN) or phenolic resin under pressure at temperatures between 1000 and 3000 °C. The heat treatment is often applied slowly over days and causes expulsion of non-carbon atoms. This produces a conjugated carbon microstructure. The original polymer backbone stays largely intact, preventing the formation of extended graphitic domains (9–12, 36, 37). The resulting microstructure is a complex one of interwoven graphitic ribbons with L_a and L_c values of ca. 50 and 15 Å, respectively (9–12, 36, 37). The accepted model for the GC microstructure is the one proposed by Jenkins and Kawamura (37). The interwoven sp^2 carbon ribbon gives rise to mechanical hardness, so the material is polishable and impermeable to gases and liquids. The density of GC (ca. 1.5) is less than HOPG, indicating that the material contains some void space (nanoporosity). Since the material is impermeable to gases and liquids, the voids are small and unconnected. Two peaks are present in the Raman spectrum for GC at 1350 and 1580 cm^{-1} with the ratio of the two reflecting the extent of microstructural disorder. Typical 1350/1580 cm^{-1} peak intensity ratios are in the 1.3–1.5 range. The material possesses a complex surface chemistry consisting of various types of carbon–oxygen functional groups at the graphitic edge plane sites (9–12).

5.2.2.1   Mechanical polishing

The surface of GC, like other solid electrodes, is gradually deactivated during exposure to the atmosphere or during electrochemical use (38, 39). Therefore, periodic pretreatment is

necessary. The most common method for activating GC is mechanical polishing. As indicated above, polishing is often a first step in any activation protocol. Polishing serves to renew the surface by cleaning, removing the effect of past history, and exposing a fresh microstructure. Since GC possesses an isotropic microstructure, a similar edge-to-basal plane ratio is always exposed after conventional polishing. Polishing should be performed under ultraclean conditions if the highest "activity" is to be achieved. Numerous polishing procedures have been reported in the literature. A good protocol to follow is the one described by Kuwana and coworkers (39, 40). In their method, the electrode is polished using successively smaller sizes of alumina on a smooth glass plate. Deagglomerated alumina powders work best in sizes from 1.0 down to 0.05 μm. The alumina is slurried in ultrapure water to make a paste. The electrode should be polished using circular motions with an even force applied. Starting from the largest grit size, the electrode should be polished and then carefully cleaned by (i) rinsing with ultrapure water and (ii) ultrasonication in the same medium for about 15 min. The GC should be placed in a clean beaker, submerged in ultrapure water and covered during the ultrasonic cleaning. Eventually, a mirror-like finish should be obtained, hence the name glassy carbon. The electrode should be used immediately after the polishing, or any pretreatment for that matter, for best results. k_{app}° for a surface-sensitive redox system like $Fe(CN)_6^{3-/4-}$ should be at least in the high 10^{-2} cm sec^{-1} range if the electrode surface is adequately cleaned and renewed.

Polishing is damaging to the material because the mechanical abrasion breaks carbon–carbon bonds. Polishing debris (e.g., a carbon and alumina microparticle layer), if not removed by thorough cleaning, will remain on the surface and affect the electrochemical properties (41). Oxygen is generally incorporated during the pretreatment as the dangling carbon bonds created on the surface readily react with oxygen in the air or from the water. Low-oxygen surfaces can be created if the polishing is done in an anaerobic environment. For example, McCreery and coworkers have produced low-oxygen GC by polishing in deoxygenated hexane (42). Unlike HOPG, the GC microstructure is isotropic and homogeneous throughout the bulk so that the same disordered microstructure is present regardless of how many layers are removed by polishing.

5.2.2.2 Solvent cleaning

Exposure to clean organic solvents is a useful method for activating GC without introducing new microstructure and surface chemistry. Usually, this pretreatment is applied in conjunction with mechanical polishing. Such is the case for the other pretreatment methods described herein for GC. As discussed above, this pretreatment method works by dissolving and/or desorbing adsorbed contaminants from the surface, generating clean edge plane (i.e., active sites) (21). Exposure times of 20–30 min are usually sufficient. Several different solvents can be used including acetonitrile, isopropanol, dichloromethane, or toluene. The solvents should be purified by distillation prior to use. AC should also be added to the distilled solvent for additional purification (21). k_{app}° for a surface-sensitive redox system like $Fe(CN)_6^{3-/4-}$ should be at least in the high 10^{-2} cm sec^{-1} range if the electrode surface is adequately cleaned and renewed.

5.2.2.3 *Vacuum heat treatment*

Vacuum heat treatment can be used to renew and activate GC (43, 44). As discussed above, this pretreatment method cleans the surface by desorbing contaminants from "active" sites and creates a low-oxygen surface by decomposing carbon–oxygen functionalities as CO and CO_2. Vacuum heat treatment generally does not alter the surface morphology or microstructure. The heat treatment is best performed under high-vacuum conditions ($<10^{-6}$ Torr). Heating the electrode to about 500 °C in the absence of oxygen is effective at desorbing contaminants. The electrode will still retain much of the surface oxygen as these functional groups do not decompose at a significant rate until temperatures >500 °C are reached. Treatment times from 10 to 30 min are usually sufficient. If higher temperatures are employed, ca. 1000 °C, then the carbon–oxygen functional groups will decompose (CO and CO_2 evolution) causing some minor pitting and new edge plane exposure. In general, this pretreatment activates the surface for electron transfer, lowers the background current, and reduces the surface functionality. k_{app}° for a surface-sensitive redox system like $Fe(CN)_6^{3-/4-}$ should be at least in the high 10^{-2} cm sec^{-1} range if the electrode surface is adequately cleaned.

5.2.2.4 *Laser activation*

Through a mechanism of contaminant desorption, this pretreatment activates GC for electron transfer (45). Short (ca. 10 nsec) and intense (ca. 10–100 MW cm^{-2}) pulses of light from a Nd:YAG or N_2 laser are applied while the electrode is immersed in a supporting electrolyte solution. Surface heating occurs as a result of the laser light being absorbed by the carbon. The heating causes the desorption of contaminants from the surface, particularly from the active edge plane, and this leads to improved rates of electron transfer for most redox systems. Since GC is a microstructurally isotropic electrode material, laser activation generally does not alter the microstructure by creating new edge plane, as is the case for HOPG. k_{app}° for a surface-sensitive redox system like $Fe(CN)_6^{3-/4-}$ should be at least in the high 10^{-2} cm sec^{-1} range if the electrode surface is adequately cleaned.

5.2.2.5 *RF plasma treatment*

Treatment in an RF plasma can be used to activate GC (46). Small RF plasma cleaners are available (e.g., Harrick Scientific) for treating electrodes at powers up to about 100 mW and pressures in the 100 mTorr range. The plasma chamber is attached to a mechanical rough pump, and sometimes also to an oil diffusion pump, in order to maintain a reduced pressure. A short 10–15 min treatment in an Ar plasma (10–100 mTorr) is useful for cleaning GC and this involves a sputtering type of mechanism in which energetic argon ions (Ar^+) collide with the surface. The electrode surface tends to be roughened after the plasma treatment. If the treatment is performed in a relatively oxygen-free gas environment, then the surface oxygen content is usually decreased as compared to the typical oxygen content for a freshly polished electrode. RF plasma treatment can also be used to chemically modify the GC surface (46). For example, researchers have incorporated surface oxygen by exposing GC to an oxygen or water/oxygen plasma (46). The alterations in the electrode surface chemistry and microstructure can range from mild to severe depending on the plasma conditions (e.g., gas phase, power, pressure, and duration).

5.2.2.6   *Hydrogen plasma treatment*

GC surfaces prepared in air and/or used in aqueous environments have edge plane and defect sites that are terminated with surface oxides of varying type and coverage (8, 10–12). The heterogeneous distribution of these functional groups can be a cause for significant variability in the electrochemical response for some redox systems and can generally lead to poor response stability. Some of these oxides are redox-active (e.g., quinone/hydroquinone couple) and others are electroinactive but ionizable (e.g., carboxylic acid). Both types of functional groups give rise to pH-dependent voltammetric and amperometric background current over a wide potential range. Several approaches have been employed for removing surface oxides from sp^2 carbon electrodes including high-vacuum heat treatment (43, 44) and mechanical polishing in an anaerobic environment (42). A relatively new pretreatment, and one analogous to vacuum heating, is hydrogen plasma treatment (47–49). Hydrogenated glassy carbon (HGC) is prepared by exposing GC to a hydrogen microwave plasma or to hydrogen gas activated by passage over a heated metal (e.g., tungsten) filament. Atomic hydrogen, not molecular hydrogen, is the principal reactant that chemisorbs at the exposed edge plane and leads to the replacement of terminal oxygen functional groups (47–49). This treatment is fundamentally different from vacuum heat treatment or mechanical polishing in an anaerobic environment because it not only removes the surface oxides but also stabilizes the surface carbon atoms by forming strong covalent C−H bonds. The hydrogenated surfaces are low in oxygen content (atomic oxygen-to-carbon ratio (O/C) <0.02), as determined by X-ray photoelectron spectroscopy (XPS), and hydrophobic with a water contact angle >65°. In fact, the oxygen content remains low even during air exposure for weeks due to the stability of the C−H bonds (49). Based on static secondary ion mass spectrometry (SIMS) results, it was proposed that the hydrogenated surface is composed of aliphatic hydrocarbon moieties (e.g., CH_3, C_3H_3, C_2H_5, C_3H_5, etc.) rather than simply hydrogen, as the chemisorption of atomic hydrogen not only replaces terminal oxygen groups but also causes ring opening reactions that lead to the formation of surface hydrocarbon moieties (48). Figure 5.2 shows a proposed surface structure for HGC.
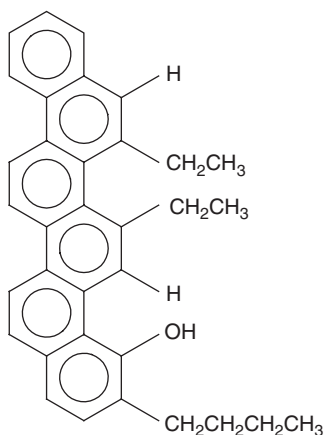
Figure 5.2   Proposed surface chemistry of hydrogenated glassy carbon (48).

HGC exhibits lower voltammetric background current, comparable electrochemical activity for several redox systems, enhanced S/B ratios, and improved response stability compared with freshly polished (i.e., oxygenated) GC. Cyclic voltammetric investigations revealed relatively rapid electrochemical reaction kinetics for $Fe(CN)_6^{3-/4-}$ and $Ru(NH_3)_6^{3+/2+}$, and slightly slower kinetics for dopamine and 4-methylcatechol. Very sluggish kinetics were found for $Fe^{3+/2+}$. For example, k_{app}° of 0.01–0.03 cm sec^{-1} were determined for $Fe(CN)_6^{3-/4-}$ and $Ru(NH_3)_6^{3+/2+}$, whereas slightly lower values of ~5 $\times$ 10^{-3} cm sec^{-1} were found for dopamine and 4-methylcatechol (48). Significantly lower rate constants of ~3 $\times$ 10^{-5} cm sec^{-1} were seen for $Fe^{3+/2+}$ (48). The low k_{app}° for $Fe^{3+/2+}$ was attributed to the absence of mediating carbonyl functional groups on the HGC surface (26, 50). The electrode response for all five redox analytes was extremely stable even after a 3-month period of air exposure. This reflects how resistive this hydrophobic surface is to deactivation (fouling) via contaminant adsorption. Further evidence for the lack of molecular adsorption (polar molecules) was revealed from chronocoulometric measurements performed with anthraquinone-2,6-disulfonate (2,6-AQDS) (51). AQDS strongly physisorbs at high coverages on the polar, oxygenated GC (51, 52). However, negligible adsorption was detected on HGC. These results demonstrate that hydrogenation is a suitable modification method for producing an active, stable, and low-oxide GC surface.

5.2.2.7   *Electrochemical polarization*

Electrochemical polarization, depending on the conditions, can improve the surface cleanliness, alter the surface microstructure, and/or change the surface chemistry. Numerous methods have been reported in the literature. Electrochemical pretreatment is best performed in conjunction with mechanical polishing and/or solvent cleaning. For many electroactive species, polarizing GC anodically at potentials from 1.5 to 2.0 V vs. Ag/AgCl is required for activation. Generally, anodic and cathodic polarization applied in unison provide the highest degree of activation. For example, a protocol used by our group to reproducibly activate GC is 5 min of potential cycling between -1.0 and 1.5 V vs. SCE (50 mV sec^{-1}) in 0.1 M phosphate buffer, pH 2, or 0.1 M HClO$_4$. This would be categorized as a "mild" pretreatment as only minor changes in background current are observed. There are also other protocols that work well for activation. The effectiveness of a particular pretreatment method for activating an electrode very much depends on the redox system under study. Engstrom described the activation of GC for several different redox systems using potential step anodization (0.5–2.0 V vs. SCE) followed by cathodization (0 to -0.5 V) in 0.1 M KNO$_3$ + 0.01 M phosphate buffer, pH 7 (53). It was proposed that three different surface conditions exist on the electrode during the course pretreatment: (i) the inactive state that results from some combination of inadequate surface cleanliness and/or minimal functional group coverage, (ii) the active surface after anodization with the oxidized form of the oxide layer and (iii) the active surface after cathodization with the reduced form of the oxide layer. Wang and Lin applied short-duration (5–60 sec) potential steps to anodic potentials between 1.0 and 2.5 V followed by steps to cathodic potentials between -1.0 and -2.0 V vs. SCE (54). The potential excursions required for activation depended on the particular redox system (e.g., phenol and uric acid). The activation was performed in neutral phosphate buffer or 1 M NaCl. Wightman and coworkers described

the activation of GC by an anodic potential step to +1.4 V vs. SCE in citrate buffer, pH 5.2, for 20 min (55). The electrode activity was assessed using $Fe(CN)_6^{3-/4-}$ and ascorbic acid. There are other potentiostatic, potentiodynamic, and galvanostatic pretreatments reported (56–59). The paper by Beilby *et al.* discusses the influence of the anodic and cathodic potentials, the ionic strength and pH of the supporting electrolyte, and the length of time of the oxidation or reduction on the degree of activation (59).

5.2.3   Pyrolyzed photoresist films (PPF)

Thin films of sp^2-bonded carbon can be produced by pyrolyzing photoresist layers. These films (PPF) are an attractive alternative to thick-film electrodes because of their smoothness and amenability to patterns. Kinoshita and coworkers were the first to report on the electrochemistry of PPF (60). McCreery and coworkers examined the formation, microstructure, chemical properties, and electrochemical behavior of these thin films in detail, and are using the material as an electrode for molecular electronic assemblies (61–64). This is a new form of conductive carbon, so a complete understanding of the interrelationship between the microstructure, surface chemistry and electrochemical properties has yet to be fully developed. In general, PPF is an electrically conducting material ($\sim 5 \times 10^{-3}$ Ω cm) that possesses a microstructure much like that of GC, but is low in surface oxygen. Presumably, some of the carbon atoms at the exposed edge plane are terminated by hydrogen during the pyrolysis. One of the most practical properties of PPF is its near-atomic smoothness as the surface roughness is on the order of 0.5 nm over square micrometer dimensions (61–64).

PPF is produced by spin coating a thin layer of photoresist onto a clean and smooth substrate, such as Si or quartz. Multiple coatings can be applied to control the final film thickness, which is usually a few micrometers. The coated substrate is then baked in an oven under atmospheric conditions at approximately 90 °C for 30 min. This step cures the photoresist layer. The substrate can then be cut into smaller pieces, if required, for placement in a tube furnace for pyrolysis. A quartz tube furnace is used for this purpose with a forming gas of 95% N_2 + 5% H_2 continuously flowing at approximately 100 sccm (61–64). The main purpose of the forming gas is to keep oxygen from reacting with the hot carbon surface. If oxygen is present then significant carbon gasification will occur. The pyrolysis is conducted by slowly raising the temperature (10 °C min^{-1}) from ambient to 1000 °C and then holding it there for 60 min. The samples are then cooled to room temperature under the constant flow of the forming gas. Film shrinkage occurs due to decomposition of the photoresist and gas evolution. The shrinkage occurs primarily in the film thickness and not so much in the lateral film dimensions. Weight loss and densification also occur during the pyrolysis. About 70% loss of the initial dry weight is typical. The weight loss, though, depends on the heat treatment temperature and, at least at low temperatures, results from the evolution of H_2O, CO, CO_2 and other gaseous decomposition products. Film densification and aromatization occur at the higher heat treatment temperatures.

The microstructure and surface chemistry of PPF have been studied as a function of the pyrolysis temperature (62–64). Raman spectra for PPF reveal the characteristic bands of sp^2 carbon at ~1358 and ~1580 cm^{-1}. The "D" (1358 cm^{-1}) and "G" (1580 cm^{-1}) bands

have been studied extensively and the peak area or intensity ratio (1358/1580) has been correlated with the extent of microstructural disorder (i.e., fraction of exposed edge plane) (62–64). The spectrum for PPF resembles that for glassy carbon. Typical 1358/1580 peak intensity ratios are 1.2–1.5, reflective of a relatively disordered microstructure. The bands narrow with increasing heat treatment temperature suggestive of more microstructural ordering. In terms of the surface chemistry, PPF is generally low in surface oxygen (O/C = ca. 2%) after pyrolysis and somewhat resistant to oxidation in air. McCreery and coworkers have shown, for example, that PPF slowly incorporates oxygen during exposure to the atmosphere over a 2-h period at room temperature, as indicated by an XPS-determined O/C that increases to only about 6% (62–64). The low-oxygen content of PPF is much like that of HGC (47–49). More remains to be learned about how the surface microstructure and chemistry change as a function of the electrode potential.

Clean PPF films possess a low C_{dl}, 5–10 μF cm^{-2}, and exhibit relatively rapid electron-transfer kinetics for several outer-sphere redox systems. For instance, k°_{app} in the low to mid 10^{-2} cm sec^{-1} range is observed for Ru(NH$_3$)$_6$$^{3+/2+}$, chlorpromazine and Fe(CN)$_6$$^{3-/4-}$ (62–64).

5.2.3.1   Mechanical polishing

Even though the adhesion of the PPF to the substrate is generally strong, pretreatment by mechanical polishing is not practical. The films are relatively thin and soft, so polishing with even a 0.05 μm diameter alumina grit would cause significant roughening and destruction of the PPF layer.

5.2.3.2   Solvent cleaning

PPF is probably best and most easily activated by solvent cleaning. As described above, soaking the electrode for 20–30 min in isopropanol (cleaned by distillation and exposure to AC) is effective at cleaning the surface without causing any roughening or microstructural damage (21). This pretreatment effectively dissolves site-blocking contaminants from the surface, particularly from the regions around the edge plane. The pretreatment only affects the surface cleanliness and does not alter the electronic properties, surface microstructure, or surface chemistry. Solvent cleaning is a good starting point for the activation of PPF.

5.2.3.3   Heat treatment

Heat treatment can be used to remove surface oxygen and clean the PPF surface. The electrodes are heat treated during the pyrolysis but the effects of past use can only be removed by a postgrowth heat treatment. For optimum results, the treatment is best performed under high-vacuum (<10^{-6} Torr) conditions. Heating the electrode to about 500°C in the absence of oxygen should be effective at desorbing contaminants. The surface oxygen content, which is low to begin with, will be retained as these functional groups do not decompose at significant rates until temperatures >500 °C are reached. Treatment times from 15 to 30 min are usually sufficient. If higher temperatures are employed, the carbon–oxygen functional groups will decompose (CO and CO$_2$ evolution) possibly leading to pitting and new edge plane site exposure. Due to differences in thermal expansion coefficient, heat

treatment at high temperature might result in film delamination from the substrate. Therefore, care should be taken to perform the heat treatment at a temperature where the PPF film is physically and chemically stable on the substrate surface. As is the case for all other heat-treated carbon electrodes, electrochemical measurements with treated PPF should be made immediately after treatment.

5.2.3.4   *Electrochemical polarization*

Depending on the severity of the conditions, electrochemical polarization can cause surface roughening and microstructural damage, as well as oxygen incorporation. An advantage of the PPF is its atomic smoothness. In most instances, one would not want to pretreat the electrode by severe electrochemical anodization (>1.5 V) or cathodization because of the microstructural damage that would be caused. McCreery and coworkers have studied the stability and surface chemistry of PPF during electrochemical polarization. The material was found to behave in much the same manner as GC during mild potentiodynamic cycling in 0.2 M $HClO_4$ between −0.5 and 1.5 V vs. Ag/AgCl (61–64). As the number of cycles was increased, the O/C increased, resulting in faster $Fe^{3+/2+}$ electron-transfer kinetics. They also examined the electrode after constant potential polarization in 0.1 M H_2SO_4 at +1.8 V for 1 min. Significant oxygen incorporation and microstructural damage occurred as reflected by an increase in C_{dl} to >50 µF cm^{-2}. If polarization is to be employed as a pretreatment, then mild conditions (<1.5 V) should be used.

5.2.4   Carbon fibers

Carbon fibers are classified as microelectrodes (Chapter 6) because of their small size. Typical diameters range from 1 to 40 µm. Microelectrodes offer advantages over conventional macroelectrodes in electroanalytical measurements in terms of (i) a lower background current (i.e., double-layer charging) due to a smaller exposed area, (ii) a smaller size that enables measurements to be made with high spatial resolution, (iii) a faster response time because of a shorter RC time constant, which enables measurements to be made with high temporal resolution and (iv) the ability to make measurements in resistive media due to low ohmic (*iR*) potential losses (65, 66). The fast response time of microelectrodes allows measurement of redox systems with large k^o. For example, k°_{app} for redox systems has been found to be in excess of 1 cm sec^{-1} (67).

Carbon fibers are manufactured from several starting materials including rayon, PAN, pitch, and lignin, with all materials possessing different chemical compositions. Fibers can also be produced by gas-phase deposition from a carbon precursor. A wide variety of synthesis and heat treatment procedures exist for the preparation and post-treatment of the fibers. For this reason, fibers are available with different exposed microstructures and surface chemistries. One has to be cognizant of this when selecting a fiber for a particular electroanalytical application. One way to classify carbon fibers is in terms of the temperature employed for their production. Generally, as the pyrolysis temperature increases, the fiber becomes more enriched with carbon and the microstructure becomes more "graphitized" or ordered. The three general classifications are (i) partially carbonized fibers at temperatures near 500 °C with up to 90 wt % carbon, (ii) carbonized fibers at temperatures between 500

and 1500 °C with 91–99 wt % carbon, and (iii) graphitized fibers at temperatures between 2000 and 3000 °C with >99 wt % carbon (68). The microstructure and surface chemistry can vary considerably from fiber type to type, depending on the source material and the fabrication procedures, and this will have a significant impact on the electrochemical properties. Furthermore, many commercial fibers receive a final surface treatment to improve their adhesion with binders in carbon–carbon composite materials. Removal of such coatings is necessary prior to electrochemical use. The most commonly used fibers in electroanalytical chemistry are the microstructurally disordered types (PAN and pitch). These fiber types have an inherently high fraction of exposed edge plane, and therefore a high active site density.

Carbon fiber microelectrodes can be used in either a disk or a microcylinder geometry. The fiber is usually sealed or insulated with pulled glass or polymeric coatings (65, 66, 69). A disk geometry is one in which the fiber is cut flush with the insulation material. A microcylinder geometry is one in which the fiber protrudes some distance (hundreds of micrometers or more) beyond the end of the insulation. Like every other type of carbon electrode, the basic electrochemical properties of carbon fibers depend on their exposed microstructure and chemical composition. Untreated fibers usually exhibit sluggish electron-transfer kinetics for most redox systems, as evidenced by poorly shaped voltammetric i–E curves. As with other carbon electrodes, pretreatment is usually a prerequisite for carbon fiber microelectrode use. The background current, C_{dl}, and the extent of molecular adsorption are strongly influenced by the exposed microstructure and surface chemistry, which are affected by the pretreatment method. These factors track the fraction of edge plane exposed, as determined from the Raman 1360/1580 peak intensity ratio, as well as the surface oxygen content. The more graphitic the exposed microstructure is, the lower C_{dl} (2–10 μF cm^{-2}) is and the lower the background voltammetric current and surface oxygen content are. Recall that C_{dl} for the basal plane of HOPG is low (i.e., in the 1–5 μF cm^{-2} range). Increased C_{dl} results, at least in part, from a higher density of electronic states at the exposed edge plane sites. This translates into a greater potential-dependent excess surface charge that is counterbalanced by greater ion accumulation and solvent dipole orientation on the solution side of the interface. The background voltammetric current increases because of the larger C_{dl}, but there can also be a contribution from pseudocapacitance associated with electroactive surface carbon–oxygen functionalities. As discussed above, the redox-active functional groups undergo electron transfer in the 0–0.5 V range (acidic solution) and their presence is manifested in a larger background current. The study of carbon fibers is challenging because they often consist of multi-phase microstructures; this means that one orientation is present on the surface, whereas another is present in the core. In addition, the fragility of the fiber, at least in the microcylinder geometry, precludes any polishing to clean and renew the surface. The anisotropic microstructure and inability to polish the surface can make response reproducibility with carbon fibers a challenge.

Figures 5.3a–e show representations of different carbon fiber microstructures (68). The fiber microstructure can be determined by Raman spectroscopy and X-ray diffraction, as discussed above for HOPG and glassy carbon. Carbon fibers come in several different microstructures, as indicated above. A concentric arrangement of the graphene sheets exists in Figure 5.3a (circumferentially orthotropic) with primarily exposed basal plane. This fiber has a single-phase microstructure that is observed for vapor-grown fibers. The physical and chemical properties of such fibers have been previously discussed (70).
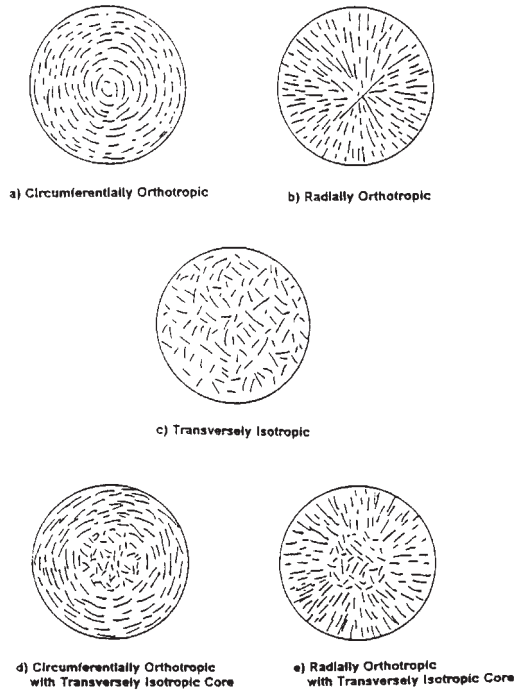
Figure 5.3   Representations of different carbon fiber microstructures.

A center void occurs because of the large energies required to bend the graphene sheets into smaller circumferences.

Figures 5.3b (radially orthotropic) and 5.3c (transversely isotropic) show single-phase microstructures. The graphene sheets are well ordered in a radial alignment with a large portion of exposed graphitic edge plane in one microstructure. A more random distribution of the graphene sheets is seen in the other with an isotropic distribution of both edge and basal plane throughout.

Diagrams of a two-phase microstructure are shown in Figures 5.3d (circumferentially orthotropic with an isotropic core) and 5.3e (radially orthotropic with an isotropic core). The exterior of the fiber has a high degree of basal character with the graphene sheets circumferentially oriented in one microstructure. The thickness of the concentric layers is less than that for the fiber type shown in Figure 5.3a. The fiber core has a random distribution of graphene sheets similar to that for glassy carbon. There is a gradual transition from the ordered surface structure to the disordered core. This fiber is an example of an onion-skin exterior and a random-core interior. The other type has an ordered radial alignment of the graphene sheets at the exterior and a more random, isotropic distribution in the core.

5.2.4.1   *Mechanical polishing*

Carbon fibers in a microcylindrical geometry are too fragile to be polished. However, a fiber in a disk geometry can be polished in a manner similar to that for GC. The same ultraclean

polishing conditions described above for GC should be employed. Care should be taken to avoid damaging the insulation layer. This means a special jig needs to be constructed to hold the microelectrode in a fixed position, if polishing by hand. Alternately, a special microelectrode beveler with a micromanipulator/electrode holder can be used. It is important that all polishing debris be removed from the electrode surface by copious rinsing and ultrasonic cleaning. To avoid damaging the end of the electrode during cleaning, it should not be allowed to "bounce" on the bottom of the solution container. It is best to suspend the microelectrode in the sonicated solution during cleaning. At least for the disk geometry, polishing is a useful first step for electrode activation. One must remember, though, that polishing can roughen the surface and alter the exposed microstructure, particularly for the fiber types with more ordered surface microstructures.

5.2.4.2   Solvent cleaning

Exposure to clean organic solvents can be useful for cleaning and activating carbon fibers. Several different solvents can be used to clean the electrode surface including acetonitrile, isopropanol, dichloromethane, and toluene. The solvents should first be distilled for purification. Reagent-grade solvents often contain impurities at levels that can cause significant electrode deactivation. AC can be added to the distilled solvents for additional purification. Soak times of 20–30 min are usually adequate. The solvent cleaning can also be performed by Soxhlet extraction.

5.2.4.3   Heat treatment

Achieving an ideal carbon fiber reference surface for studies of electrode structure–function is difficult to achieve. Another good method for cleaning carbon fibers without significantly altering the microstructure is high-vacuum heat treatment. Heating the surface in the UHV (10^{-9} Torr) to temperatures near 1000 °C for 30 min causes impurities to desorb and surface oxygen functional groups to decompose. Therefore, this pretreatment cleans the surface by desorbing contaminants and removes surface carbon–oxygen if the temperature is high enough (71). Swain, under the direction of Kuwana, studied the activation of different carbon fiber types by heat treatment (72). The heat-treated fiber surfaces are low in surface oxygen as the carbon–oxygen functionalities decompose between 500 and 900 °C (71, 72). However, the loss of surface oxygen creates dangling bonds on the surface that quickly react in the atmosphere when brought out of the vacuum chamber for use. Therefore, electrochemical measurements should be performed as soon as possible after removal from the chamber. Alternately, the heat treatment can be performed in a quartz tube furnace, carefully purged with nitrogen or argon, at a temperature of ca. 400–800 °C for 30 min. It is more difficult to remove trace levels of oxygen from the tube furnace than in the high vacuum; carbon oxidation and gasification can be a problem. Heat treatment in a tube furnace, if the temperature is kept low, ~400 °C, results in a clean surface but not one that is as low in oxygen as is achieved by vacuum heat treatment. In general, heat treatment is a good starting point for the activation of any carbon fiber type as it produces a clean and low-oxygen surface.

5.2.4.4 *Laser activation*

Laser treatment is useful for cleaning and activating carbon fibers without altering the microstructure or surface chemistry, at least if the treatment is performed under mild conditions (i.e., low incident laser power). Strein and Ewing used a pulsed N_2 laser operating at 337 nm to activate a carbon fiber microdisk electrode (73). The treatment works by both heating the surface (absorbed light), resulting in the desorption of contaminants and creation of new edge plane (e.g., active sites). The extent of edge plane formation depends on the pulse power density, pulse duration, as well as the native fiber microstructure. If significant new edge plane is exposed, then k_{app}° for different redox systems will increase as will the background voltammetric current and the surface oxygen content.

5.2.4.5 *Electrochemical polarization*

Electrochemical pretreatment is the most common method for activating carbon fibers. There are many electrochemical pretreatment methods reported in the literature. It is best to apply the pretreatment to a clean and reproducibly conditioned surface for best results. Such a surface can be obtained by mechanical polishing (disk electrodes only), solvent cleaning, or vacuum heat treatment. Usually, electrochemical pretreatment involves anodic polarization in acidic, neutral, or basic media with the magnitude of the potential, the time, and the medium being critical parameters. The polarization can be performed potentiostatically, potentiodynamically, or galvanostatically. Mild polarization in acid (<1.5 V) can be used to activate the more disordered fibers when only surface cleaning and minimal oxidation are desired. Severe polarization (>1.5 V) can be used to activate more ordered fibers by creating new edge plane. As a consequence of the edge plane formation, the background voltammetric current, the surface oxygen content, and molecular adsorption will increase. A few representative examples are given below.

Gonon and coworkers demonstrated that the response of a pyrolytic carbon fiber can be dramatically improved by immersing the fiber in a phosphate-buffered saline (PBS) solution (0.2 g L^{-1} KCl, 0.2 g L^{-1} KH_2PO_4, 0.047 g L^{-1} $MgCl_2$, 8 g L^{-1} NaCl, and 1.15 g L^{-1} Na_2HPO_4, pH 7.4) and alternating the potential between 0 and 3 V vs. Ag/AgCl at a frequency of 70 Hz and a duration of 20 sec (74). This is a rather severe treatment (the so-called French-fry method) that improved the sensitivity, reversibility, and selectivity of this particular fiber type for catecholamines. An interesting feature of the treated electrode was its ability to resolve the voltammetric oxidation of catechols from ascorbic acid. Ewing *et al.* activated PAN-based carbon fibers by potentiodynamic cycling between 0 and 1.8 V vs. SCE at 250 V sec^{-1} in pH 7.4 citrate–phosphate buffer (75). The duration of the cycling can be varied from several minutes to several tens of minutes. The anodic limit is well into the oxygen evolution regime at this solution pH so that microstructural and chemical changes (i.e., increasing the surface oxygen content) occur. The electrode sensitivity and reproducibility for various redox systems (e.g., catecholamines) were improved after pretreatment. Kovach *et al.* treated carbon fibers in a microcylinder geometry by potentiodynamic cycling between 0 and 3 V vs. SCE in phosphate buffer, pH 7.4, for 20 sec (76). This was followed by potentiostating the electrode at 0 V in the buffer solution for 30–60 min. The latter was noted to improve the response stability. Again, the anodic limit is well into the oxygen evolution regime at this solution pH so that microstructural

and chemical changes occur. Many reported pretreatments for carbon fibers involve anodic potential excursions of ~3 V (74, 76–78), which according to Adams and coworkers is "overkill" for surface oxidation as a significant portion of the current passed goes toward oxygen evolution (79). Adams and coworkers found that milder electrochemical polarization was also effective at activating carbon fibers. They reported two protocols, both in pH 7.4 PBS solution: (i) potentiodynamic cycling from 0 to 2.6 V vs. Ag/AgCl for 30 sec and (ii) potentiodynamic cycling from 0 to 1.3 V vs. Ag/AgCl for 30 sec. These are two recommended methods for activating most fiber types. The authors demonstrated that electrochemical polarization increases the electrode sensitivity toward catechols but decreases the response time and they recommended that future applications of pretreated fibers include experimental checks of the electrode response time.

5.2.5   Carbon nanotubes

These are new and interesting members of the carbon electrode family offering unique mechanical and electronic properties combined with chemical stability (80–82). So far, they have not been used extensively in electroanalytical chemistry but this is likely to change in the near future. Carbon nanotubes are formed as two structures: multi-walled (MWNT) and single-walled (SWNT) (82). MWNTs are composed of concentric and closed graphene tubules, each with a rolled-up graphene sheet. A range of diameters can be produced from a few to about 30 nm. The majority of the research in this field over the years has utilized MWNTs because of the difficulty in producing phase-pure and oriented SWNTs. An SWNT is made of a single graphite sheet rolled seamlessly with a diameter of 1–2 nm. SWNTs are usually arranged in a regular pattern of bundles that consist of tens to hundreds of tubes in contact with each other. Nanotubes can be grown in a "spaghetti mesh-like" arrangement or in an ordered array or network (82). An interesting property relevant to electrochemistry is the fact that the material can possess either metallic or semi-conducting electrical properties depending on the diameter and lattice helicity.

As discussed by Dai and others, nanotubes can be synthesized by arc discharge, laser ablation, and chemical vapor deposition (CVD) methods (82). The first two employ a solid-state precursor as the carbon source and involve vaporization at high temperatures (thousands of degrees centigrade). These well-established methods produce high-quality nanotube structures, despite the by-products that are formed. CVD utilizes a hydrocarbon source gas and a metal catalyst particle as a "seed" for nanotube growth. Growth by CVD occurs at lower temperatures (500–1000 °C) than the arc discharge or laser ablation methods. The preparation of the catalyst is a critical step in the nanotube growth. Catalysts have been prepared as thin metal layers, thin metal salt layers, and dispersed nanoparticles (83). Fe, Co, and their alloys with Mo are used as catalysts (82, 83). Both SWNTs and MWNTs can be produced by all three methods. Great progress has been made in recent years, particularly by the CVD method, producing SWNTs with high crystallinity and perfection.

Carbon nanotubes can be grown on conducting Si, Au, Pt, and glass. The first three substrates are useful for making nanotubes into electrochemical electrodes. There are three ways nanotubes have been configured as an electrochemical electrode. First, nanotubes have been made into the equivalent of a carbon paste electrode by dispersion into mineral

oil and cast into a Teflon cavity. Valentini *et al.* found that a mixture of 60% nanotube (by mass) and 40% mineral oil produced an electrode with good electrochemical properties (84). Second, the "spaghetti mesh-like" arrangement of nanotubes can be physically attached to an electrode surface. Luo *et al.* cast a network of SWNTs on a glassy carbon electrode (84). This was accomplished by dispersing 1 mg of nanotubes in *N,N*-dimethyl-formamide. Approximately 10 μL of this dispersion was dropped on the glassy carbon electrode and the solvent evaporated. The electrochemical response of this electrode, however, contains a contribution from both the nanotubes and the underlying support electrode. Third, an individual nanotube or bundle can be fabricated into a microelectrode. Crooks and coworkers reported the electrochemical behavior of a single nanotube, attached to a conducting wire and insulated with polyphenol (85). The use of this carbon type in electroanalytical chemistry is so new that there is not a wealth of literature yet available on pretreatment methods and their efficacy.

5.2.5.1 *Chemical oxidation*

Because of their structure, carbon nanotube electrodes are not amenable to conventional pretreatment. The material is too fragile for mechanical polishing and heat treatment would likely not be practical due to the way nanotube electrodes are formed (paste electrode or physically contacted to another electrode). Laser activation could be used but, so far, this pretreatment method has not been studied. One of the challenges faced while working with nanotubes is their purification after growth. Nanotubes are routinely submitted to various chemical and physical treatments to remove graphitic nanoparticle, amorphous carbon, and metal catalyst impurities (82). Chemical oxidation is often used for this purpose and therefore can serve as a pretreatment method. Purification of the nanotubes is a critical step in their application, so much work has gone into developing appropriate cleaning and dispersing treatments. In one method reported by Valentini *et al.*, the authors oxidized the nanotubes in a tube furnace at 400 °C in flowing air for 1 h (84). This was followed by exposure of the nanotubes to 6 M HCl for 4 h under ultrasonic agitation. The nanotubes were then washed with ultrapure water before being placed in 2 M HNO_3 for 20 h under ultrasonic agitation. The final step involved a copious rinse with ultrapure water. This chemical oxidation removes amorphous carbon and metal catalyst impurities and introduces significant carbon–oxygen functionalization at the exposed edge plane and defect sites.

5.2.5.2 *Electrochemical polarization*

Potentiodynamic and potentiostatic methods can also be used to activate nanotubes. Similar to chemical oxidation, electrochemical pretreatment can effectively remove impurities and cause the creation of carbon–oxygen functional groups at the exposed edge plane and defect sites. The same authors reported on an electrochemical pretreatment that involved potentiostating the electrode at +1.7 V vs. Ag/AgCl in pH 7 phosphate buffer for 3 min followed by 3 min at −1.5 V (84). Both the chemical and electrochemical oxidations improved the electrode response (smaller voltammetric ΔE_p and larger i_p values) for $Fe(CN)_6^{3-/4-}$, serotonin, and caffeic acid.

5.2.6   Diamond films

Electrically conducting diamond is a new type of carbon electrode material that is beginning to find widespread use in electroanalysis (86–88). The material possesses properties superior to other forms of carbon that include (i) low and stable background current over a wide potential range, (ii) wide working potential window in aqueous media, (iii) relatively rapid electron-transfer kinetics for several redox systems without conventional pretreatment, (iv) weak molecular adsorption, (v) dimensional stability and corrosion resistance, and (vi) optical transparency. The material is now available from several commercial sources and is not overly expensive, as commonly perceived (89).

   Diamond is often grown as a thin film on a conducting substrate, such as highly doped Si, Mo, W, or Ti, using one of the several methods: microwave plasma, hot-filament or combustion flame-assisted CVD. The most common method is microwave plasma CVD. One reason for this is the commercial availability of such reactor systems. While the mechanism of film growth is somewhat different from method to method, all serve to activate a carbonaceous source gas producing a growth precursor in close proximity to the substrate surface (90). A typical CVD reactor consists of the growth chamber and equipment associated with the particular activation method (e.g., microwave power source) as well as various accessories, such as mass flow controllers for regulating the source gas, a throttle exhaust value and controller for regulating the system pressure, a pumping system, temperature measurement capability, and the gas handling system for supplying the source gases. A block diagram of a typical CVD system is shown in Figure 5.4. The same reactor design can be used for growing carbon nanotubes, for example. In the case of microwave-assisted CVD, the microwave energy from the generator is directed to, and focused within,
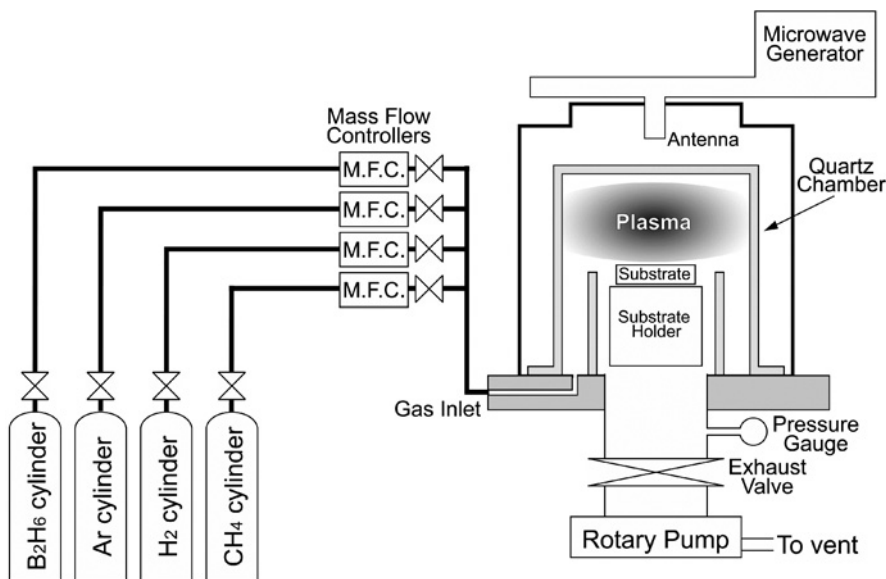
Figure 5.4   Block diagram of a typical microwave plasma CVD reactor.
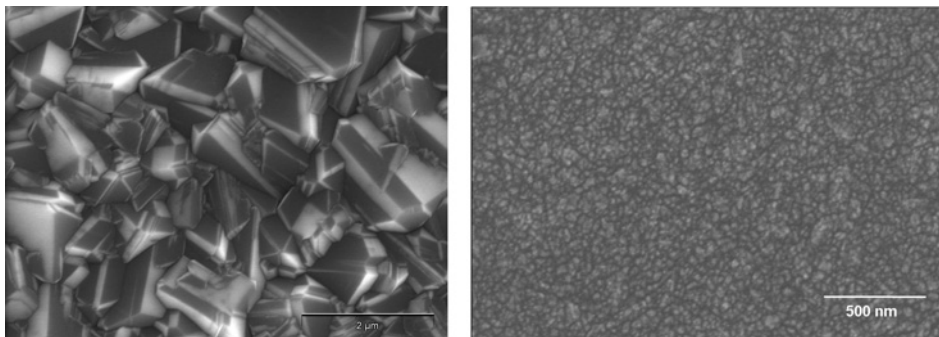
Figure 5.5 SEM images of (left) a boron-doped microcrystalline (scale bar = 2 μm) and (right) a boron-doped nanocrystalline (scale bar = 500 nm) diamond thin film grown on Si.

a quartz cavity producing a spherically shaped, glow-discharge plasma directly above the substrate. The substrate can be positioned either outside of (few mm), or immersed within, the intense discharge region. The plasma is where the reactive species involved in the diamond growth are formed. The key deposition parameters to control are the source gas composition, microwave power, system pressure, and substrate temperature.

There are two types of synthetic diamond thin film routinely produced: microcrystalline and nanocrystalline (91, 92). The classification of these two film types is based on their nominal crystallite size and morphology. Figure 5.5 shows SEM images of the two types of boron-doped diamond deposited as thin films on Si. High-quality microcrystalline diamond films are deposited from CH_4/H_2 source gas mixtures with volumetric ratios of 0.3–1.0%, microwave powers of 0.8–1 kW, pressures of 35–65 Torr, and substrate temperatures of 700–800 °C. Under these conditions, $CH_3\bullet$ is the primary growth precursor. The added hydrogen serves several critical functions: (i) abstraction of hydrogen from chemisorbed methyl groups on the growing film surface thereby producing active sites for carbon addition, (ii) activation of reactive methyl radicals in the gas phase by hydrogen abstraction, (iii) passivation of dangling bonds on the growth surface, which is important for minimizing reconstruction from sp^3 to sp^2 bonding, and (iv) gasification of any sp^2-bonded, non-diamond carbon impurity that forms on the growth surface. It can be seen from the image that microcrystalline films are well faceted with crystallite sizes on the order of a few micrometers, or greater, in lateral dimension. The individual crystallites are randomly oriented and there tends to be significant twinning. A grain boundary is present at the junction between two or more crystallites, which has structural, chemical, and electronic properties that are different from the grains.

One way high-quality nanocrystalline diamond films are deposited is from CH_4/Ar source gas mixtures using a volumetric ratio of 0.5–1.0% with little or no added hydrogen, microwave power of 0.8–1 kW, pressure of 130–160 Torr, and substrate temperature of 700–800 °C. Gruen and coworkers discovered some years ago that phase-pure nanocrystalline diamond can be grown from hydrogen-poor CH_4/Ar gas mixtures (93–103). The most remarkable difference in films grown using hydrogen-poor gas mixtures, compared with those grown from conventional hydrogen-rich mixtures, is the nanocrystallinity and

smoothness (rms roughness ~10–30 nm over large areas) of the former, as can be seen in the SEM image shown above. Noble or inert gas addition to hydrogen-rich plasmas (e.g., 0.5% CH_4/H_2) enhances the growth rate of films by increasing the $CH_3\bullet$ and atomic hydrogen concentrations in the plasma. The low excitation energy of inert gases, such as Ar or Xe, results in a plasma discharge with a higher electron density, and this leads to the higher levels of $CH_3\bullet$ and $H\bullet$. There is a fundamental change in the plasma chemistry, growth mechanism, growth rate, and film properties as one transitions from a hydrogen-rich to a hydrogen-poor plasma. In particular, hydrogen-poor plasmas have a high concentration of carbon dimer, C_2, which serves as both the primary growth and the nucleation species. The nanocrystallinity is a result of a growth and nucleation mechanism involving the insertion of C_2 into surface C−H bonds. Apparently during growth, there is sufficient hydrogen from the CH_4 to minimize surface reconstruction to an sp^2-bonded phase. The C_2 addition is believed to occur by a two-step growth mechanism (93–103). A C_2 molecule approaches the unreconstructed monohydride surface and inserts into a C−H bond. The C_2 molecule then rotates to insert its other carbon into a neighboring C−H bond on the surface. A C_2 molecule then inserts into an adjacent C−H bond, parallel to the newly inserted C_2 dimer. The original state of the surface is recovered by the formation of a bond between carbon atoms in the adjacent surface dimers. Very high rates of heterogeneous renucleation are observed on the order of 10^{10} cm^{-2}, and the resulting films consist of randomly oriented, phase-pure grains of diamond with well-delineated grain boundaries (93–103). Nanocrystalline films produced in Ar-rich plasma possess a very fine, uniform grain size (3–5 nm is typical for high-quality ultrananocrystalline diamond) and a small but non-negligible amount of sp^2-bonded carbon at the abrupt grain boundaries.

The instantaneous nucleation density during diamond growth on untreated, smooth non-diamond substrates is generally low. Therefore, substrate pretreatment is a prerequisite for achieving thin continuous films. A common substrate preparation involves either mechanical polishing with small-diameter diamond powder (0.01–1 μm) suspended in ethanol or ultrasonication in a diamond powder/solvent suspension. For example, with the latter, the diamond powder can be suspended in ethanol and the ultrasonic agitation performed in this medium. Either pretreatment results in the formation of scratches and defects, as well as the dispersion of some embedded diamond particles over the surface. Subsequent substrate washing to remove polishing debris and clusters of diamond particles from the surface is critical. The washing typically involves sequential ultrasonic cleanings in organic solvents (isopropanol, acetone, and methanol). Enhancement of the instantaneous heterogeneous nucleation density results from both the physical defects introduced and the dispersed diamond seed particles.

A number of tools are useful for characterizing the physical and chemical properties of diamond thin films including scanning electron microscopy, Raman spectroscopy, X-ray diffraction, X-ray photoelectron spectroscopy, conductivity-probe atomic force microscopy, and near-edge X-ray absorption spectroscopy. Detailed characterization of diamond electrodes has been reported in the literature. Raman spectroscopy is particularly useful. A sharp first-order phonon mode at 1332 cm^{-1} is seen for diamond. The line width is inversely related to the defect density (phonon scattering) and the line position can reflect tensile or compressive stress within the film (104, 105). Scattering intensity also is present in the 1500–1560 cm^{-1} range when the film contains non-diamond carbon impurity. This

impurity is not graphitic but possesses a mixed sp^2 and sp^3 bonding. The scattering cross-section for the non-diamond carbon is approximately 50 times greater than that for diamond, so Raman spectroscopy is particularly sensitive to the presence of non-diamond carbon impurity (106). The ratio of the $1332/1580$ cm^{-1} bands is reflective of the film quality. The higher this ratio, the lower the film quality. This is manifested in a higher voltammetric background current, a narrower working potential window, and a greater molecular adsorption (107, 108). The Raman spectral features for microcrystalline and nanocrystalline films are quite different, and the spectral features, particularly for the microcrystalline films, can change depending on the boron-doping level (109–111).

Diamond is one of the mother nature's best electrical insulators. In order to have sufficient electrical conductivity for electroanalytical measurements (<0.1 Ω cm or >10 S cm^{-1}), diamond films must be doped. The most common dopant is boron with doping levels in the 1×10^{19} cm^{-3} range, or greater, being the norm. The introduction of boron imparts p-type electrical properties to the film. Other dopants have also been used, such as nitrogen, phosphorous, and sulfur, but all suffer from either low solubility or high activation energy (90). The boron can be added to the source gas mixture in the form of B_2H_6 or $B(CH_3)_3$. B_2H_6 is the preferred gas as $B(CH_3)_3$ not only adds boron to the source gas mixture but also extra carbon. This extra carbon can alter the film morphology and decrease the quality. The electrically active boron is that which substitutionally inserts into the growing lattice. The films are rendered electrically conducting through incorporation of boron dopant atoms during deposition, although the electrical conductivity depends in a complex manner on lattice hydrogen, defects, and dangling bonds, in addition to the doping level. For example, films can be doped as high as 10^{21} cm^{-3} with little alteration of the morphology or microstructure. Typical film resistivities are <0.05 Ω cm, carrier concentrations are 10^{19} cm^{-3}, or greater, and carrier mobilities are in the $0.1–10$ cm^2 V^{-1} sec^{-1} range. Thus far, there has been little study of how to activate diamond electrodes for electron transfer. Actually, one of the interesting features of this electrode material is the fact that pretreatment is usually not required to achieve an "activated" electrode. The most active surface tends to be the hydrogen-terminated one.

5.2.6.1 *Mechanical polishing*

As mentioned above, most pretreatments of carbon electrodes initially involve mechanical polishing to remove contaminant layers and expose a fresh surface. Due to its hardness, mechanical polishing of diamond is not practical in this sense. Contaminant layers can be removed but a fresh surface will not be exposed. The polishing also likely causes the rupture of the surface carbon–hydrogen bonds leading to the incorporation of surface oxygen. If polishing is performed, then a thorough cleaning is necessary to remove all the polishing debris prior to use, particularly the alumina powder. Extensive ultrasonic cleaning in clean organic solvents (isopropanol and acetone) and ultrapure water is useful for this purpose.

5.2.6.2 *Acid washing and rehydrogenation*

Diamond electrodes tend to be quite "active" for electron transfer without pretreatment, at least for some outer-sphere redox systems. Exposure to the laboratory atmosphere does not deactivate this electrode like it does other sp^2 carbons (39). As deposited diamond

electrodes exhibit relatively rapid heterogeneous electron-transfer rate constants for several redox systems (91, 92). It is our experience that in cases where pretreatment is required, the most active diamond electrodes are produced by a two-step procedure: (i) acid washing and (ii) hydrogen plasma treatment. The acid washing involves soaking the electrode for 30 min each in a 3:1 (v/v) HNO_3/HCl solution and a 30% (v/v) H_2O_2 solution. The solutions are warmed to about 50 °C. Copious rinsing with ultrapure water is performed after each solution exposure. Exposure to these oxidizing solutions removes chemical contaminants, metal impurities, and adventitious non-diamond carbon impurity from the surface. Oxygen is also incorporated as the surface becomes much more hydrophilic. XPS-determined O/C atomic ratios increase from ~0.002 to 0.15. After water rinsing, the electrodes are transferred to the CVD reactor for a 15–30 min hydrogen plasma treatment (atomic hydrogen). This treatment removes the surface oxygen by incorporating hydrogen. The resulting film is low in surface oxygen and it is hydrophobic. In order to retain the hydrogen surface termination, the films must be slowly cooled in the presence of atomic hydrogen by lowering the power and pressure over a 5–15 min period until the electrode surface temperature is below 400 °C. Typical heterogeneous electron-transfer rate constants range from 0.02 to 0.2 cm sec^{-1} for redox systems such as $Fe(CN)_6^{3-/4-}$, $Ru(NH_3)_6^{3+/2+}$, and $IrCl_6^{2-/3-}$ (91, 92).

5.2.6.3   Solvent cleaning

Diamond thin-film electrodes in our laboratory are routinely cleaned by soaking in distilled isopropanol for 20 min prior to use. While no detailed study has been performed yet, it is presumed that the solvent exposure cleans the diamond surface by desorbing and/or dissolving contaminants. A controlled study of the effect of solvent cleaning on the electrochemical response of diamond is needed; however, it is expected that this pretreatment will be an effective, non-destructive one for activating diamond electrodes, when necessary.

5.2.6.4   Heat treatment

Although not studied as yet either, heat treatment is expected to be an effective, non-destructive method for activating diamond electrodes, if performed under the appropriate conditions. Heat treatment of boron-doped diamond cleans the surface by desorbing adsorbed contaminants, but it also can alter the electronic properties. It is expected that adsorbed contaminants would possess low activation energies for desorption; therefore, low heat treatment temperatures should be needed for cleaning. Temperatures of 250–500 °C for 30 min, either in high vacuum or a quartz tube furnace under an inert gas atmosphere, should be adequate. Exposure to this temperature is also sufficient to desorb subsurface hydrogen, which has been shown to function as a charge carrier and increase the electrical conductivity in semiconducting diamond (112–114). This reduces the number of charge carriers in the surface region. However, this carrier density is orders of magnitude lower than that arising from the substitutionally inserted boron, so little change in the electrical conductivity is expected. In contrast, heat treatment at these temperatures is also sufficient to desorb hydrogen from B–H complexes on the surface. The interacting hydrogen functions as an electron donor and compensates the boron acceptor (115). This compensation leads to a reduction in the carrier concentration. Destruction of these

complexes is expected to increase the active carrier concentration and, consequently, the film conductivity.

At heat treatment temperatures in the 700–900 °C range, the desorption of contaminants and the surface terminating hydrogen will also occur. This will create dangling bonds on the surface, which will result in surface reconstruction to form sp^2-bonded clusters and/or introduce surface oxygen once exposed to the atmosphere. For this reason, heat treatment of diamond at these high temperatures should be avoided.

5.2.6.5 *Electrochemical polarization*

Potentiostatic and potentiodynamic polarizations in either strong acid or base have been investigated, to a limited extent, as a pretreatment. Unlike most sp^2 carbon electrodes, electrochemical pretreatment does not alter the diamond microstructure, if the film quality is high, but does change the surface chemistry, causing the incorporation of oxygen. So far, there has been no controlled, systematic study of the effect of electrochemical polarization on the electron-transfer kinetics for different redox systems, so the full extent of the activation method is unknown. What has been reported is (i) converting from a hydrogen to an oxygen surface termination improves the electrode response stability toward some redox systems and (ii) in the case of adsorbed reaction products (e.g., phenol oxidation), anodic polarization can remove these adsorbed contaminants presumably by complete oxidation to CO_2 with OH• being the reactive species. One example of a severe anodic polarization applied to a microcrystalline diamond electrode was reported by Fujishima and coworkers (116). It involved potentiostating the electrode at 2.6 V vs. SCE for 4 min in pH 2 Britton–Robinson buffer. A total anodic charge of 720 mC cm^{-2} was passed. The pretreatment presumably did not alter the microstructure or crystallinity, but did increase the surface oxygen content.

5.2.7 **Tetrahedral amorphous carbon (Ta-C) films**

The use of conducting diamond as an electrochemical electrode has stimulated recent interest in the study of diamond-like carbons (DLCs) as electrode materials. Amorphous carbon thin films (0.1–20 μm thick) with a mixed sp^2- and sp^3-bonded microstructure can be produced by several deposition methods. These films, depending on their microstructure, can have hardness, strength, and chemical inertness close to that of crystalline diamond, yet be produced as a smooth and relatively stress-free film at low temperatures (<200 °C). These kinds of amorphous films include a variety of DLCs and Ta-C, which is sometimes referred to as amorphous diamond. In general, these materials have local bonding that falls between that for graphite and diamond—a mixed sp^2 (threefold coordinated) and sp^3 (fourfold coordinated) microstructure. Films can contain hydrogen or be relatively hydrogen-free, depending upon the growth conditions. The type of microstructure formed very much depends on the film deposition conditions. While their study as electrochemical electrodes is a relatively recent research undertaking, DLC and Ta-C films have been used for a number of years as wear- and corrosion-resistant coatings for cutting tools (89, 117–121).

The hardness of these coatings can be tailored from something comparable to graphite up to diamond by controlling the ratio of the sp^3 to sp^2 carbon–carbon bonding and the hydrogen content in the film. This is accomplished by adjusting the deposition conditions. The coating of stainless steel, electrically conducting Si, and other temperature sensitive materials (e.g., Ti and Al alloys, plastics, etc.) is rather commonplace nowadays. Not only do the film hardness and coefficient of friction depend on the microstructure and hydrogen content, but so do the electrical properties. The deposition of DLC films with a high level of sp^3 bonding (>80%) is possible when the carbon ions used for growth have kinetic energies in the range of 30–600 eV. Based on the pioneering work with mass selected ion beams (MSIB), DLC formation on substrates is understood by the subplantation model of Lifshitz and coworkers (122, 123) and Robertson (123). In general, DLC films are deposited from ionized carbon plasmas. Ta-C is a specific type of DLC material that is very low in hydrogen content and possesses high hardness and density.

Ta-C films can be produced by pulsed laser, vacuum-arc, laser-arc, and high-current-arc deposition (117–123). Common to all four methods is the use of a high-purity graphite target and the formation of energetic carbon ions with kinetic energies in the 30–600 eV range. These ions are accelerated toward the substrate in the presence of an electric field and they penetrate into the superficial atomic layers (subplantation model) (122, 123). There they produce a highly compressive stress, which promotes sp^3-hybridized bonding. The deposition is carried out under high-vacuum conditions to minimize loss of carbon ion kinetic energy by interaction with residual gas species. The required conditions for Ta-C deposition are the combination of sufficient carbon particle kinetic energy and low deposition temperature. A common problem with the arc deposition methods is particle emission (e.g., clusters of carbon atoms and other impurities) from the cathode. These particles can get incorporated into the deposited film and disturb the film growth. Therefore, filtering techniques have been developed to isolate the primary growth species from the impurities during deposition. Typically, ion filtration is accomplished using electromagnetic fields (122, 123).

Ta-C films can be viewed as nanostructured or nanocomposite materials. The electrical conductivity depends on the extent of sp^2-bonded carbon in the microstructure. Amorphous DLC films with high sp^3 carbon content are poor electrical conductors and therefore have limited application as electrochemical electrodes. The sp^2 carbon content has to be increased to make the films more electrically conducting. The microstructural disorder and composition (e.g., hydrogen and sp^2 carbon fraction) affect the electrical conductivity. One way this is accomplished is through ion bombardment. During ion bombardment, the sp^3 carbon bonding is gradually converted into an sp^2-bonded phase. Growing, clustering, and ordering of the sp^2 carbon domains occur during this process, as revealed by Raman spectroscopy (122–125). The extent of structural rearrangement depends on the ion energy and dose, but the change in electrical resistivity can vary from the original 10^8 to 10^{-3} Ω cm (122, 123). The ions can either be carbon, in which case no impurity is added, or others, such as nitrogen.

The electrochemical properties of electrically conducting Ta-C films have not yet been extensively studied. In fact, there have only been a couple of literature citations. Yoo *et al.* studied the electrochemical behavior of nitrogen-incorporated Ta-C thin-film electrodes (118). A low background current and a wide working potential window (>3 V) in aqueous

media were reported. Cyclic voltammetric studies of $Ru(NH_3)_6^{3+/2+}$ and Co(III)-sepulchrate revealed electrochemical reversibility at par with that of highly boron-doped diamond electrodes. In addition, the electrochemical reversibility of the Cl_2/Cl^- and quinone/hydroquinone redox systems was better than that observed for highly boron-doped diamond. Evstefeeva *et al.* performed electrochemical impedance measurements on Ta-C films annealed at 700–900 °C in vacuum or ion implanted with C^+ ions (118). $Fe(CN)_6^{3-/4-}$ was used as the redox test system to evaluate electrode activity. The authors observed that both the vacuum heat treatment and the ion implantation imparted electrochemical activity to inactive Ta-C films. There has simply not been enough work yet with this form of carbon to know how different pretreatments affect the electrochemical response. The following provides some speculation as to how this material might best be prepared for use in electroanalytical measurements.

5.2.7.1 *Mechanical polishing*

Like diamond, polishing is not practical due to the material hardness. There would simply be no new carbon exposed, but contaminant layers would be removed from the surface. There would also likely be some surface oxygen incorporation if the polishing is performed in the ambient.

5.2.7.2 *Solvent cleaning*

Solvent cleaning, as applied to other carbon electrodes, is expected to be an effective, non-damaging method of electrode pretreatment. Several different solvents can be used to clean the electrode surface including acetonitrile, isopropanol, dichloromethane, and toluene. The solvents should first be distilled for purification. Reagent-grade solvents often contain impurities at levels that can cause significant electrode deactivation. AC can be added to the distilled solvents for additional purification. Soak times of 20–30 min should be adequate. The solvent cleaning can also be performed by Soxhlet extraction.

5.2.7.3 *Heat treatment*

Heat treatment, depending on the conditions, is expected to be effective at both desorbing contaminants and improving the electrical conductivity. Low-temperature heat treatment in an inert atmosphere or in vacuum at temperatures <500 °C should be effective at desorbing contaminants. Care should be taken to minimize the presence of oxygen as significant gasification will occur at this temperature. Heat treatment at higher temperatures might also desorb hydrogen from the lattice, thereby improving the electrical conductivity as the loss of hydrogen leads to the formation of sp^2-bonded carbon (π states).

5.2.7.4 *Electrochemical polarization*

Electrochemical polarization might also be a useful pretreatment method, but this remains to be determined. Surface oxygen would certainly be incorporated during such a treatment but the extent of morphological and microstructural alteration would depend on the sp^3/sp^2 fraction of the film. The more sp^2-bonded carbon there is, the greater is the

extent of morphological and microstructural degradation expected. Conditions, such as those described for activating glassy carbon, would likely be useful for Ta-C films. For example, potentiodynamic cycling in 0.1 M KNO_3 between -0.5 and $+1.8$ V vs. SCE would introduce some surface carbon–oxygen functionality and possibly clean the surface. In summary, the activation of this type of carbon films remains an open area for research.

5.3   METAL ELECTRODES

A wide choice of solid metal electrodes exists for use in electroanalysis including platinum, gold, nickel, and palladium. Of these, platinum and gold are the most commonly used. In general, metal electrodes exhibit fast electron-transfer kinetics for many redox systems and possess a relatively wide anodic potential window. The cathodic window for some, such as platinum, is more limited due to hydrogen evolution. The background voltammetric i–E curves for metals usually are characterized by a larger overall current per geometric area than that for carbon electrodes and exhibit features or peaks associated with the formation and reduction of surface oxides, and the adsorption and desorption of H^+ and other ions. Metals have a larger C_{dl} than most carbon electrodes and this contributes to the larger background current. The presence of the surface oxides, for example, can alter the electrode reaction kinetics and mechanism for certain redox systems and this can lead to variability in the electroanalytical measurement. Due to the specific adsorption of anions, the heterogeneous electron-transfer rate constant for some redox systems at metal electrodes is quite sensitive to the electrolyte composition, more so than for carbon. For instance, anions such as Cl^-, Br^-, I^-, CN^-, S^{2-}, etc., show a strong tendency to adsorb on metal surfaces. The adsorption can block sites involved in the electrochemical reaction and alter both the reaction kinetics and the mechanism (126).

Metal electrodes can come in either bulk or thin-film form. This discussion will focus on the thin-film forms of platinum and gold. The fabrication and characterization of thin-film metal electrodes have been comprehensively described by Anderson and Winograd (127), so only a brief discussion is given herein. In general, thin films of a metal can be formed on a variety of substrates by vacuum evaporation, DC and RF sputtering, screen printing and CVD. Common substrates are glass (soda-lime and quartz), silicon, and mica. The substrates should possess a relatively smooth morphology with low surface roughness. The preparation of the substrate is a key step in the formation of well-adhering, electrically conducting and optically transparent (if needed for the application) films. Cleaning is a critical step in the substrate preparation that is sometimes overlooked. A common procedure for cleaning glass or oxide-coated silicon involves boiling in an aqueous detergent solution, rinsing with ultrapure water, followed by degreasing with clean organic solvents, such as isopropanol or methanol. When the surface is clean, distilled water will run off the surface as a continuous sheet and not bead up in the form of droplets. Mica is best prepared by cleaving the layer planes with tape or a sharp knife, which results in the exposure of a clean basal plane. The cleaning step should be performed immediately prior to film deposition.

5.3.1 Polycrystalline platinum and gold

As mentioned above, several methods can be used to deposit thin-film metal electrodes. Vacuum evaporation is performed at reduced pressures (ca. 10^{-6} Torr or lower). Deposition in the high vacuum is necessary to ensure that the mean free path of the evaporated growth species is long enough to reach the substrate. Evaporation is accomplished by melting a piece of the metal that is attached to a conductive support. This enables the metal to be resistively heated. Electron beam heating is also sometimes used. The key to keeping the deposited film chemically pure is the high-vacuum environment.

DC or RF sputtering is closely related to the cleaning process for activating electrodes described above. An electrical discharge is maintained between two electrodes, one of which is the material to be deposited (i.e., target), or a glow-discharge plasma is formed in the vicinity of the target. Both types of discharge can be formed in the presence of low-pressure (~10 mTorr) argon gas. Energetic argon ions (cations) are formed and accelerated into the negatively biased target. The ions gain kinetic energy and momentum from the accelerating bias voltage (approximately a few kV). Momentum is transferred to the target material causing the ejection of atoms or ions that deposit on the substrate with relatively high velocities. DC sputtering is best for electrically conducting targets, whereas the RF method is more useful for depositing films from insulating targets. Sputtered films often have better adhesion to the substrate than do evaporated films. This is because of the greater physical force with which they are deposited. Unlike evaporative deposition, sputter deposition methods can be carried out at lower temperatures. However, the films are not deposited in the high vacuum, so the chemical purity of the sputtered films can be lower than that of evaporated films.

The screen-printed approach for depositing thin films of metal has become popular in recent years. This approach is especially useful for producing multiple electrodes on a substrate or electrode array structures. Patterns are photolithographically formed on a screen, whose mesh contains open and blocked zones. An ink containing the metal of interest is applied to the screen and forced through the open zones onto the substrate using a squeegee blade. Once the solvent has been evaporated (air dry or an oven cure), the electrode is ready for use. In the CVD approach, molecules of a volatile precursor are transported in a carrier gas to a heated substrate. The compounds reach the substrate and react to form the desired metal film.

Both platinum and gold films are routinely deposited by vacuum deposition, sputtering, and screen-printing techniques. Macrosized electrodes can be formed or microlithography can be used to produce arrays of metal microelectrode structures. Adhesion layers are often used to produce well-adhering films. The best adhesion layers tend to be formed from metals (particularly the transition metals) that readily form oxides. The metal atoms deposited can then form covalent bonds with the oxide substrate lattice while simultaneously alloying with the metal film. Both chemical processes contribute to anchor the metal film to the substrate. In the case of gold, a thin chromium layer (~5–50 nm) is deposited on the substrate first prior to the metal deposition. Key for electrochemical applications is the burial of the chromium layer. This means that the gold films need to be >200 nm thick. Treatments have been designed to selectively remove chromium contaminant atoms from the gold surface. These include chemical etching in a $Ce(SO_4)_2/HNO_3$ solution or electrochemical etching.

In the case of platinum, chromium is also used as an adhesion layer as are niobium and titanium (128). For this metal, chemical treatments have also been developed for the removal of adhesion layer contaminants (129).

Often the final step in the growth of thin-film electrodes is annealing. The electrical resistivity of thin films of gold and platinum is usually greatly improved by annealing in either air or high vacuum. The annealing probably works by causing the coalescence of islands of metal on the surface into a more continuous film. Typical annealing temperatures are in the 400–700 °C range, sufficiently low so as to not cause the metal film evaporate.

5.3.1.1 *Mechanical polishing*

Bulk platinum and gold electrodes can be prepared for use by mechanical polishing in a manner similar to that described for GC. In order to achieve the most rapid electron-transfer kinetics, one needs to polish under ultraclean conditions. The electrode should be polished using successively smaller sizes of alumina on a smooth glass plate (38–41). Deagglomerated alumina powders work best in sizes from 1.0 down to 0.05 μm. The alumina is slurried in ultrapure water to make a paste. The electrode should be polished using circular motions with an even force applied. Starting from the largest grit size, the electrode should be polished and then carefully cleaned by (i) rinsing with ultrapure water and (ii) ultrasonication in the same medium for about 15 min. The metal electrode should be placed in a clean beaker, submerged in ultrapure water, and covered during the ultrasonic cleaning. Eventually, a mirror-like finish should be obtained. The electrode should be used immediately after the polishing, or any pretreatment for that matter, for best results. Polishing metal film electrodes is often not possible due to the thinness of these layers and the mechanical damage caused by polishing. As is the case for many types of carbon, the pretreatment of platinum and gold often involves two steps with the first being polishing. This can be followed up by laser irradiation, vacuum heat treatment, solvent cleaning, or electrochemical polarization. As is the case for carbon electrodes, several surface-sensitive and -insensitive redox systems should be used to assess the electrode activity after pretreatment.

5.3.1.2 *Heat treatment*

Vacuum heat treatment can be used to clean the electrode surface by causing the desorption of contaminants. Performing the treatment in the high vacuum ($>10^{-6}$ Torr) in the 400–900 °C range is sufficient for cleaning and activating both platinum and gold. For example, surfaces of single-crystal Au(III) can be atomically ordered and cleaned by vacuum heat treatment up to temperatures of 900 °C, as evidenced by low-energy electron diffraction (LEED) and auger electron spectroscopy (AES) (130, 131). The heat treatment can be performed in the high vacuum or in a tube furnace with an inert atmosphere, such as N_2 or Ar gas. Since this environment is not as clean as the vacuum, it is supposed that the degree of activation, as measured by the k°_{app} for different redox systems, would not be as high as that for the vacuum treatment.

5.3.1.3 *Solvent cleaning*

Solvent cleaning or solution soaking should also be effective at activating the metal electrodes, although one must be careful about the molecular adsorption of some solvent types

on the surface. This adsorption could block sites and deactivate the electrode. For metals, one should stay away from aromatic solvents and use only distilled and AC-cleaned isopropanol or dichloromethane. It is beneficial to complete the solvent cleaning by soaking the electrode in warm ultrapure water for about 30 min. In some cases, simply prolonged exposure to an acid solution is sufficient to clean metal surfaces. For example, platinum can be cleaned by simply soaking for 0.5–2 h in highly concentrated sulfuric acid of ultra-high purity (>1 M H_2SO_4).

5.3.1.4 *Laser activation*

Laser irradiation has been used by McCreery and coworkers to activate platinum electrodes (132). This involves applying pulses from a Nd:YAG laser (1064 nm) to the electrode immersed in a supporting electrolyte solution. The laser beam diameter is a few mm and output powers of 5–100 MW cm^{-2} can be employed. Importantly, the activation was performed in the presence of a few mM of CN^- anion. Several researchers have reported that CN^- stabilizes k°_{app} for $Fe(CN)_6^{3-/4-}$ by forming an adlayer that prevents electrode deactivation. The deactivation is caused by the decomposition of $Fe(CN)_6^{3-/4-}$ on the bare platinum surface. McCreery and coworkers showed that laser irradiation of platinum exposed to the air in the presence of 5 mM KCN + 1 M KCl produced k°_{app} of 0.5 cm sec^{-1}, or greater. It is presumed that similar laser irradiation of gold would activate this surface for electron transfer as well by a surface cleaning mechanism. However, one would want to avoid contacting the gold with CN^- due to the formation of soluble $AuCN_4^{-2}$ (i.e., corrosion).

5.3.1.5 *Electrochemical polarization*

A common method for cleaning platinum and gold electrodes is potential cycling in 0.1 M H_2SO_4 between the oxygen and the hydrogen evolution regimes. This process serves to oxidize contaminants at potentials where the metal oxide layer forms or where water discharge commences ($OH\bullet$ radical generation). The potential range for cycling is different for each metal and depends on the pH. For example, the cycling potential window for platinum in acidic media (pH 1) would be between -0.2 and 1.5 V vs. Ag/AgCl. Both metals form stable oxide layers on the anodic potential cycle prior to oxygen evolution that can be fully reduced to the bare metal during the cathodic sweep. Surface roughening occurs during such a cycling treatment and this can influence some measurements, particularly those in which the redox reaction involves an adsorbed state (e.g., oxygen reduction) (133). It should be noted that gold is susceptible to corrosion in the presence of Cl^-, so care should be taken when using chloride-containing supporting electrolytes.

5.3.2 Single-crystal platinum and gold

Polycrystalline gold and platinum electrodes can be converted into clean, well-ordered single-crystal electrodes by heating the respective wires in an $H_2 + O_2$ flame. This is the so-called Clavilier method (134–137). Such electrodes are prepared by melting one end of a pure wire (1 mm diameter)—a zone-refining process. The crystallinity of the bead is usually

indicated by faceting that develops. These facets possess well-defined terrace-step structures extending over a large area, as evidenced by STM (138, 139). The single-crystal bead with (1 1 1) facets is oriented by the laser beam deflection method, sealed in epoxy and polished down with alumina grit. The metal is thoroughly solvent cleaned by both rinsing and ultrasonication with the electrode suspended in the solution. Sometimes a heat treatment in an $H_2 + O_2$ flame is performed to remove polishing debris and surface damage. As a final treatment, the electrode is flame annealed and quickly quenched to expose the clean, ordered surface. This is accomplished by heating the metal in an H_2 flame for several seconds and then quickly quenching it in ultrapure water that is purged with H_2. This is done by having the quenching solution, in a special cell, right below the flame so that the electrode always is exposed to a reducing environment. This cools the electrode to room temperature in an H_2 environment. The electrode is then transferred to an electrochemical cell for use with the surface covered and protected with a droplet of ultrapure water.

5.4   SEMICONDUCTOR ELECTRODES

5.4.1   Indium tin oxide (ITO)

Indium tin oxide (ITO) is a tin-doped In_2O_3-based n-type wide-bandgap semiconductor (140–144). The two dominant markets for this and other transparent conducting oxides are architectural applications (e.g., energy efficient windows) and flat panel displays. ITO, in particular, has been used extensively for many years in spectroelectrochemical measurements that involved a combined electrochemical and spectroscopic measurement. It is generally thought that the structure of ITO tracks that of the bixbyite lattice with tin incorporated substitutionally for indium to create n-type doping (145). Its attractive properties include high electrical conductivity (10^{-5} Ω cm), high optical transparency in the visible (85%), good physical and chemical properties (at least under some conditions), and strong adhesion to many kinds of substrates. For many years, $In_xSn_{1-x}O_2$ and ZnO were the transparent, conducting oxides of focus. However, in recent years, the perception that these materials are sufficient for many applications has begun to change. This is a consequence of the acknowledgement of the limitations of existing materials as well as the realization that new materials can pave the way for new and improved devices (141). Recent work has begun to explore new binary and ternary oxide combinations, including $CdSnO_4$, $ZnSnO_4$, and $ZnIn_2O_5$ (141). It should be mentioned that these new oxides have not yet been used extensively in electroanalysis but may in the future.

The two most common ways of preparing transparent, conducting oxides are RF and DC-magnetron sputtering from an appropriate target. ITO films are often deposited by RF cathode sputtering of a 90% SnO_2–10% In_2O_3 sintering target in moderate vacuum (10^{-6} Torr) (142). Glass, quartz, and Si are the common substrates. The structural properties, surface roughness, optical transmission, and transport properties of low-temperature-deposited films will depend on the power density, total pressure, oxygen partial pressure flow rate, substrate bias, and anode-to-cathode distance (142). ITO films can also be deposited by DC-magnetron sputtering at room temperature using 10 W of power

and a total pressure of 20 mTorr (0.05% oxygen in argon) (140). Of course, the target must be of an appropriate composition.

5.4.1.1 Mechanical polishing

Polishing the thin-film electrodes is not practical due to the thinness of these layers and the mechanical damage caused by polishing.

5.4.1.2 Solvent cleaning

ITO is probably best activated by solvent cleaning. As described above, soaking the electrode for 20–30 min in isopropanol, cleaned by distillation and exposure to AC, should be effective at cleaning the surface without causing any roughening, bulk oxide reduction, or microstructural damage (21). This pretreatment works by dissolving site-blocking contaminants from the surface. Importantly, the pretreatment only affects the surface cleanliness and does not alter the electronic properties, surface microstructure, or surface chemistry. Solvent cleaning is both an end treatment as well as a good starting point for the further pretreatment of ITO. ITO is stable during exposure to methanol, toluene and hexane but unstable in dichloromethane (146). Upon exposure of ITO to this solvent, isolated film dissolution was observed, which caused an increase in the resistivity and optical transparency.

Another cleaning routinely used is washing the ITO surface with a solution of Triton X-100 (a surfactant) and water (140, 144). Other surfactant solutions might also be used for washing the surface. This is followed up by ultrasonic washing in ultrapure water and ethanol for at least 10 min each.

Donley *et al.* referred to an ITO surface cleaned by the detergent solution as "as received". They also reported four additional pretreatment/cleaning procedures that were designed to affect both the level of adventitious carbon and the control of the coverage of hydroxide on the surface (140). They adapted a *piranha treatment* that consisted of three steps: (i) heating the ITO in a 10 mM NaOH solution for 4 h at 80 °C, (ii) soaking the ITO in piranha solution (4:1 H_2SO_4/H_2O_2) for 1 min, and (iii) heating the ITO to 160 °C for 2 h. The ITO was rinsed with copious amounts of ultrapure water between each step.

The same authors reported an *RCA treatment* that involved heating the ITO in a 1:1:5 solution of $NH_4OH/H_2O_2/H_2O$ for 30 min at 80 °C. This was followed by a thorough rinsing with ultrapure water and drying with a stream of nitrogen gas.

5.4.1.3 RF plasma treatment

Cleaning by an air plasma treatment can be accomplished using a standard Harrick plasma cleaner (Model PDC-32G) at 60 W and 100–200 mTorr for 15 min. The samples should first be solvent cleaned as described above.

5.4.1.4 Heat treatment

ITO can also be cleaned and activated by vacuum heat treatment. The treatment should be performed in a vacuum that is relatively free of residual oxygen. Relatively low temperatures should be used to avoid desorbing the ITO film from the substrate or decomposing

it. For example, Chaney and Pehrsson cleaned ITO surfaces by heat treatment in UHV at 50 °C (143). Treatment times of 15–30 min should be sufficient. To the best of our knowledge, there has been no systematic study of the effect heat treatment has on the optical, electrical, or electrochemical properties of ITO.

Another similar pretreatment involves argon-ion sputtering for 45 min at 750 eV in the UHV using an argon gas pressure of 10^{-7} Torr (140). These conditions were selected to remove the adventitious carbon and surface hydroxides but not to cause extensive oxide reduction or lattice damage. Before either of these treatments, the samples should first be solvent cleaned as described above.

5.4.1.5 *Electrochemical polarization*

In general, electrochemical polarization can cause surface and bulk chemical changes in ITO as well as significant morphological and microstructural damage. Therefore, this pretreatment is not recommended. The effects of electrochemical polarization on the electrical and optical properties of ITO have been reported (146). In general, anodic polarization in strong acid (1 M HNO_3) or base (1 M NaOH) causes extensive film roughening and some isolated film loss from quartz substrates. Cathodic polarization causes metal reduction and this leads to reduced optical throughput.

5.5 CONCLUSIONS

The field of electroanalytical chemistry is as vibrant as ever today. New platforms for detection and sensing are being developed for a wide variety of chemically, biologically, and environmentally important analytes, and many of these involve some sort of electrochemical signal transduction. At the heart of any electroanalytical method is the working or indicator electrode. These methods are made possible by the unique nature of the specific working electrode material, namely the electronic, structural, and chemical properties. With few exceptions, electrode pretreatment is required for top analytical performance. If the electrode is to be activated optimally and reproducibly, one must have a good understanding of how the above-listed properties are affected by the particular pretreatment method. The goal of any pretreatment is to improve the electron transfer kinetics for the target analyte and to reduce the background signal. This chapter described some of the commonly used protocols for pretreating carbon, metal, and semiconductor electrodes. If a sensitive, reproducible, and stable electrode response is desired, then one must apply the appropriate pretreatment with an understanding of how the pretreatment affects the electrode's physical, chemical, and electronic properties.

ACKNOWLEDGMENTS

most appreciated. Some of the work described herein was performed by a talented and enthusiastic group of graduate students (Qingyun Chen, Jishou Xu, Michael Granger, Jian Wang, Maggie Witek, Matt Hupert, Shannon Haymond, Jason Stotter, Prerna Sonthalia, Grace Muna, Jason Bennett, Elizabeth McGaw, Jinwoo Park, and Yang Song).

REFERENCES

1. R. N. Adams, *Electrochemistry at Solid Electrodes*, Marcel Dekker, Inc.: New York, 1968.
2. K. R. Kneten, R. L. McCreery, *Anal. Chem.* **64**, 2518 (1992).
3. K. Kneten-Cline, M. T. McDermott, R. L. McCreery, *J. Phys. Chem.* **98**, 5314 (1994).
4. P. Chen, M. A. Fryling, R. L. McCreery, *Anal. Chem.* **67**, 3115 (1995).
5. P. Chen, R. L. McCreery, *Anal. Chem.* **68**, 3958 (1996).
6. A. Fischer, Y. Show, G. M. Swain, *Anal. Chem.* **76**, 2553 (2004).
7. M. C. Granger, M. A. Witek, J. Xu, J. Wang, M. A. Hupert, A. Hanks, M. D. Koppang, J. E. Butler, G. Lucazeau, M. Mermoux, J. W. Strojek, G. M. Swain, *Anal. Chem.* **72**, 3793 (2000).
8. R. Bowling, R. T. Packard, R. L. McCreery, *Langmuir* **5**, 683 (1989).
9. K. Kinoshita, *Carbon: Electrochemical and Physicochemical Properties*, Wiley: New York, 1988.
10. R. L. McCreery, "Carbon Electrodes: Structural Effects on Electron Transfer Kinetics", in *Electroanalytical Chemistry*, A. J. Bard, Ed., Marcel Dekker, Inc.: New York, 1991, Vol. 17, pp. 221–374.
11. R. L. McCreery, "Carbon Electrode Surface Chemistry", in *Neuromethods, Vol. 27: Voltammetric Methods in Brain Systems*, A. Boulton, G. Baker, R. N. Adams, Eds., Humana Press Inc.: New York, 1995, pp. 1–26.
12. R. L. McCreery, "Electrochemical Properties of Carbon Surfaces", in *Interfacial Electrochemistry*, A. Wieckowski, Ed., Marcel Dekker, Inc.: New York, 1999, pp. 631–647.
13. R. F. Curl, R. E. Smalley, *Science* **242**, 1017 (1988).
14. F. Tunistra, J. L. Koenig, *J. Chem. Phys.* **53**, 1126 (1970).
15. Y. Wang, D. C. Alsmeyer, R. L. McCreery, *Chem. Mater.* **2**, 557 (1990).
16. J. R. Dennison, M. Holtz, G. M. Swain, *Spectroscopy* **11**, 38 (1996).
17. A. A. Gewirth, A. J. Bard, *J. Phys. Chem.* **92**, 5563 (1988).
18. M. T. McDermott, R. L. McCreery, *Langmuir* **10**, 4307 (1994).
19. J. Xu, Q. Chen, G. M. Swain, *Anal. Chem.* **70**, 3146 (1998).
20. B. D. Bath, H. B. Martin, R. M. Wightman, M. R. Anderson, *Langmuir* **17**, 7032 (2001).
21. S. Ranganathan, T.-C. Kuo, R. L. McCreery, *Anal. Chem.* **71**, 3574 (1999).
22. R. J. Rice, R. L. McCreery, *Anal. Chem.* **61**, 1637 (1989).
23. D. T. Fagan, T. Kuwana, *Anal. Chem.* **61**, 1017 (1989).
24. F. Stevens, L. A. Kolodny, T. P. Beebe, Jr., *J. Phys. Chem. B* **102**, 10799 (1998).
25. R. J. Bowling, R. T. Packard, R. L. McCreery, *J. Am. Chem. Soc.* **111**, 1217 (1989).
26. C. A. McDermott, K. R. Kneten, R. L. McCreery, *J. Electrochem. Soc.* **140**, 2593 (1993).
27. D. C. Alsmeyer, R. L. McCreery, *Anal. Chem.* **64**, 1528 (1992).
28. R. C. Engstrom, *Anal. Chem.* **54**, 2310 (1982). R. J. Bowling, R. L. McCreery, C. M. Parr, R. C. Engstrom, *Anal. Chem.* **61**, 2763 (1989).
29. B. Zhang, E. Wang, *Electrochem. Acta* **40**, 2627 (1995).
30. C. A. Goss, J. C. Brumfield, E. A. Irene, R. W. Murray, *Anal. Chem.* **65**, 1378 (1993).
31. M. R. Deakin, K. J. Stutts, R. M. Wightman *J. Electroanal. Chem.* **182**, 113 (1985).
32. P. L. Runnels, J. D. Joseph, M. J. Logman, R. M. Wightman, *Anal. Chem.* **71**, 2782 (1999).
33. L. J. Kepley, A. J. Bard, *Anal. Chem.* **60**, 1459 (1988).

34. K. F. Blurton, *Electrochem. Acta* **18**, 869 (1973).
35. R. E. Panzer, P. J. Elving, *J. Electrochem. Soc.* **119**, 864 (1972).
36. P. J. F. Harris, *Philos. Mag.* **84**, 3159 (2004).
37. G. M. Jenkins, K. Kawamura, *Nature* **231**, 175 (1971).
38. S. Bruckenstein, J. W. Sharkey, J. Y. Yip, *Anal. Chem.* **57**, 368 (1985).
39. I.-F. Hu, D. H. Karweik, T. Kuwana, *J. Electroanal. Chem.* **188**, 59 (1985).
40. G. W. Hance, T. Kuwana, *Anal. Chem.* **59**, 131 (1987).
41. B. Kazee, D. E. Weisshaar, T. Kuwana, *Anal. Chem.* **57**, 2736 (1985).
42. P. Chen, R. L. McCreery, *Anal. Chem.* **68**, 3958 (1996).
43. K. J. Stutts, P. M. Kovach, W. G. Kuhr, R. M. Wightman, *Anal. Chem.* **54**, 1632 (1983).
44. D. T. Fagan, I.-F. Hu, T. Kuwana, *Anal. Chem.* **57**, 2759 (1985).
45. M. Poon, R. L. McCreery, *Anal. Chem.* **58**, 2745 (1986).
46. C. W. Miller, D. H. Karweik, T. Kuwana, *Anal. Chem.* **53**, 2319 (1981).
47. R. DeClements, G. M. Swain, T. Dallas, M. Holtz, R. D. Herrick, III, J. L. Stickney, *Langmuir* **12**, 6578 (1996).
48. Q. Chen, G. M. Swain, *Langmuir* **14**, 7017 (1998).
49. T.-C. Kuo, R. L. McCreery, *Anal. Chem.* **71**, 1553 (1999).
50. M. C. Granger, G. M. Swain, *J. Electrochem. Soc.* **146**, 4551 (1999).
51. J. Xu, Q. Chen, G. M. Swain, *Anal. Chem.* **70**, 3146 (1998).
52. M. T. McDermott, R. L. McCreery, *Langmuir* **10**, 4307 (1994).
53. R. C. Engstrom, *Anal. Chem.* **54**, 2310 (1982).
54. J. Wang, M. S. Lin, *Anal. Chem.* **60**, 499 (1988).
55. R. M. Wightman, M. R. Deakin, P. M. Kovach, W. G. Kuhr, K. J. Stutts, *J. Electrochem. Soc.: Electrochem. Sci. Technol.* **131**, 1578 (1984).
56. J. Wang, L. D. Hutchins, *Anal. Chim. Acta* **167**, 325 (1985).
57. D. C. Thortnon, K. T. Coby, V. A. Spendel, J. Jordan, A. Robbat, Jr., D. J. Rustrom, M. Gross, G. Ritzler, *Anal. Chem.* **57**, 150 (1985).
58. J. Mattusch, K.-H. Hallmeier, K. Štulil, V. Pacáková, *Electroanalysis* **1**, 405 (1989).
59. A. L. Beilby, T. A. Sasaki, H. M. Stern, *Anal. Chem.* **67**, 976 (1995).
60. J. Kim, X. Song, K. Kinoshita, M. Madou, R. White, *J. Electrochem. Soc.* **145**, 2314 (1998).
61. S. Ranganathan, R. L. McCreery, S. Majji, M. Madou, *J. Electrochem. Soc.* **147**, 277 (2000).
62. S. Ranganathan, R. L. McCreery, *Anal. Chem.* **73**, 893 (2001).
63. N. E. Hebert, B. Snyder, R. L. McCreery, W. G. Kuhr, S. A. Brazil, *Anal. Chem.* **75**, 4265 (2003).
64. R. P. Kalakodimi, A. M. Novak, R. L. McCreery, *Chem. Mater.* **17**, 4939 (2005).
65. R. M. Wightman, *Anal. Chem.* **53**, 1125A (1981).
66. R. M. Wightman, *Science* **240**, 415 (1988).
67. C. Amatore, A. Jutand, F. Pfluger, *J. Electroanal. Chem.* **218**, 361 (1987).
68. I. N. Ermolenko, I. P. Lyubliner, N. V. Gulko, *Chemically Modified Carbon Fibers*, VCH: Germany, 1990.
69. K. T. Kawagoe, J. B. Zimmerman, R. M. Wightman, *J. Neurosci. Methods* **48**, 225 (1993).
70. G. C. Tibbets, *Carbon* **27**, 745 (1989).
71. D. T. Fagan, T. Kuwana, *Anal. Chem.* **61**, 1017 (1989).
72. G. M. Swain, *Activation Studies of Carbon Fiber Electrodes*, Ph.D. Dissertation, University of Kansas, 1991.
73. T. Strein, A. G. Ewing, *Anal. Chem.* **63**, 194 (1991).
74. F. G. Gonon, C. M. Fombarlet, M. J. Buda, J. F. Pujol, *Anal. Chem.* **53**, 1386 (1981).
75. A. G. Ewing, M. A. Dayton, R. M. Wightman, *Anal. Chem.* **53**, 1842 (1981).
76. P. M. Kovach, M. R. Deakin, R. M. Wightman, *J. Phys. Chem.* **90**, 4612 (1986).
77. G. M. Swain, T. Kuwana, *Anal. Chem.* **63**, 517 (1991).

78. G. M. Swain, T. Kuwana, *Anal. Chem.* **64**, 565 (1992).

79. J.-X. Feng, M. Brazell, K. Renner, R. Kasser, R. N. Adams, *Anal. Chem.* **59**, 1863 (1987).

80. S. Iijima, *Nature* **349**, 315 (1982).

81. D. N. Futaba, K. Hata, T. Yamada, K. Mizuno, M. Yumura, S. Iijima, *Phys. Rev. Lett.* **95**, 056104 (2005).

82. H. Dai, *Acc. Chem. Res.* **35**, 1035 (2002).

83. K. Mizuno, K. Hata, T. Saito, S. Ohshima, M. Yumura, S. Iijima, *J. Phys. Chem. B* **109**, 2632 (2005).

84. F. Valentini, A. Amine, S. Orlanducci, M. L. Terranova, G. Palleschi, *Anal. Chem.* **75**, 5413 (2003).

85. J. K. Campbell, L. Sun, R. M. Crooks, *J. Am. Chem. Soc.* **121**, 3779 (1999).

86. G. M. Swain, "Electroanalytical Applications of Diamond Electrodes", in *Thin Film Diamond II*, C. Nebel, J. Ristein, Eds., Elsevier: New York, 2004, pp. 121–148, Chapter 4.

87. G. M. Swain, "Electrically Conducting Diamond Thin-Films: Advanced Electrode Materials for Electrochemical Technologies", in *Electroanalytical Chemistry*, A. J. Bard, I. Rubinstein, Eds., Marcel Dekker, Inc.: New York, 2004, Vol. 22, pp. 182–277.

88. D. Knigge, P. Kaur, G. M. Swain, "Recent Trends in the Chemical Modification of sp^2 and sp^3 Bonded Carbon Electrodes", in *Encyclopedia of Electrochemistry*, A. J. Bard, M. Stratmann, Eds., Wiley-VCH, 2005, Vol. 10.

89. J. C. Angus, C. E. Hayman, *Science* **241**, 913 (1988).

90. F. G. Celi, J. E. Butler, *Annu. Rev. Phys. Chem.* **42**, 643 (1991).

91. A. E. Fischer, Y. Show, G. M. Swain, *Anal. Chem.* **76**, 2553 (2004).

92. Y. Show, M. A. Witek, P. Sonthalia, G. M. Swain, *Chem. Mater.* **15**, 879 (2003).

93. Q. Chen, D. M. Gruen, A. R. Krauss, T. D. Corrigan, M. A. Witek, G. M. Swain, *J. Electrochem. Soc.* 148, E44 (2001).

94. D. M. Gruen, *MRS Bull.* **23**, 32 (1998).

95. D. M. Gruen, *Annu. Rev. Mater. Sci.* **29**, 211 (1999).

96. T. G. McCauley, D. M. Gruen, A. R. Krauss, *Appl. Phys. Lett.* **73**, 1646 (1998).

97. P. C. Redfern, D. A. Horner, L. A. Curtiss, D. M. Gruen, *J. Phys. Chem.* **100**, 11654 (1996).

98. D. Zhou, D. M. Gruen, L. C. Qin, T. G. McCauley, A. R. Krauss, *J. Appl. Phys.* **84**, 1981 (1998).

99. D. Zhou, T. G. McCauley, L. C. Qin, A. R. Krauss, D. M. Gruen, *J. Appl. Phys.* **83**, 540 (1998).

100. S. Jiao, A. Sumant, M. A. Kirk, D. M. Gruen, A. R. Krauss, O. Auciello, *J. Appl. Phys.* **90**, 118 (2001).

101. S. Bhattacharyya, O. Auciello, J. Birrell, J. A. Carlisle, L. A. Curtis, A. N. Goyette, D. M. Gruen, A. R. Krauss, J. Schlueter, A. Sumant, P. Zapol, *Appl. Phys. Lett.* **79**, 1441 (2001).

102. J. Birrell, J. A. Carlisle, O. Auciello, D. M. Gruen, J. M. Gibson, *Appl. Phys. Lett.* **81**, 2235 (2002).

103. J. Birrell, J. E. Gerbi, O. Auciello, J. M. Gibson, D. M. Gruen, J. A. Carlisle, *J. Appl. Phys.* **93**, 5606 (2003).

104. W. A. Yarbrough, R. Messier, *Science* **247**, 688 (1990).

105. M. Mermoux, B. Marcus, G. M. Swain, J. E. Butler, *J. Phys. Chem. B* **106**, 10816 (2002).

106. D. S. Knight, W. B. White, *J. Mater. Res.* **4**, 385 (1989).

107. M. C. Granger, J. Xu, J. W. Strojek, G. M. Swain, *Anal. Chim. Acta* **397**, 145 (1999).

108. J. A. Bennett, J. Wang, Y. Show, G. M. Swain, *J. Electrochem. Soc.* **151**, E306 (2004).

109. L. H. Robins, E. N. Farabaugh, A. Feldman, *J. Mater. Res.* **5**, 2456 (1990).

110. P. Gonon, E. Gheeraert, A. Deneuville, F. Fontaine, L. Abello, G. Lucazeau, *J. Appl. Phys.* **78**, 7059 (1995).

111. J. W. Ager, III, W. Walukiewicz, M. McCluskey, M. A. Plano, M. I. Landstrass, *Appl. Phys. Lett.* **66**, 616 (1995).

112. H. J. Looi, L. Y. S. Pang, A. B. Molloy, F. Jones, J. S. Foord, R. B. Jackman, *Diam. Relat. Mater.* **7**, 550 (1998).

113. F. Maier, M. Riedel, B. Mantel, J. Ristein, L. Ley, *Phys. Rev. Lett.* **85**, 3472 (2000).
114. A. Denisenko, A. Aleksov, A. Pribil, P. Gluche, W. Ebert, E. Kohn, *Diam. Relat. Mater.* **9**, 1138 (2000).
115. J. Chevallier, B. Theys, A. Lusson, C. Grattepain, A. Deneuville, E. Gheeraert, *Phys. Rev. B* **58**, 7966 (1998).
116. E. Popa, H. Notsu, T. Miwa, D. A. Tryk, A. Fujishima, *Electrochem. Solid-State Lett.* **2**, 49 (1999).
117. U. Stephan, Th. Frauenheim, P. Blaudeck, G. Jungnickel, *Phys. Rev. B* **49**, 1 (1994).
118. K. Yoo, B. Miller, R. Kalish, X. Shi, *Electrochem. Solid-State Lett.* **2**, 233 (1999). Yu. E. Evstefeeva, Yu. V. Pleskov, A. M. Kutsay, I. Bello, *Russ. J. Electrochem.* **41**, 772 (2005).
119. G. Fanchini, S. C. Ray, A. Tagliaferro, *Diam. Relat. Mater.* **12**, 891 (2003).
120. J. Benedikt, R. V. Woen, S. L. M. Van Mensfoort, V. Perina, J. Hong, M. C. M. Van de Sanden, *Diam. Relat. Mater.* **12**, 90 (2003).
121. D. A. LaVan, R. F. Padera, T. A. Friedmann, J. P. Sullivan, R. Langer, D. S. Kohane, *Biomaterials* **26**, 465 (2005).
122. O. Kutsay, I. Bello, Y. Lifshitz, C. W. Lam, W. Y. Luk, S. T. Lee, X. Meng, V. Kremnican, *Diam. Relat. Mater.* **12**, 2051 (2003).
123. W. Y. Luk, O. Kutsay, I. Bello, Y. Lifshitz, C. W. Lam, X. Meng, S. T. Lee, *Diam. Relat. Mater.* **13**, 1427 (2004). J. Robertson, *Diam. Relat. Mater.* **14**, 942 (2005).
124. A. C. Ferrari, J. Robertson, *Philos. Trans. R. Soc. Lond.: Ser. A* **362**, 2477 (2004).
125. S. Piscanec, F. Mauri, A. C. Ferrari, M. Lazzeri, J. Robertson, *Diam. Relat. Mater.* **14**, 1078 (2005).
126. M. P. Soriaga, *Prog. Surf. Sci.* **39**, 325 (1992).
127. J. L. Anderson, N. Winograd, "Film Electrodes", in *Laboratory Techniques in Electroanalytical Chemistry*, 2nd ed., P. T. Kissinger, W. R. Heineman, Eds., Marcel Dekker, Inc.: New York, 1996, p. 333.
128. A. J. Bard, J. A. Crayston, G. P. Kittlesen, T. Varco Shea, M. S. Wrighton, *Anal. Chem.* **58**, 2321 (1986).
129. M. Josowicz, J. Janata, M. Levy, *J. Electrochem. Soc.* **135**, 112 (1988).
130. F. Wagner, P. Ross, *Surf. Sci.* **160**, 305 (1985).
131. T. Yamada, N. Batina, K. Itaya, *Surf. Sci.* **335**, 204 (1995).
132. M. Poon, R. L. McCreery, *Anal. Chem.* **59**, 1615 (1987).
133. S. Motoo, N. Furuya, *J. Electroanal. Chem.* **172**, 339 (1984).
134. J. Clavilier, R. Fame, G. Guisret, R. Durand, *J. Electroanal. Chem.* **107**, 211 (1980). J. Chavilier, *ibid.* **107**, 211 (1980).
135. J. Clavilier, D. Armand, B. L. Wu, *J. Electroanal. Chem.* **135**, 159 (1982).
136. J. Clavilier, A. Rhodes, K. El Achi, M. A. Zamakhchori, *J. Chim. Phys.* **88**, 1291 (1991).
137. J. Clavilier, R. Albalat, R. Gomes, J. M. Orts, J. M. Feliu, *J. Electroanal. Chem.* **360**, 325 (1993).
138. S. Tanaka, S.-L. Yau, K. Itaya, *J. Electroanal. Chem.* **396**, 125 (1995).
139. L. Wan, S.-L. Yau, G. M. Swain, K. Itaya, *J. Electroanal. Chem.* **381**, 105 (1991).
140. C. Donley, D. Dunphy, D. Paine, C. Carter, K. Nebesny, P. Lee, D. Alloway, N. R. Armstrong, *Langmuir* **18**, 450 (2002).
141. D. S. Ginley, C. Bright, *MRS Bull.* **8**, 15 (2000).
142. D. Vaufrey, M. B. Khalifa, J. Tardy, C. Ghica, M. G. Blanchin, C. Sandu, J. A. Roger, *Semicond. Sci. Technol.* **18**, 253 (2003).
143. J. A. Chaney, P. E. Pehrsson, *Appl. Surf. Sci.* **180**, 214 (2001).
144. N. R. Armstrong, A. W. C. Liu, M. Fujihira, T. Kuwana, *Anal. Chem.* **48**, 741 (1976).
145. P. A. Cox, W. R. Flavell, R. G. Egdell, *J. Solid-State Chem.* **68**, 340 (1987).
146. J. Stotter, Y. Show, S. Wang, G. M. Swain, *Chem. Mater.* **17**, 4880 (2005).

This page intentionally left blank

– 6 –

Ultramicroelectrodes

6.1 BEHAVIOR OF ULTRAMICROELECTRODES

Robert J. Forster and Tia E. Keyes

National Centre for Sensor Research, School of Chemical Sciences,
Dublin City University, Ireland

Ultramicroelectrodes (UMEs) are electrodes with characteristic dimensions on the micrometer or sub-micrometer scale. Faster double-layer charging, reduced ohmic loss, and high mass-transport rates have allowed them to revolutionize thermodynamic, kinetic, and electroanalytical measurements (1, 2). These properties have pushed the boundaries of electrochemistry into small length scales, nanosecond timescales, hydrodynamic applications, and environments, such as liquid CO_2 and single biological cells that are not possible using conventional-sized electrodes (3, 4). The currents observed at microelectrodes typically lie in the pA to nA range, which is several orders of magnitude smaller than those observed at conventional macroelectrodes, where the radius is usually several millimeters. These reduced currents are a key element in the successful application of microelectrodes:

- **Unusual media:** Traditionally, electrochemistry suffered relative to spectroscopy because electrochemical measurements could be made only in highly ionic conducting solutions. This restriction arose because resistance between the working or sensing electrode and the reference electrode limited the precision with which the applied potential could be accurately controlled. The small electrolysis currents observed at microelectrodes often completely eliminate these ohmic effects.
- **Small volumes:** Electrochemical methods offer significant advantages over spectroscopy when working with small reactions volumes (e.g., as found in biochips and capillary electrophoresis separation systems). Electron transfer occurs at an electrode surface and the limits of detection are not compromised by a small sample volume. This property contrasts with absorption spectroscopy where the signal intensity depends directly on the path length. Moreover, electrochemistry does not require an optical waveguide to deliver the interrogating light (absorption) or collect the resulting

---

signal (emission) making the approach less costly to implement in mass diagnostic devices for analytes, such as glucose (diabetes). From a biological perspective, voltammetric measurements have been successfully performed in picoliter vials allowing single cells to be interrogated and reactions to be monitored in extremely small volumes (see Chapter 17).

- **Short timescales:** Many electrochemical events, such as electron and proton transfers, ligand exchanges, isomerizations, and ejection of leaving groups, occur on the microsecond and nanosecond time domains. To achieve a meaningful insight into these redox processes, it must be possible to measure rate constants under a wide range of experimental conditions, such as driving force, temperature, etc. However, conventional electrochemical methods cannot fulfil this role as they are restricted to millisecond, or longer, timescales. Thus, although modern laser-based spectroscopy has provided a powerful new insight into chemical processes that occur on femtosecond timescales, it is only recently that it has been possible to reach megavolts per second scan rates in cyclic voltammetry. For a solution phase reactant, this scan rate corresponds to a time resolution of a few tens of nanoseconds. This capability allows standard potentials and reaction rates of short lifetime intermediates (e.g., electronically excited states) in molecular electrochemistry. Moreover, high-speed electron transfer dynamics (e.g., of self-assembled monolayers) can be measured.

In Sections 6.1 and 6.2, we look in detail at the fundamental properties of microelectrodes, consider some of the practical aspects of using microelectrodes and discuss the experimental factors that influence the choice of electrode size.

6.1.1 Electrode response times

First, we consider the properties of a microelectrode in contact with a solution of pure electrolyte in the absence of a dissolved or immobilized redox active analyte. The objective is to understand the fundamental behavior of microelectrodes in the absence of an electroactive analyte and to discuss strategies for optimizing the electrode's temporal response. The existence of the double-layer capacitance (see Chapter 1) at the working electrode complicates electrochemical measurements at short timescales. Figure 6.1.1.1 is an equivalent circuit of an electrochemical cell where Z_F is the faradaic impedance corresponding to the
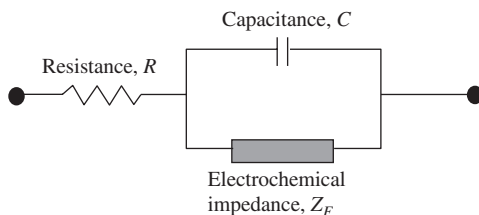
Figure 6.1.1.1 Equivalent circuit for an electrochemical cell and associated electrochemical process.

electrochemical reaction. In seeking to make transient measurements, the electrochemical cell must respond to the applied potential waveform much more rapidly than the process one is seeking to measure. However, the potential across a capacitor cannot be changed instantaneously and the double-layer capacitance must be charged through the solution resistance to change the potential across the faradaic impedance.

The time constant for this charging process is given by equation (6.1.1.1):

$$RC = \frac{\pi r_0 C}{4\kappa} \qquad (6.1.1.1)$$

where R is the cell resistance (Ω), C is the total interfacial capacitance (F), r_0 is the electrode radius (cm) and κ is the conductivity of the solution (S cm^{-1}). The RC time constant is typically hundreds of microseconds for a conventional millimeter-sized electrode placing a lower limit on the useful timescale of the order of several milliseconds. The use of UMEs with critical dimensions in the micron and even nanometer range has opened new possibilities for fast kinetic studies because of the greatly diminished capacitance of these ultrasmall probes.

For an electrode immersed in a dilute solution of supporting electrolyte that does not contain any electroactive species, a charging current, i_c, will flow following a potential step according to equation (6.1.1.2):

$$i_c(t) = \Delta E / R \exp(-t / RC) \qquad (6.1.1.2)$$

where ΔE is the magnitude of the potential step.

Figure 6.1.1.2 shows the chronoamperometric (current–time) response for a 10 μm radius platinum microelectrode where the supporting electrolyte is aqueous 0.1 M LiClO$_4$. This figure shows that current flows for approximately 10 μsec due to double-layer
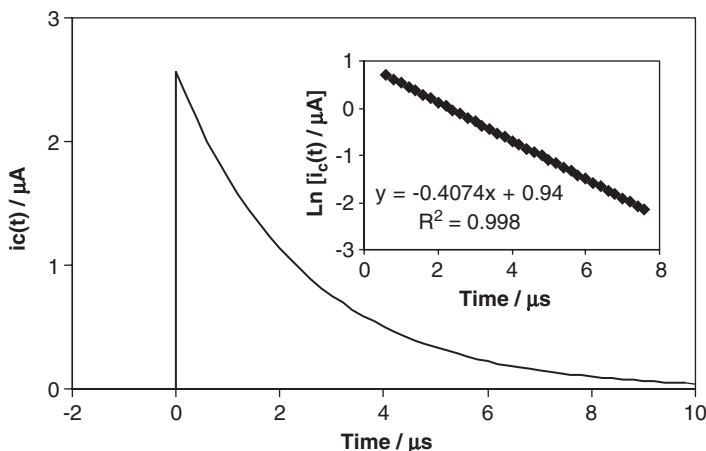
Figure 6.1.1.2   Current–time transient for a 10-μm radius platinum microelectrode in contact with an aqueous solution of 0.1 M LiClO$_4$ as supporting electrolyte following a potential step from 0.000 to 0.050 V. The inset shows the corresponding semi-log current vs. time plot.

charging. Every electrochemical measurement has a lower timescale limit that is imposed by the RC cell time constant (i.e., the product of the solution resistance, R, and the double-layer capacitance, C, of the working electrode). Meaningful electrochemical data can only be extracted at timescales that are longer than the cell time constant, typically 5–10 times the RC time constant (5). Therefore, an important objective when seeking to make transient measurements is to minimize the cell time constant.

Equation (6.1.1.2) indicates that a semi-log plot of the capacitive current vs. time should be linear with slope $1/RC$ and intercept $\ln \Delta E/R$ thus allowing the cell resistance and electrode capacitance to be determined. For the experiment illustrated in Figure 6.1.1.2, a linear semi-log plot is observed indicating that there is a single response time characterizing the electrochemical cell. This behavior is consistent with a clean, unmodified electrode surface and a well-constructed electrode (Section 6.1.3). The measured resistance and capacitance for this 10 µm radius platinum microelectrode are 19,500 $\pm$ 780 Ω and 1.5 $\pm$ 0.1 $\times$ 10^{-10} F, respectively.

As discussed in detail by Newman (6) and described by equation (6.1.1.3), the solution resistance for a disk-shaped UME is inversely proportional to the electrode radius:

$$R = \frac{1}{4\kappa r_0} \qquad (6.1.1.3)$$

Equation (6.1.1.3) shows that R *increases* as the electrode radius *decreases*. Taking the conductivity of aqueous 0.1 M $LiClO_4$ as 1.28 S m^{-1}, equation (6.1.1.3) predicts a theoretical resistance of 19,530 Ω, which is entirely consistent with the experimental result. The resistance can be a useful diagnostic of problems with the electrochemical cell (e.g., as discussed in Section 6.1.3). Surface films and imperfect seals can cause R to increase significantly. An important feature of equation (6.1.1.3) is that changes in the cell resistance with decreasing electrode radius do not have the desired effect of reducing the RC cell time constant.

Altering the potential that is applied to an electrode causes the charge on the metal side of the interface to change and some reorganization of the ions and solvent dipoles in the double layer on the solution side of the interface will occur. This process causes electrons to flow into or out of the surface giving rise to the charging or capacitive response. The double-layer capacitance for a disk-shaped UME is proportional to the area ($A = \pi r_0^2$ for an inlaid disk UME) of the electrode surface and is given by:

$$C = AC_d = \pi r_0^2 C_d \qquad (6.1.1.4)$$

where C_d is the specific double-layer capacitance of the electrode. Thus, shrinking the size of the electrode causes the interfacial capacitance to decrease with decreasing r_0^2. The capacitance determined from the data shown in the inset of Figure 6.1.1.2 is 150 pF. Taken in conjunction with a microscopic area of the 10 µm radius microelectrode of 3.8×10^{-6} cm^2 (roughness of 1.2), this specific capacitance yields an area normalized value of 39.5 µF cm^{-2}. This value is typical of that found for a clean platinum surface in contact with a dilute aqueous electrolyte. Surface contamination (e.g., by adventitious organic adsorbates) causes the interfacial capacitance to decrease by as much as a factor of two.

6.1.2 Factors that influence the electrode response time

6.1.2.1 Electrode size

Equation (6.1.1.1) suggests that the electrode response time should decrease with decreasing electrode radius. Figure 6.1.2.1 shows how the *RC* cell time constant measured in 0.1 M LiClO$_4$ depends on the radius of platinum microdisk electrodes. Consistent with equation (6.1.1.1), as the electrode radius decreases from 25 to 1 µm, the cell time constant decreases linearly from approximately 2 µsec to 80 nsec. The slope of the best-fit line is consistent with equation (6.1.1.1) where the double-layer capacitance is about 40 µF cm^{-2}. Moreover, the intercept is approximately 4.3 nsec indicating that the stray capacitance (Section 6.1.3.3) of these microelectrodes is very small. Thus, cell time constants of tens of nanoseconds can be achieved with UMEs of micron radii.

6.1.2.2 Electrolyte concentration

The overall cell resistance influences the cell time constant. Therefore, decreasing the resistance of the solution, through which the faradaic and charging currents must flow, will decrease the cell time constant. Figure 6.1.2.2 illustrates the decrease in cell time constant that is observed for a 5-µm radius platinum microdisk as the solution conductivity is systematically varied by changing the supporting electrolyte concentration from 0.05 to 2.0 M. As predicted by equation (6.1.1.1), this figure shows that a linear response is obtained and the specific double-layer capacitance is estimated as 41.7 ± 2.1 µF cm^{-2} over this range of supporting electrolyte concentrations. Figures 6.1.2.1 and 6.1.2.2 indicate that microdisk electrodes can be manufactured that respond ideally to changes in the

$y = 80.139x + 4.3159$
$R^2 = 0.9991$
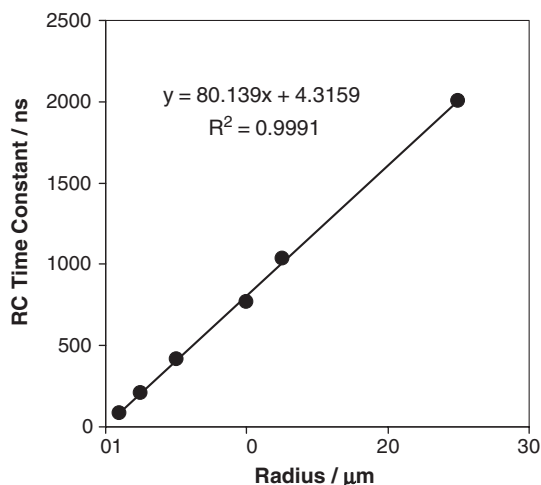
Figure 6.1.2.1 Relationship between the *RC* cell time constant and the radius of platinum microdisks where the supporting electrolyte is 0.1 M HCl. Cell time constants were measured using chronoamperometry conducted on a microsecond to sub-microsecond timescale by stepping the potential from 0.200 to 0.250 V vs. Ag/AgCl.
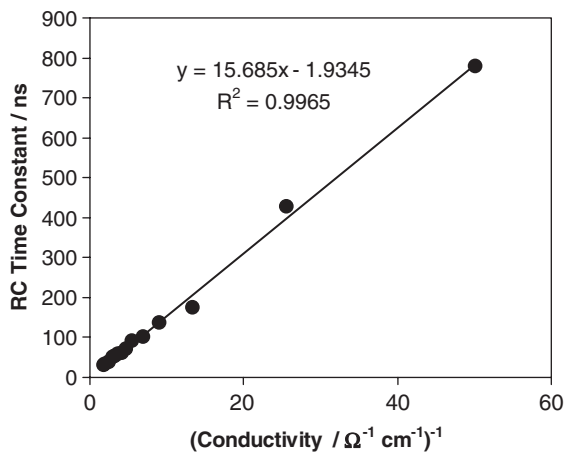
Figure 6.1.2.2   Relationship between the *RC* cell time constant of a 5-µm radius platinum microdisk and the reciprocal of the solution conductivity. Cell time constants were measured using chronoamperometry conducted on a microsecond to sub-microsecond timescale by stepping the potential from 0.200 to 0.250 V vs. Ag/AgCl.

applied potential at timescales as short as 30 nsec. Experiments performed in more conducting solutions (e.g., highly concentrated acids) indicate that *RC* cell time constants as short as 5 nsec can be achieved.

However, there are a number of practical problems associated with the design and fabrication of microelectrodes that cause micron-sized electrodes to have *RC* time constants that greatly exceed those predicted by equation (6.1.1.1).

6.1.3   Origins of nonideal responses

6.1.3.1   Electrode geometry problems

A challenge in this field is to reproducibly manufacture perfect microdisk electrodes. This is especially difficult when the radius of the microwire is less than 2 µm. Figure 6.1.3.1 illustrates some the most common structural nonidealities that can occur. Figure 6.1.3.1B illustrates an elliptical electrode caused by the wire sealing at an angle within the insulator. Figure 6.1.3.1C shows a protruding, irregular cylindrical electrode caused either by insufficient mechanical polishing or because the electrode material is very much softer than the insulator. In contrast, when the electrode material is soft (e.g., gold), it is possible to polish the working electrode to a lower level than the surrounding insulator thus creating a recessed electrode in which the opening in the insulator is of same size (Figure 6.1.3.1D), or larger than the microdisk size (Figure 6.1.3.1E). Figure 6.1.3.1F illustrates the imperfect seals that can result when heat-sealing microwires within an insulator (e.g., glass), if the thermal coefficients of expansion of the insulator and wire are not closely matched. Similarly, failure to adequately clean both the insulators and microwires can lead to imperfect seals. Table 6.1.3.1 indicates the changes in the resistance and capacitance expected for each of these nonideal electrode geometries.
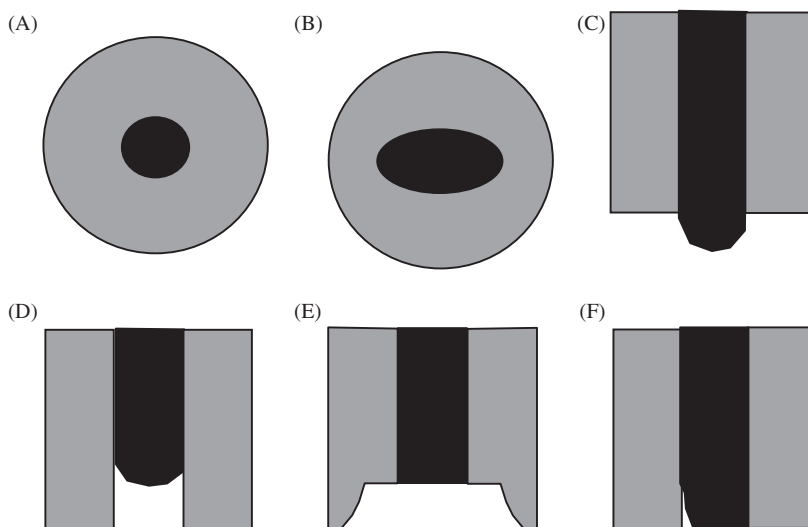
Figure 6.1.3.1 Different shapes of ultramicroelectrodes (UMEs). (A) A perfect microdisk electrode. (B) A conical disk-type planar UME due to sealing of the microwire at an angle relative to the insulating shroud. (C) An irregular cylindrical protruding from the insulator. (D) A recessed microdisk electrode. (E) A recessed electrode in which the cavity in the insulator is large than the microwire. (F) A leaky UME due to an imperfect wire-insulator seal.

Table 6.1.3.1

Effect of nonideal microelectrode geometry on resistance and capacitance[a]

Geometry	R (Ω)	C (μF cm^{-2})	Comment
Elliptical (1B)	→	↑	Capacitance increases but resistance decreases relative to ideal due to increased electrode area.
Protruding (1C)	↓	↑	Capacitance increases relative to ideal due to increased effective electrode area.
Microcavity/lagooned (1D)	↑	→	Resistance typically increases significantly relative to ideal due to difficulties of ion mass transport within pore.
Recessed (1E)	↑	→	Resistance may increase moderately but diagnostic abilities of chronoamperometry are limited.
Imperfect seal (1F)	↑	↑	Resistance and capacitance both very significantly larger than ideal.

[a]A common feature of nonideal geometry is that the capacitive current–time response following a potential step fails to decay according to a single exponential.

6.1.3.2 Surface impurities

For electrodes with radii in the micrometer range, scanning electron microscopy (SEM) provides a useful insight into the geometry of the structure formed. However, surface charging is often a difficulty even when the electrode itself is grounded and for smaller
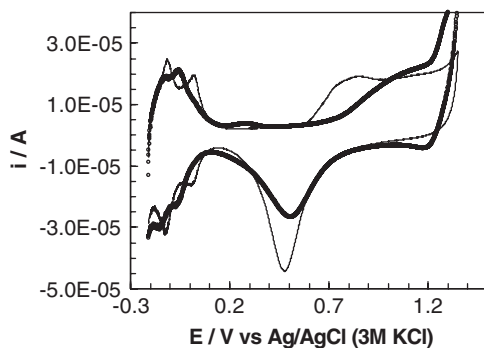
Figure 6.1.3.2   Cyclic voltammograms for a polished platinum microelectrode. The solid black line is obtained in 0.5 M H_2SO_4 (99.999%). The thick line/open circles show the effect of chloride contamination at a nanomolar concentration. Note that reduction currents are negative and oxidation currents positive in this figure.

microelectrodes, it may be necessary to destructively dissolve the insulator to expose the microwire. Even when it has been established that a close to ideal geometry microelectrode has been created, the observed resistance and capacitance behavior may deviate significantly from that predicted by theory. In particular, imperfect surface cleanliness (e.g., due to adventitiously adsorbed organics) can cause lower capacitance values and nonsingle exponential current–time transients to be observed. Electrochemical cleaning by cycling in dilute sulfuric acid represents a useful approach to producing pristine surfaces in an experimentally accessible way. Figure 6.1.3.2 illustrates two cyclic voltammograms for a 10 μm radius platinum microelectrode when electrochemically cycled in 0.1 M H_2SO_4 to create an oxide monolayer that is subsequently reduced. It is important to restrict the potential window and to avoid excessive cycling so as to prevent bulk oxidation of the metal. The microscopic or "real" area of the electrode can be determined by measuring the charge passed during the reduction of the surface oxide monolayer at approximately 0.600 V or the hydrogen adsorption/desorption peaks at approximately -0.200 V. To produce a clean electrode surface, the purity of the electrolyte significantly affects the voltammetry obtained. As illustrated in Figure 6.1.3.2, in 99.999% pure sulfuric acid, well-defined oxide monolayer formation and reduction, double layer, and hydrogen adsorption and desorption regions are observed. However, the presence of chloride even at nanomolar concentrations (e.g., arising from electrolyte leakage from the reference electrode) makes the oxide monolayer formation ill-defined, shifts the hydrogen adsorption/desorption potentials, and causes the double-layer region (expected between approximately 0.08 and 0.20 V) to be either significantly diminished or totally absent.

6.1.3.3   Experimental setup: stray capacitance

One cause of a nonideal response is stray capacitance within the electrochemical system that may arise from the electrode itself, the leads, or the electrical connections.Stray capacitance will increase the cell time constant as described by equation (6.1.3.1).

$$RC = \frac{1}{4\kappa r}(\pi r_0^2 C_0 + C_{\text{Stray}}) \tag{6.1.3.1}$$

where C_{Stray} is the stray capacitance. Although it depends on the microelectrode design and the experimental setup, this stray capacitance is typically between a few pF and several tens of pF. The cell time constant observed in these circumstances depends strongly on the relative magnitudes of the double layer and stray capacitances. At a normal-size electrode, the stray capacitance is negligible compared with the double-layer capacitance, and therefore, does not significantly affect the observed cell time constant. However, when the magnitude of the double-layer capacitance is reduced by shrinking the size of the electrode to micron and sub-micron dimensions, the stray and double-layer capacitances can become comparable. For example, taking a typical value of 40 μF cm^{-2} as the specific double-layer capacitance for a platinum electrode in contact with 1 M aqueous electrolyte solution, the double-layer capacitance of a 1 mm radius disk will be approximately 1 μF. This value is very significantly larger than the pF stray capacitance found in a typical electrochemical experiment. However, for a 1-μm radius microdisk, the interfacial capacitance will decrease by six orders of magnitude to approximately 1 pF. Therefore, stray capacitance of even a few pF will cause the observed RC time constant to increase significantly beyond the minimum value dictated by double-layer charging alone. This increased cell time constant will cause the transient response characteristics of the electrodes to become nonideal. Thus, an objective in implementing ultrafast transient techniques is to minimize the stray capacitance.

Two major sources of stray capacitance are: (i) the capacitance of the cell leads and capacitive coupling between leads, and (ii) the microelectrode itself. By using high-quality cable of minimum length (e.g., by mounting the current-to-voltage converter directly over the electrochemical cell) and by avoiding the use of switches as far as possible, stray capacitance from the electrochemical system can be minimized. However, the importance of good microelectrode fabrication and design should not be overlooked. For example, if there is a small imperfection in the seal between the insulator and the electrode material, then solution leakage will cause the RC cell time constant to increase massively and the faradaic response may become obscured by charging/discharging processes. Moreover, using silver epoxy or mercury to make the electrical connection between the microwire and a larger hook-up wire can cause the RC cell time constant to increase dramatically (7, 8). This increase arises because the electronically conducting mercury/glass insulator/ionically conducting solution junctions cause significant stray capacitance. It is important to note that these effects may only become apparent in high-frequency measurements.

6.1.3.4 Ohmic effects

When faradaic and charging currents flow through a solution, they generate a potential that acts to weaken the applied potential by an amount, iR, where i is the total current. This is an undesirable process that leads to distorted voltammetric responses. It is important to note that, as described by equation (6.1.1.3), the cell resistance *increases* with *decreasing* electrode radius. Thus, the ohmic drop is not reduced at microelectrodes relative to macroelectrodes because of reduced resistance. However, the capacitive or double-layer charging current depends on the electrode area or r_0^2. Similarly, for reversible redox reactions under semi-infinite diffusion control, the faradaic current depends on the electrode area. This sensitivity to area means that the currents observed at microelectrodes are typically six orders of magnitude smaller than those observed at

macroelectrodes. These small currents often completely eliminate ohmic drop effects even when working in organic solvents. For example, the steady-state current observed at a 5-μm radius microdisk is approximately 2 nA for a 1.0-mM solution of ferrocene. Taking a value of 0.01 Ω^{-1} cm^{-1} as the specific conductivity, then equation (6.1.1.3) indicates that the resistance will be of the order of 50,000 Ω. This analysis suggests that the *iR* drop in this organic solvent is a negligible 0.09 mV. In contrast, for a conventional macroelectrode, the *iR* drop would be of the order of 5–10 mV. Under these circumstances, distorted current responses and shifted peak potentials would be observed in cyclic voltammetry.

It is useful at this point to discuss the effect of experimental timescale on the *iR* drop observed at microelectrodes. In the following section, we discuss how the diffusion field at microelectrodes depends on the characteristic time of the experiment. In general, at short times, the dominant mass transport mechanism is planar diffusion and the microelectrode behaves like a macroelectrode. Therefore, at short times, the current *i* decreases with decreasing electrode area (r_0^2). As the resistance increases with decreasing electrode radius rather than electrode area, the product *iR* decreases with decreasing electrode radius in short timescale experiments. Thus, beyond the reduced *iR* drop because of low currents, decreasing the electrode radius from say 1 mm to 10 μm decreases the ohmic *iR* drop observed at short times by a factor of 100. In contrast, at long experimental timescales, the faradaic current depends directly on the radius making the product *iR* independent of the electrode radius and a constant value, which is inversely proportional to the solution conductivity.

6.1.4 Fundamentals of faradaic electrochemistry

Oxidation or reduction of a redox-active species at an electrode surface generates a concentration gradient between the interface and the bulk solution. This redox process requires electron-transfer across the electrode/solution interface. The rate at which electron transfer takes place across the interface is described by the heterogeneous electron-transfer rate constant, *k*. If this rate constant is large, then diffusional mass transport will control the current observed. Our objective is to describe how these diffusion fields evolve in time and then to look at experimental parameters that influence the ideality of the response. The experiment of interest involves stepping the potential from an initial value where no electrode reaction occurs, to one where electrolysis proceeds at a diffusion-controlled rate. We consider the case of a spherical electrode of radius r_s placed in a solution that contains only supporting electrolyte and a redox-active species of concentration *C**. The concentration gradient at the electrode surface is obtained by solving Fick's second law in spherical coordinates:

$$\frac{\partial C(r,t)}{\partial t} = D\left[\frac{\partial^2 C(r,t)}{\partial r^2} + \frac{2}{r}\frac{\partial C(r,t)}{\partial r}\right] \qquad (6.1.4.1)$$

The boundary conditions for the potential step experiments described above are:

$$\lim_{r \to \infty} C(r,t) = C^{\infty}$$
$$C(r,0) = C^{\infty}$$
$$C(r,t) = 0 \text{ for } t > 0$$

where r is the distance from the center of the sphere, D is the diffusion coefficient for the redox active species, and C is the concentration as a function of distance r and time t.

Equation (6.1.4.1) can be solved using Laplace transform techniques to give the time evolution of the current, $i(t)$, subject to the boundary conditions described. Equation (6.1.4.2) is then obtained:

$$i(t) = \frac{nFADC^{\infty}}{r_{\mathrm{s}}} + \frac{nFAD^{1/2}C^{\infty}}{\pi^{1/2}t^{1/2}} \qquad (6.1.4.2)$$

where n is the number of electrons transferred in the redox reaction, F is Faraday's constant, and A is the geometric electrode area.

Equation (6.1.4.2) shows that the current response following a potential step contains both time-independent and time-dependent terms. The differences in the electrochemical responses observed at macroscopic and microscopic electrodes arise because of the relative importance of these terms at conventional electrochemical timescales. It is possible to distinguish two limiting regimes depending on whether the experimental timescale is short or long.

6.1.4.1   Short times

At sufficiently short times, the thickness of the diffusion layer that is depleted of reactant is much smaller than the electrode radius and the spherical electrode appears to be planar to a molecule at the edge of this diffusion layer. Under these conditions, the electrode behaves like a macroelectrode and mass transport is dominated by linear diffusion to the electrode surface as illustrated in Figure 6.1.4.1A.

At these short times, the $t^{-1/2}$ dependence of the second term in equation (6.1.4.2) makes it significantly larger than the first and the current response induced by the potential step initially decays in time according to the Cottrell equation (Chapter 11):

$$i(t) = \frac{nFAD^{1/2}C^{\infty}}{\pi^{1/2}t^{1/2}} \qquad (6.1.4.3)$$

Figure 6.1.4.2 shows the relationship that exists between the range of useable scan rates and electrode radius subject to the condition that ohmic drop is negligible and that the dominant mass transport regime is linear diffusion (9).
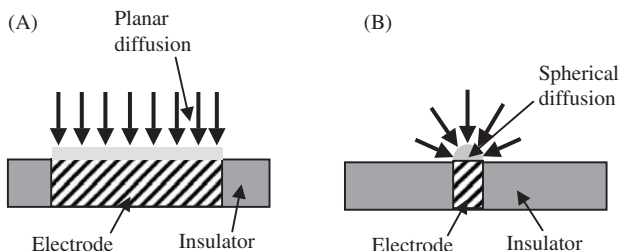
Figure 6.1.4.1   Diffusion fields observed at microelectrodes. (A) Linear diffusion observed at short times. (B) Radial (convergent) diffusion observed at long times.
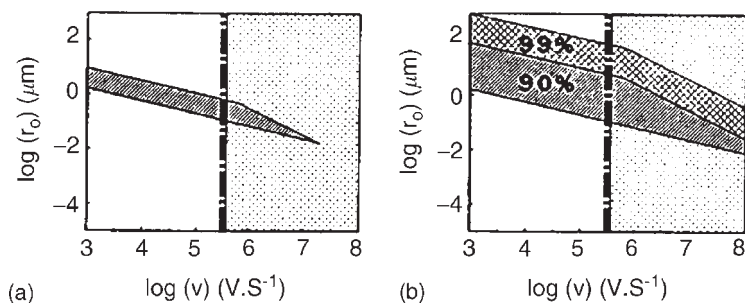
Figure 6.1.4.2 Theoretical limitations on ultrafast cyclic voltammetry. The shaded area between the slanted lines represents the radius that a microdisk must have if the ohmic drop is to be less than 15 mV and distortions due to nonplanar diffusion account for less than 10% of the peak current. (a) Without *iR* drop compensation by positive feedback, and (b) with 90 and 99% ohmic drop compensation. The dotted area in (a) and (b) represent the regions where transport within the double layer affects the voltammetric response. Limits are indicative and correspond approximately to a 5-mM anthracene solution in acetonitrile, 0.3 M tetrafluoroborate as supporting electrolyte. [Reproduced by permission of Marcel Dekker from C. Amatore, *Electrochemistry at Microelectrodes*, I. Rubenstein, Ed., 1995, Chapter 4, p. 198.]

6.1.4.2   Long times

At long times, the transient contribution given by the second term of equation (6.1.4.3) has decayed to the point where its contribution to the overall current is negligible. At these long times, the spherical character of the electrode becomes important and the mass transport process is dominated by radial (spherical) diffusion as illustrated in Figure 6.1.4.1B.

The current attains a time-independent steady-state value given by equation (6.1.4.4) for a spherical electrode.

$$i_{ss} = \frac{nFADC^{\infty}}{r_s} = 4\pi nFDC^{\infty}r_s \tag{6.1.4.4}$$

The steady-state response arises because the electrolysis rate is equal to the rate at which molecules diffuse to the electrode surface.

As "short" and "long" times are relative terms, it is useful to determine the times over which transient and steady-state behaviors will predominate and how this time regime is affected by the electrode radius.

This objective can be achieved by considering the ratio of the transient to steady-state current contributions (equations (6.1.4.3) and (6.1.4.4), respectively). This analysis gives a dimensionless parameter $(\pi Dt)^{1/2}/r_s$ that can be used to calculate a lower time limit at which the steady-state contribution will dominate the total current to a specified extent. For example, one can calculate the time required for the steady-state current contribution, i_{ss}, to be 10 times larger than the transient component, i_t. Taking a typical value of D as 1×10^{-5} cm^2 sec^{-1} for an aqueous solution, for an electrode of radius 5 mm, the experimental timescale must be longer than 80 sec. Therefore, steady state is not observed for
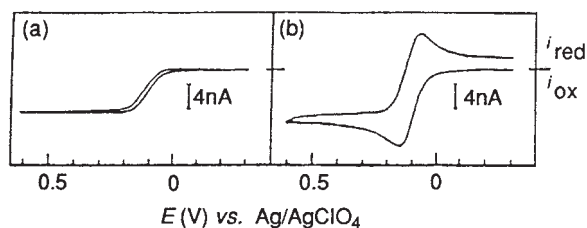
Figure 6.1.4.3 Effect of scan rate on the cyclic voltammetry of 1.0 mM ferrocene at a 6.5-μm gold microdisk where the supporting electrolyte is 0.1 M tetrabutyl ammonium perchlorate in acetonitrile. (a) Scan rate is 0.1 V sec^{-1}; (b) scan rate is 10 V sec^{-1}. [Reproduced with permission from J. O. Howell, R. M. Wightman, *Anal. Chem.* **56**, 524 (1984). Copyright 1984, American Chemical Society.]

macroelectrodes at the tens of mV sec^{-1} timescale typical of conventional cyclic voltammetry experiments. However, reducing the electrode radius by a factor of a thousand to 5 μm, means that a steady-state response can be observed for times longer than 80 μsec. As the steady-state current becomes more dominant with increasing time, steady-state responses are easily observed for microelectrodes in electrochemical experiments run at conventional timescales. Figure 6.1.4.3A shows the sigmoidal-shaped responses that characterize steady-state mass transfer in slow scan-rate cyclic voltammetry. In contrast, at short experimental timescales (high scan rates), peaked responses (Figure 6.1.4.3B) similar to those observed at conventional macroelectrodes are seen. There is no theoretical barrier to observing steady-state behavior for any size of the electrode. However, for conventional millimetre dimensioned macroelectrodes, the time taken ($>$10,000 sec) is far too long to be experimentally practical. Moreover, unintentional convection (e.g., because of building vibrations) will play an important role in the mass transport process at these long timescales.

The preceding analysis considered a spherical electrode because its surface is uniformly accessible, and a simple closed-form solution to the diffusion equation exists (10). The microdisk is the most widely used geometry, but derivation of rigorous expressions describing their experimental response is complicated because the surface is not uniformly accessible. For disks, electrolysis at the outer circumference of the disk diminishes the flux of the electroactive material to the center of the electrode. However, microdisk and microring geometries share the advantage of spherical microelectrodes in that quasi-spherical diffusion fields are established in relatively short periods of time. The steady-state limiting current obtained from these rigorous derivations is given by:

$$i_{ss} = \gamma nFDC^*r_0 \tag{6.1.4.5}$$

where γ is a shape parameter, which is 4 for a disk electrode. Consistent with equation 6.4.4.4, γ is 4π for a spherical electrode and 2π for a hemispherical electrode.

Observing a steady-state response depends on all the electrode dimensions being small, not just the radius, and is, therefore, not achieved for every geometry at the timescales considered above. For example, band electrodes whose thickness is in the micrometer range, but whose length is several millimeters, do not exhibit true steady-state responses.

However, a high analyte flux to the ends of the band often makes it possible to observe a pseudo-steady-state condition in a practical sense.

Radial diffusion gives very high rates of mass transport to the electrode surface with a mass transport coefficient of the order of D/r. Therefore, even at rotation rates of 10^4 rpm, convective transport to a rotating macroelectrode is smaller than diffusion to a 1-μm microdisk. The high flux at a microelectrode means that one does not observe a reverse wave under steady-state conditions (Figure 6.1.4.3A), because the electrolysis product leaves the diffusion layer at an enhanced rate.

6.1.5   Origins of nonideal faradaic responses

6.1.5.1   Electrode area effects

Capacitive currents are generated by events occurring within very small distances from an electrode surface and their magnitude is controlled by the microscopic area of the electrode. In most electrochemical experiments designed to probe the redox properties of solution phase reactants, the timescale of the measurement is often such that the diffusion layer is several times larger than the critical dimension (e.g., radius) of the microelectrode. For example, the depletion layer thickness, δ, can be estimated as:

$$\delta = (\pi D t)^{1/2} \qquad\qquad (6.1.5.1)$$

where D is the diffusion coefficient of the electroactive species ($cm^2\ sec^{-1}$) and t is the experimental timescale (sec). Given a characteristic diffusion coefficient of $10^{-5}\ cm^2\ sec^{-1}$, equation (6.1.5.1) reveals that the depletion layer thickness will exceed the 10 μm radius of a typical microelectrode within approximately 32 msec, which corresponds to a scan rate slower than approximately 0.8 V sec^{-1} in cyclic voltammetry (see Chapter 11). Typically, electrodes are prepared by mechanical polishing using small particle size (0.05 μm) alumina or diamond paste and the microscopic area can be a factor of two larger than the geometric one. Therefore, at the timescales usually used in electrochemical experiments, the depletion layer thickness will be much larger than the scale of roughness of a polished electrode and the electrode appears flat to molecules approaching the electrode surface.

The short RC time constants possible with microelectrodes facilitates electrochemical measurements at short timescales. For example, in a chronoamperometry experiment conducted at a nanosecond timescale, the depletion layer thickness will be of the order of a few hundred nanometers thick, which may be comparable with the length scale of the surface roughness. Under these circumstances, the depletion layer will tend to follow the structural contours of the microscopically rough surface and the area of the depletion layer will generally be larger than the geometric area. Such effects are important for electrodes partially covered by a blocking layer (e.g., due to poor fabrication) with pinholes through which the electroactive species may access the electrode surface. At short timescales, the diffusion layer thickness is small compared with the size of the active region and a depletion region will be established at each active region. The area of the overall diffusion field is the sum of the geometric areas of the individual active spots. At longer times, the

individual depletion zones begin to extend beyond the active regions, and linear diffusion is augmented by a radial component. For sufficiently long reaction times, the individual depletion layers become much thicker than the distances between the active regions and a single merged depletion layer covering the entire electrode surface (i.e., both active and inactive regions) is formed. The current response is now once again controlled by semi-infinite linear diffusion and the current magnitude is controlled by the geometric area of the electrode. Similar evolutions in the diffusion field from semi-infinite linear to radial and back to semi-infinite linear are observed when using a lithographically defined micro-electrode arrays (see Chapter 10) consisting of an ensemble of nonindependently address-able electrodes or when the electrode is a composite material based on immobilizing conducting particles (e.g., graphite) within an insulating phase (e.g., a polymer) (see Chapters 10 and 16).

6.1.5.2   Surface contamination

The electron transfer kinetics (see Chapters 1 and 15), and current response of redox-active species can be dramatically affected by the surface condition of the working elec-trode. This sensitivity to surface contamination arises because the rate of heterogeneous electron transfer decreases exponentially with increasing distance. Pretreatment of the electrode surface is often necessary to obtain reproducible results. Typically, a microelec-trode is polished with successively smaller particle size abrasive (e.g., 12.5, 5, 1, 0.3, and 0.05 μm alumina or diamond paste) so as to achieve a mirror finish. The progression of polishing should always proceed from coarse to fine abrasive, with thorough rinsing and a change of polishing pads between each step. Fabric pads attached to glass plates are typ-ically used as the platform onto which the polishing suspensions are applied. Thorough rinsing is required after each polishing and the electrodes polished using 0.05 μm alumina should be ultrasonically cleaned in deionized water for a few minutes, to remove any residual alumina.

Although mechanical polishing may provide a sufficiently clean electrode for many applications, cleaner surfaces can be produced by treating the surface with piranha solu-tion or through electrochemical cleaning. Piranha solutions are used to remove organic residues from substrates, particularly in microfabrication labs. The traditional piranha solution is a 3:1 mixture of sulfuric acid and 30% hydrogen peroxide. The solution may be mixed before application or directly applied to the material, applying the sulfuric acid first, followed by the peroxide. (*Caution: Piranha solutions are extremely energetic and may result in explosion or skin burns if not handled with extreme caution*.) Electrochemical cleaning represents a useful alternative and provided that care is taken with the potential limits and the number of cycles to prevent surface roughening, it not only generates clean surfaces but also provides the microscopic area. In a typical application, the electrode is cycled in 0.1 M $HClO_4$ by cycling between potential limits chosen to initially oxidize, and subsequently to reduce the surface of the platinum electrode. The potential is then held in the double-layer region to ensure complete reduction of any surface oxide and desorption of the hydrogen. After use, it may be sufficient to rinse the electrode surface with water and/or methanol, followed by air drying to remove adsorbed species and to ensure that the working electrode is in pristine condition. Otherwise, repolishing may be required.

6.1.5.3   Instrumental challenges

A challenge in using microelectrodes is the ability to measure very low currents (down to femto ampere, 10^{-15} A). Measuring small currents is a particular challenge when the experimental timescale is short (e.g., tens of nanoseconds are accessible using micrometer dimensioned electrodes). For example, taking values of 100 μM and 1×10^{-5} cm^2 sec^{-1} for the concentration and diffusion coefficient, respectively, the steady-state current is of the order of 200 pA for a 5-μm radius microdisk. As described by equation (6.1.4.4), the magnitude of this current will decrease with decreasing electrode radius and femtoampere currents (i.e., approximately 6000 electrons transferred per second!) will be observed for a 10-nm radius electrode. Thus, in some microelectrode experiments, potentiostats work close to the capabilities of contemporary electronics.

Consider the equivalent circuit shown in Figure 6.1.5.1 in which the objective is to measure the cell impedance given by Z_{cell}.

This circuit includes several components associated with both the electrochemical cell itself and measuring electronics. For example, the parasitic resistance and capacitance (e.g., arising from leads, switches, etc.) in the cell are described by $R_{p,cell}$ and $C_{p,cell}$, respectively, while the stray input resistance and capacitance of the measurement circuit are denoted as R_{in} and C_{in}, respectively. In the ideal current measurement circuit, R_{in} is infinite, while C_{in} and I_{in} are zero and all the current generated in the cell flows through the resistance of the measuring circuit, R_m. To measure the small currents generated at microelectrodes, R_m needs to be large (hundreds of kΩ to many MΩ). With an ideal cell and voltage source, $R_{p,cell}$ is infinite and $C_{p,cell}$ is zero and all of the current flowing into the current measurement circuit is due to Z_{cell}. The voltage developed across R_m is measured by the meter as V_m and Z_{cell} and is given by:

$$Z_{cell} = E_s R_m / V_m \tag{6.1.5.2}$$

As described by equation (6.1.5.2), the contribution from the electrode resistance to Z_{cell} increases with decreasing electrode radius and the total cell impedance can become very large. The precision with which high-impedance measurements can be made is limited for several reasons including: (a) current measurement circuits always have nonzero input capacitance, (b) an infinite input resistance cannot be achieved with real
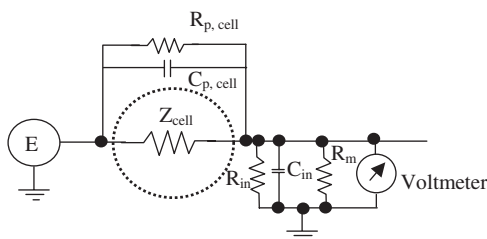
Figure 6.1.5.1   Equivalent circuit of the electrochemical cell and potentiostat measuring circuit incorporating nonideal elements.

circuits, and (c) the amplifiers used in the meter need a small but tangible input current, i.e., $I_{in} > 0$. For example, the best commercially available input amplifiers have input currents of around 50 fA, making it impossible to make absolute current measurements (DC signal) of low fA currents. Also, as discussed in Section 6.1.5c, the cell, potentiostat, and leads all contribute to parasitic resistance and capacitance components. In particular, the stray capacitance reduces the frequency or time domain over which meaningful electrochemical data can be obtained. In seeking to push the boundaries of time and media in which electrochemical measurements can be performed, fundamental physics is now influencing the experimental outcome. For example, Johnson noise associated with thermal agitation of electrons gives rise to a random fluctuation in the voltage across the resistor terminals, which may limit ultrahigh frequency, short timescale, and measurements.

REFERENCES

1. R. J. Forster, *Chem. Soc. Rev*. **23**, 289 (1994).
2. J. Heinze, *Angew. Chem. Int. Ed. Engl*. **32**, 1268 (1993).
3. B. B. Katemann, A. Schulte, E. J. Calvo, M. Koudelka-Hep, W. Schuhmann, *Electrochem. Commun*. **4**, 134 (2002).
4. J. C. Eklund, A. M. Bond, *Adv. Phys. Org. Chem*. **31**, 1 (1999).
5. A. J. Bard, L. R. Faulkner, *Electrochemical Methods: Fundamentals and Applications*, Wiley: New York, 1980.
6. J. J. Newman, *Electrochem. Soc*. **113**, 501 (1968).
7. D. O. Wipf, A. C. Michael, R. M. Wightman, *J. Electroanal. Chem*. **15**, 269 (1989).
8. L. R. Faulkner, M. R. Walsh, C. Xu, in *Contemporary Electroanalytical Chemistry*, A. Ivaska, Ed., Plenum Press: New York, 1990, p. 5.
9. W. J. Bowyer, E. E. Engelman, D. H. Evans, *J. Electroanal. Chem*. **67**, 262 (1989).
10. C. Amatore, B. Fosset, *Anal. Chem*. **68**, 4377 (1996).

6.2 MICROELECTRODE APPLICATIONS

The properties and applications of microelectrodes, as well as the broad field of electroanalysis, have been the subject of a number of reviews. Unwin reviewed the use of dynamic electrochemical methods to probe interfacial processes for a wide variety of techniques and applications including various flow-channel methods and scanning electrochemical microscopy (SEM), including issues relating to mass transport (1). Williams and Macpherson reviewed hydrodynamic modulation methods and their mass transport issues (2). Eklund et al. reviewed cyclic voltammetry, hydrodynamic voltammetry, and sonovoltammetry for assessment of electrode reaction kinetics and mechanisms with discussion of mass transport modelling issues (3). Here, we focus on applications ranging from measurements in small volumes to electroanalysis in electrolyte free media that exploit the unique properties of microelectrodes.

6.2.1   Electroanalysis at the micro- and nano-length scale

Microelectrodes have played an important role in the movement of analytical chemistry toward small-volume techniques as well as real time and spatially resolved measurement-techniques. The advantages of microelectrodes are exploited in many areas of electro-analysis, including environmental, biomedical, and material science areas. It is now possible to obtain electrochemical information at length scales ranging from meters to micrometers and even nanometers (4). As illustrated in Figure 6.2.1.1, microelectro-chemistry is a rapidly developing field that forms interdisciplinary bridges from funda-mental science to medicine, corrosion research, microelectronics, and biology.

The small physical size of microelectrodes allows the dimension of the electrochemical cell to be dramatically reduced allowing direct measurements to be performed in nanoliter and even picoliter volumes.

6.2.1.1   Electrochemical cells

Figure 6.2.1.2 illustrates the range of electrochemical cells that have been developed for microelectrochemical measurements. Significant features include the cell volume, distance of the electrodes, electrolyte flow, and optical transparency. For example, scanning electro-chemical microscopy (SECM, see Chapter 12) is performed in a macroscopic cell, but the
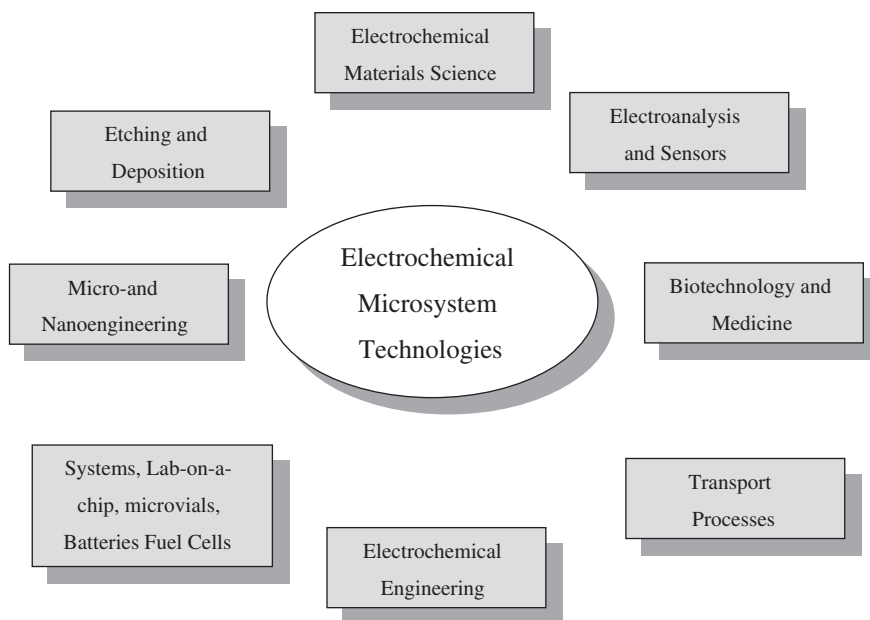
Figure 6.2.1.1   Electrochemical microsystem technologies with connections to and applications in electrochemical materials science, microengineering, electrochemical engineering, and biology and medicine.
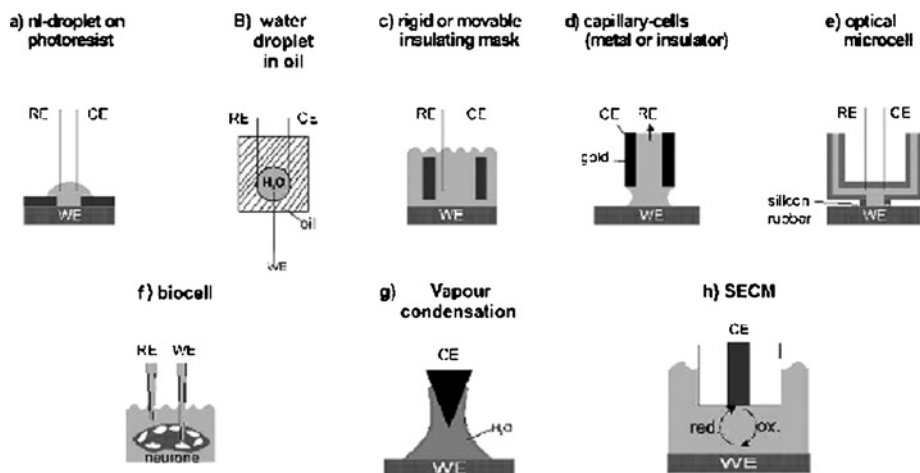
Figure 6.2.1.2 Cell constructions for microelectrochemical experiments: (a) water droplet on a photoresist electrode (8, 9); (b) water droplet in oil (10); (c) movable mask (11); (d) scanning droplet or capillary cell (12); (e) optical microcell (13); (f) biological cell (14); (g) vapour condensation cell with two electrodes or 'electrochemical nano cell' (15) and (h) SECM (16). [Reprinted from J. W. Schultze, A. Bressel, *Electrochimica Acta,* **47**, 3 (2001). Copyright (2001) with permission from Elsevier.]

local resolution is achieved by limitation of diffusion. Microelectrodes formed using lithographic techniques in which the electrode is surrounded by a hydrophobic photoresist can be used to perform electrochemical measurements in nanoliter volumes by wetting the electrode surface and introducing counter and reference electrodes into the nanoliter drop (16). Various modifications of the capillary cell and the optical microcell have been described and are similar in concept to a movable mask (10, 11). Perhaps, the smallest two-electrode electrochemical cell is that created by vapor condensation between a substrate and an SPM-tip (5) and has proven to be useful in the creation of nanodimensional structures (e.g., through "dip-pen nanolithography"). Beyond nanolithography, Bard and Fan developed an approach to detect single redox molecules using a piezoelectric positioner to move a microelectrode toward a large counter electrode to create a microvolume electrochemical cell (6). When a redox active molecule is moved from bulk solution into the microvolume defined by the two electrodes, it can be repeatedly electrolyzed to generate a measurable current. Transport of the electroactive species was dictated by Brownian motion causing the events to be infrequent.

Another approach to confining the volume is to use vials that have picoliter volumes (7). These can be fabricated with lithographic techniques. Electrochemical experiments using a standard reduction–oxidation couple, ferrocene-carboxylic acid, have been performed in volumes as small as 1 pL. Peak-shaped voltammetry and an increase in the current on the reverse wave of the cyclic voltammogram are observed in the voltammetric response when ultrasmall volumes (16 pL or less) are used. This deviation from bulk microelectrode behavior is observed only at slower scan rates in the smaller microvials. The voltammetric behavior in the small-volume experiments depends on the scan rate, vial size, and analyte concentration. A physical model based on restriction of analyte in these well-defined

microenvironments is proposed to explain the differences in current compared with that predicted by microelectrode theory in bulk solutions.

Irrespective of the sample volume, the amount of sample probed in an electrochemical experiment depends on the timescale. This sensitivity arises because, for solution phase reactants, diffusion is typically the dominant mode of mass transport. When the response is under semi-infinite linear diffusion control, the thickness of the diffusion layer, δ, is given by equation (6.1.5.1). Taking a typical diffusion coefficient of 1×10^{-5} cm^2 sec^{-1} in aqueous solution, equation (6.1.5.1) indicates that for a conventional electrochemical experiment employing an electrode of 3 mm diameter and an electrolysis time of 1 sec, a volume of approximately 10 μL will be electrolyzed. In contrast, for a 5-μm radius microelectrode and a 50-μsec electrolysis time, the volume will be less than 30 fL!

This approach can be exploited to monitor reactions involving single molecules. For example, Wightman and co-workers investigated electrochemiluminescent reactions involving individual reactant pairs (17). Their approach was to use 50 μsec potential steps at a 5-μm radius microelectrode to electrolyze a few femtoliters of 9,10-diphenylanthracene so as to generate a small population of radical anions. By allowing these radical anions to diffuse into a solution containing the radical cation of the same molecule, singlet excited states of 9,10-diphenylanthracene were created. This electronically excited state then decays back to the ground state by emission. Because of the low concentrations involved, these reactions are seen as individual light producing events.

6.2.1.2   *Analytical applications*

Microelectrodes have been used in combination with classical analytical techniques, such as anodic stripping voltammetry (ASV) to determine the concentration of a wide range of analytes, especially metal ions (18, 19). However, here we focus on more contemporary approaches that modify the surface of the microelectrode to produce sensors.

Cholesterol is a major structural component of the mammalian cell plasma membrane that regulates fluidity and permeability. It is a key component in signal transduction among cells, as well as in the immune response, cell infection, and cell surface polarity. Complete elucidation of the pathways governing the initial steps in atherogenesis requires the development of microscopic sensors capable of following the dynamics of intracellular cholesterol trafficking to and from the plasma membrane. Devadoss and Burgess (20) have probed the steady-state detection of cholesterol in the plasma membrane of a single cell using lipid bilayer-modified microelectrodes incorporating cholesterol oxidase. Their single-cell approach uses a platinum microelectrode modified with a lipid bilayer membrane containing cholesterol oxidase in which the steady-state electrode response appears to correlate with the cholesterol content of the cell plasma membrane. As shown in Figure 6.2.1.3, positioning the electrode directly adjacent to the cell (within ~1 μm or partially touching) produces an intermediate response, while contacting the cell with some force yields maximum current. The response observed adjacent to the cell may reflect detection of cholesterol efflux (i.e., solution-phase cholesterol). The apparent steady-state responses suggest that cholesterol oxidation is not limited by lateral diffusion of cholesterol in the plasma membrane to the electrode contact site (i.e., no current decay for depletion is observed).
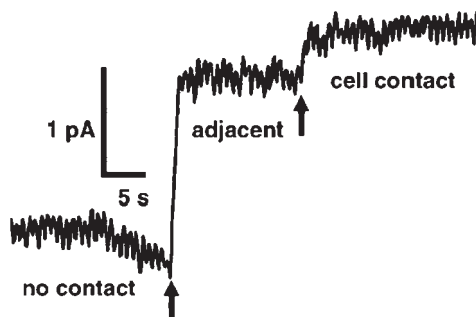
Figure 6.2.1.3 Amperometric data for detection of cellular cholesterol at a microelectrode (11.5 μm diameter) modified with a lipid bilayer membrane containing cholesterol oxidase. No contact: baseline data; no cholesterol detection. Adjacent: data for positioning the electrode within ~1 μm of (or partially touching) the plasma membrane. Cell contact: data for contacting the oocyte plasma membrane. Arrows approximate the times of changing electrode position. The buffer is 0.1 M sodium phosphate, pH 6.5. The electrode potential is 800 mV vs. NHE. [Reproduced with permission from A. Devadoss, J. D. Burgess, *J. Am. Chem. Soc.* **126**, 10214 (2004). Copyright 2004, American Chemical Society.]

6.2.2 Spatially heterogeneous systems: biological structures

In biological systems, chemical events of interest are often restricted to the interior or exterior surfaces of single cells. To provide useful information about *in vivo* biochemistry, these measurements must be performed with a high degree of spatial and temporal resolution as well as a high degree of sensitivity and selectivity (21). Spectroscopic techniques, such as fluorescence microscopy, magnetic resonance imaging, ion-mass spectrometry, and even X-ray emission imaging can provide useful information about the two-dimensional structure of biosystems. However, they are typically restricted to high analyte concentrations, millimeter rather than micrometer resolution and slow (>msec) time responses.

The mammalian brain (22) represents an extraordinarily challenging environment. At every level of organization, the brain is temporally and spatially heterogeneous: neuronal structures of differing sizes (from nanometer to meter) communicate with each other at timescales ranging from the microseconds to hours or days. Structurally, the brain contains small nuclei, such as the suprachiasmatic nucleus as well as larger nuclei that are not structurally homogeneous (e.g., the laminar structures of the cortex and hippocampus are well documented). When the objective is to elucidate the structure– function relationship of these structures, the ability to make spatially resolved measurements with microprecision is paramount. Thus, the spatial region that the chemical probe samples need to have dimensions similar to those expected for the phenomena of interest. Also, the concentrations of species present are nonuniform and the concentration of a target molecule is frequently higher close to its release site than it is in the surrounding tissue. Although the local concentration may be easily measurable, the total number of molecules in the small volume may be quite low (e.g., there are only 30,000 molecules in 50 fL of a 1 μM solution). For this reason, analysis in heterogeneous structures demands both high spatial resolution and a high mass, as opposed to concentration and sensitivity (23).

Another consequence of performing analysis at short length scales is that random processes (e.g., Brownian motion in response to a concentration gradient) can cause the instantaneously measured concentration to vary significantly from the time-averaged value. For example, equation (6.1.5.1) shows that diffusion will not significantly perturb the measured concentration over a sample interval of 1 cm for several hundred seconds. In contrast, if the concentration is measured only over 1 μm, diffusion will change the "sample" composition within a millisecond. Thus, electroanalysis becomes possible at short length scales only with the short response times of microelectrodes. It is important to note that amperometry consumes the target molecule (through oxidation or reduction) thus altering the chemical microenvironment and creating a driving force for molecular diffusion. In addition, the newly created species can interact with the sample. It is also frequently difficult to relate the measured current to concentration because of the challenge of replicating the heterogeneous nature of the sample during calibration.

Investigations elucidating neurotransmitter release have revealed the location and dynamics of neurotransmitter release through exocytotic events. A challenge in this field is to avoid fouling of the electrode surface through adsorption and carbon-fiber microelectrodes are frequently used. Neurotransmitter release occurs at short timescales making fast-scan cyclic voltammetry a powerful tool to temporally resolve neurotransmitter release. A disadvantage of electrochemistry is that the voltammetric response of each analyte is a significant fraction of the available potential window that rarely exceeds 1.5 V in aqueous media. Therefore, the task of resolving individual neurochemicals benefits greatly from advanced data analysis techniques. Wightman and co-workers evaluated the ability of cyclic voltammograms recorded at fast scan rates to resolve neurochemicals when analyzed by principal component regression (24). In their approach, a calibration set of 30 cyclic voltammograms was constructed from nine different substances at a variety of concentrations. The set was reduced by principal component analysis, and it was found that 99.5% of the variance in the data could be captured with five principal components. This set was used to evaluate cyclic voltammograms obtained with one or two compounds present in solution. In most cases, satisfactory predictions of the identity and concentration of analytes were obtained. Chemical dynamics were also resolved from a set of fast-scan cyclic voltammograms obtained with the electrode implanted in a region of a brain slice that contains dopaminergic terminals. Following stimulation, principal component regression of the data resolved the changes in dopamine and pH that were evoked. In a second test of the method, vesicular release was measured from adrenal medullary cells and the data were evaluated with a calibration set composed of epinephrine and norepinephrine. Cells that secreted one or the other were identified. Overall, the results show that principal component regression with appropriate calibration data allows resolution of substances that give overlapping cyclic voltammograms.

The utility of combining electrochemical and spectroscopic detection has also been demonstrated. Xin and Wightman demonstrated simultaneous detection of catecholamine exocytosis and calcium-ion release from single bovine chromaffin cells with a dual amperometric/calcium-selective dye-bound fluorescence sensor and demonstrated that catecholamine and calcium release were temporally and spatially correlated (25). In microelectrode measurements, individual exocytotic events associated with neurotransmitter release appear as spikes with the area of the amperometric spikes providing a

coulometric measure of the number of molecules released from each secretory event. On an average, the spikes from chromaffin cells yield an attomole of material. Despite the tiny amount of materials released, the signals are robust due to the small volume. However, because of diffusional dispersion, the concentration spikes are transient and are diluted to negligible values within a few milliseconds.

Microelectrode structures have been created that mimic aspects of brain function. Amatore and coworkers have described assemblies of paired microband electrodes that behave like a neuronal synapse (26). The generator electrode in these devices mimics a synaptic terminal, and the collector electrode functions as a postsynaptic membrane. These artificial synapses can be designed in several configurations to perform Boolean logical operations, such as AND or OR operations.

6.2.2.1   *Reactive surfaces and bioelectronics*

A number of successful bioelectronic devices have been created that exploit microelectrode technology. These include the cochlear implant and peripherally implantable stimulators (27). Other devices including retinal or cortical implants are less developed and not yet applicable. A challenge in this field is to engineer microelectrode surfaces so that they are both biocompatible and can be used to direct cell adhesion and growth (e.g., to stimulate nerve growth across an interrupted neuronal pathway).

Controlling the interfaces between cells and solid substrates is an important objective (28–30) that impacts areas as diverse as microfluidic, lab-on-a-chip separations, cellular biology, and tissue engineering. Modified surfaces offer excellent possibilities for real progress, most notably using molecular self-assembly to create low-defect density surfaces of controlled charge, hydrophobicity, and chemical reactivity (e.g., with respect to biomolecule binding (31–33)). Nishizawa recently described a strategy for the real-time local manipulation of the cell-adhesive properties of a substrate in the presence of attached living cells (34, 35). The strategy involves rapid switching of the cytophobic nature of albumin-coated substrates to a cell-adhesive surface by exposing it to an oxidizing agent, such as hypobromous acid. The oxidizing agent can be generated electrochemically at the tip of a microelectrode to create arbitrary cellular micropatterns. It is also possible to guide cellular growth and migration on substrates during cultivation. Figure 6.2.2.1 shows that the culturing of HeLa cells depends on the scanning height above the reactive surface. Approaches of this kind that facilitate the spatially controlled growth of individual cells will simplify bioassays based on cellular motility as well as contribute to cell and tissue engineering by creating micropatterned cocultures of different kinds of cell types.

6.2.3   Low conductivity media

Theoretical and practical applications of voltammetry in low ionic strength solutions have been reviewed by Ciszkowska and Stojek (36). Here, we present a selective overview of the importance of the area and the increased range of media that are now amenable to electrochemical investigation with microelectrodes.
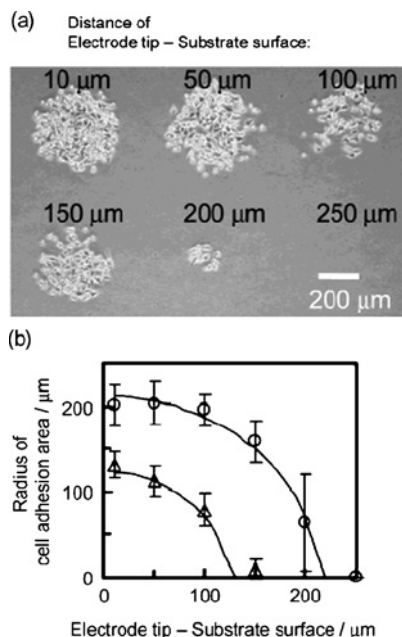
Figure 6.2.2.1   Size of cellular adhesion area at various distances between the electrode tip and the substrate surface during the electrochemical treatment. (a) Phase contrast micrograph of HeLa cells cultured for 24 h on the BSA-coated glass substrate, which was pretreated by a Br – oxidation pulse of 30 sec at the tip–surface distance indicated in the micrograph. (b) Plots of the radius of the cell adhesion area versus the distance of electrode tip–substrate surface for the electrolysis periods of 10 sec (△) and 30 sec (O). Error bars for the plots were calculated from the standard deviation of at least four cellular patterns. Solid curves were calculated assuming a diffusion-limited surface reaction. [Reproduced with permission from H. Kaji, K. Tsukidate, T. Matsue, M. Nishizawa, *J. Am. Chem. Soc*. **126**, 15026 (2004). Copyright 2004, American Chemical Society.] (for colour version: see colour section at the end of the book).

6.2.3.1   *Voltammetry in the absence of deliberately added electrolyte*

Voltammetry in highly pure water without added electrolyte is now well established (37–41). The ability to perform stripping analysis of metals without the need to add potentially contaminating supporting electrolyte is an important application (37). Ciszkowska and Osteryoung (38) have probed the voltammetric reduction of three metal cations: thallium, cadmium, and lead in solutions of various salts ($TlNO_3$, Tl_2SO_4, $Cd(NO_3)_2$, $Pb(NO_3)_2$, and $CdSO_4$), containing either no supporting electrolyte or where $LiClO_4$ or $Ca(NO_3)_2$ were added at various concentrations. The influence of migration was studied for a wide range of concentrations of the electroactive species and supporting electrolyte. As predicted by theory (39), the ratio of the limiting current, i_l, to the diffusion limited current, i_d, was 1.5 and 2 in solutions with and without excess supporting electrolyte, for the reduction of Tl^+ cation in the solutions with mono- and divalent anions.

6.2.3.2   *Voltammetry in pure liquid organics*

White and coworkers pioneered the use of microelectrodes in neat organic liquids and their theoretical interpretation (40–47). The low dielectric constant of these materials usually means that supporting electrolyte is often added to avoid catastrophic ohmic effects. A very low level of electrolyte, which results in a support ratio not higher than 0.001, helps to lower the ohmic potential drop and permits well-defined voltammetric waves to be obtained. Voltammograms were obtained for redox processes of several organic compounds, including nitrobenzene (40, 41), 4-cyanopyridine (42), aniline and pyrrole (48), acetonitrile (49), simple alcohols (50), dimethylsulfoxide (51), and DMF (52). Because the analyte concentration is so high in these experiments, water and other impurities do not influence the observed responses to any great extent.

A characteristic feature of voltammetry of pure organics is the formation of a microlayer of an ionic liquid at the electrode surface. This microlayer forms at the wave plateau, where the concentration of the substrate drops to zero and the charged product is neutralized by a counterion. For an oxidation reaction at potentials sufficiently negative of $E^{\circ\prime}$, the mole fraction of the analyte is 1. For potentials sufficiently positive of $E^{\circ\prime}$, the molar fraction of both the product and counterion is 0.5. This change in relative concentrations leads to a specific type of convection called diffusion-engendered convection (42). This thin layer of ionic liquid also leads to strong changes in the viscosity of media, which change both the activities of all species close to the electrode surface and their diffusion coefficient. These layers can be very stable especially for the electrooxidation of simple alcohols, and the electroreduction of nitrobenzene. In extreme situations, precipitation may occur at the electrode surface. White and coworkers have used interferometry (44) and voltammetry at elevated pressure (45) to probe the interfacial structure in these systems. These careful studies allow the pressure dependence of molecular transport to be investigated and have demonstrated that the interfacial layer can be compressed (45). The presence of this interfacial layer complicates the interpretation of voltammetric peak or steady-state currents because the diffusion coefficient of the analyte within the microlayer will be significantly different from that found in dilute solution. Ragsdale and White (47) used the Cullinan–Vignes equation to predict the reduction wave height of nitrobenzene in acetonitrile over a wide range of compositions. The deviations of experimental data from theoretical predictions for mole fractions of nitrobenzene less than 0.4 allowed self-association of the solution components to be detected.

6.2.3.3   *Complexation equilibria*

Traditionally, voltammetric investigations of complexation suffered relative to spectroscopy because of the need to add an excess of supporting electrolyte. A high concentration of electrolyte can cause contamination or can compete with the analyte of interest in the complexation reaction itself. The high ionic strength can cause the activity of the analyte to deviate significantly from its concentration. The ability to perform electrochemical measurements without deliberately adding supporting electrolyte may extend the range of analyte/ligand concentrations that can be investigated.

Palys and coworkers extended the work of Myland and Oldham (53) and developed a theoretical model that describes the steady-state microelectrode response for a wide range

of complexes that are inert on the experimental timescale (54). The theory shows that the steady-state limiting current depends on the type of complexation equilibrium, the type of the change in the reactant charge number, and the complex formation constant. The theory provides a good description of the experimental data found for the complexation of europium(III) with 1,4,8,11-tetraazacyclotetradecane (cyclam) in a 4:1 mixture (v/v) of methanol and dimethylsulfoxide. The influence of the concentration of the electroinactive ionic species on the limiting currents was also considered. For cases where migration contributes significantly to the transport, relationships between the measured steady-state limiting currents and β are given in the form of fitted equations.

Stojek and co-workers (55) found that in the case of neutral ligands, the shift of the half wave potential caused by the formation of the complex has the same magnitude in solutions with and without supporting electrolyte. For charged ligands, it is possible to find a value for the ligand/reactant concentration ratio above which migrational effects can be neglected. This behavior allows the classic analytical approaches to be applied to charged ligands. This approach was applied to experimental results obtained for Tl^+ with 18-crown-6 ligand in water without addition of supporting electrolyte.

6.2.4   Ultrafast electrochemical techniques

Ultrafast electrochemical techniques provide information about the kinetics and thermodynamics of redox processes that occur at sub-millisecond or nanosecond timescales. This short timescale is achieved either by making very rapid transient measurements or by using ultrasmall probes to achieve high rates of diffusion under steady-state conditions. Microelectrodes play pivotal roles in both approaches. Electrochemistry has several advantages over spectroscopy in that it provides *direct* information about electron transfer and coupled chemical reactions. In transient measurements, decreasing the lower accessible timescale depends critically on fabricating ultramicroelectrodes (UMEs) that continue to respond ideally as their critical dimension (e.g., the radius of a microdisk) decreases. The principal difficulty with transient approaches that use extremely short duration potential perturbations is ohmic drop as a small diffusion layer corresponds to a large concentration gradient, and so the current is large. The second difficulty is to produce microelectrodes with extremely short response times. It is now possible to assemble microelectrodes that respond to changes in applied potential within less than a few nanoseconds. In steady-state approaches, ultrasmall probes are required to make short timescale measurements. Various approaches that yield "nanodes" (i.e., electrodes of nanometer dimension) have been developed but the production of well-characterized nanodes remains a challenge.

6.2.4.1   Transient techniques

In transient electrochemical measurements involving a solution phase redox couple, one seeks to create a competition between the reaction of interest, electron transfer at the electrode surface or coupled homogeneous steps, and diffusion of the species to and from the electrode surface (56).

(a) Heterogeneous electron transfer dynamics

At short times, the diffusion layer thickness is much smaller than the microelectrode radius and the dominant mass transport mechanism is planar diffusion. The heterogeneous electron transfer dynamics of a diverse range of organic and inorganic species have been investigated using transient techniques. For example, cyclic voltammetry of the anthracene/anthracene anion radical has been used extensively as a reference system for characterizing new electrodes or instruments. This focus arises because the aromatic nature of the molecule leads to very small changes in the bond lengths and bond angles (i.e., the Marcus inner sphere reorganization energy is small (57)) thus causing the heterogeneous electron transfer rate constant to be large. Wightman (58) has studied this reaction using cyclic voltammetry at scan rates up to 10^5 V sec^{-1} and good agreement between the predictions of the Nicholson and Shain theory and experiment was found after correcting for the nonspherical nature of the microdisk used.

Despite the many elegant investigations that have been conducted on heterogeneous electron transfer dynamics of solution phase reactants, the magnitude of the diffusion-controlled current at short times ultimately places a lower limit on the accessible timescale. For diffusive species, the thickness of the diffusion layer, δ, is defined as $\delta = (\pi Dt)^{1/2}$ (equation (6.1.5.1)) and is, therefore, proportional to the square root of the polarization time, t. One can estimate that the diffusion layer thickness is approximately 50 Å if the diffusion coefficient is 1×10^{-5} cm^2 sec^{-1} and the polarization time is 10 nsec. Given a typical bulk concentration of the electroactive species of 1 mM, this analysis reveals that only 10,000 molecules would be oxidized or reduced at a 1-μm radius microdisk under these conditions. The average current for this experiment is only 170 nA, which is too small to be detected with low nanosecond time resolution.

Therefore, to probe the dynamics and energetics of ultrafast heterogeneous electron transfer dynamics, this diffusion limitation must be eliminated. One successful approach to achieving this objective is to use self-assembled or spontaneously adsorbed monolayers. When immobilized on an electrode surface, the electroactive species no longer needs to diffuse to the electrode to undergo electron transfer. Moreover, the electroactive species is preconcentrated on the electrode surface. For example, in the situation considered above, there will be approximately 1.7×10^{-20} mol of electroactive material within the diffusion layer. Given that the area of a 1-μm disk is approximately 3.1×10^{-8} cm^2, this translates into an "equivalent surface coverage" of about 5.4×10^{-13} mol cm^{-2}. In contrast, the surface coverage, Γ, observed for dense monolayers of adsorbates is typically more than two orders of magnitude larger with coverages of the order of 10^{-10} mol cm^{-2} being observed. This higher concentration gives rise to much larger currents that are easier to detect at short timescales. As exemplified by the work of Chidsey (59), Abruña (60), Faulkner (61), and Finklea (62), electroactively adsorbed monolayers have been developed that exhibit close to ideal reversible electrochemical behavior under a wide variety of experimental conditions of timescale, temperature, solvent, and electrolyte.

(b) Homogeneous chemical kinetics

The decrease in the lower accessible time limit possible using microelectrodes has important implications for probing the dynamics of rapid homogeneous chemical reactions.

Bimolecular reactions in solution cannot proceed faster than the rate at which molecules come into close contact. Thus, bimolecular rate constants cannot exceed the diffusion limited rate constant that is of the order of 10^9-10^{10} M^{-1} sec^{-1} in most organic solvents. As the characteristic time of cyclic voltammetry is RT/Fv, where v is the scan rate, experiments performed at MV sec^{-1} scan rates allow kinetic information, such as lifetimes that are close to the diffusion limit, to be obtained (63). As illustrated in Figure 6.2.4.1, Wightman (64) has shown that the irreversible response observed for the oxidation of anthracene at slow scan rates becomes fully reversible at a scan rate of 10^4 V sec^{-1}. This behavior is opposite to that expected when heterogeneous electron transfer is slow and suggests that the cation radical undergoes a following chemical reaction. The ability to make the voltammetric response reversible means that the formal potentials of highly reactive species can be accurately measured.

The kinetics and mechanism of homogeneous reactions following the reduction of NAD^+ and synthetic analogues continue to be investigated. Several reaction mechanisms have been observed for NAD^+ analogues, with molecules containing at least one hydrogen at the 4-position (i.e. direct analogues of NAD^+) typically undergoing a dimerisation reaction (65). The effect of changing the substitution pattern on the mechanism and kinetics of the homogeneous solution reactions of electrogenerated 1-methyl-carbamidopyridinyl radicals has been investigated. Fast-scan cyclic voltammetry (CV) and double potential
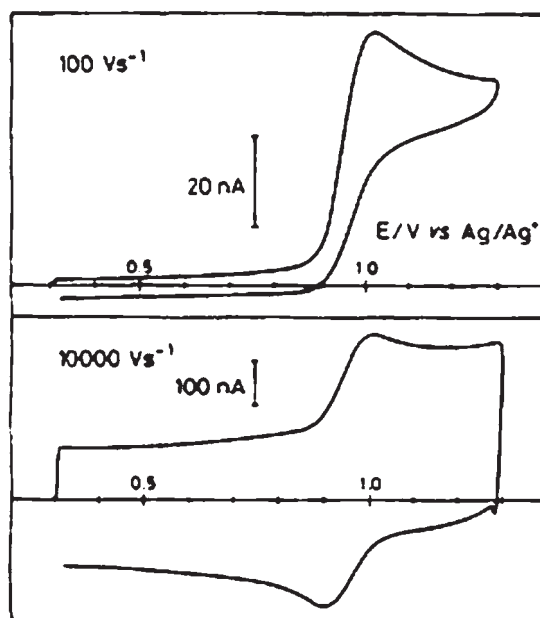

Figure 6.2.4.1   Effect of scan rate on the voltammetric response observed at a 5-μm platinum microdisk for the oxidation of 2.36 mM anthracene in DMF containing 0.6 M tetraethyl ammonium perchlorate. [Reproduced with permission from J. O. Howell, R. M. Wightman, *J. Phys. Chem*. **88**, 3915 (1984). Copyright 1984, American Chemical Society.]

step chronoamperometry (DPSC) conducted on a microsecond timescale reveal that 1-methyl-3-carbamidopyridinyl radicals react via a dimerisation mechanism involving direct coupling of the electrogenerated neutral radicals at a rate of approximately $1.6 \pm 0.1 \times 10^7$ M^{-1} sec^{-1} in DMF. The 1-methyl-4-carbamidopyridinyl and 1-methyl-3,4-dicarbamidopyridinyl radicals react via a pH-dependent ECE-DISP1 mechanism, where E, C and DISP denote electron transfer, following chemical and disproportionation reactions, respectively.

6.2.4.2   *Steady-state electrochemistry*

Under steady-state conditions, the time required for diffusion, t_D, is *not* related to the actual duration of the experiment as the diffusion layer thickness depends only on the radius. Under these conditions, t_D is approximately equal to r_0^2/D. This property has a profound impact on the size of microelectrodes required to make measurements at a steady state. Given a typical diffusion coefficient of 10^{-5} cm^2 sec^{-1}, microelectrodes with radii less than 30 nm are required to address sub-microsecond timescales. In using steady-state methods to determine kinetic parameters for fast reactions, experimental conditions are chosen so that there is mixed control by kinetics and diffusion. Aoki (66), Fleischmann (67), and Oldham (68) have addressed this issue and provided several equivalent approaches for analyzing experimental current–voltage curves. Bard and coworkers (69) developed an approach for determining kinetic parameters of simple quasi-reversible electron transfer reactions. In principle, only the one-quarter ($E_{1/4}$), one-half ($E_{1/2}$), and three-quarters ($E_{3/4}$) potentials from a single steady-state voltammogram are required, although more precise values of $k°$ and α can be obtained by fitting the full voltammogram. The analysis is independent of the electrode area and the concentration of the electroactive species, which improves the reliability of the analysis.

Parameters describing the kinetics of heterogeneous electron transfer for several solution phase redox active molecules have been reported and a representative sample is given in Table 6.2.4.1. These data show that the rate of electron transfer across the electrode/solution interface is influenced by the identity of the redox couple. These variations reflect differences in the reaction adiabaticity and activation barriers that exist for the individual systems. However, even for a single species, a considerable range of $k°$ values are observed (e.g., for the archetypal reversible couple ferrocene, reported $k°$ values range from 0.09 to 220 cm sec^{-1}). Reasons for these discrepancies include electrode fabrication protocol, purity of the ferrocene, solvent and electrolyte, and the method used to analyze the data. For high ferrocene concentrations, the electrode becomes pacified by an insoluble layer. Electrode surface blocking impedes diffusion and causes a nonproportional increase in current with increasing ferrocene concentration. Even for a standard electrochemical test system, considerable care must be taken over all aspects of the experiment, chemicals, electrode fabrication, experimental setup, as well as data collection and analysis if accurate kinetic parameters are to be obtained.

(a)   *Homogeneous chemical kinetics*
Steady-state measurements are important in studies of chemical reactivity. Steady-state measurements using electrodes of different radii provide insight into the kinetics of

Table 6.2.4.1

Rate constants for heterogeneous electron transfer determined using steady-state methods

Analyte	Electrode[a]	$k°$ (cm sec^{-1})	Reference
Anthracene	Au ring $\Delta r = 0.09$ μm; $r = 5$ μm	3.33 ± 0.05	(70)
(C_6H_6) Cr $(CO)_3{}^+$	Pt, 25 μm	≥ 0.3	(71)
$(CpCOOCH_3)_2C_o{}^+$	Pt, 23 Å-4.7 μ	130 ± 70	(72)
Cytochrome c	C, 6.3 μm	>0.4	(73)
9,10-Diphenylanthracene	Au ring $\Delta r = 90$ μm; $r = 5$ mm	5.7 ± 0.1	(70)
Ferrocene	Au ring $\Delta r = 0.09$ μm; $r = 5$ μm	0.09 ± 0.005	(70)
	C, 6 μm	2.3 ± 0.8	(74)
	Pt, 0.3-25 μm	≥ 6	(75)
	Pt, 1 μm	>2	(76)
	Pt, 16 Å-2.6 μm	220 ± 120	(72)
Fe(OEP)(N-Melm)$_2{}^+$	Pt, 1-25 μm	0.4	(77)
	Pt, 0.5-12.5 μm	0.38	(78)
	Pt, 1-25 μm	0.35	(77)
Fe(TPP) (Hlm)$_2{}^+$	Pt, 1-25 μm	0.5	(77)
Fe (TPP) py$_2{}^+$	Pt, 1-25 μm	0.6	(77)
MV$^{2+(F)}$	Pt, 22 Å-0.21 μm	170 ± 90	(72)
Naphthalene	Au ring $\Delta r = 0.2$ μm; $r = 20.5$ μm	0.88 ± 0.02	(70)
Oxygen	Pt, 12.7-250 μm	0.63 ± 0.05	(79)
Ru $(NH_3)_6{}^{3+}$	Au, 5 μm	0.076	(80)
	Pt, 1.3-4.6 μm	0.26 ± 0.13	(72)
	Pt, 11 Å-11.1 μm	79 ± 44	(72)
Tetracyanoethylene	Au ring $\Delta r = 0.2$ μm; $r = 20.5$ μm	0.15 ± 0.01	(70)
Tetracyanoquinodi-ethane	Au ring $\Delta r = 0.2$ μm; $r = 20.5$ μm	0.23 ± 0.01	(70)
Zn(TPP)	Pt, 1-25 μm	>1	(77)

[a]Dimension given is the radius of a microdisk electrode unless otherwise stated.

homogeneous reactions where the limiting current density depends on the magnitude of the homogeneous rate constant. Coupled chemical (C) and electron transfer (E) reactions (e.g. CE mechanisms, catalytic follow-up processes, as well as reactions involving disproportionation (DISP)) have been characterized. However, reactions such as chemical reactions that follow electron transfer (EC) mechanisms cannot be investigated in the same way as the current density is not influenced by the following chemical reaction. In these circumstances, the homogeneous reaction does not affect the height or shape of the reversible steady-state voltammogram. As indicated in Figure 6.2.4.2, the position of the wave on the potential axis depends on the homogeneous reaction rate and kinetic information can be obtained by probing how $E_{1/2}$ depends on the electrode radius.

6.2.5   AC electrokinetics

Electrochemical investigations are found in the areas of molecular electronics and nanotechnology. Electrochemistry can be used to produce and characterize clean surfaces (e.g., electrochemical cleaning of metals). It can direct the assembly and structure of supramolecular assemblies (e.g., by using self-assembled or spontaneously adsorbed
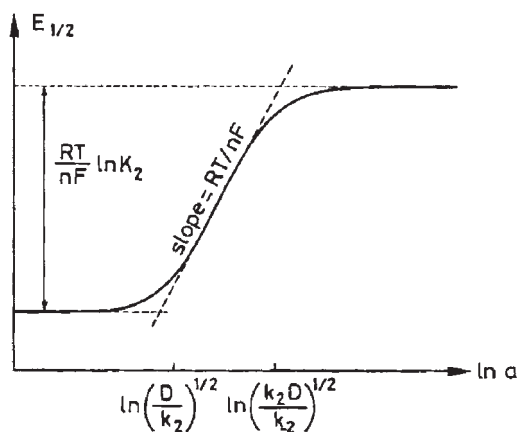
Figure 6.2.4.2 Dependence of $E_{1/2}$ for an EC reaction on the logarithm of the electrode radius. [Reproduced from K. B. Oldham, *J. Electroanal. Chem.* **313**, 3 (1991). Copyright (1991) with permission from Elsevier.]

monolayers). It can address molecular components (e.g., by switching their oxidation state). It can read their state (e.g., through measurements of the open circuit potential). Microelectrodes offer the possibility of selecting and moving nanometer dimensioned objects with precision by using AC electrokinetics. AC electrokinetics offers advantages over scanning-probe methods of nanoparticle manipulation in that the equipment used is simple, inexpensive, and has no moving parts, relying entirely on the electrostatic interactions between the particle and the dynamic electric field. There is a theoretical evidence that as manufacturing technology further improves, single particles considerably smaller than presently studied using AC electrokinetics may be manipulated.

AC electrokinetics uses an electric field created between two or more microelectrodes to induce a dipole within a cell, particle or macromolecule. With a suitable electrode design, a variety of motions including attraction, repulsion, and rotation can be induced by changing the nature of the dynamic field. These forces may be viewed as an electrostatic equivalent to optical tweezers (81) and optical spanners (82) in that they exert translational and rotational forces on a body due to the interaction between a body and an imposed field gradient. AC electrokinetic techniques, such as dielectrophoresis (83) and electrorotation (84) have been utilized for many years for the manipulation, separation, and analysis of cellular-scale particles. Recent advances in semiconductor manufacturing technology have enabled researchers to develop electrodes for manipulating macromolecules as small as 9 kDa using both attractive (85) and repulsive AC electrostatic forces and to concentrate 14 nm beads from solution (86). Trapping of single particles such as viruses and 93 nm diameter latex spheres in contactless potential energy wells (87) has also been demonstrated.

An application of AC electrokinetic phenomena is the preconcentration of a target molecule within a small volume. Crooks and coworkers (88) have achieved enrichment factors for DNA exceeding 100 using channels that are 5 mm in length, require only a single homogeneous analyte phase, and avoid complex microfluidic designs. The approach
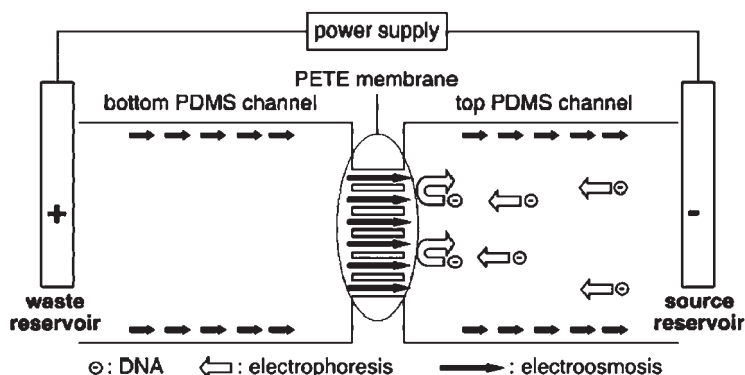
Figure 6.2.5.1   Diagram of a microfluidic concentrator. The three-dimensional microfluidic system consists of a nanoporous polyester membrane sandwiched between two poly(dimethylsiloxane) blocks, each containing a single fluidic channel (100 μm wide, 25 μm deep, and 5 mm long). [Reproduced with permission from J. Dai, T. Ito, L. Sun, R.M. Crooks, *J. Am. Chem. Soc*. **125**, 13026 (2003). Copyright 2003, American Chemical Society.]

appears versatile and should be applicable to any charged molecule or object. As illustrated in Figure 6.2.5.1, their approach relies on exerting spatial control over the electrokinetic velocity of the analyte. The electro-osmotic (eo) velocity of the buffer solution in one region of a microfluidic system opposes the electrophoretic (ep) velocity of the analyte in a second region. This results in ep transport of DNA to a location where the ep and eo velocities are equal and opposite, and DNA concentrates at this location.

When a forward bias (negative potential in the source reservoir) was applied between the electrodes, the concentration of DNA is apparent within 30 sec and reaches an enrichment factor of 11 within approximately 1 min. When the bias is reversed, DNA immediately transports through the PETE membrane indicating that concentration is not a consequence of physical blocking or size exclusion, and is trapped in the left channel (Figure 6.2.5.1) by the same balance of ep and eo velocities that were initially responsible for concentration in the right channel. This enrichment method is conceptually distinct from field-amplification stacking, isotachophoresis, micelle sweeping, size exclusion, and solid-phase extraction, but it is conceptually linked to a recent report in which micrometer-scale beads were trapped within a microfluidic channel by opposing pressure-driven flow and eo flow (89).

REFERENCES

1. P. R. Unwin, *J. Chem. Soc., Faraday Trans.* **94**, 3183 (1998).
2. D. E. Williams, J. V. Macpherson, in *Comprehensive Chemical Kinetic*s, R. G. Compton, G. Hancock, Eds., Elsevier: Amsterdam, 1999, pp. 369–438.
3. J. C. Eklund, A. M. Bond, J. A. Alden, R. G. Compton, *Adv. Phys. Org. Chem.* **32**, 1 (1999).
4. R. Kashyap, M. Gratzl, *Anal. Chem.* **70**, 1468 (1998).
5. H. Sugimura, T. Uchida, N. Kitamura, H. Masuhara, *Appl. Phys. Lett*. **63,** 1288 (1993).
6. F.-R. F. Fan, A. J. Bard, *Science* **267**, 871 (1995).
7. R. A. Clark, A. G. Ewing, *Anal. Chem.* **70**, 1119 (1998).

8. A. Michaelis, S. Kudelka, in *New Trends in Electrochemical Technology Series*, Gordon and Breach: London, 2001, Vol. 2, p. 160.

9. S. Kudelka, J. W. Schultze, *Electrochim. Acta* **42**, 2817 (1997).

10. M. M. Lohrengel, *Electrochim. Acta* **42**, 3265 (1997).

11. J. W. Schultze, V. Tsakova, *Electrochim. Acta* **44**, 3605 (1999).

12. A. W. Hassel, M. M. Lohrengel, *Electrochim. Acta* **42**, 3327 (1997).

13. A. Vogeland, J. W. Schultze, *Electrochim. Acta* **44**, 3751 (1999).

14. J. W. Deitmer, W. R. Schlue, A. Pfluegers, *Arch. Eur. J. Physiol.* **397**, 195 (1983).

15. H. Bloeß, G. Staikov, J. W. Schultze, *Electrochim. Acta* **47**, 335 (2001).

16. M. V. Mirkin, B. R. Horrocks, "Electrochemical Microsystem Technologies", in *New Trends in Electrochemical Technology Series*, J. W. Schultze, T. Osaka, M. Datta, Eds., Gordon and Breach: London, 2001, Vol. 2.

17. M. M. Collinson, R. M. Wightman, *Science* **268**, 1883 (1994).

18. M. L.Tercier, J. Buffle, *Electroanalysis* **5**, 187 (1993).

19. G. A. Daniele, M. Mazzocchin, *Anal. Chim. Acta* **273**, 3 (1993).

20. A. Devadoss, J. D. Burgess, *J. Am. Chem. Soc.* **126**, 10214 (2004).

21. R. M. Wightman, P. Runnels, K. Troyer, *Anal. Chim. Acta* **400**, 5 (1999).

22. P. L. McGeer, J. C. Eccles, E. G. McGeer, *Molecular Neurobiology of the Mammalian Brain*, Springer, 1987.

23. S. A. Brazill, S. E. Bender, N. E. Hebert, J. K. Cullison, E. W. Kristensen, W. G. Kuhr, *J. Electroanal. Chem.* **531**, 119 (2002).

24. M. L. Heien, M. A. Johnson, R. M. Wightman, *Anal. Chem.* **76**, 5697 (2004).

25. Q. Xin, R. M. Wightman, *Anal. Chem.* **70**, 1677 (1998).

26. C. Amatore, L. Thouin, J. Warkocz, *Chem. Eur. J.* **5**, 456 (1999).

27. G. M. Clark, *Cochlear Implants: Fundamentals and Applications*, Springer Verlag: New York, 2003.

28. A. Folch, M. Toner, *Annu. Rev. Biomed. Eng.* **2**, 227 (2000).

29. Y. Ito, *Biomaterials* **20**, 2333 (1999).

30. J. Shim, T. F. Bersano-Begey, X. Zhu, A. H. Tkaczyk, J. J. Linderman, S. Takayama, *Curr. Top. Med. Chem.* **3**, 687 (2003).

31. C. S. Chen, M. Mrksich, S. Huang, G. M. Whitesides, D. E. Ingber, *Science* **276**, 1425 (1997).

32. A. Brock, E. Chang, C. Ho, P. LeDuc, X. Jiang, G. M. Whitesides, D. E. Ingber, *Langmuir* **19**, 1611 (2003).

33. J. Lahann, M. Balcells, T. Rodon, J. Lee, I. S. Choi, K. F. Jensen, R. Langer, *Langmuir* **18**, 3632 (2002).

34. H. Kaji, M. Kanada, D. Oyamatsu, T. Matsue, M. Nishizawa, *Langmuir* **20**, 16 (2004).

35. H. Kaji, K. Tsukidate, T. Matsue, M. Nishizawa, *J. Am. Chem. Soc.* **126**, 15026 (2004).

36. M. Ciszkowska, Z. Stojek, *J. Electroanal. Chem.* **466**, 129 (1999).

37. J. Widera, W. H. Steinecker, G. E. Pacey, J. A. Cox, *J. Appl. Electrochem.* **33**, 121 (2003).

38. M. Ciszkowska, J. M. Osteryoung, *Anal. Chem.* **67**, 1125 (1995).

39. J. B. Cooper, A. M. Bond, K. B. Oldham, *J. Electroanal. Chem.* **331**, 877 (1992).

40. R. A. Malmsten, H. S. White, *J. Electrochem. Soc.* **133**, 1067 (1986).

41. R. A. Malmsten, C. P. Smith, H. S. White, *J. Electroanal. Chem.* **215**, 223 (1986).

42. R. B. Morris, K. F. Fischer, H. S. White, *J. Phys. Chem.* **92**, 5306 (1988).

43. J. D. Norton, S. A. Anderson, H. S. White, *J. Phys. Chem.* **96**, 3 (1992).

44. Q. Li, H. S. White, *Anal. Chem.* **67**, 561 (1995).

45. K. J. Stevenson, H. S. White, *J. Phys. Chem.* **100**, 18818 (1996).

46. S. C. Paulson, N. D. Okerlund, H. S. White, *Anal. Chem.* **68**, 581 (1996).

47. S. R. Ragsdale, H. S. White, *J. Electroanal. Chem.* **432**, 199 (1997).

48. R. L. McCarley, M. Morita, K. O. Wilbourn, R. W. Murray, *J. Electroanal. Chem.* **245**, 321 (1988).

49. J. Cassidy, S. B. Khoo, S. Pons, M. J. Fleischmann, *J. Phys. Chem.* **89**, 3933 (1985).
50. M. Ciszkowska, Z. Stojek, *J. Electroanal. Chem.* **344**, 135 (1993).
51. M. Koncka, Z. Stojek, *Electroanalysis* **7**, 1010 (1995).
52. J. Gadomska, Z. Stojek, *Electroanalysis* **10**, 307 (1998).
53. J. C. Myland, K. B. Oldham, *J. Electroanal. Chem.* **347**, 49 (1993).
54. M. Palys, Z. Stojek, M. Bos, W. van der Linden, *Anal. Chim. Acta* **337**, 5 (1997).
55. M. J. Palys, H. Sokolowska, Z. Stojek, *Electrochim. Acta* **49**, 3765 (2004).
56. M. I. Montenegro, in *Research in Chemical Kinetics*, R. G. Compton, G. Hancock, Eds., 1994, Vol. 2, p. 1.
57. R. A. Marcus, *J. Chem. Phys.* **43**, 679 (1965).
58. J. O. Howell, R. M. Wightman, *Anal. Chem.* **56**, 524 (1984).
59. C. E. D. Chidsey, *Science* **251**, 919 (1991).
60. D. Acevedo, H. D. Abruña, *J. Phys. Chem.* **95**, 9590 (1991).
61. R. J. Forster, L. R. Faulkner, *J. Am. Chem. Soc.* **116**, 5444 (1994).
62. H. O. Finklea, D. D. Hanshew, *J. Am. Chem. Soc.* **114**, 3173 (1992).
63. C. A. Amatore, A. Jutand, F. Pflüger, *J. Electroanal. Chem.* **218**, 361 (1987).
64. J. O. Howell, R. M. Wightman, *J. Phys. Chem.* **88**, 3915 (1984).
65. P. Hapiot, J. Moiroux, J. M. Savéant, *J. Am. Chem. Soc.* **112**, 1337 (1990).
66. K. Aoki, K. Tokuda, H. Matsuda, *J. Electroanal. Chem.* **235**, 87 (1987).
67. M. Fleischmann, S. Bandyopadhyay, S. Pons, *J. Phys. Chem.* **89**, 5537 (1985).
68. K. B. Oldham, C. G. Zoski, *J. Electroanal. Chem.* **256**, 11 (1988).
69. M. V. Mirkin, A. J. Bard, *Anal. Chem.* **64**, 2293 (1992).
70. A. Russell, K. Repka, T. Dibble, J. Ghoroghchian, J. Smith, M. Fleischmann, C. Pitt, S. Pons, *Anal. Chem.* **58**, 2961 (1986).
71. C. G. Zoski, D. A. Sweigart, N. J. Stone, P. H. Rieger, E. Mocellin, T. F. Mann, D. R. Mann, D. K. Gosser, M. M. Doeff, A. M. Bond, *J. Am. Chem. Soc.* **110**, 2109 (1988).
72. R. M. Penner, M. J. Heben, T. L. Longin, N. S. Lewis, *Science* **250**, 1118 (1990).
73. F. N. Büchi, A. M. Bond, *J. Electroanal. Chem.* **314**, 191 (1991).
74. A. Owlia, J. F. Rusling, *Electroanalysis* **1**, 141 (1989).
75. A. M. Bond, T. L. E. Henderson, D. R. Mann, T. F. Mann, W. Thormann, C. G. Zoski, *Anal. Chem.* **60**, 1878 (1988).
76. J. Daschbach, D. Blackwood, J. W. Pons, S. Pons, *J. Electroanal. Chem.* **237**, 269 (1987).
77. Y. Zhang, C. D. Baer, C. Camaioni-Neto, P. O'Brien, D. A. Sweigart, *Inorg. Chem.* **30**, 1682 (1991).
78. K. B. Oldham, C. G. Zoski, A. M. Bond, *J. Electroanal. Chem.* **248**, 467 (1988).
79. B. R. Scharifker, P. Zelenay, J. O'M. Bockris, *J. Electrochem. Soc.* **134**, 2714 (1987).
80. A. J. Bard, M. V. Mirkin, P. R. Unwin, D. O. Wipf, *J. Phys. Chem.* **96**, 1861 (1992).
81. J. Prikulis, F. Svedberg, M. Kall, J. Enger, K. Ramser, M. Goksor, D. Hanstorp, *Nano Lett.* **4**, 115 (2004).
82. N. B. Simpson, K. Dholakia, L. Allen, M. J. Padgett, *Opt. Lett.* **22**, 52 (1997).
83. T. B. Jones, *Electromechanics of Particles*, Cambridge University Press: Cambridge, UK, 1995.
84. U. Zimmermann, G. A. Neil, *Electromanipulation of Cells*, CRC Press, 1996.
85. M. Washizu, S. Suzuki, O. Kurosawa, T. Nishizaka, T. Shinohara, *IEEE Trans. Ind. Appl.* **30**, 835 (1994).
86. T. Müller, A. Gerardino, T. Schnelle, S. G. Shirley, F. Bordoni, G. DeGasperis, R. Leoni, G. Fuhr, *J. Phys. D: Appl. Phys.* **29**, 340 (1996).
87. M. P. Hughes, *Phys. Med. Biol.* **12**, 3639 (1998).
88. J. Dai, T. Ito, L. Sun, R. M. Crooks, *J. Am. Chem. Soc.* **125**, 13026 (2003).
89. G.-L. Lettieri, A. Dodge, G. Boer, N. de Rooij, E. Verpoorte, *Lab Chip* **3**, 34 (2003).

6.3   UME FABRICATION/CHARACTERIZATION BASICS

6.3.1   Platinum and gold inlaid disks ≥5 μm diameter

Fu-Ren F. Fan[1], Jose Fernandez[1], Biao Liu[1],
Janine Mauzeroll[2], and Cynthia G. Zoski[3]

[1]Department of Chemistry and Biochemistry, The University of Texas at
Austin, Austin, Texas 78712-0165, USA
[2]Laboratoire d'Electrochimie Moléculaire, Université Paris,
7-UMR CNRS 7591, France
[3]Chemistry Department, New Mexico State University, Las Cruces,
NM 88011, USA

6.3.1.1   Introduction

The fabrication of ultramicroelectrodes (UMEs) has been reviewed (1–3) and involves several steps. First, the end of a glass capillary is sealed such that a conical shape is obtained. A straight 25, 10, or 5 μm diameter metal wire is then positioned at the bottom of the sealed borosilicate glass capillary and put under vacuum for 30 min. The capillary is slowly sealed onto the wire using a heated resistor coil. The sealed wire is then electrically connected to a larger wire using a conducting silver epoxy. The connected tip is placed in the oven at 120 °C overnight to cure the epoxy.

This procedure can also be applied to 5 and 10 μm platinum and gold wires (where the use of soft glass capillaries is sometimes preferred). For smaller tips (1–2 μm diameter), a Wollaston wire (a metal wire covered by a silver layer) is first placed in weak nitric acid solution to dissolve the silver layer prior to sealing the tip (Section 6.3.2). A laser puller can also be used with small diameter quartz capillaries to make submicron size electrodes (Section 6.3.3). Such sealing techniques require much practice and patience.

UME tip fabrication also includes electrode polishing, sharpening, and characterization. The voltammetric behavior of the electrode is recorded to evaluate the quality of the glass/metal seal and the tip radius and that value is compared with the one observed optically. Conducting and insulating approach curves using scanning electrochemical microscopy (SECM) (see Chapter 12) can also be acquired and fitted to theory to determine the radius of the UME and the thickness of the insulating glass.

6.3.1.2   Sealing the capillary tube

Take a clean and dry Pyrex (borosilicate) glass capillary (at least 15 cm long to manipulate in a flame, inner diameter 1 mm, outer diameter 2 mm). The precleaned capillary should be moisture- and dust free so as to avoid bad sealing of the glass onto the wire. Polluting substances and water can lead to bubble formation next to the wire as the glass is melted. To circumvent this, the glass capillaries can be soaked in 1:10 diluted HNO_3, rinsed with copious amounts of distilled water, oven dried, and stored in an enclosed vial.
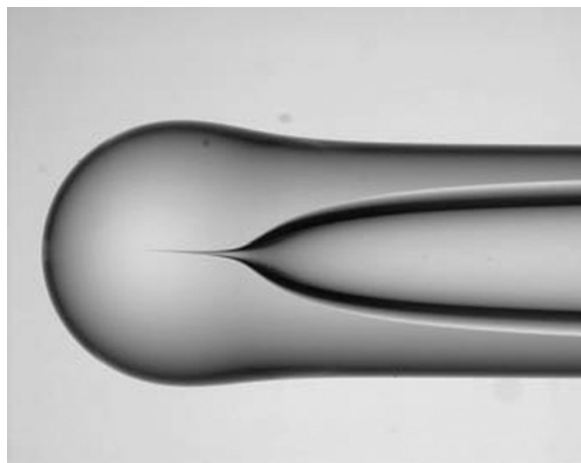
Figure 6.3.1.1   The end of a sealed glass capillary with an internal conical shape.

Use a gas/oxygen flame to seal one end of the glass capillary. Choose an adequate flame temperature, which is not too hot to avoid bending the glass. Rotate the capillary continuously on the side of the flame to obtain a conical shape (Figure 6.3.1.1). This shape must be obtained to adequately place the Pt wire in the capillary.

Check the capillary under a microscope and make sure that it is completely sealed at the base. Cut the glass capillary to about 5 cm length using a file.

6.3.1.3   Manipulating the platinum wire

Now that the capillary is sealed and shows a conical shape, a straight Pt wire must be inserted at the bottom of the capillary into the crack of the cone. Straightening the wire and positioning it is a time-consuming work and it is possible that you might have to take the wire out, straighten it several times before getting the desired results.

Using gloves, cut a piece of approximately 1.5 cm of hard (i.e., not annealed) platinum wire (5, 10, or 25 μm diameter, 99.9% purity) and rinse with acetone. The gloves are necessary to prevent finger oils from contaminating the wire.

Carefully straighten the wire with your fingers and without twisting it on a white piece of paper. This can be done by rolling the wire on a sheet of white glossy paper with a finger or the flat side of a wooden ruler. This might take several attempts.

Bring the straight wire to the edge of the paper and introduce the wire into the sealed glass capillary. At this point, special care must be taken not to bend the wire. The wire must go in straight. The use of tweezers tends to crimp the end of the wire making it difficult to fall into the glass capillary properly.

Position the wire at the bottom of the capillary in the crack of the cone (Figure 6.3.1.2) by gently tapping the capillary on the bench top. If the capillary is tapped too forcefully against the bench, the wire can sometimes bounce out of the capillary or curl up at the end. Checking under an optical microscope, the wire should be aligned as shown in Figure 6.3.1.2. If this
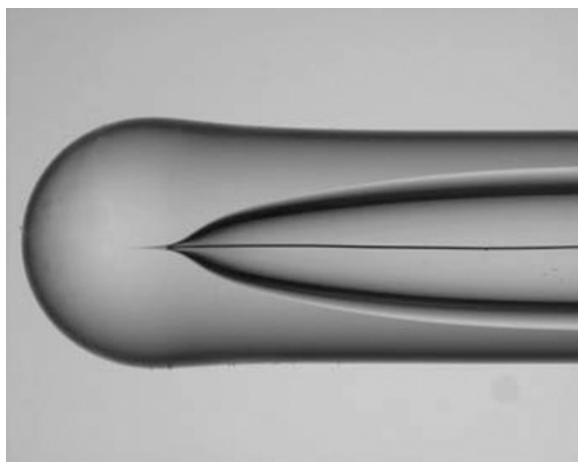
Figure 6.3.1.2 The 25 μm Pt wire is inserted at the base of the cone and remains straight. (for colour version: see colour section at the end of the book).
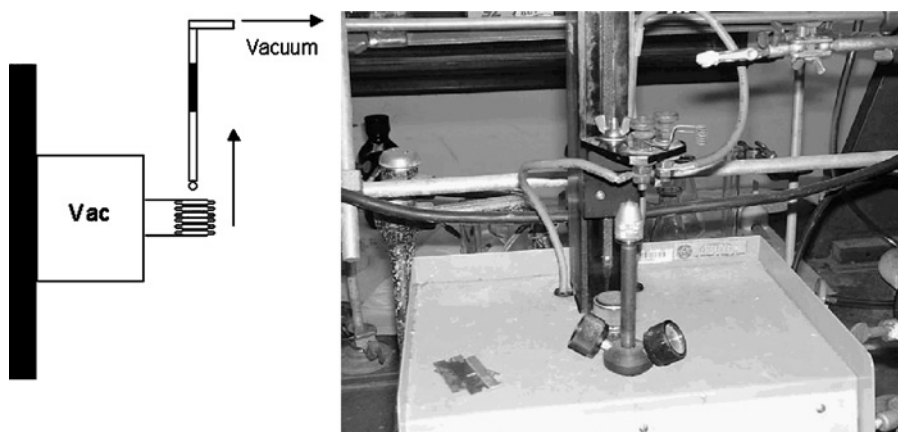
Figure 6.3.1.3 Left-hand side: Diagram of the setup where the capillary is aligned with the resistor coil. Right-hand side: Picture of the sealing setup.

is not the case, then the glass/wire assembly can be dropped through an approximately 10 cm glass tube of larger diameter, resting on a layer of Kimwipes to cushion the fall. Approximately 2 or 3 falls should align the wire in the capillary. If this does not center the wire, then it is often easiest to remove the wire from the capillary and start again.

6.3.1.4 Sealing the electrode

To seal the Pt wire into the glass capillary, a setup like that shown in Figure 6.3.1.3 is used. It is composed of a Nickel–Chromium resistor coil (gauge 18) that can be electrically

heated up to 800 °C. By turning the screw on the right-hand side of the vertical metal sup-
port, the coil can be moved vertically.

The power supply is an old pipette puller that has a 2.5-A fuse, a 120-V output, and a
maximum power of 300 W. The Nickel–Chromium wire has a thickness of approximately
1 mm. It is coiled to a length of about 1 cm, with five or six turns, and an inner and outer
diameter of 5 and 7 mm, respectively. The alligator clip above the coil is used to hold the
glass capillary and help to align it perpendicularly to the bench top.

Connect the capillary tube to a vacuum line by inserting it into rubber tubing and clamp-
ing it to the alligator clip shown in sealing setup in Figure 6.3.1.3. Align the tip such that the
capillary is perpendicular to the bench top and at the center of the resistor coil as depicted in
Figure 6.3.1.3 on the left-hand side. If the capillary is not in the center of the coil and is closer
to the sides, it will cause the capillary to bend during sealing. Take the time to make a good
alignment and to move the coil up and down the capillary.

There should be a T joint between the UME capillary and the vacuum pump. Before turn-
ing on the vacuum, check that the T joint is in the closed position such that the capillary is
not yet directly connected to the vacuum line. Turn on the vacuum. *Slowly* turn the T joint to
the open position. This must be done slowly in order not to displace the Pt wire.

Leave the capillary under vacuum for 30 min. If the pump used is bad or the evacuation
time is too short, air bubbles occur during the sealing process.

Center the glass capillary in the coil with the bottom of the capillary just inside the coil.
This means that the bottom of the tip should be approximately 1 mm (or one coil diameter)
inside the coil.

Turn on the power. The color of the coil should be orange yellow and not bright yellow.
Leave the capillary at the bottom of the coil for 20 min so that the volatile compounds and
residual moisture are evacuated.

Move the coil up the glass capillary very slowly to assure a proper sealing. Take steps of
1 mm every 5 min to seal approximately 1 cm of the capillary tube. Using a Kimwipe placed
behind the capillary, make sure that the glass does not seal past the wire. Also, be very care-
ful not to bump the setup while manipulating. If the glass capillary touches the hot sides of
the coil, the process has to be repeated from the start.

Turn the power supply and vacuum off. Wait for the glass capillary to cool down. Remove
the glass capillary and check under the microscope (Figure 6.3.1.4) to make sure that the wire
has been properly sealed.

Once sealed, electrical contact between the Pt wire and a lead wire must be made. Using
a hypodermic syringe (for example, a 3-ml syringe with a 22 G1.5 gauge needle works
best for this size glass capillary), inject a premixed silver epoxy mixture (Epotek) into the
glass capillary around the sealed wire. The epoxy must be inserted all the way down where
the Pt wire is sealed. Next introduce a conductive wire (30AWG wire for this size capil-
lary) into the tube and put the electrode in the oven (120 °C) overnight (i.e., for 10−12 h)
to cure the epoxy.

6.3.1.5   *Polishing the electrode*

A small amount of 5-min epoxy should be patched between the connection wire and the
end of the capillary to restrict the strain put on the connection wire. Allow to dry.
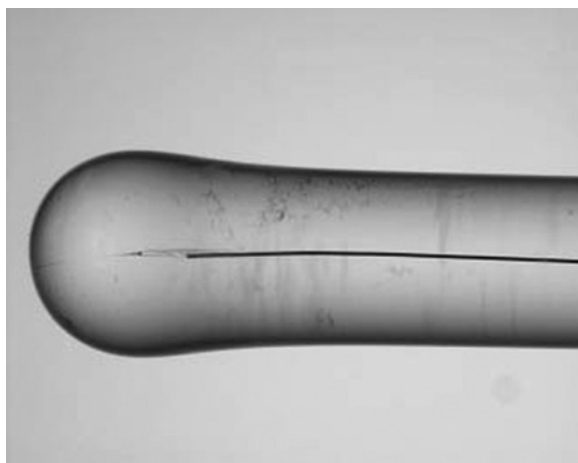
Figure 6.3.1.4 Sealed 25 μm Pt wire in a Pyrex capillary. A small air-pocket is observed at the beginning of the wire but the rest of the body is properly sealed. This is not unusual and can be shaved off during the polishing steps. (for colour version: see colour section at the end of the book).
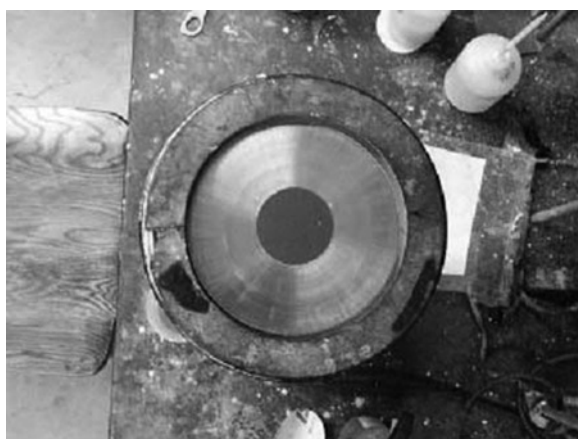
Figure 6.3.1.5 Polishing wheel.

To polish the electrode, a polishing wheel can be used as shown in Figure 6.3.1.5. Sandpaper or micropolishing cloths are put at the center of the wheel. The lower speed levels of the polishing wheel are used to polish the electrodes.

Using sandpaper (Buehler, 400 or higher grit sandpaper), remove the glass from the bottom of the tip until the sealed platinum wire is exposed and observe under a microscope (Figure 6.3.1.6). Using water on the sandpaper while polishing sometimes reduces the strain on the glass.

Polish the tip by gradually increasing the grit size of the sandpaper (400, 600, 800, 1200). Try to maintain the electrode as vertical as possible so that the tip stays completely
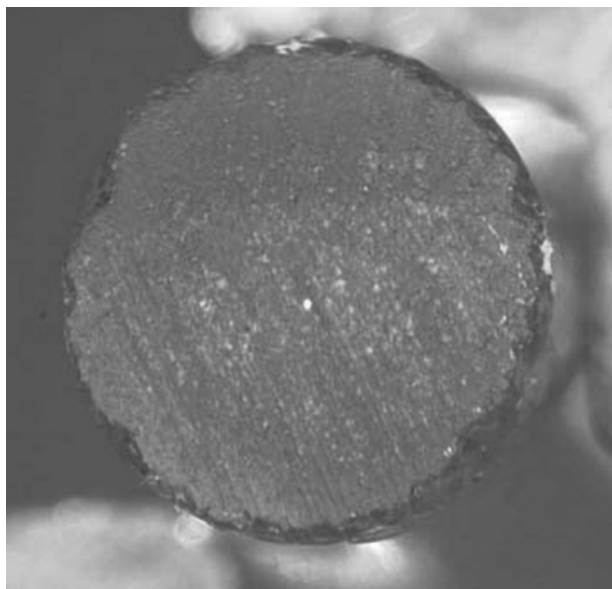
Figure 6.3.1.6   Polished capillary exposing the 25 µm Pt wire at the center. (for colour version: see colour section at the end of the book).

flat. Observe the polishing progress under the microscope. Always wash the surface of the electrode with Milli-Q water before changing from one sandpaper grit to another.

Use polishing cloth (Buehler) and solutions of alumina with different particle size (typically 1.0, 0.30, and 0.05 µm) to perform the final polishing. Always go from the larger grain size to the smallest one and use a different polishing cloth for each alumina size grain. The polishing cloths can be reused (as they are quite expensive). Make sure to wash the electrode surface extensively between alumina solutions. Decrease the particle size gradually and check under the microscope. A smooth surface must be obtained, as shown in Figure 6.3.1.7.

6.3.1.6   Checking the glass/metal seal

A steady-state voltammogram is recorded to check the seal between the glass capillary and the Pt wire. No matter how good the tip looks under the microscope, a steady-state voltammogram where the reverse scan retraces the forward scan, as shown in Figure 6.3.1.8, must be obtained. A solution of FcOH (1 mM in 0.1 M KCl) and a scan rate of 20 mV sec^{-1} were used in recording the voltammogram.

The initial potential was set to -0.2 V vs. Ag/AgCl, the reversal potential to 0.5 V, the final potential to -0.2 V, the initial scan polarity to positive, the scan rate to 0.02 V sec^{-1}, and the current sensitivity to 1×10^{-8} A.

If the steady-state voltammogram does not resemble that in Figure 6.3.1.8, one has two choices: to throw away the tip or to repeat the polishing again to remove more glass to find a better sealed segment of electrode. The most common cause for electrode failure is unsuccessful sealing.
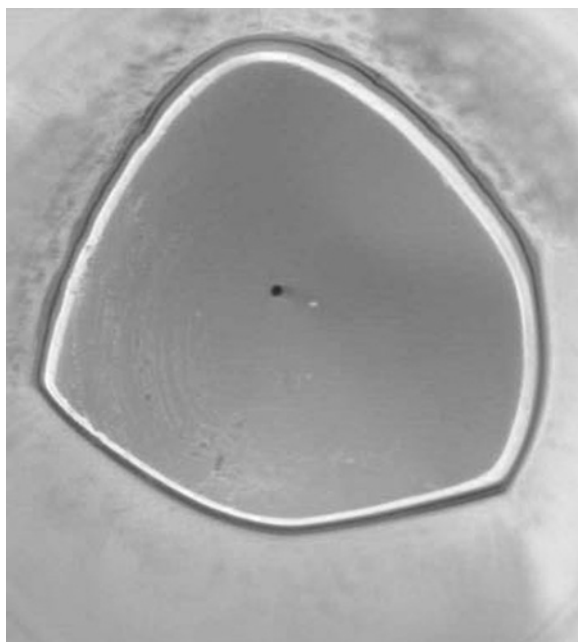
Figure 6.3.1.7   Smoothly polished 25 µm Pt UME that has been slightly sharpened.
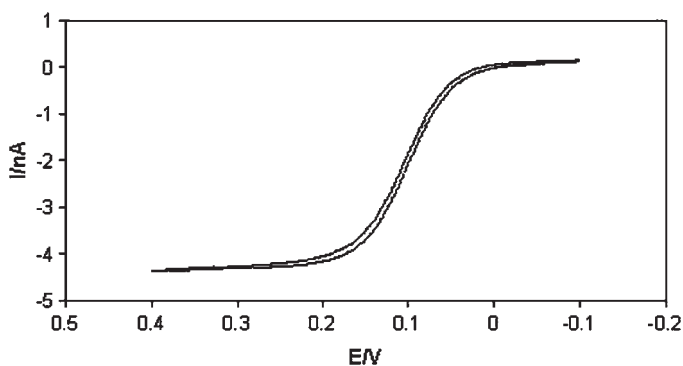
Figure 6.3.1.8   Steady-state voltammogram at a 25-µm diameter Pt disk UME in a solution of 1 mM ferrocenemethanol (FcOH) in 0.1 M KCl electrolyte. The potentials are given with respect to Ag/AgCl.

If the CV is satisfactory, the quantitative behavior of the tip can be checked by back calculating the radius of the electrode using the theoretical expression for the steady-state current. The steady-state current, i_{ss} (A = coulombs sec^{-1}), for a microdisk electrode can be expressed as:

$$i_{ss} = 4nFDaC*$$

(6.3.1.1)

where n is the number of electrons involved in the electrochemical reaction ($n = 1$ eq. mol^{-1}), F is the Faraday's constant (96,485 C eq.$^{-1}$), D is the diffusion coefficient of the reacting species (for FcOH: $D = 7 \times 10^{-6}$ cm^2 sec^{-1}), C^* is the bulk concentration of the species (1×10^{-6} mol cm^{-3}), and a is the radius of the electrode (in cm).

From the optical measurements, we know that the radius of the electrode should be 12.5×10^{-4} cm. The value extracted from the voltammogram using equation 6.3.1.1 should be very close to that value.

When micron or sub-micron size electrodes are used, it can sometimes be very difficult to optically define the radius of the electrode. It is thus useful to use available analytical expressions to determine these values (as in equation 6.3.1.1) or to monitor decreases in electrode active area as a result of adsorption processes (4).

6.3.1.7   Electrode sharpening

Electrode sharpening of the glass insulator surrounding the metal electrode is necessary in scanning probe techniques, such as SECM (see Chapter 12), in experiments where small volumes of solution are used, and in those where the electrode is inserted into small places, such as in biological cells. The goal of electrode sharpening is to reduce the ratio of the diameter of the (metal + glass) to the diameter of the metal to 10 or less, with 2–5 being optimum. Thus, the ratio of the diameter of (metal + glass) to the diameter of the metal is the so-called RG value. The process of electrode sharpening is very individualistic. However, we describe a general method below and encourage the experimentalist to make modifications. It is important to emphasize that if a UME is fabricated for routine purposes, then a larger RG $\approx$ 20 is adequate for equation (6.3.1.1) to be valid. Electrode polishing also becomes easier because one can see under an optical microscope if the metal has become recessed in the glass, such that the polishing material collects around the metal/glass seal. This is much harder to see if the metal is surrounded by glass of infinite RG.

Electrode sharpening begins with the use of 800-grit sandpaper on a polishing wheel. Hold the electrode at about a 45° angle while rotating the electrode in your fingers. Check on the RG value frequently under a microscope that is equipped with a measurement grid in the eyepiece. When RG $\approx$ 20, change to 1200-grit sandpaper and continue using the polishing wheel, but stop more frequently to check under the microscope. At about RG = 10, it is advisable to sharpen the electrode manually on the 1200-grit paper with frequent trips to the microscope.

Desirable final shapes of the electrode tip are shown in Figure 6.3.1.9.

Depending on how one does the final polishing, the overall appearance of the tip can be different as seen in Figure 6.3.1.9. On the left-hand side, 0.3 μm alumina was used to finish sharpening the tip. This yields a much smoother glass rim that is often hard to photograph and gives the appearance of a recessed disk. The use of a 1200-grit sandpaper on the right-hand side yields a more defined edge that is easier to observe. Using sandpaper is faster, but requires more skill because it is more likely that the electrode area will be scratched up by glass debris or that the side of the Pt wire will be exposed.

Again, there is no one way of sharpening a UME tip and many people end up developing a method that works best for their skill and applications.

Before collecting experimental data, it is always a good practice to repolish the electrode manually with 0.05 μm alumina and to record a steady-state voltammogram of the tip, which
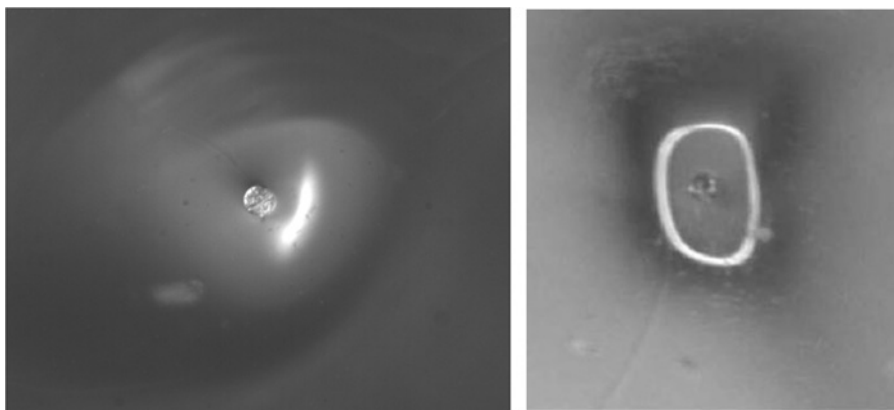
Figure 6.3.1.9   Left-hand side: 25 μm Pt tip with RG = 4; right-hand side: 25 μm Pt tip with RG = 3.

should look like that shown in Figure 6.3.1.8. It is important to note that when polishing with alumina particles greater than 0.05 μm or with grit paper, the RG value will increase. Thus, one needs to be constantly aware of the condition of the microelectrode that is being used.

REFERENCES

1. C. Amatore, in *Physical Electrochemistry: Principles, Methods and Applications*, I. Rubinstein, Ed., Marcel Dekker, Inc.: New York, 1995, p. 131.
2. R. M. Wightman, D. O. Wipf, *Electroanal. Chem.* **15**, 267 (1988).
3. F.-R. F. Fan, C. Demaille, in *Scanning Electrochemical Microscopy*, A. J. Bard, Ed., Marcel Dekker: New York, 2001, p. 75.
4. A. J. Bard, L. R. Faulkner, *Electrochemical Methods: Fundamentals and Applications*, 2nd ed., Wiley, 2001, pp. 569–571.

6.3.2   Platinum and gold inlaid disks ≤5 μm diameter

Biao Liu

Department of Chemistry and Biochemistry, The University of Texas at Austin, Austin, Texas 78712-0165, USA

6.3.2.1   *Fabrication with Wollaston wire*

The fabrication of disk-shaped Pt or Au microelectrodes of diameter less than 5 μm is similar to that described in Section 6.3.1 but employs a Wollaston wire (Goodfellow Metals, Cambridge, UK), i.e., a metal wire covered by a 50- to 100-μm silver coating (1, 2). The fabrication process is diagrammed in Figure 6.3.2.1. A 2-cm long Pt or Au Wollaston wire is inserted into one end of a 1-mm inner diameter glass capillary (Pyrex or soft glass) such

Metal wire

Silver coating

Glass

a   b   c
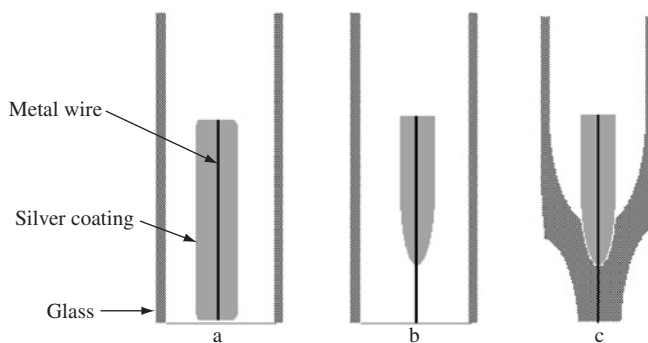
Figure 6.3.2.1   Schematic of Pt or Au UMEs with Wollaston wires. (a) Insert a 2-cm long Pt or Au Wollaston wire into one end of a glass capillary. (b) Remove the silver coating with 50% nitric acid. (3) Seal the wire into glass and polish it.

that one end of the metal wire is flush with the capillary opening. This end is then dipped into a 50% nitric acid solution to dissolve the silver coating. The quantity of nitric acid solution that fills the capillary by capillary action is controlled by judicial finger placement on the top end of the capillary so that about 3–5 mm of the metal wire is exposed. The nitric acid solution is then removed by placing the end of the capillary filled with nitric acid on a piece of filter paper or on a Kimwipe. The exposed wire must be thoroughly washed with distilled water to assure complete removal of the nitric acid. This typically requires approximately 20 separate flushings with water in the capillary by capillary action and subsequent removal via a Kimwipe. The glass capillary/wire assembly is then dried in an oven at 100 °C for 2 h. Extreme care must be taken during the dissolution of the silver coating and the washing procedure because the exposed wire is very fragile and easily broken.

The wire is secured in position by melting the glass tip of the capillary around the etched wire using a gas/oxygen flame, and then sealed into the glass using a heating coil by the same procedure as described in Section 6.3.1. It is essential that the junction between the bare and silver-coated section of the wire is sealed to prevent breakage of the wire during the use of the electrode. The electrical connection and polishing of the sealed wire are carried out by the same procedure as described in Section 6.3.1.

6.3.2.2   Fabrication with commercial pipette pullers

An alternative procedure for fabricating disk-shaped UMEs less than 5 μm diameter involves pulling metal wires into a glass capillary with the use of a commercial pipette puller (3–5) (see Section 6.3.3 for more detail). A 2-cm piece of wire with a diameter of 25 or 50 μm is inserted into a 10-cm long borosilicate or quartz capillary (1.2 mm outer diameter and 0.3 mm inner diameter) such that the wire is placed in the middle part of the capillary. It is important that microwire be classified as *annealed* and not hard be used. A laser-based pipette puller (P-2000, Sutter Instrument Co., Novato, CA) is used to pull the metal/glass assembly together. Usually two pulling programs are necessary. The first program is used to pull the glass capillary so that a firm connection between the glass and the platinum is formed. When the second program is run, the metal wire is pulled simultaneously with the glass leading to

a drastic decrease in its diameter and a simultaneous tight seal of the metal within the glass capillary. Both radii of the metal and surrounding glass can be controlled by changing the parameters of the pulling program, e.g., the temperature of heating and the strength of pulling.

Immediately after pulling, the platinum core may be covered with glass and must be exposed. In order to obtain disk-shaped UMEs, the pulled UME can be polished using a micropipette beveller (e.g., Sutter BV-10) equipped with a micromanipulator. The micromanipulator is used to move the pulled UME toward a slowly rotating abrasive disk covered with 0.05-μm alumina. The axis of the pulled UME is kept perpendicular to the plane of the abrasive rotating disk. The diameter of the exposed platinum wire increases with the length of polishing. Optical microscopy is used to check the polished UME and the polishing is stopped when a desired size is obtained. UMEs with diameter of 1–3 μm can be obtained using this procedure. Nanometer-sized electrodes can also be obtained if the polishing is carefully controlled (see Section 6.3.3).

Once fabricated, the UMEs can be characterized using SEM and steady-state voltammetry as described in Section 6.3.1. If the UMEs are used as SECM tips, the size and the shape of the tips can be evaluated using SECM (6) as described in Chapter 12.

REFERENCES

1. R. M. Wightman, D. O. Wipf, in *Electroanalytical Chemistry*, A. J. Bard, Ed., Marcel Dekker: New York, 1989, Vol. 15, p. 267.
2. A. J. Bard, F.-R. Fan, M. V. Mirkin, in *Electroanalytical Chemistry*, A. J. Bard, Ed., Marcel Dekker: New York, 1994, Vol. 18, p. 243.
3. B. D. Pendley, H. D. Abruna, *Anal. Chem.* **62**, 782 (1990).
4. Y. H. Shao, M. V. Mirkin, G. Fish, S. Kokotov, D. Palanker, A. Lewis, *Anal. Chem.* **69**, 1627 (1997).
5. B. B. Katemann, W. Schuhmann, *Electroanalysis* **14**, 22 (2001).
6. A. J. Bard, M. V. Mirkin, Eds., *Scanning Electrochemical Microscopy*, Marcel Dekker: New York, 2001.

6.3.3   Laser-pulled ultramicroelectrodes

Janine Mauzeroll[1] *and Robert J. LeSuer*[2]

[1]Laboratoire d'Electrochimie Moléculaire, Université Paris,
7-UMR CNRS 7591, France
[2]Department of Chemistry and Physics, Chicago State University,
Chicago, IL 60628

6.3.3.1   *Introduction*

This section discusses the fabrication of microelectrodes with diameters of a few micrometers to tens of nanometers using a laser-pulled technique. The methods discussed focus on the fabrication of platinum (Pt) ultramicroelectrodes (UMEs) sealed in

quartz, although the concepts can be readily applied to other glass/metal combinations. A general review of UME fabrication has been presented (1) and several publications have demonstrated the utility of laser-pulled tips (2, 3). This section provides a comprehensive description of laser-pulled UME fabrication, highlighting key steps and providing insight into trouble spots. The many parameters used in making laser-pulled UMEs add a significant amount of complexity but provide a comparable amount of flexibility in the final shape of the UME.

6.3.3.1 *Microelectrode fabrication*

(a) Equipment requirements (4)
The most important tool for fabricating pulled microelectrodes is a micropipette puller. A popular micropipette puller used for scanning electrochemical microscopy (SECM) microelectrodes is the Sutter Instrument (Novato, CA, http://www.sutter.com/) P-2000 CO_2 laser puller. A laser puller, which in 2004 cost approximately \$13k, has several advantages over resistance-based pulling systems. The most relevant of them to microelectrode fabrication are the ability to heat quartz and better control the heat distribution. Metal wire (Goodfellow) typically used is 25 μm in diameter though other diameters can be used. Platinum wire can be purchased in two different forms: hard or annealed. Annealed wire is generally softer and can be pulled at lower temperatures than hard Pt wire. However, hard Pt wire is easier to manipulate and is less likely to be damaged by mechanical stress. The parameters given below were designed for pulling annealed wire, but optimizations for hard wire configurations will be discussed as well.

Quartz capillaries (Sutter Instrument, Co.) with an outer diameter (OD) of 1 mm and inner diameter (ID) of 0.3 mm are preferred. Softer glass can be used, and must be used, if the microelectrode puller is based on resistance heating. The ID of the capillary will influence both the ability to position the wire properly and the thickness of the insulating glass sheath surrounding the metal surface of the UME. Sutter claims that their capillaries maintain a constant OD/ID ratio throughout the pull when making micropipettes. It is not clear how this translates to the construction of a UME as the wire is sealed into the glass capillary prior to pulling. Ideally, one would prefer a small OD/ID ratio as this means less insulating sheath will need to be removed during the polishing and beveling steps. However, for capillaries with the same OD, a thicker wall provides extra electrode stability as well as a smaller hole through which to align the axis of the microwire with that of the capillary.

Additional equipment includes a vacuum pump for evacuating the capillary prior to sealing along with vacuum tubing of appropriate size. After the electrode is pulled, contact can be made between the microwire and an electrode lead with either premixed silver epoxy, mercury, or a concentrated electrolyte solution. Additional larger capillaries as well as quick setting epoxy may be used to reinforce the microelectrode prior to exposing and polishing. To expose the UME wire with either sharpening or beveling, either commercial instruments (WPI or Sutter) or home built designs can be used. The basic necessities for polishing and beveling UMEs include: a method to rotate the electrode; a flat surface to apply polishing cloths of varying abrasiveness (600 or higher grit sandpaper, micropolishing cloths, 0.05 μm alumina slurries and diamond pastes, all of which can by supplied by

Buehler, Lake Bluff, IL); a method to manipulate the plane of the polishing surface; and a microscope or other method to facilitate viewing the UME tip. An optical microscope is a necessity for monitoring the various stages of pulled UME construction.

(b)   Capillary and wire preparation

All materials should be handled with gloves and kept free of dust and debris to eliminate sealing of contaminants into the glass along with the microwire. Capillaries can be cleaned with a dilute (10% v/v) nitric acid solution, rinsed with water, and allowed to dry thoroughly in an oven. Pt wire can be cleaned with either dilute nitric acid or organic solvents (acetone and hexanes) followed by a rinse with high purity (18 MΩ cm) water and a thorough drying. The next step is to straighten the microwire to be inserted into the center of the capillary. One to two centimeters of microwire should be carefully straightened by rubbing along the axis of the microwire. One should avoid twisting the microwire or introducing other mechanical stress that may result in breaks in the pulled microelectrode. Hard wire twists and bends less but requires more power in the pulling step to generate a useable UME. Using a stiff wire small enough to fit into the capillary, the Pt microwire is then positioned into the middle of the capillary so that, ideally, two symmetric microelectrodes can be produced from a pull.

(c)   Wire sealing

After positioning the microwire into the center of a capillary, it is placed into the puller and a vacuum is attached to each end of the capillary (Figure 6.3.3.1). A vacuum is applied to the capillary for up to 30 min to remove residual moisture and to minimize bubble formation in the glass during the sealing. The safety shield of the P-2000 is not designed to support the vacuum tubes that are connected to the end of the capillary to be pulled. However, it is possible to apply a vacuum to the capillary without interfering with the safety mechanisms of the pipette puller and it is strongly encouraged that the reader contacts the manufacturer before diverging from recommended instrument use. To insure that the instrument exerts no pulling force on the capillary during the sealing step, stoppers (which can be home built or purchased from Sutter) are placed on each of the pulling sleds (Figure 6.3.3.2a). When the capillary is sufficiently evacuated, a heating program is applied to seal several millimeters of the microwire into the quartz. Of the five variables available on the P-2000 laser puller, only the heating power (H) and filament (F) are important for the sealing step. Two sets of parameters have been used successfully by the authors. With a heating power set to 900, the filament size is set to 4; or heating power and filament can be set to 925 and 15, respectively. The difference between the two programs lies in the amount of wire that will be sealed in the glass. For filament 15, the laser scans slowly over 8 mm of the capillary. A filament of 4 scans the laser over 6.5 mm of the capillary more quickly. The amount of metal sealed into glass will influence the length of the taper formed during the pull. In both cases, the heating program was applied for 50 sec, followed by a 25-sec cooling time. A total of five heating/cooling cycles were performed to insure a proper seal (Figure 6.3.3.2b). Schuhmann (3) reports that much lower heating can be used successfully (H: 775; F: 5) with five cycles of 40 sec heating and 20 sec cooling. The sealing and pulling parameters are influenced by the wear and tear of individual instruments. Thus, when optimizing the sealing step, one should monitor the extent of a
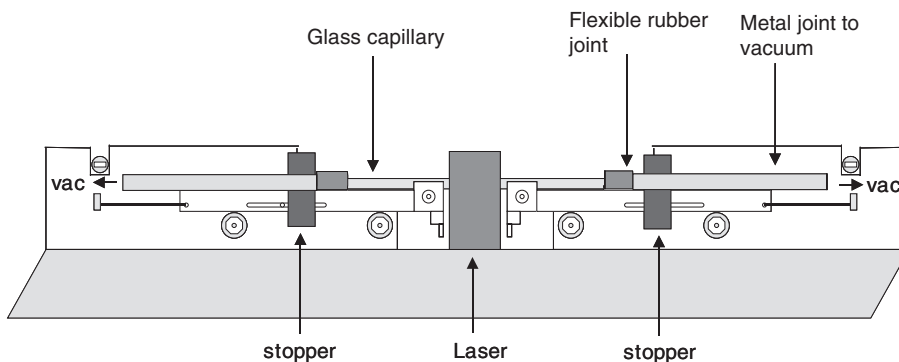
Figure 6.3.3.1   Diagram of the P-2000 laser-puller setup for the fabrication of Pt laser-pulled UME. The secured quartz capillary is connected via a rubber joint to a machine metal tube that is connected to a vacuum pump with a Y-joint. Two homemade stoppers are added to the sleds of the puller.
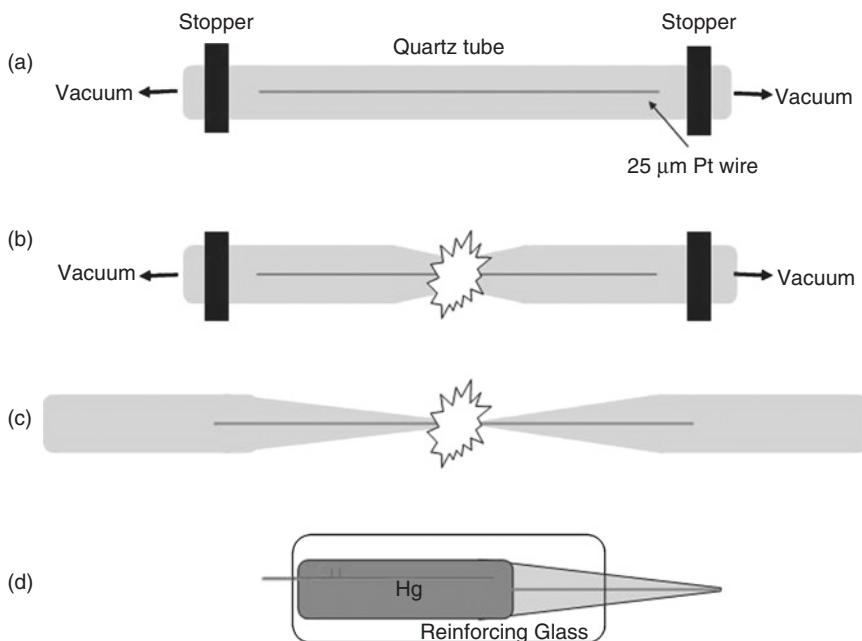
Figure 6.3.3.2   Diagram of the sealing and pulling protocol for the fabrication of Pt laser-pulled UME. (a) The straight Pt wire is inserted into the quartz capillary. The capillary is installed in the puller and connected to a vacuum. The sleds have been secured using stoppers. (b) The sealing program is run five times. (c) The pulling program is applied following the removal of vacuum and stoppers. (d) The pulled tips are electrically connected and strengthened with a larger diameter glass capillary.

seal after each cycle to minimize the amount of heating time required, because prolonged heating cycles could result in damage to the puller.

(d)   Wire pulling

The P-2000 uses five parameters to conduct a pull. The heating power, H, is the amount of heat applied to the capillary. Filament, F, can be 1 of 16 values that determines the length of capillary heated as well as the speed at which the laser is scanned (Table 6.3.3.1). For a given H, slower scan speeds and smaller scan lengths result in greater heating of the capillary. Velocity, V, determines the point at which the glass has reached the desired temperature based on changes in glass viscosity. Once the velocity is achieved, the laser is shut off. On the P-2000, the magnitude of this value is counterintuitive; a higher value for velocity means the laser will shut off when the glass reaches a lower temperature. Delay, D, is the time between the laser shutting off and the hard pull. A delay of 127 indicates that the hard pull will trigger when the laser is shut off. Values above 127 (to a maximum of 255) indicate the millisecond delay between shutting off the laser and the hard pull. Values lower than 127 allow the user to initiate the pull with the laser still on. Pull, P, is the force exerted on the capillary to create the UME. With the exception of the delay, all of the parameters have units that are not easily translated into physical quantities. Each parameter has an important effect on the shape of the microelectrode and these are summarized in Table 6.3.3.2.

Optimization of a pulling program requires patience, practice, and a bit of luck. The efficiency of UME fabrication using this technique is rarely more than 60% and when every step is taken into consideration, is typically much less. Under ideal conditions, one capillary should produce two identical microelectrodes. However, small imbalances in the pulling solenoids or imprecise calibration of the laser scanning results in less than ideal behavior.

Table 6.3.3.1

Filament number corresponding to the scan length and scan speed of the laser for the Sutter P-2000

Speed	Length (mm)				
	1.5	1.9	4.5	6.5	8
Fast	1	2	3	4	5
medium	6	7	8	9	10
slow	11	12	13	14	15

Table 6.3.3.2

Effect of pulling parameter on the shape of the pull

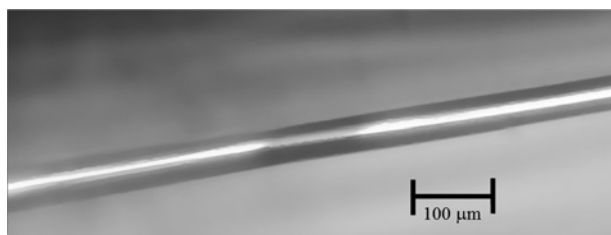| Parameter	Increase	Decrease
Heat	Smaller tip; longer taper	Larger tip; shorter taper
Velocity	Smaller tip	Larger tip
Pull	Smaller tip; longer taper	Longer tip; shorter taper

Figure 6.3.3.3   Optical micrographs of a break in the Pt wire, which occurred during the pulling step. Small cracks likely appear where the pulling force is exerted on a cooled portion of the electrode.

When attempting to optimize a pulling program, one should start with one of the programs listed here or a program suggested by the manufacturer that closely resembles the desired dimensions. Only one parameter should be adjusted at a time (for the P-2000, Sutter recommends changing values other than *F* in intervals of 5). The P-2000 reports the time required to pull the UME, and this value can be diagnostic of the success of the pull. To maximize the reproducibility of a parameter set, the values should be adjusted such that a pull takes between 4 and 6 sec to complete.

Two very similar procedures have been used by the authors with similar success. The first performs the pull within 25 sec of the final heating step, such that the quartz has not completely cooled prior to the pull. The laser is turned off, the vacuum tubes removed from the capillary and the stoppers removed from the pulling sleds followed by a pull using the parameters: *Heat*: 875; *Filament*: 2; *Velocity*: 130; *Delay*: 150; *Pull*: 200. This procedure results in electrode tapers of 3–5 mm and metal disk diameters from 200 nm to 4 μm. Alternatively, the sealed capillary can be cooled to room temperature prior to executing a pull using the parameters: *Heat*: 875; *Filament*: 2; *Velocity*: 50; *Delay*: 120; *Pull*: 200. This method results in electrodes with tapers of roughly 1 cm and electrodes as small as 3 nm diameter have been fabricated.

It is important to inspect a pulled UME to insure continuity of the Pt wire. Oftentimes, small cracks from 1 to 100 μm will occur. These cracks typically occur either where the glass begins to taper or at the very tip of the UME and are most likely due to a section of Pt wire being pulled when it has cooled too much. Cracks at each of these locations can be avoided by systematically optimizing the pulling parameters (Figure 6.3.3.3). When a crack is at the start of a taper, the glass surrounding that portion of wire likely absorbs much of the heat from the laser and the Pt microwire does not melt sufficiently. Either a smaller velocity or higher heat value can be used to supply more heating to the capillary at this stage of the pull. When the crack occurs at the tip of the UME, the wire has cooled too much toward the end of the pull, and the delay between the hard pull and the laser shut off trigger should be lowered. Note that by changing these values, the shape of the UME will change as well, so parameters should be changed only enough to eliminate the break in the Pt wire.

(e)   *Electrical connection and reinforcement*

Connection of an electrode lead to the unsealed Pt wire can be made with mercury, silver epoxy, or a concentrated electrolyte solution. Mercury is the easiest material for

making electrical contact but can easily be displaced and results in loss of contact. An electrolyte solution can be used for making electrical contact but problems related to a shift in electrode potentials and the possibility of solution evaporation over time can occur. Silver epoxy provides a solid contact with the least amount of capacitance. However, delivery of the epoxy into a small capillary is challenging. To deliver mercury into a 0.3-mm ID capillary, a long syringe was custom made from HPLC-like needles that could fit onto a typical disposable syringe (SGE Inc., Austin, TX). We have had the most success with Hg contacts and Schuhmann (3) reports good results with silver epoxy. To provide additional stability, the UME can then be sealed in a larger, reinforcing glass tube using 5-min epoxy. This step is sometimes avoided since it is critical that the axis of the UME be parallel to the reinforcement tube. However, rotation of the UME/reinforcement tube while the epoxy dries gives a satisfactory result. Figure 6.3.3.2 summarizes the four steps of UME fabrication using a laser puller.

(f)   Exposing the metal surface

The authors used a home built beveller to expose the Pt disk and sharpen the UME; however, commercial bevellers are available (WPI or Sutter). Generally, solid-surface bevellers use a high quality lapping film that is widely used in the fiber optics industry and can be easily replaced if the abrasive is damaged or saturated with glass particles. Other models rely on optically-flat mirrored glass disks, wetted with an abrasive slurry to bevel fluid-filled microelectrodes that are commonly used in microinjection applications. In the former case, the beveller spins at 4000 rpm to provide sufficient cutting force to produce a sharp, uniform tip in a very short time. The latter model spins at 60 rpm and is said to be preferred for pipettes that are 1 μm or less. Fluid-filled pipettes are hollow and much more delicate than pulled tips and so in designing our home-built system, we elected to work with high spin rates so that a minimum amount of time would be needed to expose and shape the tips. Only one touch to the polishing cloth is necessary to change the surface of the electrode and the least amount of manipulation is desirable.

The home-built beveller consisted of a rotating-disk electrode combined with a flat surface that could be translated up and down and tilted (Figure 6.3.3.4a). To expose the Pt surface, the UME is wrapped in Teflon tape, placed in a rotating-disk electrode setup (Pine Instrument, Co., Grove City, PA) and rotated at 5000 rpm. The desired polishing material is applied onto a flat surface, which is brought in contact with the rotating UME. Touching the tip of the UME to the abrasive surface can be observed as an oscillation of the long quartz end. This procedure is repeated until a reasonable CV response is obtained. The procedure is repeated with various polishing materials, typically starting with wet 1200 grit sandpaper and finishing with 0.05 μm alumina on a polishing cloth, until the CV response of the UME is ideal (Figure 6.6.3.4b).

Alternatively, the exposing step can be performed using hydrofluoric acid (2).Unlike polishing, HF etching will produce a conical or cylindrical UME. Although this may cause complications in the quantitative analysis of data, a protruding metal tip minimizes the difficulties of crashing the insulating sheath into a surface, and precise knowledge of zero tip/substrate distance can be obtained. Very small UMEs have been obtained by dipping a pulled tip in 49% HF solution for 3 sec three times (Figure 6.3.3.5). Concentrated HF solutions dissolve quartz very quickly, especially on UMEs with taper thicknesses less than
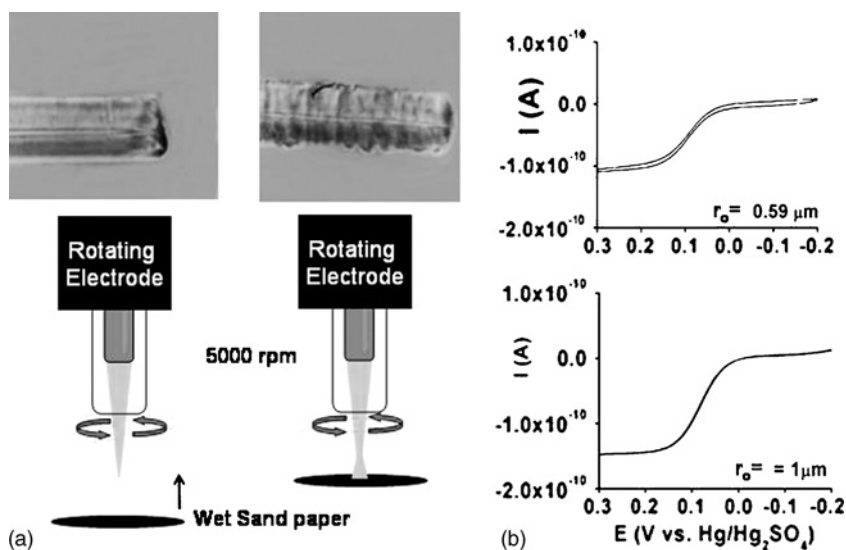
Figure 6.3.3.4 (a) Exposing the Pt surface using a homebuilt beveller. (b) Voltammetric response of exposed tips in 1 mM ferrocenemethanol/0.1 M KCl.

1 μm. Very little work has been done with HF etching of UMEs. However, as the SECM theory for conical tips has been developed (5), this method should be explored as a viable alternative to mechanical polishing.

(g) Sharpening and etching

The final step in making an UME for SECM techniques is also the most challenging. The goal is to remove enough of the insulating glass sheath from the tip of the electrode such that the diameter of the sheath is (ideally) less than 10 times the diameter of the metal disk. Like sharpening a pencil, quartz surrounding the exposed Pt disk can be removed by polishing the UME at an angle. A flat surface with fine grit (600+) sandpaper is tilted and brought into contact with the UME. Unlike exposing the metal surface, where a UME slightly off the rotation axis was advantageous, UME sharpening requires the tip to be on the rotation axis in order to avoid asymmetry in the sharpening and, worse, breaking of the UME. Quartz tapers are surprisingly flexible and can withstand a small amount of bending, thus allowing contact between the tip and the abrasive surface to be observed (Figure 6.3.3.6a). UMEs sharpened in this way result in insulating sheath diameters that are approximately 10–20 times larger than the disk diameter (Figure 6.3.3.6b).

6.3.3.2   Microelectrode characterization

(a)   Voltammetry

Voltammetric techniques are used in analyzing the qualities of a new UME as discussed in Section 6.3.1. Slow scan (<100 mV sec^{-1}) linear sweeps should result in a scan rate
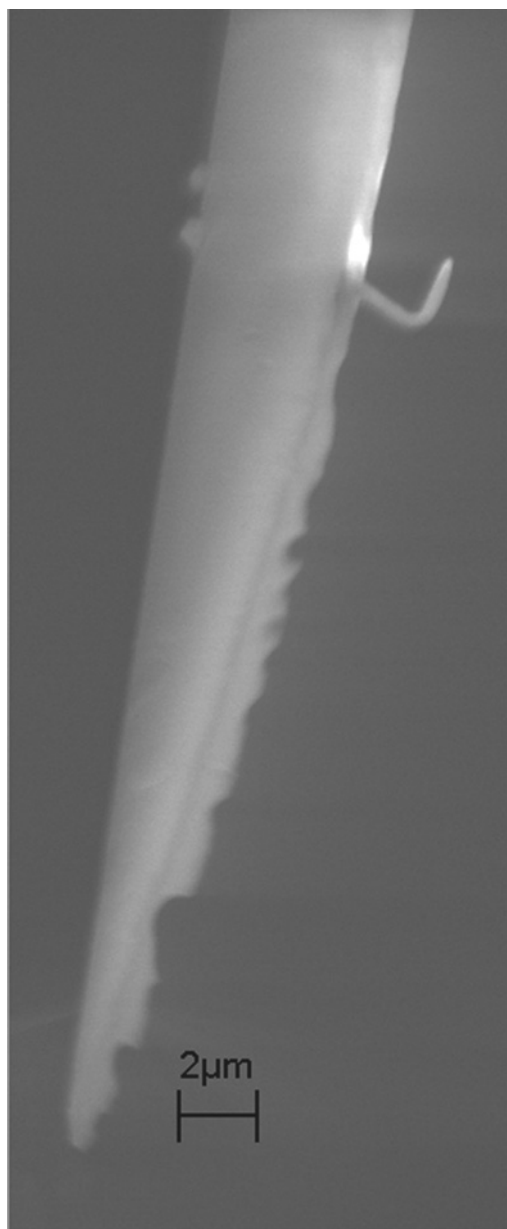
Figure 6.3.3.5 Scanning electrochemical micrograph (SEM) of an etched HF UME. Etching of a sealed Pt UME in concentrated HF for several seconds can provide electrodes with very small RGs. However, the etching process is not easily controlled and can yield nonideal results.
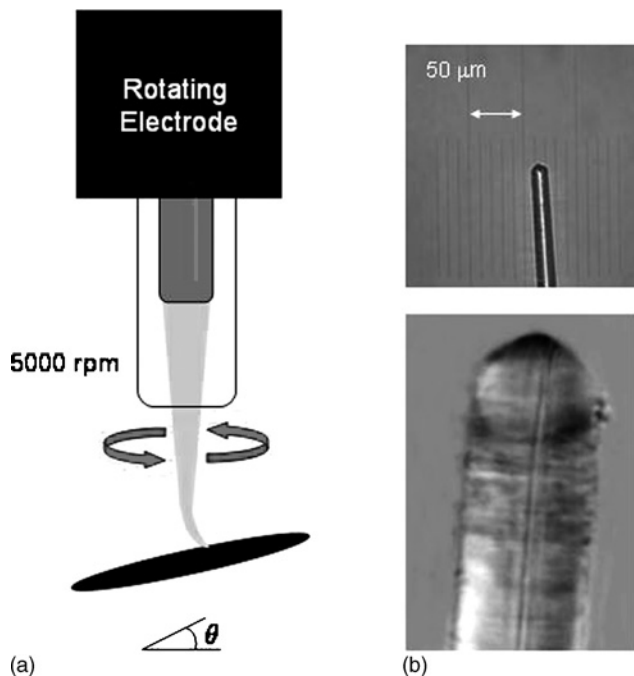
Figure 6.3.3.6   (a) Sharpening of the exposed Pt UME using the homebuilt beveller. (b) Optical micrographs of a sharpened UME.

independent sigmoidal curve with a current height equal to nFr_0DC^* where n is the number of electrons transferred, F is the Faraday constant, r_0 is the radius of the disk, D is the diffusion coefficient, and C^* is the concentration of the electroactive component in solution. Ideal voltammetric behavior consists of a steady-state plateau in the forward portion of the potential sweep and a reduced capacitive hysteresis on the return portion of the sweep. As seen in Figure 6.3.3.4b, pulled-laser UMEs behave like ideal UMEs in terms of retraceability, reduced capacitance, and stability of the steady-state current. In electrochemical studies where small analyte concentrations are of interest, these tips are well suited (6). These electrodes maintain a well-shaped sigmoidal behavior even at high scan rates and the lack of background current indicates that the electrodes are tightly sealed.

Measuring the resistance between a UME and an indium/gallium alloy is an alternative method of estimating the electrode surface area of a UME (2). This method has been incorporated into some commercial bevellers for monitoring exposure of the UME disk during polishing. However, this method has the disadvantage of contaminating the electrode with the alloy.

Neither voltammetry nor resistance methods can easily differentiate between planar and nonplanar geometries, and other techniques need to be used in order to fully characterize a UME. Two other techniques, SECM (see Chapter 12) and scanning electron microscopy (SEM), help to differentiate between an inlaid disk, recessed, and conical-shaped UMEs.
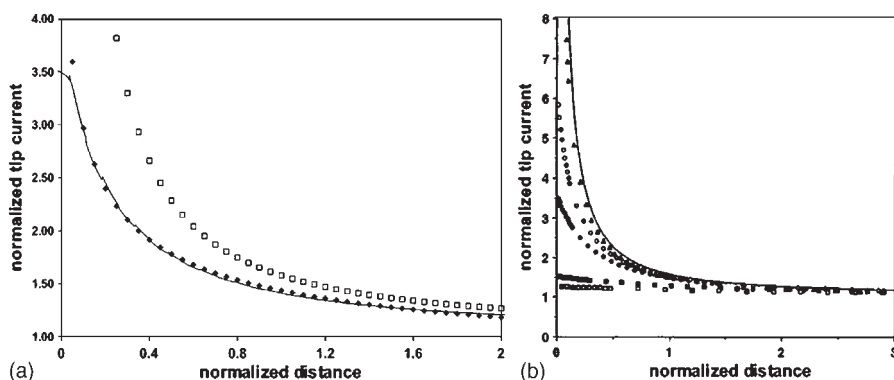
Figure 6.3.3.7 (A) Steady-state current–distance curves for mercury/Pt (25 µm diameter) hemispherical tip (line) as compared with theoretical behavior of a planar disk (□) and hemispherical (●). [Reproduced with permission from J. Mauzeroll, E. A. Hueske, A. J. Bard, *Anal. Chem.* **75**, 3880–3889 (2003). Copyright 2003, American Chemical Society.] (B) Steady-state current–distance curves for a "lagooned" tip over a planar conductive substrate corresponding to different values of the parameter *l/a* (where *l* is the depth of metal recession and *a* is the tip radius) and the analogous working curve for a disk-shaped tip. *l/a*: 10 (□), 5 (■), 1 (●), 0.5 (○), and 0.1 (△). The upper curve was computed for a disk-shaped tip from equation S11 of reference (2). [Reproduced with permission from Y. Shao, M. V. Mirkin, G. Fish, S. Kokotov, D. Palanker, A. Lewis, *Anal. Chem.* **69**, 1627 (1997). Copyright 1997, American Chemical Society.]

Feedback mode SECM experiments (Figure 6.3.3.7a) can distinguish between different UME geometries of conventional size (7–13). In the case of laser-pulled tips, present SECM theory can also distinguish between inlaid and noninlaid geometry (Figure 6.3.3.7b). The feedback current response for a recessed and a convex geometry (hemispherical, conical, and spherical) will both result in a lower normalized current response than that of the inlaid geometry (2). In positive feedback mode, the recessed geometry will yield a positive feedback response when slightly recessed and what appears to be kinetically controlled behavior when deeply recessed. It will also have a maximum current related to the contact of the glass opening with the metal surface and the sealing of the microcavity. The convex geometries will yield positive feedback and present a short circuit current when put in contact with the conductive substrate.

SEM can be used to "visually" inspect UMEs (Figure 6.3.3.8). Images allow one to determine the approximate diameter and geometry of a UME as well as to determine the electrode RG and observe if the disk is centered in the quartz. The biggest difficulty in obtaining suitable SEM images is that the large amount of insulating material surrounding a small, conductive disk sometimes results in a significant amount of distortion due to charging of the quartz sheath.

6.3.3.3   *Microelectrode maintenance and storage*

Maintenance of UMEs is a misnomer because the time it takes to "repair" a nonfunctioning electrode can be better spent fabricating a new UME. However, broken or fouled

Figure 6.3.3.8   Scanning electron micrographs of 50-nm radius conductive Pt disk somewhat displaced toward the edge of the 1-μm radius glass ring. [Reproduced with permission from Y. Shao, M. V. Mirkin, G. Fish, S. Kokotov, D. Palanker, A. Lewis, *Anal. Chem.* **69**, 1627 (1997). Copyright 1997, American Chemical Society.]

UMEs can be cut to larger diameters (2–5 μm) and used as conventional electrodes for many months. Electrodes can be stored dry, typically on a glass slide or taped to some other surface to protect the fragile tip, or they can be stored in distilled water to minimize contamination from air pollutants. Unlike larger (25 μm diameter) microelectrodes, polishing is not a suitable cleaning method unless an increase in the electrode area is acceptable. UMEs on the order of 1 μm diameter and larger can, in principle, be polished and sharpened by hand without increasing the electroactive area. Fouled UMEs can sometimes be cleaned electrochemically via cycling through the potential window of 0.5 M H_2SO_4 for 20 min (14). It is also possible to renew a UME by bathing it in the vapor of refluxing HNO_3 followed by electrochemical reduction of the PtO surface (15). One should note, however, that with very small UMEs, the formation of an oxide layer and its subsequent removal can result in the active surface becoming recessed.

6.3.3.4   Conclusions

This section has described the fabrication of sub 100 nm electrodes based on a laser-pulling technique. Because laser-pulled UMEs with an inlaid disk geometry require a mechanical sharpening step, micrometer to submicrometer dimensions might be the practical limit for electrodes fabricated with this technique. If an inlaid disk is not a requirement, the lower limit of electrode size can be extended to the 10 nm region by using HF-etching techniques to expose a conical surface.

The push towards nanometer sized electrodes brings with it challenges in some of the fundamental assumptions made in electrochemistry as discussed in reference (16).

REFERENCES

1. A. J. Bard, M. V. Mirkin, *Scanning Electrochemical Microscopy*, Marcel Dekker, Inc.: New York, 2001.
2. Y. Shao, M. V. Mirkin, G. Fish, S. Kokotov, D. Palanker, A. Lewis, *Anal. Chem.* **69**, 1627 (1997).
3. B. B. Katemann, W. Schuhmann, *Electroanalysis* **14**, 22 (2002).
4. The companies listed are those that have been used by the authors, but their inclusion in this chapter is neither an endorsement nor a statement that they are the only companies that provide such services.
5. C. G. Zoski, B. Liu, A. J. Bard, *Anal. Chem.* **76**, 3646 (2004).
6. J. Mauzeroll, A. J. Bard, Proc. Natl. Acad. Sci. USA **101**, 7862 (2004).
7. M. V. Mirkin, F. R. F. Fan, A. J. Bard, *J. Electroanal. Chem.* **328**, 47 (1992).
8. C. Demaille, M. Brust, M. Tionsky, A. J. Bard, *Anal. Chem.* **69**, 2323 (1997).
9. Q. Fulian, A. C. Fisher, G. Denuault, *J. Phys. Chem. B* **103**, 4387 (1999).
10. Q. Fulian, A. C. Fisher, G. Denuault, *J. Phys. Chem. B* **103**, 4393 (1999).
11. Y. Selzer, D. Mandler, *Anal. Chem.* **72**, 2383 (2000).
12. C. G. Zoski, M. V. Mirkin, *Anal. Chem.* **74**, 1986 (2002).
13. N. J. Gray, P. R. Unwin, *Analyst* **125**, 889 (2000).
14. B. Liu, A. J. Bard, M. V. Mirkin, S. E. Creager, *JACS* **126**, 1485 (2004).
15. R. N. Adams, *Electrochemistry at Solid Electrodes*, Marcel Dekker, Inc.: New York, 1969.
16. C. Amatore, in *Physical Electrochemistry: Principles, Methods and Applications*, I. Rubinstein, Ed., Marcel Dekker, Inc.: New York, 1995, p. 131.

6.3.4   Platinum conical ultramicroelectrodes

Biao Liu

Department of Chemistry and Biochemistry, The University of Texas at Austin, Austin, Texas 78712-0165, USA

6.3.4.1   Introduction

Conical-shaped ultramicroelectrodes (UMEs) are of special interest in connection with the imaging of surfaces, in kinetic studies, in probing thin films, and in probing minute environments, such as single cells. The most common fabrication procedure is by the etching of platinum wire or carbon fibers followed by coating with an insulating material except at the apex of the electrode. In this section, the fabrication of both blunt and sharp conical electrodes are discussed.

6.3.4.2   Blunt conical UMEs

Pt conical UMEs are constructed from 25 μm or 50 μm diameter Pt or Pt–Ir wires. A 2-cm length of Pt wire is connected to a conductive wire with silver epoxy (Epotek, H20E, Epoxy Technology, Inc., Billerica, MA). The ensemble is then enclosed in a glass capillary, which

a

b
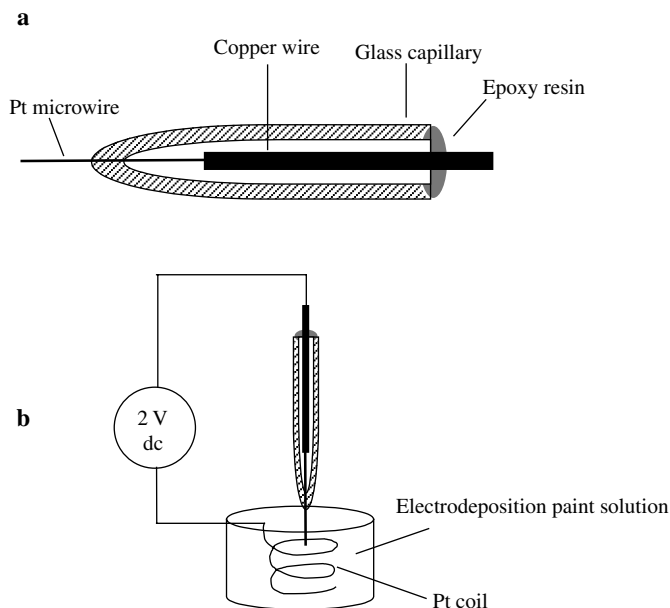
Figure 6.3.4.1 Schematic of the setup for the fabrication of Pt conical UMEs. (a) A Pt wire is sealed into glass capillary. (b) The etched wire is insulated with electrophoretic paint.

has first been drawn to a fine point using a pipette puller, such that ~5 mm of the microwire is protruding. The Pt wire is sealed in the glass capillary by melting the glass tip of the capillary around the wire using a heating coil or by heating over a gas/oxygen flame (Figure 6.3.4.1).

The Pt wire is then electrochemically etched in a solution containing saturated $CaCl_2$ (60% by volume), H_2O (36% by volume), and concentrated HCl (4% by volume) (1). Other etching solutions, such as concentrated $NaNO_2$ (2, 3), NaCN, or NaOH (4, 5) can also be used. About 2 mm of the wire is immersed in the solution. An alternating voltage of ~5 V rms is applied between the Pt wire and a large area carbon plate electrode using a Variac transformer. As the etching proceeds at the air/solution interface, bubbles form at the Pt/solution interface. The Variac transformer is switched off immediately upon cessation of bubbling as the top part of the electrode in air loses contact with the solution. The electrode shape at this point is not perfectly conical and has a longer sharp protrusion from the tip (i.e., the etched wire is very sharp). This is "trimmed" by turning the Variac transformer back on and very rapidly immersing the tip into the etching solution for very short (<1 sec) periods several times. Repeated "trimming" may be necessary to get a desired aspect ratio of the conical electrode. After "trimming", the wire is thoroughly rinsed with deionized water. The etched wire is then dipped for ~3 sec in a 3:1 $HCl:HNO_3$ solution to clean the Pt surface, washed with copious amounts of deionized water, and then dried in an oven at 110 °C for 2 h.

The etched conical Pt tips are then coated with an insulating material, except at the apex of the tip. A number of coating procedures have been reported in the literature,

including RF sputtering of insulating materials (6), dipping the tip in a varnish (7, 8) or molten paraffin (9), and translating the tip through a molten bead of glass (5, 10), poly(α-methylstyrene) (5), or apiezon wax (4, 11) held on a heated support. The etched Pt UMEs have also been coated by electrodepositing insulating layers onto the metal surface (2, 3, 12–15).

A commonly used anodic electrophoretic paint consists of poly(acrylic acid) (PAAH) with an excess of base added to make it water-soluble by deprotonation of the acidic groups thus forming the PAA$^-$ species. Prior to use, the anodic paint is diluted with water (1:15 by volume). The etched wire is immersed in the dilute aqueous paint solution and positioned in the center of a Pt coil (0.5 mm diameter), as shown in Figure 6.3.4.1b. A dc potential of ~2 V is applied between the etched wire and the Pt coil until the current reaches a steady state (after ~30 sec). The anodic current flow produces a local pH decrease at the electrode surface, induced by water oxidation, and generates water insoluble PAAH that deposits onto the etched metal surface. The insulated electrode is removed from solution and dried at 150 °C for 3 min. During heat curing, the insulating layer shrinks so that the sharp end of the tip is exposed, while the shaft of the tip is completely insulated. Usually, the entire coating procedure is repeated one or two times with more dilute anodic paint solution (1:20 by volume) to insure any pinholes formed in the first curing are sealed. The exposed end of the conical electrodes prepared using the approach described above is usually nanometer sized.

6.3.4.3   Sharp conical UMEs

Recently, an approach has been developed to prepare micrometer-sized conical Pt electrodes (16). In this method, the conical Pt microelectrodes are constructed from 25 μm diameter Pt wire. The Pt wire is electrochemically etched as described above. Working under an optical microscope, the etched Pt wire is inserted into one end of a pulled glass capillary with an inner diameter of ~20 μm such that the sharp end of the Pt tip is flush with the capillary opening, which is then melted around the Pt wire by using a gas/oxygen flame. The glass capillary is placed on the stage of an optical microscope, and the etched wire is inserted into the capillary until the sharp end of the wire is flush with the capillary opening. The inserting process is monitored under the optical microscope. The 20-μm diameter glass capillary is prepared by pulling a borosilicate glass tube (O.D. = 1.0 mm, I.D. = 0.58 mm) with a micropipette puller (Model P-2000, Sutter Instrument Co.). A one-line program can be used in the pulling with the parameters: Heat = 300, Filament = 4, Velocity = 35, Delay = 200, and Pull = 0.

Careful control of the flame temperature and heating time is critical to obtaining a well-sealed tip. Thus, the Pt tip/capillary assembly is held in the cone part of the flame near the nozzle outlet for ~2 sec. The melted glass retracts from the tip on cooling, giving conical Pt electrodes with the base radius of the cone of $\approx$ 5–10 μm and the cone height of $\approx$ 10–20 μm, as shown in Figure 6.3.4.2.

Once fabricated, the conical electrodes can be characterized by scanning electron microscopy (SEM), transmission electron microscopy (TEM), steady-state voltammetry (SSV), and scanning electrochemical microscopy (SECM) (see Chapter 12).

The conical UMEs are first characterized by steady-state voltammetry to get an estimate of the radius from the limiting current. When using steady-state voltammetry in this way,

25 μm
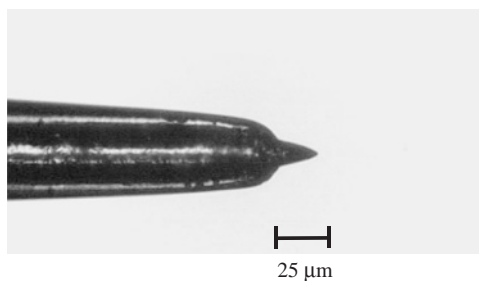
Figure 6.3.4.2   The optical image of a micrometer-sized conical Pt electrode. (The photo was provided by the Electrochemistry Laboratory of the Department of Chemistry and Biochemistry, University of Austin at Texas.)
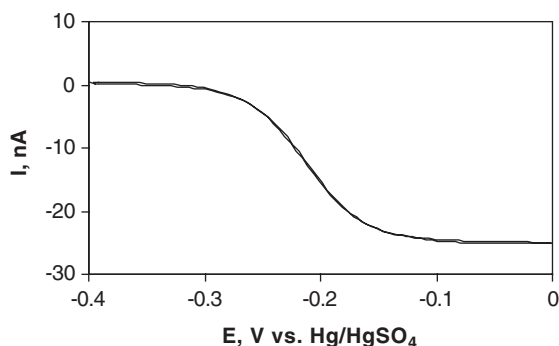
Figure 6.3.4.3   Steady-state voltammogram of a conical Pt tip in an aqueous solution contained 1 mM ferrocenemethanol and 0.1 M KCl. The potential scan rate was 20 mV sec^{-1}.

well-characterized systems having rapid heterogeneous electron transfer are used. Commonly used aqueous systems include the oxidation of ferrocenemethanol and the reduction of ruthenium hexamine. Figure 6.3.4.3 shows a typical CV obtained at a conical Pt. In steady-state voltammetry at UMEs, the current–potential curve is sigmoidal in shape. The voltammetric response for a well-insulated UME shows little hysteresis on the return scan. Large hysteresis on the return scan is an indication that the sweep rate is too fast, or that there is a poor seal between the insulator and metal wire. The apparent electrochemical radius of the electrode is calculated from the diffusion-limited plateau current, i_{lim}, assuming a hemispherical or disk geometry.

$$i_{\text{lim}} = 2\pi nFDC^* r_{\text{o}} \qquad \text{(hemisphere)} \qquad (6.3.4.1)$$

$$i_{\text{lim}} = 4nFDC^* r_{\text{o}} \qquad \text{(disk)} \qquad (6.3.4.2)$$

where n is the number of electrons, F is Faraday's constant, D is the diffusion coefficient, C^* is the bulk concentration of electroactive species, and r_{o} is the radius of a hemisphere or a disk. Using these equations, the electrode radius for a specific UME geometry can be determined and compared with values obtained from electron microscopy images.
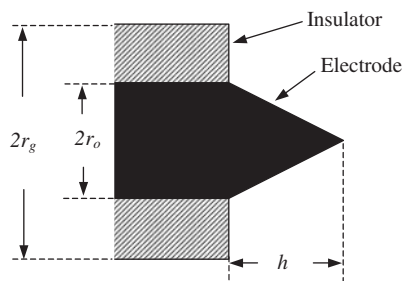
Figure 6.3.4.4   The schematic of a finite conical electrode.
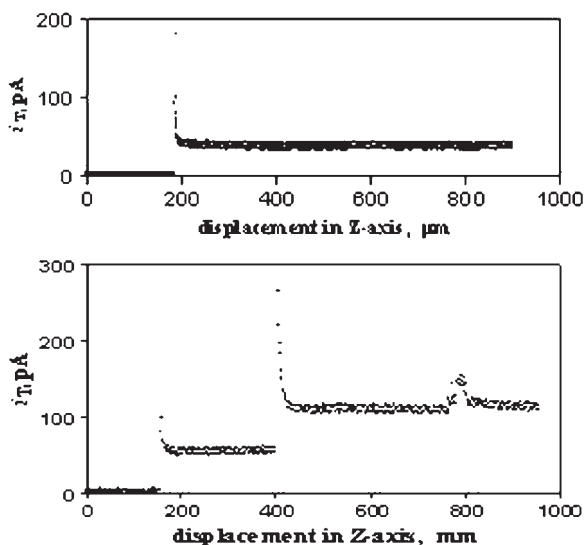
Figure 6.3.4.5   The electrochemical approach curves of a Pt UME insulated with electrophoretic paint to an air/solution interface. (a) Electrode insulation is good. (b) Electrode insulation is poor. The solution contained 10 mM $K_3Fe(CN)_6$ and 0.1 M KCl. The tip potential was 0.1 V vs. Ag/AgCl. (The data was from the Electrochemistry Laboratory of the Department of Chemistry and Biochemistry, University of Austin at Texas.)

SEM and TEM have also been used for the characterization of conical UMEs. From SEM or TEM images, one can obtain an estimate of the radius of the electrode as well as the radius of the insulating material (2, 17). The side-view images can also provide information regarding whether the metal or fiber is in the plane of, recessed within, or protruding from the insulating material.

SECM has proven to be a valuable tool for the characterization of conical UMEs to obtain the geometrical parameters of a UME, including the insulating sheath (11, 16, 18, 19). Electrode characterization with SECM is based on approach curve measurements of a UME tip current, i_T, as a function of the tip–substrate separation, d, over either a

conducting or insulating substrate (refer to Chapter 12 for the theory and application of SECM). The SECM approach curves depend on the ratio of the base radius of the cone (r_o) to the height of the cone (h) and on the thickness of the insulating sheath (RG = r_g/r_o, where r_g is the radius of the insulating sheath, Figure 6.3.4.4). The shape parameters of a conical electrode, including r_o, h, and RG can be obtained by fitting experimental SECM approach curves to theoretical ones (16).

SECM can also be used to gain information about the quality of the insulation on the conical tips. An approach curve is obtained at the air/solution interface, where the solution contains a redox mediator such as $Fe(CN)_6^{3-}$. The potential sufficient to reduce $Fe(CN)_6^{3-}$ is applied to the tip and the tip current is monitored as the tip is moved from air into the aqueous ferricyanide solution. Figure 6.3.4.5a shows the air/solution approach curve for a finite conical tip insulated with anodic paint. No current flows until the tip first enters the solution, where the current then rises sharply in an UME transient, which decays to a constant steady-state current value. This constant value is maintained as more of the tip is immersed in solution. Figure 6.3.4.5a indicates that the tip is completely insulated with only the very end of the tip uncovered. In contrast, a poorly insulated tip showed leaks along the sides as more of the tip is immersed into the solution (Figure 6.3.4.5b). The tip current increases stepwise as more of the tip enters the solution. This behavior is an indication of pinholes in the insulating film.

REFERENCES

1. F. R. F. Fan, C. Demaille, in *Scanning Electrochemical Microscopy*, A. J. Bard, M. V. Mirkin, Eds., Marcel Dekker: New York, 2001, pp. 75–110.
2. C. J. Slevin, N. J. Gray, J. V. Macpherson, M. A. Webb, P. R. Unwin, *Electrochem. Commun.* **1**, 282 (1999).
3. J. L. Conyers, H. S. White, *Anal. Chem.* **72**, 4441 (2000).
4. L. A. Nagahara, T. Thundat, S. M. Lindsay, *Rev. Sci. Instrum.* **60**, 3128 (1989).
5. R. M. Penner, M. J. Heben, N. S. Lewis, *Anal. Chem.* **61**, 1630 (1989).
6. T. Abe, K. Itaya, I. Uchida, *Chem. Lett.* 399 (1988).
7. A. A. Gewirth, D. H. Craston, A. J. Bard, *J. Electroanal. Chem.* **261**, 477 (1989).
8. C. M. Vitus, S. C. Chang, M. J. Weaver, *J. Phys. Chem.* **95**, 7559 (1991).
9. B. Zhang, E. Wang, *Electrochim. Acta* **39**, 103 (1994).
10. R. M. Penner, M. J. Heben, T. L. Longin, N. S. Lewis, *Science* **250**, 1118 (1990).
11. M. V. Mirkin, F.-R. F. Fan, A. J. Bard, *J. Electroanal. Chem.* **328**, 47 (1992).
12. C. E. Bach, R. J. Nichols, H. Meyer, J. O. Besenhard, *Surf. Coatings Technol.* **67**, 139 (1994).
13. B. W. Mao, J. H. Ye, X. D. Zhuo, J. Q. Mu, Z. D. Fen, Z. W. Tian, *Ultramicroscopy* **42–44**, 464 (1992).
14. K. Potje-Kamloth, J. Janata, M. Josowicz, *Ber. Bunsenges. Phys. Chem.* **93**, 1480 (1993).
15. T. G. Strein, A. G. Ewing, *Anal. Chem.* **64**, 1368 (1992).
16. C. G. Zoski, B. Liu, A. J. Bard, *Anal. Chem.* **76**, 3646 (2004).
17. J. J. Watkins, J. Chen, H. S. White, H. D. Abruna, E. Maisonhaute, C. Amatore, *Anal. Chem.* **75**, 3962 (2003).
18. Y. H. Shao, M. V. Mirkin, G. Fish, S. Kokotov, D. Palanker, A. Lewis, *Anal. Chem.* **69**, 1627 (1997).
19. J. V. Macpherson, P. R. Unwin, *Anal. Chem.* **72**, 276 (2000).

6.3.5   Flame-etched carbon nanofibers

Ran Tel-Vered

Department of Chemistry and Biochemistry, The University of Texas at Austin, Austin, Texas 78712-0165, USA

6.3.5.1   Introduction

Of the more prominent advantages in the preparation of flame-etched carbon fiber electrodes are that they can be easily obtained at minimal cost and with short fabrication times (1, 2). Moreover, their preparation involves only benign materials, avoiding the need for corrosive substances and high voltages that are often used in wet-etching techniques. Following flame etching and electrophoretic insulation, the radius of curvature of the carbon fiber at the apex ranges between several tens to less than 200 nm, primarily depending on variations in the etching time, flame temperature, and the exact position of the tip in the flame.

6.3.5.2   Probe preparation

Borosilicate tubes (Sutter Instrument Co., Novato, CA) of 1.0 mm outer diameter and 0.58 mm inner diameter are immersed in 0.5 M HNO_3 for 15 min and sonicated for 10 min in deionized water. The tubes are then pulled using a laser pipet puller (Model P-2000, Sutter Instrument Co.), employing the following pulling parameters: heat = 385, filament = 4, velocity = 30, delay = 150, and pull = 0. This yields micropipet tips with inner diameters of approximately 20 μm and tapers that are approximately 0.5 cm in length. Approximately 1 cm of a 10-μm diameter carbon fiber (Strem Chemicals, Newburyport, MA) is attached to one end of a straight Ni–Cr wire using a small amount of silver epoxy and cured in an oven for 45 min at 100 °C. The wire/fiber assembly is then manually inserted into the top of the micropipet and pushed through so that approximately 3 mm of the fiber protrudes from the micropipet tip. At that point, epoxy cement is applied for sealing the other side of the capillary to form a stable connection between the Ni–Cr wire and the glass. The capillary is then sealed around the carbon fiber using a cool low oxygen natural gas flame by inserting the pipet tip into the flame for approximately 0.5 sec. To ensure hermetic seals, the tips are immersed in DI water and then examined with an optical microscope. At this stage, tips that show a slight intake of water are resealed in the flame whereas electrodes that show slight bending caused by the flame treatment are discarded. The part of the carbon fiber that protrudes from the glass pipet is then flame etched in an oxygen-rich (bright blue color) natural gas flame to a length of 50 μm or less (Figure 6.3.5.1). During this step, it is very important to etch the carbon alone, without melting the glass seal. This is done by a very slow manual approach of the fiber to the vicinity of the outer region at the base of the flame (Figure 6.3.5.2) and periodic observation by optical microscopy to monitor the progress of etching. An orange glow from the carbon fiber indicates that etching is proceeding. Insulation of the etched carbon fiber is carried out by
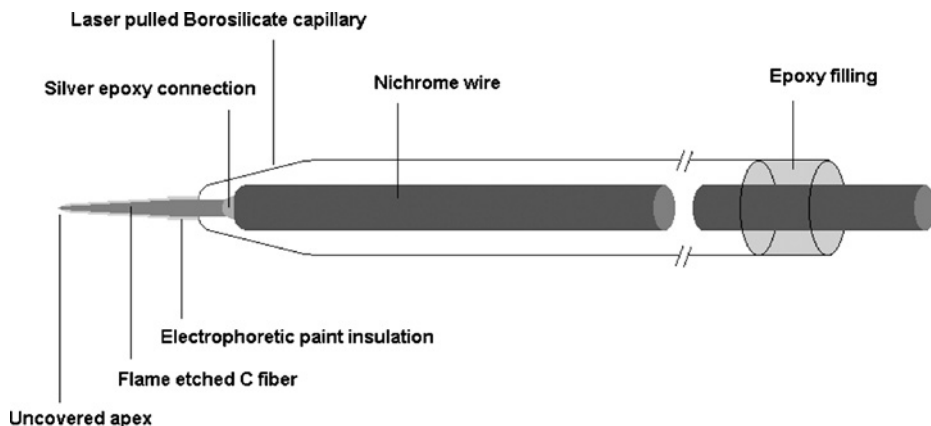
Figure 6.3.5.1   Schematic drawing of a flame-etched carbon nanofiber electrode.
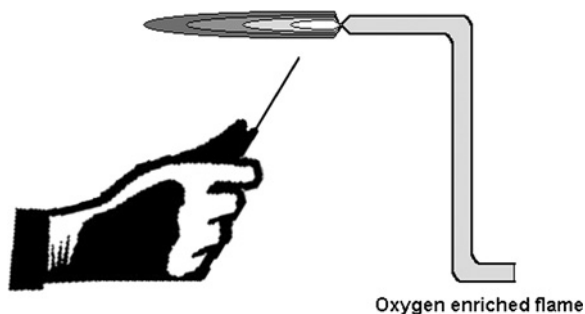
Figure 6.3.5.2   Slow, manual approach of the fiber to the outer region at the base of the flame.

using anodic electrophoretic paint (Glassophor ZQ 84-3225 from BASF, Münster, Germany). The etched fiber is immersed into a 1:20 solution of the paint in water and a Pt coil surrounding the tip serves as the reference/auxiliary electrode. A dc potential of 2.2 V is applied to the carbon electrode for 40 sec, typically showing a gradual decrease in the oxidation current from several tens of nanoamperes to a steady value of 0.2–1.0 nA, depending on the length of the etched fiber. The electrode assembly is then washed with DI water and heated at 150 °C for 3 min, allowing the deposited paint polymer film to fuse and shrink while exposing the tip apex (3). The entire deposition and heating process is repeated once more to ensure good insulation of the fiber. A typical oxidation current during the second deposition is in the range of tens of picoamperes.

6.3.5.3   Tip characterization

To probe for pinholes in the electrophoretic paint insulation, the carbon nanofiber electrodes are tested with a scanning electrochemical microscope (SECM, see Chapter 12)
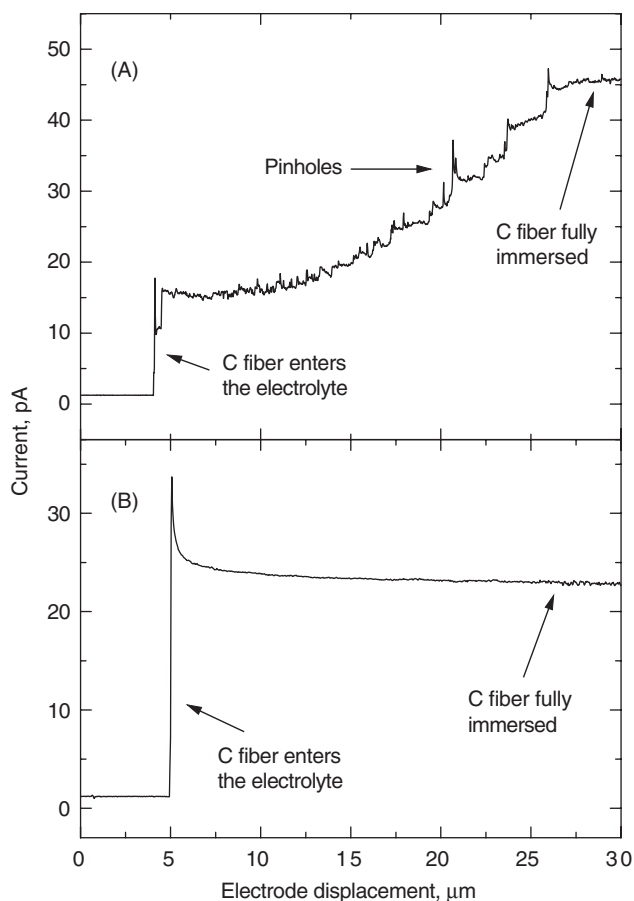
Figure 6.3.5.3   Approach from air into liquid for a flame-etched carbon nanofiber with (A) and without (B) pinholes. The electrolyte is 1 mM ferrocenemethanol (FcOH) in 0.1 M KCl. Tips are held at 0.35 V vs. Ag/AgCl. Approach rate: 200 nm sec^{-1}.

amperometric technique known as approach into liquid (4). Figure 6.3.5.3 presents an example for both properly (A) and poorly (B) insulated tips. The carbon tip is positioned in air approximately 500 μm above the surface of a 1-mM ferrocenemethanol (FcOH) in 0.1 M KCl solution and polarized to 0.35 V vs. Ag/AgCl where a steady-state FcOH oxidation current is expected to occur when exposed parts of carbon are in contact with the electrolyte solution. In the next stage, the tip is slowly (200 nm sec^{-1}) lowered toward the solution, until an initial touch between the exposed carbon apex and the electrolyte is achieved as indicated by a combined faradaic/charging current jump. The tip is further scanned down until no increase in the measured current can be detected, corresponding to a full immersion inside the solution. As the tip is held above the mediator's oxidation potential, any current spikes along the scanned path can be attributed to pinholes in the
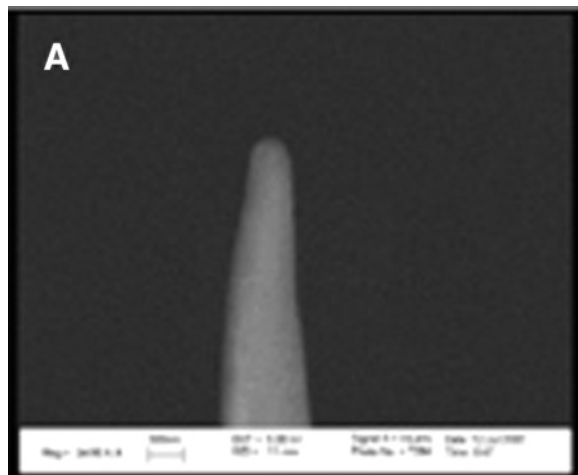
Figure 6.3.5.4   SEM image of a carbon nanofiber after insulation with electrophoretic paint. Beam energy is 5.00 kV and the focal distance is 11 mm.

electrophoretic paint layer. It is important to note that although the occurrence of pinholes decreases sharply by flame etching the carbon fiber to only a few micrometers in length; and that in most cases, no holes are detected even at very slow scans, tiny pinholes can still be undetectable due to the small currents associated with their size.

Scanning electron microscopy (SEM) is effective in characterizing the geometry, radius, and shape of the flame-etched carbon nanofiber. Figure 6.3.5.4 shows a hemispherical tip apex supporting a radius of curvature of nearly 150 nm. In practice, smaller tips down to $r = 50$ nm can be fabricated depending on variations in the etching time, flame temperature, and the exact position of the tip in the flame. For a properly insulated tip (such as the one in Figure 6.3.5.3A), a comparison between the visible radius (r_{vis}) measured by SEM and the steady state electrochemically evaluated radius (r_{ec}) measured by cyclic voltammetry at a slow scan rate in the presence of a nerenstian redox mediator, shows a good correlation with the equation for a hemisphere with an error of less than 10%, and hence:

$$r_{vis} \sim r_{ec} = i_{ss} / 2\pi n F D_o C_o^*$$ (6.3.5.1)

where D_o is the diffusion coefficient of the mediator species, C_o^* is the mediator bulk concentration, and i_{ss} is the steady-state diffusion limiting current.

The good agreement between the radii measured by the different methods indicates that for properly insulated fibers, most of the electroactive area is concentrated at the very end of the apex and that the contribution of undetected pinholes to total faradaic current is negligible. Furthermore, the correlation between the radii is useful in evaluating the aspect ratio (H) at the nanofiber apex. A closer look at Figure 6.3.5.4 shows a radius of curvature that is nearly 150 nm. As the tip starts to broaden right from its apex, this geometry corresponds to an aspect ratio of approximately $H = 0.5$ or less. Such carbon nanofiber tips are especially useful for electrochemically probing surfaces, as they possess a conical

geometry that facilitates closer approach to the substrate and maintain high sensitivity to redox feedback currents in accordance with the small H value.

REFERENCES

1. T. G. Strein, A. G. Ewing, *Anal. Chem.* **64**, 1368 (1992).
2. W. H. Huang, D. W. Pang, H. Tong, Z. L. Wang, J. K. Cheng, *Anal. Chem.* **73**, 1048 (2001).
3. C. J. Slevin, N. J. Gray, J. V. Macpherson, M. A. Webb, P. R. Unwin, *Electrochem. Commun.* **1**, 282 (1999).
4. Y. Lee, A. J. Bard, *Anal. Chem.* **74**, 3626 (2002).

6.3.6   Electrochemically etched carbon fiber electrodes

Anthony Kucernak

Department of Chemistry, University of Tennessee, Knoxville,
TN 37996, USA

6.3.6.1   Introduction

Etched insulated carbon fiber electrodes can be prepared from a suitable source of graphitized carbon fibers (e.g., PANEX®33 CF, 95% Carbon, Zoltek Corporation, MO, USA), copper wire, colloidal graphite (e.g., type G303 from Agar Scientific Ltd., UK), and a cathodic electrophoretic paint (e.g., Clearclad HSR, from LVH Coating Ltd., UK). Etching of the electrodes requires a variable voltage AC source (50 Hz, 1–10 V_{ac}), an AC current meter capable of measuring in the μA range and a suitable linear translation stage. Insulation of the electrode requires a DC power supply (0–20 V), linear translation stage, microscope, and oven. Testing of electrodes requires a high-gain low-noise potentiostat.

The processes involved in the production of these electrodes involve mounting the carbon fibers, etching them to produce a sharp tip, and subsequent insulation of the tip so that only the very end of the tip is exposed (1, 2). Testing of the electrode is then performed to determine whether there are any pinholes in the insulation.

6.3.6.2   Preparation and etching of electrodes

Individual single fibers of about 5–6 mm in length are attached to one end of a 1-mm diameter copper wire with a drop of colloidal graphite. The mounted fiber can then be left to cure in air at room temperature for several hours. Prior to etching of the fiber, it is successively rinsed with ethanol and water. A linear translation stage is prepared with a screw connector so that the mounted carbon fiber can be affixed to the stage via the copper wire. The screw connector also provides electrical contact to the power supply. The configuration is displayed in Figure 6.3.6.1. The mounted fiber is then gently translated into the etching solution (0.01 M NaOH) with about $0.5-1$ mm of the fiber immersed. A 50-Hz
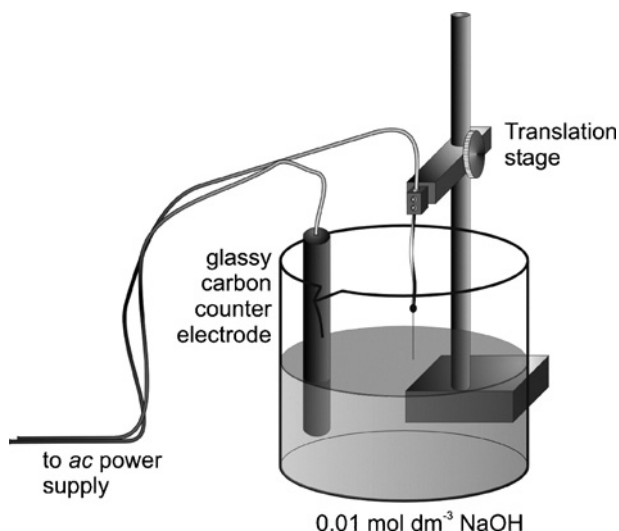
Figure 6.3.6.1   Schematic diagram of the experimental configuration used to etch the mounted carbon fiber electrodes.

AC voltage is then applied between the mounted fiber and a glassy carbon rod auxiliary electrode for a defined period.

The magnitude of the applied AC voltage and its duration has a critical effect on the shape of the resultant tip, as does the source of carbon fiber. In order to produce good electrodes, the cone-angle of the tip should be around 30° – if the angle is much smaller, then the tip will be overly fragile and liable to break during handling. If the cone angle is much larger, then it becomes difficult during the insulation process to prevent the end of the electrode from being coated. In general, three different etching regimes can be characterized as shown in Figure 6.3.6.2.

When the applied potential is too high (Figure 6.3.6.2(a), $V_{applied} = 8$ V_{ac}), etching of the carbon proceeds at a very fast rate ($i \sim 70$ μA) accompanied by significant amounts of gas evolution. The measured current quickly decays away and the resulting electrode shows a severely pitted and etched end without any tapering of the fiber. If the applied potential is reduced (Figure 6.3.6.2(b), $V_{applied} = 5$ V_{ac}), the measured AC current is significantly reduced ($i \sim 5$–15 μA) and the etching proceeds predominantly at the electrolyte/air interface, leading initially to a fiber with a "neck" in it. Etching of the immersed portion of the fiber appears to be quite slow. If etching is allowed to continue, eventually the neck becomes so narrow that the immersed section of the fiber drops off, and the current becomes very small. At still lower applied potentials (Figure 6.3.6.2(c), $V_{applied} = 3$ V_{ac}), etching occurs much more slowly ($i \sim 2$–6 μA), but homogeneously distributed along the entire length of the fiber, leading initially to a significantly thinned carbon electrode. These thin carbon electrodes are quite fragile, and easily destroyed. Continued etching leads to eventual total dissolution of the carbon except for a sharp tip formed at the electrolyte/air interface. Tips produced at either of the lower potentials typically have radius of curvatures <50 nm and are suitable for the subsequent steps.
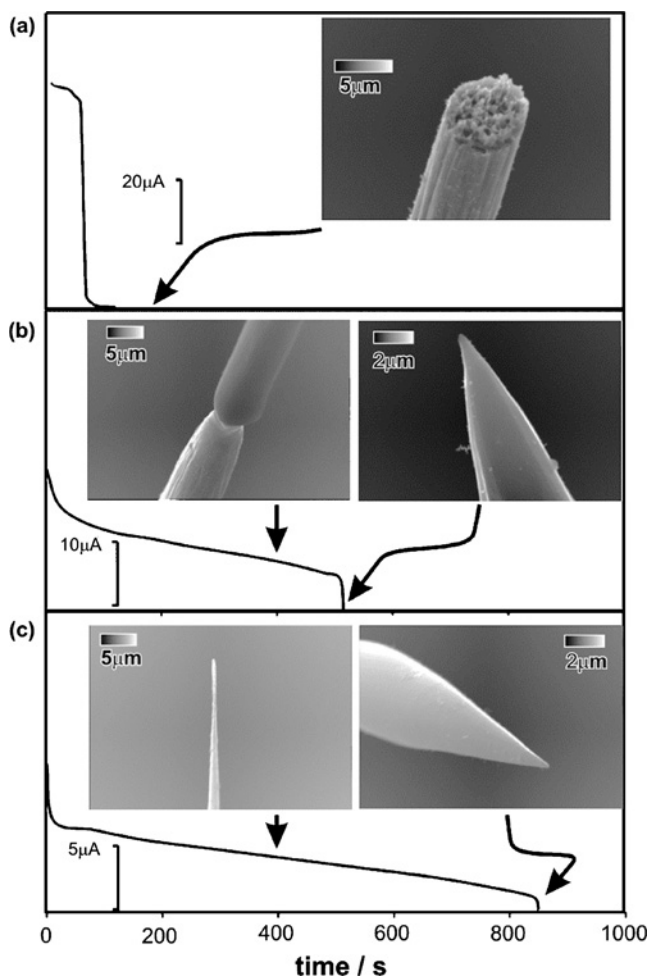
Figure 6.3.6.2 Variation of AC current with time and SEM images of the different tip morphologies obtained at different times during the etching of Zoltek PANEX®33 CF carbon fibers in 0.01 M NaOH as a function of applied AC voltage. (a) 8 V_{ac}; (b) 5 V_{ac}; (c) 3 V_{ac}.

After etching, the fibers are rinsed with water to remove any residual alkaline solution and left to dry prior to the insulation step.

6.3.6.3 Insulation of etched carbon fiber electrodes

The insulation process involves two separate stages: electrophoretic deposition of paint onto the tip surface followed by a curing step at high temperatures during which the paint particles fuse together. As some shrinkage of the deposited film will occur accompanying the heating process, the insulating film tends to retract slightly from the tip apex, allowing the surface of the tip apex to be exposed in a natural and spontaneous way without the need

for any manual intervention. This is a major advantage of the electrophoretic deposition process in making nanometer-sized electrodes compared with other insulating techniques. However, the shrinkage process also brings about some complexities. To be able to expose the tip end during the heating stage, a thin paint layer must be deposited. Otherwise, a fully insulated electrode would be produced even after the subsequent heating stage. In contrast, if the coating layer is too thin, pinholes tend to be left in the film, probably caused by rough protrusions on the surface of the fiber. These additional pinholes will provide an additional faradaic current contribution, bringing about uncertainties in the voltammetric response.

Cathodic electrophoretic paint is the preferred polymeric material used to insulate the carbon fibers as the negative potentials required for deposition avoid any possibility of further oxidative dissolution of the carbon fiber. The usual approach for electrophoretic deposition is to suspend the article being coated in an appropriate suspension of polymer particles and polarising the item versus a secondary electrode.

A modification of this process allows the formation of a tapering deposit of polymer particles so that after the curing process, the shaft of the carbon electrode is coated by a relatively thick layer of polymer, whereas closer to the tip, the polymer layer becomes thinner. The modification of the process involves immersing the carbon electrode in the electrophoretic solution and translating the entire electrode so that the tip of the electrode almost breaks the surface. As shown in Figure 6.3.6.3(a), the tip apex remains in contact with the solution by a very thin liquid meniscus. Such an arrangement will lead to virtually no deposition on the very end of the tip, and an increase in deposition density moving away from the tip. Figure 6.3.6.3(b) shows an overhead photomicrograph taken with side illumination. Light reflects off the meniscus, and produces a small bright patch where the meniscus exists.

A deposition voltage of 5–7 V employed for 60–90 sec is used during the first deposition. Subsequent deposition steps employ the same potential and a deposition time of 20–40 sec. A glassy carbon auxiliary electrode was used, and again, no effect of auxiliary electrode position was obvious. After deposition, spray rinsing is used to remove any loose solution from the fiber. The copper-fiber assembly is then heated at ~195 °C for about 30 min to let the deposited film cure. This heat cure process hardens the film and fuses the resin particles together forming an insulating film. Repeated deposition and cure steps are performed to obtained electrodes with smaller effective radii. Typically two deposition/curing cycles are performed to produce relatively large electrodes, and up to five cycles are performed to produce carbon electrodes with the smallest active surface area.

The final step is to seal the copper-fiber assembly into a glass tube with epoxy resin. Only the insulated carbon fiber should be allowed to protrude from the epoxy sealed glass tube. Electrodes may be re-used and have lifespans of a few weeks.

6.3.6.4   *Testing of insulated carbon fiber electrodes*

Assuming that the exposed portion of the electrodes fabricated above possess a hemispherical shape, then the diffusion-limited current is expected to follow (3):

$$i_d = 2\pi nFDC^* r_{eff} \tag{6.3.6.1}$$

where D and C* are respectively the diffusion coefficient and the bulk concentration of electroactive species in the electrolyte, r_{eff} is the effective radius of the electrode, and n is
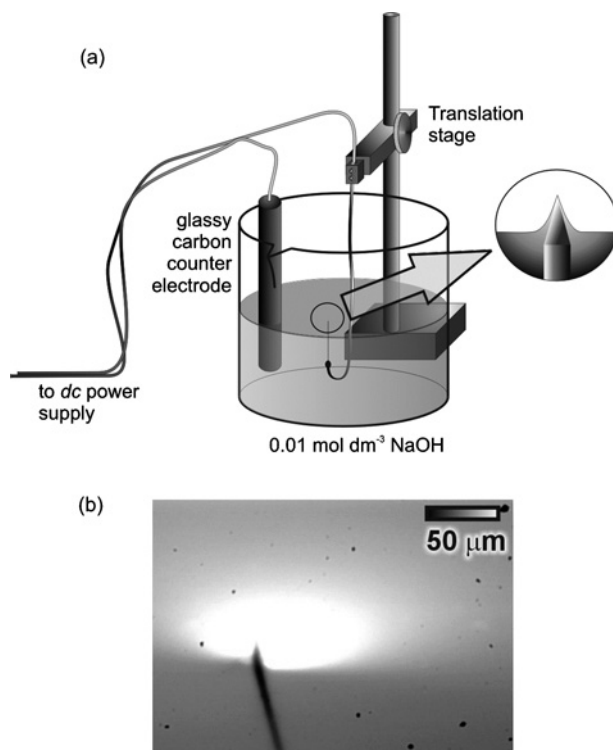
Figure 6.3.6.3   (a) Schematic diagram of the "inverted deposition" configuration used during the electrophoretic deposition of insulator onto the etched carbon electrode. (b) Photomicrograph of surface of electrophoretic paint showing the carbon fiber disappearing into the solution and the extent of the meniscus (white disk) made visible by illumination parallel to the surface of the paint solution.

the number of electron involved in the electrode reaction. Thus, the value of r_{eff} can be determined from the measured steady-state limiting current in the presence of excess supporting electrolyte by using equation (6.3.6.1) with the known values of D, C^*, and n.

The quality of the coating of the electrode may be assessed in a nondestructive manner by measuring the diffusion limited current response as a function of the extent of immersion of the electrode into a suitable electrolyte solution. An example is shown in Figure 6.3.6.4, which displays two overlapping cyclic voltammograms for an insulated carbon fiber electrode with and effective radius of 4.3 nm inserted only ~5–10 µm and inserted 3 mm into an electrolyte containing 0.01 M K_3FeCN_6 + 0.5 M KCl. The absence of any difference between the two scans suggests that there are no defects in the insulation along the shaft of the electrode.

A more destructive approach to assessing the quality of the coating may be performed by polarising the electrode in an electrolyte containing a suitable metal salt (e.g., 0.005 M $CuSO_4$) at a potential at which metallic copper will deposit, and examining the electrode under an SEM after the electrode has been removed. The presence of any defects will be evident by the obvious growth of copper deposits at sites away from the tip.
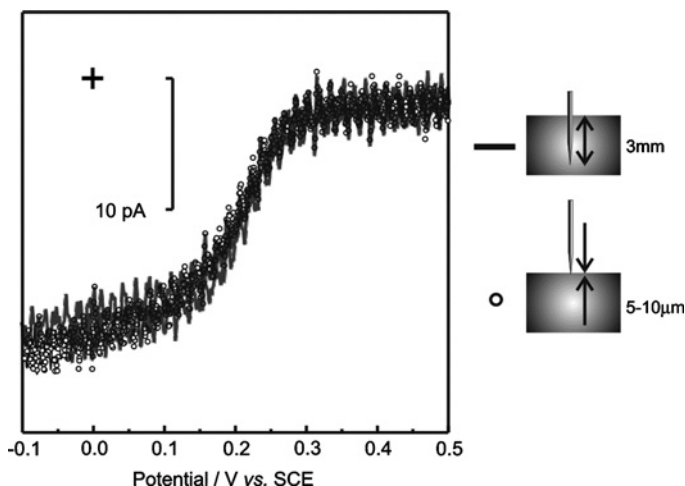
Figure 6.3.6.4 Comparison of the cyclic voltammograms for the reduction of 0.01 M K_3FeCN_6 in 0.5 M KCl on a carbon electrode with an effective radius of 4.3 nm as a function of the distance the electrode is immersed into the solution. ○: 5–10 μm; —: 3 mm. $dE/dt = 0.05$ V sec^{-1}.

REFERENCES

1. S. L. Chen, A. Kucernak, *Electrochem. Commun.* **4**, 80 (2002).
2. S. Chen, A. Kucernak, *J. Phys. Chem. B* **106**, 9369 (2002).
3. M. I. Montenegro, M. A. Queiros, J. L. Daschbach, *Microelectrodes: Theory and Applications*, Kluwer Academic Press: Dordrecht, The Netherlands, 1991.

6.3.7   Gold spherical microelectrodes

Christophe Demaille

Laboratoire d'Electrochimie Moléculaire, Université Paris
7-UMR CNRS 7591, France

6.3.7.1   *Spherical microelectrodes: self-assembly of gold nanoparticles*

(a)   *Fabrication technique*

This original ultramicroelectrode (UME) fabrication technique, developed by Bard and coworkers (1a,b), makes use of the finding of Schiffrin and coworkers (2) who showed that, in the presence of dithiol linkers, gold nanoparticles self-assemble to form an electrically conductive gold-like material. By confining the dithiol linker molecules inside the micrometer-sized tip of a glass micropipette, that was then immersed into a solution of gold nanoparticles, the dithiol–nanoparticle encounter could be restricted to the very tip of
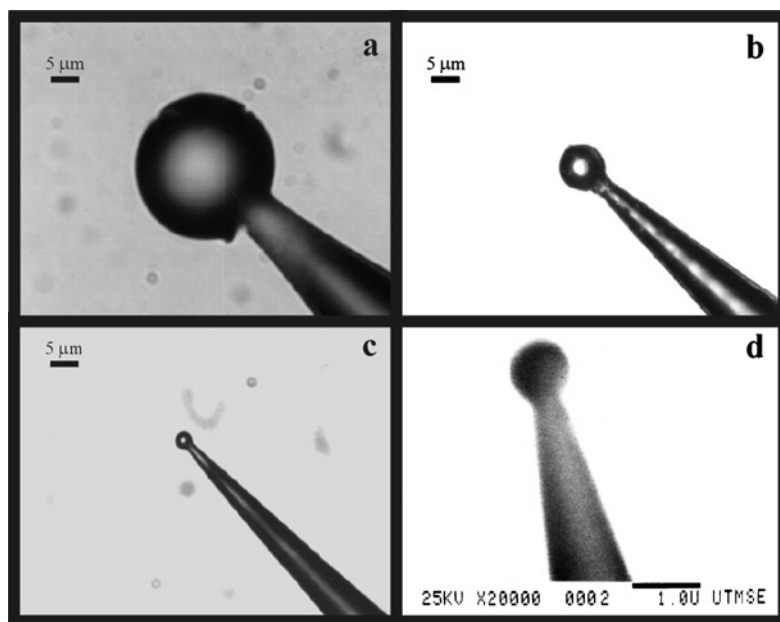
Figure 6.3.7.1   Optical (a–c) and scanning electron (d) microscope images of spherical gold UMEs self-assembled at the very tip of micropipettes. The horizontal scale bar in (d) represents 1 µm. Electrode diameters: (a) 26 µm, (b) 8 µm, (c) 3 µm, and (d) 0.9 µm. (Reprinted with permission from reference (1a), Copyright © 1997 American Chemical Society.)

the micropipette, thus limiting the growth of the self-assembled material to this region. This method was observed to result in the formation of perfectly spherical structures at the micropipette tip, as seen in Figure 6.3.7.1.

The complete self-assembly process of the spherical gold microstructures is represented schematically in Figure 6.3.7.2 and is described in detail below.

Quartz capillaries are pulled to form micropipettes having a tip orifice of a size ranging from 0.1 to 1 µm depending on the pulling conditions, using for example, a Sutter Instrument (Novato, CA) P2000 laser puller. The micropipette is then immersed in a 1,9-nonanedithiol solution in 2-propanol for ~1 h in order to fill the micropipette tip with a small amount of the dithiol solution. The micropipette is then thoroughly rinsed with toluene and immersed in a toluene solution containing octylammonium-protected ~8-nm gold nanoparticles prepared as described by Schiffrin and coworkers (2). The sphere then self-assembles at the tip of the capillary in ~2 h with the final diameter depending on the dithiol concentration and on the micropipette size. As a rule of thumb, the sphere diameter ranged from 2 to 20 times the micropipette tip diameter for dithiol concentrations ranging, respectively, from 1 to 5 mM. Spheres of a diameter ranging from 1 to 30 µm can be reproducibly assembled by this technique. Larger spheres can be produced but they tend to become mechanically unstable. Submicrometer-sized spheres can also be assembled but only with a low yield.
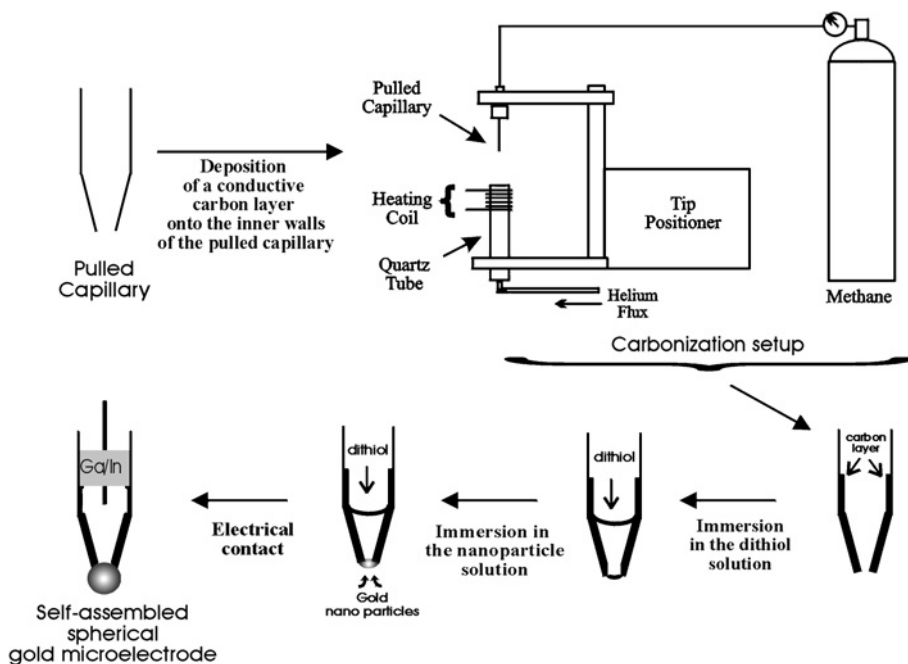
Figure 6.3.7.2   Schematic representation of the self-assembled spherical gold UME fabrication technique. (Adapted with permission from reference (1a,b)).

To use the self-assembled spheres as UMEs, electrical contact has to be established between the sphere and the macroscopic end of the supporting micropipette. The solution proposed by Bard and coworkers (1c) was to coat the inner walls of the pulled micropipette by a thin layer of pyrolitic carbon extending from the top to the very tip of the capillary. This carbon film deposition technique was adapted from previous work (3). The carbonization setup, presented in Figure 6.3.7.2, was constructed for better control of the carbon film quality and is used as follows. The micropipette, held in a gas-chromatography ferrule, is filled with methane under high pressure (240–500 psi) and introduced into a quartz tube heated to ~1000 °C. The quartz tube is continuously flushed with helium to avoid methane combustion. The heat source originally proposed was a Bunsen-burner (3), but it can be conveniently replaced by a Nichrome wire coil (1c). For a given micropipette size, the appropriate pressure is the one for which methane bubbles start to come out from the micropipette when immersed in water. A better quality film is formed when oxygen is pumped out from the micropipette before filling with high-pressure methane. Deposition of a thin conducting carbon film onto the inner walls of the capillary occurs when the micropipette is introduced into the quartz tube and passed *slowly* back and forth through the heated zone. This ensures that the interior of the micropipette is properly coated while the micropipette tip is still open. To gain better control of the car-bonizing process, the motion of the micropipette into the heated tube can be controlled via the use of a mechanical positioner. Carbon-coated micropipettes are then used in the

sphere assembly process detailed above. A small amount of gallium indium eutectic, introduced from the macroscopic side of the micropipette, establishes the final connection between the carbon layer and the biasing circuit, as shown in Figure 6.3.7.2.

(b) Electrochemical behavior: self-assembled spherical UMEs

Although it has been demonstrated that the nanoparticles maintain their individualities within the self-assembled spheres (1a,b), the electrochemical behavior of the self-assembled UMEs is similar to that of UMEs made of bulk gold. In particular, voltammetric peaks corresponding to gold oxide formation/reduction (4) were recorded at the self-assembled spherical UMEs in acidic media. Integration of the gold oxide reduction peak yielded an electrode surface roughness of 1.0, which confirmed the remarkable smoothness of the self-assembled spheres. The use of the self-assembled spherical structures as UMEs was tested both in aqueous solution and in acetonitrile. In both cases, ideally shaped reversible steady-state cyclic voltammograms (5a) (Section 6.1) were recorded, as shown in Figure 6.3.7.3.

Recording of such well-defined voltammetric signals, especially in nonaqueous solvent, together with the fact that this ideal behavior was maintained even at the highest scan rate explored (10 V sec^{-1}), shows that the self-assembled spherical UMEs are not porous and are tightly sealed to the supporting glass capillary surface.

Self-assembled spherical electrodes have been successfully used as SECM amperometric probes both in positive and negative feedback modes (1a,b) (Chapter 12). A very close tip–substrate separation could be attained due to the great smoothness of the self-assembled structures.

The self-assembled spherical electrodes have a fabrication success rate over 70%. In some instances, the presence of a golden conducting film adjacent to the sphere was seen on the outside wall of the micropipette tip. This thin film could be removed by
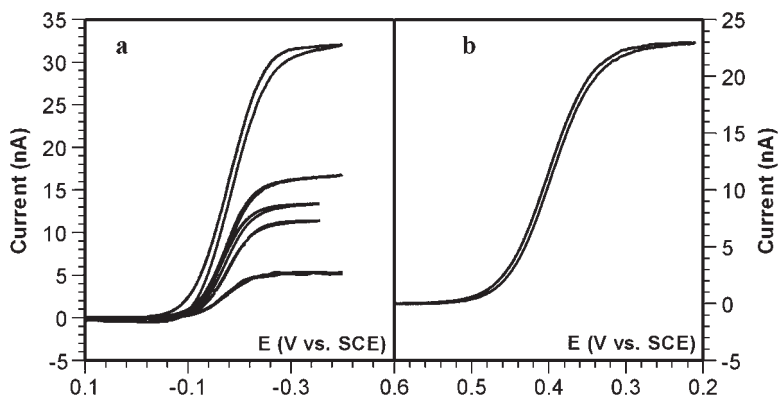
Figure 6.3.7.3 Cyclic voltammograms recorded at self-assembled gold UMEs. (a) In a 7.5-mM aqueous solution of hexaamineruthenium (III) chloride, 1 M KCl electrolyte. UME diameters (top to bottom): 10, 5, 4, 3, and 1.7 μm. (b) In a 6.5-mM solution of tetracyanoquinodimethane in acetonitrile, 0.1 M tetrabutylammonium tetrafluoroborate electrolyte. UME diameter: 6 μm. (Reprinted with permission from reference (1a), Copyright © 1997 American Chemical Society.)

briefly dipping the micropipette tip in a dilute aqua-regia solution (HNO_3/HCl/H_2O 1:3:10, caution! highly corrosive solution!). The self-assembled spherical electrodes were observed to be quite robust and could be handled without any particular caution. Indeed, when used as SECM probes, these microelectrodes even survived brief contacts with a hard substrate surface. Fall-out of the sphere from the supporting glass capillary has been observed, but only as a result of very harsh handling. Self-assembled gold UMEs have been stored in air for at least a week without any loss of their mechanical stability (6).

6.3.7.2   Submicrometer-sized spherical electrodes produced by spark-induced melting

(a)   Fabrication technique

In this technique developed by Abbou et al. (7), a spark-discharge of controlled intensity is used to melt the tip of a sharpened (etched) gold microwire, which balls-up instantaneously upon cooling. Extremely smooth spherical structures of controllable sizes, ranging from 0.1 to 1 μm in diameter, can be formed in this way (Figure 6.3.7.4).

Successive steps for the fabrication of gold spherical UMEs from these preformed structures are summarized graphically in Figure 6.3.7.5.

(b)   Sharpening the tip of a gold microwire by electrochemical etching

Sharpened gold microwires, the starting material for this technique, are produced by electrochemical etching of commercial gold microwires (60 μm in diameter) in a saturated $CaCl_2$:water:ethanol solution (10:40:5 v:v:v), under a DC-voltage of +7 V. Etching is complete in ~2 min and results in giving the extremity of the microwire a smooth conical aspect.

(c)   Spark-induced melting of the tip of the etched gold microwire

The diameter of the gold sphere ultimately formed at the tip of the etched microwire depends on the intensity of the spark-discharge, which can be controlled by the use of the spark-generating setup presented in Figure 6.3.7.6.

The electronic circuit shown in Figure 6.3.7.6 was designed to generate a *single* high-voltage pulse of an amplitude as high as 6 kV required to trigger the arc discharge. Most of the electronic components necessary to built such a high-voltage generating circuit can
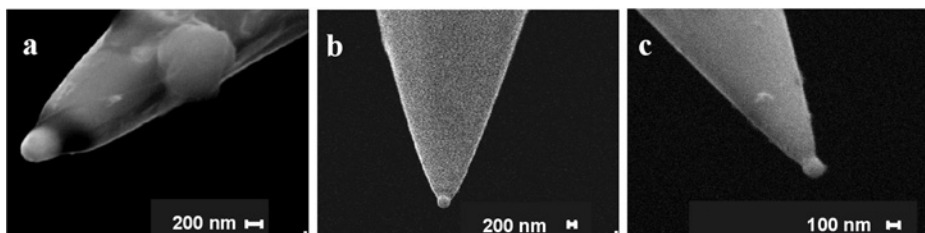
Figure 6.3.7.4   Scanning electron microscopy images of spherical gold UMES formed by spark-induced localized melting of the tip of etched gold microwires. To form the submicrometer spheres shown, the spark-generator (Figure 6.3.7.6) was operated in an open-circuit configuration with the following settings: $R = 0$, $d_s = 0.5$ mm, the shielding gas was air (a) or helium (b and c). (Adapted with permission from reference (1). Copyright © 2002 American Chemical Society.)
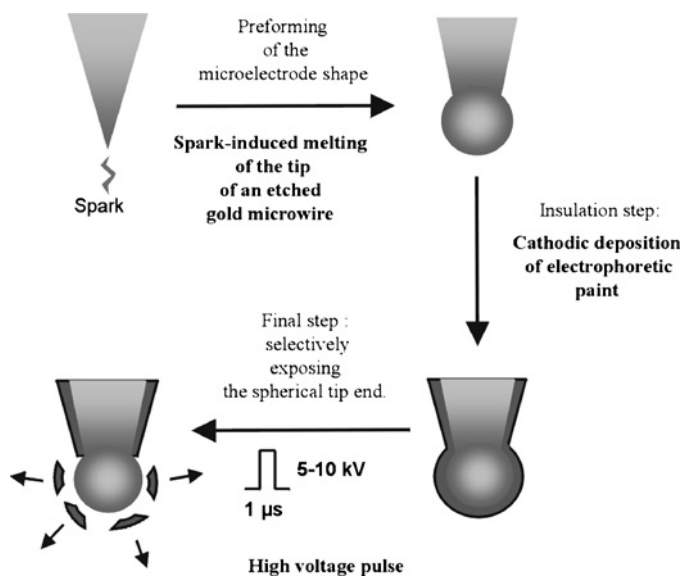
Figure 6.3.7.5 Schematic representation of the technique to fabricate submicrometer-sized spherical gold electrodes.

be found in commercial electric gas-lighters. The sharpened gold wire, as the anode, is connected to the low-voltage terminal of the circuit while a sharpened tungsten wire, used as a cathode, is connected to the high-voltage ($-$) terminal. Using the home-made positioning apparatus shown in Figure 6.3.7.6b, the gold microwire can be positioned exactly facing the tungsten wire. The spark-discharge intensity can be controlled by varying both the distance, d_s, separating the extremities of the gold and the tungsten wires, and the value of the resistance, R, in series with the cathode. The smaller the value of d_s, and conversely, the higher the value of R, the smaller the diameter of the sphere formed. It was shown that for d_s values of ~1 mm, spheres of a diameter ranging from ~10 μm to a few μms were formed when R was increased from 1 to 500 kΩ. It was observed that spheres as small as ~1 μm in diameter could reliably be formed for d_s ~ 0.5 mm and R ~ 1 MΩ. Submicrometer-sized spheres could only be formed when the setup was used in an *open-circuit* configuration; that is, when the gold wire was disconnected from the electronic setup, while d_s was kept at ~0.5 mm and R set to zero. A further decrease of the sphere diameter could be obtained by continuously blowing helium within the inter-electrode gap during the spark generation. Helium has a much larger thermal conductivity than air, so that more heat is driven away from the wire and very small spheres, of a diameter of ~100 nm, were then observed to form. To use the spheres as microelectrodes, the body of the gold microwire must be insulated. This was achieved by electrophoretic deposition of an insulating cathodic paint as described below.

(d) Insulation of the gold microwire

The gold microwire, bearing the preformed sphere at its tip, is immersed in a solution containing cathodic electrophoretic paint (BASF, Cathodip™ FT83-0250) diluted in a
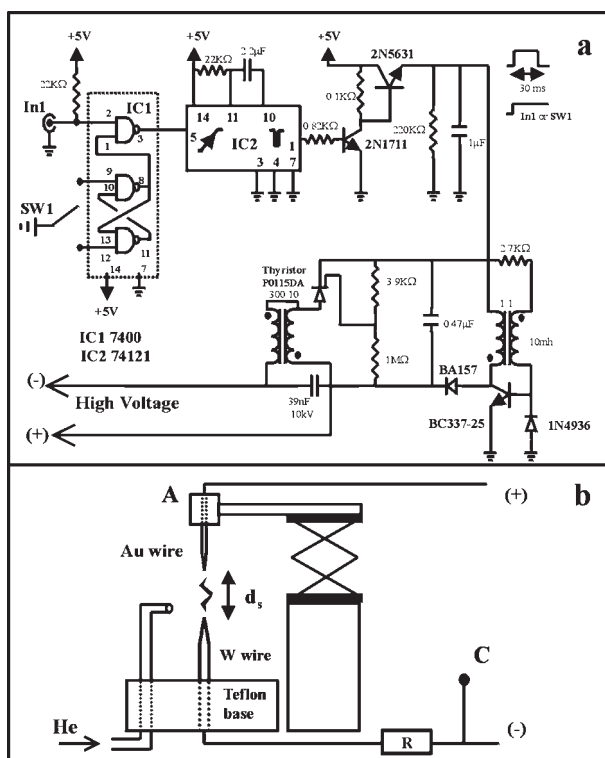
Figure 6.3.7.6 Schematic diagram of the high-voltage single pulse/spark generator setup. (a) Schematics of the electronic circuit of the high-voltage single pulse generator. (b) Diagram of the microwire positioning setup. The configuration shown is the closed-circuit configuration used to pre-form spherical microstructures at the end of etched gold microwires. In the open-circuit configuration, the gold wire is disconnected from the (+) terminal in point *A*. When this setup is used for the selective exposure of UMEs, the painted microwires are connected in point *C* and the resistance *R* is short-circuited. (Reprinted with permission from reference (1). Copyright © 2002 American Chemical Society).

1:1 (v:v) ratio by water, and acidified by 3 mM acetic acid. The gold microwire is then connected to a potentiostat as the cathode of a two-electrode configuration, the anode being a platinum coil. The potential of the microwire is scanned from 0 to -5 V at a rate of 50 mV sec^{-1} to trigger deposition of the paint. At such a negative potential, protons are reduced and the ensuing local pH rise causes the deprotonation of the NH_3^+ moieties borne by the polymer chains composing the cathodic paint that then precipitate onto the gold microwire surface. After deposition, the gold microwire is rinsed with water and placed in an oven heated to 180 °C for 20 min. This thermal curing step results in the cross-linking of the amine-bearing chains by diisocyanate linkers also present in the paint composition. When the painted gold microwires were characterized in an aqueous solution of ferrocenedimethanol by cyclic voltammetry, no faradaic current was recorded. This behavior was observed for more than 80% of the painted wires and demonstrates that the cured paint

layer forms a perfectly insulating coating over the entire surface of the gold microwire. A technique to selectively expose only the preformed spherical extremity of the microwires follows below.

(e) Selective exposure of the spherical end of the microwire

This technique makes use of the same spark-generating setup described above, but the gold microwire connected to the (+) terminal of the setup is here a sacrificial microwire, whereas the microwire to be exposed is connected to the high-voltage (−) terminal of the setup in point *C* of Figure 6.3.7.6(b), i.e., in *parallel* to the spark-generating circuit. The spark is thus generated between the tungsten and the sacrificial gold wire *and not* at the painted microwire. However, being connected to the high-voltage terminal of the setup, the painted microwire experiences the same sudden high-voltage pulse as the tungsten cathode does. The highest voltage experienced by the painted microwire can be controlled by varying the interelectrode spacing d_s; the smaller d_s the lower the voltage reached. Typical values of d_s in the 0.5−2 mm range translate to an applied voltage of 1.5–6 kV. It was observed that, once subjected to this high-voltage pulse, painted microwires systematically exhibited sigmoidal-shaped cyclic voltammograms typical of UMEs (5a) (Figure 6.3.7.7).

The high-voltage pulse resulted in exposure of a small portion of the insulating film covering the microwire. The size of the exposed area, as determined from the plateau current of the steady-state voltammogram (5b), corresponds to the diameter of the spherical tip-end of the microwire, as measured from SEM images. In addition, when a spherical microelectrode, fabricated as described above, was used to reduce Fe^{2+} ions in solution, the resulting iron deposit was observed to grow exclusively onto the spherical tip-end of
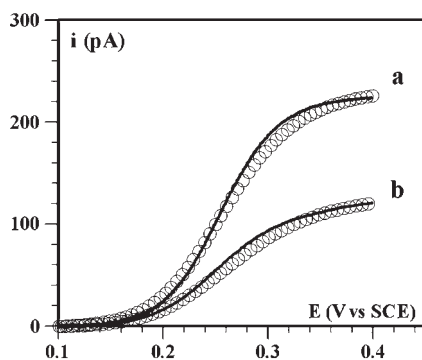
Figure 6.3.7.7 Cyclic voltammetry of ferrocenedimethanol at submicrometer-sized spherical gold UMEs produced by spark-induced melting of the tip of etched gold microwires. The cyclic voltammograms (a and b) were recorded, respectively, at the UMEs shown in the SEM pictures (a and b) of Figure 6.3.7.4. From the value of the plateau currents, the UME diameters were estimated to be of (a) 250 nm and (b) 150 nm. The scan rate was of 20 mV sec^{-1}. The forward and backward traces of each voltammogram are perfectly superimposable at this scan rate. The open circles correspond to the fit of the whole voltammogram using the equation given in the text and the following parameter values: $E° = 235$ mV vs. SCE, $D = 7.4 \times 10^{-6}$ cm^2 sec^{-1}, $k_s = 0.4$ cm sec^{-1}, $\alpha: = 0.5$. Ferrocenedimethanol is at a concentration of 1 mM in 0.1 M KH_2PO_4.

the microelectrode. All of the above conclusively show that the high-voltage pulse method actually results in *selectively* exposing the preformed spherical tip-end of the microwires. The physical reasons behind such remarkable selectivity is not absolutely clear. It is thought that the high electric field created at the very end of the microwire blows away the insulating paint covering the spherical structure. This process seems to be facilitated by the bottle-neck shape of the extremity of the preformed electrodes (Figure 6.3.7.4) as much poorer results were obtained with nonpreformed (simply etched and painted) microwires.

(ƒ) Electrochemical characterization of spherical gold UMEs

From the value of the plateau current i_{ss} of the cyclic voltammograms recorded in an aqueous solution of ferrocenedimethanol, the radius r_o of the submicrometer-sized spherical gold UMEs could be obtained using the expression: $i_{ss} = 4\pi FDC^*r_0$, where D is the diffusion coefficient of ferrocenedimethanol and C^* is its concentration (Section 6.1) (5b). The cyclic voltammograms were fitted using the theoretical expression for steady-state voltammograms at spherical UMEs (5a).

$$i = \frac{i_{ss}}{1 + \exp[-F(E - E^\circ)/RT] + (D_0/r_0 k_s)\exp[-\alpha F(E - E^\circ)/RT]} \qquad (6.3.7.1)$$

where k_s and E° are, respectively, the heterogeneous electron transfer rate constant and standard potential of ferrocenedimethanol (7). The good fit obtained (Figure 6.3.7.7, open circles) demonstrates the ideal voltammetric behavior of the spherical submicrometer-sized gold UMEs.

Another interesting aspect of the cyclic voltammetric response recorded at these spherical gold UMEs is the absence of hysteresis between the forward and backward traces of the voltammograms. This is indicative of the relatively low capacitance of the microelectrodes resulting from the good insulating property of the reticulated paint film. A typical value of ~5 pF was reported for the capacitance of the spherical UMEs. This value is low enough for the capacitive charging current not to interfere with the cyclic voltammetry signals for scan rates as high as a few volts per second. It was also reported that the UMEs could be used in a large potential window, ranging from − 1.2 to +1.7 V/SCE in a pH 4.4 aqueous solution without damaging the insulating coating film. The spherical UMEs can be fabricated as described with an overall success yield of ~60%. The microelectrodes can be stored in air for as long as a year without any degradation of their electrochemical behavior (8).

This fabrication technique was also successfully applied to combined AFM-SECM probes (7, 9). Following a reported technique (10), the gold microwire was bent to a right angle ~1 mm away from one of its ends while its other end was flattened between stainless-steel plates. The flattened part of the microwire serves as a flexible AFM cantilever arm while its short extremity is converted into a spherical microelectrode following the method described above. The AFM-SECM experiments using these combined probes, confirmed the ideal behavior of the spherical gold microelectrodes formed by the spark-method.

REFERENCES

1. (a) C. Demaille, M. Brust, M. Tsionsky, A. J. Bard, *Anal. Chem.* **69**, 2323 (1997); (b) F.-R. F. Fan, C. Demaille, in *Scanning Electrochemical Microscopy*, A. J. Bard, M. V. Mirkin, Eds., Marcel Dekker: New York, 2001, pp. 81–91; (c) *Ibid*, pp. 94–99.
2. (a) M. Brust, D. Bethell, D. J. Schiffrin, C. J. Kiely, *Adv. Mater.* **7**, 795 (1995); (b) D. Bethell, M. Brust, D. J. Schiffrin, C. J. Kiely, *J. Electroanal. Chem.* **409**, 137 (1996).
3. (a) Y.-T. Kim, D. M. Scarnulis, A. G. Ewing, *Anal. Chem.* **58**, 1782 (1986); (b) D. K. Y. Wong, L. Y. F. Xu, *Anal. Chem.* **67**, 4086 (1995).
4. D. A. J. Rand, R. Woods, *J. Electroanal. Chem.* **31**, 29 (1971).
5. (a) M. V. Mirkin, A. J. Bard, *Anal. Chem.* **64**, 2293 (1992); (b) C. Amatore, in *Physical Electrochemistry. Principles, Methods and Applications*, I. Rubinstein, Ed., Marcel Dekker: New York, 1995, pp. 131–208.
6. A. J. Bard, M. Brust, C. Demaille, M. Tsionsky, Unpublished results (1995).
7. J. Abbou, C. Demaille, M. Druet, J. Moiroux, *Anal. Chem.* **74**, 6355 (2002).
8. J. Abbou, C. Demaille, Unpublished results (2004).
9. J. Abbou, C. Demaille, A. Anne, *J. Am. Chem. Soc.* **126**, 10095 (2004).
10. (a) J. V. Macpherson, P. R. Unwin, *Anal. Chem.* **72**, 276 (2000); (b) J. V. Macpherson, M. A. Webb, P. R. Unwin, *Anal. Chem.* **73**, 550 (2001).

6.3.8   Hg microhemispherical electrodes

Janine Mauzeroll

Laboratoire d'Electrochimie Moléculaire, Université Paris,
7-UMR CNRS 7591, France

6.3.8.1   Introduction

The Hg/Pt ultramicroelectrodes (UMEs) described here are hemispherical in shape and can be used in both electrochemical and scanning electrochemical studies (scanning electrochemical microscopy (SECM), Chapter 12 of this handbook) when it is necessary to work in negative potential regions where proton reduction occurs at Pt. Examples include the detection of Tl(I) as a surrogate for K(I) in studies of ion transport through channels in membranes (1, 2) or in studies where a very negative redox couple, like methyl viologen, is needed.

This section describes the deposition and characterization of a Hg hemisphere on Pt UMEs (3). Two methods of fabricating hemispherical Hg/Pt UMEs are described: electrodeposition from an inorganic mercury solution or from controlled contact of the Pt UME with a mercury drop. Electrochemical characterization can be performed using linear sweep voltammetry, amperometry (see Chapter 11) and SECM feedback experiments (see Chapter 12).

6.3.8.2   Importance of the choice of substrate

Ideally, the solid support should be easily wet by and have a low solubility in mercury. In the case of glassy carbon, the surface is poorly wet leading to the formation of scattered

mercury droplets (4). For metals like gold, platinum and silver, the formation of inter-metallic compounds at the base metal can occur. Thermal evaporation experiments have shown that the formation of inter-metallic species leads to a potential window that extends to less negative potentials than that of the hanging mercury drop electrode (HMDE) (5). Since the dissolution of Pt is hindered by the presence of surface oxides, Pt supports can still be used in voltammetric studies following the deposition of a sufficiently thick mercury layer (6). Also, in the case of a Hg–Au amalgam UME, Mandler and coworkers (7) have demonstrated the use of such probes in SECM studies of surface reactions catalyzed by Pt. Another possible substrate material is iridium. Osteryoung and coworkers fabricated and studied Ir (8) and Ir/Pt (9) alloy-based mercury UMEs. They are very useful for electrochemical studies but are more brittle than Pt UMEs.

6.3.8.3   *Hg/Pt hemispherical UME fabrication by electrodeposition*

The solid support for the Hg hemisphere is a conventional Pt UME as reported in detail in Section 6.3.1 of this Handbook and other published work (10).

(a)   *Solutions*
To deposit mercury onto a Pt UME, a 10 mM $Hg_2(NO_3)_2$ (J.T. Baker Chem. Co., Phillipsburg, NJ) in 0.1 M KNO_3 solution acidified to 0.5% with HNO_3 is used. Following deposition, cyclic voltammetry and SECM characterization experiments use 1 mM in cobalt sepulchrate trichloride (Aldrich), hexamineruthenium (III) chloride (Strem Chem., Newbury Port, MA), or methyl viologen (Aldrich) redox couples. The supporting electrolyte used is formed by 0.1 M KCl solutions buffered by a 1:1 molar ratio of NaH_2PO_4/Na_2HPO_4 of total concentration of 0.01 M at pH 7. All solutions are prepared with Milli-Q (Millipore Corp.) reagent water and degassed with Ar for 30 min prior to all experiments.

(b)   *Instruments*
A CHI Model 900 scanning electrochemical microscope (CH Instruments, Austin, TX) can be used to control UME tip potentials, obtain approach curves and monitor the tip to underlying substrate distance. Voltammetric and SECM experiments can be performed either with the SECM head in a glove bag under positive pressure or the SECM cell covered with parafilm and in the presence of an argon blanket. Where SECM characterization is not possible, any potentiostat can be used to deposit and characterize the Hg/Pt UME.

(c)   *Reaction cell*
To monitor mercury deposition in situ, a microscope reaction cell can be used. The working Pt UME and counter electrode are inserted through a hole at the base of the cell while the reference electrode is positioned in a side compartment as shown in Figure 6.3.8.1. Once mounted on an optical microscope equipped with a water immersion objective (Olympus FLxw40), a camera and personal computer can then be used to record images of the mercury deposition.

(d)   *In-situ mercury deposition*
Mercury is deposited onto a Pt UME from a $Hg_2(NO_3)_2$ solution in a three-electrode setup and controlled by a potentiostat. A 1 mm Pt wire serves as a counter electrode and a fritted
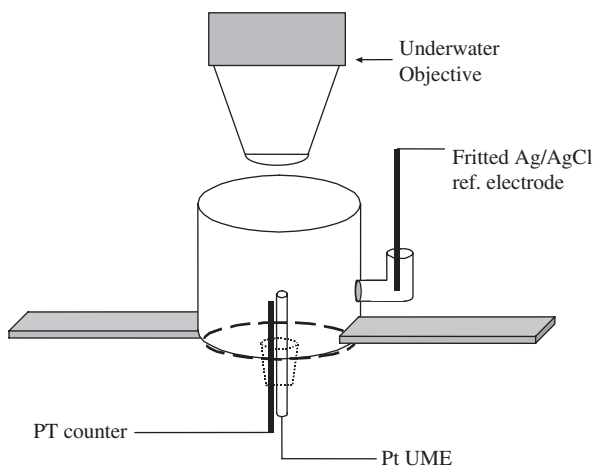
Figure 6.3.8.1 Experimental setup for the formation of Hg/Pt hemispherical UME by electrode-position from a $Hg_2(NO_3)_2$ solution with 0.1 M KNO_3 acidified to 0.5% with HNO_3 as supporting electrolyte. This glass cell was joined at the base with a microscope slide. The underwater objective was lowered into solution and the deposition curve recorded during a 300 sec potential step of −0.1 V vs. Ag/AgCl. Reprinted with permission from reference (3). Copyright, the American Chemical Society.

Ag/AgCl electrode serves as a reference electrode. The deposition curve is recorded during a 300 sec potential step of −0.1 V vs. Ag/AgCl. In the first stages of deposition, a very thin layer of inter-metallic species (Pt_2Hg) is formed (5). This is followed by the spontaneous formation of mercury nuclei (Figure 6.3.8.2a) close to the edge of the Pt/glass interface where the current density is the highest (11). With time, the nuclei coalesce until a full hemisphere is formed. This coalescence alters the surface area of the electrode and leads to indentations in the current deposition curves (Figure 6.3.8.2b). These results are consistent with previously reported work (7).

(e) Hg/Pt hemishperical UME characterization: voltammetry

The electrochemical behavior and stability of a Hg UME is evaluated using linear sweep voltammetry. After mercury deposition, proton reduction shifts to more negative potentials from that seen at bare Pt by about 800 mV (Figure 6.3.8.2c). Dirty or damaged electrodes only shift the potential by about 200 mV and show prewaves characteristic of Pt micro arrays. Clean UMEs with a thick mercury deposit, however, are well behaved.

Proton reduction at Pt is catalyzed by methyl viologen. Electrochemical studies of this couple in aqueous media must, therefore, be performed at a mercury electrode. The methyl viologen voltammogram at the Hg UME is well behaved (Figure 6.3.8.3a) and confirms good coverage of the Pt disk.

The change in geometry from a disk to a hemisphere can be observed by the change in limiting current in voltammograms of $Ru(NH_3)_6^{3+}$ (Figure 6.3.8.3a). This follows theoretical equations of the steady-state current at microelectrodes (see Section 6.1 in Chapter 6 of this handbook) where the ratio of the limiting current of a disk UME (12)
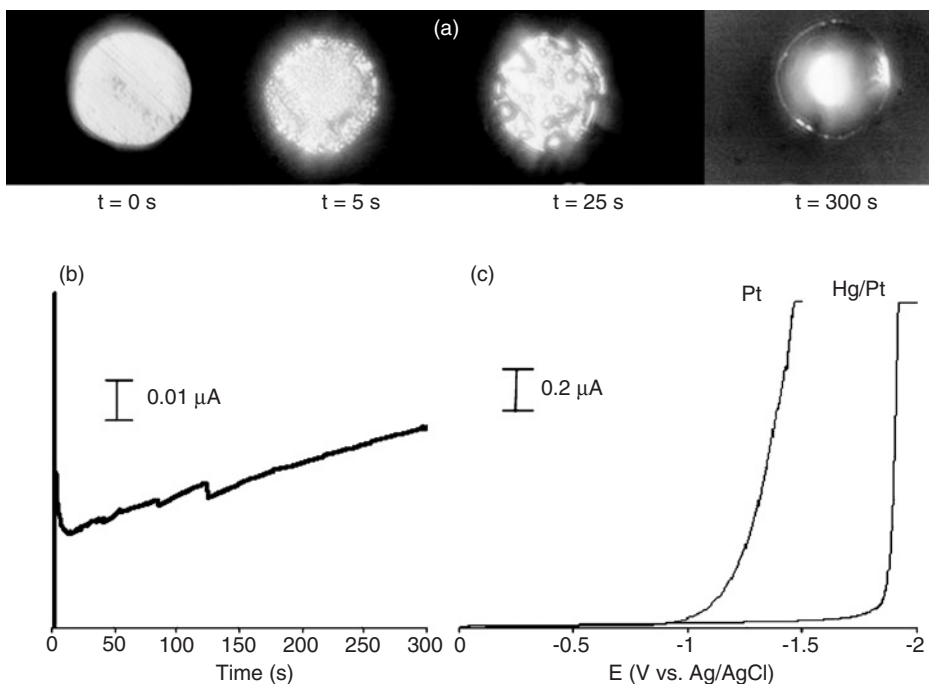
Figure 6.3.8.2   Characterization of a 25 μm Hg/Pt hemispherial UME. (a) In-situ micrographs of mercury deposition (0–300 sec) from a 10 mM $Hg_2(NO_3)_2$ solution with 0.1 M KNO_3 supporting electrolyte acidified to 0.5% with HNO_3. (b) The deposition curve recorded during a 300 sec potential step of −0.1 V vs. Ag/AgCl. A 1 mm Pt wire served as the counter electrode and a fritted Ag/AgCl electrode served as the reference electrode. (c) Current potential curves at Pt and Hg/Pt UMEs in 0.1 M KNO_3. Reprinted with permission from reference (3). Copyright, the American Chemical Society.

and that of a hemispherical UME is close to $\pi/2$. The observed change of steady-state current (i_h/i_d = 1.47) from the Pt UME to the Hg UME is close to this value for $Ru(NH_3)_6^{3+}$, confirming the near hemispherical geometry of the UME. A similar increase in the steady-state ratio (i_h/i_d = 1.57) was observed for cobalt sepulchrate trichloride (Figure 6.3.8.3a). Thus, both the optical and voltammetric analyses confirm the hemispherical geometry of the UME.

(f)   Hg/Pt hemispherical UME characterization: SECM
Theory (13, 14) and applications of SECM are discussed in Chapter 12. Relevant here is the effect of UME tip geometry on SECM approach curves as shown in Figure 6.3.8.3b–d. Approach curves to a Hg/Pt hemispherical UME are compared with those at a Pt disk for three redox couples and the comparison demonstrates the reduced sensitivity of the Hg/Pt hemispherical UMEs relative to Pt disk electrodes in terms of SECM feedback experiments. The Hg/Pt experimental approach curves are consistent with an analytical approximation
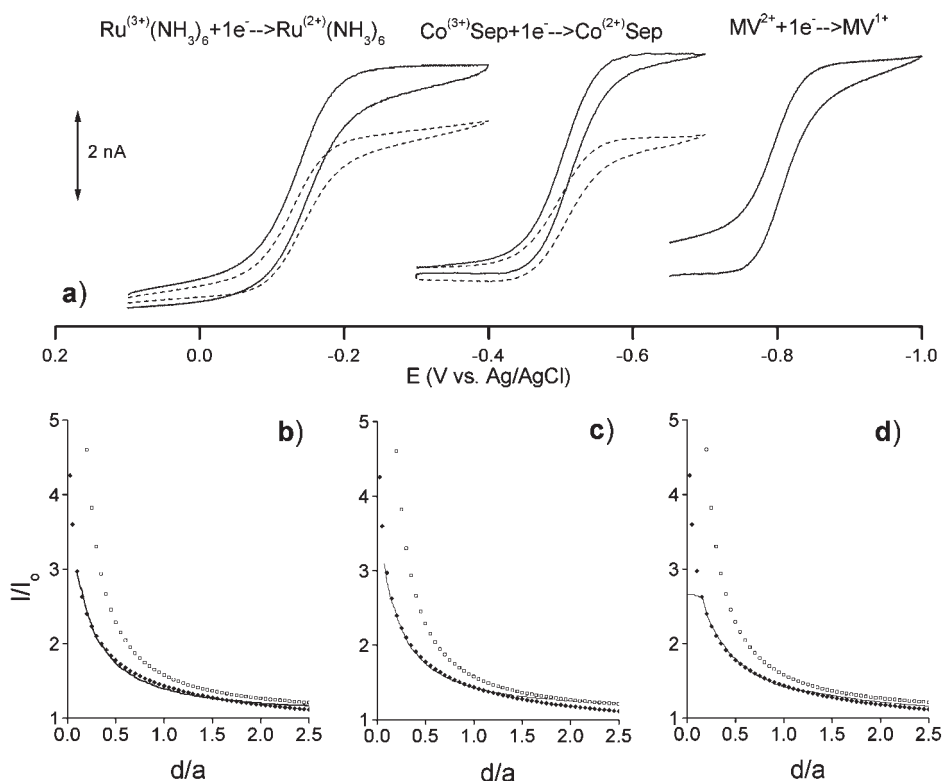
Figure 6.3.8.3 (a) Voltammetric behavior of the 25 μm (--) Pt UME and (solid line) Hg/Pt hemispherical UMEs in 1 mM Ru(NH$_3$)$_6$Cl$_3$, cobalt sepulchrate trichloride, and methyl viologen in 0.1 M KNO$_3$. (b) Positive feedback SECM fitting of the (□) finite disk theory, (♦) hemispherical disk theory, and (line) experimental results for the 1 mM Ru(NH$_3$)$_6$Cl$_3$. (c) Positive feedback SECM fitting of the (□) finite disk theory, (♦) hemispherical disk theory, and (line) experimental results for the 1 mM cobalt sepulchrate trichloride in 0.1 M KNO$_3$. (d) Positive feedback SECM fitting of the (□) finite disk theory, (♦) hemispherical disk theory, and (line) experimental results for the 1 mM methyl viologen. Reprinted with permission from reference (3). Copyright, the American Chemical Society.

for positive feedback (±1%) (normalized current vs. distance) for a hemispherical UME developed by Selzer and Mandler (15):

$$\frac{i_T}{i_{T,\infty}} = 0.873 + \ln(1 + L^{-1}) - 0.20986 \exp\left[-\frac{L - 0.1}{0.55032}\right] \qquad (6.3.8.1)$$

where i_T is the tip current, $i_{T,\infty}$ is the steady-state current when the tip is far from the substrate and L is the ratio of the tip to substrate spacing (d) and the active electrode radius (12.5 μm) (i.e., $L = d/r_0$). The response is significantly different from that reported for a disk UME (16):

$$\frac{i_T}{i_{T,\infty}} = 0.68 + \frac{0.7838}{L} + 0.3315 \exp\left[-\frac{1.0672}{L}\right] \qquad (6.3.8.2)$$

Previously reported studies of gold spherical UMEs prepared by self-assembly of gold nanoparticles (17) show similar behavior (see Section 6.3.7).

6.3.8.4   Hg/Pt hemispherical UME fabrication by contact to a mercury pool

(a)   Solution
The supporting electrolyte used is identical to that in the first protocol. The redox couples used for electrochemical characterization are 2 mM hexamineruthenium (III) chloride (Strem Chem., Newburyport, MA) and 0.1 mM Tl(I) nitrate (Aldrich). All solutions are prepared using Milli-Q (Millipore Corp.) reagent water and degassed with Ar for 30 min prior to all experiments.

(b)   Instruments
A CHI Model 900 scanning electrochemical microscope (CH Instruments, Austin, TX) can be used to control UME tip potentials, obtain approach curves and to approach a Pt UME to a mercury pool. Similar results can be achieved with a micromanipulator and an independent potentiostat.

(c)   In-situ mercury deposition
A Hg/Pt UME can be formed by applying –1.1 V vs. Hg/Hg_2SO_4 (Radiometer, Copenhagen, Denmark)) at a Pt UME and contacting it with the mercury (Bethlehem Instr., Hellertown, PA) of an HDME (Metrohm Instr., Herisau, Switzerland) or a Hg pool in phosphate buffer (Figure 6.3.8.4a).

(d)   Hg/Pt hemispherial UME characterization: voltammetry
As shown in Figure 6.3.8.4b, a 0.5 V overpotential for hydrogen evolution is observed in deaerated phosphate buffer (pH = 7) following Hg deposition onto Pt. The response shown in Figure 6.3.8.4b suggests full coverage of Pt by Hg. The extension of the potential window allows the detection of Tl(I) electrochemistry at the Hg/Pt UME (Figure 6.3.8.4c). The voltammogram shows a stable steady-state current for the Tl(I) reduction and a characteristic stripping peak for the oxidation of the Tl amalgam.

(e)   Hg/Pt hemispherical UME characterization: SECM
Hg/Pt hemispherical UME show positive feedback with $Ru(NH_3)_6^{2+}$ when approaching an HMDE (Figure 6.3.8.5) or a Hg pool. The experimental approach curves fit theory developed by Selzer and Mandler (15) for a hemispherical UME as described in Section 6.3.8.2. Reproduction of the voltammetric and SECM characterization confirms the equivalency of the two methods used to form Hg/Pt hemispherical UMEs.

   In SECM experiments, the close approach of the disk UME is often hampered by the insulating sheath, which may strike the substrate due to misalignment of the tip. The protrusion of the active electrode area as in the mercury hemisphere permits an uninhibited approach and a better estimation of the true zero distance.

6.3.8.5   Microelectrode maintenance and storage

Once formed, the mercury hemisphere is firmly attached to the Pt substrate and can withstand washing; however, it cannot be stored in air and left to dry. When dry, the hemisphere
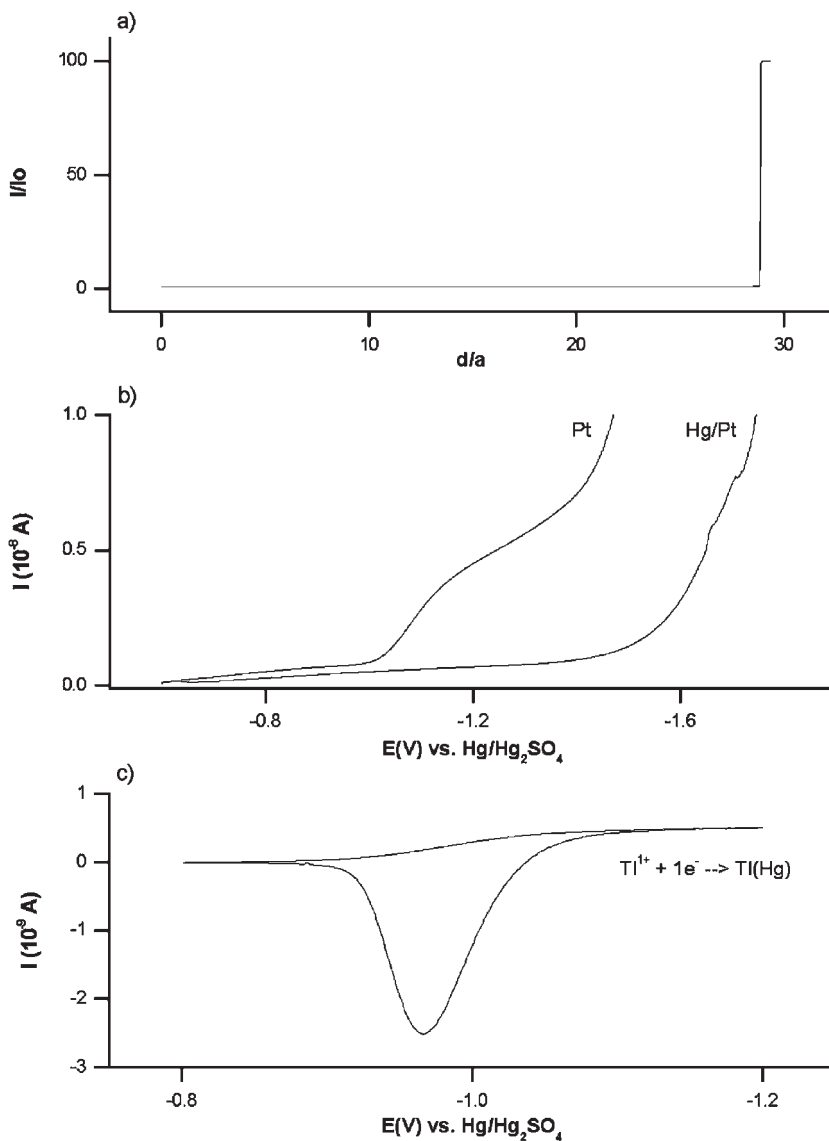
Figure 6.3.8.4   Formation and characterization of the Hg/Pt hemispherical submarine UME. (a) The Pt submarine electrode in phosphate buffer (pH = 7) as it approached the HMDE while poised at -1.1 V vs. Hg/Hg_2SO_4. Upon contact with the HMDE, a hemispherical mercury layer is deposited onto the Pt UME. (b) Hydrogen evolution at Pt and Hg/Pt submarine UME in phosphate buffer. (c) Voltammogram of the 10^{-4} M Tl(I) at the Hg/Pt submarine electrode in phosphate buffer. Reprinted with permission from reference (2). Copyright the American Chemical Society.
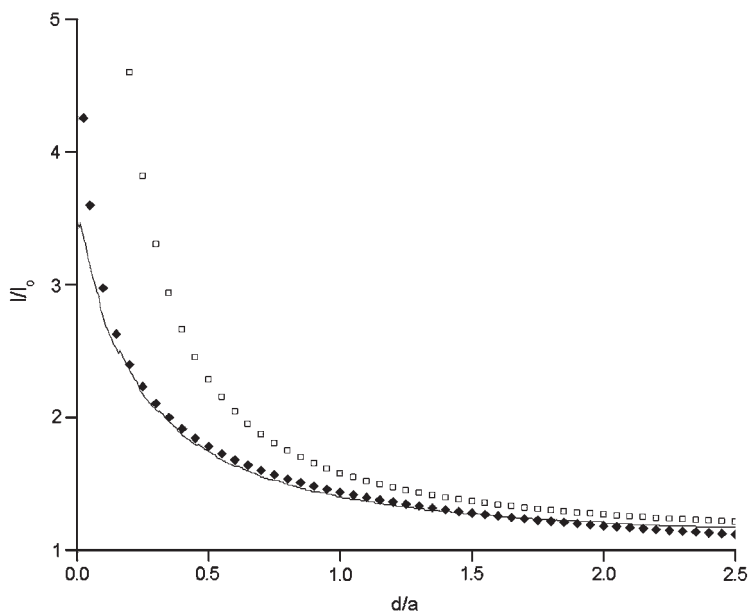
Figure 6.3.8.5   Positive feedback SECM curve fitting of (line) Hg/Pt hemispherical submarine UME approach curve to (♦) hemispherical SECM theory and (❑) disk SECM theory for a 2 mM hexamineruthenium chloride solution in phosphate buffer (pH = 7). The Hg/Pt hemispherical UME approached an HMDE. Reprinted with permission from reference (2). Copyright the American Chemical Society.

shrinks and sometimes exposes Pt as a result of surface tension changes. Hg UMEs should therefore be stored in a degassed potassium nitrate solution.

The main limitation of Hg/Pt UMEs is their reusability. For studies where the redox couples do not adhere to the mercury or form an amalgam, electrochemical cycling and storage in PBS is sufficient. In cases where amalgam formation is important, no amount of cycling is able to completely remove all traces of amalgam. Many times, it is easier to mechanically polish the UME to remove the mercury and expose a fresh Pt surface. In SECM studies, where mechanical polishing implies an increase in RG, this cleaning method can become cumbersome.

6.3.8.6   Conclusions, limitations and prospects

Hg/Pt hemispherical UMEs can be fabricated by two methods which produce identical UMEs and characterized using optical and electrochemical instrumentation. Voltammograms are well behaved and the extension of the potential window to more negative potentials facilitates the use of mediators such as methyl viologen. Approach curves recorded over conductors for different redox couples show good agreement with hemispherical theory (3).

These electrodes can be used in voltammetric, amperometric, and SECM studies in negative potential regions where proton reduction occurs at Pt. They are also very smooth and

easily adaptable to stripping voltammetry studies. Their positive potential region is limited by stripping (oxidation) of the mercury deposit.

REFERENCES

1. M. Rueda, I. Navarro, G. Ramirez, F. Prieto, C. Prado, A. Nelson, *Langmuir* **15**, 3672 (1999).
2. J. Mauzeroll, M. Buda, A. J. Bard, F. Prieto, M. Rueda, *Langmuir* **18**, 9453 (2002).
3. J. Mauzeroll, E. A. Hueske, A. J. Bard, *Anal. Chem.* **75**, 3880 (2003).
4. H. P. Wu, *Anal. Chem.* **66**, 3151 (1994).
5. Z. Yoshima, *Bull. Chem. Soc. Jpn.* **1981**, 556 (1981).
6. K. R. Wehmeyer, R. M. Wightman, *Anal. Chem.* **57**, 1989 (1985).
7. Y. Selzer, I. Turyan, D. Mandler, *J. Phys. Chem. B* **103**, 1509 (1999).
8. J. Golas, Z. Galus, J. Osteryoung, *Anal. Chem.* **59**, 389 (1987).
9. C. Wechter, J. Osteryoung, *Anal. Chim. Acta* **234**, 275 (1990).
10. F.-R. F. Fan, C. Demaille, in *Scanning Electrochemical Microscopy*, A. J. Bard, Ed., Marcel Dekker: New York, 2001, p. 75.
11. B. Sharifer, G. J. Hills, *J. Electroanal. Chem.* **130**, 81 (1981).
12. R. M. Wightman, D. O. Wipf, *Electroanal. Chem.* **15**, 267 (1988).
13. A. J. Bard, F.-R. F. Fan, J. Kwak, O. Lev, *Anal. Chem.* **61**, 132 (1989).
14. J. M. Davis, F.-R. F. Fan, A. J. Bard, *J. Electroanal. Chem. Interfacial Electrochem.* **238**, 9 (1987).
15. Y. Selzer, D. Mandler, *Anal. Chem.* **72**, 2383 (2000).
16. M. Arca, A. J. Bard, B. R. Horrocks, T. C. Richards, D. A. Treichel, *Analyst* **119**, 719 (1994).
17. C. Demaille, M. Brust, M. Tsionsky, A. J. Bard, *Anal. Chem.* **69**, 2323 (1997).

6.3.9   Clarke oxygen microelectrode

Katherine B. Holt

Department of Chemistry and Biochemistry, The University of Texas at Austin, Austin, Texas 78712-0165, USA

6.3.9.1   Introduction

Platinum and carbon ultramicroelectrodes (UMEs) are commonly used to determine the concentration of dissolved oxygen in solution, by measuring the current for the reduction of oxygen (1, 2). However, difficulties with signal stability are often encountered, associated with interference by other electroactive species, or poisoning of the electrode surface by adsorbed impurities. These problems can be overcome by covering the electrode with a membrane that is permeable to oxygen but not to other solution species, as first proposed by Clarke in his design for the membrane oxygen electrode (3–6). If both working and counter electrodes are placed behind the membrane, with electrochemical contact maintained through a thin layer of immobilized electrolyte, then measurements of oxygen concentration in the gas phase are possible. The use of an UME tip as the basis for a Clarke
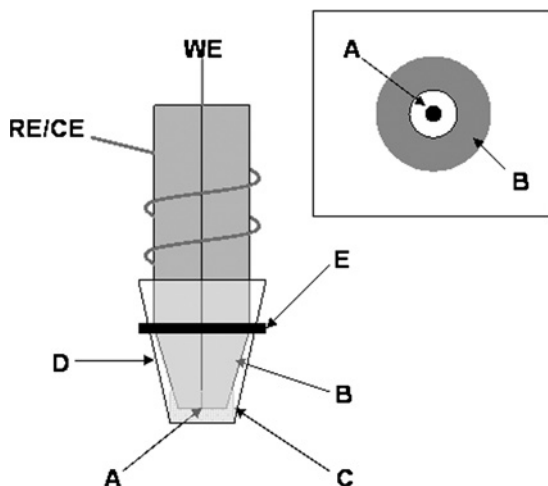
Figure 6.3.9.1   Schematic diagram of membrane UME-based oxygen sensor: (A) 25 µm diameter disk Pt working electrode sealed in glass; (B) Ag layer acting as reference/counter electrode; (C) electrolyte layer forming electrolytic contact between working and reference electrodes; (D) 10 µm thick high density polyethylene (HDPE) membrane; (E) rubber o-ring. Inset: bottom view of electrode surface; (A) 25 µm diameter disk Pt working electrode sealed in glass; (B) Ag paint creating a ring reference/counter electrode. [Reprinted with permission from M. Carano, K. B. Holt, A. J. Bard, *Anal. Chem.* **74**, 5071 (2003). Copyright 2003. The American Chemical Society.]

membrane electrode allows the gas-phase measurement of oxygen concentration to be extended to scanning electrochemical microscopy (SECM, see Chapter 12) (7).

6.3.9.2   Construction and electrochemical response of Clarke UME

(a)   Construction
The fabrication of the Clarke UME is illustrated schematically in Figure 6.3.9.1. It consists of a 25 µm Pt disk working electrode sealed in glass with a silver coating on the outside of the glass acting as a reference/counter electrode. Electrochemical contact between the two electrodes is made possible by a thin electrolyte layer maintained behind an oxygen-permeable membrane pulled over the tip and held in place with an o-ring.

(b)   UME oxygen sensor
The basis of the electrode is a 25 µm diameter Pt wire sealed in glass by the procedure described in Section 6.3.1 and elsewhere (8). For use in SECM, the electrode is sharpened to a tip using sandpaper to reduce the RG to values of 3–4. It is important that a thin membrane can be pulled tightly over the tip without tearing, so care must be taken during sharpening that the glass edges remain relatively smooth. After sharpening, a layer of silver paint (GC Electronics) is applied to the outside of the glass from the tip to approximately two-thirds of the length of the electrode. The electrode is placed in a 110 °C oven for 1 h to evaporate the solvents from the silver paint solution. Contact is made to the silver layer by coiling a wire around the body of the electrode and then painting over the wire with
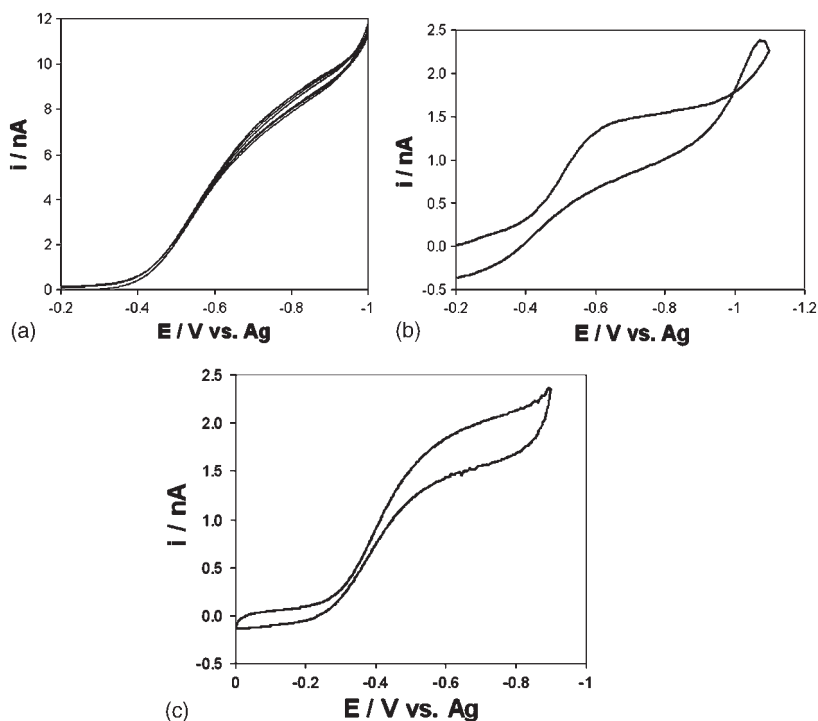
Figure 6.3.9.2 (a) Typical CV (scan rate 0.2 V sec^{-1}) for the reduction of oxygen in air-saturated 0.2 M pH 7 PBS at a bare 25 μm Pt disk–Ag ring UME, after 10 min continuous cycling; (b) CV (scan rate 0.2 V sec^{-1}) for the reduction of oxygen in air-saturated 0.2 M NaNO$_3$ solution for 25 μm Pt disk–Ag ring UME covered with 10 μm thick HDPE membrane containing drop of 0.2 M pH 7 PBS electrolyte; (c) CV (scan rate 0.2 V sec^{-1}) for the reduction of oxygen in air for 25 μm Pt disk–Ag ring UME covered with a 10 μm thick HDPE membrane containing drop of 0.2 M pH 7 PBS electrolyte. [Reprinted with permission from M. Carano, K. B. Holt, A. J. Bard, *Anal. Chem.* **74**, 5071 (2003). Copyright 2003. The American Chemical Society.]

silver paint. The electrode is left overnight in the oven to ensure all solvents are evaporated from the silver paint. Before use, the tip is polished thoroughly with 1, 0.3 and 0.05 μm alumina to remove any silver paint in contact with the Pt disk working electrode.

The most important factor in operation of an oxygen electrode is that a reproducible limiting current for oxygen reduction is obtained which does not deteriorate over time. For this reason, reproducible and stable cyclic voltammograms (CVs) for the bare electrode should be obtained in solution before the membrane electrode is constructed. Repeated cycling in the oxygen reduction region, from 0 V to −1.2 V vs. Ag/AgCl should result in a stable oxygen reduction current after 20 min, as shown in Figure 6.3.9.2a. Formation of surface oxides by electrochemical oxidation should be avoided. Typically, oxygen reduction currents of ~10 nA should be obtained for a 25 μm diameter disk electrode in an air-saturated solution (oxygen concentration = 0.27 mM, $D_s = 2 \times 10^{-5}$ cm^2 sec^{-1}).

(c)   Electrolyte

Any inert aqueous electrolyte solution is suitable for use in a Clarke electrode (4–6). There may be some benefits to using a buffered electrolyte solution because the product of the four-electron reduction of oxygen is the hydroxide ion, which causes a localized shift in pH at the electrode surface during use. However, satisfactory behavior is obtained using unbuffered solutions.

The electrolyte layer should be reduced to the smallest possible thickness, dictated by the roughness of the tip surface and the stretching of the membrane. However, the layer should not be too thin, as it is essential to maintain good electrochemical contact between the working and reference electrodes and also to allow the efficient removal of the hydroxide ion products from the surface of the cathode. The thickness of the electrolyte layer may be estimated by adding a redox active species to the electrolyte layer and performing SECM approach curves (see Chapter 12) to an insulator. An estimate of electrolyte layer thickness of 20–60 μm was obtained for a typical Clarke UME using this technique (7).

The lifetime of the electrolyte layer, that is the time before the composition changes due to the build up of hydroxide ions, depends on the rate at which oxygen is reduced. Probes with cathodes of UME dimensions, producing currents in the nA range, will typically have a longer electrolyte life than probes using cathodes of macro-dimensions, with a similar electrolyte thickness. In this case, it was found that the Clarke UME behaved reproducibly, without changing the membrane or electrolyte, for up to 8 h. If deactivation begins to occur, or if the oxygen reduction current becomes unstable, then the membrane and electrolyte layer should be replaced and the Pt electrode repolished.

(d)   Membrane

Membranes suitable for use in a Clarke electrode must be readily permeable to oxygen, but not to species that interfere with the oxygen reduction process. They should also be largely nonpermeable to water molecules so that the integrity of the electrolyte layer is maintained when used in the gas phase. Typical membrane materials used for Clarke electrodes include polytetrafluoroethylene (PTFE), polyethylene, polystyrene, collodion and polyvinyl chloride (4, 5). Thicknesses generally range from 10 to 50 μm. For the Clarke UME, a 10 μm thick high density polyethylene (HDPE) membrane was used, as it is commonly available, being the constituent of most supermarket plastic bags. A square of 30 mm × 30 mm was cut and a drop (0.5–1 μL) of electrolyte placed in the center. The tip was placed in contact with the electrolyte drop and the membrane pulled around the tip and secured using a rubber o-ring. The membrane must be pulled tightly against the surface of the working electrode; however care must be taken not to tear the membrane during this procedure. The solution and gas-phase CVs for oxygen reduction in air-saturated solution and in air should then be recorded to ensure the integrity of the membrane.

The response time, τ, of the electrode is the time taken for 99% of the current change on alteration of oxygen concentration and can be calculated according to the equation (5):

$$\tau = 0.53 z_m^2 / D_m \qquad\qquad (6.3.9.1)$$

where z_m is the thickness of the membrane and D_m is the diffusion coefficient of the oxygen through the membrane. Assuming a 10 μm thick membrane, with $D_m = 1 \times 10^{-7}$ cm^2 sec^{-1}
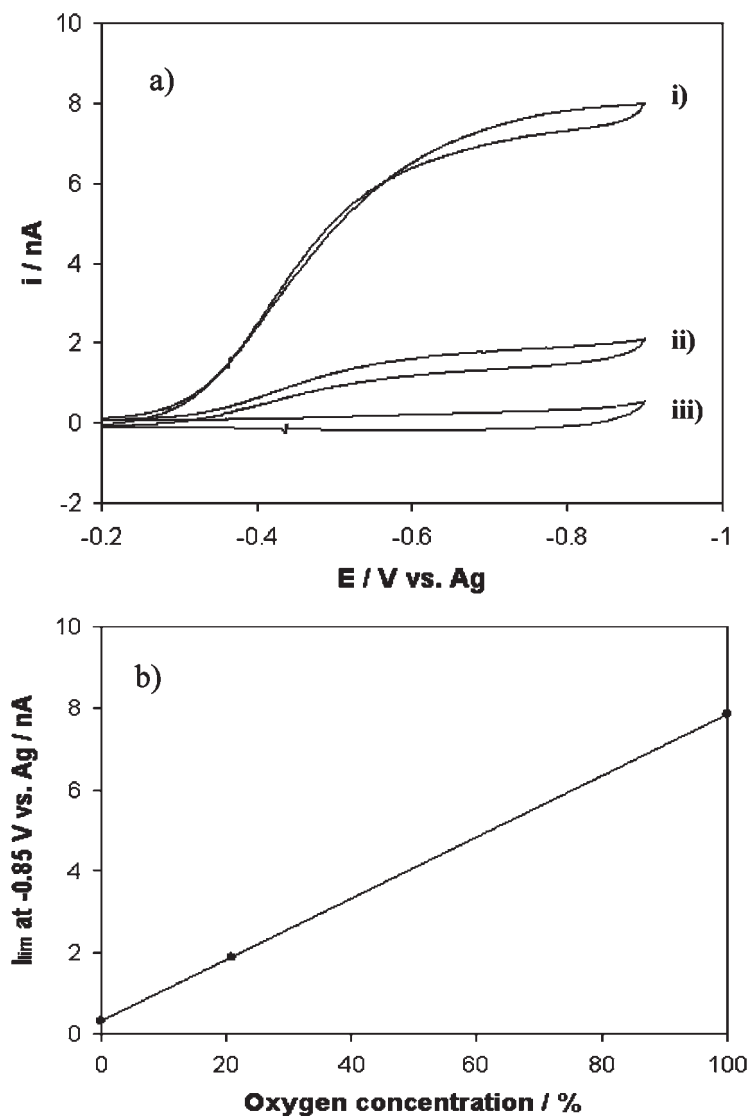
Figure 6.3.9.3   (a) Cyclic voltammograms (scan rate 0.05 V sec^{-1}) in the gas-phase for the reduction of oxygen at 25 μm Pt disk–Ag ring UME with 10 μm thick HDPE membrane and 0.1 M pH 7 PBS electrolyte in: (i) 100% oxygen; (ii) air (20.9% oxygen); and (iii) argon (0% oxygen). (b) Calibration plot for the relationship between tip current at −0.85 V and gas-phase oxygen concentration for a 25 μm Pt disk–Ag ring UME with 10 μm thick HDPE membrane and 0.1 M pH 7 PBS electrolyte. [Reprinted with permission from M. Carano, K. B. Holt, A. J. Bard, *Anal. Chem.* **74**, 5071 (2003). Copyright 2003. The American Chemical Society.]

in the gas phase, a value of $\tau = 5$ sec is obtained. In contrast, the UME response time without a membrane is ~70 ms, as given by the expression $\tau = r^2/D_s$, where r is the radius of the electrode. The increase in response time for the Clarke UME should be taken into consideration for time-dependent applications.

6.3.9.3   *Typical electrochemical behavior of Clarke UME*

If the membrane is pulled tightly against the electrode and there are no holes, a CV similar to that in Figure 6.3.9.2b should be obtained for a Clarke UME, in air-saturated solution ($[O_2] = 0.27$ mM). Compared with the CV obtained without a membrane, in the same solution (Figure 6.3.9.2a), the oxygen reduction current is smaller, due to the reduced diffusion coefficient of oxygen through the membrane. For a 25 μm disk electrode with a 10 μm thick HDPE membrane, limiting currents of 1.5–2 nA are typical for oxygen reduction in an air-saturated solution. This corresponds to a diffusion coefficient, $D_{m,s}$, for oxygen through the membrane in solution, of 1×10^{-6} cm² sec⁻¹. The exact value of the limiting current will vary according to the tightness of the membrane and thickness of the electrolyte layer, but should be of this order. Currents closer to 10 nA indicate a hole in the membrane, or that the membrane is too loose.

Figure 6.3.9.2c shows a typical CV for a Clarke UME in air. The limiting current is ~2 nA, corresponding to diffusion coefficient of oxygen through the membrane in the gas phase, $D_{m,a}$, of 1×10^{-7} cm² sec⁻¹. Limiting currents of the order of 10 nA indicate that diffusion through the membrane is not rate-limiting and that the membrane is too loose, or has a hole. The limiting currents obtained indicate that different diffusion coefficients are obtained for oxygen diffusion through the HDPE membrane in solution and in the gas phase. Diffusion of oxygen through the membrane is actually faster when the electrode is used in the solution phase, which may be attributed to water incorporation into the membrane polymer matrix (9). It is therefore important to calibrate the electrode according to the medium in which it will be used. Figure 6.3.9.3a shows typical oxygen reduction CVs obtained for the Clarke UME in the gas phase, at (i) 100% oxygen flow, (ii) 20.9% oxygen (air) and (iii) 0% oxygen (100% argon). Figure 6.3.9.3b shows the limiting current of the CVs at -0.85 V vs. Ag plotted against oxygen concentration, showing that a linear response is obtained. For use in the solution phase, the membrane electrode should be calibrated using degassed, air-saturated and oxygen-saturated solutions.

Several unique complications are encountered when using a Clarke UME as a SECM tip (7). Increased response time of the membrane UME and convection in the gas phase mean that conventional approach curves cannot be obtained. In addition, care must be taken during imaging not to touch the substrate surface with the membrane, as changes to the tip current are then observed, due to deformation of the membrane and electrolyte layer.

REFERENCES

1. C. Lee, J. Kwak, A. J. Bard, *Proc. Natl. Acad. Sci. USA*. **87**, 1740 (1990).
2. B. R. Horrocks, G. Wittstock, in *Scanning Electrochemical Microscopy*, A. J. Bard, M. V. Mirkin, Eds., Marcel Dekker: New York, 2001, p. 490.
3. L. C. Clark, *T. Am. Soc. Art. Int. Org*. **2**, 41 (1956).

4. M. L. Hitchman, in *Measurement of Dissolved Oxygen*, P. J. Elving, J. D. Winefordner, Eds., I. M. Kolthoff, Ed. Emeritus, John Wiley & Sons: New York, 1978.

5. I. Fatt, *The Polarographic Oxygen Sensor: Its Theory of Operation and Its Application in Biology, Medicine and Technology*, CRC Press: Cleveland, OH, 1976.

6. J. Linek, V. Vacek, J. Sinuke, P. Benes, "Measurement of Oxygen by Membrane-Covered Probes", in *Ellis Horwood Series in Analytical Chemistry*, Ellis Horwood: New York, 1988.

7. M. Carano, K. B. Holt, A. J. Bard, *Anal. Chem*. **74**, 5071 (2003).

8. A. J. Bard, F. -R. F. Fan, M. V. Mirkin, in *Electroanalytical Chemistry*, A. J. Bard, Ed, Marcel Dekker: New York, 1994; Vol. 18, pp 243–373.

9. H. Yasuda, W. Stone, *J. Polym. Sci.* **4**, 1314 (1966).

6.3.10   Nitric oxide microsensors

Youngmi Lee

Department of Chemistry, University of Tennessee, Knoxville,
TN 37996, USA

Nitric oxide (NO) had been considered nothing more than toxic gas (e.g., air pollutant) until its physiological functions were discovered in the 1980s (1). NO (enzymatically produced within mammalian cells) plays critical roles in vasodilatation (1), inhibition of platelet adhesion and activation (2), mediation of anti-tumor activities (3, 4), and neurotransmission (5). Quantitative measurement of NO at biological levels is challenging not only because biological cells generate a trace-amount of NO, but also because NO decays relatively fast to form nitrite (NO_2^-) and/or nitrate (NO_3^-) by reaction with NO scavengers (e.g., oxygen, hemoglobin)(6). Electrochemical detection with the use of a NO microsensor is advantageous for real-time quantitative analysis of NO generated from its sources (e.g., biological samples as well as synthesized materials which generate NO). The small dimension of a NO microsensor allows one to estimate the local concentration of NO in close proximity to the NO source (7). The fabrication and characterization of planar amperometric NO microsensors and electrochemical NO measurements using the NO microsensors are discussed in this section.

6.3.10.1   *Electrochemical detection of NO*

Nitric oxide can be electrochemically oxidized to nitrite and then to nitrate via a three-electron transfer reaction. The overall reaction is:

$$NO + 2H_2O \underset{k_b}{\overset{k_f}{\rightleftharpoons}} 4H^+ + NO_3^- + 3e^- \qquad (6.3.10.1)$$
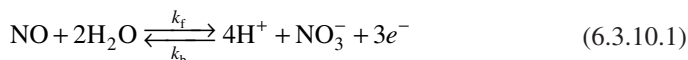
The oxidation of NO to nitrite and the subsequent oxidation of nitrite to nitrate cannot be clearly discriminated due to their similar oxidation potentials (8). To detect NO electrochemically, the complete three-electron oxidation of NO to nitrate (at ca. 0.9 V vs. Ag/AgCl) at the surface of a working electrode is accomplished (9, 10) amperometrically

by polarizing the working electrode at a constant potential sufficient for the complete oxidation of NO to nitrate. The oxidation current is directly proportional to NO concentration.

Electrochemical oxidation of NO at the surfaces of novel electrode materials (e.g., platinum, gold, glassy carbon, carbon fiber) is known to be kinetically slow. However, accelerated electron-transfer kinetics of NO oxidation have been reported for a variety of chemically modified electrodes with polymeric metalloporphyrin films (11, 12) and platinized Pt (13). These electrodes require less positive potentials for NO oxidation to nitrate (~0.65−0.75 V vs. Ag/AgCl) and generate higher current (5–10 fold) than bare metal electrodes.

To fabricate NO sensors, chemically modified electrodes are commonly covered with an additional membrane layer. This increases the selectivity for NO by cutting off other easily oxidized and interfering species. A variety of membranes (e.g., cellulose acetate (14, 15), Nafion (16)) have been used to modify the surface of working electrodes via electropolymerization or classic dip coating methods.

6.3.10.2 *Fabrication of NO microsensors*

NO sensors based on chemically modified electrodes have been reported to exhibit both enhanced electrode kinetics and larger currents compared with bare solid electrodes. Wire-type NO microsensors have also been widely used due to their larger sensing areas (17). In fact, most commercially available NO microsensors are of the wire-type. However, it is the planar configuration of sensors that is essential in gaining access to concentration profiles of analytes (especially for unstable analytes) as a function of distance from a source. Amperometric NO microsensors have been thoroughly reviewed (18). Despite the advantage of a planar configuration, few NO microsensors of this type have been reported.

Planar NO microsensors are constructed similarly to the planar metal disk microelectrodes commonly used in scanning electrochemical microscopy (SECM, see Chapter 12). The working electrodes are prepared as follows: (i) The metal (e.g., Pt) disk electrode is encased in glass and the surrounding glass sheath reduced as described in Section 6.3.1 and in reference (19). The bare metal electrode is then chemically modified to enhance the kinetics for electrochemical oxidation of NO on its surface.

For a platinized Pt-based Clark-type NO microsensor (13), the surface of a bare Pt disk electrode is electrochemically platinized by cyclic voltammetry in a platinizing solution (3% chloroplatinic acid in water). As the potential is scanned (from +0.6 to –0.35 V vs. Ag/AgCl) using cyclic voltammetry (see Chapter 11), Pt(IV) ions are electroplated on the bare Pt disk electrode to create a porous and roughened electrode surface. The platinized Pt electrode has a larger active surface area as demonstrated by the larger recorded currents and lower detection limits for NO measurements compared with bare Pt electrodes as shown in Figure 6.3.10.1.

In this Clark-type NO microsensor, a PTFE gas permeable membrane was used for selectivity specific to NO. A capillary structure with the bottom end simply covered with a thin PTFE gas permeable membrane (~30 μm thick) was used as an outer sleeve of the sensor. A platinized Pt working electrode with a Ag wire reference electrode coiled around its glass sheath was inserted into the outer sleeve filled with an internal solution (aqueous 30 mM NaCl and 0.3 mM HCl solution as recommended by Shibuki) to optimize kinetics of NO oxidation at the platinum working electrode of the NO gas sensor (20). The Pt
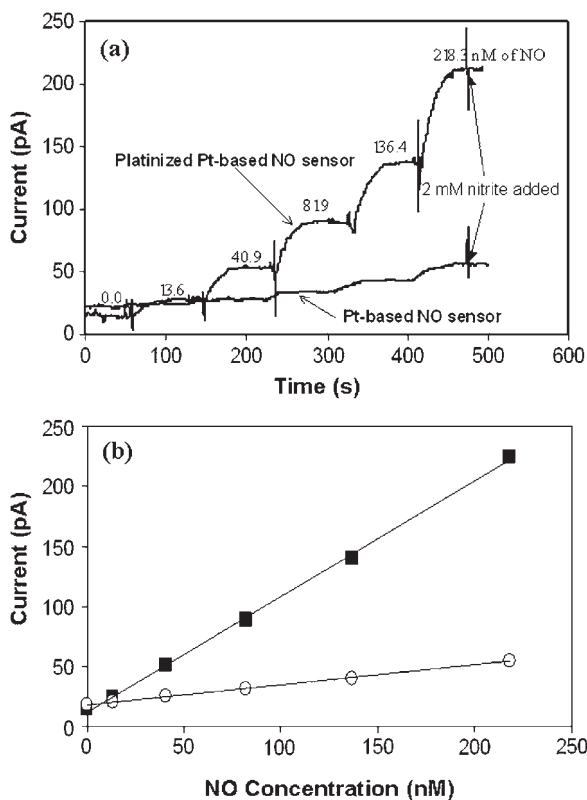
Figure 6.3.10.1 (a) Typical dynamic response curves for bare Pt-based NO microsensors and platinized Pt-based NO microsensors; (b) Corresponding calibration curves for bare Pt-based NO microsensors (■) and platinized Pt-based NO microsensors (○). [Reprinted with permission from Y. Lee, B. K. Oh, M. E. Meyerhoff, *Anal. Chem.* **76**, 545–553 (2004). Copyright 2004, American Chemical Society.]

electrode was pushed smoothly toward the PTFE membrane to cause the inner working electrode to protrude from the end plane of the outer sleeve without tearing the membrane. Therefore, the dimension of the NO microsensor is the sum of the inner electrode diameter and the membrane thickness.

Other types of planar NO microsensors include Pt microelectrodes chemically modified by electrodeposition of metalloporphyrin-like nickel(II) complexes. For example, tetrasulfonated phthalocyanine tetrasodium (NiTSPc) was electrodeposited on the bare electrode surface by repetitive cyclic voltammetry (21). Alternatively, electrode functionalization using nickel(4-*N*-tetramethyl)pyridyl porphyrin (NiTmPyP) as an electrocatalyst was also carried out by applying multiple pulses in differential pulse amperometry (22). In this case, the electrocatalyst was entrapped in a NO selective polymer network of a negatively charged acrylic acid resin that prevented access by anionic interfering species.

6.3.10.3   *Characterization of NO microsensors*

Effective NO sensors have high selectivity for NO, good sensitivity (low detection limit), linearity, fast response times, and long-term stability. These features can be evaluated using dynamic sensor response curves in which the sensor current (proportional to the concentration of NO) is recorded at a constant working electrode potential (sufficient to oxidize NO to nitrate) while a given amount of NO standard solution is successively added to the stirred deaerated background solution. The NO standard solution is prepared by bubbling NO gas into the same kind of deaerated solution as the sample background solution (assuming a concentration of NO in this saturated solution of 1.9 mM (23)).

  The sensitivity (in *A/M*) and the linear dynamic range for any given sensor are determined from calibration curves (i.e., plots of the steady-state currents from the dynamic response curves vs. the corresponding NO concentrations). Typical dynamic response curves and calibration curves are shown in Figure 6.3.10.1. Compared with sensors based on a bare Pt electrode, NO sensors based on a platinized Pt electrode have significantly improved sensitivity. The stability of a NO sensor is tested through the reproducibility of calibration curves obtained with time. Electrochemically stable sensors should generate similar and reproducible calibration curves in repeated measurements regardless of sensor operating time. The selectivity of a NO sensor is determined by monitoring sensor responses in the presence of interfering species which can be easily oxidized at the redox potential for NO. For example, in the same experimental setup used for obtaining NO dynamic response curves, sensor currents are monitored in the presence of varying amounts of possible interferents (e.g., dopamine, ascorbic acid, nitrite, etc.) instead of NO added into the solution. No (or little) response of the NO sensor to the addition of these species verify the selectivity of the sensor exclusively for NO. Lastly, response times are calculated as the time required to reach a certain percentage (e.g., 90%) of the steady-state response currents when NO concentration changes. The response time depends primarily on the thickness of the membrane covering the bare or platinized Pt electrode. Fast response times are essential for real-time detection of unstable analytes with short life-time (like NO). Therefore, it is important to fabricate NO sensors with thin gas permeable membranes.

6.3.10.4   *Bulk vs. surface NO measurements*

When the concentration of an analyte is constant (i.e., the analyte molecules are homogeneously distributed) through a sample solution, a sensor generates an identical signal (only proportional to the analyte concentration) regardless of its location in the solution. [Note that the sensor should be positioned away from the container walls so that mass transport of analytes to the sensor is unhindered.] In contrast, the position of a sensor becomes a key factor when the concentration of an analyte is highly location dependent as in measurements of NO generated from biological samples (e.g., mammalian endothelial cells) or NO releasing materials. Because the life-time of NO is relatively short, positioning an NO microsensor near the surface of its source is crucial to detecting NO before it decays. Recently, it was reported that NO-microsensor signals measured over endothelial cells were a function of the distances between the sensor and the surfaces of NO generating cells (22). In fact, a higher current was measured at a shorter distance over the same cells.

This result indicates that the distance of the sensor from the NO source plays an important role in quantitative measurements of NO.

The effect of the size of a sensor on the levels of NO detected near the surface of its source has been investigated (13). A larger sensor exhibited a higher signal even at the same distance from the surface of the same NO releasing samples. The higher signal also occurred in NO sensors having different insulating sheath sizes but with an equal electrode area. This result was attributed to a NO trapping effect where the large insulating sheath of a large sensor prevents free diffusion of NO generated from the sample, thus leading to falsely elevated NO local concentrations near the large NO sensor (relative to levels at the same distance when no sensor was present). Therefore, the sensor distance from NO sources and the sensor size and geometry must be known for accurate NO measurements near NO generating samples.

REFERENCES

1. L. J. Ignarro, G. M. Bugga, K. S. Wood, R. E. Byrns, G. Chaudhuri, *Proc. Natl. Acad. Sci. USA* **84**, 9265–9269 (1987).
2. M. W. Radomski, R. M. J. Palmer, S. Moncada, *Proc. Natl. Acad. Sci. USA* **87**, 5193–5197 (1990).
3. C. F. Nathan, J. B. Hibbs, *Curr. Opin. Immunol.* **3**, 65–70 (1991).
4. J. M. Langrehr, R. A. Hoffman, J. R. Lancaster, R. L. Simmons, *Transplantation* **55**, 1205–1212 (1993).
5. A. Ohta, H. Takagi, T. Matsui, J. Hamai, S. Iida, H. Esumi, *Neurosci. Lett.* **158**, 33–35 (1993).
6. D. D. Thomas, X. Liu, S. P. Kantrow, J. R. Lancaster, *Proc. Natl. Acad. Sci. USA* **98**, 355–360 (2001).
7. M. Feelish, J. Stamler, Eds., *Methods in Nitric Oxide Research*, John Wiley: Chichester, 1996.
8. J. T. Maloy, A. J. Bard, R. Parsons, T. Jordan, Eds., *Standard Potentials in Aqueous Solution*, Marcel Dekker: New York, 1985, Chap. 7.
9. F. Bedioui, S. Trévin, J. Devynck, *Electroanalysis* **8**, 1085–1091 (1996).
10. F. Bedioui, N. Villeneuve, *Electroanalysis* **15**, 5–18 (2003).
11. T. Malinski, Z. Taha, *Nature* **358**, 676–678 (1992).
12. S. Trévin, F. Bedioui, J. Devynck, *Talanta* **43**, 303–311 (1996).
13. Y. Lee, B. K. Oh, M. E. Meyerhoff, *Anal. Chem.* **76**, 545–553 (2004).
14. A. Meulemans, *Neurosci. Lett.* **171**, 89–93 (1994).
15. A. Cserey, M. Gratzel, *Anal. Chem.* **73**, 3965–3974 (2001).
16. F. Bedioui, S. Trévin, J. Devynck, *J. Electroanal. Chem.* **377**, 295–298 (1994).
17. A. Dickson, J. Lin, J. Sun, M. Broderik, H. Fein, X. Zhang, *Electroanalysis* **16**, 640–643 (2004).
18. F. Bedioui, N. Villeneuve, *Electroanalysis* **15**, 5–18 (2003).
19. A. J. Bard, F. -R. Fan, J. Kwak, O. Lev., *Anal. Chem.* **61**, 132–138 (1989).
20. K. Shibuki, *Neurosci. Res.* **9**, 69–76 (1990).
21. A. Pailleret, J. Oni, S. Reiter, S. Isik, M. Etienne, F. Bedioui, W. Schuhmann, *Electrochem. Commun.* **5**, 847–852 (2003).
22. S. Isik, M. Etienne, J. Oni, A. Biochi, A. Reiter, W. Schuhmann, *Anal. Chem.* **76**, 6389–6394 (2004).
23. D. R. Lide, Ed., *Handbook of Chemistry and Physics*, CRC Press, Inc.: Boca Raton, Ann Arbor, Boston, 1990–1991.

6.3.11   Glass nanopore electrodes

Bo Zhang, Gangli Wang, and Henry S. White

Department of Chemistry, University of Utah, Salt Lake City,
UT 84112, USA

6.3.11.1   *Introduction*

The truncated conical-shaped glass nanopore electrode (for brevity, hereafter referred to as a "glass nanopore electrode" or GNE) comprises a Pt microdisk electrode sealed at the bottom of a conical-shaped pore in glass (1). The radius of the pore orifice can be varied between 5 nm and 1 μm. The GNE was developed as a structurally simple platform for nanopore-based sensors and for investigating molecular transport through orifices of nanoscale dimensions.

Fabrication of a GNE, depicted in Figure 6.3.11.1, involves four general steps: (i) electrochemically etching a small diameter Pt wire to produce a sharp tip with a radius of curvature of a few nanometers; (ii) sealing the sharpened Pt tip into a glass capillary; (iii) polishing the capillary until a Pt nanodisk is exposed; and (iv) electrochemically etching the exposed Pt to produce a truncated cone-shaped nanopore in glass, the bottom of the pore defined by a Pt microdisk electrode. Each step can be performed in an electrochemical laboratory without any specialized equipment.

Owing to the conical shape of the pore, transport of redox molecules from the bulk solution to the electrode surface, Figure 6.3.11.2, is largely determined by the solution resistance in vicinity of the pore orifice (2). This geometry-based localization of the pore resistance to the orifice, originally described by Martin and coworkers (3, 4), suggests that transport selectivity can be achieved by chemical modification of the interior glass surface near the pore orifice. Two additional advantages are associated with the conical shape
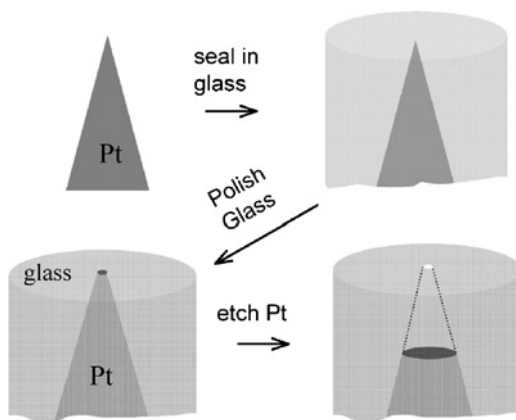
Figure 6.3.11.1   Fabrication of a GNE.
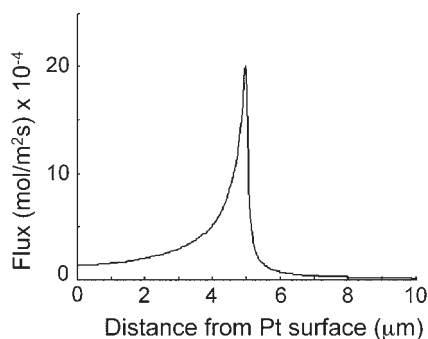
Figure 6.3.11.2 Flux as a function of position at a GNE. Note that the flux reaches a maximum value at the pore orifice, rather than at the electrode surface. This behavior is a result of the diffusion resistance being localized at the pore orifice (5).

pore. First, higher ionic conductance can be achieved with conical-shaped pores relative to straight cylindrical pores, without sacrificing the ability to localize the resistance to the pore orifice. Second, the steady-state flux of molecules (or ionic conductivity) in a conical-shaped pore *is independent of the pore depth* for pores that have a depth $>20\times$ the orifice radii (2). This characteristic is advantageous in the fabrication of nanopores. As with other types of micro- and nanometer-scale electrodes, the GNE can be used for quantitative measurements in highly resistive solution without suffering from prohibitive Ohmic potential losses (5).

6.3.11.2 Fabrication (6)

Fabricating a nanopore in glass, Figure 6.3.11.1, is primarily limited by the initial sharpness of the Pt tip and the ability to expose a very small Pt disk by polishing the glass.

(a) Pt tip preparation

A 25-µm diameter Pt hard wire (Alfa-Aesan, 99.95%), about 4 cm in length, is attached to a stiff W wire using Ag conductive epoxy. The W/Pt wire is then carefully inserted into a glass capillary, leaving ~2 cm of the Pt wire out of the capillary. The end of the Pt wire (~1 cm) is immersed vertically into a 15% $CaCl_2$ solution prepared from a 1:1 (v/v) mixture of H_2O and acetone and an ac voltage of 3 V is applied between the Pt tip and a larger Pt wire, resulting in vigorous bubbling at the Pt tip. The ac voltage is removed as the bubbling ceases, indicating complete etching of the wire to the solution/air interface. The sharpened Pt tips were cleaned by rinsing in H_2O, EtOH, and piranha solution. Tips prepared by this method were found by transmission electron microscopy to have radii of curvature of ~50 nm. The tips were further sharpened by electropolishing in dilute H_2SO_4 using the procedure described by Libioulle *et al.* (7). The etched Pt tip is inserted into 0.1 M H_2SO_4 solution and positive 15 V pulses (vs. a large Pt electrode) of 16 µs duration were applied using a homemade waveform generator at a repeating frequency of 4 kHz for ~1 sec. A −1.1 V dc voltage is then applied to the Pt wire for ~60 sec to reduce any remaining surface oxide. This two-step electropolishing process is repeated three times. Pt tips
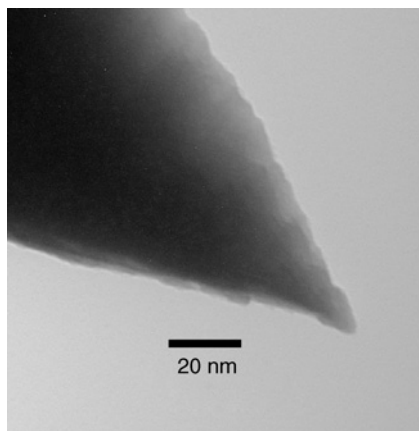
Figure 6.3.11.3   Sharpened Pt wire with ~2 nm tip radius (8).

with apex radii less than 20 nm, Figure 6.3.11.3, as measured by transmission electron microscopy, are obtained by this method.

(b)   Sealing the Pt tip in glass

Soda–lime (Warner Instruments Inc., i.d. = 0.75 mm; o.d. = 1.65 mm) and Pb-doped Corning 8161 glass (Warner Instruments Inc., i.d. = 1.10 mm; o.d. = 1.50 mm) capillaries were chosen based on their low softening temperature (700 and 604 °C, respectively), electrical properties, and thermal expansion coefficients (6, 8). The softening temperatures of these glasses are ~1100 °C lower than the melting point of Pt (1769 °C), allowing the Pt tip to be sealed without melting. Following step (i), the W/Pt wire is pulled back into the capillary, leaving ~5 mm of glass extending past the Pt tip. The glass capillary is inserted into the center of a ceramic tube without touching the tube, and the outside of the ceramic tube is heated using a H_2-O_2 torch. During heating, the glass capillary is rotated slowly by hand, allowing the softened glass to collapse around the end of the sharpened Pt wire. Approximately 3 mm of solid glass extends past the end of the Pt tip.

(c)   Exposing the Pt nanodisk

The glass-sealed Pt electrodes are sanded using 400, 800, 1200 grit papers until the glass gap between the Pt tip and its mirror image, viewed under an optical microscope (40×) is less than ~1 μm. The electrode is then polished on microcloth wetted with an aqueous slurry of 50 nm aluminum oxide power (Alfa Aesar) containing 0.1 M KCl. An electrical continuity measurement employing a simple electrical circuit is used to determine when the dc resistance between the W wire extending from the top of the capillary and the wetted polishing cloth decreased below ~2 GΩ (8). Electrode radii (a) are determined at this point by measuring the diffusion-limited voltammetric current (i_d) for the oxidation of 5 mM ferrocene (Fc) in CH_3CN, using the equation $i_d = 4nFDC^*a$, where n is the number of electrons transferred, F is Faraday's constant, and D is the diffusion coefficient of Fc (2.4×10^{-5} cm^2 sec^{-1}). An example is shown in Figure 6.3.11.4. For larger electrodes ($a > 75$ nm), the electrochemical measurement yields values that are within 20% of values
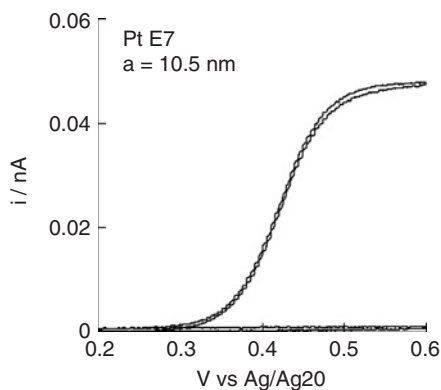
Figure 6.3.11.4 Voltammetric response of a 10.5-nm radius Pt nanodisk electrode corresponding to the oxidation of ferrocene in acetonitrile. Also shown is the $i-V$ response prior to exposing the Pt disk.

determined by scanning electron microscopy (SEM). The radii of smaller nanodisks are difficult to measure by SEM due to surface charging of the glass surface.

(d) Etching the Pt disk to create a pore

The Pt surface of the nanodisk electrode is electrochemically etched in a 15% $CaCl_2$ solution (pH ~ 5.5) with the entire cell placed in an ultrasonic bath to increase the rate of transport of the etching products out of the pore. A 5 V ac voltage is applied between the Pt nanoelectrode and a Pt wire counter. Large nanodisk electrodes (>100 nm) required significantly shorter etching times (10–20 sec) than smaller nanodisk electrodes (<50 nm, 5–20 min) to generate a pore in the glass with a depth at least 10× the pore orifice radius. The electrode is then rinsed with water.

6.3.11.3 Characterization of GNEs (2)

Determination of the GNE geometry requires experimental measurement of at least three of the four geometrical parameters shown in Figure 6.3.11.5: the pore depth (d), orifice radius (a), microdisk radius at the pore base (a_p), and the pore half-cone angle (θ).

(a) Pore orifice radius

The value of a is also equal to the radius of the Pt disk prior to etching the Pt to generate the pore. The disk radius is determined by measuring the steady-state diffusion-limited current in a solution containing millimolar concentrations of a redox-active molecule. The accuracy in determining a based on i_d depends on whether the geometry of the pore walls after etching faithfully reproduces the shape of the original Pt wire surface. Scanning electron microscopy images have shown that the orifice radius is within 20% of the original Pt disk radius after etching the Pt.

(b) Half-cone angle

Values of θ are determined to within 1° by optical and electron microscopy of the etched Pt wire prior to sealing it in glass. The angle θ is constant except at the very apex of the sharpened wire. Limitations of a varying θ near the tip of the wire have been discussed (2).
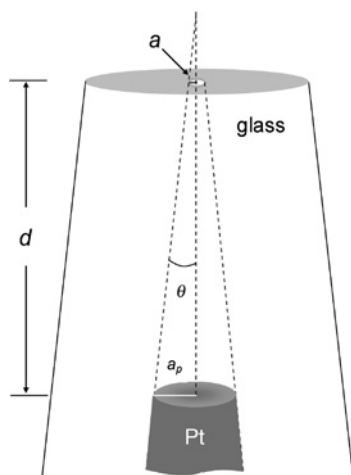
Figure 6.3.11.5   Geometrical parameters of a GNE (2).

(c)   Radius of Pt disk at the bottom of the pore
At sufficiently high scan rates in a voltammetric experiment, the current becomes limited by planar diffusion of redox molecules initially present in the pore and adjacent to the Pt surface. The voltammetric response of the GNE is identical to that of a shielded macroscopic planar electrode in this limit (2). The value of a_p is determined from the slope of a plot of the voltammetric peak current, i_p, versus the square root of scan rate, $v^{1/2}$, according to the expression:

$$i_p = 2.69 \times 10^5 \, n^{3/2} D^{1/2} C^* v^{1/2} \pi a_p^2 \tag{6.3.11.1}$$

(d)   Pore depth
A value of d is obtained by geometry if a, θ, and a_p are previously measured by the above methods. Alternatively, at intermediate scan rates, the GNE behaves as a thin-layer electrochemical cell, exhibiting symmetrical cathodic and anodic voltammetric peaks corresponding to redox molecules initially present in the pore. This thin-layer cell response is superimposed on the steady-state diffusion current (equation (6.3.11.3), presented below in Section 6.3.11.4) and the peak current is approximated by:

$$i_p = i_{lim} + \frac{n^2 F^2 v}{4RT} C_b V_p \tag{6.3.11.2}$$

where R is the gas constant, T is absolute temperature, and V_p is the pore volume. If any pair of geometrical parameters is known (e.g., θ and a_p), then d can be computed from the value of V_p obtained from a linear plot of i_p versus v.

6.3.11.4   Voltammetric response of GNEs

The transient and steady-state voltammetric responses of GNEs have been analyzed by simulation, theory, and experiment (1, 2). An approximate analytical expression for the diffusion-limited steady-state current at a GNE, $i_{\lim}$, is given by equation (6.3.11.3):

$$i_{\lim} = 4nFaDC^* \left[\frac{(1 + (d/a)\tan\theta)}{(4d/a\pi) + (1 + (d/a)\tan\theta)} \right] \qquad (6.3.11.3)$$

where all variables and constants are defined above. Equation (6.3.11.3) is derived from the general definition of the limiting current, $i_{\lim} = nFC^*/R_{MT}$, where R_{MT} is the steady-state mass-transfer (diffusion only) resistance comprising the internal pore resistance, R_{in}, and the external solution resistance, R_{ex}. The latter is equivalent to the mass-transport resistance at a disk electrode, $R_{ex} = 1/4Da$. For small cone angles, $\theta < 20°$, the pore resistance can be approximated as $R_{in} = d/Da\pi(a + d\tan\theta)$ with reasonable accuracy ($<5\%$ error), which, when combined with the above expression for R_{ex} and R_{MT}, yields equation (6.3.11.3).

In the limit $d \to 0$, the GNE geometry reduces to that of a disk electrode of radius a and equation (6.3.11.3) reduces to:

$$i_{\lim}^{d=0} = 4nFaDC^*, \qquad (6.3.11.4)$$

the well-known expression for the steady-state limiting current at a disk-shaped electrode. Conversely, in the limit $d \to \infty$, corresponding to a very deep pore, equation (6.3.11.3) reduces to:

$$i_{\lim}^{d \to \infty} = 4nFaDC^* \left[\frac{\tan\theta}{4/\pi + \tan\theta} \right] \qquad (6.3.11.5)$$

A key prediction of equation (6.3.11.5) is that $i_{\lim}^{d \to \infty}$ is independent of d, a consequence of the radial divergent flux within a conical-shaped pore. For typical values of θ obtained in preparing GNEs (~10°), the current (equation (6.3.11.1)) asymptotically approaches the depth-independent value (equation (6.3.11.5)) when the pore depth is at least 20× greater than the radius of the pore orifice. For instance, for a pore with a 20-nm radius orifice, any pore depth greater than ~400 nm will yield a similar value of the steady-state limiting current. Experimental measurements of $i_{\lim}$ as a function of d confirm the behavior predicted by the above set of equations (2).

Figure 6.3.11.6 shows typical behavior of a GNE with a 74-nm radius orifice (including the voltammetric response of the nanodisk electrode *prior to* etching the Pt to create a pore). Etching the pore to micrometer depths results in an ~75% decrease in the steady-state current relative to the unetched nanodisk electrode, in quantitative agreement with equation (6.3.11.5) using the measured value of $\theta \sim 10°$. This current reflects the rate atwhich ferrocene diffuses across the pore orifice (mol sec^{-1}). When the same GNE is re-etched to create an even deeper pore, the voltammetric response displays a "thin-layer" shape, corresponding to oxidation of the ferrocene molecules initially within the pore. The thin-layer response of the GNE can be exploited to detect very small numbers of
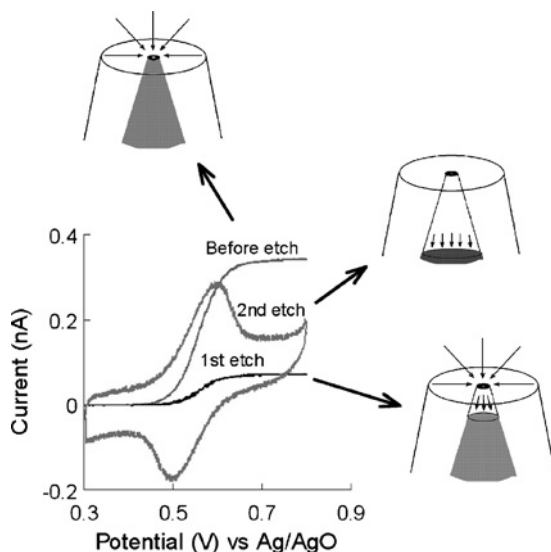
Figure 6.1.11.6   Voltammetric response of a GNE in a 5 mM ferrocene/acetonitrile solution as a function of pore depth. The radius of the Pt nanodisk prior to etching is 74 nm. All curves were recorded at 10 mV sec^{-1}.

molecules contained within the pore. Finite-element simulations of the transient voltammetric response have also been reported and are in good agreement with experimental observations (1, 2).

REFERENCES

1. B. Zhang, Y. Zhang, H. S. White, *Anal. Chem.* **76**, 6229 (2004).
2. B. Zhang, Y. Zhang, H. S. White, *Anal. Chem.* **78**, 477 (2006).
3. S. Lee, Y. Zhang, H. S. White, C. C. Harrell, C. R. Martin, *Anal. Chem.* **76**, 6108 (2004).
4. E. A. Heins, Z. S. Siwy, L. A. Baker, C. R. Martin, *Nano Lett.* **5**, 824–1829 (2005).
5. Y. Zhang, B. Zhang, H. S. White, *J. Phys. Chem.* **110**, 1768 (2006).
6. The fabrication of glass GNEs is rapidly evolving at the time of this writing. The description presented here is adapted from reference (2) and from: G. Wang, B. Zhang, J. R. Wayment, J. M. Harris, H. S. White, unpublished results, University of Utah, 2006.
7. L. Libioulle, Y. Houbion, J. -M. Gilles *Rev. Sci. Instrum.* **66**, 97 (1995).
8. B. Zhang, J. Galusha, G. Wang, R. J. White, E. N. Ervin, R. Jones, C. Cauley, H. S. White, A. J. Bergren, unpublished results, University of Utah, 2006.

– 7 –

Potentiometric Ion-Selective Electrodes

Shigeru Amemiya

Department of Chemistry, University of Pittsburgh, 219 Parkman Avenue, Pittsburgh, PA 15260, USA

7.1 INTRODUCTION

Potentiometric ion-selective electrodes (ISEs) are one of the most important groups of chemical sensors. The application of ISEs has evolved to a well-established routine analytical technique in many fields, including clinical and environmental analysis, physiology, and process control. The essential part of ISEs is the ion-selective membrane that is commonly placed between two aqueous phases, i.e., the sample and inner solutions that contain an analyte ion. The membrane may be a glass, a crystalline solid, or a liquid (1). The potential difference across the membrane is measured with two reference electrodes positioned in the respective aqueous phases

reference electrode 2 ‖ sample solution | membrane | inner solution ‖ reference electrode 1

(cell 1)

Under equilibrium conditions, the measured potential (or emf of the cell), E, can be expressed as

$$E = E_I^0 + \frac{RT}{z_I F} \ln a_I^W \tag{7.1.1}$$

where z_I is the charge of the analyte ion, I, a_I^W is its activity in the sample solution, and the constant term, E_I^0, is unique for the analyte and also includes the sum of the potential differences at all the interfaces other than the membrane/sample solution interface. This well-known "Nernst" equation for ISEs represents their unique response properties, i.e., Nernstian responses, where the sensor signal, E, is proportional to logarithm of the analyte activity rather than the activity itself. The slope in an E versus $\ln a_I^W$ (or more commonly $\log a_I^W$) plot is used for identification of the analyte based on the charge. A wide range of the analyte activity can be determined because of the logarithmic dependence of the

Handbook of Electrochemistry
Edited by C.G. Zoski

potential on the analyte activity. Moreover, a very low analyte activity can be determined only by measuring the potential difference rather than detecting a very small signal. A well-known example is a glass membrane pH electrode, which has a detection limit of down to 10^{-12} M for H^+.

How can we create such a membrane for a wider range of analytes? The most successful approach is to use ion-selective liquid membranes (2, 3). The liquid membranes are hydrophobic and immiscible with water, and most commonly made of plasticized poly(vinyl chloride). The selectivity is achieved by doping the membranes with a hydrophobic ion (ionic site) and a hydrophobic ligand (ionophore or carrier) that selectively and reversibly forms complexes with the analyte (Figure 7.1). Whereas the technique has been well established experimentally since the 1960s, it is only recently that the response mechanisms are fully understood. In this chapter, principles of liquid membrane ISEs will be introduced using simple concepts of ion-transfer equilibrium at water/liquid membrane interfaces. Non-equilibrium effects on the selectivity and detection limits will also be discussed. This information will enable practitioners of ISEs to better optimize experimental conditions and also to interpret data. Additionally, examples of ISEs based on commercially available ionophores are listed. More comprehensive lists of ionophore-based ISEs developed so far are available in recent IUPAC reports (4–6).
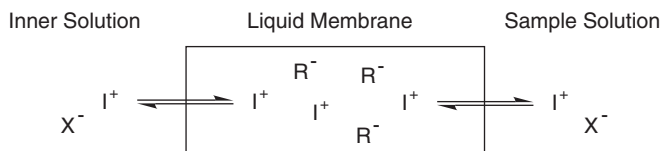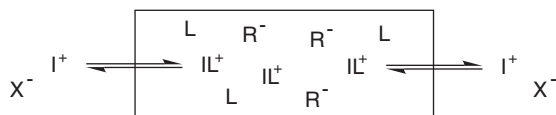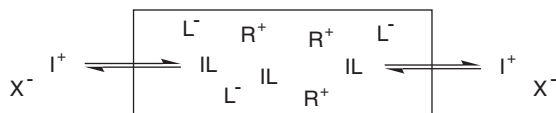
Figure 7.1   Schematic view of the equilibrium between sample, ion-selective membrane, and inner filling solution (cell 1). The cation-selective membranes are based on (A) cation exchanger (R^-), (B) electrically neutral ionophore (L) and anionic sites (R^-), and (C) charged ionophore (L^-) and cationic sites (R^+). The aqueous solutions contain an analyte cation (I^+) and its counter anion (X^-). Adapted from reference (2).

7.2 CLASSIFICATION AND MECHANISM

7.2.1 Phase boundary potential

Potentiometric responses of liquid membrane ISEs depend on a change in the phase boundary potential at the membrane/sample solution interface, which is controlled by bulk equilibrium (7). When an ion, i, with charge z_i is transferred across the interface between the sample and membrane phases, the ion-transfer reaction is defined as

$$i^{z_i} \text{ (membrane)} \rightleftharpoons i^{z_i} \text{ (sample)} \tag{7.2.1}$$
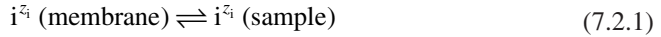
Under equilibrium conditions between the two phases, the electrochemical potentials of the ion in the sample and membrane phases, $\bar{\mu}_i^W$ and $\bar{\mu}_i^M$, respectively, is equal

$$\bar{\mu}_i^M = \bar{\mu}_i^W \tag{7.2.2}$$

which is equivalent to

$$\mu_i^{M,0} + RT \ln a_i^M + z_i F \phi^M = \mu_i^{W,0} + RT \ln a_i^W + z_i F \phi^W \tag{7.2.3}$$

where a_i^W and a_i^M are the ion activities in the sample and membrane phases, respectively, $\mu_i^{W,0}$ and $\mu_i^{M,0}$ are the standard chemical potentials of the ion in the respective phases, and ϕ^W and ϕ^M are the inner potentials in the respective phases. Rearrangement of equation (7.2.3) gives the phase boundary potential, $\Delta_W^M \phi$, as a function of the ion activities

$$\Delta_W^M \phi = \frac{RT}{z_i F} \ln \frac{k_i a_i^W}{a_i^M} \tag{7.2.4}$$

with

$$\Delta_W^M \phi = \phi^M - \phi^W \tag{7.2.5}$$

$$k_i = \exp\left[-\frac{RT(\mu_i^{M,0} - \mu_i^{W,0})}{z_i F} \right] \tag{7.2.6}$$

where k_i is the so-called single ion distribution coefficient. Equations (7.2.1) and (7.2.4) for the ion-transfer reactions are counterparts of the half reaction and the Nernst equation for redox reactions at liquid/solid electrode interfaces, respectively.

To obtain a Nernstian response to the ion, its membrane activity must be constant and independent of the sample activity so that equation (7.2.4) can be simplified to

$$\Delta_W^M \phi = \text{constant} + \frac{RT}{z_i F} \ln a_i^W \tag{7.2.7}$$

where the constant term is $(RT/z_i F) \ln(k_i/a_i^M)$. The activity term of equation (7.2.7) is the origin of the activity term of equation (7.1.1) for Nernstian responses. Also, the constant

term of equation (7.1.1) includes that of equation (7.2.7) so that, in an E versus $\log a_i^W$ plot, not only the response slope but also the intercept depends on the transferred ion, which is an expression of the ion selectivity. In any potentiometric experiment, the sample solutions of an analyte ion (primary ion) also contain its counter ions and, in most cases, its co-ions (interfering ions). Nernstian responses can be obtained when the primary ion is the only major ion that is selectively transferred across the interface between the two phases as demonstrated below.

7.2.2   Ion-exchanger-based ISEs

Since the sample solutions always contain similar concentrations of an analyte ion and its counter ions, the primary requirement for Nernstian responses is selective membrane permeability for the analyte against the aqueous counter ions. The selectivity can be obtained simply by doping a membrane with ionic sites that have a charge opposite to that of the analyte. This type of membrane electrode based on ionic sites is called ion-exchanger-based ISEs or more specifically, ionophore-free ion-exchanger-based ISEs because any liquid membrane ISE has an ion-exchange capability for Nernstian responses. Table 7.1

Table 7.1

Membrane compositions and selectivity coefficients of ion-exchanger-based ISEs

Ion	Membrane composition[a]	$\log k_{I,J}^{pot\,b}$	Method	Reference
Na^{+c}	DOS (66.15), PVC (33.40), NaTFPB (0.45)	H^+, (0.8); K^+, (0.5); Ag^+, (0); $N(CH_3)_4^+$, (1.6); Mg^{2+}, (-2.2); Ca^{2+}, (-2.2); Cu^{2+}, (-2.2); Cd^{2+}, (-2.2)	FIM	(9)
Cl^{-c}	oNPOE (66), PVC (33), TDDMACl (1)	F^-, -1.8; Br^-, 1.3; I^-, 3.3; HCO_3^-, -1.4; NO_2^-, 1.1; NO_3^-, 2.0; SCN^-, 3.8; ClO_4^-, 5.1; acetate$^-$, -1.5; SO_4^{2-}, -1.6	SSM	(10)

[a]The weight percentages of ionic site, plasticizer, and PVC are given in parentheses.
[b]Unbiased selectivity coefficients are given in parentheses.
[c]The selectivity coefficients were determined for another primary ion (Pb^{2+} and NO_2^- for the cation- and anion-exchange electrodes) and then recalculated for the present ion.
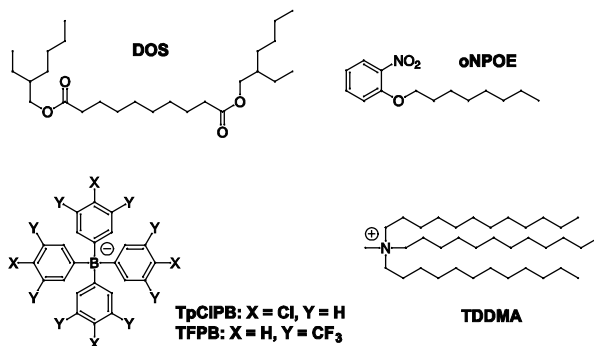
lists examples of the electrodes and the structures of representative ionic sites and membrane plasticizers. Cation selectivity against anions can be obtained by doping a membrane with an analyte salt of a tetraphenylborate derivative as an anionic site, whereas anion selectivity can be obtained by doping a membrane with an analyte salt of a lipophilic tetraalkylammonium as a cationic site.

When a membrane doped with anionic sites is in contact with an aqueous solution of I^+X^-, I^+ is exchanged across the interface (Figure 7.1A). The aqueous counter ion is excluded from the membrane phase because of the "common ion" effect. Transfer of an aqueous counter ion into the membrane phase must be followed by simultaneous transfer of the analyte so that the electroneutrality is maintained in the two phases. The salt-extraction process can be defined as

$$I^+(\text{water}) + X^-(\text{water}) \rightleftharpoons I^+(\text{membrane}) + X^-(\text{membrane}) \tag{7.2.8}$$

Also, the equilibrium reaction can be quantified by salt-partitioning constant, K_P, as defined by

$$K_P = k_I k_X = \frac{a_I^M a_X^M}{a_I^W a_X^W} \tag{7.2.9}$$

The high membrane concentration of the analyte as a counter ion of the ionic sites shifts the equilibrium such that the aqueous counter ion is excluded from the membrane. Thus, the concentration of the aqueous anion in the cation-selective membrane doped with anionic sites is negligible in the charge balance in the membrane phase

$$[I^+]_M = [R^-]_M + [X^-]_M \approx [R^-]_M \tag{7.2.10}$$

where brackets indicate the membrane concentration of the species. Since the membrane concentration of the analyte is fixed by the concentration of the anionic site, the phase boundary potential given by equation (7.2.4) depends only on the analyte activity in the sample solution, resulting in a Nernstian response.

While ion-exchanger-based ISEs provide a very high selectivity against the counter ions of an analyte, a drawback is the lack of the selectivity against the co-ions. The selectivity against interfering co-ions is primarily determined by hydrophobicity of the ions as quantified by k_i. It is well known that selectivity of anion-exchanger-based ISEs among inorganic anions follows so-called Hofmeister series

$$ClO_4^- > SCN^- > I^- > NO_3^- > Br^- > Cl^- > HCO_3^- > SO_4^{2-} > F^- \tag{7.2.11}$$
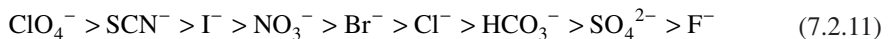
This selectivity sequence means that, for example, Cl^- in the membranes can be easily replaced with more hydrophobic anions. When it is completely replaced with another anion, the phase boundary potential becomes independent of the sample activity of Cl^- and is determined by that of the interfering anion. The ion-exchange equilibrium is defined as

$$X^-(\text{membrane}) + Y^-(\text{water}) \rightleftharpoons X^-(\text{water}) + Y^-(\text{membrane}) \tag{7.2.12}$$
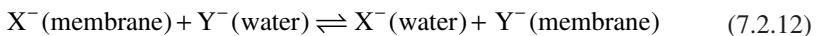
with the ion-exchange equilibrium constant, K_E

$$K_E = \frac{k_Y}{k_X} = \frac{a_X^W a_Y^M}{a_X^M a_Y^M} \tag{7.2.13}$$

When Y^- is more hydrophobic than X^-, $k_Y > k_X$, so that K_E is >1. In the sample solution containing both X^- and Y^-, X^- can be more easily replaced by Y^- at higher activity of Y^- and lower activity of X^-. Because of this selectivity mechanism, ion-exchanger-based electrodes were developed mostly for hydrophobic ions such as organic ions and drugs for pharmaceutical applications (8).

7.2.3 Neutral-ionophore-based ISEs

Selectivity of ion-exchanger-based ISEs can be modified by adding an electrically neutral ionophore to the membranes (Figure 7.1B). Examples of ISEs based on commercially available neutral ionophores are summarized in Table 7.2. The neutral-ionophore-based electrodes were first developed using an antibiotic such as valinomycin as a K^+-selective ionophore (K^+-1). In addition to naturally occurring ionophores, many neutral ionophores were synthesized for alkaline cations, alkaline earth cations, heavy metal ions, and inorganic anions.

When a membrane containing anionic sites is doped with a cation-selective neutral ionophore, the cationic analyte in the membrane phase forms complexes with the ionophore

$$I^+(\text{membrane}) + L(\text{membrane}) \rightleftharpoons IL^+(\text{membrane}) \tag{7.2.14}$$
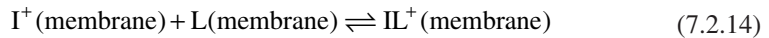
where the formation constant, β, is given by

$$\beta = \frac{a_{IL}^M}{a_I^M a_L^M} \tag{7.2.15}$$

When the formation constant is large enough and the membrane contains an excess amount of the free ionophore, the complexation reaction proceeds completely so that most analytes in the membrane are in the complexed form. Therefore, the charge balance in the membrane phase can be simplified as

$$R_T = [I^+]_M + [IL^+]_M \approx [IL^+]_M \tag{7.2.16}$$

where R_T is the total concentration of ionic sites (anionic sites in this example). Also, combination of the mass balance equation for the ionophore with equation (7.2.16) gives the membrane concentration of the free ionophore as

$$[L]_M = L_T - [IL^+]_M \approx L_T - R_T \tag{7.2.17}$$

Table 7.2

Membrane compositions and selectivity coefficients of ISEs based on commercially available neutral ionophores and their complexation constants

Ion	Membrane composition[a]	$\log k_{I,J}^{pot\,b}$	Method	$\log \beta\ (n)^c$	Reference
H+	H+-1 (1), PVC (30), oNPOE (69), KTpClPB (70)	Li+, −6.9; Na+, −5.6	FIM	−	(13)
Li+	Li+-1 (1), oNPPE/TEHP[d] (70), PVC (28), KTpClPB (71)	H+, −2.6; Na+, −2.5; K+, −2.4; Rb+, −1.5; Cs+, −1.2; NH$_4$+, −2.4; Mg^{2+}, −4.1; Ca^{2+}, −3.8; Sr^{2+}, −3.9; Ba^{2+}, −3.7	SSM	5.33 (1)	(14)
Li+	Li+-2 (2.5), PVC (33), oNPOE (66), KTpClPB (15)	H+, −2.6; Na+, −1.9; K+, −3.2; Rb+, −3.1; Cs+, −3.8; NH$_4$+, −3.8; Mg^{2+}, −2.4; Ca^{2+}, −1.0; Sr^{2+}, −0.9; Ba^{2+}, −1.1	SSM	10.40 (1)	(15)
Na+	Na+-1 (0.66), o-NPOE (70), PVC (28), KTpClPB (50)	H+, −2.2; Li+, −2.5; K+, −2.0; Cs+, −2.1; NH$_4$+, −2.7; Mg^{2+}, −2.9; Ca^{2+}, −2.6	SSM (FIM)[e]	10.27 (1)	(16)
Na+	Na+-2 (1), o-NPOE (65), PVC (33), KTpClPB (11)	H+, −0.8; K+, −1.5; Mg^{2+}, −3.8; Ca^{2+}, −1.6	SSM	10.91 (2)	(17)
K+	K+-1 (1.2), DOS (65), PVC (33), NaTFPB (60)	Na+, −4.1 (−4.5); Mg^{2+}, −5.2 (−7.5); Ca^{2+}, −5.0 (−6.9)	SSM	10.10 (1)	(18)
K+	K+-2 (2), oNPOE (33), PVC (65), KTpClPB (70)	Li+, −3.8; Na+, −3.2; NH$_4$+, −2.1; Mg^{2+}, −5.0; Ca^{2+}, −4.5	SSM	10.04 (1)	(19)
Cs+	Cs+-1 (0.4), PVC (33.2), oNPOE (66.3), KTpClPB (62)	Li+, −3.3; Na+, −2.1; K+, −3.2; Rb+, −0.8; Rb+, −1.0; Mg^{2+}, −3.0; Ca^{2+}, −3.5	SSM	−	(20)
NH$_4$+	NH$_4$+-1 (3), PVC (30), BEHS (66.5), KTpClPB (25)	Li+, −3.5; Na+, −2.4; K+, −1.0; Rb+, −1.5; Cs+, −2.4; Mg^{2+}, −4.0; Ca^{2+}, −3.8; Sr^{2+}, −3.6; Ba^{2+}, −4.0	SSM	−	(21)
Mg^{2+}	Mg^{2+}-1 (1), PVC (33), oNPOE (65), KTpClPB (50)	H+, +6.5; Li+, −0.9; Na+, −2.3; K+, −1.2; Rb+, −0.6; Cs+, +0.3; Ca^{2+}, +1.5; Sr^{2+}, +0.3; Ba^{2+}, +0.3	SSM	13.84 (3)	(22)
Mg^{2+}	Mg^{2+}-2 (2), oNPOE (66), PVC (32), KTpClPB (100)	Li+, −3.6; Na+, −3.0; K+, −1.4; Rb+, −0.5; Cs+, +0.6; NH$_4$+, −2.0; Ca^{2+}, −2.5; Sr^{2+}, −2.9; Ba^{2+}, −2.3	SSM	−	(23)
Ca^{2+}	Ca^{2+}-1 (0.46), oNPOE (66), PVC (33), NaTFPB (50)	Na+, −3.4 (−8.3); K+, −3.8 (−10.1); Mg^{2+}, −4.6 (−9.3)	SSM	29.2 (3)	(24)

(*Continued*)

Table 7.2 (Cont.)

Ion	Membrane composition[a]	$\log k_{I,J}^{\text{pot}\,b}$	Method	$\log \beta\ (n)^c$	Reference
Ca²⁺	Ca²⁺-2 (1), oNPOE (64), PVC (34.5), KTpClPB (69)	H⁺, −4.4; Li⁺, −2.8; Na⁺, −3.4; K⁺, −3.8; Mg²⁺, −4.4	SSM	24.54 (2)	(25)
Ca²⁺	Ca²⁺-3 (2), oNPOE (66), PVC (32), KTpClPB (100)	H⁺, −3.7; Li⁺, −4.1; Na⁺, −4.1; K⁺, −4.5; Rb⁺, −4.2; Cs⁺, −4.0; NH₄⁺, −4.2; Mg²⁺, −5.0; Sr²⁺, −1.0; Ba²⁺, −2.0	SSM	−	(23)
Ba²⁺	Ba²⁺-1 (1), PVC (33), oNPOE (66), KTpClPB (65)	H⁺, −1.6; Li⁺, −3.2; Na⁺, −2.7; K⁺, −2.7; Rb⁺, −2.9; Cs⁺, −2.9; NH₄⁺, −3.2; Mg²⁺, −7.8; Ca²⁺, −1.8; Sr²⁺, −0.2	SSM	−	(26)
Cu²⁺	Cu²⁺-1 (1.2), PVC (57.2), oNPOE (34.3), KTpClPB (24)	Na⁺, −2.7; K⁺, −2.3; Mg²⁺, −3.6; Ca²⁺, −3.6; Sr²⁺, −3.7; Mn²⁺, −2.5; Ni²⁺, −3.2; Co²⁺, −4.0; Zn²⁺, −2.2 Cd²⁺, −4.4; Pb²⁺, −0.7	FIM	−	(27)
Ag⁺	Ag⁺-1 (1.1), DOS (66), PVC (32), KTpClPB (29)	Na⁺, −3.4 (−6.2); K⁺, −3.3 (−5.7); Ca²⁺, −4.0 (−8.0); Pb²⁺, −4.3 (−6.0); Cu²⁺, −4.1 (−7.7)	SSM	−	(24)
Pb²⁺	Pb²⁺-1 (1.57), DOS (66.15), PVC (33.40), NaTFPB (34)	H⁺, (−7.5); Na⁺, (−7.5); K⁺, (−6.9); Ag⁺,[f] (9.5); N(CH₃)₄⁺, (−6.5); Mg²⁺, (−13.9); Ca²⁺, (−13.1); Cu²⁺, (−4.0); Cd²⁺, (−6.3)	SSM	−	(9)
Pb²⁺	Pb²⁺-2 (1.24), DOS (66.15), PVC (33.40), NaTFPB (17)	H⁺, (4.4); Na⁺, (3.5); K⁺, (4.5); Ag⁺, (21.8); N(CH₃)₄⁺, (6.7); Mg²⁺, (−1.7); Ca²⁺, (−1.1); Cu²⁺, (0.3); Cd²⁺, (−0.3)	SSM	−	(9)
Cl⁻	Cl⁻-1 (2), DOS (65), PVC (33), TDDMACl (1)	F⁻, −5.2; Br⁻, −0.7; I⁻, −0.7; HCO₃⁻, −4.7; NO₃⁻, −2.5; SCN⁻, −0.3; ClO₄⁻, −0.2; acetate⁻, −5.2; salicylate⁻, −0.8; SO₄²⁻, −5.5; HPO₄²⁻, −5.2	SSM	−	(28)
CO₃²⁻	CO₃²⁻-1 (9.7), DOS (59.0), PVC (2 9.5), TDDMACl (13.8)	Cl⁻, −5.0; Br⁻, −3.6; NO₃⁻, −1.8; SCN⁻, 0.5; salicylate⁻, 3.6; SO₄²⁻, −5.0; HPO₄²⁻, −5.0	SSM	−	(29)

[a]The weight percentages of ionophore, plasticizer, and PVC are given in parentheses. The amount of ionic sites is in mol% relative to the ionophore.
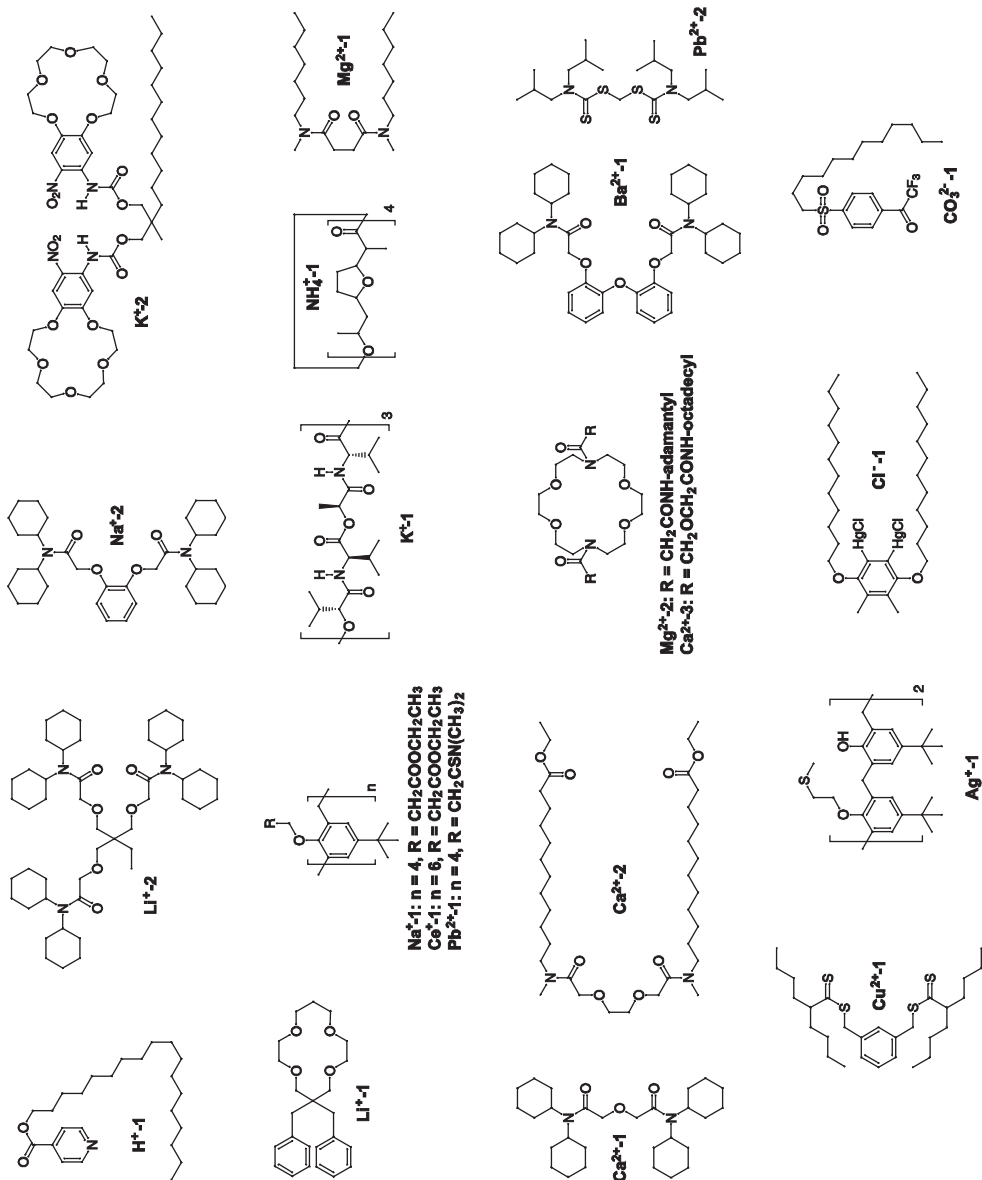[b]Unbiased selectivity coefficients are given in parentheses.
[c]Data from reference (30). n is the assumed stoichiometry.
[d]98:2 mixture of o-nitrophenyl phenyl ether and tris(2-ethylhexyl)phosphate.
[e]SSM for monocations and FIM for dications.
[f]Obtained with oNPOE.

where L_T is the total concentration of the ionophore. Since the membrane contains both free and complexed ionophores, the free analyte concentration in the membrane phase is buffered to be low and independent of the sample composition. Combination of equations (7.2.15)–(7.2.17) gives the free analyte concentration, and subsequently its activity as

$$a_I^M = \frac{\gamma_{IL}^M R_T}{\beta \gamma_L^M (L_T - R_T)} \qquad (7.2.18)$$

where γ_{LM}^M and γ_L^M are the membrane activities of the complexes and the free ionophore, respectively. The sample-independent membrane activity results in the Nernstian response to the analyte ion. Moreover, because of the complexation process, the analyte in neutral-ionophore-based membranes is more stabilized than that in ion-exchanger-based membranes. The lower free analyte activity in the membrane phase shifts the ion-exchange equilibrium (see equation (7.2.12) for anions) such that the analyte is not exchanged with an interfering ion at a lower analyte activity or at a higher interfering-ion activity in the sample solution, leading to higher selectivity for the analyte.

While selective complexation makes the membrane more permeable to the analyte ion than the co-ions, selectivity against counter ions in neutral-ionophore-based membranes is achieved by ionic sites, not by the ionophore. In fact, the ionophore–analyte complexation decreases the free analyte activity in the membrane to enhance the salt extraction into the membrane phase, which may result in counter-ion interference due to Donnan exclusion failure (7). Although the PVC matrix has inherent negative sites as an impurity (11), the concentration is so low that the anionic sites were initially introduced in cation-selective ISEs based on neutral ionophores to suppress the counter-ion interference (12).

7.2.4 Charged-ionophore-based ISEs

Another way to improve selectivity against interfering co-ions is to use electrically charged ionophores. Commercially available charged ionophores and selectivity of the ISEs based on them are listed in Table 7.3. This system appears to be an ion-exchanger-based membrane based on the ionic sites that form a complex with an analyte selectively. For example, Ca^{2+}-selective electrodes based on organophosphate compounds are well-known examples of charged-ionophore-based ISEs although they have also been called ion-exchanger-based electrodes because of the ion-exchange capability. In this case, the charged ionophore provides selectivity for Ca^{2+} against both anions and other cations simultaneously. Another important class of charged ionophores is positively charged metalloporphyrins for anions (31). For example, membranes doped with a chloride salt of Mn(III)prophyrins respond selectively to Cl^-, which is due to selective coordination of Cl^- to the positively charged metal center.

Despite the dual selectivity inherent to the charged ionophores, they have been studied much less than neutral ionophores, limiting the number of examples. This is partially because of the belief that the membranes with charged ionophores are less suited for potentiometric ISEs than those with neutral ones (32), which turned out to be wrong only recently. When a membrane is doped only with an electrically neutral complex of a

Table 7.3

Membrane compositions and selectivity coefficients of ISEs based on commercially available charged ionophores

Ion	Membrane composition[a]	$\log k_{I,J}^{pot}$	Method	Reference
H^+	H^+-2 (0.7), PVC (33), oNPOE (66), TDDMACl (50)	Li^+, -9.6; Na^+, -9.5; K^+, -9.4	FIM	(34)
Ca^{2+}	Ca^{2+}-4 (1), DOPP (66), PVC (33)	H^+, 0.2; Li^+, -1.2; Na^+, -2.0; K^+, -2.3; Rb^+, -2.2; Cs^+, -2.4; NH_4^+, -1.6; Mg^{2+}, -1.6; Ba^{2+}, -1.6; Sr^{2+}, -0.9	SSM	(35)
Ca^{2+}	Ca^{2+}-5 (1), DOS (65), PVC (33), TDDMACl (48)	H^+, 1.0; Li^+, -1.6; Na^+, -1.4; K^+, -1.1; Rb^+, -1.1; Cs^+, -1.1; NH_4^+, -0.9	SSM	(35)
Sr^{2+}	Sr^{2+}-1 (1.2), PVC (33), oNPOE (65), KTpClPB (50)	Mg^{2+}, -4.9; Ca^{2+}, -3.5; Ba^{2+}, 0.8	SSM	(36)
Cl^-	Cl^--2 (5), NPOE (90), 1-decanol (4), TDDMATpBClPB (1)[b]	Br^-, 0.3; I^-, 1.3; NO_2^-, 0.5; NO_3^-, -0.9; ClO_4^-, 1.5; acetate$^-$, -3.7; SO_4^{2-}, -5.9	SSM	(37)
NO_2^-	NO_2^--1 (1),[c] NPOE (65), PVC (33), KTpClPB (36.6)	F^-, -3.9; Cl^-, -3.7; Br^-, -3.3; I^-, -2.2; HCO_3^-, -3.7; NO_3^-, -3.5; SCN^-, 0.2; ClO_4^-, -2.2; acetate$^-$, -3.8; SO_4^{2-}, -4.1	SSM	(10)

[a]The weight percentages of ionophore, plasticizer, and PVC are given in parentheses. The amount of ionic sites is in mole percent relative to the ionophore.
[b]Used as a supporting electrolyte so that the weight percentage is given in the parentheses.
[c]The ionophore structure is given in Figure 7.6.
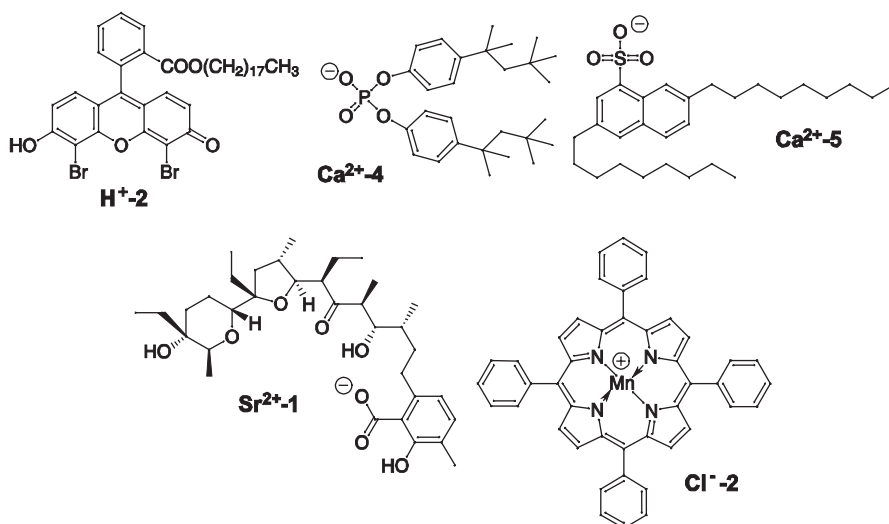
negatively charged ionophore and a cationic analyte, the complex partially dissociates in the membrane

$$I^+(\text{membrane}) + L^-(\text{membrane}) \rightleftharpoons IL(\text{membrane}) \tag{7.2.19}$$
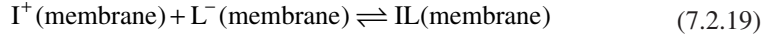
The reaction can be quantified with a formation constant as defined by equation (7.2.15) for neutral ionophores. In contrast to the neutral ionophore system, free charged ionophore does not exist in excess in the membrane so that complex dissociation is enhanced. With a sufficiently large formation constant, the analyte activity in the membrane phase is given as

$$a_I^M = \sqrt{\frac{\gamma_{IL}^M \gamma_I^M L_T}{\gamma_L^M \beta}} \tag{7.2.20}$$

The analyte activity depends only on the square root of the formation constant rather than the constant itself, which contrasts with the case of neutral ionophores. While the constant analyte activity in the membrane phase results in a Nernstian response, the membrane activity is relatively high and uncomplexed analytes are available for exchange with an interfering ion.

It was recently found that use of ionic sites in charged-ionophore-based ISEs improves the selectivity against interfering co-ions by providing excess free ionophores (10, 33). Figure 7.1C illustrates a charged-ionophore-based membrane that contains a salt of a cationic site and the charged ionophore in addition to the ionophore–analyte salt. Since the ionophore interacts weakly with the cationic site, the salt of the cationic site dissociates efficiently. Excess free ionophore provided from the ionic-site salt shifts the complexation equilibrium in equation (7.2.19) such that the ionophore–analyte complexation is enhanced. With the assumption that the ionophore–ionic-site salt dissociates completely, the charge and mass balances in the membrane phase are given as

$$[L^-]_M = R_T \tag{7.2.21}$$

$$L_T = [L^-]_M + [LM]_M \tag{7.2.22}$$

Combination of equations (7.2.21) and (7.2.22) with an expression for the formation constant gives the membrane activity of the free analyte as

$$a_I^M = \frac{\gamma_{IL}^M (L_T - R_T)}{\beta \gamma_L^M R_T} \tag{7.2.23}$$

With the ionic sites, most analyte is in the complexed form so that the membrane activity is not only independent of the sample solution but also very low. Equation (7.2.23) with the buffering effect by ionophore is very similar to equation (7.2.18) for neutral ionophores. Therefore, charged-ionophore-based membranes must be doped with ionic site to improve the selectivity against interfering co-ions. In this specific example, the charge sign of ionic sites is opposite to that of the ionophore, which is not always the case (34).

Charge sign of ionic sites significantly affects the selectivity of charged-ionophore systems as discussed in Section 7.3.2.

7.3 EQUILIBRIUM POTENTIOMETRIC RESPONSES

7.3.1 The Nikolsky–Eisenman equation and phase boundary potential model

Most ionophores form complexes not only with the analyte ion but also with the aqueous co-ions. Interference by co-ions is a major origin of experimental errors in the analysis. The Nernst equation (7.1.1), however, does not describe the contribution of the interfering ions to the measured potential. Traditionally, the influence of the interfering ions on the potentiometric responses has been described using the Nikolsky–Eisenman equation (38)

$$E = E_I^0 + \frac{RT}{z_I F} \ln\left(a_I + \sum_{I \neq J} k_{IJ}^{pot} a_J^{z_I/z_J} \right)$$

(7.3.1)

where k_{IJ}^{pot} is the selectivity coefficient for the analyte ion, I, against an interfering co-ion, J, and a_J and z_J are the sample activity and charge of the interfering ion. In a solution containing no interfering ion, equation (7.3.1) is equivalent to the Nernst equation (7.1.1) for the ion. Also, with only an interfering ion in a solution, equation (7.3.1) can be simplified to a Nernst equation for the interfering ion as

$$E = E_J^0 + \frac{RT}{z_J F} \ln a_J$$

(7.3.2)

with

$$E_J^0 = E_I^0 + \frac{RT}{z_I F} \ln k_{IJ}^{pot}$$

(7.3.3)

Therefore, the selectivity coefficient can be determined by potential measurements in separate solutions containing only the analyte or interfering ion (Figure 7.2A: the separate solution method, SSM). With potentials E_I and E_J at sample activities of the respective ions, a_I (SSM) and a_J (SSM), or with the intercepts of the E versus log a plots, the selectivity coefficient is given as

$$k_{IJ}^{pot} = \frac{a_I(SSM)}{a_J(SSM)^{z_I/z_J}} \exp\left[\frac{z_I F(E_J - E_I)}{RT} \right] = \exp\left[\frac{z_I F(E_J^0 - E_I^0)}{RT} \right]$$

(7.3.4)

Importantly, the potentials must be measured in activity ranges in which the electrode responses are Nernstian to the ions (39). While this requirement for equilibrium conditions
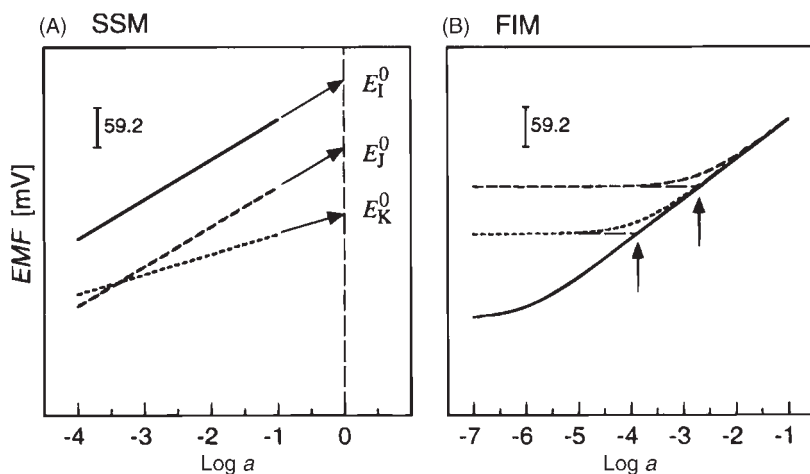
Figure 7.2 Representation of the separate solution method (A; SSM) and fixed interference method (B; FIM) under equilibrium conditions. Solid lines, response to monovalent primary ion; dashed and dotted lines, monovalent and divalent interfering ions, respectively. In the case of the FIM, the arrows indicate the detection limit. From reference (39). Copyright 2000 American Chemical Society.

can be checked experimentally, it is not always satisfied because of the non-equilibrium effects as discussed in Section 7.4.

The selectivity coefficient can also be determined by measuring the cell potentials at different analyte concentrations in the presence of a fixed concentration of an interfering ion (Figure 7.2B: the fixed interference method, FIM). In this case, the Nernstian response at high analyte activities is represented by equation (7.1.1). The constant potential at low analyte activities is determined by the interfering ion, whereas the Nernstian response to the interfering ion at the fixed activity should be confirmed in additional experiments (39). Linear extrapolations of these responses at high and low activities result in a cross point, which is defined as a detection limit. The selectivity coefficient can be obtained as

$$k_{IJ}^{pot} = \frac{a_I(DL)}{a_J(FIM)^{z_I/z_J}} \tag{7.3.5}$$

where $a_I(DL)$ is the analyte activity at the detection limit and $a_J(FIM)$ is the fixed activity of the interfering ion.

Despite the wide use of the Nikolsky–Eisenman equation and the selectivity coefficients, it is not so obvious whether this equation is valid when both analyte and interfering ions significantly contribute to the phase boundary potentials (for example, near the detection limit in Figure 7.2B). The equation was originally derived under equilibrium conditions for ions with the same charge number (specifically, $z_I = z_J = 1$) and then extended empirically (40). The experimental potentiometric responses in mixed ion solutions may deviate from the Nikolsky–Eisenman equation when the (1) experimental

conditions are not at equilibrium and (2) empirically extended equation is not valid, i.e., when the charge numbers are different.

To address the theoretical limitation of the Nikolsky–Eisenman equation, a more general description of the equilibrium responses of liquid membrane ISEs in mixed ion solutions was proposed (41). The model is based on phase boundary potentials under an equilibrium exchange of an analyte and an interfering co-ion at the membrane/sample solution interface. With ionophore-based membranes, the ion-exchange process is followed by complexation of the ions with an ionophore, where free ionophore was assumed to be always present in excess to simplify the model. The charge of the ions was not fixed so that their effect on the potentiometric responses can be addressed by the model. Under equilibrium conditions, the model demonstrated that the Nikolsky–Eisenman equation is valid only for ions with the same charge ($z_I = z_J$). The selectivity coefficient, however, can still be used in the new model to quantify the potentiometric responses in the mixed ion solution. For example, the potentiometric responses to a monovalent cation in the presence of a divalent cation are given as

$$E = E_I^0 + \frac{RT}{F} \ln \left[\frac{a_I}{2} + \frac{1}{2} \sqrt{a_I^2 + 4a_J (k_{IJ}^{pot})^2} \right] \tag{7.3.6}$$

Figure 7.3 shows potentiometric responses to Na^+ in the presence of Ca^{2+} as obtained with an Na^+-selective electrode based on a neutral ionophore (Na^+-2). Equation (7.3.6) fits the

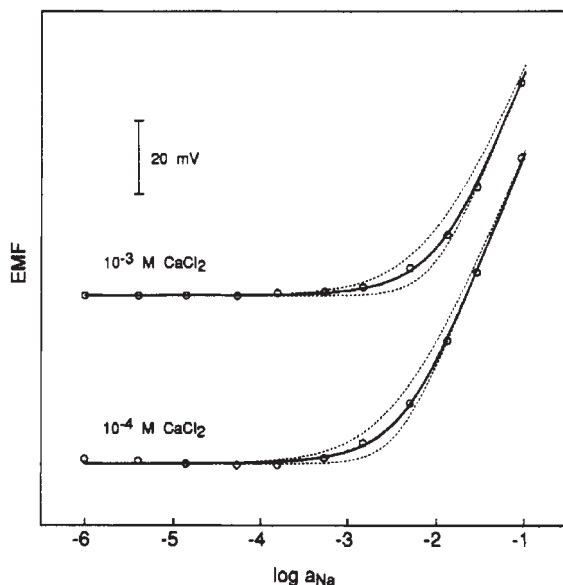**Figure 7.3**   Sodium calibration curves in a background of 0.001 or 0.0001 M CaCl$_2$, for an Na^+-selective electrode based on a membrane of Na^+-2 in DOS/PVC (2:1, w/w). Solid line according to equation (7.3.6); dotted lines according to Nicolsky–Eisenman equation (7.3.1) when Na^+ (upper curve) or Ca^{2+} (lower curve) is assumed to be the primary ion. From reference (41). Copyright 1994 American Chemical Society.

experimental responses better than the Nikolsky–Eisenman equation. More recently, the model was extended to describe the simultaneous responses for any number of monovalent, divalent, and trivalent ions (42).

7.3.2 Effect of ionic sites on selectivity

Besides hydrophobicity of ions and stability of their ionophore complexes, the concentration and charge of the ionic sites in the membrane phase also affect the ion selectivity of ionophore-based ISEs. This effect was first found for neutral-ionophore-based ISEs (14, 43), then for charge-ionophore-based ISEs (10, 33), and most recently implemented in an equilibrium phase boundary potential model generalized for both systems with primary and interfering ions of any charges and their complexes of any stoichiometries (34).

In ionophore-based ISEs, the analyte ion must be buffered to achieve a low and sample-independent membrane activity for a selective Nernstian response. This condition is satisfied when the membranes contain both free and complexed ionophores (Figure 7.4A: ionophore-based response mechanism). The membrane responds to an ion, i, on the basis of an ionophore-based mechanism when the concentration and charge of ionic sites satisfy the following relationship based on mass and charge balances in ionophore-based membranes (34):

$$-\frac{|z_i|}{z_i}\left(z_L + \frac{z_R R_T}{L_T}\right) < \frac{|z_i|}{n_i} \tag{7.3.7}$$

where z_L and z_R are the charges of the ionophore and the ionic sites, respectively, and n_i is the stoichiometry of the ionophore–ion complexes. Otherwise, free ionophore in the membrane is depleted by complexation with the ion so that the potentiometric responses become independent of the complexation process and are determined by the excess free ions as in the case of ionophore-free ion-exchanger electrodes (Figure 7.4B: ionophore-independent

(A)   Ionophore-based mechanism

$$L^{z_L} \quad iL_{n_i}^{(z_i + n_i z_L)} \rightleftharpoons i^{z_i}$$
$$R^{z_R}$$

(B)   Ionophore-independent mechanism

$$iL_{n_i}^{(z_i + n_i z_L)} \quad i^{z_i} \rightleftharpoons i^{z_i}$$
$$R^{z_R}$$
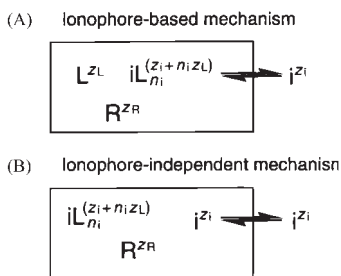
Figure 7.4 Schematic diagram of the major components in membranes that respond according to (A) an ionophore-based mechanism and (B) an ionophore-independent mechanism. In the latter case, the membranes contain a high concentration of free analyte ions but no significant concentration of free ionophore. The boxes designate the membrane phases: i, the primary or interfering ion; R^{z_R}, the lipophilic ionic site; L^{z_L}, the ionophore; and $iL_{n_i}^{z_i + n_i z_L}$, the 1:n_i complexes of the ion with the ionophore. From reference (34). Copyright 2000 American Chemical Society.

mechanism). Also, the response mechanism of the same membrane to an interfering ion depends on the charge and complexation stoichiometry of the ion. When $|z_J|/n_J \geq |z_I|/n_I$, equation (7.3.7) is satisfied simultaneously for primary and interfering ions so that the membrane responds to both ions on the basis of an ionophore-based mechanism, where the ionic sites do not affect the selectivity significantly. With $|z_J|/n_J < |z_I|/n_I$, the membrane responds to the analyte and interfering ions on the basis of ionophore-based and ionophore-independent mechanisms, respectively, when the following equation is satisfied:

$$\frac{|z_J|}{n_J} < -\frac{|z_I|}{z_I}\left(z_I + \frac{z_R[R_T]}{[L_T]}\right) < \frac{|z_I|}{n_I} \tag{7.3.8}$$

When $|z_J|/n_J < |z_I|/n_I$, the selectivity can be dramatically improved by optimizing the concentration and charge of ionic sites to satisfy equation (7.3.8). Figure 7.5 shows the effect of anionic sites on the Mg^{2+} selectivity of a neutral-ionophore-based ISE as determined by the SSM (14). The selectivity coefficients strongly depend on the membrane concentration of the anionic sites and result in optimum values against most ions with 120 mol% anionic sites relative to the ionophore concentration. With 1:1 complexes between the ionophore and Mg^{2+}, a large amount of the free ionophore is available for the ion in the membrane with 120 mol% anionic sites, i.e., ionophore-based mechanism. Ca^{2+} and
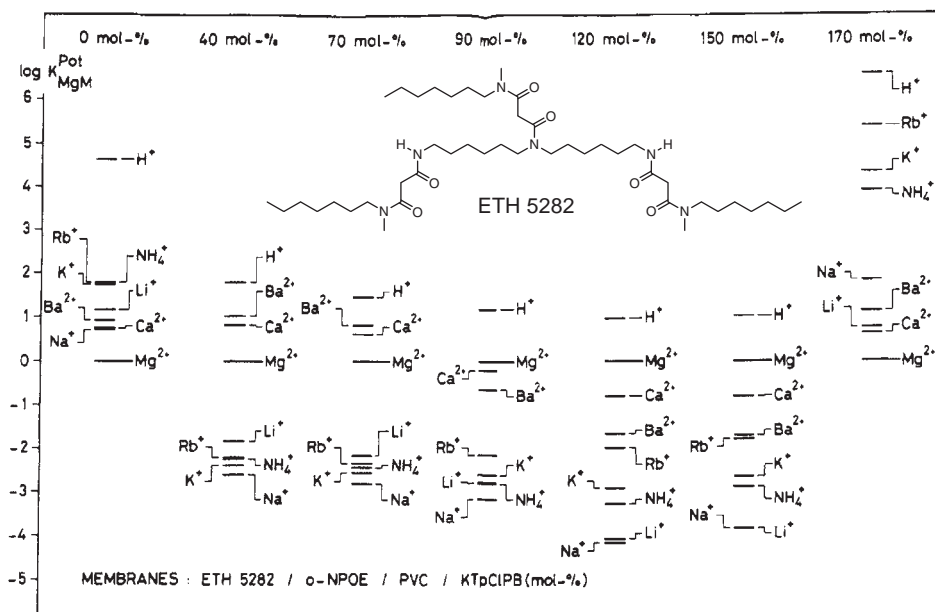
Figure 7.5 Selectivity coefficients, $\log k_{MgJ}^{pot}$, of liquid membranes containing neutral ionophore ETH 5282 and oNPOE as the membrane solvent as determined by the SSM. From reference (14). Copyright 1991 American Chemical Society.
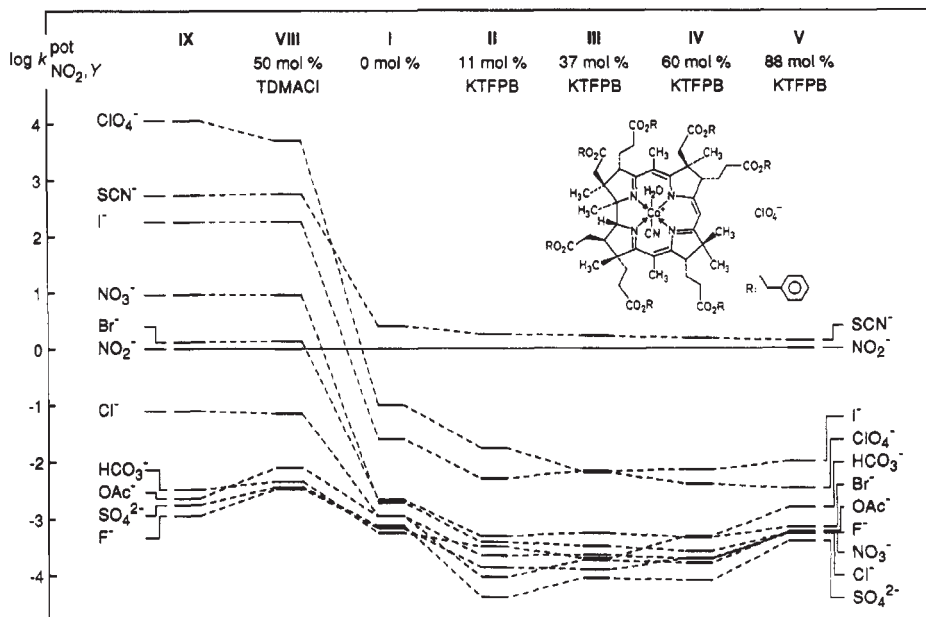
Figure 7.6 Selectivity coefficients, $\log k_{NO_2, J}^{pot}$ of liquid membranes containing charged ionophore NO_2^--1 and oNPOE as the membrane solvent as determined by the SSM. The membrane IX is based only on an anion exchanger TDDMA. Selectivity coefficients of the membranes III and IX are also listed in Tables 7.3 and 7.1, respectively. From reference (10). Copyright 1994 American Chemical Society.

Ba^{2+}, however, form 1:2 complexes so that the free ionophore in the same membrane is depleted in contact with the separate solutions containing these ions. Since the interfering ions remain partially uncomplexed in the membrane phase, the electrode responds to the interfering ions on the basis of an ionophore-independent mechanism.

The effect of ionic sites on the selectivity is more complicated for charged ionophores because not only the concentration but also the charge of the sites affects the selectivity. Figure 7.6 shows the effects of ionic sites on the selectivity of NO_2^--selective electrodes based on a positively charged ionophore (NO_2^--1). As discussed in Section 7.2.4, addition of anionic sites improves the selectivity by increasing free ionophore concentration in the membrane. Most anions coordinate to the metal center of the ionophore for 1:1 complexation so that the selectivity coefficient depends slightly on the site concentration. Free anions are introduced by doping a membrane with cationic sites, resulting in a selectivity similar to that of ionophore-free anion-exchanger electrodes. In this example, $|z_I|/n_I = |z_J|/n_J$ so that the membranes function on the basis of the same mechanism (ionophore-based or ionophore-independent mechanism) to the primary and interfering ions. This example supports that charged ionophores require ionic sites of opposite charge (10, 33), which is not always true (34).

Figure 7.7 shows selectivity coefficients for Sr^{2+} against other alkaline earth cations as obtained with an electrode based on lasalocid (Sr^{2+}-1) as a negatively charged ionophore.
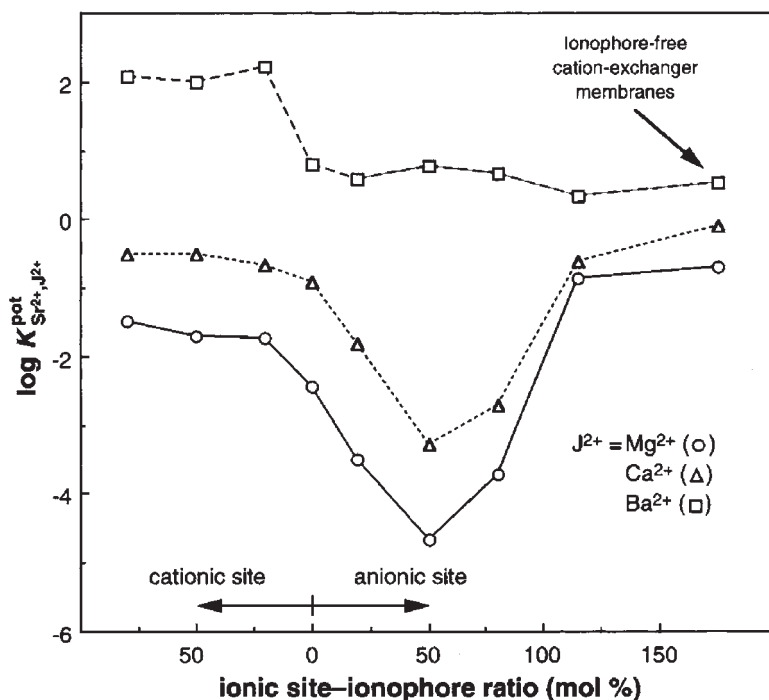
Figure 7.7 Selectivity coefficients, $\log k_{SrJ}^{pot}$, as determined with the SSM for oNPOE–PVC (2:1, w/w) membranes based on lasalocid (Sr^{2+}-1) and ionic sites. Selectivity coefficients of the membranes with 50 mol% anionic sites are also listed in Table 7.3. From reference (34). Copyright 2000 American Chemical Society.

As predicted by the generalized mode (34), the highest selectivity was achieved by addition of anionic sites rather than cationic sites. Also, the selectivity coefficients against Ca^{2+} and Mg^{2+} give the minimum values as observed with an Mg^{2+}-selective electrode based on a neutral ionophore, suggesting difference of complexation stoichiometry among the divalent cations. The selectivity dependence on the concentration and charge of ionic sites can be explained by formation of 1:1 and 1:2 complexes for the analyte and interfering ions, respectively. Importantly, the concentration and charge of ionic sites that give the highest selectivity can be calculated (14, 34), even when each analyte and interfering ion forms more than one type of complexes with different stoichiometries (34).

7.3.3 Apparently "non-Nernstian" equilibrium responses

The Nikolsky–Eisenman equation and a more general phase boundary model discussed in Section 7.3.1 are based on a common assumption that a well-defined amount of a free ionophore is always present in the membrane, implying that the membrane always functions on the basis of an ionophore-based mechanism. As discussed in Section 7.3.2, however, the
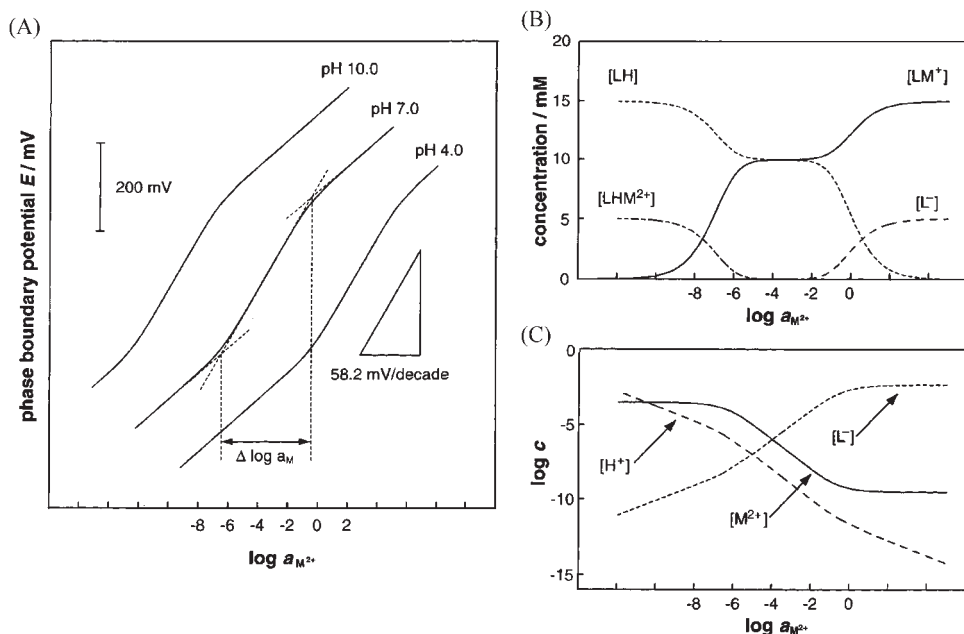
Figure 7.8 (A) Calculated phase boundary potentials as a function of the activity of a divalent cation in the sample solution for a membrane with an acidic ionophore and anionic sites. Responses are shown for sample solutions of pH 4.0, 7.0, and 10.0. Calculated equilibrium concentrations of (B) the deprotonated ionophore, L^-, and its complexes, LH, LM^+, and LHM^{2+}, and (C) the deprotonated ionophore and the free primary ion, M^{2+}, and hydrogen ion, H^+, in the membrane phase for pH 7.0. From reference (44). Copyright 1998 American Chemical Society.

concentration and charge of ionic sites can be such that the free ionophore can be depleted for some ions. Recently, potentiometric responses of the latter systems in mixed ion solutions were studied theoretically and experimentally to establish a novel response mechanism where equilibrium potentiometric responses can be apparently "non-Nernstian" in a wide activity range (44–46).

The apparently "twice-Nernstian" responses of ISEs based on acidic ionophores (Figure 7.8A) are the first examples of apparently "non-Nernstian" responses that could be explained on the basis of equilibrium phase boundary potentials (44). In this system, the acidic ionophores such as lasalocid (Sr^{2+}-1) in their deprotonated form, L^-, can bind both to dications, M^{2+}, as primary ions and to H^+ ions as secondary ions. With the assumption of 1:1 complexes for both ions and equilibrium exchange of the ions at the membrane/sample interface, the potentiometric response was demonstrated to depend simultaneously on the two ions over several orders of magnitude of the sample primary-ion activity in pH-buffered solutions. In the "twice-Nernstian" response region, the ionophores in the complexed forms with H^+ and M^{2+} are present simultaneously, whereas free ionophores are depleted (Figure 7.8B). The free M^{2+} concentration in the membrane phase is inversely proportional to the sample activity (Figure 7.8C), which results in a
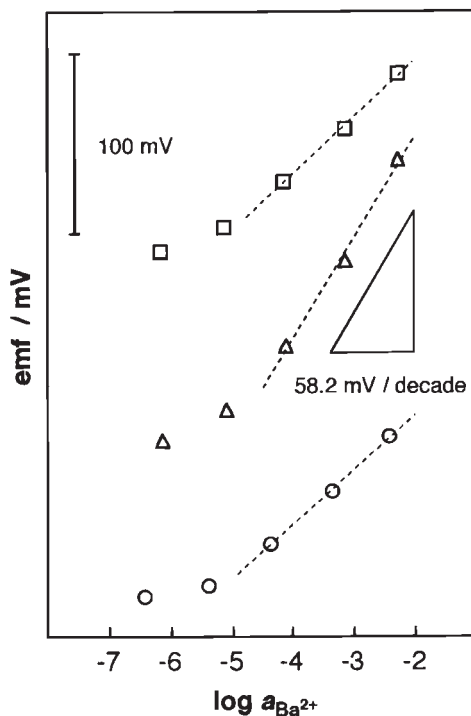
Figure 7.9   Potentiometric responses to Ba^{2+} as obtained with oNPOE–PVC (2:1, w/w) membranes based on lasalocid (Sr^{2+}-1) and 50 mol% KTpClPB: (□) pH 2.0 (10 mM HCl), (Δ) pH 4.0 (1 mM $(CH_3COO)_2Mg/HCl$), and (○) pH 7.0 (0.1 M Tris/HCl). The three response curves have been shifted vertically for enhanced clarity. From reference (44). Copyright 1998 American Chemical Society.

response slope twice as large as the Nernstian slope. This result contrasts to conventional Nernstian responses of ionophore-based ISEs, for which the membrane activity of the free primary ion is buffered with the ionophore and remains sample-independent. As predicted theoretically, these ISEs gave Nernstian, apparently twice-Nernstian, and again Nernstian responses to the primary dications when samples of high, intermediate, and low pH were used, respectively (Figure 7.9).

Analogously, apparently "super-Nernstian" responses to monoanions as observed with metalloporphyrin-based ISEs were shown to result from the formation of OH^--bridged metalloporphyrin dimers in the ISE membranes (31, 45). Apparently super-Nernstian responses to F^- with slopes from -70 to -85 mV/decade were obtained with membranes based on Ga(III)octaethylporphyrin and anionic sites, which were quantitatively explained as responses co-determined by F^- as the primary ion and OH^- ions as the secondary ion with 1:1 and 1:2 complexation stoichiometry, respectively.

More recently, a generalized phase boundary potential model that describes apparently "non-Nernstian" equilibrium responses of ionophore-based ISEs was developed (46). The model predicts that ionophore-based ISEs can give three types of apparently non-Nernstian

equilibrium responses, i.e., apparently "super-Nernstian", "sub-Nernstian", and "inverted-Nernstian" responses (response slopes with a sign opposite to that of the conventional Nernstian responses). The response slopes depend on the charge numbers of the primary and secondary ions and on the stoichiometries of their complexes with the ionophore

$$\frac{\partial E}{\partial \log a_I^W} = \frac{RT \ln 10}{z_I F} \left(\frac{1}{1 - n_I z_J / n_J z_I} \right) \tag{7.3.9}$$

where $n_I z_J \neq n_J z_I$. The generalized model also revealed other requirements for apparently "non-Nernstian" equilibrium responses such as binding site and formation constants of the ionophore, and the concentration and charge of the ionic sites.

7.4   NON-EQUILIBRIUM POTENTIOMETRIC RESPONSES

7.4.1   Mixed ion-transfer potentials

ISEs are operated under open circuit condition, where no significant current flows. When a Nernstian response is obtained, only one ion is exchanged significantly between the membrane and sample phases so that there is no net current carried by the ion at the interface. In contrast, when co-extraction of the analyte and its aqueous counter ion (Donnan exclusion failure) or exchange of the analyte and its interfering co-ion occurs at the interface, the partial current carried by each ion, I_i, may become significant. The partial currents, however, cancel each other so that the total current at the interface, I, is zero

$$I = \sum_i I_i = 0 \tag{7.4.1}$$

The non-equilibrium ion-exchange processes can cause deviation of the potentiometric responses from those predicted by the Nikolsky–Eisenman equation and the equilibrium phase boundary potential model.

   The non-equilibrium effects on potentiometric responses can be described using the concept of mixed ion-transfer potential (47). When ion transfers at a sample solution/membrane interface are fast enough, a local equilibrium at the interface is always achieved. The salt-extraction and ion-exchange processes, however, induce concentration polarization of the ions near the interface so that the potential is determined by the interfacial ion concentration as

$$E_{mix} = E_i^0 + \frac{RT}{z_i F} \ln \frac{\gamma_i^{W,S} c_i^{W,S}}{\gamma_i^{M,S} c_i^{M,S}} \tag{7.4.2}$$

where E_{mix} is the mixed ion-transfer potential, E_i^0 is a constant term unique for the ion, $c_i^{W,S}$ and $c_i^{M,S}$ are the ion concentrations at the water and membrane sides of the interface, respectively, and $\gamma_i^{W,S}$ and $\gamma_i^{M,S}$ are the activity coefficients of the ion at the respective
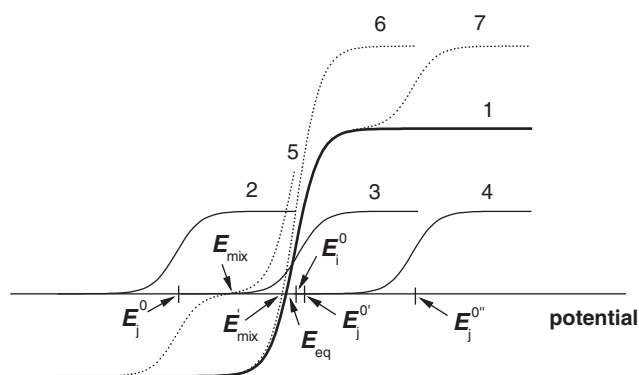
Figure 7.10   Schematic representation of the partial current versus potential curves for the transfer of primary ion, I (curve 1), and interfering ions, J, with different E_J^0 values (curves 2–4) across the sample solution/membrane interfaces. Curves 5–7 represent the total current versus potential relationships corresponding to curves 2–4, respectively. The curves are calculated using equations (7.4.2) and (7.4.3). See also reference (47).

sides of the interface. The interfacial concentrations are related to the partial current carried by the ion, which can be obtained under steady-state diffusion layer approximation as

$$\frac{I_i}{z_i FA} = \frac{D^W}{\delta^W}(c_i^{W,S} - c_i^W) = -\frac{D^M}{\delta^M}(c_i^{M,S} - c_i^M) \tag{7.4.3}$$

where A is the interfacial area, D^W and D^M are the diffusion coefficients of the ion in the sample and membrane phases, respectively, δ^W and δ^M are the thickness of the steady-state diffusion layers in the respective phases, and c_I^W and c_I^M are the bulk concentrations of the ion in the respective phases.

Consider an ion-exchanger-based membrane doped with a salt of a cationic analyte and an anionic site, which is in contact with a sample solution containing both the analyte and an interfering cation. Under steady-state conditions, combination of equations (7.4.2) and (7.4.3) for the analyte ion gives the partial current versus potential relationship based on transfer of the analyte ion between the membrane and sample phases as illustrated by curve 1 in Figure 7.10. The potential at zero current in the curve, E_{eq}, corresponds to the equilibrium potentiometric response of the membrane in the absence of the interfering ion in the sample solution. Also, the partial current versus potential relationship is obtained for transfer of the interfering ion from the sample solution to the membrane phase as represented by curves 2–4 depending on hydrophobicity of the ion. Because of the zero-current condition, the measured potential must be such that the partial current carried by the interfering ion exactly cancels current carried by the analyte. Therefore, in the presence of the interfering ion, the measured potential shifts from the equilibrium potential to a mixed ion-transfer potential (see curves 5–7).

The concept of this mixed ion-transfer potential was recently extended to quantify the non-equilibrium responses of neutral-ionophore-based ISEs (48). Figure 7.11 shows the
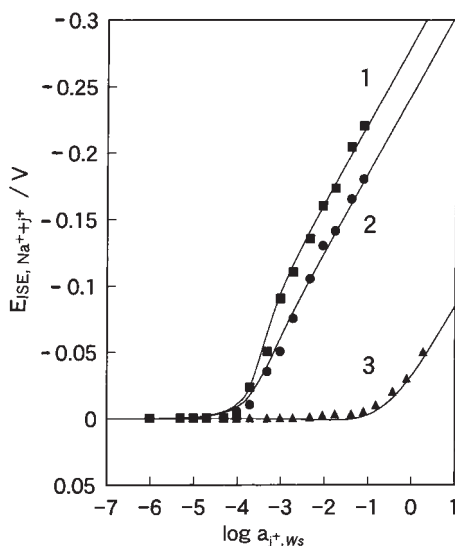
Figure 7.11 Potentiometric responses of Na$^+$-ISE to (■) Rb$^+$, (●) K$^+$, and (▲) Li$^+$ in sample solutions containing 1 mM Na$^+$. The membrane is a nitrobenzene solution of 0.05 M dibenzo-18-crown-6 and 1 mM NaTFPB as a neutral ionophore and anionic sites, respectively. Solid lines represent theoretical curves. From reference (48).

effect of the interfering ions on the potentiometric responses in a solution containing a fixed concentration of the analyte Na$^+$. When 10^{-4} to 10^{-3} M Rb$^+$ is added to the sample solution as a more preferred interfering ion, the potential increases from the equilibrium potential determined by Na$^+$, resulting in a super-Nernstian response (curve 1). In this activity region, the analyte ion in the membrane is significantly replaced with the interfering ion so that the potential is based on mixed ion-transfer potentials. Since the interfering ion is significantly depleted at the sample side of the interface, the measured potential is lower than the equilibrium potential as extrapolated from the Nernstian response at higher interfering-ion activities. In contrast, addition of a more discriminated Li$^+$ gives a sub-Nernstian response even in a high activity range (curve 3), where Na$^+$ in the membrane phase is only partially replaced with Li$^+$. Good fits of the experimental potentials with the theoretical ones demonstrate usefulness of this concept for quantifying the non-equilibrium effects on the potentiometric responses.

7.4.2   Elimination of non-equilibrium effects in separate solutions

Liquid membranes are usually soaked in an analyte solution, which is high in activity, overnight before measurements so that all exchangeable ions in the membranes are replaced with the analyte ion for a Nernstian response. This process is called conditioning. When a membrane conditioned in an analyte solution is in contact with the separate solution of an

interfering ion, the ion-exchange process at the interface may cause a non-equilibrium effect. The membranes give sub-Nernstian or no responses to highly discriminated ions, where the responses to the discriminated ions are masked by the analyte ion released from the membranes. Therefore, the selectivity coefficients thus determined are upper limits rather than those determined thermodynamically.

The non-equilibrium effects on the selectivity determination can be eliminated by measuring the bi-ionic potential in the following cell (49, 50):

$$\text{solution (I) | membrane (I) || membrane (J) | solution (J)} \qquad \text{(cell 2)}$$

where the membrane compositions are the same except for the exchangeable ions given in parentheses. With this cell, the measured potential is the difference between the equilibrium phase boundary potentials at the left and right membrane/solution interfaces as determined by distributions of ions I and J, respectively, as far as the liquid junction potential between the two membranes is negligibly small. Therefore, an unbiased selectivity coefficient can be obtained directly from the measured potential difference, $E_I - E_J$, using equation (7.3.4) for the SSM, where the analyte and interfering-ion activities correspond to those in the solutions at the left- and right-hand sides of the cell, respectively.

On the basis of a similar concept, a more simple method was proposed for determination of unbiased selectivity coefficients (24). With this method, a membrane is conditioned in a solution of a highly discriminated ion rather than the highly preferred analyte ion so that the membrane gives a Nernstian response to the discriminated ion. Then, the potentiometric responses to a less discriminated ion are measured. Whereas a super-Nernstian response based on a mixed ion-transfer potential may be observed in a lower activity region, completion of the ion-exchange process at the interface at higher activities results in a Nernstian response. The procedure is carried out in the rigid sequence of exposure of the membranes to the ions of interest from a highly discriminated one to a highly preferred one, allowing a determination of the unbiased selectivity coefficients against a series of the ions. Figure 7.12 shows the potentiometric responses of K^+-selective membranes based on a neutral ionophore valinomycin (K^+-1), which were conditioned in a KCl solution and in an NaCl solution. When conditioned in highly discriminated Na^+, the membrane gives Nernstian responses to all ions (even to more discriminated Ca^{2+} and Mg^{2+}) so that the selectivity coefficients can be determined under equilibrium conditions by the SSM. In contrast, the membrane conditioned in a K^+ solution gives almost no response to the discriminated ions because of the non-equilibrium effect.

Importantly, the unbiased selectivity coefficients are thermodynamically meaningful. When an interfering ion, such as tetraethylammonium ion for cation-selective electrodes, does not bind to an ionophore, the selectivity coefficient for an ion of interest against such an interfering ion can be used to determine the formation constant of the ion–ionophore complexes (9). For example, when a neutral ionophore forms $1:n_i$ complexes with an ion, i, and does not bind to an interfering ion, j, the formation constant is given as

$$\beta_{n_i} = \frac{k_{ij}^{\text{pot}}(\text{IE})}{k_{ij}^{\text{pot}}(\text{L})(L_T - n_i R_T / z_i)^{n_i}} \qquad (7.4.4)$$
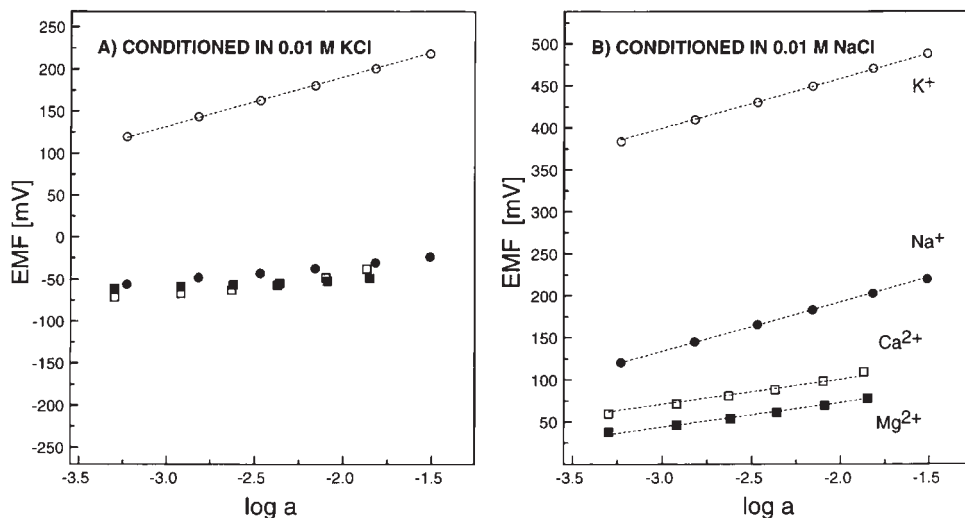
Figure 7.12 Potentiometric responses of liquid membranes based on valinomycin (K^+-1) and NaTFPB conditioned in (A) 0.01 M KCl and (B) 0.01 M NaCl to (○) K^+, (●) Na^+, (■) Mg^{2+}, and (❑) Ca^{2+}. Dotted lines with Nernstian response slopes of 58.4 and 29.2 mV for monovalent and divalent cations, respectively. From reference (2). Copyright 1997 American Chemical Society.

where k_{ij}^{pot}(IE) and k_{ij}^{pot}(L) are the unbiased selectivity coefficients as obtained with an ion-exchanger-based membrane and an ionophore-based membrane, respectively, which contain the same concentration of ionic sites.

Formation constants can also be determined by measuring the potential of the following cell (51):

solution (i) | ion-exchanger-based membrane (i) ‖ ionophore-based membrane (i) | solution (i)

(cell 3)

Whereas the potential is transient because of the gradual mixing of the membrane components, the initial potential is directly related to the formation constants without requirement of a reference ion. Assuming the same ionophore and ion as equation (7.4.4), the formation constant is given by

$$\beta_{n_i} = \frac{\exp(z_i F E_M / RT)}{(L_T - n_i R_T / z_i)^{n_i}}$$

(7.4.5)

where E_M is the potential of cell 3 with the same aqueous solutions measured using the same reference electrodes. This technique is called the sandwich method and can be used to determine equilibrium constants for complexation, ion-exchange, and salt-partitioning processes (51, 52).

Table. 7.4.

Formal complex formation constant, $\log \beta_n$, and stoichiometries, n, of ionophore–ion complexes in PVC membranes[a]

Ion	$Pb^{2+}-1$[b]		$Pb^{2+}-2$[b,c]		K^+-1[d]		K^+-2[d]	
	$\log \beta_n$	n	$\log \beta_n$	n	$\log \beta_n$	n	$\log \beta_n$	n
Li^+	–	–	–	–	(6.74)[e]	(1)[e]	4.22	1
Na^+	3.1	1	<3	1	(6.65)[e]	(1)[e]	6.00	1
K^+	<3	1	<3	1	9.95	1	8.10	1
Ag^+	–	–	12.6	1	–	–	–	–
Pb^{2+}	15.9	1	<3	1	–	–	–	–
Cu^{2+}	12.1	1	<3	1	–	–	–	–
Cd^{2+}	10.0	1	<3	1	–	–	–	–

[a]The ionophore structures are given in Table 7.2.
[b]Determined using a reference ion in DOS/PVC membranes.
[c]The ionophore is also known as a Ag^+ ionophore because of its strong binding with Ag^+.
[d]Determined by the sandwich method in DOS/PVC membranes.
[e]Determined using two ionophores. From reference (53).

The formation constants determined so far for representative neutral ionophores and the primary ions are listed in Table 7.2. Also, Table 7.4 lists the formation constants for both primary and interfering ions and reveals the very high complexation selectivity of the ionophores.

7.4.3 Effects of transmembrane ion flux on detection limit

Potentiometric responses of liquid membrane ISEs can be explained in most cases by considering ion-transfer processes only across the membrane/sample solution interfaces. It, however, was recently found that ion flux across the bulk membrane affects the interfacial processes and subsequently determines the detection limit (54, 55). When the analyte concentration in the sample solution is very low, a much higher analyte concentration in the inner solution drives the analyte flux from the inner solution to the sample solution. Therefore, the analyte activity at the sample side of the interface is determined not by the sample concentration but by the transmembrane ion flux. The analyte flux can be balanced by the flux of the aqueous counter ion from the inner solution to the sample solution (Figure 7.13A), maintaining the electroneutrality in the membrane and the two aqueous phases. Also, the counter flux of the interfering co-ion from the sample solution to the inner solution can balance the analyte flux (Figure 7.13B and C).

Pretsch and co-workers demonstrated for the first time that a detection limit of liquid membrane ISEs can be as low as the picomolar range by controlling the transmembrane flux (54). Figure 7.14 shows the responses of the same Pb^{2+}-selective electrodes with different inner solution compositions. When Pb^{2+} is buffered in the inner solution containing EDTA, the detection limit can be improved by almost five orders of magnitudes down to ~10^{-12} M. The low Pb^{2+} concentration in the inner solution suppresses the co-extraction
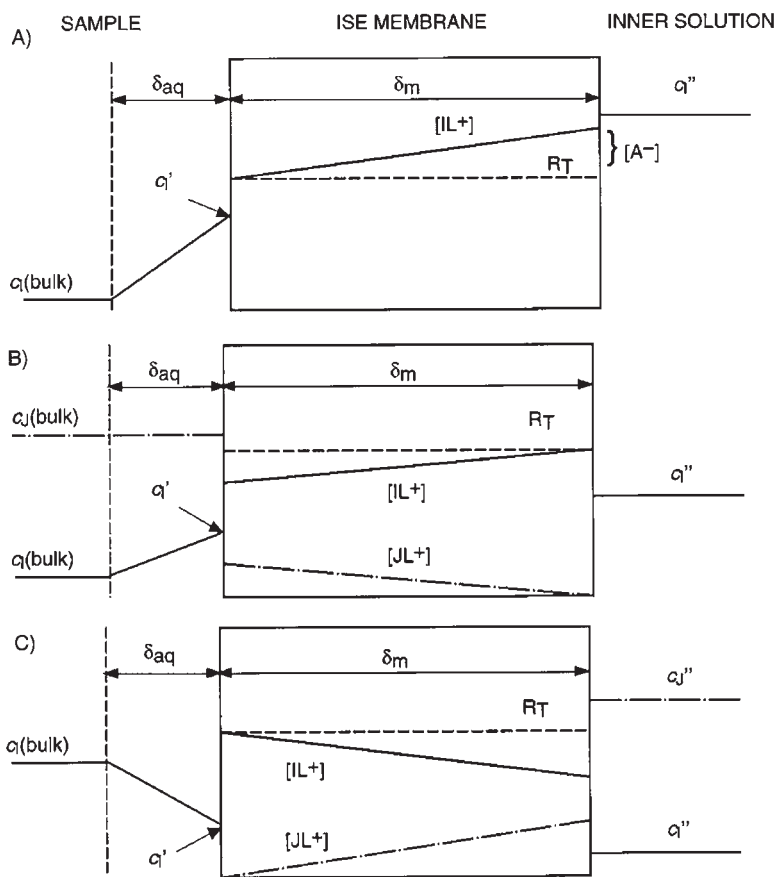
Figure 7.13 Schematic representation of the processes influencing the lower detection limit of ISEs based on an ionophore (L) forming 1:1 complexes with the monovalent primary (I^+) and interfering ions (J^+). Gradients are generated in the aqueous Nernstian phase boundary (thickness δ_{aq}) because of (A) co-extraction of I^+ and A^- from the inner solution and (B and C) partial exchange of primary ions by interfering ones at the sample and reference side, respectively. From reference (55). Copyright 1999 American Chemical Society.

at the inner solution side of the membrane, decreasing the Pb^{2+} flux directed to the sample solution. A high Na^+ concentration in the inner solution further decreases the membrane concentration of Pb^{2+} at the side of the inner solution by ion exchange, resulting in dramatic improvement of the detection limit. An improvement of detection limit was also observed for an interfering ion Na^+. The subsequent Nernstian response to Na^+ allows determination of the unbiased selectivity coefficient.

So far, detection limits of liquid membrane ISEs for Pb^{2+}, Cd^{2+}, Ag^+, Ca^{2+}, K^+, NH_4^+, ClO_4^-, and I^- have been improved to nanomolar and picomolar levels (56). The transmembrane ion flux at a Pb^{2+}-selective membrane was directly detected using scanning electrochemical microscopy (57). Potentiometric ISEs, however, are a passive
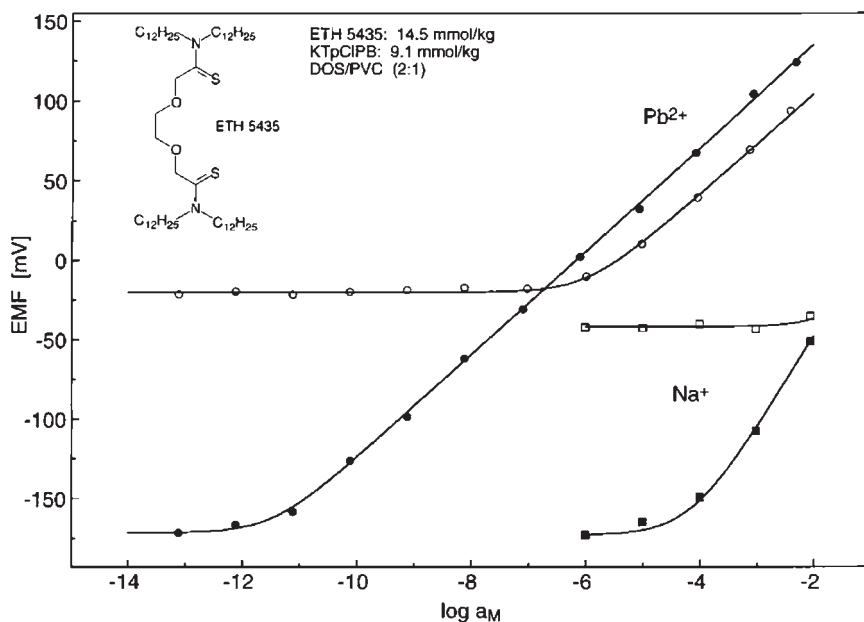
Figure 7.14 Response of two Pb^{2+} ISEs with the same membrane but different internal electrolytes. Conventional (empty symbols): 1:1 mixture of 10^{-3} M $PbCl_2$ and 0.1 M $MgCl_2$. New (full symbols): 1 mL of 0.1 M $Pb(NO_3)_2$ in 100 mL of 0.05 M EDTA-Na_2; measured pH 4.34. Calculated activities: 10^{-12} M Pb^{2+} and 10^{-1} M Na^+. From reference (54). Copyright 1997 American Chemical Society.

electrochemical sensor so that control of the transmembrane flux is a challenging task. An optimum composition of the inner solution strongly depends on the sample composition (55). When the transmembrane flux of an analyte toward the inner solution becomes much larger than the analyte flux sustainable from the bulk sample solution to the interface, the analyte is completely depleted at the sample side of the interface (Figure 7.13C), where the phase boundary potential becomes insensitive to the analyte in a low sample activity range and then changes only at higher activities, resulting in a super-Nernstian response. Besides optimization of the membrane and inner solution compositions, detection limits were lowered by suppressing the transmembrane ion flux by applying an external current (58) or by enhancing the analyte flux to the membrane surface with a rotating-electrode configuration (59) though more instrumentation is necessary.

Effects of the transmembrane flux on the detection limits were also studied theoretically (60). The phase boundary potential model in mixed ion solutions as discussed in Section 7.3.1 was extended by implementing the steady-state transmembrane flux to demonstrate that the detection limit of a highly selective electrode, $c_I(DL)$, is given approximately as

$$c_I(DL) = \sqrt{\frac{q[R_T]}{z_I} k_{IJ}^{pot} c_J^W} \tag{7.4.6}$$

with

$$q = \frac{D^M \delta^W}{\delta^M D^W} \tag{7.4.7}$$

where $z_I = z_J$, δ^M is approximated to be equal to the membrane thickness, and $k_{IJ}^{pot} c_J \ll q[R_T]/z_I \approx 10^{-6}$ M for highly selective electrodes. Comparison of the detection limit under the transmembrane ion flux conditions given by equation (7.4.6) with that under equilibrium conditions given by equation (7.3.5) reveals that the non-equilibrium effect worsens the detection limit, i.e.,

$$\frac{c_I(DL)}{c_I^{eq}(DL)} = \sqrt{\frac{q[R_T]}{z_I k_{IJ}^{pot} c_J}} > 1 \tag{7.4.8}$$

where $c_I^{eq}(DL)$ is the detection limit under equilibrium conditions as given by equation (7.3.5) with activity coefficients of 1. Therefore, elimination of the transmembrane flux will improve the detection limit to the thermodynamically determined one. A possible approach is the use of solid-contact ISEs where a membrane is directly mounted on a solid electrode without an inner solution so that the major source of the transmembrane ion flux is eliminated. Although establishment of a reliable electrical contact at the membrane/electrode interface is challenging, there are a few examples of solid-contact ISEs with nanomolar detection limits (61). Potentiometric measurements under complete two-phase equilibrium will be an idealistic condition not only for practical application with a low detection limit but also for fundamental characterization of the membrane equilibrium.

7.4.4   Non-equilibrium responses for polyion detection

While selectivity and detection limit are biased by the non-equilibrium effects, it is interesting to point out that liquid membrane ISEs for polyions were successfully developed by taking advantage of mixed ion-transfer potentials (62). Two typical examples of the electrodes are those for heparin and protamine. Heparin is a highly sulfated polysaccharide (M_r 5000–25,000), which is extensively used as an anticoagulant in many medical procedures for prevention of blood clotting, especially during open heart surgery. Protamine is a naturally occurring polycationic protein rich in arginine (M_r ~4500), which is used to neutralize the anticoagulant activity of heparin. These electrodes are based on membranes doped with an anion-exchanger tridodecylmethylammonium (TDDMA) for heparin or with a negatively charged ionophore dinonylnaphthalene sulfonate (Ca^{2+}-5) for protamine. Equilibrium partitioning of such multiply charged ions between the membrane and aqueous phases results in a very small potential change as predicted by the Nernst equation (Figure 7.15). However, a non-equilibrium ion-exchange process between a polyion in the aqueous phase and a counter ion of the ion-exchanger sites in the membrane phase causes a large potential change, resulting in a non-equilibrium super-Nernstian
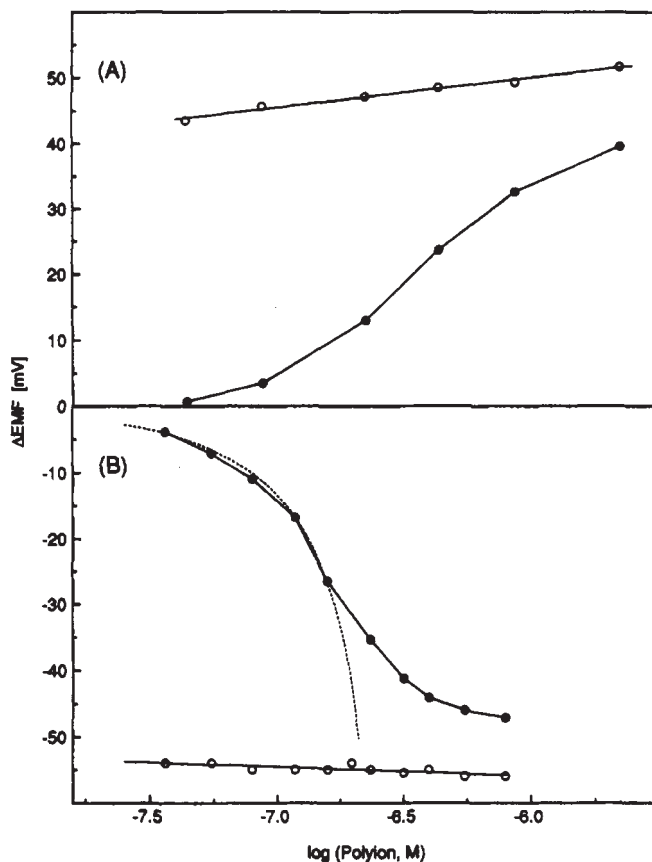
Figure 7.15   Potentiometric responses of (A) protamine and (B) heparin sensors in 0.12 M NaCl solution at different response times: (●) 5 min and (○) 24 h. The membranes were composed of 66 wt% PVC, 32.5 wt% plasticizer (oNPOE and DOS for respective polyions), and 1.5 wt% ion exchangers (Ca^{2+}-5 and TDDMA, respectively). Dotted line, theoretical curve. From reference (62). Copyright 1994 American Chemical Society.

response. This classical response mechanism based on mixed ion-transfer potentials turned out to be analytically useful for detection of biological polyions even beyond protamine and heparin. Moreover, rotating-electrode potentiometry was first developed for the polyion sensors to improve the detection limit (63), where a higher ion flux from the bulk sample solution to the membrane surface is achieved by reducing the diffusion layer thickness.

7.5   CONCLUSIONS

Development of various ionophores in the last four decades has allowed detection of more than 60 analyte ions with liquid membrane ISEs (3). Recent progress in the theory of liquid

membrane ISEs has clarified the response mechanisms so that several long-standing problems of practical importance in the field have been solved. Potentiometric responses in mixed ion solutions can be explained and quantified under both equilibrium and non-equilibrium conditions. The effect of ionic sites on the potentiometric response is fully understood so that the optimum membrane compositions for the highest selectivity can be predicted theoretically. Most impressively, finding and controlling the transmembrane ion flux now allows detection of trace amounts of ions at the picomolar level by ion-selective potentiometry.

These theoretical advances have led to the development of potentiometric methods for quantifying fundamental membrane processes. The stoichiometry of the ionophore–ion complexation in the membrane phase can be determined by studying the effects of ionic sites on potentiometric selectivity. Such a study also reveals whether an ionophore serves as a neutral or a charged ionophore (64). Formation constants of the complexes with the corresponding stoichiometry can be determined from the unbiased selectivity coefficients or more directly by the sandwich method. Quantitative information about the complexation processes in the membranes, which eventually limits practical performances of the electrodes, will be useful for future design of selective ionophores.

Non-equilibrium processes at the sample/membrane interface and across the bulk membrane bias the selectivity and detection limits of the electrodes. Elimination of these non-equilibrium effects by operating the electrodes under complete equilibrium conditions will be of both practical and fundamental significance. While non-equilibrium responses are useful for potentiometric polyion-selective electrodes, it is not obvious whether potentiometry based on mixed ion-transfer potentials is a better transduction mechanism than amperometry/voltammetry based on selective polyion transfer (65, 66). Ion-transfer electrochemistry at polarized liquid/liquid interfaces is introduced in Chapter 17 of this handbook.

REFERENCES

1. W. R. Fawcett, *Liquids, Solutions, and Interfaces: From Classical Macroscopic Descriptions to Modern Microscopic Details*, Oxford University Press: New York, 2004.
2. E. Bakker, P. Bühlmann, E. Pretsch, *Chem. Rev.* **97**, 3083 (1997).
3. P. Bühlmann, E. Pretsch, E. Bakker, *Chem. Rev.* **98**, 1593 (1998).
4. Y. Umezawa, P. Bühlmann, K. Umezawa, K. Tohda, S. Amemiya, *Pure Appl. Chem.* **72**, 1851 (2000).
5. Y. Umezawa, K. Umezawa, P. Bühlmann, N. Hamada, H. Aoki, J. Nakanishi, M. Sato, K. P. Xiao, Y. Nishimura, *Pure Appl. Chem.* **74**, 923 (2002).
6. Y. Umezawa, P. Bühlmann, K. Umezawa, N. Hamada, *Pure Appl. Chem.* **74**, 995 (2002).
7. R. P. Buck, E. Lindner, *Acc. Chem. Res.* **31**, 257 (1998).
8. V. V. Cosofret, R. P. Buck, *Crit. Rev. Anal. Chem.* **24**, 1 (1993).
9. A. Ceresa, E. Pretsch, *Anal. Chim. Acta* **395**, 41 (1999).
10. U. Schaller, E. Bakker, U. E. Spichiger, E. Pretsch, *Anal. Chem.* **66**, 391 (1994).
11. A. Van den Berg, P. D. van der Wal, M. Skowronska-Ptasinska, E. J. R. Sudholter, D. N. Reinhoudt, P. Bergveld, *Anal. Chem.* **59**, 2827 (1987).
12. J. H. Boles, R. P. Buck, *Anal. Chem.* **45**, 2057 (1973).
13. U. Oesch, Z. Brzozka, A. Xu, B. Rusterholz, G. Suter, H. V. Pham, D. H. Welti, D. Ammann, E. Pretsch, W. Simon, *Anal. Chem.* **58**, 2285 (1986).

14. R. Eugster, P. M. Gehrig, W. E. Morf, U. E. Spichiger, W. Simon, *Anal. Chem.* **63**, 2285 (1991).

15. M. Bochenska, W. Simon, *Mikrochim. Acta* **III**, 277 (1990).

16. T. Grady, A. Cadogan, T. McKittrick, S. J. Harris, D. Diamond, M. A. McKervey, *Anal. Chim. Acta* **336**, 1 (1996).

17. M. Huser, P. M. Gehrig, W. E. Morf, W. Simon, E. Lindner, J. Jeney, K. Tóth, E. Pungor, *Anal. Chem.* **63**, 1380 (1991).

18. E. Bakker, *J. Electrochem. Soc.* **143**, L83 (1996).

19. E. Lindner, K. Tóth, J. Jeney, M. Horvath, E. Pungor, I. Bitter, B. Agai, L. Toke, *Mikrochim. Acta* **I**, 157 (1990).

20. A. Cadogan, D. Diamond, M. R. Smyth, G. Svehla, M. A. McKervey, E. M. Seward, S. J. Harris, *Analyst* **115**, 1207 (1990).

21. D. Siswanta, H. Hisamoto, H. Tohma, N. Yamamoto, K. Suzuki, *Chem. Lett.* 945 (1994).

22. M. V. Rouilly, M. Badertscher, E. Pretsch, G. Suter, W. Simon, *Anal. Chem.* **60**, 2013 (1988).

23. K. Suzuki, K. Watanabe, Y. Matsumoto, M. Kobayashi, S. Sato, D. Siswanta, H. Hisamoto, *Anal. Chem.* **67**, 324 (1995).

24. E. Bakker, *Anal. Chem.* **69**, 1061 (1997).

25. U. Schefer, D. Ammann, E. Pretsch, U. Oesch, W. Simon, *Anal. Chem.* **58**, 2282 (1986).

26. M. W. Laubli, O. Dinten, E. Pretsch, W. Simon, F. Vogtle, F. Bongardt, T. Kleiner, *Anal. Chem.* **57**, 2756 (1985).

27. S. Kamata, H. Murata, Y. Kubo, A. Bhale, *Analyst* **114**, 1029 (1989).

28. M. Rothmaier, U. Schaller, W. E. Morf, E. Pretsch, *Anal. Chim. Acta* **327**, 17 (1996).

29. C. Behringer, B. Lehmann, J.-P. Haug, K. Seiler, W. E. Morf, K. Hartman, W. Simon, *Anal. Chim. Acta* **233**, 41 (1990).

30. Y. Qin, Y. Mi, E. Bakker, *Anal. Chim. Acta* **421**, 207 (2000).

31. L. Gorski, E. Malinowska, P. Parzuchowski, W. Zhang, M. E. Meyerhoff, *Electroanalysis* **15**, 1229 (2003).

32. W. E. Morf, *The Principles of Ion-Selective Electrodes and of Membrane Transport*, Elsevier: New York, 1981.

33. V. V. Egorov, V. A. Repin, T. A. Ovsyannikova, *J. Anal. Chem.* **47**, 1235 (1992).

34. S. Amemiya, P. Bühlmann, E. Pretsch, B. Rusterholz, Y. Umezawa, *Anal. Chem.* **72**, 1618 (2000).

35. Y. Mi, C. Green, E. Bakker, *Anal. Chem.* **70**, 5252 (1998).

36. U. Schaller, E. Bakker, E. Pretsch, *Anal. Chem.* **67**, 3123 (1995).

37. P. C. Hauser, N. D. Renner, A. P. C. Hong, *Anal. Chim. Acta* **295**, 181 (1994).

38. G. G. Guilbault, R. A. Durst, M. S. Frant, H. Freiser, E. H. Hansen, T. S. Light, E. Pungor, G. Rechnitz, N. M. Rice, T. J. Rohm, W. Simon, J. D. R. Thomas, *Pure Appl. Chem.* **48**, 127 (1976).

39. E. Bakker, E. Pretsch, P. Bühlmann, *Anal. Chem.* **72**, 1127 (2000).

40. Y. Umezawa, K. Umezawa, H. Sato, *Pure Appl. Chem.* **67**, 508 (1995).

41. E. Bakker, R. V. Meruva, E. Pretsch, M. E. Meyerhoff, *Anal. Chem.* **66**, 3021 (1994).

42. M. Nägele, E. Bakker, E. Pretsch, *Anal. Chem.* **71**, 1041 (1999).

43. P. C. Meier, W. E. Morf, M. Läubli, W. Simon, *Anal. Chim. Acta* **156**, 1 (1984).

44. S. Amemiya, P. Bühlmann, Y. Umezawa, *Anal. Chem.* **70**, 445 (1998).

45. E. D. Steinle, S. Amemiya, P. Bühlmann, M. E. Meyerhoff, *Anal. Chem.* **72**, 5766 (2000).

46. S. Amemiya, P. Bühlmann, K. Odashima, *Anal. Chem.* **75**, 2997 (2003).

47. T. Kakiuchi, M. Senda, *Bull. Chem. Soc. Jpn.* **57**, 1801 (1984).

48. Y. Yoshida, M. Matsui, K. Maeda, S. Kihara, *Anal. Chim. Acta* **374**, 269 (1998).

49. G. M. Shean, *J. Membr. Sci.* **2**, 133 (1977).

50. S. Koizumi, T. Imato, N. Ishibashi, *J. Membr. Sci.* **132**, 149 (1997).

51. Y. Mi, E. Bakker, *Anal. Chem.* **71**, 5279 (1999).

52. Y. Qin, E. Bakker, *Anal. Chem.* **74**, 3134 (2002).

53. E. Bakker, E. Pretsch, *Anal. Chem.* **70**, 295 (1998).

54. T. Sokalski, A. Ceresa, T. Zwickl, E. Pretsch, *J. Am. Chem. Soc*. **119**, 11347 (1997).

55. T. Sokalski, T. Zwickl, E. Bakker, E. Pretsch, *Anal. Chem.* **71**, 1204 (1999).

56. E. Bakker, E. Pretsch, *Anal. Chem.* **74**, 420A (2002).

57. R. E. Gyurcsanyi, E. Pergel, R. Nagy, I. Kapui, B. T. T. Lan, K. Toth, I. Bitter, E. Lindner, *Anal. Chem*. **73**, 2104 (2001).

58. K. Pergel, R. E. Gyurcsanyi, K. Toth, E. Lindner, *Anal. Chem.* **73**, 4249 (2001).

59. T. Vigassy, R. E. Gyurcsanyi, E. Pretsch, *Electroanalysis* **15**, 1270 (2003).

60. A. Ceresa, A. Radu, S. Peper, E. Bakker, E. Pretsch, *Anal. Chem.* **74**, 4027 (2002).

61. J. Sutter, E. Lindner, R. E. Gyurcsanyi, E. Pretsch, *Anal. Bioanal. Chem.* **380**, 7 (2004).

62. B. Fu, E. Bakker, J. H. Yun, V. C. Yang, M. E. Meyerhoff, *Anal. Chem.* **66**, 2250 (1994).

63. Q. S. Ye, M. E. Meyerhoff, *Anal. Chem.* **73**, 332 (2001).

64. E. Bakker, E. Malinowska, R. D. Schiller, M. E. Meyerhoff, *Talanta* **41**, 881 (1994).

65. Y. Yuan, S. Amemiya, *Anal. Chem.* **76**, 6877 (2004).

66. J. Guo, Y. Yuan, S. Amemiya, *Anal. Chem.* **77**, 5711 (2005).

– 8 –

Chemically Modified Electrodes

Grant A. Edwards, Adam Johan Bergren, and Marc D. Porter

Iowa State University, Ames, IA 50011, USA

8.1   INTRODUCTION

Electrode surfaces are modified in a quest to render an electrochemical function either not possible or difficult to achieve using conventional electrodes. Targeted improvements include increased selectivity, sensitivity, chemical and electrochemical stability, as well as a larger usable potential window and improved resistance to fouling. Furthermore, electrodes with tailored surfaces enhance fundamental studies of interfacial processes. Therefore, the need for improved electrode performance and logically designed interfaces is rapidly growing in many areas of science.

The definition of a chemically modified electrode (CME) is: a conducting or semiconducting material that has been coated with a monomolecular, multi-molecular, ionic, or polymeric film (termed adlayer; see Figure 8.1) which alter the electrochemical, optical, and other properties of the interface (1, 2). The conductive and semiconductive substrates are derived from conventional electrode materials (see Chapter 5), while the adlayers are widely diverse in their origins and properties. This diversity extends or enhances the range and scope of electrochemical techniques.

Ideally, the properties of the adlayer impart a predictable function to the electrode. Recent improvements in surface characterization techniques enable a molecular-level understanding of modified interfaces. These techniques, coupled with electrochemical characterizations, not only provide a means to verify the function, but also serve as a basis for refinements of the modification strategy to further enhance its performance.

The extensive nature of electrode modification procedures prevents a comprehensive description of all types of modified electrodes, their uses, and the techniques used to characterize them. This chapter therefore focuses on providing the reader with concepts central to electrode modification through several examples of established systems. Specialized reviews are noted in each section, where appropriate; these and topical texts (3–10) should be consulted for more detailed information.
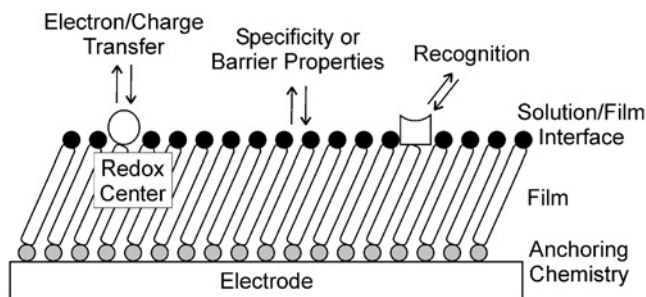
Figure 8.1   Generic illustration of a modified electrode. The film (or adlayer) is anchored to a conventional electrode to enhance performance or achieve a specialized function.

8.2   SUBSTRATE MATERIALS AND PREPARATION

The substrate is the platform electrode that supports the adlayer. Commercially available or custom fabricated substrates can be used. While any conventional electrode material can serve as a substrate, some materials are more convenient to modify. Of the conductive metals, Au, Ag, and Pt are the most commonly modified (11). These surfaces benefit from the ease with which reproducible and clean surfaces can be produced and maintained in the laboratory environment. Carbon electrodes (12, 13) are also commonly employed for similar reasons. Other metals and semiconductors are used less frequently, but are nonetheless high-profile materials (4, 5).

In most electrode preparation schemes, the electrode surface is treated before modification to provide reproducible surface attributes. These procedures often involve conventional electrode treatments (see Chapter 5), with adaptations or additions where needed. The pretreatment is critical: the electrochemical behavior of a derivatized electrode is often sensitive to small variations in the substrate properties (e.g., crystallinity, roughness, chemical functionality). Thus, preparation procedures must frequently be refined through trial and error to achieve the desired performance. On the other hand, the function of the electrode can often be fine-tuned by changing pretreatment variables, enhancing the versatility of a modification scheme.

Specific functional groups may also be necessary for some modification strategies. In these cases, pretreatment methodologies can include steps designed to create a high population of active sites on the substrate surface. Likewise, requirements of adlayer characterization methods may require specific substrate properties. For example, atomically smooth surfaces are preferable for high-resolution scanning tunneling microscopic (STM) characterizations of adlayer structures. Thus, the intended application of the modified electrode, requirements of surface characterization techniques, and the modification chemistry often direct the choice of substrates and pretreatment procedures.

8.3   MODIFIED ELECTRODE TYPES

Modified electrodes can be classified by the film–substrate attachment method (e.g., physisorption, chemisorption, and covalent attachment) and film composition (e.g., clays,

zeolites, sol-gels, polymer, and DNA). Choice of modification methods and film identity stems from the demand of the end-application. Multiple combinations of attachment methodologies and film compositions may be realized. The anchoring mechanisms, structural characteristics, and electrochemical uses of some example systems are discussed within this section.

8.3.1   Langmuir-Blodgett

The Langmuir-Blodgett (L-B) assembly technique (8, 14, 15) offers a versatile way to prepare a modified electrode. L-B layers are created by transferring organized monomolecular films from a liquid phase in a Langmuir trough onto a solid support. Attractive non-covalent interactions hold the film in a cohesive unit on the electrode surface. However, the weak nature of these forces limits adlayer stability.

   L-B films are useful in biological studies, as they can easily be prepared to act as mimics of lipid membranes. Thus, modified electrodes of this type are often used in studies of transport phenomena (16) and enzyme activity. These electrodes are also often used as molecular recognition sensors (17–20) and in molecular electronics (20–22).

8.3.1.1   *Structural description and preparation*

Langmuir-Blodgett films are formed by the deposition of a Langmuir film onto a solid substrate. Langmuir films are composed of an organized monolayer of amphiphilic molecules at a liquid/gas interface. These molecules, by virtue of possessing a hydrophobic tail and a hydrophilic head, are spontaneously oriented at a liquid/gas interface. For example, a sparingly water-soluble amphiphile spread onto an aqueous phase results in partial solubilization of the head group, while the hydrophobic tail group extends partially into the gaseous phase to minimize the free energy of the system. The resulting film is depicted in Figure 8.2. Some amphiphiles commonly used in the construction of Langmuir films are given in Table 8.1. Films with mixed composition can be prepared by spreading mixtures of amphiphiles onto a common solvent (20, 23). Homogeneous or phase segregated films result from the chemical properties of the molecules spread at the interface.
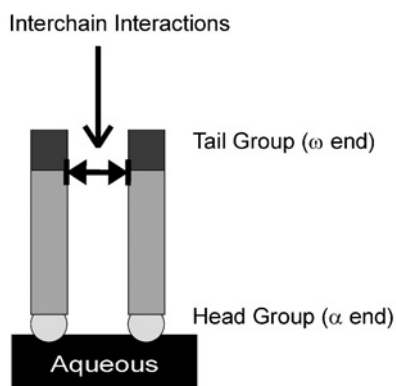
Figure 8.2   Diagram of a Langmuir film (only two molecules are shown for clarity).

Table 8.1

Functionalized aliphatic amphiphiles used to form Langmuir-Blodgett films[a]

Molecule	Formula	Attributes
Acids	$C_nH_{2n+1}COOH$	Easy to vary n
Alcohols	$C_nH_{2n+1}OH$	Difficult to form L-B layers
Esters	$C_nH_{2n+1}COOR$	Form monolayers and multilayers
Amides	$C_nH_{2n+1}CONH_2$	Form alternating multilayers
Amines	$C_nH_{2n+1}NH_2$	Alternate with acids
Nitriles	$C_nH_{2n+1}CN$	

[a]Other examples include aromatics, heterocycles, highly conjugated molecules (dyes), porphyrins, pthalocyanines, fullerenes, polymers and biological compounds (phospholipids, pigments, peptides, and proteins).
Source: Adapted from reference (8) with the permission of Cambridge University Press.
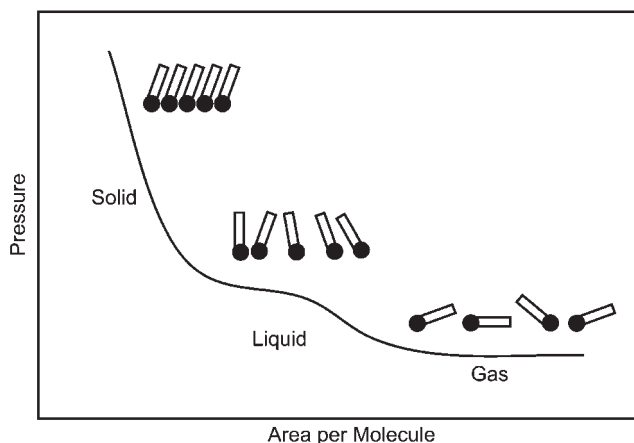
Figure 8.3   Two-dimensional phase diagram of a Langmuir film. Reproduced from: K. Kolasinski, *Surface Science: Foundations of Catalysis and Nanoscience*, John Wiley & Sons, Ltd.: Chichester, 2002. Copyright 2002 by John Wiley & Sons, Limited. Reproduced with permission.

After a desired composition (single- or multi-component) is achieved, lateral pressure is applied to increase the two-dimensional film concentration. In practice, pressure is applied using a moveable barrier in a Langmuir trough. As the film is compressed, the system goes through a series of phase transitions, as shown in Figure 8.3 At the end of the compression cycle, a highly ordered two-dimensional film is formed.

After creation of the compressed film, it can be transferred to an electrode surface. The characteristics of the substrate can tremendously affect the quality of the resulting Langmuir-Blodgett film (20), and dictate how the initial layer is transferred. Figure 8.4 depicts a common film transfer method, where a hydrophilic substrate is vertically lifted through a Langmuir film. The attractive forces between the surface and the head groups result in transfer of the layer, such that the film physisorbs on the electrode surface. These
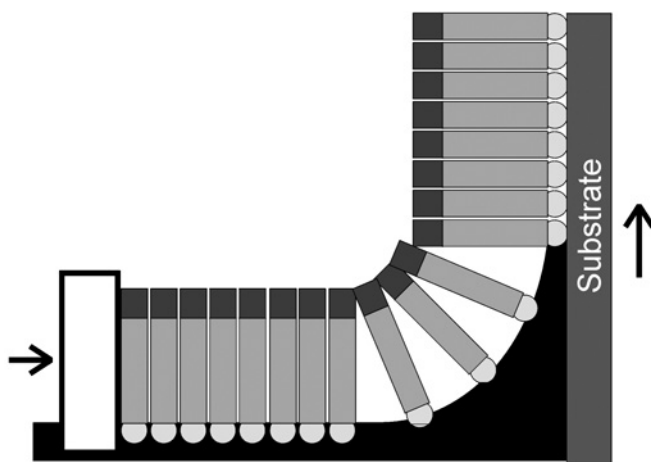
Figure 8.4   Receding deposition of an L-B film. Adapted from reference (8) with the permission of Cambridge University Press.

forces are often sufficient to exclude solvent molecules from the interface between the solid support and the film. Upon careful transfer, the electrode-supported adlayer retains the packing density and orientation of the precursor Langmuir film.

Extending deposition transverses the substrate downwards from the gas phase through the Langmuir film into the liquid layer, orienting the head groups away from the surface. Conversely, the example shown in Figure 8.4 is termed receding deposition; as the substrate is withdrawn from the liquid, hydrophilic head groups are deposited directly onto the substrate surface. Multiple layers can be deposited by repeated cycles in which the substrate is raised and/or lowered through the Langmuir film.

Complex layer architectures can be developed using different deposition cycles. Figure 8.5 shows some examples of layers that can be created, where X, Y, Z, and A-B-A types are represented. X-type films are created by repeated extending deposition, resulting in head-to-tail orientation of molecules in adjacent layers. Z-type layers are formed from successive receding deposition cycles. Alternating extending and receding deposition results in a Y-type film, orienting the monomolecular layers in a head-to-head and tail-to-tail configuration. Mixed multilayers (termed A-B-A layers) are deposited using more than one amphiphile, and a multiple tank trough, with a variety of possible structural features.

8.3.1.2   *Overall characteristics*

The power of the L-B technique is the vast array of possible layer types and orientations. However, the forces that hold the film in a coherent unit on the substrate surface consist of van der Waals interactions. These forces are much smaller than those resulting in chemical bond formation. Thus, L-B layers may not be stable for long periods of time or in harsh environments. Moreover, specialized equipment is required to create them, and special care must be taken to ensure reproducible and well-ordered films. This approach is particularly demanding with respect to high-purity reagents and liquids, and surface preparation procedures.
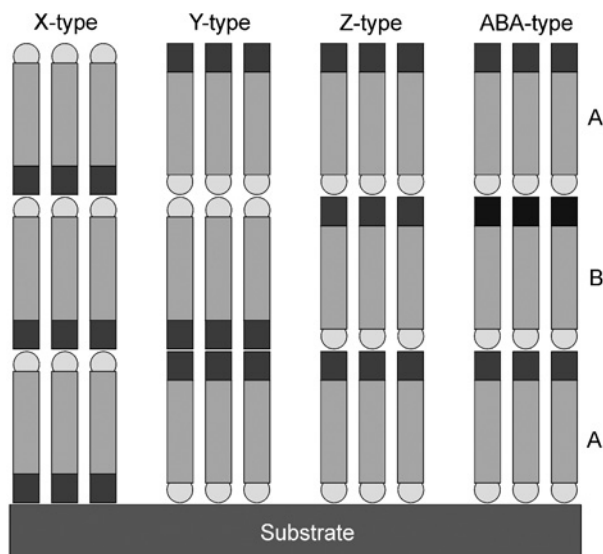
Figure 8.5 Langmuir-Blodgett film types. Adapted from reference (8) with the permission of Cambridge University Press.

8.3.1.3   *Applications*

L-B films often resemble lipid membranes. Thus, electrodes modified with these layers are particularly relevant as mimics in studies of biological functions, including transport phenomena (16), enzyme activity (20), and molecular recognition (17–20, 22). Finally, the ability to control the thickness of an L-B layer on the nanometer scale is well-suited for studies of molecular electronics and nanotechnology (20–22).

8.3.2   Self-assembly

Modification of a substrate surface by spontaneous adsorption (24), now more commonly referred to as self-assembly, is one of the most utilized modification pathways. These films are typically bound to the substrate by chemisorption; however, intermolecular forces within the film are also important. Chemisorption is the strong adsorption of a molecule onto a surface through the spontaneous formation of a chemical bond (1). This chemical bond forms between a functional group in the molecule and a site on the electrode. Monomolecular layers prepared by chemisorption are known as self-assembled monolayers (SAMs). These adlayers can be used to impart the desired function to the electrode directly, or can serve as a foundation for more complex electrode architectures.

8.3.2.1   *Structural description and preparation*

A schematic illustration of a SAM is shown in Figure 8.6. Chemisorption occurs through the head group, or α-end. A spacer chain separates the head group from the tail group,
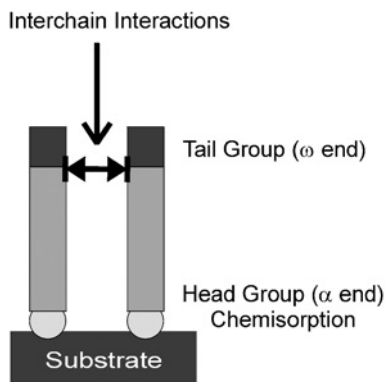
Figure 8.6 Schematic of a self-assembled monolayer. Adapted from reference (6) with permission.

or ω-end. The head group is responsible for the largest energetic contribution to self-assembly, while the tail group strongly influences interfacial properties. The microscopic structure of the film is dependent on the forces acting between the spacer chain and tail groups, and include dispersive (or van der Waals), electrostatic, and steric interactions. Densely packed layers are formed when the spacer chains and tail groups maximize attractive forces and have comparable van der Waals radii. Less dense and more disordered adlayers may also form as a consequence of repulsive interactions, mismatches in packing radii, and/or registry with the substrate, but are still suitable for a wide range of studies.

SAMs are created by exposure of an adsorbate precursor (liquid or vapor) to a suitable substrate. Usually, the substrate is immersed in a dilute solution ($10^{-4}-10^{-3}$ M) for a predetermined time (seconds to days) after which the electrode is removed, rinsed copiously with neat solvent, and dried before use. Mixed monolayers can be formed by the simultaneous deposition of multiple precursors from the same solution. However, caution must be exercised since the solution concentration ratio usually does not reflect the resulting surface composition.

Many sulfur-containing functional groups chemisorb onto metal electrodes (11, 25–30). For example, thiols and disulfides spontaneously adsorb on gold. Thiols also chemisorb at silver, copper, platinum, and mercury; however, gold is by far the commonly used substrate electrode due to its relative inert nature. Several examples of SAMs that have been reported in the literature are listed in Table 8.2. A detailed discussion of an example (alkanethiolates on gold) is given below.

8.3.2.2 Formation and structure of alkanethiolates on gold

Alkanethiolates on gold (Au-S-$(CH_2)_n$-X) serves as an ideal system for demonstrating the important concepts and techniques used in the fabrication, characterization, and application of SAM-based modified electrodes. There are many excellent examples of their application in practical and fundamental areas related to electroanalytical and surface chemistry

Table 8.2

Examples of modifying layers formed by chemisorption

Molecule	Electrode material
RSH	Au (29), Ag (31), Pt (4), Cu (30), Hg (32)
RSSR′	Au (26)
RSR′	Au (33)
R_3P	Zr (34, 35)
RNC	Au (36–40), Pt (41), Cu (36)
RCOOH	Ag (6), Al_2O_3 (6)
$R(OArCH(NH_2)_2)_2$	Au (42)
Silanes	Hydroxlyated surfaces (6, 43)

Note: A more extensive table could be found in reference (25).

(6, 43, 44). However, the adsorption mechanism and the resulting structural details of these adlayers are complicated (45, 46).

The assembly mechanism of alkanethiols onto gold from the liquid phase (45–55) and the vapor phase (56) has been investigated using scanning tunneling microscopy (STM) and other techniques. A generalized mechanism is illustrated in Figure 8.7. The adsorption process is characterized by two distinct stages. The first stage results from the affinity of the thiol head group for the Au surface, driving the formation of a disordered layer with sub-monolayer coverage, as depicted in Figure 8.7A−C. During this stage, the surface becomes saturated with molecules having an average orientation parallel to the surface; the layer does not reach its full thickness. The second stage, shown in Figure 8.7D−E, proceeds over a longer time scale, and is driven by interactions (van der Waals forces) between the spacer chain and tail groups. These lateral interactions orient the molecules more perpendicular to the surface, allowing the coverage and thickness to increase to packing density limits. This combination of head-group binding and intermolecular forces leads to an equilibrium structure characterized by high packing density (formation of a full monolayer), molecular ordering (all-trans zigzag conformation of sequences with the alkane chains), and stability.

Although SAMs are capable of forming dense adlayers, many subtle variables, especially during the early stages of formation (57, 58), can result in the variation of the microscopic film structure. These differences can significantly alter the behavior of the electrode.

SAMs are stable within an extended potential window: –0.8 to +0.8 V vs. Ag/AgCl (59). However, the pH of the solution can alter these limits. Nevertheless, the positive limit is defined by oxidation of the adlayer. Furthermore, electrochemical experiments have revealed that upon cathodic potential sweeps, a surface wave is observed that corresponds to the one-electron reduction of a complete monolayer of thiolates (60). The film packing density can be determined from integration of the peak current obtained upon reductive desorption. Moreover, insights into the structural features and formation mechanism is available from reductive desorption data (59). This desorption process limits the cathodic potential possible for SAM modified electrodes.
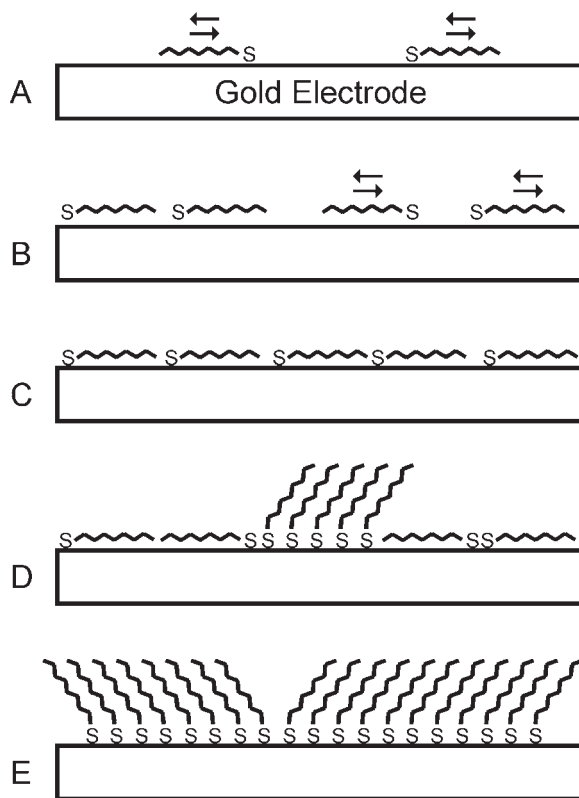
Figure 8.7 Illustration of the self-assembly mechanism of alkanethiols onto gold. Adapted from reference (56) with permission. Copyright 1996 AAAS.

Extensive surface characterizations have been applied to alkanethiolates on gold. For instance, X-ray photoelectron spectroscopy (XPS) has been used to identify the electronic state of the adsorbed sulfur atom as a thiolate (26) with a partial charge of -0.2 (61). STM has also been used extensively to interrogate the resulting adlayer structure. The binding site of the sulfur head-group has been speculated to occur at threefold hollow sites at Au(111), forming a $(\sqrt{3} \times \sqrt{3})R30°$ adlayer, as shown in Figure 8.8 (62, 63). There are also numerous studies indicating more complicated lattice structures, showing that perhaps, many different structures are possible (43).

8.3.2.3 Overall characteristics

The main limitation of self-assembly is the requirement of a specific functional group that will drive assembly onto the substrate of interest. Moreover, the rational design and formation of tailored mixed systems are complicated by an interwoven multi-step assembly mechanism. Fortunately, these limitations could be overcome on most occasions, and self-assembly allows facile control of interfacial properties at the molecular level (64).
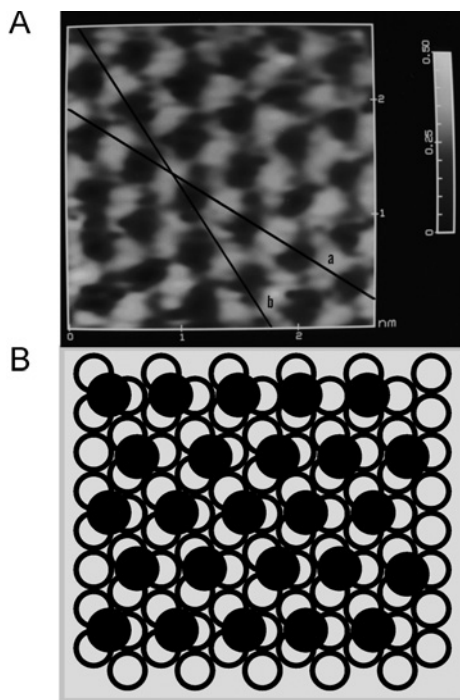
Figure 8.8 (A) STM image of ethanethiolate on Au(111). (B) Representation of the $(\sqrt{3} \times \sqrt{3})R30°$ overlayer structure of a thiolate monolayer. Open circles represent Au atoms while filled circles represent S atoms (not to scale). Adapted from reference (63) with permission.Copyright 1991 American Chemical Society.

Although SAM precursors are amphiphilic molecules, as in L-B films, SAMs are more stable due to the specific nature of chemisorption. Thus, the preparation of SAMs is much more facile and the resulting adlayers are more stable. Functionalities can also be introduced into the adlayer that allows for further modification of the interface. Therefore, SAMs are attractive as coatings in many applications.

8.3.2.4 Applications

SAMs are widely used in electrochemistry to block access of solution-based molecules (11). A well-defined thickness between the substrate surface and redox couple is provided by SAMs with electroactive tail groups (11, 65–72). The spacer chain is used to hold the redox center away from the surface of the electrode, enabling studies of long-range heterogeneous electron transfer.

The use of SAMs as a facile way to attach other functionalities to the electrode surface has been exploited in the development of chemical sensors (44, 45). Functionalities presented at the electrode easily modulate the selectivity of the electrode surface for an analyte of interest. Cyclodextrins, calixarenes, and other molecules with size and shape specificity

can be tethered to the surface of the SAMs lending chemical specificity to the electrode surface (73, 74). SAM modified electrodes are also utilized in biomimetics (45), studies of interfacial phenomenon (25), nanotechnology (25), and molecular electronics (45).

8.3.3 Covalent attachment

By taking advantage of traditional synthetic chemistry, surface-based functional groups can be modified through the formation of new chemical bonds (4, 5, 75). These covalent attachment schemes are used to modify the surface of an electrode. The reactions used for derivatization are determined by the identity of the chemical components on the electrode surface. Therefore, the choice of the modifier must account for the reactivity of the target surface site.

Covalent anchoring can result in stable, reusable modified electrodes. However, adlayer stability is not guaranteed (especially for organosilane linkages) and increased robustness may be offset by the complicated preparation required for many covalent modification schemes. Moreover, highly organized layers are often difficult to achieve, and reproducibility of the fine structure of the layer can be limited.

8.3.3.1 *Overall description and electrode pretreatment*

A variety of functional groups exist on the surface of many common electrode materials. Enrichment of these groups is normally required to realize acceptable reactive site population (4, 5). Additional activation steps can be employed to increase the efficiency of coupling (i.e., by converting the functional group to a more reactive form). The enrichment and activation steps can be accomplished in a single step, or may require multiple steps. Figure 8.9 illustrates common covalent electrode modification schemes.
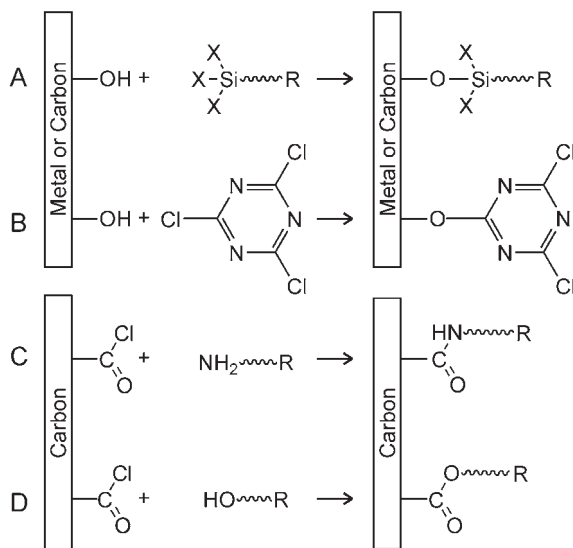
Figure 8.9   Covalent modification schemes (4, 5, 76).

8.3.3.2   Covalent modification of carbon electrodes

Considering the scope of organic chemistry, carbon electrodes are an obvious choice as a substrate for covalent anchoring schemes (5). The bulk of carbon electrode materials are extended networks of fused aromatic rings (see Chapter 5). The terminal surface region of the network is often rich in reactive sites. Oxygen-containing functional groups (i.e., carboxylic acids and alcohols) and sp^2 hybridized carbon atoms have been exploited in covalent modification strategies (5).

There are two categories of covalent modification schemes for carbon electrodes: (1) chemical and (2) electrochemically assisted. Common functional groups on carbon electrodes include carboxylic acids, alcohols, and ketones. Most chemical methods employ carboxylic acid or hydroxyl groups, while electrochemically assisted modification can occur by direct reactions with aromatic surface carbon atoms.

(a)   Chemical reactions at carbon

Organosilane chemistry can be used to anchor modifying layers to any hydroxyl-containing moiety, as shown in Figure 8.9A. Thus, organosilanes are commonly used to modify carbon electrodes. In practice, dense hydroxyl group populations are formed by reduction of acids. The silane can be used directly as the adlayer or serve as a linker molecule.

Although silane chemistry provides a very versatile method for modification of carbon electrode surfaces, it is difficult to obtain ordered layers with well-defined thickness (see Figure 8.10). Moreover, these layers show poor reproducibility and stability, and thus far have mainly been used in fundamental studies (43).

Hydroxyl groups can also be reacted with cyanuric chloride (76–79), as shown in Figure 8.9B. Each cyanuric chloride moiety has three reactive sites, which can be used for
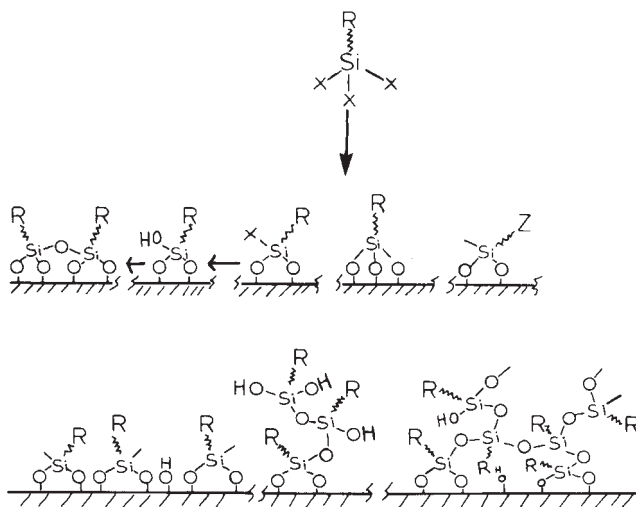
Figure 8.10   Organosilane reactions with metal oxide surfaces. Reproduced from reference (5) with permission. Copyright 1984 Marcel Dekker, Inc.

immobilization. This leaves one or two reactive sites for the formation of an adlayer of amines, alcohols, Grignard reagents, or hydrazines (5).

On the other hand, carboxylic acid groups, due to their rich synthetic chemistry and natural occurrence on carbon electrode surfaces, are often used in covalent anchoring of adlayers onto carbon electrodes. The surface density of carboxylic acid groups can be increased by heating the electrode in air or by oxygen plasma treatment (77). To increase the efficiency of the reaction between surface sites and amines or alcohols, the carboxylic acids are often converted to acid chlorides (e.g., using thionyl chloride). After activation, these surfaces can be further reacted with amines and alcohols to allow attachment of other functional groups or electrode-modifying layers (Figure 8.9C–D). Often, these reactions are used to tether electroactive groups to the surface, and the resulting systems are used in electron transfer studies (5).

(b)   Electrochemically assisted reactions at carbon

A powerful strategy to covalently derivatize carbon electrodes with monolayers and multilayers utilizes electrochemical reactions (75). Electron transfer is used to activate a heterogeneous chemical reaction. The adlayer is formed after generating the highly reactive species by oxidation or reduction of the solution-based molecule or a surface-based functional group. In most electrochemically assisted modification schemes, the reaction involves a carbon radical.

Electrochemically assisted modification of carbon electrodes has been accomplished by oxidation of amines (80, 81) and arylacetates (82), reduction of aryl diazonium salts (83), and anodization (oxidation) in a solution with alcohols (75). Of these schemes, reduction of diazonium salts, shown in Figure 8.11, provides a particularly convenient pathway for carbon electrode modification.

The electrochemical reduction of aryl diazonium salts is generally carried out in acetonitrile or acid solutions (75). This method allows diverse functionality (84, 85), and the possibility of monolayers or multilayers (86, 87). Although a high adlayer coverage can be obtained (88), the blocking efficiency depends on the details of the modification procedures (89). The convenience and diversity offered by diazonium reduction have led to the application of this modification procedure in areas ranging from studies of electron transfer kinetics (90), molecular electronics (91), sensor design (92), and even in the chemical modification of carbon stationary phases in liquid chromatography (93).

8.3.3.3   Covalent modification of metal electrodes

Many different metals can be electrochemically oxidized, providing a high density of hydroxyl groups (4, 5). Organosilane and cyanuric chloride chemistry can be utilized to
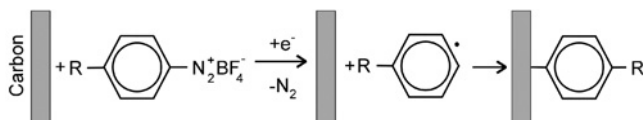

Figure 8.11   Reaction scheme for covalent attachment by phenyldiazonium reduction. Adapted from reference (75) with permission.

modify oxidized metal surfaces as shown in Figure 8.9A–B, analogous to carbon electrodes (10, 43).

8.3.4   Clay modified electrodes

Clays possess many properties that make their use as electrode modifiers intriguing. These features include abundance, low cost, diversity, high chemical stability, negligible toxicity, and pliability (94–98). The diversity stems from differences in chemical composition, charge, size, and major associated ions (95). Clays can also withstand highly oxidizing environments and temperatures (98). Therefore, they are often used as electrode modifiers when the experiments demand harsh conditions where the integrity of other adlayers would be compromised. Perhaps most importantly, the structural composition of clays imparts functions that are particularly amenable to electrochemistry. An overview of the chemical and physical characteristics is necessary to understand their utility in electrochemistry.

8.3.4.1   Structural description

Clays are abundant throughout the world; approximately 4250 distinct clay minerals have been identified (98), of both natural and synthetic origin. Clays are phyllosilicate minerals, so-called because of their sheet-like (1:20 thickness:length) structure (99). The sheets (phyllo) consist of aluminosilicate networks composed of silicon oxide tetrahedra (SiO_4) or aluminum oxide octahedra (AlO_6). These sheets form layers (platelets) when oxygen atoms are shared between two or more adjacent sheets, and can combine in various ways to form many different types of clays.

   Clays are categorized by a tetrahedral:octahedral numbering system. A 1:1 layer is composed of one tetrahedral sheet linked to one octahedral sheet. 2:1 layers are also common, where one octahedra is sandwiched between two tetrahedral sheets (99). Some of the common clay materials are presented in Table 8.3.

   Clay platelets may be dispersed or stacked in pseudo-crystalline arrangements. Regular groupings of layers in face-to-face, edge-to-face, or edge-to-edge configurations (and combinations of these) result (96) in crystals having grain sizes in the colloidal range (<2 μm) (99). Cohesive van der Waals and electrostatic forces hold the grains together when present in a modifying layer on the substrate. The surface of a platelet contains oxygen or hydroxide groups, imparting a hydrophilic nature to the region between two platelets. Therefore, this region can swell and accommodate water molecules (98).

   The number of different clays is greatly extended by replacement of the Al^{3+} or Si^{4+} cations in the crystalline lattice (i.e., Mg^{2+}, Fe^{2+}, or Li^+ for Al^{3+}) (98). Usually, the replacement cations are less positively charged, resulting in an inherent excess negative charge on each platelet. Exchangeable cations, on the other hand, such as Na^+ and Ca^{2+}, reside in the aqueous interlayer region, neutralizing the excess negative charge and electrostatically binding the platelets. Thus, the cation-exchange capacity (CEC) of clays is generally large. The natural occurrence of anion-exchange clays is far more infrequent than cation-exchange clays. However, anion-exchanged clays have been prepared synthetically. An outline of the different types of clay is presented in Table 8.3.

Table 8.3

Clay materials commonly used to modify electrodes

	Tet:Oct	Name
Cation–exchange	1:1	Kaolinite
		Halloysite
	2:1	Prototype montmorillonite
		Montmorillonite
		Nontronite
		Illite
		Hectorite
		Laponite
		Saponite
		Vermiculite
Anion exchange	2:1	Chlorite
	0:1	Brucite
		Hydrotalcite
		Layered double hydroxide

Source: Adapted from reference (95) with permission.

8.3.4.2 *Pretreatment*

Before immobilization on the substrate, the clay must be treated to ensure uniform and predictable properties. Naturally occurring clays contain particulate and chemical impurities. Moreover, the native ionic species in the interlayer region may vary, requiring different procedures to realize effective and reproducible ion-exchange properties. Pretreatment steps also influence the conductivity and porosity of the clay.

The heterogeneity inherent in natural clays can be overcome by simple treatments. The following procedure is described by Bard and Mallouk (96), while similar treatments involving freeze drying have been presented (94, 100). First, large particles are removed by decanting an aqueous suspension of the clay. The decanted suspension is stirred in a concentrated (1 M) solution of NaCl for 48 h to ensure Na^+ is the major interlayer ion. This solution is centrifuged and washed, then dialyzed to remove excess electrolyte. Finally, a last centrifugation step is used to ensure the solution contains particles under 0.2 µm in diameter. Other impurities can be removed by procedures that are more specialized. Iron oxide, for example, can be removed from the interlayer region by dithionite and citrate treatments (96) without disturbing the iron content of the crystalline lattice.

Pillared clays are prepared by intercalation of bulky cations (e.g., $[Al_{13}O_4(OH)_{28}]^{3+}$) to provide a fixed spacing between platelets (96). A well-defined interlayer spacing (between 10 and 20 Å) is adjustable by changing the cation identity. Pillared clays are utilized to provide a regular cavity size, allowing the incorporation of molecular guests of specific size.

8.3.4.3 *Immobilization*

The plastic nature of clays makes their immobilization onto a solid substrate electrode straightforward: spin-coating, drop-casting, and screen-printing techniques have all been successfully implemented (97, 98). Covalent attachment using silane linkages has also

been reported (95). Other, less common methods include Langmuir-Blodgett film transfer and electrophoretic deposition, and have resulted in hybrid films (films containing other amphiphilic molecules), and extremely smooth films, respectively (97). Drop-casting and spin-coating are the most commonly reported techniques for immobilizing clays on electrodes (96). However, clay materials are also often utilized in composite carbon paste electrodes (97). It is important to note that the electrolyte identity and concentration, and the solvent in which the clay is dissolved prior to deposition affect the structure of the film (94–96), and therefore the function of the resulting electrode.

8.3.4.4 *Applications*

Clay modified electrodes are used in fundamental studies of electron transfer, and in the construction of sensor devices. The ionic aqueous environment in the interlayer region is highly amenable to electrochemical processes. Furthermore, this environment is controllable and fairly innocuous, allowing many different species to retain their activity. Molecular recognition, chemical catalysis, electrocatalysis, and preconcentration of analyte molecules are all applications of this class of modified electrodes. A condensed list of clay modified electrodes is given in Table 8.4. Reference (96), Table 6.1 on pages 280–281 contains a more comprehensive list.

The ion-exchange properties of clay materials lead to several practical applications. The analytical signal results from heterogeneous electron transfer between electroactive ions and the substrate. This signal arises from the permeation of electroactive molecules through the clay layer to the underlying electrode. Thus, electroactive ions (e.g., dissolved metals) can be preconcentrated through ion-exchange, and quantified with high sensitivity and selectivity using stripping voltammetry (98). Analytes that do not appreciably permeate the clay film can be determined by a mediation reaction.

Neutral molecules can also be incorporated into clay materials by taking advantage of their sorption properties. The mild environment of the interlayer region provides an ideal matrix for biologically active molecules. Thus, biosensors can be constructed by incorporation of enzymes into the film (98). The enzyme can then act as a mediator for the target biomolecule.

Table 8.4

Electrochemical uses of clay modified electrodes

Electrode materials	Analyte	Benefits
Glucose oxidase in nontronite on GC	Glucose	Stable, reusable, reduced interference
Nafion-coated nontronite on GC	Methyl viologen	Reduced interference
Nafion-coated nontronite on GC	Uric acid, dopamine	Reduced interference
Mercury-plated nontronite on GC	Cu^{2+}, Zn^{2+}	Enhanced selectivity
Cellulose acetate membrane with montmorillonite or nontronite	$[Cu(NH_3)_4]^{2+}$	Trace analysis of Cu^{2+}
Screen-printed nontronite	Codeine, amitole, purine bases	FIA and voltammetry
Nontronite stabilized catalyst	Dopamine	LOD 0.54 nM

Source: Information adapted from reference (98).

Finally, the properties of the solution should be considered. Competition between electrolyte cations and analyte molecules for ion-exchange sites within the film make high concentrations of electrolyte undesirable. Moreover, small variations in the electrolyte concentration can have a large effect on the interlayer spacing of the clay material. pH also affects the stability and electrochemical response of the film. Furthermore, some solvents may degrade the film. For example, polar organic molecules are known to intercalate, dramatically changing the interlayer spacing in some clays (96).

8.3.5   Zeolite modified electrodes

A class of aluminosilicates called zeolites offer a number of chemical, physical, and structural characteristics that merit use as electrode modifiers (7, 101–106). The chemical composition of zeolites is similar to that of clays; however, zeolites are three-dimensional aluminosilicate crystals rather than two-dimensional sheet structures. This distinction imparts unique chemical and physical properties that can be exploited for preconcentration, size and shape selectivity, and catalysis. However, molecules that can be incorporated into zeolites are more limited due to spatial constraints of the zeolite cavity.

8.3.5.1   *Structural description*

A zeolite is an inorganic molecule consisting of a base matrix of aluminosilicates arranged in a three-dimensional crystal (107–112). They have high ion-exchange capacities due to charge excesses inherent in their structure. The distinguishing feature of zeolites is the three-dimensional framework, which results in channels and cages of molecular dimensions. These apertures act as molecular sieves, allowing the passage of small, appropriately shaped molecules. Once within a zeolite, chemical reactions are often facilitated through geometric confinement. That is, the molecule or molecules are forced into a configuration that increases their reaction probability. These combined properties (ion-exchange, size and shape selectivity, and catalytic activity) are particularly useful in electrochemistry.

The basis of the three-dimensional structure of zeolites is the framework of tetrahedral silicon and aluminum oxide rings shown in Figure 8.12. Bridging oxygen atoms are shared between the silicon and aluminum atoms in variable ratios, giving rise to diversity in the types of ring structures that can be formed. These rings come together in the third dimension because of the extended tetrahedral bonding scheme. Therefore, different ring structures result in different cage dimensions and geometries. Figure 8.13 depicts structures of four zeolite types, exemplifying the porous, cage-like openings with dimensions on the molecular scale. Approximately 40 different naturally occurring zeolites have been discovered (96).

The structure of the AlO_2/SiO_2 network induces a fixed negative charge at each Al atom (see Figure 8.12). Associated cations maintain electroneutrality, with common species being Na^+, K^+, Ca^{2+}, Mg^{2+}, H^+, NH_4^+, and some organic cations (96); these cations are exchangeable. The strong acid nature, arising from terminal hydroxyl groups at the crystal faces (104), is key to the catalytic activity of zeolite–acid catalyzed reactions.
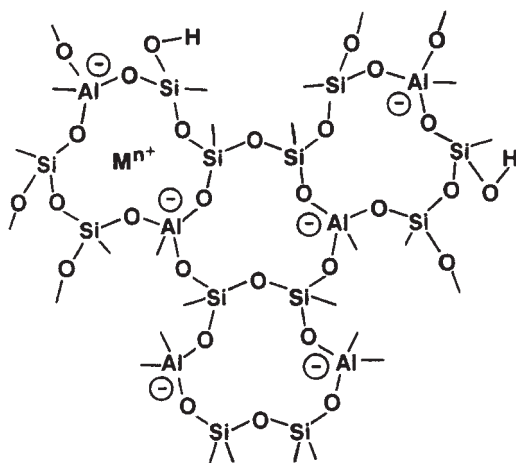
Figure 8.12   Chemical structure of an aluminosilicate zeolite, illustrating the Al-O-Si network, the terminal hydroxyl groups, and the fixed anionic sites (with charge compensating cations). Reproduced from reference (104) with permission.
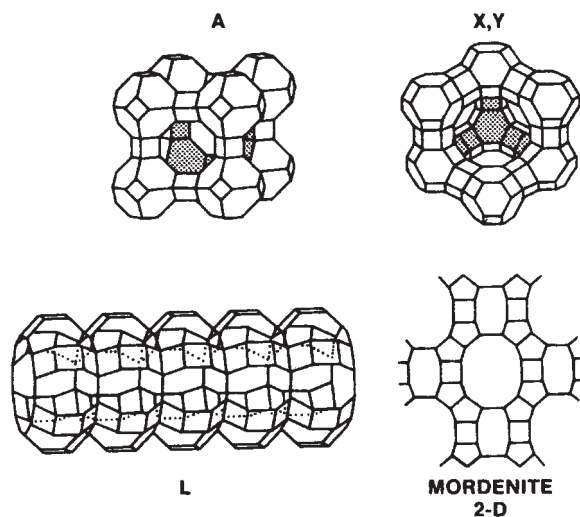
Figure 8.13   Three-dimensional representations of the framework structure of zeolite types A, XY, L, and a two-dimensional framework structure of mordenite. The vertices of lines in the above structures indicate the Si or Al atoms, with bridging oxygen slightly displaced from the lines. Reproduced from reference (102) with permission. Copyright 1990 American Chemical Society.

Expansive efforts to identify new zeolites have been driven by their importance in industrial applications (112). The most prominent industrial use is cracking of crude oil. These efforts have resulted in the preparation of numerous synthetic zeolites. There are five broadly defined classes of synthetic zeolites, as outlined in Table 8.5.

Table 8.5

Classes of zeolites (reference (96))

Abbreviation	Name	General structure
$AlSiO_4$	Aluminosilicate	$AlSiO_4$
AlPO	Aluminophospate	$AlPO_4$
SAPO	Silicoaluminophosphate	$SiPO_4$
MAPO[a]	Metal-containing aluminophospate	$AlPO_4$
MAPSO[a]	Metal-containing silicoaluminophosphate	$SiPO_4$

[a]Doped with Li, Be, Mg, or transition elements.
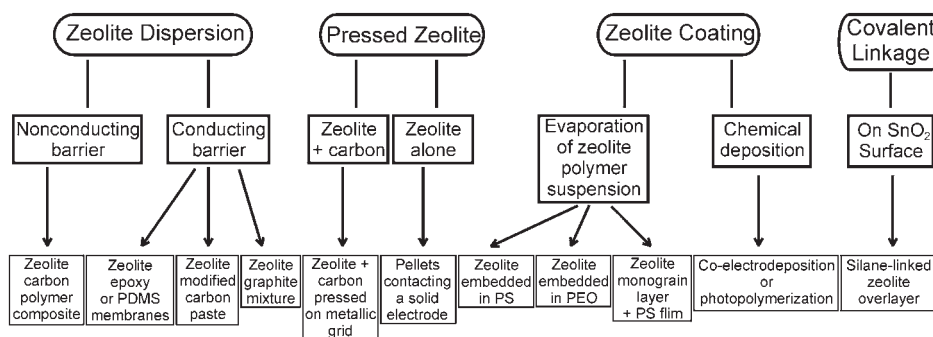
Figure 8.14 Strategies applied to prepare zeolite modified electrodes. (PDMS: polydimethylsiloxane; PS: polystyrene; PEO: polyethylene oxide). Reproduced from reference (106) with permission.

8.3.5.2 *Immobilization*

Many different procedures for modification of electrode surfaces by zeolites have been proposed (106). In practice, fabrication of zeolite modified electrodes is complicated by at least two factors: first, zeolites are electrically insulating, and second, immobilization of the film by physical or chemical bonding is difficult. Most successful zeolite modification schemes employ composites, where polymers or conductive powders are used as a matrix to support the zeolite. In any successful scheme, electroactive analyte molecules and counter-ions must be able to undergo rapid mass transport within the zeolite-based film.

Four different strategies for immobilizing zeolites on the surface of an electrode can be identified (106). The desired zeolite can be: (1) dispersed within a solid matrix; (2) compressed onto a conductive substrate; (3) embedded in a polymeric film; or (4) covalently anchored. Figure 8.14 outlines these broad approaches and the many different possible electrode structures. Further elaboration on these immobilization schemes can be found in Tables I and II of references (102) and (106), respectively. These references also contain specific examples of preparation procedures for zeolite modified electrodes.

Table 8.6

Applications of zeolite modified electrodes

(1) Molecular recognition
Molecular discrimination
Self-assembled multi-component systems
(2) Charge and mass transport characterization
Ion-exchange
Diffusion (analytes and counter-ions)
Electron transfer mechanisms
Intrazeolite effects
(3) Electroanalysis
Amperometry (preconcentration, indirect detection)
Potentiometry (membranes)
(4) Electrocatalysis
Mediation by exchanged species
Encapsulated species
Dispersion electrolysis
(5) Batteries
Reactant hosts
Dispersion electrolysis

Source: Reproduced from reference (104) with permission.

8.3.5.3   Applications

The unique three-dimensional aluminosilicate crystalline lattice of zeolites gives rise to three intriguing characteristics (104). These characteristics are: high cation-exchange capacity, sensitive molecular recognition (size and shape selectivity), and good catalytic activity. These properties give rise to the use of zeolite modified electrodes in sensor development, and electrocatalysis (106). These and other applications are outlined in Table 8.6. More detailed descriptions can be found in recent reviews (7, 96, 102–106), with extensive lists compiled by Rolison (Table II in (102)) and Walcarius (Tables 1 and 3 in (105) and Table 1 in (106)).

8.3.6   Sol-gel modified electrodes

Amorphous sol-gel materials have become increasingly appealing as electrode modifiers in the past 20 years (113). The initial interest in these materials was based on applications of their optical characteristics (silica, zirconia, and other transparent oxides) (113). As electrochemists sought convenient methods for combining different metal oxides in a crystalline product, their interest in sol-gel materials was sparked.

Sol-gel materials possess attractive properties which can be exploited as electrode modifiers in electrochemical detection schemes (114, 115). These properties include: high adsorption capacity, acid/base functionality, and thermal stability. Moreover, the inclusion of functional groups, enzymes, and proteins in sol-gels is easily achieved, expanding the possible applications.

8.3.6.1   *Structural description*

The term sol-gel is used to describe a broad class of solid structures created through gelation of a colloidal suspension (i.e., sol) (113). Upon dehydration, a xerogel, or "dry gel" state forms. Subsequent heat treatment can be used to remove unreacted organic residues, increase stability and density, or introduce crystallinity (113).

The chemical composition of sol-gels is typically a basic inorganic oxide. A common example of a sol-gel is silica gel, which has particular utility as stationary phase supports in chromatographic columns. The sol-gel materials used for electrode modification are typically created from two different classes of material: inert and redox active. Many different types of sol-gels are derived from these classes, as outlined in Table 8.7 (113).

The first class, inert inorganic sol-gels, are not redox active (e.g., silica, alumina, and zirconia) (113). In the gel form these materials have a large surface area, high ion-exchange capacity (due to surface hydroxyls), and exhibit good adhesion to metal oxide and ceramic supports.

The second class of sol-gels contains redox-active metal oxides, such as tungsten oxide, vanadium pentoxide, manganese oxide, and other transition metal oxides. Moreover, many n-type semiconductors such as zinc oxide, barium titanate, and titanium dioxide can be used in this class (113). The structures of these gels are sensitive to the pH and oxidation state of the precursors. Many redox-active sol-gels exhibit electrochromism (different oxidation states exhibit different colors, allowing spectroscopic determination of redox states). These gels can also accommodate the reductive insertion of lithium and other moieties.

Introduction of guest species into class one and two sol-gels can be accomplished through a variety of techniques (113), including chemical reactions and impregnation schemes. These procedures yield many different types of sol-gels that can be classified

Table 8.7

Classification of sol-gel materials and attributes relevant to electrode modification

Sol-gel classes	Attributes
(1) Inert, inorganic materials	Electroinactive (silica, alumina, and zirconia)
(2) Redox-active metal oxides	Electroactive (vanadium pentoxide, manganese oxide, tungsten oxide, etc.)
Modified sol-gel types	Definition
Organic–inorganic hybrids	Inclusion of organic functionalities
(i) Covalently bound	Creation of sol-gel-C bond during/after formation of gel
(ii) Doped	Molecules incorporated in the sol starting solution (large-scale catalysts or electrode modifiers)
(iii) Impregnated	Adsorption or precipitation of organic compounds onto prepared gels
(iv) Intercalated	Materials are placed into a swelled gel that are encapsulated upon dehydration
Macroscopic and microscopic inclusion	Encapsulated unicellular microorganisms, whole cells, and powders

Source: Information adapted from reference (113).

(113) as outlined in Table 8.7. The different methods for modification of class one and two sol-gels are outlined below.

Sol-gel networks can be further modified by covalently linking molecules to the matrix. These linkages can be added before or after sol-gel formation. To introduce the modifier before formation, it is important that the bond between the precursor and modifier be resistant to attack by the reactive groups of the precursor involved in gel formation. Carbon–silicon bonds are typically used for this purpose. Alternatively, the gel can be derivatized after formation, through a wider range of steps (e.g., using silanes) with direct covalent attachment to the sol-gel matrix by inorganic or organic reactions. Moreover, by combination of these two approaches, a functionalized precursor can be designed for secondary reactions with other types of molecules.

Compounds can be introduced into the gel network by entrapment (113). Doping involves the addition of a molecular guest to the sol-gel precursor solution. Alternatively, the gel may be modified by impregnation after formation by precipitation–adsorption or intercalation into the oxide network by swelling agents. When modifying the gel with small molecules, care must be exercised because doping, impregnation, and intercalation procedures often result in electrodes with guests that are prone to loss through leaching. Therefore, these techniques are more useful for immobilization of large catalysts or organic modifiers (113).

In addition to molecular guests, macroscopic species can be used to form composite materials, using the sol-gel as a matrix. To this end, conductive powders and other species have been incorporated in sol-gels (113). These large-scale objects are usually captured in the network during gel formation. Electrodes with unique qualities can be fabricated using these procedures. For example, a gel doped with conductive carbon particles results in a carbon paste-like electrode, having the electrochemical activity of carbon in conjunction with the robust mechanical characteristic of the sol-gel material. Furthermore, metal particles or conductive polymers can be used to increase the redox activity of the resulting electrode. Polymers can be incorporated by initiating a polymerization reaction within a preformed sol-gel matrix, introduction of a preformed polymer during gelation, or concurrent polymerization and polycondensation.

8.3.6.2   Immobilization

In constructing a sol-gel modified electrode, thin films may be necessary due to the insulating properties of the gel (115). Thus, they are often fabricated by growing a thin film on the substrate. For such cases, sol-gels with high adhesion characteristics are ideal (most sol-gels adhere to metal, metal oxide, and semiconducting electrode materials). When necessary, more robust linkages can be formed by covalent bonding through silane chemistry. Incorporation of charge mediators, chromophores, organometallic catalysts, preconcentration agents, ionophores, and active proteins into the sol-gel matrix provide the basis for the function of the electrode.

To overcome the limitations of conductivity, bulk-modified sol-gels can be used (113). These electrodes incorporate conductive materials into the gel. The resulting structures are able to serve as a carbon-paste-like electrode (see Chapter 5). The sol-gel backbone is solid-like, providing a mechanically robust and convenient electrode embodiment.

This property is combined with the attributes of the conductive elements incorporated in the gel, allowing many novel functions to be realized.

8.3.6.3 Applications

The properties of sol-gels that are useful in electroanalysis include abrasion and corrosion resistance, ionic conductivity, optical transparency, and electrochromism. These, along with the ease with which sol-gels can be constructed with variable chemical composition have led to their use in electrocatalysis (116), sensing, and as robust reference electrodes (113). Other applications are summarized in references (113, 115). Table 1 in (115) includes an in-depth list of useful sol-gel modified electrodes.

8.3.7 Polymer modified electrodes

The extended nature of a polymer network provides many opportunities for enhancing electroanalytical measurements and enabling studies of long-range interfacial phenomena. The relative thickness of a polymeric film allows a high number of active sites on the electrode surface, increasing utility in sensor design (117–120) and fundamental studies (4). For example, polymer modified electrodes can be used to study extended charge transport phenomena or electron transfer mediation reactions (121–123).

These modifiers are classified by the type of polymer (5). To this end, four classes are identified: redox, ion-exchange, conductive, and nonconductive, as shown in Figure 8.15. The first three classes of polymers are able to participate in electron transfer events; the distinction between them lies in the mode of electron-transport that dominates their observed behavior, as shown in Figure 8.16 (4). Nonconducting polymers are used to create selective physical barriers or for surface passivation (118).

A variety of methods exist for immobilization of polymeric films on substrate surfaces. These can be divided into two broad classes: coating a preformed polymer or polymerization-deposition. A dissolved polymer can be adsorbed onto a substrate by drop-casting, dip-coating, or spin-coating (124). Alternatively, a polymerization reaction can be initiated with the electrode immersed in the monomer solution to create a polymer-coated substrate.

Anchoring of polymer films is accomplished through the same forces that immobilize other films. They are easily physisorbed, due to high molecular weight and hydrophobicity. Therefore, as long as these interactions are not altered, for example, by a strong solvent for the polymer, the film remains stable. A synopsis of the characteristics, construction, and uses of each of the four classes of polymer modified electrodes follows.

8.3.7.1 Redox polymers

Redox polymers and co-polymers contain redox-active molecules covalently incorporated into the polymer. Each redox site is capable of exchanging electrons with other sites within the polymer or guests, as shown in Figure 8.17A. Only those sites in close proximity to the solution–polymer interface typically participate in electron transfer with solution-based redox couples. However, electron transfer with the substrate only occurs at immobilized sites in close proximity to the polymer–substrate interface. Thus, an analytical signal is
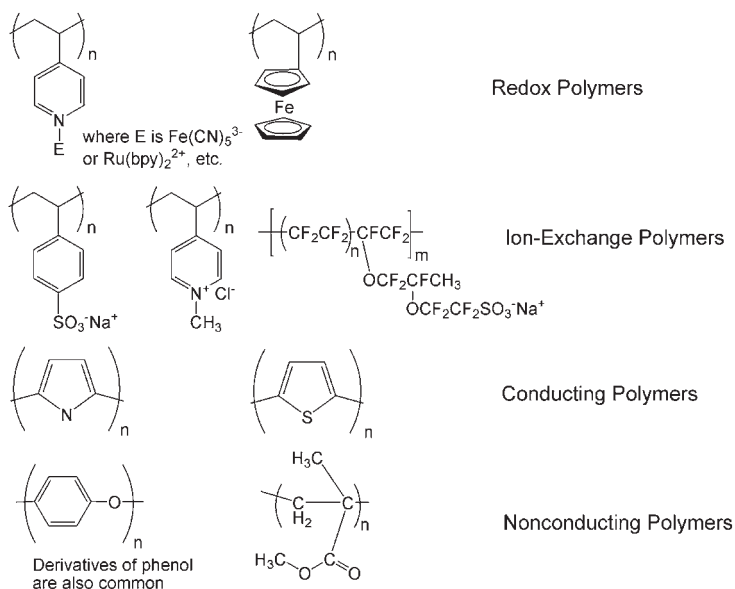
Figure 8.15 Examples of common polymers used to modify electrodes.
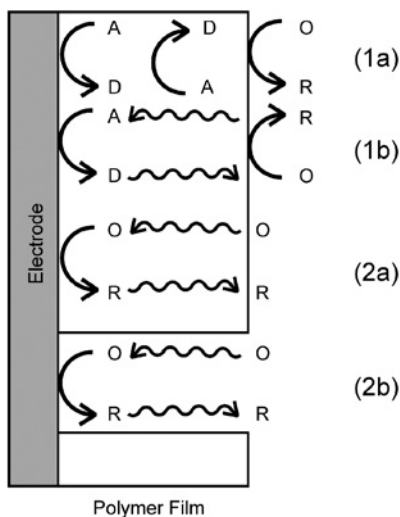
Figure 8.16 Illustration of four electron-transfer modes in polymer modified electrodes. Polymers containing redox molecules (where A + e = D) can mediate electrons to a solution-based analyte (where O + e = R) through an electron hopping mechanism (1a), or by diffusion of free redox molecules within the film (1b). Permeable polymer layers, on the other hand, provide a suitable chemical environment for diffusion of O through the layer (2a) or contain channel/pinholes where electron-transfer occurs (2b). This material is adapted with permission from: A. J. Bard, *Integrated Chemical Systems: A Chemical Approach to Nanotechnology*; John Wiley & Sons, Inc.: New York, 1994. Copyright 1994 John Wiley & Sons, Inc.

Figure 8.17 Schematic representation of the processes that take place in a redox-containing polymer film consisting of (A) a redox polymer and (B) an ion-exchange polymer filled with free redox molecules. Filled circles depict the reduced form of the couple and open circles the oxidized form. Smooth arrows show electron-transfer events between the two forms, and wavy arrows indicate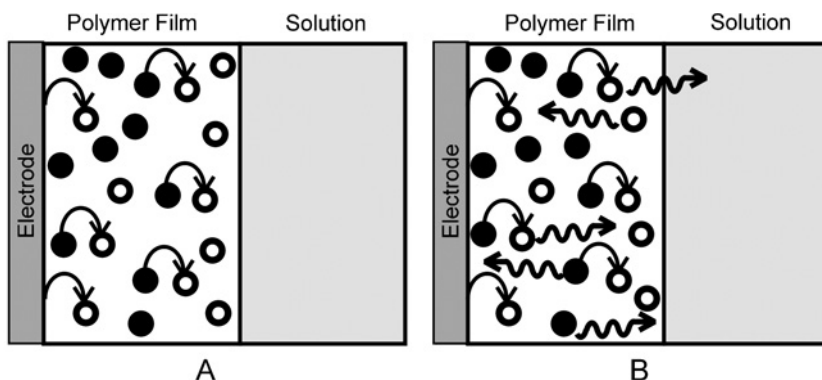 diffusional processes. This material is adapted from reference (4) with permission. Copyright 1992 John Wiley & Sons, Inc.

derived from electrons that are effectively shuttled by electron hopping through the polymer film. The extended nature of this electron hopping network has contributed greatly to our understanding of neural networks and other biological systems (122).

The synthesis of redox polymers is generally performed before deposition (124). First, a polymer is synthesized by condensation or addition polymerization with at least one monomer that is redox-active. The polymer is immobilized on the substrate by dip-coating, drop-casting, or spin-coating. These procedures must be carefully applied if homogeneous and pinhole free films are needed.

Redox polymers can also be covalently coupled to a substrate surface (5). A preformed polymeric film is covalently bound to the substrate by reaction of active sites on the surface and functional groups within the polymer. The main advantage of this second synthetic route is the stability provided by tethering the polymer.

Electron transfer events within this class of modified electrodes involve the transformation of a molecule between stable oxidation states; therefore, transport of counter-ions within the film must be realized to maintain electroneutrality. Electron hopping between the redox centers is often rate-limited by ion transport. Although control of the spacing of redox centers within the polymer may provide experimental advantages, ion transport limitations must be overcome. As a result, only when closely spaced, fast-reacting redox sites reside in the film, will significant extended electron hopping be observed.

The main drawback of redox polymer electrodes, both in fundamental studies and in chemical analysis, stems from the difficulty in controlling the concentration and spatial organization of redox sites within the film (4). The main use of redox polymer modified electrodes has been in fundamental studies of electron transfer mechanisms. These electrodes are also used as electrochemical sensor devices, but on a much more limited scale (117). Many of these limitations are overcome by the use of ion-exchange polymers, as outlined below.

8.3.7.2   Ion-exchange polymers

A powerful and elegant way to overcome the limitations encountered in redox polymers makes use of ion-exchange polymers (5). This class of modified electrode can be constructed using any polymer with ion-exchange properties by exchanging the native counter-ion for an appropriately charged electroactive ion. This ion will serve as the electron transfer site within and on the surface of the film. The result is a layer with the ability to transport electrons as illustrated in Figure 8.17B.

In contrast to redox polymers, the electroactive molecules can diffuse between the ion-exchange sites on the polymer, resulting in a number of advantages. The polymer backbone need not flex for effective electron transfer like a redox polymer film, and therefore, occurs at a much faster rate. The concentration of redox sites in the film can be easily controlled through the ion-exchange process. Furthermore, the requirements of the redox molecule are greatly relaxed (any redox-active ion can be used). However, the active ion is prone to leaching from the ion-exchange polymer. This complication usually can be overcome by dosing the contacting solution with a small amount of the associated ion.

The preparation of ion-exchange redox polymer modified electrodes usually involves two steps. A preformed ion-exchange polymer (e.g., Nafion®) is immobilized on the electrode surface through drop-casting, spin-coating, or dip-coating. The desired redox ion (carrying the appropriate charge) is ion-exchanged into the polymer. Thus, variation of the polymer identity allows cationic or anionic redox molecules to be used.

The ease of preparation and the variety of electron active ions make ion-exchange polymers amenable to fundamental studies of electron transfer mechanisms. The systematic variation of the concentration (effective density) of redox sites within a coating has been useful in the construction of electron hopping models (4). These models are based on the apparent rate of electron diffusion through the film. Because the redox centers are able to diffuse within the polymer, the apparent rate is related to two parameters: redox molecule diffusion and the rate of electron self-exchange.

Ion-exchange polymers on electrode surfaces can also be used to perform practical tasks, such as preconcentration of ionic analyte molecules, and electron transfer mediation.

8.3.7.3   Electrically conductive polymers

The third class of polymer modified electrodes includes those derived from electrically conductive polymers. These materials have special structural properties (such as highly conjugated π-bonds) that facilitate the conduction of electrons through delocalized electronic bands (125). The electron transfer mechanism, therefore, occurs by movement of electrons through overlapping and unoccupied electronic energy states. Conductive polymers have several positive attributes, especially related to their synthesis and application.

The intrinsic conductivity of many conductive polymers is typically in the semiconducting range ($10^{-14}-10^2\ \Omega^{-1}\ cm^{-1}$). The polymer is often doped to increase conductivity into the range associated with metallic materials ($1-10^5\ \Omega^{-1}\ cm^{-1}$) (126). Doping is accomplished by injection of positive or negative charge using chemical reagents or
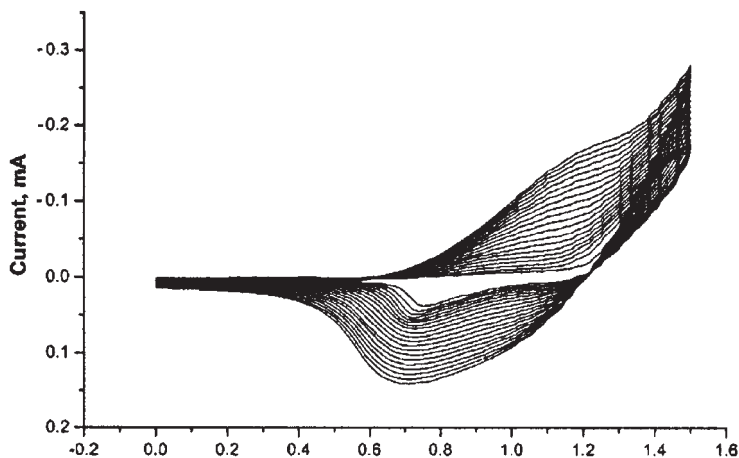
Figure 8.18   Cyclic voltammogram of 0.010 M fluorene in 0.20 M tetrabutylammonium tetrafluoroborate in acetonitrile at a Pt working electrode, scan rate 100 mV s^{-1}. Reproduced from reference (127) by permission of The Electrochemical Society, Inc.

electrochemical reactions (126), creating charge-carriers in the form of excess electrons or holes. Small ions are also incorporated during doping to maintain electroneutrality.

Although conductive polymers can be made by a variety of methods, electropolymerization is by far the most convenient method in constructing a polymer modified electrode. The polymerization proceeds by an electrochemical reaction at the electrode surface, resulting in immobilization of a polymer film. For example, Figure 8.18 shows current–potential curves for electropolymerization of fluorene. The peaks in each curve show the deposition of an additional layer of polyfluorene (127). The peak currents during electropolymerization of different types of polymer can increase or decrease with each subsequent scan depending on the electron transfer characteristics of the polymer and the deposition rate (127, 128).

The advantages offered by electropolymerization stem from the versatility and convenience provided by direct reaction of the monomer at the electrode surface. Moreover, after formation on the electrode surface, charge injection (doping) is easily controlled and optimized using potential programs and/or changing the electrolyte identity (126). Other advantages include facile, reproducible control over film thickness and the ability to use diverse electrode geometries and form thick films (up to ~1 μm) (126). The solution conditions required for the synthesis are unusually mild, allowing entrapment of biological molecules while retaining their activity (126).

The most common use for conductive polymer modified electrodes has been in the construction of sensor electrodes. These can be very selective and sensitive, and made to enhance the analysis of many different molecular entities. Thus, many different inorganic, organic, and biological species have been targeted (117).

8.3.7.4   Nonconductive polymers

Nonconducting polymers are not involved in electron transfer reactions, and therefore are partially or totally passivating. However, these polymers are useful in constructing permselective films. These films are deposited on substrate surface by the same methods as other polymers: dip-coating, spin-coating, drop-casting, or electropolymerization. The most elegant and useful approach to construct a highly selective modified electrode using a nonconducting polymer film is molecular imprinting.

The distinguishing feature of molecularly imprinted polymer films stems from the addition of a recognition molecule to the polymerization solution (129–131). During the reaction of monomer, the recognition molecule becomes trapped within the newly formed polymer. After polymerization, the recognition molecule is removed, resulting in structural voids having a structure that is complementary to the recognition molecule (129). Although imprinted polymer modified electrodes can be made using a nonconductive polymer template, the imprinting process is a generic one; any type of polymer can, in principle, be used.

The synthetic protocols needed to produce imprinted polymers are not trivial. However, successful construction of an imprinted polymer modified electrode is extremely rewarding: obtaining sites having affinities comparable to antibodies may be possible (129). Unlike current biorecognition elements, the selectivity of the imprinted layer remains high in a variety of environments. This stability results from the robust nature of the polymeric material. Recently, combinatorial approaches are being utilized for optimization of synthetic protocols in order to overcome synthetic challenges of creating these films (129, 131).

8.3.8   DNA modified electrodes

Deoxyribonucleic acid (DNA) is increasingly used for molecular recognition purposes (132–134). Electrodes modified with DNA, therefore, are useful in the construction of electroanalytical sensors. Analytes, including carcinogens, drugs, and mutagenic pollutants with high binding affinities for DNA, will be important in testing water, food, soil, and plant samples. Electroactive molecules may be detected directly upon binding to DNA bound at the electrode surface. Indirect detection of electroinactive molecules may be accomplished by monitoring changes in the signal attributed to the bound DNA (134). Sensors can also be used to detect gene sequences (134) such as mutations associated with human diseases. Further information on DNA modified electrodes, including fabrication (i.e., immobilization of DNA using many of the techniques discussed above) and application can be found in references (134–142).

8.4   CONCLUSIONS AND PROSPECTS

The properties of chemically modified electrodes that have driven their development include: increased selectivity and sensitivity, chemical and electrochemical stability, larger usable potential windows, and resistance to fouling. Chemically modified electrodes will

remain important tools in applied and fundamental science. This area has blossomed upon development of a molecular-level understanding of the synthesis and characterization of interfacial architectures. This will continue as new and improved surface characterization techniques are developed. However, challenges remain in the successful construction of modified electrodes; especially needed are advances in our understanding of the subtleties of adlayer formation processes and the related fundamental electron transfer mechanisms.

REFERENCES

1. R. A. Durst, A. J. Bäumner, R. W. Murray, R. P. Buck, C. P. Andrieux, *Pure Appl. Chem.* **69**, 1317–1323 (1997).
2. W. Kutner, J. Wang, M. L'Her, R. P. Buck, *Pure Appl. Chem.* **70**, 1301–1318 (1998).
3. C. R. Martin, C. A. Foss, Jr., "Chemically Modified Electrodes", in *Laboratory Techniques in Electroanalytical Chemistry*, 2nd ed., P. T. Kissinger, W. R. Heineman, Eds., Marcel Dekker, Inc.: New York, 1996.
4. R. W. Murray, "Molecular Design of Electrodes Surfaces", in *Techniques of Chemistry*, J. William H. Saunders, A. Weissberger, Eds., John Wiley and Sons, Inc.: New York, 1992, Vol. 22.
5. R. W. Murray, "Chemically Modified Electrodes", in *Electroanalytical Chemistry*, A. J. Bard, Ed., Marcel Dekker, Inc.: New York, 1984, Vol. 13, pp. 191–368.
6. A. Ulman, *An Introduction to Ultrathin Organic Films From Langmuir-Blodgett to Self-Assembly*, Academic Press: San Diego, 1991.
7. A. Walcarius, "Implication of Zeolite Chemistry in Electrochemical Science and Applications of Zeolite-Modified Electrodes", in *Handbook of Zeolite Science and Technology*, S. M. Auerbach, K. A. Carrado, P. K. Dutta, Eds., Marcel Dekker, Inc.: New York, 2003, pp. 721–783.
8. M. C. Petty, *Langmuir-Blodgett Films: An Introduction*, Press Syndicate of the University of Cambridge: New York, 1996.
9. D. H. Karweik, C. W. Miller, M. D. Porter, T. Kuwana, "Prospects in the Analysis of Chemically Modified Electrodes", *Surface Analysis*, 1982, 89–119, American Chemical Society Conference Proceedings.
10. J. A. Cox, M. E. Tess, T. E. Cummings, *Rev. Anal. Chem.* **15**, 173–223 (1996).
11. H. O. Finklea, "Electrochemistry of Organized Monolayers of Thiols and Related Molecules on Electrodes", in *Electroanalytical Chemistry: A Series of Advances*, A. J. Bard, I. Rubinstein, Eds., Marcel Dekker, Inc.: New York, 1996, Vol. 19, pp. 109–335.
12. R. L. McCreery, K. K. Cline, "Carbon Electrodes", in *Laboratory Techniques in Electroanalytical Chemistry*, 2nd ed., P. T. Kissinger, W. R. Heineman, Eds., Marcel Dekker, Inc.: New York, 1996.
13. R. L. McCreery, "Carbon Electrodes: Structural Effects on Electron Transfer Kinetics", in *Electroanalytical Chemistry*, A. J. Bard, Ed., Marcel Dekker, Inc.: New York, 1984, Vol. 17, pp. 191–368.
14. K. B. Blodgett, *J. Am. Chem. Soc.* **56**, 495 (1934).
15. K. B. Blodgett, *J. Am. Chem. Soc.* **57**, 1007–1022 (1935).
16. A. Mälkiä, P. Liljeroth, K. Kontturi, *Anal. Sci.* **17**, i345–i348 (2001).
17. J. Gong, X. Lin, *Electrochim. Acta* **49**, 4351–4357 (2004).
18. M. Ferreira, L. R. Dinelli, K. Wohnrath, A. A. Batista, O. N. Oliveira, Jr., *Thin Solid Films* **446**, 301–306 (2004).
19. T. Miyahara, K. Kurihara, *J. Am. Chem. Soc.* **126**, 5684–5685 (2004).
20. G. G. Roberts, *Adv. Phys.* **34**, 475–512 (1985).

21. L. M. Goldenberg, M. C. Petty, A. P. Monkman, *J. Electrochem. Soc.* **141**, 1573–1576 (1994).
22. L. M. Goldenburg, *J. Electroanal. Chem.* **379**, 3–19 (1994).
23. M. K. Ram, N. S. Sundaresan, B. D. Malhotra, *J. Phys. Chem.* **97**, 11580–11582 (1993).
24. A. T. Hubbard, *Chem. Rev.* **88**, 633–656 (1988).
25. J. C. Love, L. A. Estroff, J. K. Kriebel, R. G. Nuzzo, G. M. Whitesides, *Chem. Rev.* **105**, 1103–1169 (2005).
26. C. D. Bain, H. A. Biebuyck, G. M. Whitesides, *Langmuir* **5**, 723–727 (1989).
27. R. G. Nuzzo, D. L. Allara, *J. Am. Chem. Soc.* **105**, 4481–4483 (1983).
28. R. G. Nuzzo, F. A. Fusco, D. L. Allara, *J. Am. Chem. Soc.* **109**, 2358–2368 (1987).
29. M. D. Porter, T. B. Bright, D. L. Allara, C. E. D. Chidsey, *J. Am. Chem. Soc.* **109**, 3559–3568 (1987).
30. P. E. Laibinis, G. M. Whitesides, D. L. Allara, Y.-T. Tao, A. N. Parikh, R. G. Nuzzo, *J. Am. Chem. Soc.* **113**, 7152–7167 (1991).
31. M. M. Walczak, C. Chung, S. M. Stole, C. A. Widrig, M. D. Porter, *J. Am. Chem. Soc.* **113**, 2370–2378 (1991).
32. A. Demoz, D. J. Harrison, *Langmuir* **9**, 1046–1050 (1993).
33. E. B. Troughton, C. D. Bain, G. M. Whitesides, R. G. Nuzzo, D. L. Allara, M. D. Porter, *Langmuir* **4**, 365–385 (1988).
34. T. E. Mallouk, H. Lee, L. J. Kepley, H.-G. Hong, S. Akhter, *J. Phys. Chem.* **92**, 2597–2601 (1988).
35. T. E. Mallouk, H. Lee, L. J. Kepley, H.-G. Hong, *J. Am. Chem. Soc.* **110**, 618–620 (1988).
36. U. B. Steiner, W. R. Caseri, U. W. Suter, *Langmuir* **8**, 2771–2777 (1992).
37. A. C. Ontko, R. J. Angelici, *Langmuir* **14**, 1684–1691 (1998).
38. A. C. Ontko, R. J. Angelici, *Langmuir* **14**, 3071–3078 (1998).
39. M. J. Robertson, R. J. Angelici, *Langmuir* **10**, 1488–1492 (1994).
40. K.-C. Shih, R. J. Angelici, *Langmuir* **11**, 2539–2546 (1995).
41. J. J. Hickman, C. Zou, D. Ofer, P. D. Harvey, M. S. Wrighton, P. E. Laibinis, C. D. Bain, G. M. Whitesides, *J. Am. Chem. Soc.* **111**, 7271–7272 (1989).
42. F. Auer, B. Sellergren, A. Swietlow, A. Offenhauser, *Langmuir* **16**, 5936–5944 (2000).
43. A. Ulman, *Chem. Rev.* **96**, 1533–1554 (1996).
44. S. Flink, F. C. J. M. van Veggel, D. N. Reinhoudt, *Sensors Update* **8**, 3–19 (2001).
45. F. Schreiber, *J. Phys.: Condens. Matter* **16**, R881–R900 (2004).
46. N. Sandhyarani, T. Pradeep, *Int. Rev. Phys. Chem.* **22**, 221–262 (2003).
47. N. Camillone, III, *Langmuir* **20**, 1199–1206 (2004).
48. G. Hahner, C. Wöll, M. Buck, M. Grunze, *Langmuir* **9**, 1955–1958 (1993).
49. D. Qu, M. Morin, *J. Electroanal. Chem.* **524–525**, 77–80 (2002).
50. C.-J. Zhong, N. T. Woods, G. B. Dawson, M. D. Porter, *Electrochem. Commun.* **1**, 17–21 (1999).
51. R. Subramanian, V. Lakshminarayanan, *Electrochim. Acta* **45**, 4501–4509 (2000).
52. M. Cohen-Atiya, D. Mandler, *J. Electroanal. Chem.* **550–551**, 267–276 (2003).
53. W. Pan, C. J. Durning, N. J. Turro, *Langmuir* **12**, 4469–4473 (1996).
54. D. S. Karpovich, G. J. Blanchard, *Langmuir* **10**, 3315–3322 (1994).
55. C. D. Bain, G. M. Whitesides, *J. Am. Chem. Soc.* **111**, 7164–7175 (1989).
56. G. E. Poirier, E. D. Pylant, *Science* **272**, 1145–1148 (1996).
57. M. Byloos, H. Al-Maznai, M. Morin, *J. Phys. Chem. B* **105**, 5900–5905 (2001).
58. J. H. Teuscher, L. J. Yeager, H. Yoo, J. E. Chadwick, R. L. Garrell, *Faraday Discuss.* **107**, 399–416 (1997).
59. C. A. Widrig, C. Chung, M. D. Porter, *J. Electroanal. Chem.* **310**, 335–359 (1991).

60. M. M. Walczak, D. D. Popenoe, R. S. Deinhammer, B. D. Lamp, C. Chung, M. D. Porter, *Langmuir* **7**, 2687–2693 (1991).
61. C.-J. Zhong, R. C. Brush, J. Andregg, M. D. Porter, *Langmuir* **15**, 518–525 (1999).
62. C. E. D. Chidsey, D. N. Loiacono, *Langmuir* **6**, 682–691 (1990).
63. C. A. Widrig, C. A. Alves, M. D. Porter, *J. Am. Chem. Soc.* **113**, 2805–2810 (1991).
64. C.-J. Zhong, M. D. Porter, *Anal. Chem.* **67**, 709A–715A (1995).
65. C. Miller, P. Cuendet, M. Grätzel, *J. Phys. Chem.* **95**, 877–886 (1991).
66. C. Miller, M. Grätzel, *J. Phys. Chem.* **95**, 5225–5233 (1991).
67. S. Terrettaz, A. M. Becka, M. J. Traub, J. C. Fettinger, C. J. Miller, *J. Phys. Chem.* **99**, 11216–11224 (1995).
68. A. M. Becka, C. J. Miller, *J. Phys. Chem.* **96**, 2657–2668 (1992).
69. A. M. Becka, C. J. Miller, *J. Phys. Chem.* **97**, 6233–6239 (1993).
70. J. F. Smalley, S. W. Feldberg, C. E. D. Chidsey, M. R. Linford, M. D. Newton, Y.-P. Liu, *J. Phys. Chem.* **99**, 13141–13149 (1995).
71. J. J. Sumner, K. S. Weber, L. A. Hockett, S. E. Creager, *J. Phys. Chem. B* **104**, 7449–7454 (2000).
72. K. Weber, L. Hockett, S. Creager, *J. Phys. Chem. B* **101**, 8286–8291 (1997).
73. F. Davis, C. J. M. Stirling, *Langmuir* **12**, 5365–5374 (1996).
74. M. Weisser, G. Nelles, G. Wenz, S. Mittler-Neher, *Sens. Actuators, B* **38–39**, 58–67 (1997).
75. A. J. Downard, *Electroanalysis* **12**, 1085–1096 (2000).
76. A. M. Yacynych, T. Kuwana, *Anal. Chem.* **50**, 640–645 (1978).
77. J. F. Evans, T. Kuwana, *Anal. Chem.* **49**, 1632–1635 (1977).
78. J. F. Evans, T. Kuwana, M. T. Henne, G. P. Royer, *J. Electroanal. Chem.* **80**, 409–416 (1977).
79. A. W. C. Lin, P. Yeh, A. M. Yacynych, T. Kuwana, *J. Electroanal. Chem.* **84**, 411–419 (1977).
80. B. Barbier, J. Pinson, G. Desarmot, M. Sanchez, *J. Electrochem. Soc.* **137**, 1757–1764 (1990).
81. R. S. Deinhammer, M. Ho, J. W. Andregg, M. D. Porter, *Langmuir* **10**, 1306–1313 (1994).
82. C. P. Andrieux, F. Gonzalez, J.-M. Savéant, *J. Am. Chem. Soc.* **119**, 4292–4300 (1997).
83. M. Delamar, R. Hitmi, J. Pinson, J. M. Savéant, *J. Am. Chem. Soc.* **114**, 5883–5884 (1992).
84. J. K. Kariuki, M. T. McDermott, *Langmuir* **15**, 6534–6540 (1999).
85. P. Allongue, M. Delamar, B. Desbat, O. Fagebaume, R. Hitmi, J. Pinson, J.-M. Savéant, *J. Am. Chem. Soc.* **119**, 201–207 (1997).
86. J. K. Kariuki, M. T. McDermott, *Langmuir* **17**, 5947–5951 (2001).
87. F. Anariba, S. H. DuVall, R. L. McCreery, *Anal. Chem.* **75**, 3837–3844 (2003).
88. Y.-C. Liu, R. L. McCreery, *J. Am. Chem. Soc.* **117**, 11254–11259 (1995).
89. A. J. Downard, M. J. Prince, *Langmuir* **17**, 5581–5586 (2001).
90. H.-H. Yang, R. L. McCreery, *Anal. Chem.* **71**, 4081–4087 (1999).
91. F. Anariba, J. K. Steach, R. L. McCreery, *J. Phys. Chem. B* **109**, 11163–11172 (2005).
92. A. J. Downard, A. D. Roddick, A. M. Bond, *Anal. Chim. Acta* **317**, 303–310 (1995).
93. J. A. Harnisch, D. B. Gazda, J. W. Anderegg, M. D. Porter, *Anal. Chem.* **73**, 3954–3959 (2001).
94. A. Fitch, *Clays and Clay Minerals* **38**, 391–400 (1990).
95. S. M. Macha, A. Fitch, *Mikrochim. Acta* **128**, 1–18 (1998).
96. A. J. Bard, T. Mallouk, "Electrodes Modifed with Clays, Zeolites, and Related Microporous olids", in *Molecular Design of Electrode Surfaces*, R. W. Murray, Ed., John Wiley & Sons, Inc.: New York, 1992, Vol. XXII, pp. 271–312.
97. Z. Navrátilová, P. Kula, *Electroanalysis* **15**, 837–846 (2003).
98. J.-M. Zen, A. S. Kumar, *Anal. Chem.* **76**, 205A–211A (2004).

 99. B. Velde, Ed., *Clay and the Environment: Origin and Mineralogy of Clays*, Springer-Verlag: Berlin, 1995.
100. P. K. Ghosh, A. J. Bard, *J. Am. Chem. Soc.* **105**, 5691–5693 (1983).
101. M. D. Baker, C. Senaratne, *Anal. Chem.* **64**, 697–700 (1992).
102. D. R. Rolison, *Chem. Rev.* **90**, 867–878 (1990).
103. D. R. Rolison, C. A. Bessel, *Acc. Chem. Res.* **33**, 737–744 (2000).
104. D. R. Rolison, R. J. Nowak, T. A. Welsh, C. G. Murray, *Talanta* **38**, 27–35 (1991).
105. A. Walcarius, *Electroanalysis* **8**, 971–986 (1996).
106. A. Walcarius, *Anal. Chim. Acta* **384**, 1–16 (1999).
107. J. Dwyer, A. Dyer, *Chem. Ind.* (7), 237–240 (1984).
108. J. Dwyer, *Chem. Ind.* (7), 258–269 (1984).
109. A. Dyer, *Chem. Ind.* (7), 241–245 (1984).
110. L. V. C. Rees, *Chem. Ind.* (7), 252–257 (1984).
111. R. P. Townsend, *Chem. Ind.* (7), 246–251 (1984).
112. J. M. Newsam, *Science* **231**, 1093–1099 (1986).
113. O. Lev, Z. Wu, S. Bharathi, V. Glezer, A. Modestov, J. Gun, L. Rabinovich, S. Sampath, *Chem. Mater.* **9**, 2354–2375 (1997).
114. M. M. Collinson, A. R. Howells, *Anal. Chem.* **72**, 702A–709A (2000).
115. A. Walcarius, *Electroanalysis* **10**, 1217–1235 (1998).
116. Q. Wang, G. Lu, B. Yang, *Langmuir* **20**, 1342–1347 (2004).
117. B. Adhikari, S. Majumdar, *Prog. Polym. Sci.* **29**, 699–766 (2004).
118. M. Yuqing, C. Jianrong, W. Xiaohua, *Trends Biotechnol.* **22**, 227–231 (2004).
119. J.-K. Park, P. H. Tran, J. K. T. Chao, R. Ghodadra, R. Rangarajan, N. V. Thakor, *Biosens. Bioelectron.* **13**, 1187–1195 (1998).
120. A. Ciszewski, G. Milczarek, *Talanta* **61**, 11–26 (2003).
121. M. Kavanoz, H. Gülce, A. Yildiz, *Turk. J. Chem.* **28**, 287–297 (2004).
122. C. E. D. Chidsey, R. W. Murray, *Science* **231**, 25–31 (1986).
123. L. R. Faulkner, *Chem. Eng. News* **62**, 28–45 (1984).
124. A. J. Bard, L. R. Faulkner, *Electrochemical Methods: Fundamentals and Applications*, 2nd ed., John Wiley & Sons, Inc.: New York, 2001.
125. H. S. Nalwa, *Handbook of Organic Conductive Molecules and Polymers*, John Wiley & Sons, Inc.: New York, 1997.
126. J.-C. Vidal, E. Garcia-Ruiz, J.-R. Castillo, *Microchim. Acta* **143**, 93–111 (2003).
127. H. S. Sharma, S.-M. Park, *J. Electrochem. Soc.* **151**, E61–E68 (2004).
128. S. Sadki, P. Schottland, N. Brodie, G. Sabouraud, *Chem. Soc. Rev.* **29**, 283–293 (2000).
129. S. A. Piletsky, A. P. F. Turner, *Electroanalysis* **14**, 317–323 (2002).
130. M. C. Blanco-López, S. Gutiérrez-Fernández, M. J. Lobo-Castañón, A. J. Miranda-Ordieres, P. Tuñón-Blanco, *Anal. Bioanal. Chem.* **378**, 1922–1928 (2004).
131. K. Haupt, K. Mosbach, *Chem. Rev.* **100**, 2495–2504 (2000).
132. N. D. Popovich, H. H. Thorp, *Electrochem. Soc. Interface* **11**, 30–34 (2002).
133. M. E. Napier, C. R. Loomis, M. F. Sistare, J. Kim, A. E. Eckhardt, H. H. Thorp, *Bioconjugate Chem.* **8**, 906–913 (1997).
134. M. Mascini, I. Palchetti, G. Marrazza, *Fresenius J. Anal. Chem.* **369**, 15–22 (2001).
135. T. G. Drummond, M. G. Hill, J. K. Barton, *Nat. Biotechnol.* **21**, 1192–1199 (2003).
136. M. Fojta, *Electroanalysis* **14**, 1449–1463 (2002).
137. J. J. Gooding, *Electroanalysis* **14**, 1149–1156 (2002).
138. E. Katz, I. Willner, J. Wang, *Electroanalysis* **16**, 19–44 (2004).
139. F. Lucarelli, G. Marrazza, A. P. F. Turner, M. Mascini, *Biosens. Bioelectron.* **19**, 515–530 (2004).

140. E. Palacek, M. Fojta, M. Tomschik, J. Wang, *Biosens. Bioelectron.* **13**, 621–628 (1998).
141. H. H. Thorp, *Trends Biotechnol.* **21**, 522–524 (2003).
142. J. Wang, G. Rivas, X. Cai, E. Palecek, P. Nielsen, H. Shiraishi, N. Dontha, D. Luo, C. Parrado, M. Chicharro, P. A. M. Farias, F. S. Valera, D. H. Grant, M. Ozsoz, M. N. Flair, *Anal. Chim. Acta* **347**, 1–8 (1997).

This page intentionally left blank

– 9 –

Semiconductor Electrodes

Santosh K. Haram

Department of Chemistry, University of Pune, Ganeshkhind,
Pune 411007, India

9.1 INTRODUCTION

Electrochemistry with semiconductor electrodes represents an interesting and highly inter-
disciplinary area of science—especially in physical chemistry. It involves concepts of
physics including band structure, zone theory, and charge transport as well as chemical
concepts including electrodics, photochemistry, surface chemistry, catalysis, and Marcus
theory. Semiconductor electrodes have been used in a variety of applications including liq-
uid junction solar cells, photolytic splitting of water, pollutants and organic molecules,
semiconductor processing, and sensor technology.

It is instructive to examine first the historical evolution of this field. The use of a semi-
conductor as an electrode in an electrochemical cell was first demonstrated by E. Becquerel
in 1839. He observed a photovoltaic effect when AgCl electrode was illuminated with
UV light. The 'Becquerel effect' was not clearly understood until 1954, when researchers
from Bell Laboratories studied photoelectrochemistry on Ge single crystals. They demon-
strated that photochemical reactions occurring at Ge electrodes are affected substantially
by the impurity levels in Ge. Based on these experiments and the zone theory that was
developing at that time, the Becquerel effect was modeled as a photoinduced charge sep-
aration at the AgCl–liquid interface. The effect was further tested with other semiconduc-
tor electrodes such as Si, GaAs, GaP, CdS, CdSe, ZnS, ZnSe, ZnTe, TiO_2, $SrTiO_3$, and
Ta_2O_5. Electron transfer theories were also rapidly evolving during this period, starting
from homogeneous systems at heterogeneous metal–electrolyte interfaces leading, in turn,
to semiconductor–electrolyte junctions.

Until the early 1970s, the work was fundamental in nature and mainly of academic inter-
est. The report by Fujishima and Honda (1) in 1972 describing photoassisted splitting of
H_2O to H_2 and O_2 on TiO_2, however, suggested the possibility of using semiconductor elec-
trodes in converting solar energy into the chemical/electric energy. Electrolysis of water
using sunlight is extremely attractive because (a) the hydrogen evolved can be stored more
easily than either electricity or heat and (b) it is non-polluting, renewable, inexhaustible,

Handbook of Electrochemistry
Edited by C.G. Zoski

and very flexible with respect to conventional fuel alternatives. This report was published during a period when the entire world was, for the first time, experiencing soaring gasoline prices due to fossil fuel depletion. This led to an intense interest in understanding the semiconductor–electrolyte interface (SEI) pertaining to renewable energy sources and remains an active area of research. The goal is to discover an ideal SEI, which can deliver an efficiency of about 15% without fouling the electrodes. To date, there has been limited success due to the inverse relationship between photocorrosion and efficiency. Oxide semiconductors such as TiO_2 and ZnO are stable against photocorrosion to some extent but deliver poor efficiency due to a wide band gap. Sulfides and selenides are more efficient due to an optimum band gap but are unstable under sunlight.

Despite the limited success of semiconductor electrodes in solving energy problems, they provide an interesting alternative to traditionally used working electrode materials in electrochemical investigations. An important advantage of semiconductor electrodes is that the electrochemical response can be varied extensively by simply changing the impurity levels, surface treatments, or surface adsorption. In this way, semiconductor electrodes have a major edge over conventional metal electrodes where the properties of a given metal electrode are less easily controlled. This property of semiconductor electrodes has potential applications in developing sensors.

The photoelectrochemistry of semiconductor electrodes will not be the focus of this chapter due to the thousands of articles and reviews available in the literature. Instead, the semiconductor as an electrode in the 'dark' will be discussed. The journey begins with zone theory, which addresses the energetics of semiconductors. Next is the interface between the semiconductor and electrolyte, which is described using Gerischer's model. We then enter the solution side and use the Marcus theory to explain the distribution of energy states associated with solvent reorganization energy. We discuss how electrochemical techniques such as cyclic voltammetry (CV, see Chapter 11) and scanning electrochemical microscopy (SECM, see Chapter 12) can be used to deduce the energetics of the interface and kinetics of electron transfer, respectively. We describe measurements on suspended quantized semiconductor particles by simple electrochemical methods. We also describe various methods of preparing semiconductor electrodes.

9.2 SEMICONDUCTOR BASICS

9.2.1 Band theory of solids

The properties of semiconductor electrodes and their differences compared with metal electrodes can be understood by examining their electronic structure. Semiconductors are unique in their electronic properties due to their band structure. The origin of the energy bands is generally discussed using *band or zone theory*, where the motion of a single electron in the crystal lattice is considered. It is assumed that there is no interaction between individual electrons or between the electrons and lattice points (the potential energy is zero). Therefore, the model is sometimes referred to as the *nearly free electron model*.

The time-dependent Schrödinger equation for a *free electron* is written as

$$-\frac{\hbar^2}{2m_e}\nabla^2\Psi(x,y,z) = E\cdot\Psi(x,y,z) \tag{9.2.1}$$

where m_e is rest mass of a free electron, E is the kinetic energy, Ψ is a single electron wave function, and $\nabla^2 = \partial^2 / \partial x^2 + \partial^2 / \partial y^2 + \partial^2 / \partial z^2$. The solution for equation (9.2.1) is given by

$$\Psi_k(r) = \frac{1}{\sqrt{V}} \cdot e^{i \cdot k \cdot r} \tag{9.2.2}$$

where $r = (x, y, z)$ is the position vector and k is the wave vector given by $k^2 = k_x^2 + k_y^2 + k_z^2$. The multiplier, $1/\sqrt{V}$, is a normalization constant that accounts for the presence of the electron in the volume element, V. Based on the *de Broglie wavelength* (2) associated with microscopic particles, the linear momentum and kinetic energy of the electron in a single crystal can be expressed in terms of k by the expressions

$$\mathbf{P} = \hbar \cdot k \tag{9.2.3}$$

and

$$E(k) = \frac{\hbar^2 k^2}{2 \cdot m_0} \tag{9.2.4}$$

where $\hbar = h / 2\pi$ and h is Planck's constant. A plot of energy $E(k)$ vs. k is given in Figure 9.1a, where the relationship is essentially parabolic and the allowed energy values are distributed *continuously* from zero to infinity. In a real crystal, however, electrons interact with the periodic potential field, $U(\mathbf{r})$, created by orderly arranged ions in the lattice such that

$$U(\mathbf{r}) = U(\mathbf{r} + \mathbf{R}) \tag{9.2.5}$$

where $\mathbf{R}$ is the unit vector. In this situation, the electron wave scatters on these lattice points. It is analogous to the diffraction of X-rays on a periodic lattice governed by Bragg's law. The electronic waves, which satisfy Bragg's condition, scatter on the lattice points and cannot propagate in the lattice. It leads to the formation of forbidden energy gaps in the
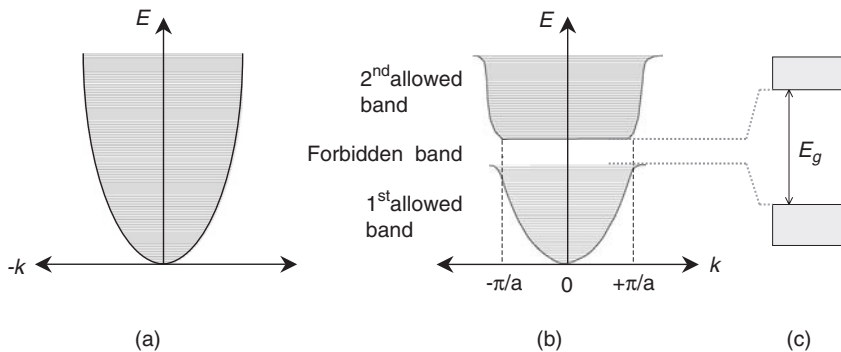

Figure 9.1   (a) Plot of energy E vs. wave vector k for the free electron, which suggests that the electron can acquire any value of energy or all transitions are allowed. (b) The effect of scattering of the electron at periodic lattice points, which gives rise to gaps of forbidden energy levels. Lower hashed area within $\pm \pi / a$ is called the first allowed band or *first Brillouin zone*, where a is the lattice constant along the '*a*' direction in the crystal. Upper hashed area is called the *second Brillouin zone*. (c) More familiar band structure for a solid. It is a plot of electronic energy vs. distance.

band, called *band gaps*. The region in the k space between $\pm\pi/a$ has allowed energy states and is called the *first Brillouin zone*. It is shown in Figure 9.1b. A more familiar picture of the band structure to the chemist is depicted in Figure 9.1c where an average value of the energy along three axes vs. distance in arbitrary unit is plotted. The electrons are filled in these allowed bands similar to the filling of electrons in the atomic and molecular orbitals. The probability that an electron can occupy a particular energy level E is governed by Fermi–Dirac statistics and is expressed as

$$f(E) = \frac{1}{1 + e^{(E - E_F)/k_B T}} \tag{9.2.6}$$

where E_F refers to the *Fermi level*. From a chemist's point of view, E_F represents an electrochemical potential of electrons ($\bar{\mu}_e$) in the solid. k_B is the Boltzmann constant. The probability distribution function $f(E)$ as a function of E at various temperatures is plotted in Figure 9.2a. In a solid, the energy states are not distributed uniformly throughout the energy values. Rather, the number of states per unit volume (i.e., density of states) increases with increasing energy value. The density of (available) states in an energy interval dE as a function of E is given by (3)

$$g(E)\,dE = \frac{4\pi}{h^3}(2m)^{3/2} E^{1/2}\,dE \tag{9.2.7}$$

which is plotted in Figure 9.2b. The product of equations (9.2.6) and (9.2.7) will lead to the following expression that represents the density of occupied states:

$$N(E)\,dE = F(E)\cdot g(E)\,dE \tag{9.2.8}$$

The function is plotted in Figure 9.2c and represents the density of states within the energy interval dE. The hashed area represents the density of occupied states. Depending on the
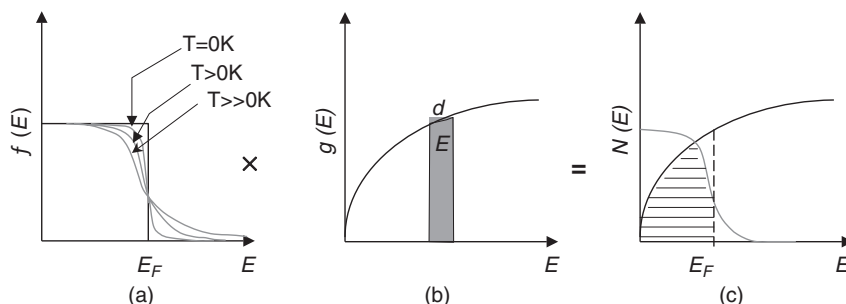

Figure 9.2 (a) Fermi–Dirac distribution function for a single electron at various temperature values. E and E_F are the energy of the allowed states and Fermi energy, respectively. (b) Density of state (DOS) as a function of energy. It represents density of available states in the energy interval dE and at energy E. (c) When Fermi–Dirac distribution function blends with density of available states, one gets density of occupied states shown as hashed area. Please note the position of E_F, below which all the states are occupied and above all the states are empty.
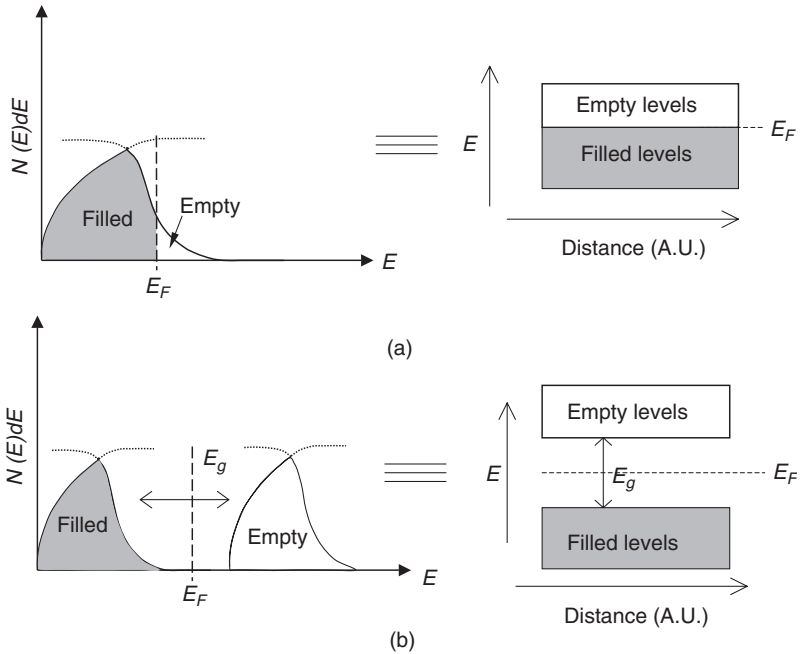
Figure 9.3 Band structure of (a) metal and (b) semiconductor. Left-hand side illustrations in both cases are a more explicit depiction of band theory. Right-hand side illustrations are more familiar and approximate.

number of valence electrons available and the probability distribution ($f(E)$), the bands can be either partially or completely filled. Materials with partially filled bands are classified as metals. If the band is completely filled and the immediate higher energy band is empty, then the material has properties of either an insulator or a semiconductor. These possibilities are shown in Figure 9.3.

For semiconductors (and insulators), the completely filled lower band is called the valence band (VB) and the higher energy band immediately above it is called the conduction band (CB). The average energy gap between these two bands is called the *band gap* (E_g). Based on equation (9.2.8), the density of energy states above the CB edge E_c is given by

$$N_c = \frac{8\sqrt{2\pi}}{h^3}(m_e^*)^{3/2}(E - E_c)^{1/2} \tag{9.2.9}$$

Similarly, the density of states below the VB edge E_v is given by

$$N_v = \frac{8\sqrt{2\pi}}{h^3}(m_h^*)^{3/2}(E - E_v)^{1/2} \tag{9.2.10}$$

where m_e^* and m_h^* are effective masses[1] of an electron and a hole in the crystal, respectively. For semiconductors ($E_g \leq$ ca. 1 eV), thermal energy at room temperature ($k_B T$) is sufficient to promote a few electrons from the VB to the CB. The corresponding density of electrons in the CB (n) and density of holes in the VB (p) are given by

$$n = N_c \exp\left(-\frac{E_c - E_{F,n}}{k_B T}\right) \tag{9.2.11}$$

and

$$p = N_v \exp\left(-\frac{E_v - E_{F,p}}{k_B T}\right) \tag{9.2.12}$$

where $E_{F,n}$ and $E_{F,p}$ are corresponding Fermi energies of electrons and holes, respectively. At equilibrium, the Fermi levels of electrons and holes are equal. That is

$$E_{F,n} = E_{F,p} = E_F \tag{9.2.13}$$

which leads to

$$n = n_0; \qquad p = p_0 \tag{9.2.14}$$

where n_0 and p_0 are the respective densities of electrons in the CB and holes in the VB at equilibrium. Substituting the equilibrium condition described in equation (9.2.14) into equations (9.2.11) and (9.2.12) leads to

$$n_0 p_0 = N_c N_v \exp\left(\frac{E_c - E_v}{k_B T}\right) = n_i^2 \tag{9.2.15}$$

At room temperature (300 K), the equation simplifies to

$$n_i = p_i \approx 2.5 \times 10^{19} \exp\left(-\frac{E_g}{2k_B T}\right) \tag{9.2.16}$$

The mobility of electrons in the CB and holes in the VB imparts conductivity to the semiconductor as illustrated in Figures 9.4a and b. This type of semiconductor is called an '*intrinsic*' semiconductor.

Electron–hole pairs can also be introduced by substitution of acceptor and donor atoms by a process called *doping*. These 'doped' semiconductors are called *extrinsic* semiconductors.

---

[1]The effective mass of an electron in a crystal is given as $m_e^* = \hbar^2/(d^2E/dk^2)$, which is different from the rest mass of an electron, m_e. The equation suggests that the mass of an electron in the crystal changes with the curvature of the Brillouin zone (Figure 9.1b). For most of the values of k, $m_e^* = m_e$. However, near the edges of the zone, i.e., $k = \pm n\pi/a$, m_e^*, differs considerably from m_e. At the bottom of the zone, (d^2E/dk^2) is positive and the effective mass is positive. At the top of the zone, (d^2E/dk^2) is negative and the effective mass is negative. Physically, it represents an exchange of momentum with the lattice as the moving electron gets retarded near the Brillouin zone boundaries.
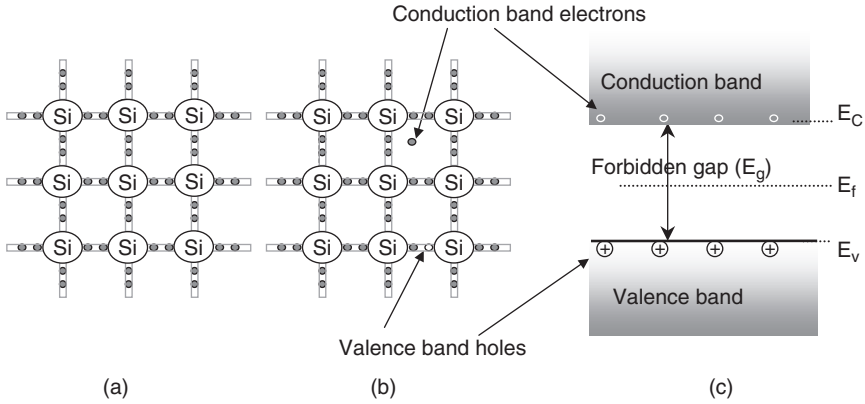
Figure 9.4 Two-dimensional representation of crystal structure of an intrinsic semiconductor such as Si crystal. The original tetrahedral structure is oversimplified to a square one for clarity. Dark spots in the sketch illustrate shared valence electrons among Si atoms and form covalent bonds. (a) Situation at 0 K where no ionization takes place. (b) At higher temperature, valence electrons gain sufficient energy and are delocalized, which form the holes in the VB. (c) Energy diagram for the intrinsic semiconductor crystal. Mobility of holes in VB and the electrons in CB imparts conductivity to the intrinsic semiconductor crystal.

For example, if Si crystal is doped with P, As, or Sb atoms (group V elements), donor states are created in the band gap. For a moderately doped semiconductor (ca. $N_D = 10^{-14}$ donor atoms per cm^3), these states lie ca. 0.02–0.03 eV below the CB. Thus, even at room temperature, these states get fully ionized by promoting electrons into the CB. The presence of electrons in the CB is due not only to their promotion from the VB but also from the ionized donor states. Thus, the overall density of electrons in the CB due to doping is given by

$$n = (n_0 N_D)^{1/2} \exp\left(-\frac{E_D}{2k_B T}\right) \tag{9.2.17}$$

where E_D is the energy gap between donor states and E_c; it has a magnitude of approximately 0.02–0.03 eV at room temperature as Figures 9.5a and b illustrate. The density of electrons in the CB is increased compared with the density of holes in the VB. The observed conductivity is attributed to CB electrons, which are called *majority carriers*. Such a material is called an *n-type semiconductor*.

If Si crystal is doped with trivalent impurity atoms (e.g., B, Al, Ga, and In), then the acceptor levels are introduced into the band gap approximately 0.02–0.03 eV above the VB. Thus, the electrons from the VB get promoted to the acceptor levels, leaving holes behind. The overall density of holes in the VB is given by

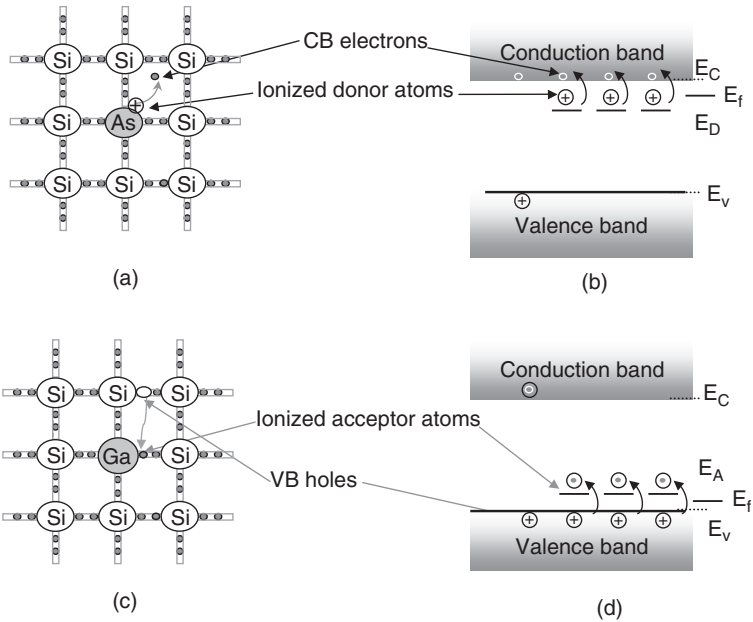$$p = (p_0 N_A)^{1/2} \exp\left(-\frac{E_A}{2k_B T}\right) \tag{9.2.18}$$

Figure 9.5   (a) Two-dimensional representation and (b) corresponding energy bands for n-doped Si. An extra valence electron from As atom is ionized and occupies the CB of Si. Similarly, (c) and (d) are respective illustrations for p-doped Si. Valence electron from Si occupies the vacancy created (acceptor levels) at Ga atoms, thus leaving a hole in the VB for conduction. Note the shift in position of the Fermi level (E_F) due to doping.

where E_A is the energy gap between acceptor states and E_v; it is approximately 0.02–0.03 eV at room temperature as shown in Figures 9.5c and d. In this case, there are more holes in the VB than electrons in the CB. Thus, the holes are majority carriers and electrons are the minority carriers. The material is referred to as a *p-type semiconductor*.

9.2.2   Size quantization in semiconductors

It is generally assumed that the electronic properties of a semiconductor are independent of crystal size. However, recent studies have shown that if the particle size of the semiconductor is less than approximately 10 nm, then many of their physicochemical properties appear to be substantially different from analogous properties of a bulk material. This is because the electrons and holes are confined in the region of space defined by potential barriers that are comparable to or smaller than their respective *de Broglie* wavelengths so that allowed energy states become discrete (or quantized). This effect is referred to as the size quantization effect (SQE) or the quantum size effect. SQE is also observed in the noble metals (4). For semiconductors, the critical dimension for SQE depends upon the effective masses of the electrons (m_e^*) and the holes (m_h^*). For example, for $m^* \sim 0.05$, the critical dimension is approximately 30 nm. Thus, for semiconductors, SQE is observed in
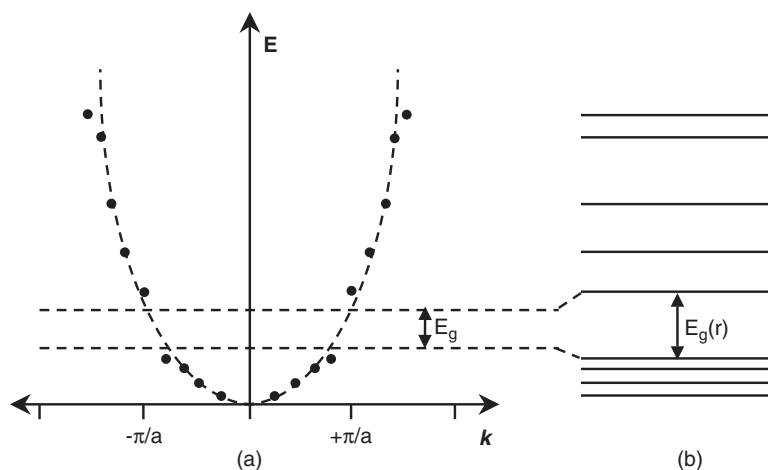
Figure 9.6 (a) Schematic plot of the energy E vs. wave vector k for the electron confined in a size-quantized semiconductor crystal. The dark dots over the parabola indicate the discrete and allowed energy values for the transition. (b) The band structure in the form of discrete energy states that suggest 'molecular-like states' for the size-quantized particles. E_g indicates the band gap for the bulk semiconductor, whereas $E_g(r)$ indicates energy separation between the highest occupied molecular orbital (HOMO) and the lowest unoccupied molecular orbital (LUMO) in the case of size-quantized particles, where $E_g(r) > E_g$.

the nanometer size regime and the particles are called nanoparticles or size-quantized particles. The band structure for the semiconductor in its size-quantized state is illustrated in Figure 9.6. As can be seen, the energy bands observed in a bulk semiconductor (Figure 9.1b) are replaced by discrete states, which leads to a dramatic change in its electronic properties. Currently, there is intense scientific and technological interest in size-quantized semiconductor structures. This is because electronic properties such as optical, catalytic, electrical, and redox potentials can be tuned and manipulated in fascinating ways by controlling the dimension, rather than just the chemical composition alone.

SQE is modeled similarly to the 'particle in a box problem', in which the smaller the 'box', the larger is the lower energy eigen value. The correlation for energy states between bulk material and corresponding size-quantized particle is schematically depicted in Figure 9.7.

It suggests that on decreasing the particle size, the energy of the first electronic transition of the semiconducting material shifts toward higher energy, which can be measured by using UV–vis absorption spectra. The blue shift in the absorption peak as a function of size for CdSe size-quantized particles (5) is shown in Figure 9.8. Furthermore, phase transition pressure, melting point, optical, optoelectronic, catalytic, and magnetic properties of *nanomaterials* differ from those of bulk solids and also from the molecular species from which they are made. Chemists can view this as a *giant molecule* or a new state of matter.

Two models have been used to explain SQE in the case of semiconductor nanoparticles. The first model is an effective mass approximation (6–11) developed for relatively larger particles. The second model assumes a tight-binding framework for well-defined small
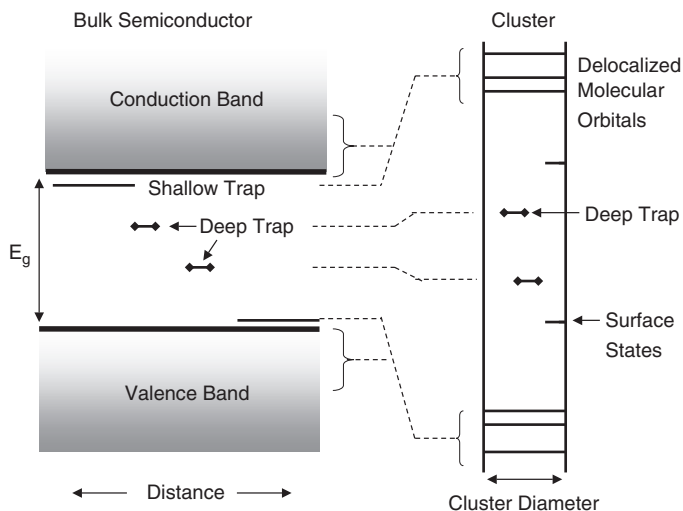
Figure 9.7   Spatial electronic state correlation diagram relating cluster states to bulk crystal states. Adapted from reference (6).
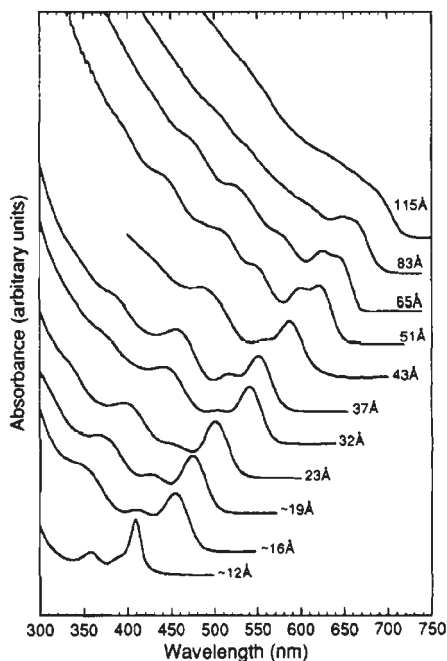

Figure 9.8   UV–vis spectra recorded for various sizes of trioctylphosphine oxide (TOPO)-capped CdSe clusters dispersed in hexane. Blue shift in the absorption edge is due to a larger separation between electronic states with decrease in particle diameter. Reprinted with permission from reference (5). Copyright 1993, American Chemical Society.

clusters (12). In the effective mass approximation, the electrons and holes are considered to be trapped in the spherical potential well. It is characterized only by a continuum of a solid having a dielectric constant ε. Electrons and holes are considered to be well separated from each other and uncorrelated. Variational methods (13) have been employed to solve the resulting Hydrogenic Hamiltonian. The ground-state energy of the *exciton* (minimum energy required to produce the electron–hole pair) is given by (11)

$$E_d = \frac{2\hbar^2\pi^2}{d^2}\left[\frac{1}{m_e^*}+\frac{1}{m_h^*}\right] - \frac{3.572e^2}{\varepsilon d} - \frac{0.124e^4}{\hbar^2\varepsilon^2}\left[\frac{1}{m_e^*}+\frac{1}{m_h^*}\right]^{-1} \qquad (9.2.19)$$

where m_e^* and m_h^* are the respective effective masses of the electron and the hole, and d and ε refer to the diameter and dielectric constant of the semiconductor particles, respectively. The effective mass approximation gives a good understanding of the blue shift of the optical absorption threshold. However, it fails in the case of small crystallites due to the oversimplified description of the crystal potential.

A better description of the band structure for nanoparticles can be obtained by considering the tight-binding framework model (12). In this model, the atomic structure of a solid is implicitly considered. The energy levels are obtained by using the semi-empirical tight-binding theory. The energy levels and wave functions are, respectively, the eigen values and eigen vectors of the Hamiltonian matrix **H**. Its bases are either atomic orbitals or a linear combination (hybridization) of them. The numerical calculation results obtained for CdS and ZnS nanocrystallites are summarized in Figures 9.9a and b, respectively.
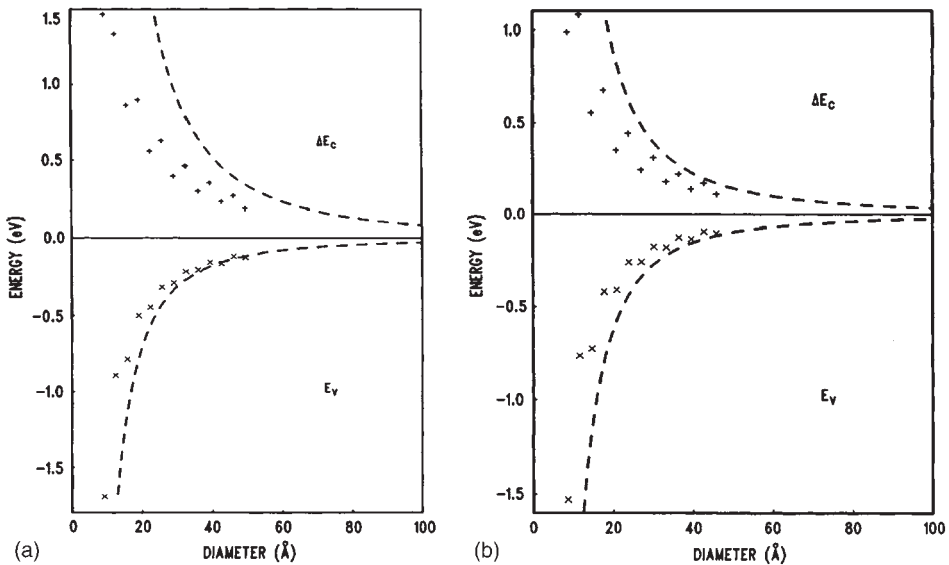
Figure 9.9   (a) Variation of band edge as a function of diameter of CdS clusters. The origin is taken as bulk values. The variational results are represented as '×' in the figure. $\Delta E_c = E_c - 2.5$ eV(+). The dashed curves are the results of the effective mass approximation. (b) Similar results for ZnS cluster. $\Delta E_c = E_c - 3.7$ eV(+). Reprinted with permission from reference (12). Copyright 1989 by the American Physical Society.
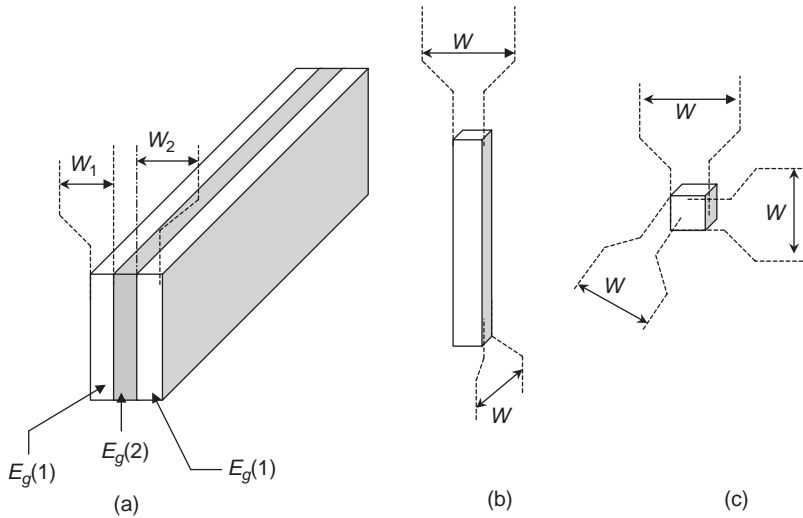
Figure 9.10 Three quantization configurations in semiconductors. (a) Confinement of charge carriers in 'two dimensions' called a quantum well. A narrow band gap ($E_g(2)$) is sandwiched between two wide band gap ($E_g(1)$) semiconductors. The charged carriers are trapped in a two-dimensional potential well. (b) Confinement of charge carriers in 'one dimension' called quantum wires. (c) Confinement of charge carriers in 'zero dimension' called quantum dots. 'w' represents width of confined direction, which is of the order of 1–20 nm. Adapted from reference (14).
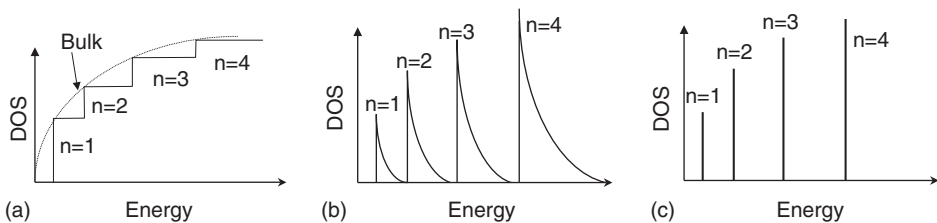

Figure 9.11 The density of electronic states (DOS) as a function of energy for three size regimes: (a) quantum well—DOS is a step function, (b) quantum wire, and (c) quantum dots. For the quantum wire, DOS distribution is in between a quantum well and quantum dots.

Semiconductor nanoparticles that arise due to the confinement of electrons/holes in zero spatial dimension are called quantum dots. Quantum wires and quantum films or wells arise when the charge carriers in the corresponding semiconductor are confined in one or two spatial dimensions. These dimensional confinements and corresponding density of states are illustrated in Figures 9.10 and 9.11, respectively.

9.3 ENERGETICS OF A SEMICONDUCTOR

Key factors in the utilization of semiconductor electrodes in electrochemical cells and devices are (a) knowledge of the relative location of the energy levels in the

semiconductor and solution and (b) understanding the role of surface states in the charge transfer. Two important parameters are the *Fermi level* (E_F) of the semiconductor and the corresponding electrochemical potential ($\bar{\mu}_{e,redox}$) of electrons in solution. The Fermi level was introduced in Section 9.2. From equation (9.2.6), the probability of finding an electron at $E = E_f$ is found to be 1/2. Thus, the Fermi level can also be defined as the energy level where the probability of an electron occupying it is one half. The probability of occupying levels above E_F is 0 and below E_F is 1. In case of an intrinsic semiconductor, E_F is expressed as

$$E_F = \frac{3}{4} k_B T \ln\left(\frac{m_h^*}{m_e^*}\right) + \frac{E_C + E_V}{2} \tag{9.3.1}$$

At absolute zero, the first term in equation (9.3.1) vanishes and

$$E_F \approx \frac{E_C + E_V}{2} = \frac{E_g}{2} \tag{9.3.2}$$

Thus, E_F lies about midway in the forbidden region as illustrated in Figure 9.4c. The position of E_F also depends upon the relative density of electrons and holes. For example, for the case of an n-type semiconductor ($N_D \approx 10^{15}$ cm^{-3}), E_F lies midway between E_c and E_D. Similarly, for the case of a p-type semiconductor, E_F lies midway between E_v and E_A, as illustrated in Figures 9.5b and d. From a chemist's point of view, E_F is simply the electrochemical potential of the electron in a given phase (in the present context, it is a semiconductor phase) that is expressed as

$$E_F^\alpha = \bar{\mu}_e^\alpha = \mu_e^\alpha - e\phi^\alpha \tag{9.3.3}$$

where μ_e^α and ϕ^α are the chemical potential and the inner potential[2] of an electron in phase α, respectively. It is measured in electron volts (eV) with reference to the energy of an electron in a vacuum, which is assumed to be zero. Similarly, the electrochemical potential of electrons in a dilute redox solution is given by

$$\bar{\mu}_{e,redox} = \mu_{e,redox}^0 + k_B T \ln\left(\frac{[O]}{[R]}\right) \tag{9.3.4}$$

where [O] and [R] are the concentrations of oxidized and reduced species, respectively. Redox potentials are expressed with reference to the normal hydrogen electrode (NHE) whose reduction potential is the assigned standard of 0.0 V at all temperatures.[3] In order to compare the energetics of a redox reaction with those of a semiconductor, we need to

---

[2]Inner potential ϕ is defined as the work done to bring a unit positive charge from the vacuum level to the phase α electric force field ε. Thus, $\phi = \int_\infty^{(x,y,z)} \varepsilon(x,y,z)\,dl$.
[3]Standard free energy change of formation ($\Delta_f^\circ G$) for a hydrogen atom from ions is assumed to be zero at all temperatures. It implies that $E^0(H_2(1 \text{ atm})/H^+(a=1)) = 0.0$ V with $\Delta_f^\circ G = -nFE^\circ$.

express $\bar{\mu}_{\text{e,redox}}$ on a vacuum or absolute scale. As discussed, $\bar{\mu}_{\text{e,redox}}$ of a redox system is equivalent to the Fermi level $E_{\text{F,redox}}$; that is

$$E_{\text{F,redox}} = \bar{\mu}_{\text{e,redox}} \tag{9.3.5}$$

On an absolute scale, it is given by

$$E_{\text{F,redox}} = E_{\text{ref}} - eU_{\text{redox}} \, (\text{in eV}) \tag{9.3.6}$$

where U_{redox} is the redox potential in volts vs. NHE and E_{ref} is the energy of the reference electrode vs. this absolute scale. The standard reduction potential of the NHE (0.0 V) is accepted to be equivalent to -4.5 eV on an absolute scale (15).

$$E_{\text{F,redox}} = -4.5\,\text{eV} - eU_{\text{redox}} \tag{9.3.7}$$

The position of bands of various semiconductors using the vacuum and electrochemical scales is shown in Figure 9.12. In fact, this is an important bridge between semiconductor physics and electrochemistry. For example, Si has $E_{\text{F}} = -4.8$ eV on a vacuum scale. The corresponding value with reference to NHE in solution is +0.3 V.
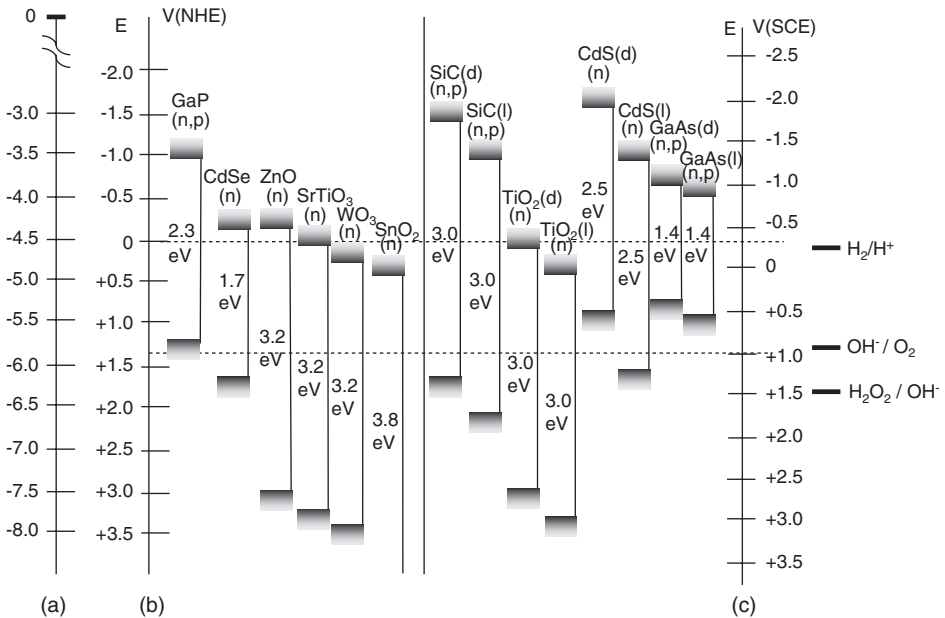

Figure 9.12   Position of energy bands of various semiconductors with respect to vacuum and electrochemical scales (adapted from reference (14)). The scale marked as (a) is for the vacuum scale. The scale marked as (b) is for the normal hydrogen electrode (NHE) scale and the scale marked as (c) is for saturated calomel electrode (SCE) scale.
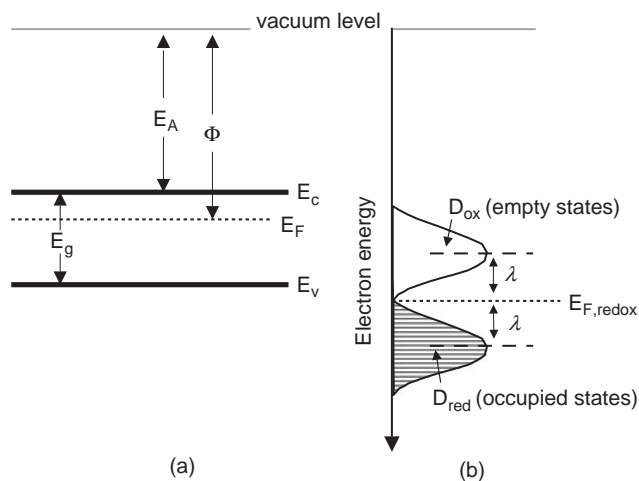
Figure 9.13   (a) Energy levels in the semiconductor. E_A and Φ stand for the electron affinity and work function of the semiconductor, respectively. (b) Energy distribution of occupied and unoccupied states of a redox couple. Adapted from reference (14).

A redox couple will also have a distribution of energy levels similar to semiconductors. These were first described by Gerischer (16, 17) in terms of a Gaussian-type distribution function, which is given by

$$D_{\mathrm{ox}} = \exp\left[-\frac{(E - E_{\mathrm{F,redox}} - \lambda)^2}{4k_{\mathrm{B}}T\lambda} \right] \tag{9.3.8}$$

and

$$D_{\mathrm{red}} = \exp\left[-\frac{(E - E_{\mathrm{F,redox}} + \lambda)^2}{4k_{\mathrm{B}}T\lambda} \right] \tag{9.3.9}$$

where D_{ox} and D_{red} are the distribution functions for oxidized and reduced species, respectively. λ is the solvent reorganization energy from electron transfer theory (18). A detailed picture of energy levels of semiconductor bands and a distribution of occupied and unoccupied states for a redox couple are given in Figure 9.13.

9.3.1   Semiconductor–electrolyte interface (SEI)

When the semiconductor and redox solution are brought in contact with each other, their Fermi levels must match at equilibrium. If they differ initially, then charge transfer must take place between these phases to eliminate the disparity in their Fermi levels. For example, if
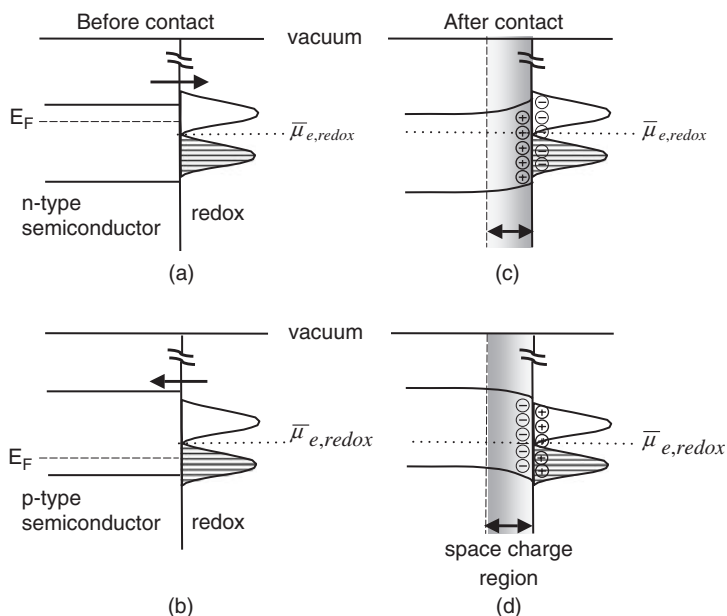
Figure 9.14   Energetics of the semiconductor–electrolyte interface, when n- and p-type semiconductors are brought in contact with the redox couple having $\overline{\mu}_{e,redox}$ in between the band gaps. (a and b) The situations before contact. (c and d) The situations after contact. Arrows shown in (a) and (b) show the direction of electron flow before equilibrium is established.

E_F of an n-type semiconductor lies above the $\overline{\mu}_{e,redox}$ of the solution as shown in Figure 9.14a, then to remove the difference in Fermi energies, the electrons will flow from the semiconductor to the solution side.

Thus, the semiconductor will acquire a positive charge and the solution will become negatively charged as shown in Figure 9.14c. Similarly, a p-type semiconductor will acquire a negative charge with respect to the solution as shown in Figure 9.14d. In the case of moderately doped semiconductors, the density of states available on the surface is not sufficient to accommodate these excess charges. Therefore, charges will be distributed inside the semiconductor region at a distance on the order of approximately 10–1000 nm. This region is called the *space charge region*. The resultant electric field in the space charge region affects the local energy of the electrons. Thus, the electrochemical potential of electrons in the semiconductor is different near the space charge region than that of the bulk of the semiconductor. It appears as *band bending* in the Gerischer diagram.

Thus, if charge separation occurs in this region, electrons in the CB will have a tendency to 'roll down' into the bulk. At the same time, holes in the VB will 'bubble out' on the surface. Thus, the space charge region is responsible for charge separation at the SEI. The potential difference created between the bulk of the semiconductor and the interface due to band bending is called the barrier height ($\Delta\phi$). It is depicted in Figure 9.15. There will also be a potential gradient toward the solution side due to the Helmholtz layer as shown in Figure 9.16.
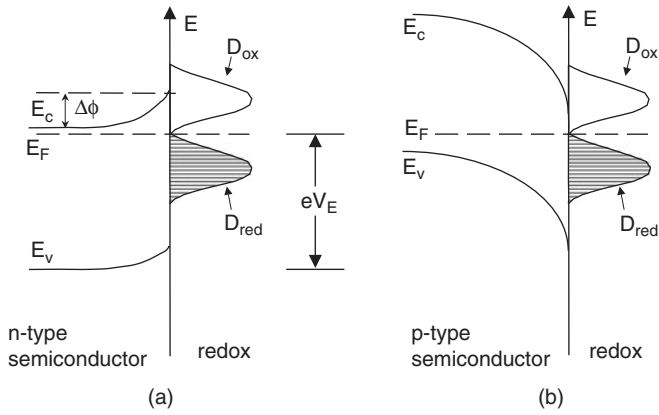
Figure 9.15   Details of the semiconductor–electrolyte interface for (a) n-type and (b) p-type semiconductors. $\Delta\phi$ represents the barrier height. Adapted from reference (14).
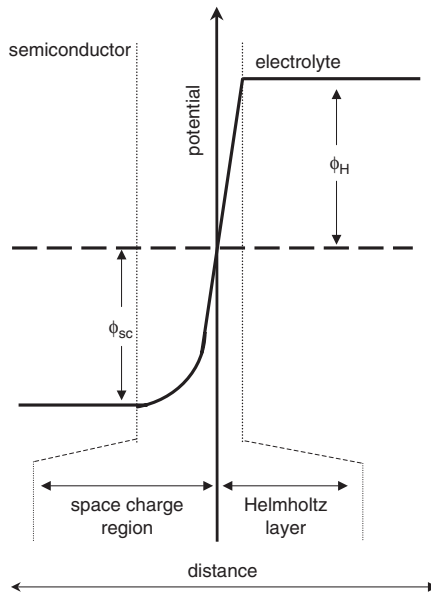
Figure 9.16   Potential distribution across the SEI. ϕ_{SC} and ϕ_H are potential drops across space charge and Helmholtz regions, respectively. Adapted from reference (14).

Thus, the SEI can be modeled as two parallel plate capacitors in series. Because the value of the space charge region capacitor is generally smaller than that of the Helmholtz layer, it dominates the overall capacitance of the SEI.

One of the important advantages in using a semiconductor as an electrode is that the energetics of the SEI can be modulated by applying a potential bias.

Figure 9.17   Effect of applied potential on the structure of the SEI. The corresponding current–voltage curve is also shown for n-type semiconductor. The negative bias increases from left to right side of the figure. Situation (a) occurs at extremely positive bias from E_{fb}. The flow of current is attributed to the tunneling process, when diode *breaks down*. In situations (b) and (c), the electron transfer takes place, overcoming the barrier height, which progressively reduces with more and more negative bias. Situation (d) is a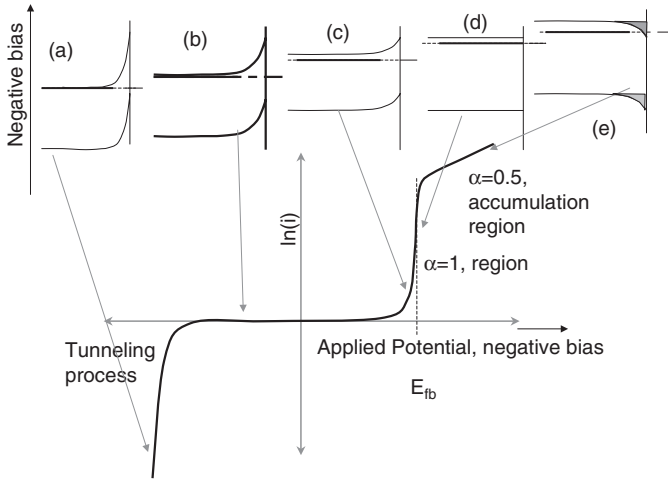n unique one at which bands become flat and current increases exponentially. Further increase in the negative bias leads to inverted bands and semiconductor starts behaving like a metal.

Figure 9.17 shows the effect of an applied bias on the structure of the SEI. On applying a negative bias to an n-type semiconductor, $\Delta\phi$ is reduced and at a particular value of EMF, it is eliminated completely. The applied potential at which no space charge region exists is called a *flat-band potential* E_{fb}, which is related to the barrier height by the expression

$$-\Delta\phi = E - E_{fb} \tag{9.3.10}$$

The capacitance of the space charge region C_{sc} can be related to $\Delta\phi$ by the *Mott–Schottky* equation

$$\frac{1}{C_{sc}^2} = \left(\frac{2}{e\varepsilon\varepsilon_o N_D} \right)\left(-\Delta\phi - \frac{kT}{e} \right) \tag{9.3.11}$$

Thus, a plot of $1/C_{sc}^2$ vs. applied potential E (a *Mott–Schottky plot*) can be used to determine the E_{fb} of the SEI.

9.4   SEMICONDUCTOR ELECTRODES

9.4.1   Electron transfer at semiconductor–electrolyte interface

An observed current in an electrochemical cell is usually viewed as charge transfer across the electrode–solution interface. Consequently, it is not necessary to use individual electrons

or holes in theoretical calculations. The electron transfer can be modeled as an adiabatic process (19, 20) in which an 'electron cloud' interacts with an electron acceptor (cloud) in a solution (redox); that is, the (symmetrically) favorable configuration in terms of spatial and angular momentum compatibility is achieved on matching the energy levels.

In the case of metallic electrodes (e.g., Pt), the observed cathodic current for the reaction

$$O + ne \rightarrow R \tag{9.4.1}$$

at a given potential E is given by

$$i \approx nFAk'_f C_o(x = 0) \tag{9.4.2}$$

where n and F are the number of electrons involved in elementary steps and Faraday's constant, respectively, A is the area of the electrode and $C_o(x = 0)$ is the surface concentration of the oxidized species O. k'_f is the heterogeneous rate constant ($cm\ s^{-1}$) of the electron transfer, which is an exponential function of E and the transfer coefficient (α). In metals, the electron density near the Fermi level is very high compared with the concentrations of O and R. Therefore, there is hardly any change in electron density at steady state so that the rate of electron transfer is often limited by the surface concentration of ions and it follows pseudo-first-order kinetics.

In the case of a semiconductor electrode, densities of electrons and holes are limited. Therefore, the current is often governed by the density of the charge carriers (17) that can be treated as individual reactants. Thus, in the case of charge transfer across an SEI, a bimolecular heterogeneous rate constant must be considered. Unlike metals, the charge transfer can follow two different pathways.[4] It can occur by electron transfer from the CB to O and by electron transfer from R to the VB. The latter case is viewed as a transfer of holes from the VB to R as illustrated in Figure 9.18. Unlike a metal electrode, its concentration can be varied over a wide range by simply controlling the applied potential E.

Consider the SEI as shown in Figure 9.14 where $\bar{\mu}_{e,redox}$ of ions lies between E_{VB} and E_{CB}. The semiconductor electrode is immersed in a well-stirred solution so that the
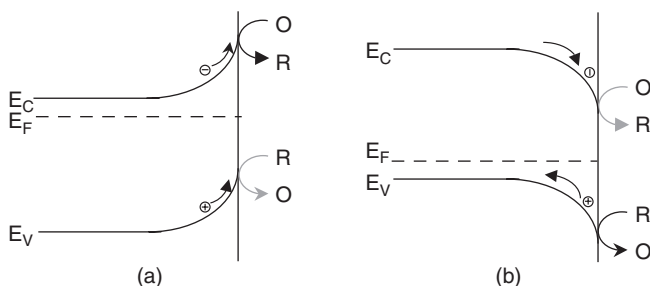

Figure 9.18   Electron transfer reaction at SEI in dark for (a) n-type and (b) p-type semiconductors. Faint arrows indicate that the process is less dominating.

---

[4]In this model, complications often arise in the charge transfer due to surface states. These states lie between the VB and CB and are not considered.

current is not limited by the mass transfer of ions in the solution. In the dark, the electron transfer will be dominated by the majority carriers in the semiconductor. Thus, in case of an n-type semiconductor, there are excess electrons (from the donor states) in the CB compared with the holes present in the VB. The transfer of electrons from the CB to O in solution will proceed at a higher rate than the electron transfer from R to the holes in the VB. Thus, the reduction of O will take place in solution. Since the electrons need to overcome $\Delta\phi$ in order to pass current in the forward direction, a net cathodic current will flow according to

$$i = nFAk_f n_{sc} C_o (x = 0) \tag{9.4.3}$$

where k_f (cm^4 sec^{-1}) is the bimolecular heterogeneous rate constant for the forward reaction (reduction) and n_{sc} (cm^{-3}) is the density of electrons in the space charge region. Similarly, for the p-type semiconductor, oxidation of R would be the most favorable process. Similar to equation (9.4.3), the net anodic current for given potential is expressed as

$$i = nFAk_b p_{sc} C_R (x = 0) \tag{9.4.4}$$

where k_b (cm^4 sec^{-1}) is the heterogeneous rate constant for the backward reaction (oxidation) and p_{sc} (cm^{-3}) is the density of holes in the space charge region. This represents the situation where no external bias is applied to the interface and the system is driven by the barrier height ($\Delta\phi$). At equilibrium, both rates will be equal and no net current will flow at the SEI.

When an EMF (E) is applied to the electrode, the heterogeneous rate constants (k_f and k_b) will vary with E according to the Butler–Volmer equations

$$k_f = k^\circ \exp\left[-\frac{\alpha F(E - E^{\circ\prime})}{RT} \right] \tag{9.4.5}$$

and

$$k_b = k^\circ \exp\left[\frac{(1-\alpha)F(E - E^{\circ\prime})}{RT} \right] \tag{9.4.6}$$

where $E^{\circ\prime}$ is the formal reduction potential of the redox O/R couple and k° is the standard rate constant that can be related to the exchange current density i_0 at the interface. Its value depends upon the overlap of the electronic wave function of the semiconductor and the redox couple (21). The higher the overlap, the more facile are the kinetics and the faster is the charge transfer. The heterogeneous rate constants k_f or k_b depend upon the potential drop ($\Delta\phi'$) at the Helmholtz layer across the SEI, which may change with applied potential.[5] It follows that the quantity ($E - E^{\circ\prime}$) can be replaced by $\Delta\phi'$ in equations (9.4.5) and (9.4.6). Thus, these equations are applicable to both metal and semiconductor electrodes.

---

[5]This is a property of the interface at the solution side and is therefore applicable to metal electrodes also.

Unlike metals, semiconductors have a space charge region. Therefore, the applied potential will affect the composition of the space charge region through the equations

$$n_{sc} = N_D \exp\left[-\frac{F(E - E_{fb})}{RT}\right] \tag{9.4.7}$$

and

$$p_{sc} = N_A \exp\left[\frac{F(E - E_{fb})}{RT}\right] \tag{9.4.8}$$

Here again, $(E - E_{fb})$ is equal to the amount of band bending that is also the barrier height ($\Delta\phi$). The applied bias changes the magnitude of the barrier height and thus controls the current in the cell. This is analogous to the current through a metal–semiconductor Schottky barrier (22). Under these conditions, variation of E mainly affects n_{sc} and p_{sc} in an n- and a p-type semiconductor, respectively. This means that the slope of a plot of $\ln(i)$ vs. E will be RT/F that implies that $\alpha = 1$ (23). For an n-type semiconductor, if E is made more negative than E_{fb}, then the electrons accumulate at the semiconductor surface, called an *accumulation layer*. In this situation, n_{sc} is no longer a function of E, which was earlier governed by equation (9.4.7). Thus, the applied potential will change k_f as per equation (9.4.3); that is, there will be a change in potential drop in the Helmholtz region ($\Delta\phi'$). Semiconductor electrodes essentially behave like a metal with $\alpha \approx 1$. Similar arguments are applicable to a p-type semiconductor when a potential more positive than that of E_{fb} is applied. If we substitute equations (9.4.5) and (9.4.7) into equation (9.4.3) and plot a Tafel plot, it would typically follow the function as shown in Figure 9.17. In this illustration, current is assumed to be purely faradaic and not limited by mass-transfer processes. Thus, in using semiconductor electrodes experimentally, the density of charge carriers is controlled as function of potential; this feature is lacking in metal electrodes.

9.4.2 Illuminated semiconductor electrodes

Consider the situation of an SEI between an n-type semiconductor electrode and redox couple, which we have discussed in Section 9.3. On illuminating this interface with a light having photon energy ($h\nu$) greater than the band gap (E_g) of the semiconductor,[6] a transition of electrons from the VB to the CB will occur, leaving behind holes in the VB. The *charge pairs* generated in the bulk of the semiconductor will eventually neutralize each other and the energy will dissipate in terms of heat (lattice vibrations).

However, the charge pairs generated near the SEI experience a potential gradient due to the space charge region. The electrons promoted in the CB *experience* the lower energy in

---

[6]The feasibility of excitation of an electron from the VB to the CB is allowed if the angular momenta of the photon and electron are conserved during excitation. The semiconductor is then called a direct band gap semiconductor. For example, CdS, CdSe, GaAs, InP, etc., are direct band gap semiconductors, whereas Si is an indirect band gap semiconductor.
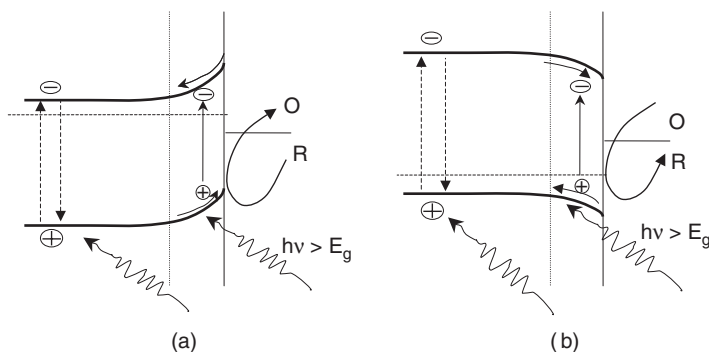
Figure 9.19   n-Type semiconductor–electrolyte interface under the illumination. (a) Charge pair generated in the bulk gets eventually annihilated and generates heat. (b) Charge pair generated in the space charge region gets separated from each other due to the potential gradient. Holes *bubbled out* at the interface can oxidize the redox R into O. Thus, net oxidation reaction will take place at the SEI of n-type semiconductor on illumination.
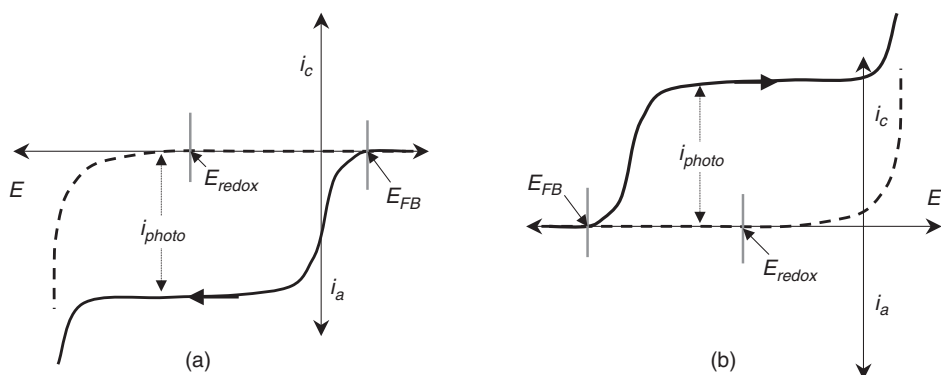

Figure 9.20   *i–v* curve for semiconductors/redox junction in dark (dotted line) and on illumination (hard line) for (a) n-type semiconductor, which on illumination leads to photoanodic current, and (b) p-type semiconductor, which on illumination leads to photocathodic current. The onset for photocurrents in both the diagrams suggests the flat-band potential, E_{fb}.

the bulk of the semiconductor and thus '*roll back*' into the bulk. In contrast, holes experience an opposite force field and thus '*bubble out*' at the interface. The situation is demonstrated in Figure 9.19. The holes, which are 'surfaced' at the SEI, have an effective redox potential equal to that of the VB edge and thus oxidize R into O. The electrons travel in the semiconductor bulk and proceed into the external circuit, which eventually reduces O at the counter electrode. Thus, in the case of an n-type semiconductor, the reduction will be facilitated in the dark. However, on illumination, oxidation is prevalent. Therefore, irradiation of an n-type semiconductor promotes an oxidation reaction called *photo-oxidation* at the semiconductor surface. The corresponding steady-state current–potential curves are drawn in Figure 9.20.

9.4.3 Cyclic voltammetry (CV) at semiconductor electrodes

Cyclic voltammetry (please see Chapter 11) (24) has been extensively used to probe the behavior of SEI in the dark and under illumination. Bard and co-workers (21, 25–27), Wrighton and co-workers (28, 29), Lewis and co-workers (30, 31), and Chazalviel *et al.* (32) have carried out pioneering work in this field. These studies unambiguously demonstrated the use of CV to deduce critical parameters of SEI including, for example, E_V, E_c, and E_{fb}. In Section 9.4.1, it was demonstrated that a change in EMF at a semiconductor electrode results in a large change in the density of charge carriers at an SEI. Only the redox couples, which are energetically closer to the VB and CB, are expected to undergo charge transfer. For example, Laser and Bard (21) recorded CVs with a single-crystal TiO_2 electrode in redox couples chosen such that their E_{redox} accommodates the entire potential window from the VB to the CB.

The various redox couples used in this experiment and their potentials on TiO_2 and Pt are listed in Table 9.1. The idea was to judge the position of energy bands based on the reversibility of the CV for redox couples of known potentials. Based on these results, three

Table 9.1

Electrochemical data for redox couples

	Pt	TiO_2	
	E_0 (V vs. SCE)	E_{pc}	E_{pa} (V vs. SCE)
$Ru(bipy)_3^{3+}$	+1.3	+0.36	None
	−1.3	−1.34	−1.27
	−1.49	−1.52	−1.46
	−1.73	−1.77	−1.70
Th•+	+1.23	+0.40	None
10-MP•+	+0.82	+0.28	None
TMPD•+	+0.22	−0.31	None
Ox-1•+	−0.42	−0.80	None
	−1.30	−1.65	None (adsorption probe)
p-BQ	−0.52	−1.00	None
	−1.64 (irreversible)	−1.89	None
$Ru(TPTZ)_2^{3+}$	−0.81	−0.90	−0.72
	−0.97	−1.09	−0.88
	−1.63	−1.76	−1.55
	−1.88	−2.03	−1.83
AQ	−0.94	−1.12	Some oxidation beginning at ca. −0.90
	ca. −1.61 (quasi-reversible)	−1.84	−1.44
DBM	−1.55	−1.68	−1.44
9,10-DPA	−1.84	−1.93	−1.74
A	−1.94	−2.06	−1.80

Reprinted with permission from reference (33). Copyright 1975, American Chemical Society.
[a]Abbreviations used in this table: Th, thianthrene; 10-MP, 10-methylphenothiozine; TMPD, *N,N,N′,N′*-tetramethyl-*p*-phenylenediamine; Ox-1, oxazine-1; *p*-BQ, *p*-benzoquinone; AQ, anthraquinone; DBM, dibenzoylmethane; 9,10-DPA, 9,10-diphenylanthracene; A, anthracene.

potential regions were identified: (a) a region positive to approximately -0.8 V, where a redox couple, which is reversible at platinum, becomes totally irreversible at TiO_2. In some cases, the reduction wave was shifted by about 1 V more negative compared with that recorded on platinum. However, on illumination of the SEI, quasi-reversibility was observed. (b) In the second potential region, negative to about -0.8 V, there is no change in the redox profile on TiO_2. The reduction of all redox couples on TiO_2 is reversible, similar to that recorded on a Pt electrode. (c) In the third potential region, redox couples that reduce at potentials positive of 0.4 V on platinum are reduced between $+0.3$ and $+0.4$ V at TiO_2 irrespective of their reduction potentials on Pt.

The redox reaction observed in the first potential region between approximately -0.8 and $+0.3$ V is attributed to electron transfer through a rectifying junction; this explains the irreversibility of the CV curve and the quasi-reversibility observed under illumination. This behavior indicates that the redox potentials of the chosen redox couple are within the band gap region. The behavior of the CV more negative than -0.8 V can be attributed to the formation of an accumulation layer and metallic behavior of the semiconductor. This behavior indicates that the redox potential is above E_C. The CV behavior in the third potential region positive of $+0.4$ V is attributed to the mediation of electron transfer through the surface state. Based on these results, the suggested band diagram for TiO_2 electrode is depicted in Figure 9.21.
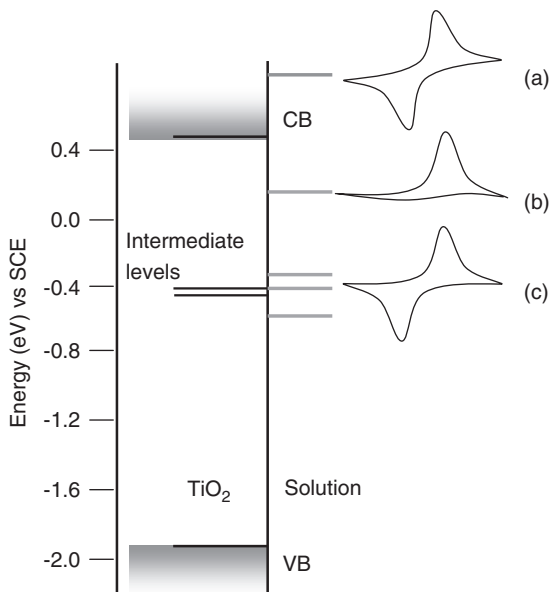
Figure 9.21   Band diagram for n-type single-crystal TiO_2 electrode based on CV measurements. (a) CV recorded for redox having redox potential above E_C. Reversibility of CV indicates metallic behavior of the electrode. (b) CV recorded for a redox having redox potential below E_C. Irreversibility of CV indicates rectifying nature of the junction. (c) Same CV for redox couples having redox potentials negative to ca. -0.3 V, indicating electron transfer through the surface states in this potential region.

Figure 9.22   Determination of flat-band potential by CV. Reversible redox couple with two-electron transfer systems is chosen such that $E_{0(1)}$ lies in the CB and $E_{0(2)}$ lies in the band gap.

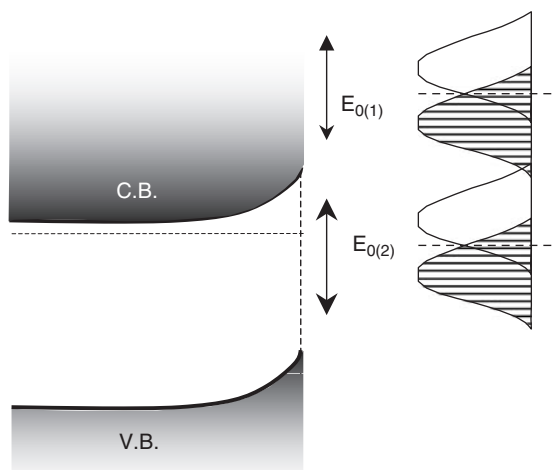Thus, with the help of voltammetric experiments in a judiciously chosen redox couple, one can pinpoint various energy states in the bulk as well as on the surface of the semiconductor. This model was further supported by CV results obtained on WSe_2 in aqueous solution (34, 35), GaAs in molten salt (36), Si, n-type ZnO, CdS, and GaP electrodes in acetonitrile (21), and CdS, GaP, GaAs, and p-type Ge in N,N'-dimethylformamide (37).

To obtain information about the energetics of semiconductor electrodes using CV, it is not necessary to have a series of redox couples whose E_{redox} are distributed in the entire band structure. In fact, one can pinpoint the flat-band position E_{fb} by recording CVs for just one redox couple having two-electron systems, A^+/A and A^{2+}/A^{1+}, with respective redox potentials $E_{0(1)}$ and $E_{0(2)}$, such that these potentials lie above and below E_C. The situation is sketched in Figure 9.22.

A typical result reported (38) on an n-MoS_2 electrode with redox couples BF and TMPD[7] is depicted in Figure 9.23. Note that both TMPD and BF exhibit two reversible one-electron waves at Pt as shown in Figures 9.23a and c. However, at MoS_2 in the dark, there is one reversible wave under the same condition and at the same potential as at Pt (refer to Figures 9.23b and d).

This situation indicates that the electrode is degenerated at that potential and behaves like a metal. The second oxidation wave appears on illumination, which was not seen in dark. As discussed in Section 9.4.2, photo-oxidation at an n-type semiconductor is prevalent if the redox potential lies within the band gap. Thus, the second wave observed upon illumination was assigned to the oxidation of $TMPD^+$ to $TMPD^{2+}$ or BF^+ to BF^{2+}. Quite interestingly for BF, the CVs recorded in the dark and under illumination are separated by approximately 0.20 V. The onset of a photocurrent for both TMPD and BF is at

---

[7]BF and TMPD refer to biferrocene and N,N,N′,N′-tetramethyl-p-phenylenediamine, respectively.
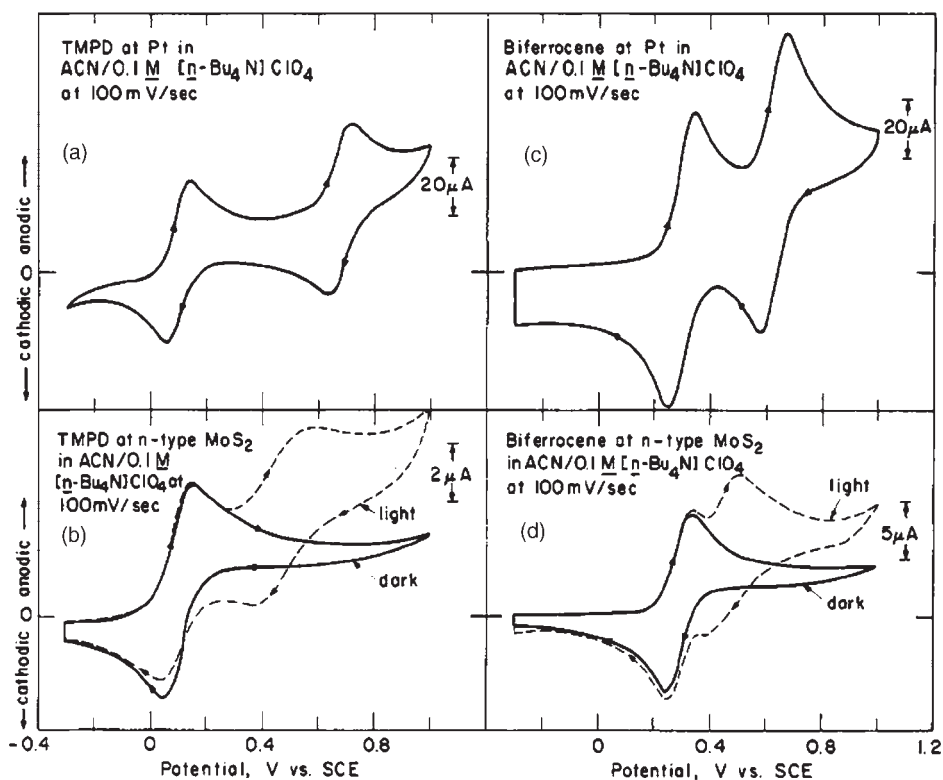
Figure 9.23   Comparison of CV for TMPD (a and b) and biferrocene (c and d) at Pt and MoS$_2$ (dark or illuminated). Illumination was with 632.8-nm light at 50 mW cm^{-2}. Reprinted with permission from reference (38). Copyright 1979, American Chemical Society.

approximately +0.3 V. Thus, one can bracket E_{FB} between 0.3 and 0.5 V where a second wave appears on illumination.

Though CV has been extensively used to probe the SEI, there are very few papers that describe the analytical theory for the CV response of a semiconductor electrode in the dark as well under illumination. Of the few, the prominent one is developed by Lewis and co-workers, where analytical solutions have been proposed for a redox couple that is adsorbed on the surface (30) as well as one having diffusion freedom (31) in solution. The model was later supported by relevant experiments (39). The equivalent circuit used for the simulation is shown in Figure 9.24.

The additional circuit elements account for the effect of capacitance (C_d) at the electrode–solution interface, background current (I_Z), and solution resistance (R_s). Figure 9.25 represents some of the results that were compared with simulated CVs obtained for an Si electrode in 1.2 mM Me$_2$CoCp$_2$PF$_6$ (redox)/1.0 M TEABF$_4$ (supporting electrolyte) in acetonitrile in an electrochemical cell having a Pt counter electrode and at various illumination periods. As can be seen, there is an excellent agreement between simulations and experiments.
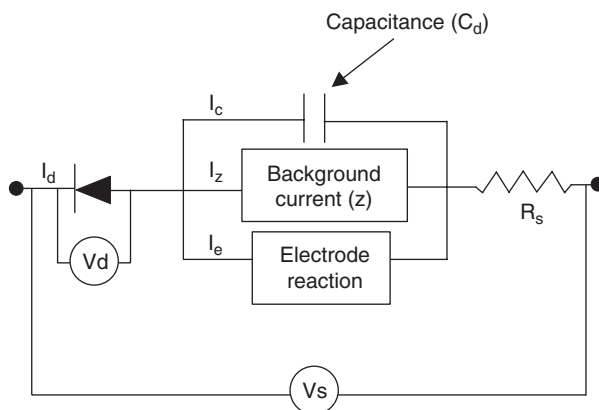
Figure 9.24   The equivalent circuit used as a model for the ideal semiconductor–liquid interface, including the effects of capacitance at the metal electrode–solution interface (C_d), background current (Z), and series resistance losses in the electrolyte (R_s). Adapted from reference (39).

9.4.4   Fermi-level pinning in semiconductor electrodes

Most of the results discussed in Section 9.4.3 have been explained on the basis of a simple model for an ideal SEI, which was first proposed by Gerischer (16). In the model, the redox system in solution is considered to have fluctuating energy levels (distribution functions, clarify with Figure 9.13) described by Marcus (19). The band structure of the interface will be decided by bulk energy levels of the semiconductor and redox couple. Charge transfer takes place between the semiconductor and redox states by tunneling through Helmholtz layers. However, as seen in Section 9.4.3 with the TiO_2/redox system, identical CVs were observed over a particular potential range irrespective of the redox potential. This suggests that there are states on the surface[8] that are involved in the charge transfer. If these states are present in the band gap, then the charge transfer will be preferentially mediated by a surface state as illustrated in Figure 9.26.

The energetics of the SEI will now be driven by surface states rather than by the bulk state of the semiconductor. In such a situation, the barrier height (or band bending), which can be changed by choosing the appropriate redox couple (41), is now more sensitive to the parameters as a result of surface pretreatment, cleaning of the surface, adsorption, etc. It appears as if the Fermi level of a semiconductor is 'pinned' at the given energy. The phenomenon is called *Fermi-level pinning*. Historically, this phenomenon is reported for a semiconductor/metal Schottky barrier in which surface states of the semiconductor give rise to a fixed barrier height, independent of the metal (42, 45). It has

---

[8]The surface of any solid is energetically different from that of the bulk. This is due to a variety of reasons including unsatisfied valence of surface atoms, formation of oxide layers, and adsorption of foreign atoms and molecules. It amounts to a different set of energy states at the surface than that of the bulk, which are called surface energy states or simply 'surface states'.
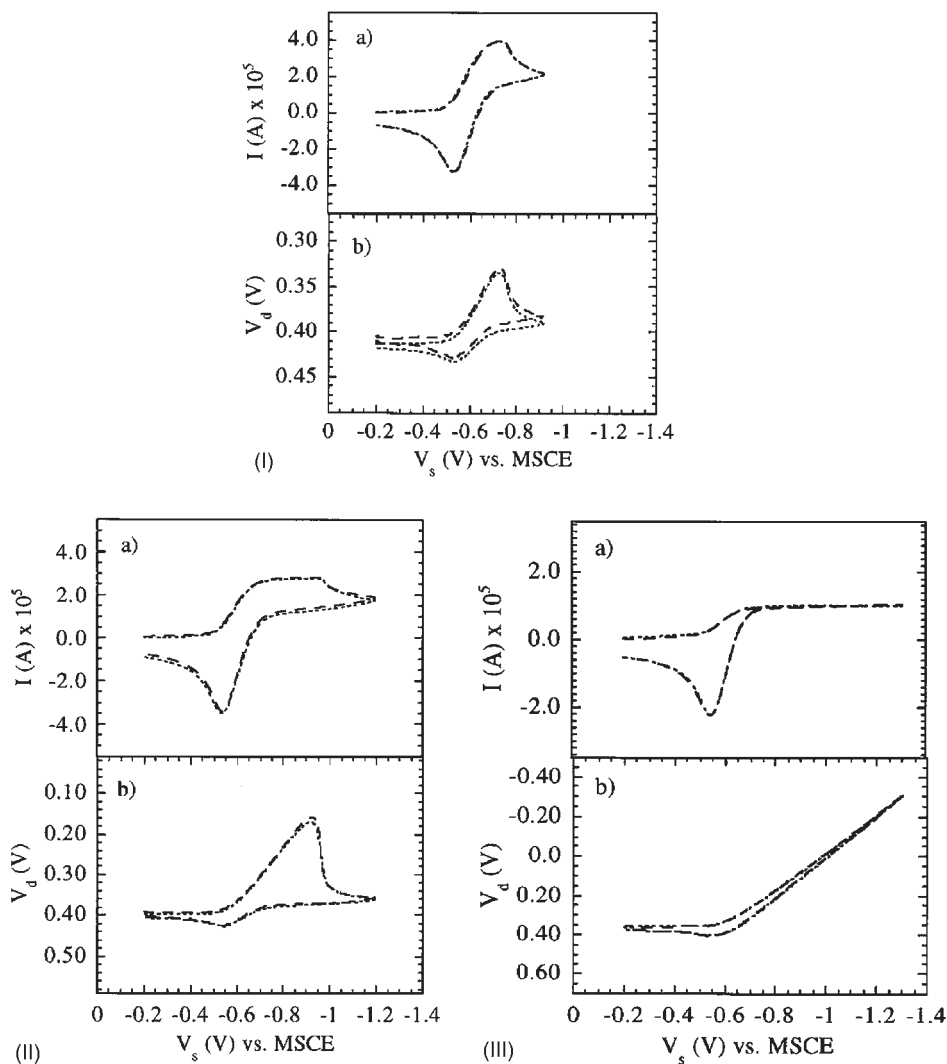
Figure 9.25 Experimental (dash) and simulated (dotted) cyclic voltammograms of n-Si photodiode at various levels of illumination (various values of light-induced current (I_L)). At (I) $I_L = 4.40 \times 10^{-5}$ A, (II) $I_L = 2.80 \times 10^{-5}$ A, and (III) $I_L = 1 \times 10^{-5}$ A. All figures with label (a) are I–V curves and label (b) are plots of voltage drop across photodiode (V_d) as a function of applied voltage V_s vs. SCE. Reprinted with permission from reference (39). Copyright 1998, American Chemical Society.

been further identified in the case of various semiconductors including GaAs (26, 46), Si (32, 40), n-CdSe (47), and n-CdS (48) in solutions. These investigations suggest that ionic semiconductors (large band gap oxides) give more ideal behavior (41) than the covalent (e.g., GaAs) and elemental semiconductors (e.g., Si) do. Thus, the observed Fermi energy pinning can be unambiguously attributed to the surface states. Note that

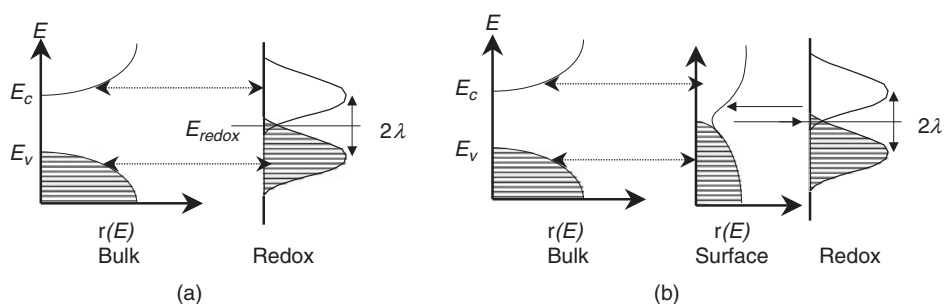**Figure 9.26**   Schematic diagrams for energy vs. density of states for semiconductor–electrolyte interface (SEI). (a) An ideal interface described by Gerischer's model, where direct transfer of charge between bulk energy states of semiconductor and redox takes place, and (b) transfer of charge mediated through surface states. The hashed curves represent filled states. λ represents solvent reorganization energy from Marcus theory. Adapted from reference (40).
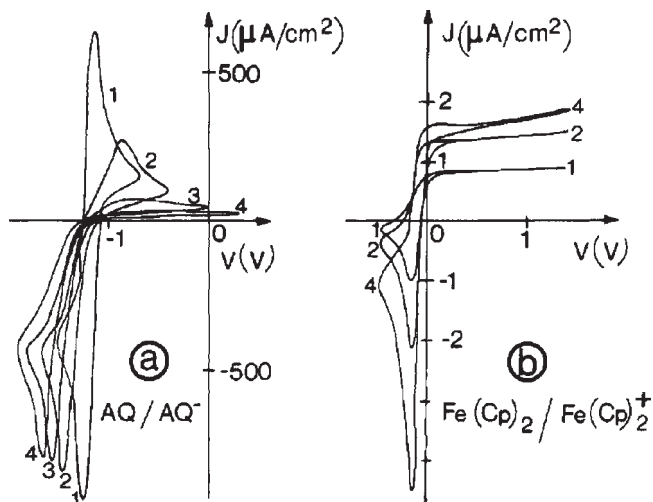
Figure 9.27   CVs for two representative redox systems (a) AQ/AQ^- and (b) $Fe(Cp)/Fe(Cp)^+$ at different durations of immersion, t: (1) $t = 5$ min, (2) $t = 30$ min, (3) $t = 1$ h, and (4) $t = 2$ h. The increase of the cathodic peak in part (b) is due to the increase of the (initially zero) ferricinium concentration upon potential cycling. Reprinted with permission from reference (32). Copyright 1981, American Chemical Society.

due to the dynamic nature of the SEI interface, the surface constituents may change with time; this amounts to time-dependent electrochemical behavior.

Consider the following example. Figure 9.27 shows a CV recorded on an n-Si electrode immersed in acetonitrile with two redox couples: anthraquinone and its monoanion (AQ/AQ^-) and ferrocene/ferrocenium ($Fe(Cp)_2/Fe(Cp)_2^{1+}$). In this experiment, care was taken in the experimental set-up so that once the electrode was introduced into the cell, it was not further exposed to the external atmosphere. Thus, effects due to surface oxidation

were minimized. As shown in Figure 9.27a, the electrochemistry of AQ/AQ$^-$ initially gives a reversible CV similar to that obtained on a Pt electrode; this is indicative of a complete non-rectifying junction. As time passes (from curves 1 to 4 in Figure 9.27), the anodic peak reduces and finally disappears completely (curve 4) and the junction becomes rectifying. A similar observation was also found for the Fe(Cp)$_2$/Fe(Cp)$_2^{1+}$ couple (refer to Figure 9.27b). Interestingly, the photocurrent measurements carried out with these and various other redox couples exhibited the conversion of the barrier height to a single value ($\Delta\phi \approx 0.7$ eV), irrespective of the redox potential of the couples. All of these results suggest a change in the interface with immersion time in solution from a *non-pinning* to a completely *pinned regime*, and the behavior can be attributed to a change in the surface properties due to adsorption. This behavior has also been reported in the case of CdS (49), GaAs (50), InP (29, 51), and CdTe (52) electrodes.

9.4.5 Characterization of the SEI by scanning electrochemical microscopy (SECM)

Scanning Electrochemical Microscopy (SECM) (53) is an electroanalytical technique that has been used to study the kinetics of electron transfer in a variety of substrates (54–58). However, there are very few reports about its use in investigating the SEI (23, 59–64). A detailed description of SECM is given in Chapter 12. There are also many review articles that deal extensively with this technique (65–68).

In short, SECM is a scanning probe technique similar to STM or atomic force microscopy (AFM). A tip current arises due to an electrochemical reaction (faradaic process) at an ultra-microelectrode (UME) tip (see Chapter 6). The tip generally consists of a Pt wire of diameter between 1 and 25 μm that is sealed in a glass capillary and polished to get a flat electrode surface. A typical voltammogram recorded on a UME is shown in Figure 9.28b. It is a sigmoidal, steady-state current–potential curve without any hysteresis.
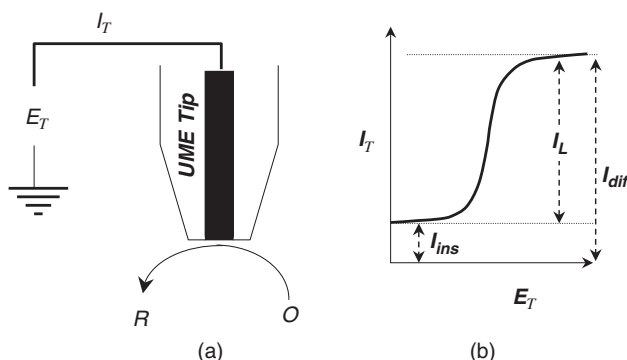

Figure 9.28   (a) An electrochemical reaction occurring at UME and (b) a corresponding voltammetric response. E_T and I_T stand for applied tip potential and measured tip current, respectively. I_L stands for limiting current.
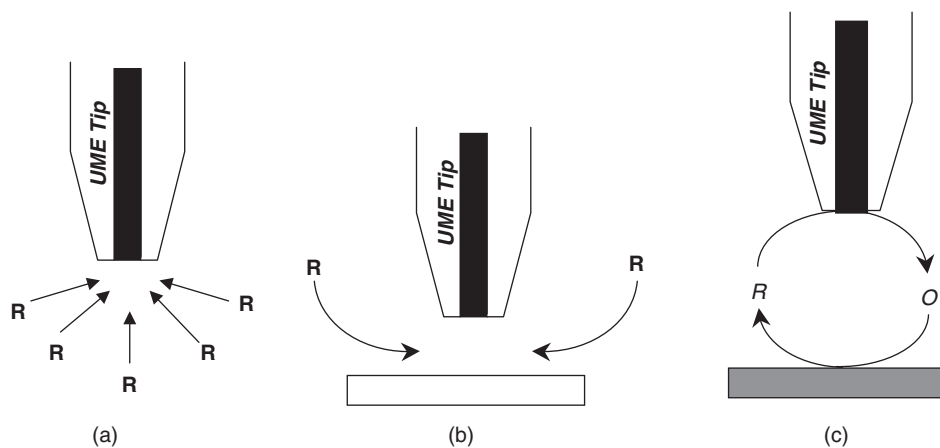
Figure 9.29 Feedback modes of SECM operations. The UME tip is poised at a potential E_T such that R will oxidize to O. (a) UME is freely hanging in the redox solution, $i_T = i_{T,\infty}$; (b) UME near the insulating substrate, the diffusion is blocked, called negative feedback, $i_T < i_{T,\infty}$; (c) UME near the conducting substrate, positive feedback from the substrate as O gets reduced back to R that leads to $i_T > i_{T,\infty}$.

To study the kinetics of electron transfer, SECM can be operated in two modes: a feedback mode (53, 69) and a substrate generation-tip collection mode (53). In the feedback mode, a mediator redox couple is required to probe the interface. The tip is poised to a potential well above E_{redox}. The steady-state current observed due to hemispherical diffusion of O toward the tip is expressed as (Figure 9.29a)

$$i_{T,\infty} = 4nFD_0C_0^*a \tag{9.4.9}$$

where a is radius of the tip. When a tip poised with a potential $>E_{redox}$ is brought very close (dimension on the order of the radius of the UME tip) to a substrate (in our case, the substrate is the semiconductor), then the diffusion of species O to the substrate will be blocked (Figure 9.29b), leading to a corresponding decrease in the tip current i_T.

A plot of tip current vs. distance between the tip and the substrate is called an approach curve and the decrease in current due to the blocking of diffusion to the tip is called *negative feedback*. In certain situations, R is regenerated back to O by the substrate as shown in Figure 9.29c. The result is a large flux of O to the tip and a corresponding increase in the tip current. Thus, the current at the tip increases as a function of its distance d from the substrate and the rate at which O is regenerated at substrate. This is called *positive feedback*. Typically, blocked diffusion is observed over an insulating substrate while positive feedback is observed over a conducting substrate when the kinetics of the redox process are reversible. Intermediate values of i_T are observed when electron transfer at the substrate is limited. In such situations, it is possible to deduce the rate constant of the charge transfer reactions.

Conventional techniques have limitations in studies of electron transfer kinetics at an SEI. In transient techniques such as CV, parallel processes such as electrode corrosion, charging of the double layer, and interference of *IR* drop contribute significantly to the

measured current as the electrode is poised to a desired potential. Hence, there is often a lack of agreement between an observed i–E curve and a proposed theory. Any attempt to use a low concentration of a redox couple to reduce the IR drop is likely to increase the contribution of the electrode corrosion current to the measured current. Steady-state voltammetric measurements with rotating disk electrodes (RDE) (23), wall jet electrodes (70, 71), or UMEs overcome these difficulties to some extent but it is very difficult to use semiconductors in an inlaid disk configuration.

These limitations can be overcome by SECM. One of the important advantages of SECM is that the tip does not need to be a semiconductor. Therefore, any semiconductor electrode can be probed using a Pt UME tip, for example. Since very small currents are measured at the UME tip, the IR drop is minimal. Additionally, the UME tip quickly reaches a steady state due to the small area of the electrode so that effects due to double layer charging are avoided. Because the UME tip is poised at a potential specific to the redox couple used, corrosion processes taking place at semiconductor electrode do not contribute to the tip current.

In the SECM feedback mode, the tip can be used to generate a high local concentration of a mediator. For example, if the semiconductor electrode is expected to reduce O to R from a solution of reduced species R, then the species O can be generated locally near the semiconductor surface underneath the tip by poising the tip at a sufficiently positive potential as shown schematically in Figure 9.30a.

If the semiconductor electrode does not reduce O to R, then the current at the tip will decrease due to blocked diffusion. The resulting tip current vs. distance approach curve can be fitted to the equation for an approach over an insulator. If the semiconductor substrate is poised to a potential sufficiently negative (E_S), then R is regenerated on the surface and the tip current increases. A typical plot of tip current (i_T) vs. substrate potential (E_S) is shown in Figure 9.30b. At intermediate values of E_S, the tip current may be limited by the heterogeneous rate constant (k_{et}) involved in the electron transfer reaction at the substrate.

The total tip current, i_T, can be expressed as the sum of the current due to the diffusion of O in the gap between the tip and the semiconductor surface, i_{ins}, and the feedback current due to regeneration of R at the substrate in the gap, i_{fb} (23)

$$i_T = i_{ins} + i_{fb} \qquad (9.4.10)$$

The current component i_{fb} is the current at substrate i_s. Thus,

$$i_s = i_{fb} \qquad (9.4.11)$$

Therefore, the flux or mass transport rate (mol s^{-1} cm^{-2}) at the semiconductor substrate is given by

$$m_o = \frac{i_s}{nFAC_o^*} = \frac{i_T - i_{ins}}{nFAC_o^*} \qquad (9.4.12)$$

where C_o^* is the bulk concentration of the redox molecule. For a uniformly accessible electrode, the current due to an irreversible electron transfer is given by

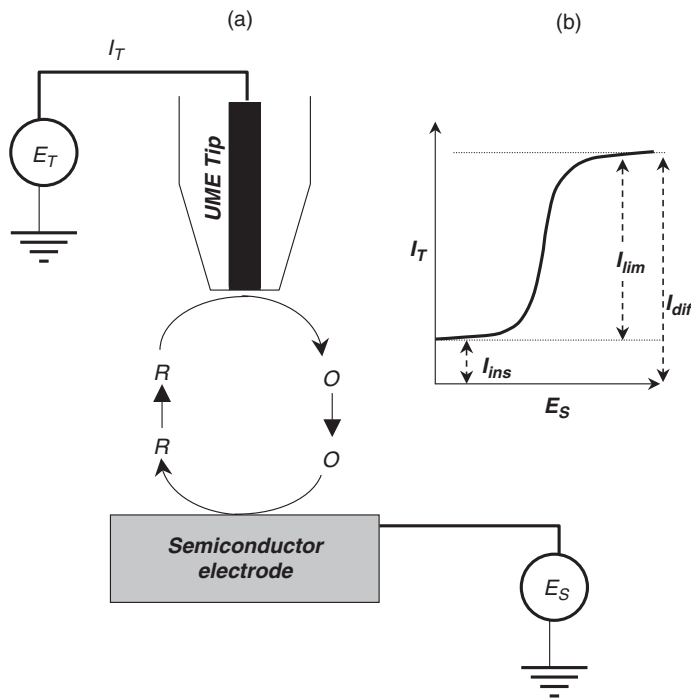$$i = \frac{nFAC_o^* m_o}{1 + (m_o / k)} \qquad (9.4.13)$$

Figure 9.30 Schematics of the feedback SECM for measurements of electrochemical heterogeneous rate constant at semiconductor electrode. (a) UME tip is poised at positive potential, so that R will get oxidized to O at diffusion control rate. When the tip is closed to the substrate surface, O may get re-reduced at semiconductor electrode, depending on the potential at which semiconductor electrode is polarized (E_s). Thus, I_T depends upon rate of reduction of O on semiconductor surface. (b) A steady-state irreversible voltammogram (I_T vs. E_s).

where k is the electrochemical heterogeneous rate constant that follows Butler–Volmer kinetics according to

$$k = k_0 \exp\left[\frac{\alpha nF(E - E^{\circ\prime})}{RT}\right] \tag{9.4.14}$$

where α is transfer coefficient and $E^{\circ\prime}$ is the formal redox potential. Thus, the heterogeneous rate constant for a reaction taking place at semiconductor electrodes can be determined from SECM feedback approach curves.

Figure 9.31 shows a typical steady-state voltammogram ($i_T - E_s$) reported by Bard and co-workers (23) for the oxidation of $Ru(NH_3)_6^{2+}$ on p-WSE$_2$ in 0.5 M Na_2SO_4. A UME tip was poised more negative than the $E_{1/2}$ (-0.23 V vs. saturated calomel electrode (SCE) in Na_2SO_4) of $Ru(NH_3)_6^{2+/3+}$ so that $Ru(NH_3)_6^{3+}$ generated at the p-WSe$_2$ semiconductor is reduced to $Ru(NH_3)_6^{2+}$ on the Pt tip.
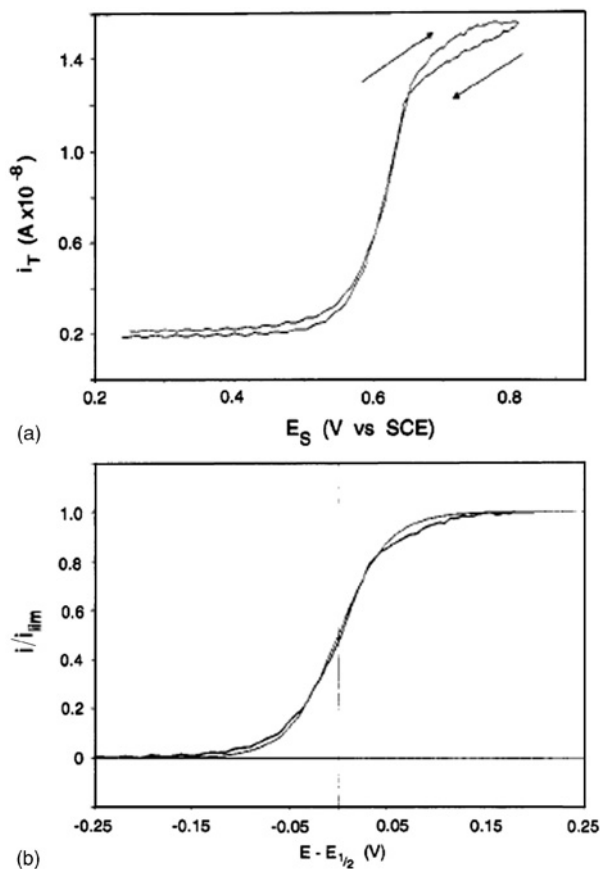
Figure 9.31   Kinetic voltammograms (i_T vs. E_s) for the oxidation of $Ru(NH_3)_6^{2+}$ on p-WSe$_2$ in 0.5 M Na$_2$SO$_4$. The tip was 10-μm diameter platinum and the concentration of $Ru(NH_3)_6^{2+}$ in the bulk solution was 4.78 mM. (a) A raw data and (b) a fitted voltammogram (bold line is experimental). Reprinted with permission from reference (23). Copyright 1994, American Chemical Society.

The potential of the substrate, i.e., p-WSE$_2$, was scanned from a region where $Ru(NH_3)_6^{2+}$ is not oxidized (below +0.66 V vs. SCE, which is the V_{FB} of p-WSE$_2$) to a potential region where the accumulation layer forms. As can be seen in Figure 9.31a, there is a transition from a low-current to a high-current regime at ca. +0.6 V, which fits very well to the theory (refer to Figure 9.31b). The m_0 and k_{et} values estimated for various redox concentrations are listed in Table 9.2.

SECM in the feedback mode has also been used to study the photoelectron transfer kinetics at an illuminated CdS/MV$^{2+/1+}$ interface (63). The set-up used for these measurements is shown in Figure 9.32. In these experiments, CdS films were back-illuminated in the solution of a redox species (e.g., MV^{1+}) and a hole scavenger (e.g., triethanolamine (TEOA)). The Pt tip was poised for the oxidation of MV^{1+}, which is reduced back to MV^{1+}

Table 9.2

Kinetic data for the oxidation of $Ru(NH_3)_6^{2+}$ on p-WSe$_2$/0.5 M Na$_2$SO$_4$

$Ru(NH_3)_6^{2+}$ (mM)	m_o (cm sec^{-1})	$E_{1/2} - E^{\circ\prime}$ (V)	k° (10^{-16} cm sec^{-1})	K_{et} (10^{-17} cm^4 sec^{-1})
4.8	0.038	0.846	1.9	6.5
4.8	0.046	0.850	1.9	6.6
4.8	0.046	0.852	1.8	6.1
4.8	0.046	0.850	1.9	6.6
4.8	0.042	0.858	1.3	4.4
4.8	0.023	0.831	2.0	6.9
4.8	0.019	0.825	2.1	7.2
2.8	0.046	0.861	1.3	4.3
2.8	0.046	0.862	1.2	4.2
1.7	0.048	0.855	1.7	5.7
1.7	0.048	0.855	1.7	5.7
1.0	0.049	0.859	1.4	4.9
1.0	0.051	0.855	1.8	6.0
1.0	0.050	0.859	1.5	5.1
			1.7 ± 0.6^a	5.7 ± 1.0^a

Reprinted with permission from reference (23). Copyright 1994, American Chemical Society.
^{a}Mean value.
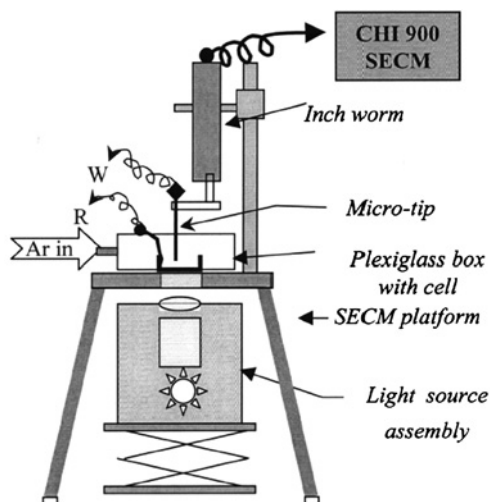
Figure 9.32 The set-up used for PET-SECM measurements. CdS film was back-illuminated. The cell was enclosed in the Plexiglas box. The positive pressure of Ar was always maintained in the box throughout the experiment in order to avoid air oxidation of MV^{1+}. Adapted from reference (63).

on the illuminated CdS film. Figures 9.33 and 9.34 show approach curves recorded for various light intensities and TEOA concentrations, respectively. As expected, there is a transition of the approach curve from insulating to conducting behavior on increasing either the light intensity or the TEOA concentration.
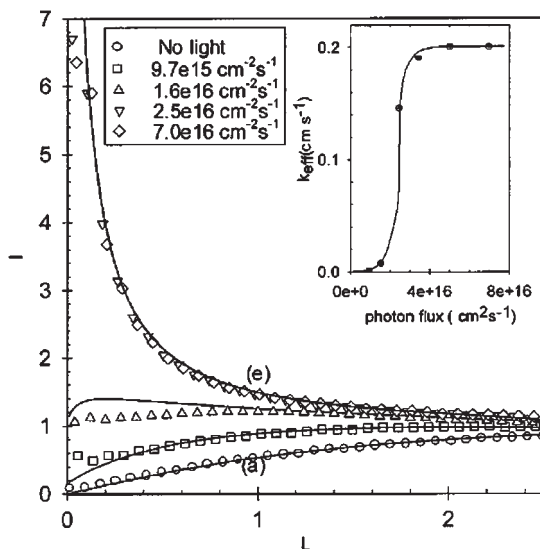
Figure 9.33 Approach curves recorded at various light intensities on CdS film in 0.1 mM MV$^+$ as a redox, 50 mM TEOA as a hole scavenger, and 0.1 M KCl supporting electrolyte in an inert atmosphere. (a) In the dark and (e) high intensity of illumination. The values of photon flux are given in the box. The solid lines are fitting to theory at various values of k_{eff}. The inset depicts a plot of k_{eff} vs. photon flux. The hyperbolic nature of the curve was attributed to the mass-transfer limit reached at high photon flux. The actual k_{eff} could be higher than 0.2 cm sec^{-1} at higher illumination at those intensities. Reprinted with permission from reference (63). Copyright 2001, American Chemical Society.

SECM in the *substrate generation and tip collection mode* (72) has been used for the estimation of spatially localized active sites on semiconductor electrodes (60, 61, 73). In this mode, electroactive species are generated by a redox reaction at the substrate and detected by a UME probe either amperometerically or potentiometrically. A typical set-up used for these kinds of experiments is given in Figure 9.35.

The corresponding SECM images obtained by these measurements are given in Figure 9.36a.

A local current density as large as 0.14 A cm^{-2} was observed for the oxidation of Br$^-$, which is four orders of magnitude higher than the average current density. These data also suggested that sites smaller than ca. 10 μm diameter are the most active for oxidation. Similar work has also been reported for Ta$_2$O$_5$ electrodes (60). Figure 9.37 shows the SECM image obtained for the oxidation of I^- on a Ta$_2$O$_5$ substrate. These results again suggest that a small cluster provides the most active site for the oxidation of I^-.

In another set of novel SECM experiments, a ZnO microelectrode (ca. 50 μm) was used as the UME tip instead of platinum and used to record steady-state voltammograms in various redox couples. The rates of electron transfer between the semiconductor tip and redox species such as ferricinium (FC$^+$), dimethyl-ferricinium (diM$^+$), and decamethyl-ferricinium (DM$^+$) have been estimated (64). Figure 9.38 shows steady-state voltammograms recorded with a 100-μm diameter ZnO microelectrode in various concentrations of diM$^+$.
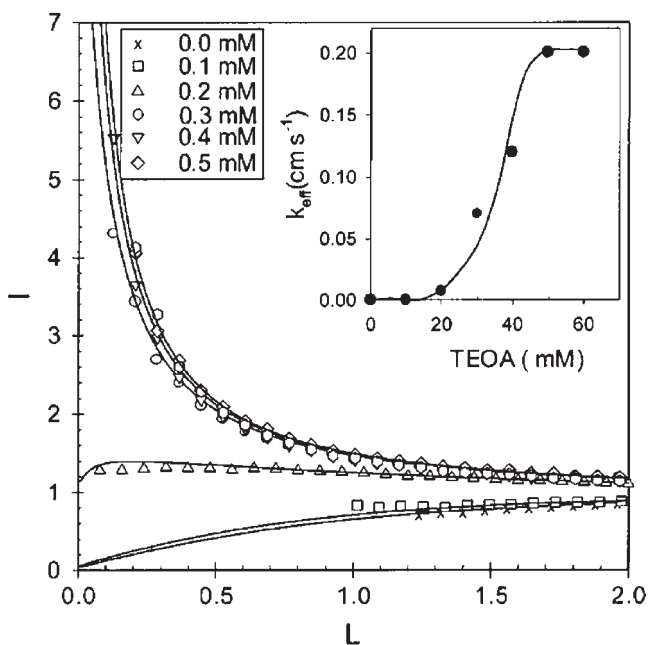
Figure 9.34   Approach curves recorded at various TEOA concentrations. [MV$^+$] 0.1 mM in 0.1 M KCl. The solid lines are fitting to theory at various values of k_{eff}. The inset depicts a plot of k_{eff} vs. [TEOA]. Reprinted with permission from reference (63). Copyright 2001, American Chemical Society.
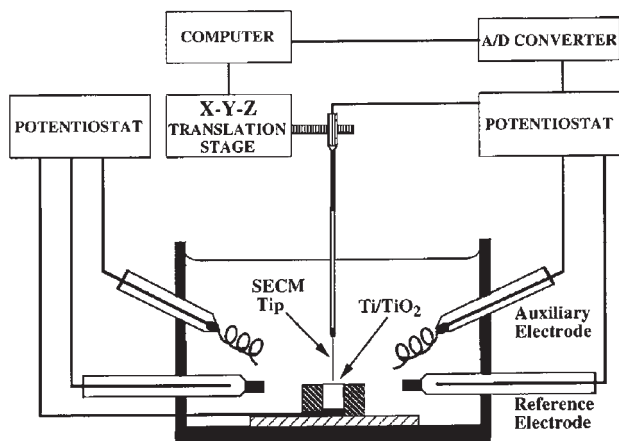
Figure 9.35   SECM set-up described in reference (71) for the determination of spatial distribution of active sites on semiconductor electrodes. Substrate potential (E_s) and the tip potential (E_T) were controlled independently by bi-potentiostat. Redox species generated on substrate were collected using UME tip, which is raster over surface by x–y piezo. The contrast is generated by the tip current i_T measured at (x, y) coordinates. Reprinted with permission from reference (73). Copyright 1998, American Chemical Society.
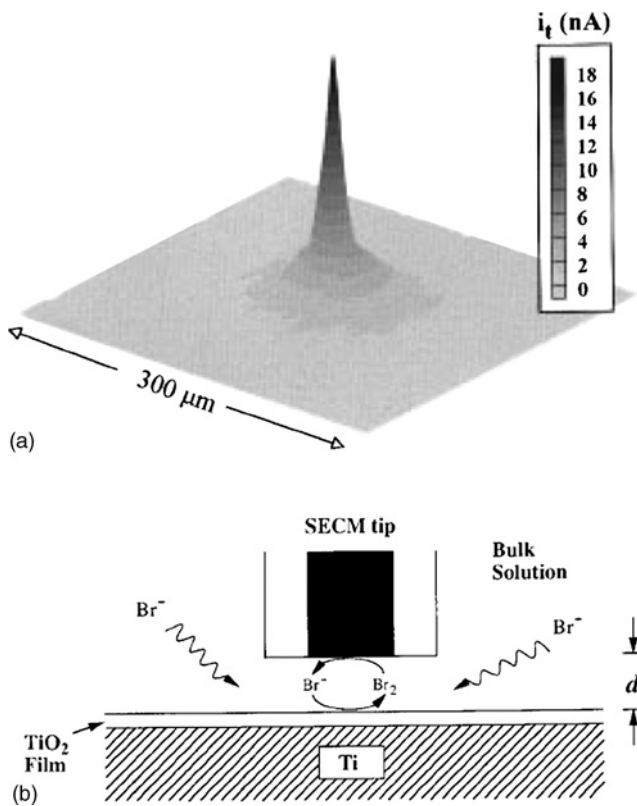
Figure 9.36 (a) 300 × 300 μm SECM image of the electroactive site in a solution containing 50 mM KBr and 10 mM H_2SO_4. The potential of Ti/TiO_2 electrode (E_s) was held at 1.5 V to oxidize Br^-. The potential of SECM tip (E_T) was held at 0.0 V, sufficiently negative to reduce Br_2 at the mass-transport limited rate. SECM tip was scanned at a height, d, of 5 μm above Ti/TiO_2 electrode. The image was recorded after the current at Ti/TiO_2 electrode had decayed to a steady-state value. (b) Schematics depicting SECM tip positioned above an oxide-covered Ti electrode. The tip radius and tip-to-Ti electrode separation are drawn approximately to scale. TiO_2 film (ca. 65 Å) is much thinner than drawn. Reprinted with permission from reference (73). Copyright 1998, American Chemical Society.

The steady-state current densities obtained from these data can then be approximately related to rate constants by the expression

$$j = Fk_{et}[\text{diM}^+] = Fk_0(e_{sf})[\text{diM}^+] \tag{9.4.15}$$

where k_{et} and k_0 are the pseudo-first-order rate constant (cm sec^{-1}) and the bimolecular rate constant (cm^4 sec^{-1}), respectively, and e_{sf} is the surface concentration of electrons that is related to E_{fb} by the following relationship:

$$e_{sf} = N_d \exp\left[\frac{(E - E_{fb})e}{k_B T}\right] \tag{9.4.16}$$
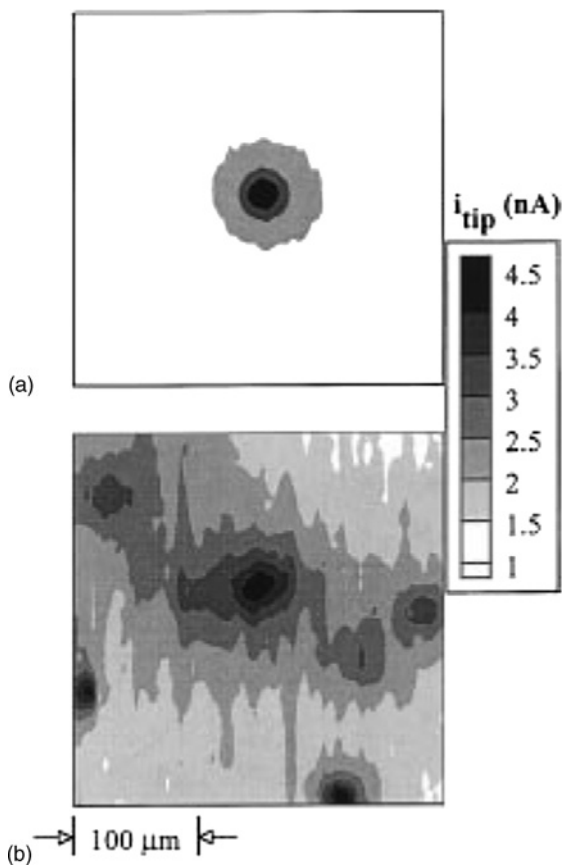
Figure 9.37 Representative SECM images (300 × 300 μm) of Ta/Ta$_2$O$_5$ electrode in a solution containing 10 mM KI and 0.1 M K$_2$SO$_4$. The dark regions correspond to sites of high activity for the oxidation of I$^-$ at Ta/Ta$_2$O$_5$ electrode: (a) an isolated site and (b) a cluster of sites. Four-micrometer radius SECM tip was scanned at 10 μm s^{-1} at a tip-to-surface separation, $d = 5$ μm, $E_T = 0.0$ V, and $E_s = 1.0$ V vs. Ag/AgCl. Reprinted with permission from reference (59). Copyright 1999, American Chemical Society.

where E is the applied bias to the ZnO UME. A plot of the log of current density vs. applied potential is expected to be a straight line and the extrapolation at $E = E_{fb}$ gives values of k_0 as shown in Figure 9.39. These have been estimated to be 4×10^{-18} and 7×10^{-23} cm^4 s^{-1}, respectively, at $E = E_{fb}$.

9.5 TYPES OF SEMICONDUCTOR ELECTRODES

9.5.1 Single crystal and epitaxial film electrodes

The theory for semiconductor electrodes discussed in the previous sections is applicable to materials having long-range order in the lattice, as demonstrated by single-crystal material
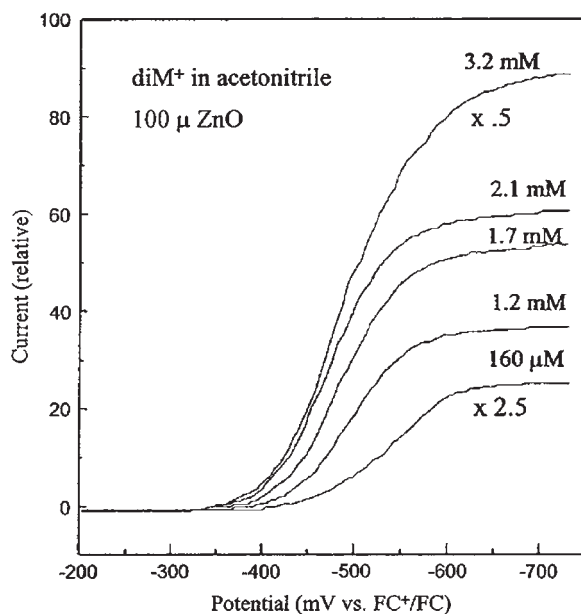
Figure 9.38 An example of a concentration study is given here for diM⁺ in which [diM⁺] is increased from 0.16 to 3.2 mM. The plateau current at a 100-μm diameter ZnO electrode was found to be linear with [diM⁺] and the range of $E_{1/2}$ values was within 30 mV of the average of 510 mV, indicating that the rate constant did not change significantly with concentration. Reprinted with permission from reference (64). Copyright 2000, American Chemical Society.
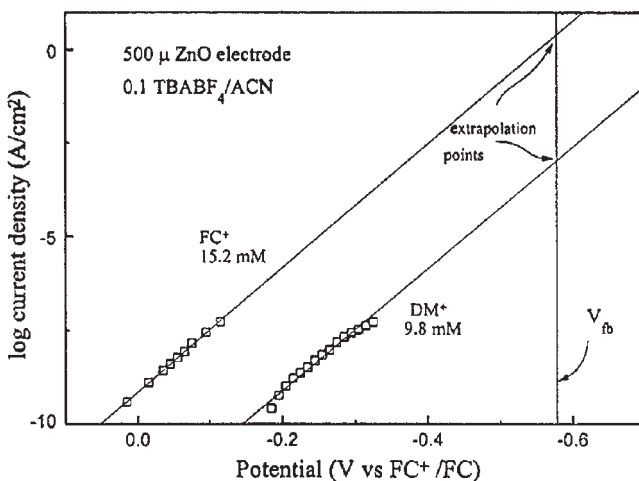
Figure 9.39 A plot of log of current density at steady state vs. applied bias at various concentrations of FC⁺ and DM⁺ on 500 μm ZnO electrode. The reduction current is extrapolated to V_{fb} and $k°$ is extracted from the result by the use of equations (9.4.15) and (9.4.16). Reprinted with permission from reference (64). Copyright 2000, American Chemical Society.

and epitaxial films. Their interfacial properties are spatially uniform and reproducible. Thus, many equations describing the transport and transfer of charges in them can be applied with accuracy. Layered metal dichalchogenide (LMD) semiconductors such as MoS_2, WSe_2, and $SnSSe_2$, however, have anisotropic crystallographic properties that strongly influence the bulk and surface properties of the electrodes. Nevertheless, the molecularly smooth, chemically inert, and reproducible van der Waals surface of LMDs can easily be obtained by simply piling of the upper few layers with the help of adhesive tapes (34).

It is often difficult to obtain single crystals of semiconductors except for a few such as Si, GaAs, and InP that are routinely used by electronic industries. In a few cases, it is possible to grow a film of a few atomic layers thickness on the substrate with matching lattice parameters; these are called epitaxial layers. Techniques such as molecular beam epitaxy (MBE) and metal organic chemical vapor deposition (MOCVD) have been employed (74–77) for this purpose. It is also possible to grow a thick film (up to few micrometers) with long-range ordering; this is a semiconductor single-crystal membrane (78).

One of the important limitations in using single-crystal and epitaxial films as electrodes is that they are very expensive to prepare. Therefore, most of the studies have been undertaken with polycrystalline electrodes.

9.5.2 Polycrystalline electrodes

It is relatively easier to prepare electrodes of many semiconducting materials in which the size of the individual crystallites is small with respect to the diffusion length of the charge carriers. These charge carriers get scattered across the boundaries of the crystallites, called *grain boundaries*, and this poses a serious limitation in applying the Gerischer model for charge transfer. Additionally, the efficiency of charge transport is greatly compromised so that quantification of the electronic properties of the polycrystalline semiconductor electrodes is often difficult. Despite this problem, the preparation and characterization of polycrystalline electrodes have been intensely investigated. The rationale for this interest is the low-cost preparation of polycrystalline electrodes with a large surface area. The following sections describe methods of fabricating such electrodes.

9.5.2.1 *Electrochemical deposition of semiconductor films*

Electrochemical deposition has emerged as a powerful tool for growing high-quality semiconductor films (79) and nanostructures on a suitable substrate. Recent efforts have been focused on achieving atomic-level control on the growth process, which leads to the formation of well-ordered, epitaxial deposits of the desired material. Various baths used for electrodeposition of semiconductor films are listed in Table 9.3.

For chalcogenide films, a suitable complex of metal ions and selenium (H_2SeO_3) or a sulfur source is allowed to reduce simultaneously. The role of the complexing agent is twofold: (a) it avoids the reaction between the precursors in the bulk solution and (b) it helps in shifting the reduction potential of the metal ions to an optimum value so that one

Table 9.3

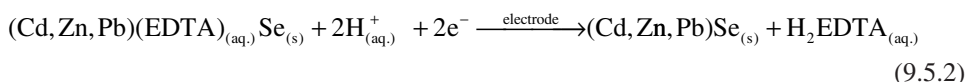Chemical bath conditions reported for deposition of semiconductors

Films	Bath	Substrate	Potential/ current	Bath temperature	References
CdSe	50 mM Cd(ClO$_4$)$_2$ + 5 mM Se in DMSO	Mica, Au	Galvanostatic	90–140 °C	(80–82)
CdSe	50 mM CdSO$_4$ or CdCl$_2$ + 0.3 M SeO$_2$	Ti, Ni	Potentiostatic	R.T.	(83)
Cu$_2$O	CuSO$_4$ + NaOH + lactic acid	Cu	Galvanostatic	R.T.	(84)
ZnO	Zn(NO$_3$)$_2$ + tetra-sulfonated metallothiocyanine	ITO	Potentiostatic	70 °C	(85)
CdS	CdCl$_2$ + S in DMSO	ITO	Galvanostatic	R.T.	(86)
Ge	GeI$_4$ in ionic liquids	Pt	Potentiostatic	R.T.	(87)
Ag$_2$Se	AgNO$_3$ + KSCN + SeO$_2$	ITO	Potentiostatic	R.T.	(88)
CuInSe$_2$	CuCl + InCl$_3$ + KSCN	Au	Potentiostatic	R.T.	(89)
PbSe	Lead acetate + SeO$_2$	ITO	Potentiostatic	R.T.	(90)

R.T.: room temperature.

can bring both potentials to a value that facilitates simultaneous reductions. Plausible steps in the electrochemical reactions include

$$HSeO_3{}^{2-}(aq.) + 5H^+(aq.) + 4e^- \rightarrow Se(s) + 6H_2O \qquad (9.5.1)$$
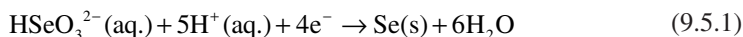
where due to proton involvement in the mechanism, an acidic pH facilitates the reaction

$$(Cd, Zn, Pb)(EDTA)_{(aq.)} Se_{(s)} + 2H^+_{(aq.)} + 2e^- \xrightarrow{\text{electrode}} (Cd, Zn, Pb)Se_{(s)} + H_2EDTA_{(aq.)}$$
$$(9.5.2)$$

where Se formed on the electrode may also get reduced further through the mechanism

$$Se_{(s)} + 2H^+_{(aq.)} + 2e^- \rightarrow H_2Se_{(aq.)} \qquad (9.5.3)$$
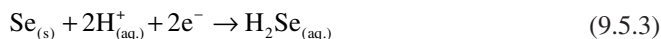
One of the major obstacles in electrodeposition of high-quality films of binary semiconductors is that one of the constituent elements may get plated simultaneously, leading to non-stoichiometric films. Thus, subsequent heat treatment is necessary to produce a film of acceptable quality. This problem can be overcome by sweeping the potential between a range where both constituents are reduced. For example, in the deposition of CdSe films, the potential was swept between -0.4 and -0.8 V vs. SCE in a low concentration of Se, which led to stoichiometric films. Using this technique, one can control the thickness of the film up to a few monolayers (83). By choosing the appropriate substrate and under-potential for deposition, it is possible to achieve an epitaxial growth of a semiconductor nanostructure called electrochemical atomic-layer epitaxy (ECALE) (91). The advantage of this method is that several kinds of structurally well-ordered thin films of compound semiconductors such as GaAs, CdTe, CdSe, and ZnS can be deposited.

Though it is relatively easy to carry out the electrodeposition from an aqueous bath, its major disadvantage is the narrow potential window available for the deposition. This problem has been overcome by carrying out the deposition in non-aqueous solvents. Moreover, elemental S and Se have the desired solubility in solvents such as *N,N*-dimethylformamide (DMF) and dimethyl sulfoxide (DMSO). Baranski and Fawcett were first to report the electrodeposition of CdSe films using non-aqueous baths of DMF (92) and DMSO (93). Non-aqueous solvents are also known to result in a deposition having nanocrystalline form (82). Use of cadmium salts having anions with adsorbing properties (such as Cl^- and Br^-) has been reported to result in deposition of CdSe nanoparticles (94). Precise control over bath temperature is known to control the size of the nanoparticles (82).
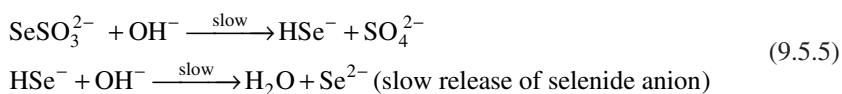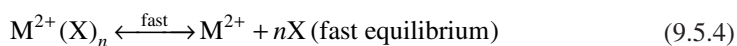
Besides non-aqueous solvents, it is possible to use room-temperature ionic liquids (RTILs) as media for electrodeposition (87). RTILs are fused organic salts that are in the liquid state at room temperature. They possess a wide range of liquid temperatures, in some cases higher than 400 °C, and have intrinsically useful characteristics including negligible vapor pressure, a wide liquid range and thermal stability, high ionic conductivity, and a large electrochemical window (95). Endres *et al.* demonstrated the electrodeposition of elemental semiconductors such as Ge films and nanoparticles in RTIL, namely 1-butyl-3-methylimidazolium hexaflurophosphate (87, 96).

9.5.2.2   *Electroless deposition of semiconductor films*

Electroless deposition (ED) or chemical bath deposition (CBD), in general, consists of a spontaneous deposition of films on a conducting or an insulating substrate by carrying out a redox reaction in solution. These techniques have been known for hundreds of years for silvering mirrors. CBD has also been used for a long time to deposit semiconducting films. Various group II–VI materials such as lead, zinc, and cadmium chalcogenides in the form of films have been prepared routinely by this method. There are many review articles that describe this method (74, 75, 97, 98) in detail.

The basis of the CBD method is the slow release of anions (sulfide or selenides) with free metal ions (Cd^{2+}, Zn^{2+}, or Pb^{2+}) into a solution such that their concentration just exceeds the solubility product of semiconductor. In the bath, a low concentration of the cations is maintained by their complexation with ligands such as TEOA and/or ammonia. The anions are formed by hydrolysis of thiourea, in the case of sulfide, or hydrolysis of selenosulfate or selenourea, in the case of selenides. The material is precipitated due to a super-saturation condition when the concentration of sulfide/selenide anions exceeds the solubility product of CdS/Se.

A general reaction scheme for the deposition of group II–VI semiconductor films is as given below (98–101):

$$M^{2+}(X)_n \xleftrightarrow{\text{fast}} M^{2+} + nX \text{ (fast equilibrium)} \tag{9.5.4}$$

$$SeSO_3^{2-} + OH^- \xrightarrow{\text{slow}} HSe^- + SO_4^{2-}$$

$$HSe^- + OH^- \xrightarrow{\text{slow}} H_2O + Se^{2-} \text{ (slow release of selenide anion)} \tag{9.5.5}$$

$$(NH_2)_2CS + 2OH^- \xleftrightarrow{\text{fast}} S^{2-} + 2H_2O + H_2CN_2 \text{ (slow release of sulfide anion)} \quad (9.5.6)$$

$$M_{aq.}^{2+} + S_{aq.}^{2-} \rightarrow MS_{solid}$$
$$\text{or} \quad\quad\quad\quad\quad\quad\quad\quad\quad\quad\quad\quad\quad\quad\quad\quad (9.5.7)$$
$$M_{aq.}^{2+} + Se_{aq.}^{2-} \rightarrow MSe_{solid}$$

$$(CdSe)_n + nH_2O \xleftrightarrow{\text{fast}} nCd^{2+} + nHSe^- + nOH^- \text{ (redissolution of thermodynamically}$$
$$\text{unstable nuclei)} \quad (9.5.8)$$

$$(CdSe)_n + (CdSe)_m \rightarrow (CdSe)_{n+m} \text{ (aggregation)} \quad\quad\quad (9.5.9)$$
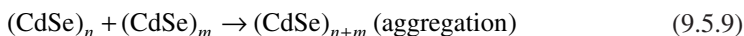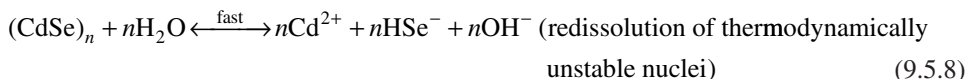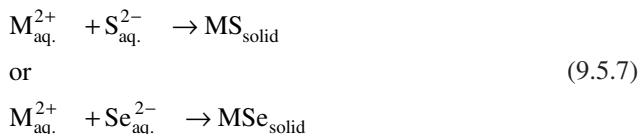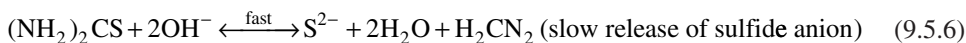
The rate-determining step in this series of plausible reactions is probably the slow release of selenide or sulfide by equation (9.5.5). Sulfide/selenide anions are consumed by two different mechanisms: one by nucleation and the other by growth of existing nuclei. The second step (i.e., growth) seems to be energetically more favorable.

AFM investigations of the electroless deposited CdS film on mica (102) suggest that the film can also be formed by ion-by-ion deposition on the substrate. This is in addition to the usually accepted notion of precipitation of clusters on the substrate that are already formed in the solution by homogeneous precipitation. Three plausible mechanisms are illustrated in Figure 9.40. In our experience, the film formed by deposition of clusters is powdery or chalky (refer to the mechanism illustrated in Figure 9.40b), and can be wiped off by tissue paper.

The ion-by-ion deposition growth, however, leads to an adherent mirror-like film, which cannot be pulled off even by a scotch adhesive tape. Ion-by-ion deposition methods have also been demonstrated for tandem deposition of CdS and ZnS thin films and $Zn_{1-x}Cd_xS$ composites (103) on conducting glass. The effects of chelating agent, pH, and type of counter anions on the quality of ion-by-ion deposition have also been investigated (104).
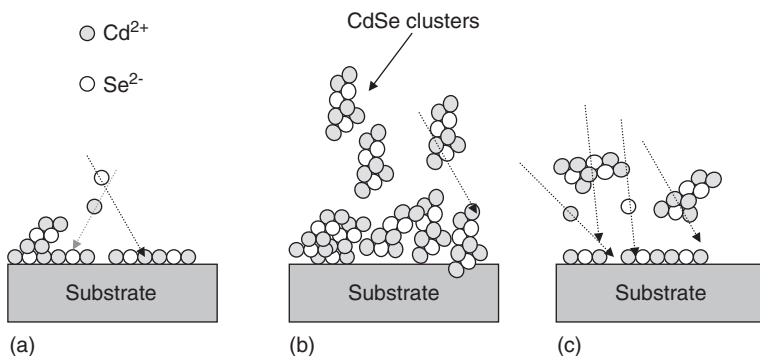

Figure 9.40 Three speculated mechanisms for the formation of semiconductor films by ED method: (a) ions are adsorbed on the substrate one by one, heterogeneous precipitation; (b) some of the clusters formed in the solution are deposited on the substrate; (c) mixed mechanism.

It is possible to use the substrate as one of the precursors. Deposition of thin films of $Cu_{2-x}Se$ has been carried out by reacting a Cu substrate or a Cu film electrodeposited on Pt or Ti with H_2SeO_3 at an acidic pH (105, 106).

(a)   Electroless deposition bath for the preparation of CdS and ZnS films

Various baths have been proposed for the ED of CdS thin films (98, 100, 103). As described in Section 9.5.2.2, a complex of Cd^{2+} ions is allowed to react with sulfide ions formed by the hydrolysis of thiourea. In principle, Na_2S or H_2S can also be used as the sulfurating agent but the reaction proceeds so fast that the deposition results in a powdery deposit. A typical protocol used by many authors for the deposition of CdS thin films on borosilicate- and indium tin oxide (ITO)-coated glasses is as follows:

One hundred and fifty milliliters, 0.2 M TEOA is mixed with 10 mL, 0.1 M cadmium acetate solution in a 250 mL reagent bottle. After stirring for about 30 min, 10 mL of 0.2 M thiourea is added. The solution is stirred for approximately 10 min. One milliliter of 30% NH_4OH solution is added to the bath. All of the contents are then transferred into a pre-heated (60 °C) and thermostated crystallization dish with a lid. Prior to the addition, about eight precleaned glass slides are arranged vertically in PTFE, with a ring-shaped holder having vertical notches. The solution is stirred continuously during the deposition. After an hour, the substrates are withdrawn and transferred immediately to preheated (60 °C) distilled water to avoid peeling of the films due to the thermal shock. After cooling to room temperature, the films are rinsed with a copious amount of distilled water and dried under vacuum.

The quality of the films is strongly dependent on the cleaning and pretreatment of the substrates. Prior to deposition, the glass slides are etched with *Piranha* solution.[9] ITO-coated slides are cleaned with a solution of 2 M KOH in 2-propanol. After cleaning, these are stored in distilled water. In our experience, acidic surfaces do not give a desired deposition. We observed that etched slides soaked overnight in ammonia solution lead to a uniform deposit. So far, the reason is not clearly understood. Hydroxyl groups formed on the surface possibly lead to the formation of $Cd(OH)_2$ on the surface that, perhaps, acts as nucleation center (97). ZnS films can also be prepared using a similar strategy. Various baths used for these films have been reported by O'Brien and McAleese in detail (97).

(b)   Electroless deposition bath for the preparation of CdSe films

CdSe films are deposited by reacting Cd^{2+} ions with Se^{2-} ions that are generated *in situ* by the hydrolysis of Na_2SeSO_3 in ammonium hydroxide. Ammonium ions in the solution also act as complexing agents that facilitate the slow release of Cd^{2+} ions in the solution (99). Better results are obtained by using separate complexing agents such as amines. The protocol suggested by Hodes (98) for the ED of CdSe is as follows:

Two milliliters of 0.5 M Cd^{2+} is diluted with approximately 3.4 mL of distilled water. To this, 2.1 mL of 0.7 M potassium salt of nitrilotriacetic acid (KNTA)-complexing agent is

---

[9]Mixture of 30% H_2O_2 and concentrated H_2SO_4 in 1:3 ratio. Extreme precaution is necessary in handling the solution. Experiments should not be done without a proper fume-hood.

added. The pH of the solution is adjusted to 8 and 5 mL of 0.2 M Se (Na$_2$SeSO$_3$) is added to it. After stirring, the solution is transferred to the thermostated bath containing precleaned slides and the deposition is carried out as described previously.

Na$_2$SeSO$_3$ is prepared by refluxing Se metal powder with concentrated Na$_2$SO$_3$ solution (107). Typically, to prepare a 50 mM solution of Na$_2$SeSO$_3$, 0.0987 g of Se powder is refluxed with 0.5 g Na$_2$SO$_3$ in 20 mL distilled water in a round bottom flask fitted with an air condenser for 3–4 h. An excess concentration of Na$_2$SO$_3$ is necessary to prevent decomposition of Na$_2$SeSO$_3$ back into Se and Na$_2$SO$_3$. After cooling down, the solution is filtered and diluted to 25 mL in a standard measuring flask. This solution should be used immediately for the synthesis.

9.6   NANOSTRUCTURED SEMICONDUCTOR ELECTRODES (NSSE)

The effect of size quantization on the electronic properties of semiconductors, discussed in Section 9.2.2, demonstrates that semiconductor electrodes made of nanostructured particles are of great practical interest. Based on size quantization, these films can be categorized into: (a) thin semiconductor films deposited or epitaxial growth on a substrate where the SQE is due to the space confinement in two dimensions (i.e., a quantum well) and (b) particulate films of size-quantized nanoparticles that may be several micrometers thick; their properties are due to the combined effect of film and isolated size-quantized particles. Both the situations are illustrated in Figure 9.41.
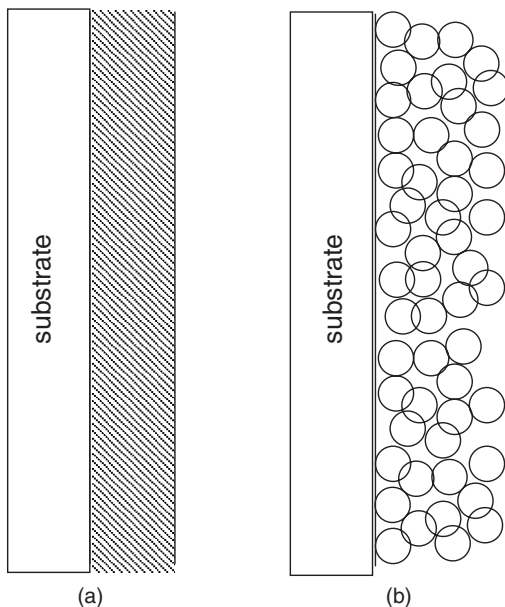

(a)   (b)

Figure 9.41   Types of nanostructured semiconducting films: (a) quantum well prepared by epitaxial growth in nanometer thickness and (b) particulate film in micrometer thickness.

9.6.1   Epitaxial methods for the preparation of NSSE

Nozik and Memming have worked extensively on the electrochemistry and photoelectro-chemistry of quantum well semiconductor electrodes (14). As discussed in Section 9.5.1, the quantum wells are produced by either MBE or MOCVD method. Both of these techniques are capable of creating epitaxial layers exhibiting quantum size effects. Their properties can be varied by film thickness, interfacial abruptness, and crystalline perfection.

In MBE, ultra-high vacuum chambers are outfitted with a number of evaporation cells. Each cell has a shutter to control the molecular flux. The molecular beam can be pulsed within 0.1 sec and the growth rate can be controlled within a few Å sec^{-1}. During the growth, the substrate temperature is maintained at ca. 500–700 °C. Atomic species most commonly used include Al, In, Sb, Be, Ge, Se, Te, Cd, Hg, Zn, Mn, Pb, and Si. The most common quantum well electrodes produced by MBE are the III–V semiconductors binary and ternary compounds. Some II–VI quantum well structures have also been prepared.

MOCVD is used only to prepare III–V semiconductors. Using this method, the group III metals are introduced in the form of their organometallic vapors. Each reacts with the gaseous precursors of non-metalloid group V components of the desired semiconductor compound to form a crystalline, epitaxial film on a hot substrate. For example, Ga, Al, and In are commonly introduced in the form of their trimethyl compounds. As and P are introduced in the form of arsine or tetrabutylarsine and phosphine or tetrabutylphosphine, respectively. Organometallics are introduced in the reaction chamber by passing hydrogen gas at a controlled flow rate through liquid organometallics. The single-crystal substrate is kept on the graphite block preheated at 650–750 °C.

9.6.2   Preparation of particulate films

Nanocrystalline particulate films, which exhibit pronounced quantum size effects in three dimensions, are of great interest due to applications in solar cell (108–112) and sensor (57, 113–115) applications. They exhibit novel properties due to not only the SQE manifested by individual nanoparticles but also the total surface area. Unlike MBE and MOCVD methods used to prepare quantum well electrodes, these electrodes can be prepared by conventional chemical routes described in Section 9.5.2.2. For example, II–VI semiconductor particulate films were prepared by using low concentrations of precursors and by controlling the temperature of the deposition bath. Hodes demonstrated the SQE for CdSe thin films deposited by an electroless method (98). The blue shift in the spectra of CdSe films has been demonstrated to be a function of bath temperature. As described in Section 9.5.2.1, electrodeposition of semiconductors in non-aqueous solvents leads to the formation of size-quantized semiconductor particles. On a single-crystal substrate, electrodeposition methods result in epitaxial growth (116, 117), and demonstrate quantum well properties.

Nanoparticles can be 'anchored' on a substrate by forming covalent bonds between the substrate and the capped nanoparticles. For example, ITO glass can be modified by (3-mercaptopropyl)trimethoxysilane (MPTMS), which leads to the formation of thiol
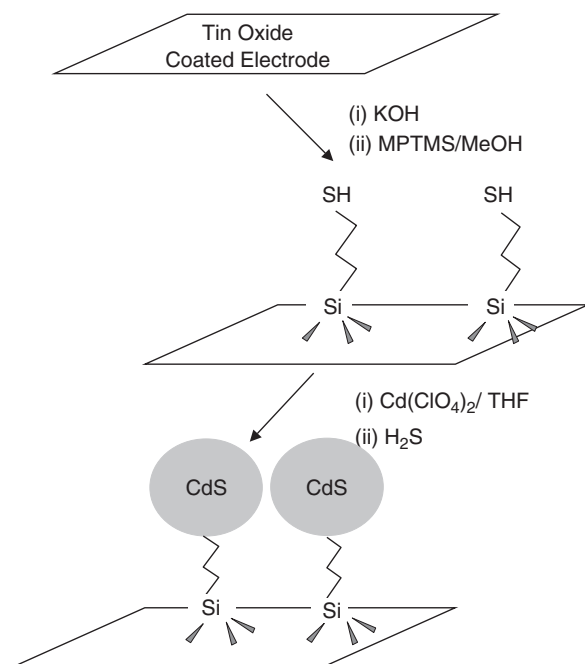
Figure 9.42   Schematic for surface modification of ITO glass with (3-mercaptopropyl)trimethoxysilane (MPTMS) followed by anchoring of CdS nanoparticles to the pendant thiol group. Adapted from reference (118).

pendants on the glass surface (118–120). Nanoparticles can be anchored to ITO glass through these pendants, as shown in Figure 9.42.

Similar work has been reported by Bard and co-workers where CdS nanoparticles were attached to a gold substrate using hexanedithiol (121). Using this method, it is possible to deposit multilayers that form an addressable three-dimensional quantum dot structure. Template methods have been used to deposit semiconductors of various shapes and sizes. For example, Li demonstrated the use of anodic aluminum oxide (AAO) templates to deposit CdS nanowires with a large aspect ratio (122).

Fendler's group recognized that semiconductor nanoparticle films can be synthesized by exposing a fatty acid monolayer complex of Cd^{2+} ions to gases (123, 124) such as H_2S. These films are called Langmuir–Blodgett (LB) films; they can be transferred to a suitable substrate for further characterization and use. The LB technique was further refined by Pan *et al.* to form LB films with CdS nanorods (125). Yoneyama and co-workers reported the fabrication of two-dimensional organized CdS nanoparticle films by cross-linking 2-aminoethanol-capped CdS nanoparticles with glutaraldehyde prior to their transfer to the substrate (126), as shown in Figure 9.43.

Coulombic interaction between capped particles can be used to organize the particles on the substrate (127–129). In one such example, polyacrylate-capped CdS nanoparticles were synthesized and assembled layer by layer on poly(diallyldimethylammonium chloride)
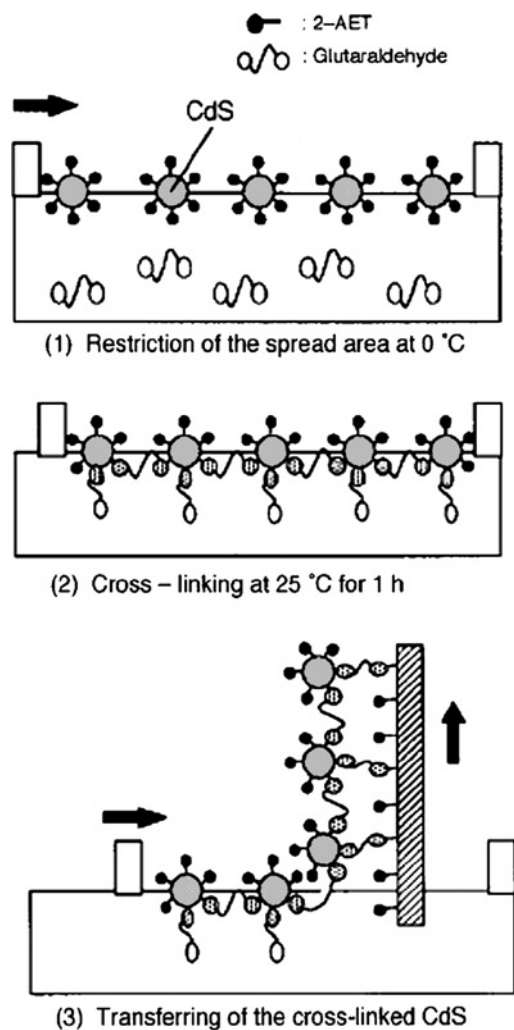
Figure 9.43 Schematic illustration of two-dimensional cross-linking of 2-aminoethanethiol-capped CdS nanoparticles spread on air–water interface that is transferred on suitable substrate. Reprinted with permission from reference (126). Copyright 1999, American Chemical Society.

coated on various substrates by virtue of the coulombic attraction between the negatively charged polyacrylate surface of the particles and cationic polyelectrolyte on a substrate. It is depicted schematically in Figure 9.44.

9.6.3 Electrochemistry on nanostructured semiconductors

Electrochemistry on nanostructured semiconductors may be classified according to the mode of charge transfer between the nanophase materials, the substrate, and the redox couple. The
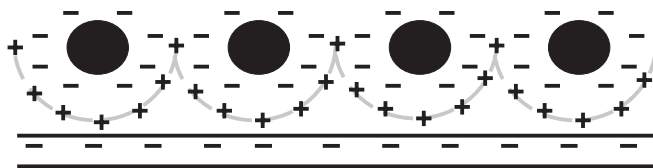
Figure 9.44   A schematics for coulombic interaction between particles and support; negatively charged polyacrylate-capped Q-CdS embedded in positively charged polyelectrolyte. Adapted from reference (127). Copyright 2001, American Chemical Society.

electrochemistry involved in charge transfer between an electrode modified with semiconductor nanoparticles and a redox couple in solution is similar to that discussed in Section 9.4 for bulk materials. A series of papers published by Gratzel and co-workers (109, 110), Liu and Kamat (130), Hodes (98, 117), and Fendlar and co-workers (62) report the electrochemistry of particulate films including TiO_2, ZnO, CdS, and CdSe pertaining to photoelectrochemical (PEC) applications.

Studies on charge transfer between addressable semiconductor nanoparticles and redox couples are quite novel. Riley and co-workers reported PEC measurements on CdS nanoparticles 'tailored' to ITO glass by a covalent linkage (118) as shown in Figure 9.42. A plot of photocurrent vs. the wavelength of light, called an action spectrum, recorded on these devices as a function of the size of the nanoparticles is shown in Figure 9.45. This group further investigated the kinetics of charge transfer between well-addressed tailored particles and the redox couple by electrochemical impedance spectroscopy and photocurrent transient measurements (119, 120).

9.6.4   Electrochemistry on suspended semiconductor nanoparticles

Photoelectrochemical (PEC) measurements on small semiconductor particles are of interest because of their possible applications in photocatalysis in addition to being a fundamental probe to study photolytic and electron transfer reactions at interfaces. The energetics of the particles differ, however, from the bulk. For extremely small particles, the Fermi level shifts to more negative values due to the quantum size effect. With slightly larger particles, photogenerated electrons can have energy that is different from that of the CB edge E_c of the bulk semiconductor in contact with the same solution. Thus, measurements of the energetics of dispersed particles are very important in deciding whether a given particle is in a position to reduce or oxidize the species in the solution. One of the ways to measure these properties is to collect the photogenerated electrons at an inert metal electrode immersed in the particle dispersion. The potential of the electrode can be adjusted such that it will be in position to collect the electrons, which will give an idea about the redox properties of the electrons photogenerated on the particles. Such a measurement carried out on a TiO_2 suspension is shown in Figure 9.46, where the onset of the anodic photocurrent suggests the position of the Fermi level in the particles.

These types of measurements have been confirmed for various semiconductor dispersions (27, 131–133) including TiO_2, In_2O_3, SnO_2, CdS, WO_3, and Fe_2O_3, and demonstrated that the
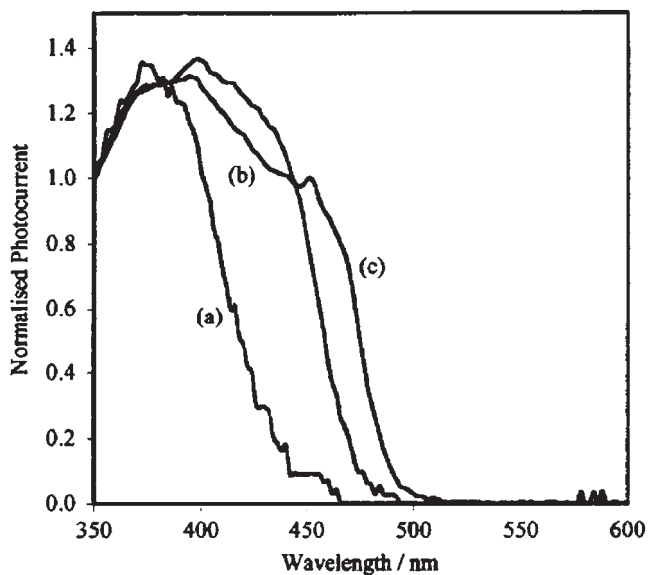
Figure 9.45 A plot of normalized photocurrent vs. wavelength of illumination, called action spectrum for CdS nanoparticle-modified ITO glass electrode. Particle size of CdS increases from (a) 2 nm and (b) 4 nm to (c) 10 nm diameter. The onset of action spectra shows red shift as a function of size, which is in concordance with the SQE. From reference (118). Reproduced by permission of The Royal Society of Chemistry.
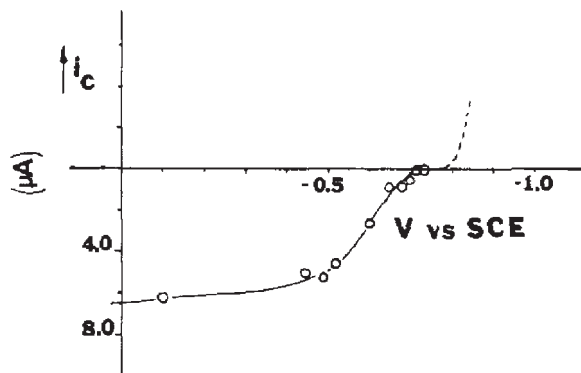
Figure 9.46 Photocurrent voltage response of suspended TiO_2 particles at In_2O_3 electrode. The anodic photocurrent indicates the electron transfer from the particles to electrode. From the onset, the potential for the photogenerated electrons was estimated to be -0.46 V vs. NHE. Reprinted with permission from reference (27). Copyright 1981, American Chemical Society.

Fermi level of particles is a function of irradiation intensity. The photo-onset potentials were shifted toward more negative values as a function of the photon flux. These experiments were supported by a blue shift of the absorption peak in the UV–vis spectra measured immediately after a high-intensity flash (134). This phenomenon is known as the 'Burstein shift' (135). Various potentials were applied to dispersions on an optically transparent electrode,

and the UV–vis spectra were recorded as a function of applied potentials (136). The change in absorption values was observed after a certain critical potential. It was observed that as particle size decreases, the critical potential shifts toward more and more negative values. These measurements were attributed to the quantum size effect.

The energetics of these particles have also been studied by CV and differential pulse voltammetry (127). The cyclic voltammograms recorded on alkylthiolate-capped PbS nanoparticles (3 nm diameter) in acetonitrile (137) are shown in Figure 9.47.

The peaks observed in the CVs were attributed to the redox reactions occurring due to the electrochemical decomposition of the PbS particles. For example, quasi-reversible cathodic peaks marked as I, II, and III were attributed to the reduction of PbS to Pb. The anodic peaks marked IV and V were attributed to the anodic stripping of deposited lead. The CVs recorded on Q-CdS particles in DMF however gave a cathodic and anodic peaks at extreme potential values as shown in Figure 9.48.

The peak positions marked as A1 and C1 were found to be shifted with particle diameter as shown in Figure 9.49.

In fact, there is a direct correlation between potential separation between peaks A1 and C1 and the observed band gap for various size particles. It is summarized in Table 9.4.

Based on these results, peak A1 is attributed to electron transfer from the highest occupied molecular orbital (HOMO) to the electrode and peak C1 is attributed to electron transfer from the electrode to the lowest unoccupied molecular orbital (LUMO), thus introducing the concept of 'electrochemical band gap' for semiconductor nanoparticles. Such a band gap was also observed earlier for extremely small metal nanoparticles (4). The decomposition of compound semiconductor particles on charge transfer poses a serious limitation on these studies, which was overcome by carrying out these measurements on
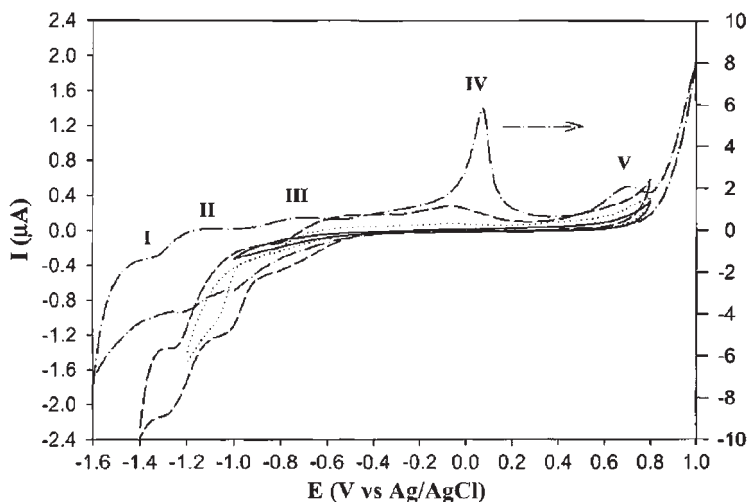

Figure 9.47   CVs recorded on hexanethiol-capped PbS nanoparticles in acetonitrile. Peaks marked (I), (II), and (III) are attributed to the reversible reduction of PbS. Anodic peaks marked (IV) and (V) are attributed to the oxidation and stripping of Pb from the electrode. Reprinted with permission from reference (137). Copyright 2000, American Chemical Society.
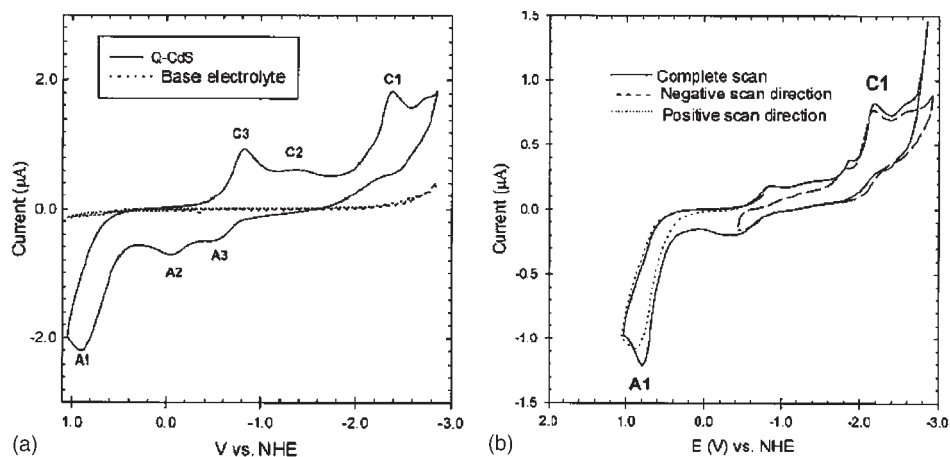
Figure 9.48   CVs recorded on thioglycol-capped CdS nanoparticles in DMF: (a) in full potential range and (b) at various starting potentials which suggests that peaks C1 and C2 are due to oxidation product from A1 and the peaks A2 and A3 are due to reduction products from C1. Reprinted with permission from reference (138). Copyright 2001, American Chemical Society.

elemental semiconductor nanoparticles such as Si (139). Differential pulse voltammograms (DPV) recorded on Si nanoparticles in DMF are shown in Figure 9.50.

Reversible peaks at about +0.09 and −0.7 V were attributed to the transfer of electrons from the HOMO and the LUMO to the electrode. The separation between these two peaks matches very well with the band gap obtained by spectroscopic methods. The reversibility of these peaks suggests that elemental semiconductor nanoparticles such as Si do not decompose on charge transfer. The peaks observed in the range −0.7 to −2.3 V are attributed to quantum double layer charging (140, 141), which is commonly observed in the case of monolayered protected clusters (MPCs).

9.7   SEMICONDUCTOR ELECTRODE APPLICATIONS

Semiconductor electrodes show electronic properties different from those of metal electrodes due to the space charge region present at SEI. The electric field gradient in the space charge region facilitates the separation of charge pairs generated at the SEI. This property of the SEI leads to numerous applications of semiconductor electrodes in the field of solar energy conversion (130, 131) and in sensor (132, 133) applications. Attention will be focused on the basic principles behind the use of semiconductor electrodes in these applications.

9.7.1   Solar cells

Solar cell applications can be broadly classified into two types: (a) photolytic or photoassisted conversion including the oxidation of water to H_2 and O_2 or decomposition of
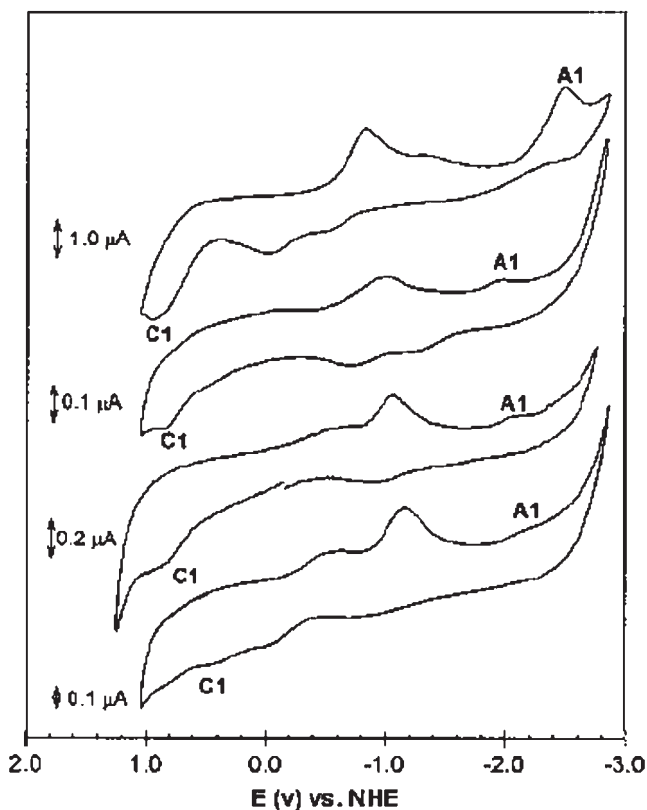
Figure 9.49 CVs recorded on various sizes of thioglycol-capped CdS nanoparticles. As the parti-
cle size increases from top to bottom, the separation between A1 and C1 decreases. Reprinted with
permission from reference (138). Copyright 2001, American Chemical Society.

Table 9.4

Correlation of optical and electrochemical band gaps for fractions I–IV

Fraction	ΔE (V)[a]	ΔE (V)[b]	Band gaps[c] (eV)	Size[d] (nm)
I	[e]	2.63	3.06	4.5
II	2.47	2.98	3.10	4.3
III	2.53	2.88	3.13	4.2
IV	2.96	3.39	3.23	3.9

ΔE refers to the peak separation between Al and Cl. Reprinted with permission from reference (138). Copyright
2001, American Chemical Society.
[a]C1–A1 peak separation at 10 mV s^{-1}.
[b]C1–A1 peak separation at 100 mV s^{-1}.
[c]Estimated from UV–vis absorption peaks.
[d]Estimated from electronic spectra.
[e]Peak not well defined.
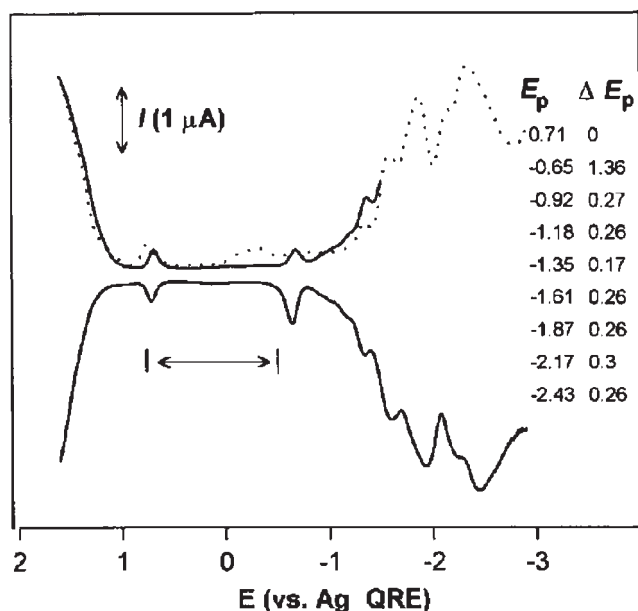
Figure 9.50 Differential pulse voltammogram (DPV) recorded on 1.74 nm Si nanoparticles. The reversible peaks near +0.09 and −0.7 V are attributed to the electron transfer through HOMO and LUMO of Si NPs. Reprinted with permission from reference (139). Copyright 2002, AAAS.

organic pollutants (142, 143) and (b) conversion of solar energy into electric energy using PEC solar cells or wet-photovoltaic cells.

The basic principle in both types is based on charge separation at the depletion semiconductor–electrode interface. As discussed in Section 9.3.1, in the case of direct band gap semiconductors, if the incident photon energy is higher than the band gap, the electrons are promoted into the VB by creating holes in the CB. The charge pairs generated in the depletion region are separated under the influence of the electric field gradient. For example, in the case of n-type semiconductors, holes will 'bubble out' at the SEI and can be used to carry out a desired oxidation. Electrons will travel through the semiconductor bulk, pass through the external circuit, and can be used to carry out a desired reduction at the counter electrode as shown in Figure 9.51a. Thus, a semiconductor electrode can be effectively used as a photocatalyst in carrying out photoassisted chemical conversion.

In PEC solar cells, the redox molecules used are reversibly oxidized and reduced at the semiconductor electrode and counter electrode. The current flowing through the external circuit can be used to drive a load and the device will effectively convert solar into electrical energy as shown in Figure 9.51b. Unfortunately, the decomposition potentials of most semiconductors lie in their own band gaps, leading to photocorrosion of the semiconductor surface, and put a question mark on the use of these devices. Oxide semiconductors such as TiO_2 and ZnO are more stable against photocorrosion but they absorb only in the UV region and are thus less efficient for terrestrial applications.
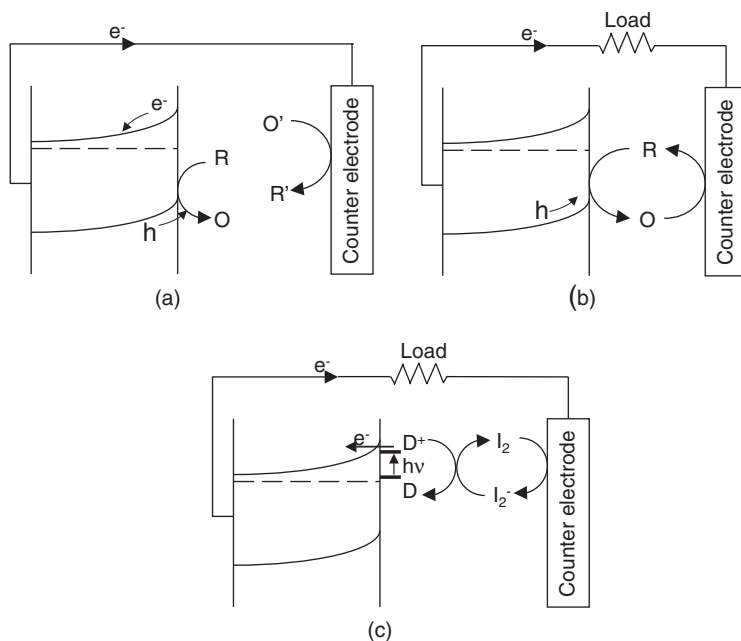
Figure 9.51   Schematics of (a) photochemical cell, where two different molecules undergo redox reaction, which leads to the photoassisted decomposition of molecules; (b) PEC solar cell, where same redox gets reduced and oxidized reversibly at photoelectrode and counter electrode, and thus net conversion of light into the electricity; (c) dye-sensitized PEC solar cell. The light is absorbed by dye molecule (D) and in an excited state, it injects the electron to CB. Electron travels through external circuit and reduces the mediator molecule, for example, I_2 into I_2^-. I_2^- reduces D^+ and the dye is regenerated for next electron transfer.

This problem is partially solved by sensitizing the electrode with a dye that absorbs in the visible region as illustrated in Figure 9.51c. Upon photoexcitation, the dye molecule injects a photoelectron in the CB that rolls down into the bulk semiconductor, passes through the external circuit, and reduces the redox mediator at the counter electrode. The reduced form of the mediator may diffuse and reduce the oxidized dye that completes the cycle. TiO_2-based PEC cells are more efficient when particulate films are used; these are referred to as 'Gratzel cells'. Among the various dyes explored for this purpose, ruthenium bipyridine complexes and their analogs have proven to be most efficient. However, these are not economically viable due to the cost of ruthenium, and thus have not yet been commercialized.

9.7.2   Sensors

The surface chemistry of semiconductors in sensor applications has been reviewed by Ellis and co-workers (144). Here, the basic principles behind the use of semiconductor

electrodes as sensors are discussed. The origin of the transduction mechanism of semi-conductor electrodes can be realized using the band structure of the interface. It is characterized by not only E_C, E_V, and E_F positions on the surface but also surface states present in the band gap. The molecule to be sensed will interact with these energy levels by the processes of adsorption and desorption. These can influence the rate of surface recombination, producing observable changes in the electrical or optical properties of semiconductors. For example, the surface states present in the band gap are an efficient mediator for non-radiative recombination, leading to low photoluminescence (PL) yields for most 'pinned' systems. An adsorption-induced shift in the energy position of surface traps away from the band gap can produce an increase in the semiconductor PL intensity. For the n-type semiconductor, adsorbed donors can effectively return the surface-trapped charge to the semiconductor bulk, thereby reducing the surface electric field at the depletion layer. It may cause a contraction of its width so that both the PL intensity and the bulk conductance are expected to increase.

The depletion region of the semiconductor is not only an insulating layer but also relatively non-emissive and hence commonly referred to as a 'dead layer'. If we oversimplify the semiconductor interface into a near-surface non-emissive zone and an underlying emissive zone, then the adsorption-induced PL behavior is quantitatively related to changes in the thickness of the dead layer according to

$$\frac{PL_0}{PL_x} = \exp(-\alpha' \Delta X) \tag{9.7.1}$$

where PL_0 and PL_x are initial and adsorption-induced PL intensities, respectively. α' is the semiconductor absorptivity, corrected for self-absorption, and ΔX is the resulting change in dead layer thickness from D_0, the initial dead layer thickness, to D_x in the presence of adsorbate (145, 146). Based on a similar argument, adsorption of acceptors should decrease PL yield and conductance. If the thickness of the semiconductor film approaches the width of the depletion layer, a measurable change in the conductivity of the sample can be used as a method of analyte detection.

ACKNOWLEDGMENTS

REFERENCES

1. A. Fujishima, K. Honda, *Nature* **37**, 238 (1972).
2. D. A. McQuarrie, *Quantum Chemistry*, Viva Book Private Limited: New Delhi, 2003.
3. C. Kittel, *Introduction to Solid State Physics*, Vth ed., Wiley Eastern Limited: New Delhi, 1976.
4. S. Chen, R. S. Ingram, M. J. Hostetler, J. J. Pietron, R. W. Murray, T. Gregory Schaaff, J. T. Khoury, M. M. Alvarez, R. L. Whetten, *Science* **280**, 2098 (1998).

5. C. B. Murray, D. J. Norris, M. G. Bawendi, *J. Am. Chem. Soc.* **115**, 8706 (1993).
6. L. E. Brus, *J. Phys. Chem.* **90**, 2555 (1986).
7. L. E. Brus, *J. Chem. Phys.* **79**, 5566 (1983).
8. L. E. Brus, *J. Chem. Phys.* **80**, 4403 (1984).
9. R. Rossetti, J. L. Ellison, J. M. Gibson, L. E. Brus, *J. Chem. Phys.* **80**, 4464 (1984).
10. S. V. Nair, S. Sinha, K. C. Rustagi, *Phys. Rev. B* **35**, 4098 (1897).
11. Y. Kayanuma, *Solid State Commun.* **59**, 405 (1986).
12. P. E. Lippens, M. Lannoo, *Phys. Rev. B* **39**, 10935 (1989).
13. I. N. Levine, *Quantum Chemistry*, 5th ed., Pearson Education: Singapore, 2000.
14. A. J. Nozik, R. D. Memming, *J. Phys. Chem.* **100**, 13061 (1996).
15. H. Reiss, A. Heller, *J. Phys. Chem.* **89**, 4207 (1985).
16. H. Gerischer, *J. Phys. Chem.* **27**, 48 (1961).
17. H. Gerischer, *J. Phys. Chem.* **95**, 1356 (1991).
18. R. A. Marcus, *J. Phys. Chem.* **94**, 1050 (1990).
19. R. A. Marcus, *J. Chem. Phys.* **24**, 966 (1956).
20. R. A. Marcus, *Can. J. Chem.* **37**, 138 (1959).
21. D. Laser, A. J. Bard, *J. Am. Chem. Soc.* **80**, 459 (1976).
22. V. L. Rideout, *Thin Solid Films* **48**, 261 (1978).
23. B. R. Horrocks, M. V. Mirkin, A. J. Bard, *J. Phys. Chem.* **98**, 9106 (1994).
24. R. Nicholson, I. Shain, *Anal. Chem.* **36**, 706 (1964).
25. P. A. Kohl, A. J. Bard, *J. Am. Chem. Soc.* **99**, 7531 (1977).
26. F.-R. F. Fan, A. J. Bard, *J. Am. Chem. Soc.* **102**, 3676 (1980).
27. W. W. Dunn, Y. Aikawa, A. J. Bard, *J. Am. Chem. Soc.* **103**, 3456 (1981).
28. A. Aruchamy, M. S. Wrighton, *J. Phys. Chem.* **84**, 2848–2854 (1980).
29. R. N. Dominey, N. S. Lewis, M. S. Wrighton, *J. Am. Chem. Soc.* **103**, 1261 (1981).
30. P. G. Santangelo, G. M. Miskelly, N. S. Lewis, *J. Phys. Chem.* **92**, 6359 (1988).
31. P. G. Santangelo, G. M. Miskelly, N. S. Lewis, *J. Phys. Chem.* **93**, 6128 (1989).
32. J. N. Chazalviel, T. B. Truong, *J. Am. Chem. Soc.* **103**, 7447 (1981).
33. S. N. Frank, A. J. Bard, *J. Am. Chem. Soc.* **97**, 7427 (1975).
34. F.-R. F. Fan, H. S. White, B. L. Wheeler, A. J. Bard, *J. Am. Chem. Soc.* **102**, 5142 (1980).
35. J. A. Baglio, G. S. Calabrese, D. Jed Harrison, E. Kamieniecki, A. J. Ricco, M. S. Wrighton, G. D. Zoski, *J. Am. Chem. Soc.* **105**, 2246 (1983).
36. P. Singh, K. Rajeshwar, J. DuBow, R. Job, *J. Am. Chem. Soc.* **102**, 4676 (1980).
37. L.-S. R. Yeh, N. Hackerman, *J. Phys. Chem.* **82**, 2719 (1978).
38. L. F. Schneerneyer, M. S. Wrighton, *J. Am. Chem. Soc.* **101**, 6496 (1979).
39. P. G. Santangelo, M. Lieberman, N. S. Lewis, *J. Phys. Chem. B* **102**, 4731 (1998).
40. J. N. Chazalviel, *J. Electrochem. Soc.* **129**, 963 (1982).
41. M. L. Rosenbluth, N. S. Lewies, *J. Phys. Chem.* **93**, 3735 (1989).
42. J. Bardeen, *Phys. Rev.* **71**, 717 (1947).
43. C. A. Mead, W. G. Spitzer, *Phys. Rev. A* **134**, 713 (1964).
44. W. G. Spitzer, C. A. Mead, *J. Appl. Phys.* **34**, 3061 (1963).
45. S. Kurtin, T. C. McGill, C. A. Mead, *Phys. Rev. Lett.* **22**, 1433 (1969).
46. A. J. Bard, A. B. Bocarsly, F.-R. F. Fan, E. G. Walton, M. S. Wrighton, *J. Am. Chem. Soc.* **102**, 3671 (1980).
47. B. L. Wheeler, N. Hackerman, *J. Phys. Chem.* **92**, 1601 (1988).
48. S. Nakabayashi, A. Kira, *J. Phys. Chem.* **95**, 9961 (1991).
49. M. Bruening, E. Moons, D. Cahen, A. Shanzer, *J. Phys. Chem.* **99**, 8368 (1995).
50. S. Bastide, R. Butruille, D. Cahen, A. Dutta, J. Libman, A. Shanzer, L. Sun, A. Vilan, *J. Phys. Chem. B* **101**, 2678 (1997).

51. N. Prokopuk, N. S. Lewis, *J. Phys. Chem. B* **108**, 4449 (2004).
52. S. Tanaka, J. A. Bruce, M. S. Wrighton, *J. Phys. Chem.* **85**, 3778 (1981).
53. A. J. Bard, F.-R. F. Fan, J. Kwak, O. Lev, *Anal. Chem.* **61**, 132 (1989).
54. F.-R. F. Fan, M. V. Mirkin, A. J. Bard, *J. Phys. Chem.* **98**, 1475 (1994).
55. O. D. Uitto, H. S. White, *Anal. Chem.* **73**, 533 (2001).
56. D. T. Piercet, A. J. Bard, *Anal. Chem.* **65**, 3598 (1993).
57. B. R. Horrocks, D. Schmidtke, A. Heller, A. J. Bard, *Anal. Chem.* **65**, 3605 (1993).
58. Y. Selzer, D. Mandler, *J. Phys. Chem. B* **104**, 4903 (2000).
59. S. B. Basame, H. S. White, *Anal. Chem.* **71**, 3166 (1999).
60. S. B. Basame, H. S. White, *Langmuir* **15**, 819 (1999).
61. S. B. Basame, H. S. White, *J. Phys. Chem.* **99**, 16430 (1995).
62. X. K. Zhao, L. L. McCormick, J. H. Fendler, *Chem. Mater.* **3**, 922 (1991).
63. S. K. Haram, A. J. Bard, *J. Phys. Chem. B* **105**, 8192 (2001).
64. S. Rodman, M. T. Spitler, *J. Phys. Chem. B* **104**, 9438 (2000).
65. L. A. Bottomley, J. E. Coury, P. N. First, *Anal. Chem.* **68**, 185R (1996).
66. M. A. Poggi, E. D. Gadsby, L. A. Bottomley, *Anal. Chem.* **76**, 3429 (2004).
67. A. J. Bard, F.-R. Fan, M. V. Mirkin, in *Electroanalytical Chemistry*, A. J. Bard, Ed., Marcel Dekker: New York, 1994, Vol. 18, p. 243.
68. A. J. Bard, F.-R. F. Fan, M. V. Mirkin, *Physical Electrochemistry: Principles, Methods and Applications*, I. Rubinstein, Ed., Marcel Dekker: New York, 1995.
69. A. J. Bard, D. O. Wipf, *J. Electrochem. Soc.* **138**, 469 (1991).
70. C. A. Koval, J. B. Olson, *J. Phys. Chem.* **92**, 6726 (1988).
71. J. V. Macpherson, P. R. Unwin, *Anal. Chem.* **71**, 4642 (1999).
72. R. D. Martin, P. R. Unwin, *Anal. Chem.* **70**, 276 (1998).
73. S. B. Basame, H. S. White, *J. Phys. Chem. B* **102**, 9812 (1998).
74. K. L. Chopra, *Thin Film Phenomena*, McGraw Hill Book Company: New York, 1969.
75. K. L. Chopra, R. C. Kainthla, D. K. Pandya, A. P. Thakoor, in *Physics of Thin Films*, G. Hass, M. H. Francombe, J. L. Vossen, Eds., Academic Press: New York, 1982, Vol. 12, p. 201.
76. K. L. Chopra, S. Major, D. K. Pandya, *Thin Solid Films* **102**, 1 (1983).
77. H. Kikimoto, *J. Cryst. Growth* **95**, 360 (1989).
78. K. C. Lee, *J. Electrochem. Soc.* **95**, 360 (1990).
79. D. K. Roe, L. Wenzhao, H. Gerischer, *J. Electroanal. Chem. Interface Electrochem.* **136**, 323 (1982).
80. I. Ruach-Nir, Y. Zhang, R. Popovitz-Biro, I. Rubinstein, G. Hodes, *J. Phys. Chem. B* **107**, 2174 (2003).
81. Y. Golan, L. Margulis, I. Rubinstein, G. Hodes, *Langmuir* **8**, 3, 749 (1992).
82. D. Xu, G. Guo, Yuguo Guo, Y. Zhang, L. Gui, *J. Mater. Chem.* **13**, 360 (2003).
83. A. M. Kressin, V. V. Doan, J. D. Klein, M. J. Sailor, *Chem. Mater.* **3**, 1015 (1991).
84. J. Barton, A. Vertegel, E. Bohannan, J. Switzer, *Chem. Mater.* **13**, 952 (2001).
85. T. Yoshida, M. Tochimoto, D. Schlettwein, D. Wohrle, T. Sugiura, H. Minoura, *Chem. Mater.* **11**, 2657 (1999).
86. M. Lawrence, J. Dodelet, *J. Phys. Chem.* **89**, 1395 (1985).
87. F. Endres, *Phys. Chem. Chem. Phys.* **3**, 3165 (2001).
88. R. Chen, D. Xu, G. Guo, Y. Tang, *J. Mater. Chem.* **12**, 1437 (2002).
89. M. Kemell, M. Ritala, M. Leskela, *J. Mater. Chem.* **11**, 668 (2001).
90. H. Saloniemi, T. Kanniainen, M. Ritala, M. Leskela, R. Lappalainen, *J. Mater. Chem.* **8**, 651 (1998).
91. T. Torimoto, A. Obayashi, S. Kuwabata, H. Yasuda, H. Mori, H. Yoneyama, *Langmuir* **16**, 5820 (2000).

92. A. S. Baranski, W. R. Fawcett, *J. Electrochem. Soc.* **127**, 766 (1980).

93. A. S. Baranski, W. R. Fawcett, K. Gatner, A. C. McDonald, J. R. McDonald, *J. Electrochem. Soc.* **130**, 579 (1983).

94. Y. Mastai, D. Gal, G. Hodes, *J. Electrochem. Soc.* **147**, 1435 (2000).

95. B. M. Quinn, Z. Ding, R. Moulton, A. J. Bard, *Langmuir* **18**, 1734 (2002).

96. F. Endres, S. Z. E. Abedin, *Chem. Commun.* **8**, 892 (2002).

97. P. O'Brien, J. McAleese, *J. Mater. Chem.* **8**, 2309 (1998).

98. G. Hodes, *Isr. J. Chem.* **33**, 95 (1993).

99. D. R. Pratt, M. E. Langmuir, R. A. Boudreu, R. D. Rauh, *J. Electrochem. Soc.* **28**, 1627 (1981).

100. T. L. Chu, S. S. Chu, N. Schultz, C. Wang, C. Q. Wu, *J. Electrochem. Soc.* **139**, 2443 (1992).

101. F. Zhou, P. R. Unwin, A. J. Bard, *J. Phys. Chem.* **96**, 4917 (1992).

102. M. L. Breen, J. T. Woodward, D. K. Schwartz, A. W. Apblett, *Chem. Mater.* **10**, 710 (1998).

103. Y. F. Nicolau, M. Dupuy, M. Brunel, *J. Electrochem. Soc.* **137**, 2915 (1990).

104. M. Sasagawa, Y. Nosaka, *Phys. Chem. Chem. Phys.* **3**, 3371 (2001).

105. S. K. Haram, K. S. V. Santhanam, *Thin Solid Films* **238**, 21 (1994).

106. S. K. Haram, K. S. V. Santhanam, M. Neumann-Spallart, C. Levy-Clement, *Mater. Res. Bull.* **27**, 1185 (1992).

107. B. Pejova, M. Najdoskia, I. Grozdanova, S. K. Deyb, *Mater. Lett.* **43**, 269 (2000).

108. H.-Y. Byun, R. Vittal, D. Y. Kim, K.-J. Kim, *Langmuir* **20**, 6853 (2004).

109. A. J. McEvoy, M. Gratzel, in *Encyclopedia of Electrochemistry*, B. Stratman, Ed., Wiley-VCH: Weinheim, Germany, 2002, Vol. 6, p. 397.

110. A. Z. M. Zukalova, L. Kavan, Md. K. Nazeeruddin, P. Liska, M. Grätzel, *Nano Lett.* **5**, 1789–1792 (2005).

111. D. B. Mitzi, *J. Mater. Chem.* **14**, 2355 (2004).

112. J. Bisquert, A. Zaban, P. Salvador, *J. Phys. Chem. B* **106**, 8774 (2002).

113. O. Chyan, J.-J. Chen, F. Xu, J. A. Sees, L. H. Hall, *Analyst* **125**, 175 (2000).

114. A.-M. L. Nickel, F. Seker, B. P. Ziemer, A. B. Ellis, *Chem. Mater.* **13**, 1391 (2001).

115. J. Karlsson, M. Armgarth, S. Odman, I. Lundstrom, *Anal. Chem.* **62**, 542 (1990).

116. R. Liu, A. A. Vertegel, E. W. Bohannan, T. A. Sorenson, J. A. Switzer, *Chem. Mater.* **13**, 508 (2001).

117. B. Alperson, H. Demange, I. Rubinstein, G. Hodes, *J. Phys. Chem. B* **103**, 4943 (1999).

118. S. Drouard, S. G. Hickey, D. J. Riley, *Chem. Commun.* **1**, 67 (1999).

119. S. G. Hickey, D. J. Riley, *J. Phys. Chem. B* **103**, 4599 (1999).

120. S. G. Hickey, D. J. Riley, E. J. Tull, *J. Phys. Chem. B* **104**, 7623 (2000).

121. K. Hu, M. Brust, A. J. Bard, *Chem. Mater.* **10**, 1160 (1998).

122. Y. Li, D. Xu, Q. Zhang, D. Chen, F. Huang, Y. Xu, G. Guo, Z. Gu, *Chem. Mater.* **11**, 3433 (1999).

123. X. K. Zhao, Y. Yuan, J. H. Fendler, *J. Chem. Soc., Chem. Commun.* **18**, 1248 (1990).

124. X. K. Zhao, J. H. Fendler, *J. Phys. Chem.* **95**, 3716 (1991).

125. Z. Y. Pan, G. J. Shen, L. G. Zhang, Z. H. Lu, J. Z. Liu, *J. Mater. Chem.* **7**, 531 (1997).

126. T. Torimoto, N. Tsumara, M. Miyake, M. Nishisawa, T. Sakata, H. Mori, H. Yoneyama, *Langmuir* **15**, 1853 (1999).

127. L. I. Halaoui, *Langmuir* **17**, 7130 (2001).

128. Y. Sun, E. Hao, X. Zhang, B. Yang, J. Shen, L. Chi, H. Fuchs, *Langmuir* **13**, 5168 (1997).

129. S. S. Shankar, S. Chatterjee, M. Sastry, *Phys. Chem. Commun.* **6**, 36 (2003).

130. D. Liu, P. V. Kamat, *J. Phys. Chem.* **97**, 10769 (1993).

131. T. Sagara, Y. Aikawa, M. Sukigara, *J. Phys. Chem.* **91**, 1173 (1987).

132. C.-Y. Liu, A. J. Bard, *J. Phys. Chem.* **93**, 3232 (1989).

133. J. K. Leland, A. J. Bard, *J. Phys. Chem.* **91**, 5076 (1987).

134. C.-Y. Liu, A. J. Bard, *J. Phys. Chem.* **93**, 7749 (1989).

135. E. Burstein, *Phys. Rev.* **93**, 632 (1954).

136. P. Hoyer, H. Weller, *Chem. Phys. Lett.* **221**, 379 (1994).

137. S. Chen, L. A. Truax, J. M. Sommers, *Chem. Mater.* **12**, 3864 (2000).

138. S. K. Haram, B. M. Quinn, A. J. Bard, *J. Am. Chem. Soc.* **123**, 8860 (2001).

139. Z. Ding, B. M. Quinn, S. K. Haram, L. E. Pell, B. A. Korgel, A. J. Bard, *Science* **296**, 1293 (2002).

140. D. T. Miles, R. W. Murray, *Anal. Chem.* **75**, 1251 (2003).

141. J. F. Hicks, A. C. Templeton, S. Chen, K. M. Sheran, R. Jasti, R. W. Murray, *Anal. Chem.* **71**, 3703 (1999).

142. T. L. Villarreal, R. G. Mez, M. Neumann-Spallart, N. Alonso-Vante, P. Salvador, *J. Phys. Chem. B* **108**, 15172 (2004).

143. A. Heller, *Acc. Chem. Res.* **28**, 503 (1995).

144. F. Seker, K. Meeker, T. F. Kuech, A. B. Ellis, *Chem. Rev.* **100**, 2505 (2000).

145. A. A. Burk, P. B. Johnson, A. B. Ellis, *J. Appl. Phys.* **59**, 1621 (1986).

146. K. Mettler, *Appl. Phys.* **12**, 75 (1977).

This page intentionally left blank

– 10 –

Microelectrode Arrays

Sabine Szunerits[1] and Laurent Thouin[2]

[1]LEPMI, UMR CNRS/INPG/UJF 5631, ENSEEG, Institut National Polytechnique de Grenoble, Domaine Universitaire, 38042 Saint Martin d'Hères, France
[2]Ecole Normale Supérieure, Département de Chimie, UMR CNRS 8640 Pasteur, 24 rue Lhomond, 75231 Paris Cedex 05, France

10.1   INTRODUCTION

The behavior of microelectrodes (radius smaller than 50 μm) differs from conventional-sized electrodes (radius 1 mm or greater) in that nonlinear diffusion is the predominant mode of transport. This difference in mass transport from the bulk solution toward the electrode has several important implications that make microelectrodes very attractive in many areas of electroanalytical chemistry. These include reduced ohmic potential drop, a decreased time constant, a fast establishment of steady-state signals, and an increased signal-to-noise ratio.

Since the beginning of the 1980s (1, 2), the development of microfabrication techniques has allowed these electrodes to become widely used even though the benefits of the properties of small electrodes was recognized much earlier. Microelectrodes have thus been employed for those applications demanding electrochemistry in restricted volumes, in solutions of high resistance as well as in short-time regimes (1, 2). For a more detailed discussion about microelectrodes, see Chapter 6.

It was around the same time that the first reports on microelectrode arrays appeared. Both experimental and theoretical works (3–27) have demonstrated the advantages of such electrode assemblies, which result from the specific mass transport of electroactive materials or diffusion regimes taking place at their interface. These include the following:

(1)   As long as the microelectrodes in the array do not interact with each other, a steady-state current is monitored at long times. This regime is a characteristic of the spherical or hemispherical diffusion achieved at individual electrodes of the array.
(2)   In conditions where individual diffusion layers overlap, the array may be considered as a single macroelectrode at which planar diffusion occurs.

Handbook of Electrochemistry
Edited by C.G. Zoski

(3)   Arrays of microelectrodes exhibit higher signal-to-noise ratios than macroelectrodes having an equivalent surface area. Lower current detection limits can be achieved that are important for electrochemical detectors in measuring small quantities of materials.

(4)   Interactions between individual electrodes in the arrays permit regeneration of electroactive substances through redox cycling or collection of very unstable intermediates.

Owing to these advantages, miniaturized electrochemical sensors for probing electroactive species at particular microscopic locations are in demand. This miniaturization is particularly important for diverse applications in biology where *in situ* measurements on living organisms are of interest. The aim of this chapter is to give a comprehensive understanding of the different types of microelectrode arrays (random, ordered, paired, etc.) and a general classification scheme based on their operating mode or electrochemical properties. An overview of the diverse methods employed to construct microelectrode arrays together with some recent areas where microelectrode arrays have been used will be presented. The specific properties of microelectrode arrays can, however, not be understood without a fundamental understanding of the diffusion on microelectrode arrays. A basic discussion around these phenomena will be given.

10.2   CLASSIFICATION OF MICROELECTRODE ARRAYS

The shapes of the electrodes in the array are limited mainly by the way the array is fabricated and by one's imagination. Microelectrode arrays are classified according to the design of the array and the function/use of the array.

10.2.1   Microelectrode designs

Individual electrodes in an array may assume a disordered (random) or periodical arrangement. Random microelectrode arrays are characterized by a statistical distribution of electrodes that may be of identical or dissimilar dimension and shape. Ordered microelectrode arrays generally consist of an ensemble of electrodes of identical dimensions with a periodic arrangement.

10.2.1.1   Random microelectrode arrays

The main advantage of such arrays (Figure 10.1A) is the ease with which they can be fabricated. They are mostly formed by sealing single metal wires (Pt, Au, Ag, Cu, Ni, etc.) or conducting carbon fibers into an insulating matrix, such as glass or an epoxy resin. The disadvantage is that they are geometrically ill-defined and, therefore, do not permit a clear comparison with theoretical predictions. The ill-defined spacing between conducting surfaces can lead to overlapping diffusion layers. Electrode dimensions and interelectrode distances ranging from tenths of angstroms to micrometers are possible.

One of the first random microelectrode arrays reported consisted of sealing a bundle of individually conducting carbon fibers into epoxy (29). This array consisted of five layers of 20 electrodes where each electrode had a radius of 5 μm. Each disk was located at least six diameters from its nearest neighbor electrode so that diffusional cross-talk between
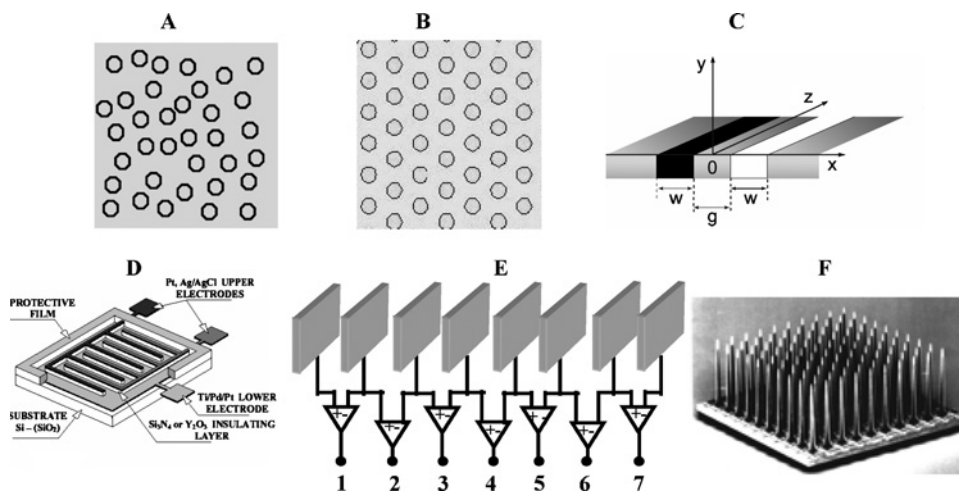
Figure 10.1   Classification of microelectrodes: (A) random array, (B) ordered array, (C) paired electrode, schematic representation of a double band assembly, (D) interdigitated array, schematic presentation of IDA electrodes vertically arranged (E) linear array, (F) three-dimensional array, Utah electrode array (reprints from reference (28)). (for colour version: see colour section at the end of the book).

disks did not occur. This array has proven to be advantageous as a flow rate independent amperometric detector.

A recent addition to this class of arrays is the construction of self-assembling arrays. Statistical arrays of microspheres with random radii have been realized by depositing mercury on an inactive substrate (30, 31) or by partial covering of a conducting electrode by a monolayer of insulating organic film (32, 33). In the same way, arrays of disk electrodes of a few hundred angstroms diameter have been made from polymeric membranes. The irradiation and local polymerization of the membranes led to the formation of transmembrane pores of calibrated dimensions in which platinum or gold were deposited (7, 18, 20). Opto-electrochemical microring arrays based on the deposition of gold around optical fibers (34–36) have recently been reported.

10.2.1.2   *Ordered microelectrode arrays*

The design of microelectrode arrays with well-defined geometries is largely preferred for electroanalytical, biological, as well as theoretical purposes. An ordered microelectrode array configuration, where each electrode in the array is regularly spaced with respect to another is shown in Figure 10.1B. A notable advantage of ordered arrays is their ability to be fabricated using silicon technology procedures, such as photolithography, which also accommodates bulk fabrication. The most common electrode materials are gold deposited on silica substrates, but platinum, iridium, and diamond have also been used. These devices do not endure mechanical pretreatment (polishing and removal of some coating on the electrode) but this is a minor problem, as their high interelectrode reproducibility and inexpensive nature permits disposability. Still, high-quality ordered microelectrode arrays are not easy to be fabricated and found. Regular arrays with well-defined geometries generally consist of parallel band

electrodes or disk electrodes arranged in a hexagonal array. These two geometries are preferred because their symmetry allows modeling of diffusion at these assemblies. Specific geometries have included an ensemble of microdisks sealed in a hexagonal or a square array (37–47), or parallel microbands of identical nature or alternatively polarized as an anode or a cathode. This latter configuration is generally known as paired electrodes (48–58) (Figure 10.1C) or as interdigitated electrode arrays (Figure 10.1D) (16, 20, 24, 27, 59–83).

A popular variation of ordered microelectrode arrays is the two-dimensional array (Figure 10.1E) (84) where the diffusion properties extend in two dimensions rather than three dimensions. Linear arrays with up to 16 electrodes have been reported and used for the investigation of anatomical muscle properties (85) and for basic and applied studies of the neuromuscular system (84).

10.2.1.3   Three-dimensional microelectrode arrays

This geometry has found wide application in biosensing and in recording electrical neural signals from nervous systems. Planar microelectrode arrays are not advantageous for acute tissue slice experiments. However, by using three-dimensional electrodes, it is possible to monitor the electrical activity of the tissue directly after placing it onto the electrodes. The geometry of the electrodes improves the penetration into the tissue slice, thereby reducing the distance between the active cells and the electrode. These arrays have a cylindrical structure (Figure 10.1F) and are mostly based on the etching of silicon wafers. Another configuration of a three-dimensional microelectrode array is based on the etching of optical fiber bundles and covering the surface with gold (36, 86). McKnight *et al.* have recently reported the fabrication and characterization of a microarray of individually addressable vertically aligned carbon nanofiber electrodes (87).

10.2.2   Microelectrode array behavior

Microelectrode arrays can be classified according to the way the array is operating.

10.2.2.1   Microelectrode arrays as amplifiers

If all of the microelectrodes in the array are polarized at the same potential, higher currents per unit area are possible (88). The signal-to-noise ratio of each individual electrode can be preserved and this so-called amplification effect is maintained as long as no overlap between individual diffusion layers occurs. Amplification remains effective at long times if the interelectrode spacings are at least 10 times larger than the radius of an individual microelectrode on the array. For a microelectrode of 5 μm radius, a minimal spacing of 50 μm would be necessary (88, 89).

10.2.2.2   Individually addressable arrays

Identical or different potentials can be applied to each electrode in an individually addressable array allowing multiparametric analysis while avoiding diffusional cross-talk. The development of an individually addressable microelectrode array places sophisticated demands on microfabrication technology. The conventional way to individually address each electrode of an array is to connect an electrode line to a corresponding bonding pad

at the end of a circuit chip (39, 90, 91). The electrochemical measurements are then carried out on each electrode either simultaneously, or sequentially. When carried out sequentially, however, recording a complete cyclic voltammogram on a 64 individually addressable microelectrode array can take up to 3 h (92) depending on the scan rate.

Simultaneous current measurements are possible using integrated circuits (ICs) where the addressing hardware is built onto each microelectrode array chip (40, 93). Such an approach was recently reported in which 64 individually addressable gel-integrated Hg-plated Ir-based microelectrodes were used (46, 94). The IC is based on a double multiplexing system and a single potentiostat. This was the first system reported allowing simultaneous recording of complete voltammograms for a large number of individually addressable microelectrodes with fast dynamic techniques, such as square wave anodic stripping voltammetry. This probe has been used for real-time, high spatial resolution concentration profile measurements at interfaces (46). The use of complementary metal oxide semiconductor (CMOS) technology (42, 95, 96), the major type of transistor set nowadays (97), permits local amplification just behind the electrodes to significantly decrease the electrode density. The main drawback of the standard CMOS technology is that it uses aluminum alloys as the metallic layer. This alloy shows limited stability in physiological solutions and is not biocompatible; therefore, it is not a suitable electrode material for biologically oriented investigations. However, by modifying the electrode surfaces, these arrays can be adapted for studies in biological media. Such an approach was reported by Berdondini *et al.* who electrolessly deposited gold from gold cyanide plating solutions (98).

10.2.2.3   *Generator/collector scheme*

Although all efforts in the individually addressable configuration are put into avoiding interactions between the electrodes in the array through overlap of individual diffusion layers, cross-talk in the collector/generator mode between closely spaced electrodes is the basic principle of their functioning. The simplest configuration for a generation/collection scheme is the paired electrode configuration mentioned above (Figure 10.1C). The intermediate generated on one electrode (the generator), diffuses to the other electrode (the collector), where it can be regenerated to the reactant initially present in bulk solution (Figure 10.2). In contrast to the rotating disk electrode where the regenerated species is swept into the bulk solution, the regenerated species at the collector electrode can diffuse back to the generator electrode and participate in the redox cycle again. The recycling or feedback between the paired electrodes results in amplifying the generator current far above the value it would have were the collector electrode disconnected (51, 53). Band electrodes are mostly used for the generator/collector mode and are fabricated generally by a sandwich method (48, 51–57).

A more sophisticated version of the paired electrode is the interdigitated array electrode (IDA). The IDA is an outgrowth of lithographic microfabrication technology (16, 20, 24, 27, 59–74, 76–83). The IDA consists of a series of parallel microband electrodes in which alternating microbands are connected together forming a set of interdigitated electrode fingers (Figure 10.1D). Typical dimensions of an individual microband "finger" are 100–200 nm in height, 1–10 μm in width and 5–10 mm in length. The typical interfinger separation (gap) is 1–10 μm. The potential of each finger set of electrodes can be controlled independently of the other relative to that of a reference electrode. The gap between the "fingers" is small enough so that for a sufficiently long electrolysis, diffusional coupling can
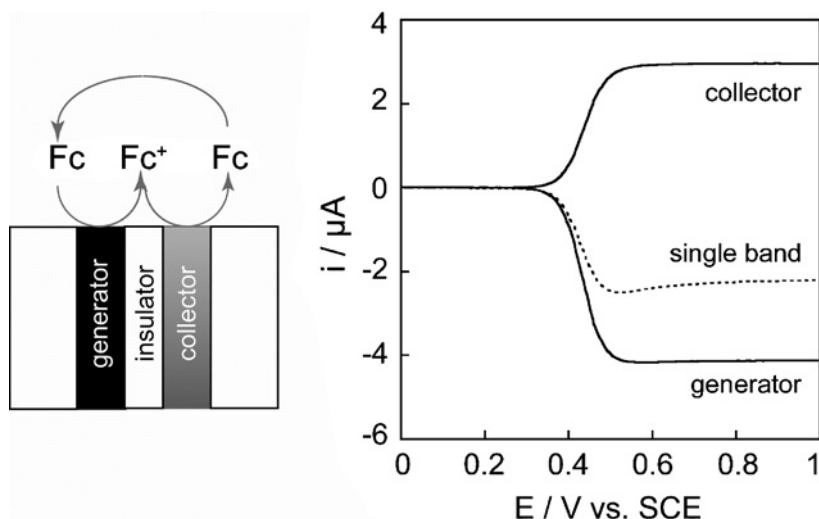
Figure 10.2   Generator/collector scheme: oxidation of 2 mM ferrocene (Fc) in 0.1 M $n\text{Bu}_4\text{BF}_4$/ CH$_3$CN. Dashed line: single band experiment (only one electrode is biased). Solid lines: generator/ collector experiment with $E_{\text{collector}}$ = 0 V/SCE. Band width, w = 5 μm; gap width, g = 2.5 μm; and scan rate, v = 0.1 V sec^{-1}.

occur between fingers and a collector/generator scheme similar to a paired electrode is set (Figure 10.2). With interdigitated electrodes, the small gap dimensions and the use of an array rather than a single generator/collector electrode pair results in very large collection efficiencies (larger than 0.98), which give the IDA an advantage in detecting trace amounts of electroactive species.

10.3   THEORY: DIFFUSION AT MICROELECTRODE ARRAYS

A quantitative description of mass transport to microelectrode arrays must take into account possible interactions between the diffusional fields of individual microelectrodes. The major complication arises from the difficulty in describing and modeling these inter- actions, which depend on the way the microelectrodes are arranged within the array but also on the way, the array is being operated.

10.3.1   Arrays of electrodes operating at identical potentials

When each electrode in the array is operating at the same potential, the overall response of the electrode array depends on two parameters: the density of the electrode distribution and the relative dimensions of the electrodes with regard to the thickness of the diffusion layer, δ, developing at each active element of the array. In other words, for a given array geometry, its electrochemical behavior will be strongly dependent on the time scale of the electrochemical perturbation (21, 26).
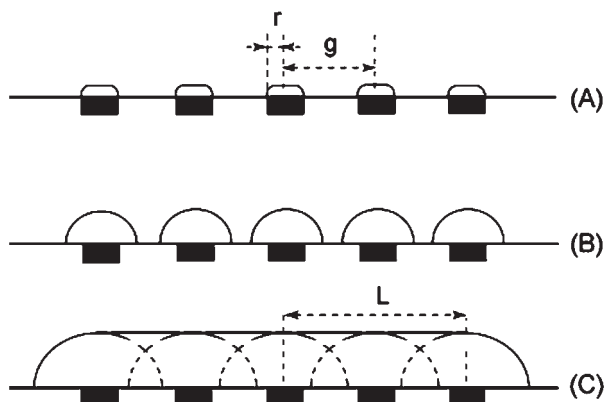
Figure 10.3 Schematic representation of diffusion layers of concentration profiles developing at arrays of electrodes at different times of the electrochemical perturbation: (A) planar diffusion at short times, (B) hemispherical or cylindrical diffusion at intermediate times, and (C) planar diffusion and overlap of individual diffusion layers at longer times.

When the duration of the experiment is sufficiently short for the diffusion layer to be small with respect to the radius r of the electrodes, planar diffusion is observed at each electrode and the current monitored at the array is proportional to the sum of geometric areas S^{el} of the individual active elements (Figure 10.3A). Under these conditions, the detected current is given by the well-known Cottrell equation:

$$(Dt)^2 \ll r, \qquad i = \frac{nFS^{el}DC*}{\sqrt{\pi Dt}} \tag{10.1}$$

At longer times, the individual diffusion layers become larger than the electrode dimensions and a transition regime occurs whose characteristics depend on the distance d separating two active elements of the array. When this distance is relatively large in comparison to the size of the diffusion layers, steady-state or quasi-steady-state diffusion takes place at each element depending on their shape (Figure 10.3B). The current is still equal to the sum of the currents at each active element but is proportional to the total active area S^{el} with a proportionality factor, which depends on the shape of the electrodes. This factor is introduced by $\delta(r)$, which is the equivalent diffusion layer thickness at each electrode under steady-state regime:

$$r \ll (Dt)^2 \ll d, \qquad i = \frac{nFS^{el}DC*}{\delta(r)} \tag{10.2}$$

This relation is only valid when the distance d separating the electrodes is much larger than their dimensions. If this is no longer the case, the diffusion layers developing at adjacent electrodes interpenetrate each other before reaching the steady- or quasi-steady-state diffusion regime observed separately at each element. The overlap of individual diffusion layers results in an apparent global diffusion layer that extends over the array in a planar diffusion regime (Figure 10.3C). In this condition, the array behaves like a large electrode

having an area equal to the geometric area of the entire array S^{array}, including the total active area S^{el} and insulating zones S^{insul} (i.e., $S^{array} = S^{el} + S^{insul}$):

$$d \ll (Dt)^2 \ll L, \quad i = \frac{nFS^{array}DC*}{\sqrt{\pi Dt}} \tag{10.3}$$

The situation where no diffusional overlap occurs presents a major interest for independently addressable arrays. At short times, the electrodes behave independently and the array performs like a simple current amplifier. This amplification is small compared with that achieved by classical electronic means. At long times, the current corresponds to an electrode of a dimension equal to that of the entire array. As the noise in electrochemical experiments is related to the capacity of the conductor and thus proportional to its surface area, the signal-to-noise ratio under these conditions is improved by a factor equal to S^{array}/S^{el}. This ratio can be improved up to two orders of magnitude and even more with the present technologies developed in nanolithography. This great advantage has been used for low current detection in the design of electrochemical detectors adapted for chromatography purposes (15, 83, 99).

Another advantage concerns heterogeneous electron transfer kinetics at such electrode interfaces. When the size of the active elements and distances separating the sites are small compared with the diffusion layer thickness, nonlinear diffusion is confined to a layer, which is adjacent to the array surface. As a result, considerable torsions of flux lines occur near each active element and the local rate of diffusion is drastically enhanced compared with that occurring far from the array surface where linear diffusion prevails (14). Even though the array behaves like a larger electrode, high diffusion rates may be generated locally on the arrays while keeping a relatively low overall diffusion rate. One must note that if the array is considered as a single large electrode at which planar diffusion occurs, the evaluation of the heterogeneous kinetics will be strongly affected, leading to an underestimation of the electron transfer rate (see Section 10.5.1). The same applies to fast homogeneous kinetics for which the kinetic layers are smaller than the distance separating two electrodes in the array (14).

All the limiting behaviors and their transitions described above have been observed experimentally at electrode arrays (19, 29, 74, 100–103). These situations have been treated theoretically for cases in which the active areas are uniform in size and situated in regular arrays (3, 9, 10, 13, 22, 104–106). Some differences have been observed among the calculations especially in the description of diffusion regimes at intermediate times, while the separate diffusion fields merge into a single larger field. It is only during this critical interval that the currents or diffusion regimes depend on the way the electrodes are arranged in the array. At shorter times, the electrodes behave as if they were individually separated and at longer times, the individual active areas are no longer distinguishable. The problem in dealing with mass transport to arrays of electrodes arises from the coupling between the expansion in three dimensions of the individual diffusion layers and the two-dimensional distribution of the electrodes in the array. The earliest theories of diffusion at arrays of electrodes have been developed to analyze the electrochemical responses at partially blocked surfaces of large electrodes (5, 9, 14, 101, 107, 108). Rigorous solutions of diffusion at statistical arrays are obviously impossible

and are generally adapted from those estimated at regular arrays by the introduction of statistical corrections (22, 108, 109). This is why the problem has been most frequently undertaken with microelectrodes packed in regular arrays. The common approach is to approximate the surface of the array as an ensemble of independently performing diffusion domains. The electrodes are supposed to be distributed in a regular two-dimensional lattice (square or hexagonal lattice form) with elements considered as the base of semi-infinite unit cells. Because of symmetry considerations, there is no flux of species at the boundary between the unit cells. Simplification of the problem is usually achieved with this construction by using a cylindrical geometry (Figure 10.4). Results have been obtained analytically (9, 105) and numerically (3, 10, 13, 104, 106, 107). Analytical solutions of the models give accurate results but appear limited to the semi-infinite diffusion regime at short and long time ranges (see Section 10.5.1). Good agreement between experimental data and results based on simulations were reported over the entire time regime taking into consideration the transient character of radial diffusion by explicit finite-difference techniques (10) and using the hopscotch algorithm (106). The transition from spherical to planar diffusion at arrays of electrodes has also been treated as the overlap of equivalent diffusion zones in the case of square, hexagonal, and random arrays (22). The analytical expressions show that the current is significantly reduced if the distribution of microelectrodes is random as compared with when the microelectrodes are regularly distributed. More recently, the diffusion processes for a finite number of active elements have been investigated with regular (110, 111) or arbitrary distributions (112), in thin layer cells (110) or taking into account convection influences of the solution (111).
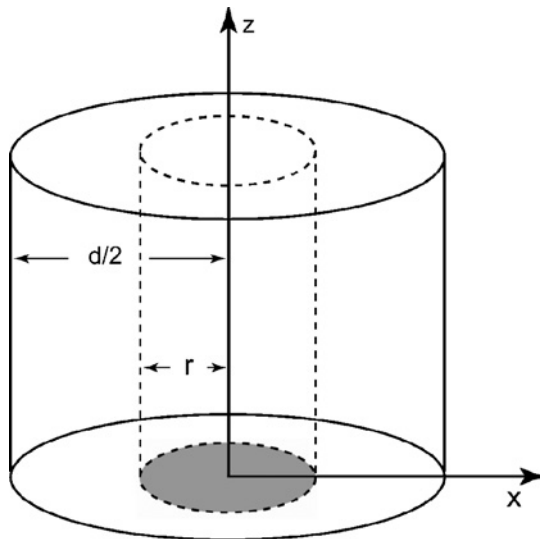

Figure 10.4   Approximate model of individual elements in arrays of electrodes with cylindrical coordinates. The electrode surface is represented in gray and insulating surface in white.

10.3.2   Arrays of electrodes operating in generator/collector mode

The intrinsic difficulties of modeling diffusion at arrays of electrodes are increased in the generator/collector mode because the transport equations must be solved numerically rather than analytically. The discontinuities between electrodes and insulators are amplified as the two adjacent electrodes interact with each other leading to cross talk at their immediate borders. Moreover, the communication between each electrode involves long-distance diffusional pathways, which connect the electrodes by their opposite borders. As a consequence, all numerical techniques have to deal with fine space grids between the electrodes to describe precisely the diffusion pathways at distances exceeding the electrode dimensions. The problem must be solved simultaneously at two different scales depending on the distance z from the array surface. For these reasons, simulations performed in real space are extremely difficult to handle as they require grid spaces perfectly adapted to the problem under investigation with a large number of points or nodes to be treated together. In an effort to reduce the number of grid elements required, simulations at electrodes arrays have employed exponential space grids (54, 74) or particular grid discretization (77) with the advantage of producing a high grid density in the vicinity of the electrodes without a dramatic increase in the overall number of elements required for the simulation of the complete diffusion layer. However, one major disadvantage is that the grid lines do not follow the actual lines of flux to the electrode surface especially at the edges of the electrodes where they are strongly curved. Moreover, it is impossible to define precisely a single grid accounting for the time-dependent shape of the concentration profiles.

An alternative to these difficulties consists of performing simulations in a nonreal space, which leads to linearization of isoconcentration and flux lines. The use of a conformal map is particularly useful and adapted for modeling diffusion at these assemblies. In many cases, it provides a simple way to estimate the steady-state currents for each type of electrode (26). This method has been used to describe analytically the current at interdigitated arrays (24, 76). In addition, the Schwarz–Christoffel transformation (Figure 10.5) allows the best change of space according to the geometry of the assemblies and time scale of experiments (27, 48, 51–53, 77, 113). Looking at a compromise between the simplicity of the transformed space and ease of formulations, it is possible to convert the real space into a conformal space, which affords a set of isoconcentration lines that is considerably more regular (Figure 10.6). Beyond the ease of calculations, these transformations allow simple comparisons or equivalences to be made between the different types of arrays. Indeed, it has been demonstrated for symmetry reasons that configurations like double-band, triple-band, and interdigitated electrodes have equivalencies (53). The nature of the original configuration is reflected only by the relative sizes of distance separating the electrodes and electrode dimensions. Nonetheless, the nature of the exact configuration is reflected through the rapidity with which the quasi-steady-state or steady-state regime is achieved.

Conformal mapping techniques often allow explicit analytical equations to be formulated for steady-state currents observed at electrode arrays in a generator/collector mode (48, 52, 53, 114). The steady-state regime is experimentally the most useful regime in these operating conditions. Under steady-state conditions, the enhanced cross-talk between electrodes leads to a reduced diffusional flux of species toward the solution as time proceeds. A steady-state regime is rapidly reached in the generator/collector mode in
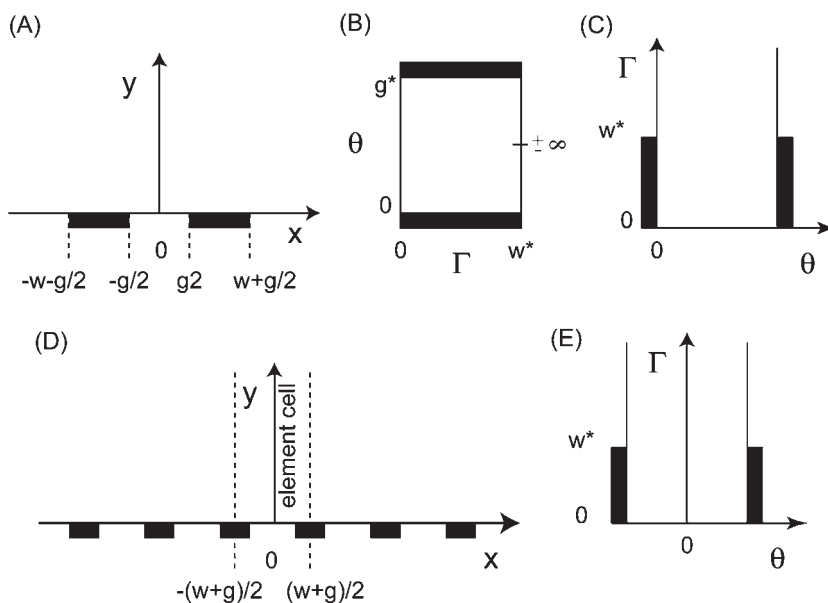
Figure 10.5 Schematic representation of band electrodes in real space and after Schwarz–Christoffel transformations. Double-band assembly in real space (A) and conformal space (B, C) for steady-state (B) and non-steady-state (C) conditions. Interdigitated array of band electrodes in real space (D) and conformal space (E).

Figure 10.6 Theoretical concentration profiles calculated in the conformal space of a double-band assembly (Figure 10.3C) operating in generator/collector mode in near-steady-state conditions. $w/g = 1$ and $g/2(Dt)^{-1/2} = 0.1$. C^* is the bulk concentration of the reactant in solution.

contrast to arrays of electrodes operating at the same potential. The greater the feedback and collection efficiency between the electrodes, the more rapid is the approach to the steady state. The conformal space also allows effective numerical simulations to be performed under non-steady-state cond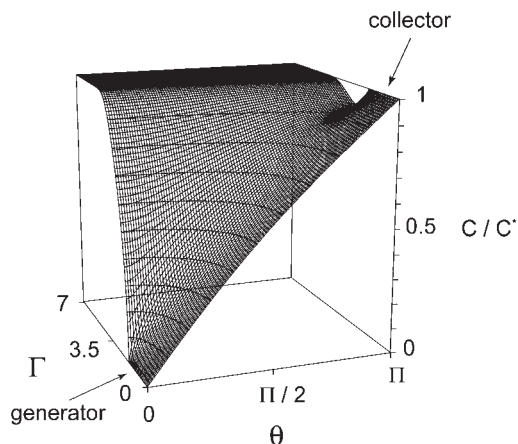itions whenever planar diffusion is significantly altered by nonplanar diffusion. Under non-steady-state conditions, the grid lines do not necessarily follow those of the conformal map, but the map is advantageous over other configurations as it more closely approximates the actual grid. A smaller number of nodes are necessary to obtain a numerical solution with the accuracy required. These conformal techniques also allow the effect of electrode perturbation on the electrochemical response to be evaluated for simple geometries. It has been demonstrated for double-hemicylindrical electrodes that these effects are no longer negligible when the resulting heights of the electrodes from the insulating plane become comparable to their widths or to the distance separating the electrodes (114).

   All the descriptions above clearly show the strong correlation between collection efficiency, feedback, and steady-state character of the currents detected at electrode arrays. This can be established more rigorously by analyzing the response at a paired-electrode assembly operating in a generator/collector mode. The cross-talk between the two electrodes is characterized by two parameters: the collection efficiency coll(t) and the amplification factor ampl(t), with coll(t) = i_c/i_g and ampl(t) = i_g/i_b. The currents i_c, i_g, and i_b are, respectively, the currents at the collector, generator, and single electrode (i.e., when the second electrode is not connected). The collection efficiency reflects the capture yield of species at the collector that were produced at the generator. The amplification factor is related to the feedback of species from the collector to the generator. The relationship between these two parameters depends on the configuration of the assembly and is a function of time (Figure 10.7A). The collection and amplification factors increase with time and tend toward a steady-state limit theoretically (1/ampl(∞) = 0 and coll(∞) = 1), which is not easily reached experimentally due to the diffusional escape of species toward the solution. It is noteworthy that even if the steady-state limit is never achieved experimentally for

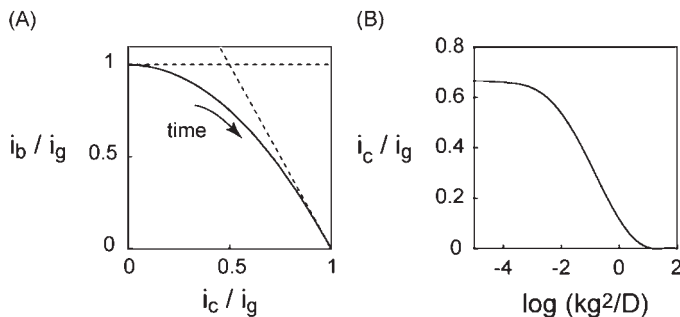**Figure 10.7** Double-band assembly operating in generator/collector mode. (A) Relationship between feedback (1/ampl(t) = i_b/i_g) and collection efficiency (coll(t) = i_c/i_g) in absence of a chemical reaction. (B) Effect of a chemical reaction (EC mechanism) on the collection efficiency as a function of kg^2/D. $w/g = 2$ and $g/2(Dt)^{-1/2} = 0.005$. k is the first-order rate constant of the chemical reaction.

micrometric arrays, an intermediate regime is attained. In these conditions, a simple relation exists between coll(*t*) and ampl(*t*):

$$coll(t) = 1 - \eta / ampl(t) \tag{10.4}$$

with $\eta = 0.5$ for a double-band assembly (113), $\eta = 0.25$ for a triple-band configuration (one generator flanked by two collectors) (31) and even smaller for an interdigitated array. The η value accounts for the extent of diffusional escape toward the solution according to the configuration of the assembly. It thus reflects the time dependence or rapidity in which the steady-state regime is achieved. Indeed, this regime is approached faster for an interdigitated array whereas it remains a virtual limit for a double-band configuration of micrometric size.

The collection efficiency is related to the geometry of the assembly itself but depends also on the lifetime of species produced at the generator. Indeed, one of the main interests of these assemblies is their capability to address kinetic problems. When this lifetime exceeds the time required to diffuse between the two electrodes, the collection efficiency is thus maximal according to the configuration of the assembly. In contrast, when the generated species is no longer stable, the collection efficiency tends to be zero. In this case, the temporal notion is replaced by a spatial notion linked to the dynamics of diffusion taking place between the electrodes. This is true whatever the geometry of the assembly provided that the duration of the experiment is sufficiently long for the diffusion layer developing at the generator to extend over the collector. The collection efficiency is thus a function that compares the relative values of lifetime with the time of flight over the distance separating the two electrodes (Figure 10.7B). Under these conditions, experimental determinations of rate constants or electrochemical mechanism need preliminary working curves to be established with respect to the configuration and geometry of the device (27, 53). This remains valid even if the generator/collector mode is employed in an electroanalytical approach for diffusion layer titrations in which the reactant is produced at the generator and reacts with the target analyte. As the collection efficiency is very sensitive to the heterogeneous kinetics of electron transfer at the generator (49), the need for analytical measurements to proceed with quantitative simulation appears to be obvious. Moreover, the array and especially the distance between the generator and collector must be adapted to the kinetics under investigation. Indeed, for the majority of molecules, the diffusion coefficient is equal to $D \approx 10^{-5}$ cm^2 sec^{-1}, which means that a lifetime of 1 ms requires formally a interelectrode distance of about 1 μm (Figure 10.7B).

10.4   FABRICATION OF MICROELECTRODE ARRAYS

Numerous methods for fabricating microelectrode arrays have been devised depending on the type of array required (6, 20, 35, 41, 49, 62, 63, 65, 115–134).

Low-aspect-ratio (ratio of the height of the microelectrode divided by its lateral dimension is larger than 0.2) microelectrode arrays are fabricated using conventional silicon-based microfabrication technologies, such as lithographic techniques to yield arrays of thin films of metallic or carbon electrodes on a silicon substrate. These arrays often have limited stability and life times as a result of defects in the metal layer; poor resistance to corrosion is

observed together with subsequent swelling and delamination of the metal layers. These microfabricated arrays are typically fragile and cannot be cleaned using conventional cleaning methods, for example, polishing, washing with solvents, and sonication. They are mostly cleaned using reactive ion etching with oxygen plasma.

High-aspect-ratio (ratio of the height of the microelectrode divided by its lateral dimension is larger than 2) microelectrode arrays are mostly fabricated using silicon micromachining, silicon microfabrication, or techniques involving bundling of multiple metal wires. These arrays are mostly designed to penetrate brain tissue to permit highly localized electrical stimulation and/or recording signals from neural tissue. These arrays are more robust compared with arrays formed by lithography and the surface is rather easy to clean. However, solid wire electrode arrays do not have more than a handful of electrodes in the array. The Utah Electrode Array contains about 100 electrodes but is less prone to delamination.

10.4.1   Mechanical methods

A variety of methods have been used in fabricating microdisk electrodes (see Chapter 9). One of the most successful methods is that in which a wire is sealed in glass and the surface is subsequently polished (or etched away) until the electrode is revealed (135). The manufacturing of microdisk arrays is based on the same technique as for simple electrodes. Although lithographic methods or silicon technology are the preferred ways in industry for the mass fabrication of ordered arrays, these techniques are not always accessible to most analytical users of microelectrodes. There is thus demand for the availability of inexpensive, conventionally manufactured microelectrodes. These processes, which are mostly mechanical methods, are at present limited due to the poor reproducibility of the manufacturing methods. Mechanical methods, summarized in Figure 10.8, can be classified according to how the array is constructed. A major limitation is that a careful polishing technique has to be employed. Otherwise, the electrodes have a tendency to recess below the surface of the insulating sheet leading to voltammograms that are slightly different from those for a perfectly coplanar electrode. Careful design is essential to ensure that the diffusion layers at each microelectrode do not interfere with others.

10.4.1.1   Wire techniques

One of the current technologies involves sealing conducting wires (gold, platinum, and carbon fibers) into an insulating material (epoxy resin and glass tube), which is resistant to water and some organic solvents, such as acetonitrile and methanol (Figure 10.8A) (29, 65, 90, 117, 137). Electrical contact between the metal wires is made by using silver epoxy resin. This method was used by Schwarz *et al.* (137), in developing microelectrode arrays of gold and platinum with different numbers of single electrodes in the array. They showed that the construction of disk as well as band microelectrode arrays is possible using this mechanical method. The ordered arrays were constructed by clamping the metal wires on an H-shaped body made of bronze. The wires are fixed in notches with fixed internal distance of 120–130 μm between the single wires. Then the wires are put into a mould and
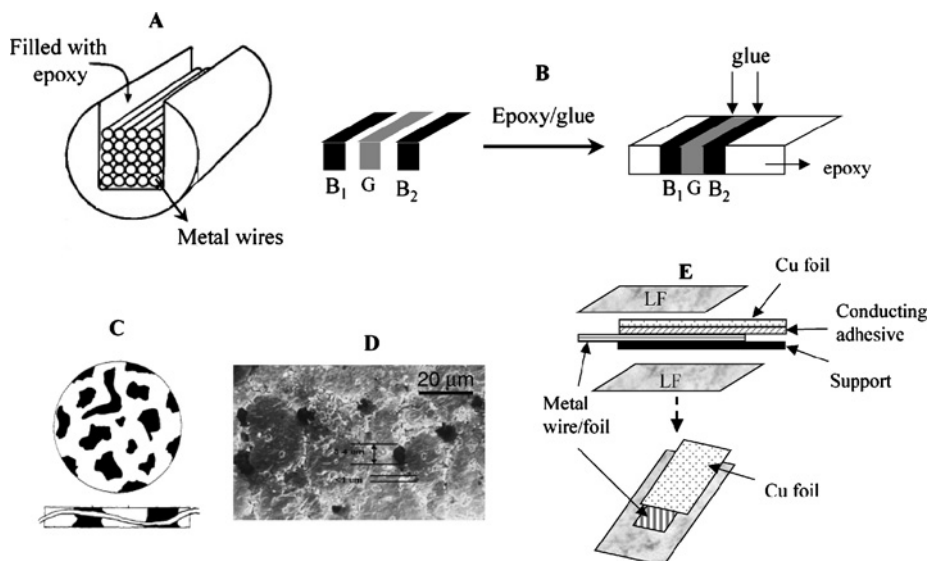
Figure 10.8   Construction principles of microelectrode arrays: (A) wire technique, (B) sandwich method, (C) composite formation (reprint with permission from reference (15)), and (D) Sonochemical formation, electrical micrograph with permission from reference (136).

epoxy resin is poured in to give a cube-shaped epoxy resin body. Arrays of disks as well as band electrodes were constructed in this way.

Band electrodes were formed by pressing gold foils with resin-impregnated glass silk fabric, as the insulation layer, at temperatures of 120–150 °C (137). The distance between the bands is 120 μm and the length of the bands is 600 μm with 2 mm width. The electrodes are provided with an electrical connector at the end of the contact cap. The radii of the sensor surfaces are 2 mm, with complete lengths of 25 mm.

Carbon fibers have been used for array construction because they are more rigid than gold. The construction of carbon fiber arrays consisting of five layers of 20 electrodes was introduced by Caudill *et al.* (29) and used as a flow rate independent amperometric detector. Sleszynski *et al.* (25) reported the design of ensembles based on reticulate vitreous carbon embedded in epoxy resin.

10.4.1.2   Sandwich method

Sandwich techniques (Figure 10.8B) are ideal for the construction of double-band assemblies (53, 113). The schematic of a double-band electrode is seen in Figure 10.1C. An insulator (Mylar film of 2.5 μm thickness, insulating gap) is placed between two sheets of platinum foil (5 μm) and the entire assembly inserted between two pieces of soft glass (about 3 mm thick and 8 mm width). Each layer of this sandwich is sealed with a small amount of epoxy resin, before firmly pressing into position. After hardening of the epoxy, each platinum foil was independently connected to an electrical copper lead with silver epoxy. This assembly can be glued into a glass tube (1 cm internal diameter).

The cross-section of this assembly can be exposed by saw yielding an assembly of two-paired microband electrodes.

An inexpensive and general method for the construction of microelectrode arrays is based upon thermal lamination of metal foils, which is very similar to the sandwich technique described before (138). The polyester/polyethylene laminating foil used is resistant to DMSO as well as to DMF. Electrical connections to the foil have been established either by spot welding a thin metal wire contact to the foil or by using a piece of copper foil with a conducting adhesive on one side. Gold, platinum, and silver microbands were fabricated in this way in addition to disks ranging from 10 to 125 μm. A linear array of microdisk electrodes was prepared by laminating two gold meshes (Figure 10.8E).

10.4.1.3   Formation of compositions (composite electrodes)

Ke−I graphite electrodes are composite electrodes with islands of graphite particles in a sea of Ke−I (13). Each island of graphite is in effect a microelectrode, each separated from other microelectrodes by insulating regions of Ke−F. The electrode surface is thus considered to consist of an array of microelectrodes (Figure 10.8C). It can be considered as a partially blocked solid carbon electrode. The electrode can be fabricated by mixing graphite (particle size of less than 1 μm) with Ke−F (150–450 μm particle size) with a mortar and pestle. This mixture was put into a vacuum chamber to remove the air from the composite and heated to 300–325 °C for 5 min. As the pressure increased, the heater turned off resulting in the composite pellet, which was mounted on a glass tube and sealed in place with epoxy. The dimensions of active and inactive sites on the electrode surface can be adjusted by varying the Ke−I particle size and carbon content. The graphite particles incorporated in an inert binder were found to exhibit microelectrode character in the range of 5–25% graphite. These electrodes are widely used as oxidative working electrodes in flowing streams because of their favorable noise and detection limit.

Another composite electrode is constructed by filling the voids of reticulated vitreous carbon with nonconductive epoxy to produce two-dimensional electrode materials (25). Reticulated vitreous carbon has been used as a three-dimensional highly porous electrode material and has been used in flowing systems as well as in thin slices as an optically transparent electrode.

Electrodes constructed of a single piece of material, such as reticulated vitreous carbon, have the advantage of good electrical contact to each conducting surface, but possess the attendant disadvantage that the magnitude of the interdistance spacing between the electrodes is limited by the requirement that the material be dimensionally stable. Microcellular foams made out of carbonized poly(acrylonitrile) (PAN) foams have been shown to be advantageous as the interelectrode spacing increases as the void fraction of the foam also increases. These foams are prepared via a thermally induced phase separation that allows control of density, pore size, and large void volume (97%). By incorporating an insulator into this matrix, an array can be made of average conducting particle size of 1 μm and smaller (139). Cylindrical samples of PAN foams were fashioned by using a simple drill press. The drill was suspended over a lab jack where the sample was placed. As the jack was raised, the drill slowly turned cutting the fragile foam structure. Filling of the foam with epoxy was accomplished in a vacuum through capillary action.

10.4.1.4   *Sonochemical fabrication*

Arrays can also be fabricated by sonochemical ablation of polydiamidobenzene ultra thin films deposited on gold-coated glass slides (136). These electrodes were then immersed in a beaker containing distilled water and sonicated for an hour using a 25-kHz sonic bath. The sonic bath employed 12 transducers geometrically arranged and bonded to the base of the stainless steel tank. 1,2-Diaminobenzene dihydrochloride can be electropolymerized at conductive surfaces via a two-electron process to form essentially defect-free insulation polymer films of less than 100 nm thickness. The rational underpinning of this work is that sonochemical ablation of thin insulation polymer films at electrode surfaces may expose localized areas each of which can act as localized microelectrodes and collectively as a microelectrode array. Ultrasound in the kHz range passing through solvents, such as water causes thermal agitation and localized hotspots of up to several hundreds to a few thousand K. This in turn gives rise to the formation of superheated vapor bubbles, which are cooled by the solvent at ambient temperature and asymmetrically implode with the ejection of micro-jets of solvents at speeds of up to several hundreds $msec^{-1}$. This micro-jet can cause the shattering of hard brittle solids. Soft polymer may, however, be ablated by such jets. A SEM image for a 60-sec sonicated electrode assembly is shown in Figure 10.8D showing the cavitations of the polymer surface. The size of the cavities are about 3 ± 1 μm or sub-micron diameter.

10.4.2   Template approaches

A general template method for preparing nanomaterials has been investigated by Martin and others for the formation of micro- and nanoelectrode arrays (140). The method entails synthesis of the desired metal (or polymer, protein, semiconductor, carbon nanowire) within the cylindrical and monodisperse pores of a membrane or another porous material (Figure 10.9) (see also Section 16.2 in Chapter 16).

Both acid anodized aluminum (alumite membrane) (141, 142) and nuclear track-etched membranes have been used as a template. The nuclear track-etched membranes are prepared by irradiation/chemical etching (143) and contain linear, cylindrical pores of nearly uniform pore diameter. This ensures that the holes in the template are circular and approximately of the same diameter. More recently, porous nano-channel glass (144), and etched wafers of micro-channel plate glass have served as templates (125). The advantage of using porous membranes as templates can be found in their function as arrays of microelectrodes. They exhibit small potential drops, which make the electrochemical measurements possible when
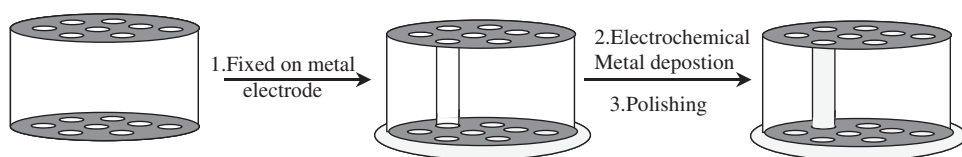

Figure 10.9   Schematic diagram of the procedure used to prepare the microelectrode array using templates. (for colour version: see colour section at the end of the book).

a low-concentration electrolyte is used. Furthermore, membranes with pore radii ranging from 6 μm to 50 Å and pore densities, ranging from 1×10^5 pores cm^{-2} to about 6×10^8 are commercially available allowing the formation of arrays with a broad range of element radii. The ability to control the length of the electrodes formed in the template is another important feature of the template method. The length of the wire can be controlled by varying the deposition time (electrochemical plating method) or by varying the thickness of the template in the electroless plating approach. The template technique is so advanced that gold metal wires as small as 80 Å in diameter can be produced (142).

The fabrication of these arrays presents three challenges:

(1) Preparation of the porous template
(2) Electrodeposition of the metal within the hollow parts of the template
(3) Final preparation of the array following electrodeposition

One of the earliest applications of the template method was to prepare ensemble microscopic (7, 18) and nanoscopic electrodes (116, 141). Such electrodes were prepared by electrochemically depositing noble metals within the pores of the commercially available polymeric filtration membranes. The fabrication of a microelectrode "ensemble" based on the electrochemical deposition of platinum into the pores of a track-etched microporous polycarbonate host membrane was first shown in 1987 by Charles Martin (7). The word ensemble was used to describe the final device because the elements in the device are not evenly spaced. The procedure is simple, and requires only routine and inexpensive electrochemical instrumentation. It was ultimately found that electroless plating allowed for more uniform metal deposition (116). Both plating methods are important for the fabrication of the array, and further considerations continue in the following.

10.4.2.1 *Electrochemical plating method*

Electrodeposition of metallic wires throughout the void spaces of porous nanostructure templates was first shown by Possin in 1970 (145), who developed an electrochemical synthesis method for producing different single metal wires in a 15-μm thick mica wafer with the density of the pores in the order of 10^4 pores cm^{-2}. As the membranes employed have cylindrical pores of uniform diameter a micro- as well as nanometer-sized cylinder or fibril of the desired material is obtained in each pore (7, 146–150).

To electrodeposit metal throughout the channels of the template, the porous material is mounted on a metal-coated glass substance; typically, a metal-coated glass slide (Figure 10.9). The slide provides support for the template and the metal coating on the slide provides the electrical connection needed to drive the electrodeposition. The templates are often coated on one side with a thin metal layer (100 nm of titanium, platinum, or gold) through sputtering in the vacuum at an angle of 45° with respect to the plane of the wafer. This allows the metal to deposit uniformly on the edges of the template as well as a short distance into the channels. These metalized templates adhere well to the glass and provide a surface from which the electrodeposited metal can grow. Ideally, the metal film should completely occlude the channel ends, providing a continuous conducting surface in the channels. Large channels (>1 μm) cannot be efficiently occluded by sputtering

layers of metal from which wire growth can be initiated. The template can be bound to the metal-coated slide using epoxy applied around the periphery: a light downward force applied to the center of the template during the epoxy step followed by curing to ensure that the template maintains good electrical contact. Electrodeposition is often enhanced at elevated temperatures and the solutions are often chemically harsh. Thus, a hard, inert epoxy is needed to withstand harsh conditions. Electrodeposition of gold, platinum, silver, copper, nickel, rhodium, and cobalt in templates has been reported (7, 125, 141, 142, 145, 150–152) as well as deposition of polymer (149), semiconductors (153), and carbon (154) into these templates.

10.4.2.2   *Electroless metal deposition*

Electroless deposition of metals is based on the deposition and reduction of metallic ions (reducing agents are formaldehyde, hydrazine, hydroxylamine) (155–158) from a solution to a surface without applying an electrical potential (159). The key feature of the electroless deposition process is that gold deposition begins at the pore wall. The advantage of the electroless method is that the surface to be coated does not need to be electrochemically conductive. The key requirement of an electroless deposition bath of this type is to arrange the chemistry such that the kinetics of homogeneous electron transfer from the reducing agent to the metal ion is slow. This is essential because otherwise the metal ion would simply be reduced in the bulk solution. A catalyst that accelerates the rate of metal-ion reduction is thus applied to the surface to be coated. In this way, metal ions are reduced only at the surface and the surface becomes coated with the desired metal.

Electroless deposition of various metals into templates was pioneered by Martin who also showed that more uniform metal films are obtained as thicker metal layers are formed (116). Furthermore, the electroless deposition chemistry allows routine fabrication of gold disk electrode arrays, in which the disk can have a diameter as small as 10 nm. To make the electroless deposition process compatible with the membrane chemistry, a "sensitizer" (Sn^{2+}) was first applied to the surface of the membrane, by simply immersing the membrane in a solution of $SnCl_2$/trifluoroacetic acid (0.026/0.07 M) (Figure 10.10).
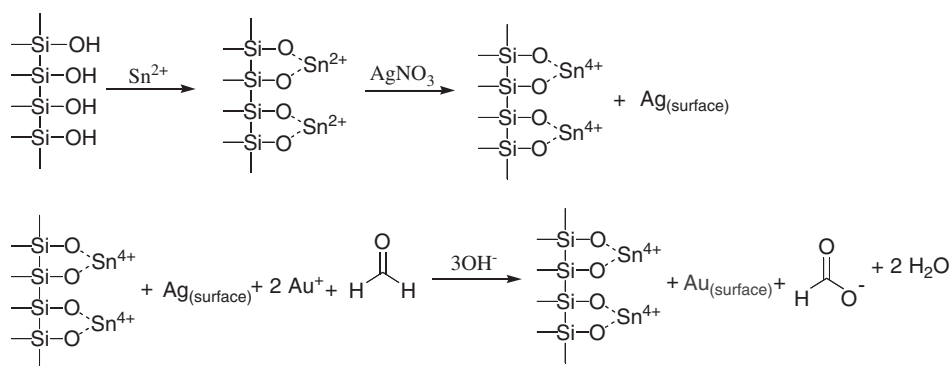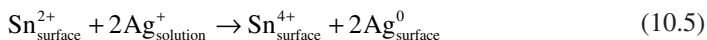

Figure 10.10   Schematic diagram of the electroless procedure used to deposit gold into templates.

The Sn^{2+} sensitized polycarbonate membrane is then activated by immersion in an aqueous solution of $AgNO_3$ for some minutes. This causes a redox reaction in which the surface-bound Sn^{2+} is oxidized to Sn^{4+} and the Ag^+ is reduced to elemental Ag together with some silver oxide. As a result, the pore walls become coated with discrete nanoscopic Ag particles. A gold-coated membrane can be obtained by immersing it into a Au plating bath ($Na_3Au(SO_3)_2$) (commercially available from Technic Inc., Craston, RI: OROMERSE SO Part B) in the presence of formaldehyde and Na_2SO_3. The Ag particles are galvanically displaced by gold as gold is the more noble material. Furthermore, the silver particles show excellent catalytic sites for the oxidation of formaldehyde:

$$Sn^{2+}_{surface} + 2Ag^{+}_{solution} \rightarrow Sn^{4+}_{surface} + 2Ag^{0}_{surface} \tag{10.5}$$

$$Au^{+}_{solution} + Ag^{0}_{surface} \rightarrow Au^{0}_{surface} + Ag^{+}_{solution} \tag{10.6}$$

Another way of filling the pores of a template with conducting material is filling its pores with carbon paste (18). This is, however, really difficult to do and takes a long time and a lot of patience. The carbon paste was prepared by mixing Carbopack C powder (particle size diameter is 150–180 μm) with vacuum grease using a glass mortar and pestle, which also reduced the size of the carbon particles to 100–300 nm in diameter. By rubbing the paste into the pores of the membrane, after first removing the poly(vinylpyrrolidine) wetting agent by ultrasonicating the membrane in glacial acetic acid, until the carbon paste began to leak out from the opposite side of the membrane. This procedure was repeated and placed onto the surface of a macrosized carbon paste electrode and held in place with a rubber O-ring (Figure 10.11).

Recently, electroless deposition of gold on optical fibers forming ring microelectrodes was reported by Szunerits and Walt (35, 36). Hundreds of gold-coated and -insulated optical fibers were bundled together in a coherent way to form an opto-electrochemical ring electrode array (Figure 10.12). The advantage of microelectrode arrays were thus combined with the imaging properties offered by optical fiber bundles providing users with two levels of control and selectivity. Much of the work on this opto-electrical device has been performed using electrochemiluminescence (ECL) (refer to Chapter 13) as the detection method.
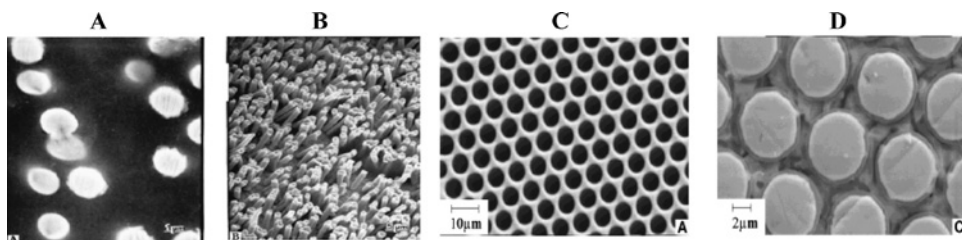
Figure 10.11 Electron micrograph of (A) the surface of an microelectrode array prepared from a microporous polycarbonate host membrane (diameter of 1 μm) (reprint with permission from reference (7)); (B) Pt fibrils obtained after the polycarbonate host membrane is dissolved away from the microelectrode array (reprint with permission from reference (7)); (C) SEM micrograph of the surface of a microchannel glass wafer etched but unfilled (reprint with permission from reference (125)); (D) etched and with Rh-filled array (125) (reprint with permission from reference (125)).

Figure 10.12   Electrochemiluminescence (ECL) imaging using an opto-electrochemical microring array. (for colour version: see colour section at the end of the book).
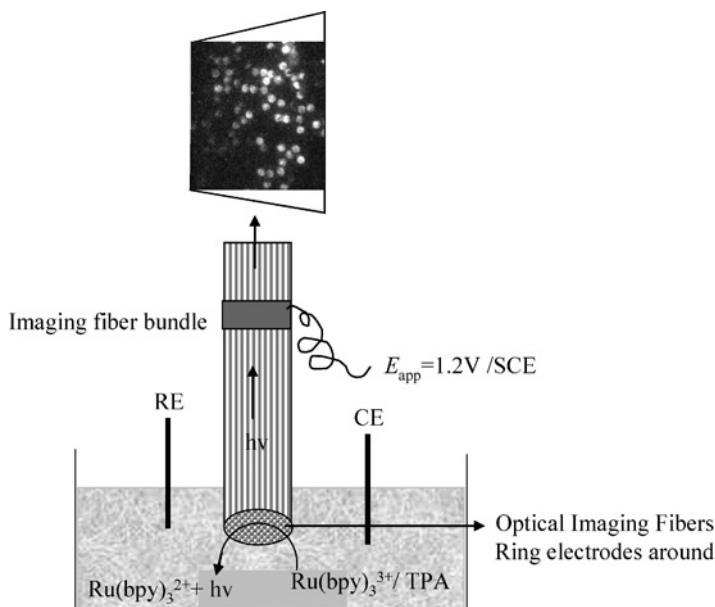
10.4.3   Lithographic techniques

Lithographic methods have the advantage of being highly controllable and reproducible over mechanical and template approaches. Fabrication of highly sophisticated electrode geometries is a possibility that has been utilized only to a limited extent so far. Lithography, in general, is a technique that transfers a copy of a master pattern onto the surface of a solid material, such as a silicon wafer, and advances in lithographic techniques can be found in the comprehensive literature (160, 161). Photolithography and soft lithography with reactive ion etching have been widely used for the fabrication of electrode arrays and will be discussed in more detail here.

10.4.3.1   *Photolithography (lift off and reactive ion etching)*

The most widely used form of lithography is photolithography. This is partly because of the fact that in the ICs industry, pattern transfer from masks onto thin films is accomplished almost exclusively via photolithography. Photolithographic methods all share the same operational principle: exposure of an appropriate material to electromagnetic radiation (near UV: 350–500 nm, Mercury lamps; deep UV: 150–300 nm, KrF excimer laser, X-ray, soft X-ray (EDU)) introduces a latent image into the material as a result of a set of chemical changes (usually a change in solubility) in its molecular structure. The resolution of photolithography increases as the wavelength of the light used for the exposure decreases. With 193 nm light from an ARF eximer laser and synthetic fused silica lenses,

patterns as small as 150 nm are achieved (162). However, it has been pointed out that photolithographically produced electrodes are difficult to resurface by means of polishing (163). One should keep in mind that the procedure of polishing electrodes between measurements is out of the question when it comes to practical applications, such as process monitoring or in situ investigations.

Three steps are important for the success of photolithography and for forming microelectrode arrays:

(1)   Photo mask design
(2)   Photoresist step
(3)   Development

(a)   *Photo mask design*

Although a scanned aperture can be used to write arbitrary patterns, the predominant use of photolithography is in replicating a pattern on a mask into a layer of photoresist. Such a mask, also called photo mask, is either a nearly optical flat glass, which is transparent to near UV or a quartz plate, transparent to deep UV covered with a metal absorber pattern (about 800 Å thick chromium layer). Such a mask is either placed in physical contact with the resists (contact mode), or an image of the mask is reduced and projected into the resists with an optical system (projection mode).

(b)   *Photoresist step*

In addition to advances in the physics and engineering of new light sources and projection optics, clear designs for the chemistries of the photoresist have been critical to the success of photolithography. Photoresists must meet several rigorous requirements: high sensitivity, high contrast, good etching resistance, good resolution, easy processing, high purity, minimal solvent use, low cost, and a high glass transition temperature, T_g. Most resists are amorphous polymers. At temperatures above the glass transition temperature, these polymers exhibit viscous flow with motion of the polymer chain segments. At a temperature below T_g, the motion of the segments is halted and the polymer behaves as a glass rather than as a rubber. Thus, heating the resists film above the T_g enables the film to anneal into its most stable energetic state, the rubber state. Here, the solvent easily can be removed from the polymer matrix through soft-bake. The photoresist is dispensed from a vicious solution of the polymer into the wafer laying on a wafer plate in a resist spinner.

The principle components of photoresists are a polymer, a sensitizer, and a casting solvent. During radiation, the polymer changes structure. The solvent allows spin coating and thin layer formation on a wafer surface. Sensitizers control the chemical reactions in the polymeric phase. There are two types of resists: positive and negative resists. We talk about a positive resist when the photochemical reaction during exposure weakens the polymer by rupture or scission of the main and side polymer chains. The exposed resists become more soluble in developing solutions. The development rate for the exposed resist is larger than for the unexposed one. A negative resist is where the reaction strengthens the polymer by random cross-linking, thus, becoming less soluble. The best known positive photoresist is poly(methylmethacryalte) (PMMA). PMMA becomes soluble through chain scission under deep UV illumination with the maximal sensitivity at 220 nm. Negative photoresists are mostly based on cross-linking of polymer chains, rendering the exposed

parts of the resist insoluble. One negative resist commonly used is a bis(aryl)azide rubber resist, whose matrix is cyclized poly(*cis*-isoprene). Upon photolysis, this resist loses nitrogen and generates a highly reactive nitrene, which undergoes a series of reactions that result in the cross-linking of the resin. New types of resists include polyimides, polyamic acids, photosensitive polyimide precursors, SU-8 (an epoxy-based transparent photoresist). All the resists are deposited through spin coating, which is of primary importance to the effectiveness of pattern transfer.

(c) Development

The development of the resin to form microelectrode arrays is mostly based on the "lift-off process" (164). A solvent dissolves the remaining soluble positive photoresist underneath the metal, starting at the edge or lip of the unexposed photoresist and lift off the metal in the process (Figure 10.13). When the photoresist is removed, all metal on top of the photoresist strip strips off automatically while metal on the top of the photoresist lines stays.

Photolithographically patterned gold microelectrodes have been used extensively (165). Pishko *et al.* reported recently the fabrication of glucose, lactate, and pyruvate sensor arrays by depositing electrostatically complexed monolayers on lithographically patterned individually addressable, gold microelectrodes. Standard photolithographic techniques combined with metal deposition were used to fabricate gold arrays of both SiO_2/Si and flexible Mylar substrates.

Reaction Ion Etching is another possibility for the development of photolithographically treated surfaces (Figure 10.14). It is based on insulating a silicon wafer by growing a high-quality silicon dioxide (SiO_2) layer. A semiconductor interface like silicon is often
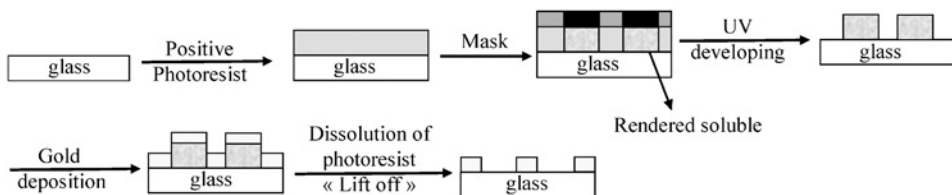

Figure 10.13   Gold microelectrode array made using photolithography (positive resin) and lift off. (for colour version: see colour section at the end of the book).
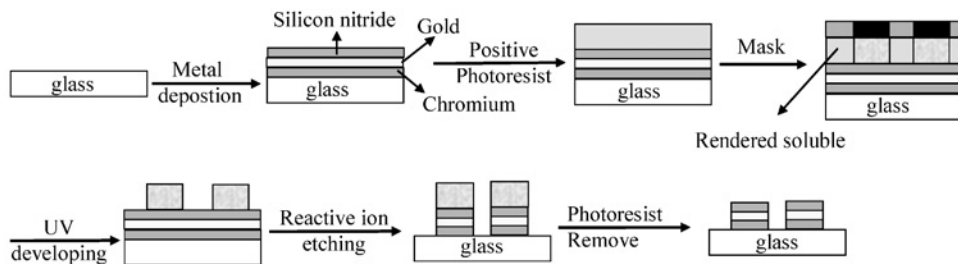

Figure 10.14   Photolithography and reactive ion etching. (for colour version: see colour section at the end of the book).

preferred over glass as it is perfectly flat and withstands the subsequent processing steps. Onto the SiO_2, a thin metal film (10–100 nm) is deposited followed by deposition of an insulating film, Si_3N_4, on top of the metal using plasma chemical vapor deposition (CVD). This multilayer surface is modified with a photoresist, covered with a photomask, exposed to UV light, and developed. The area, which is not protected with resin, is exposed to reactive ion etching to etch away the top insulator and the metal. The advantage of reactive ion etching is that the patterns have extremely sharp and vertical steps.

10.4.3.2   Other lithographic techniques (X-ray, electron-beam, ion-beam)

The improvement in optical resolution can be achieved either by increasing the numerical aperture or by reducing the wavelength of the illuminating light. This is a consequence of equation 10.7. The theoretical resolution of an optical system for projection printing is limited by Rayleigh diffraction:

$$R = k_1 \lambda / \text{NA} \tag{10.7}$$

where λ is the wavelength of the illumination system, NA is the numerical aperture of the lens system, and k_1 is a constant dependent on the imaging technology and process control but typically must be >0.7 for adequate production yield.

The most likely technology to push beyond photolithography is X-ray lithography. X-ray lithography is superior to optical lithography because of the use of shorter wavelength and a very large depth of focus. UV photons are scattered at all interfaces, leading to standing waves and proximity effects, X-rays are absorbed but do not scatter. Furthermore, in comparison to electron lithography and ion-beam lithography, no charged particles are directly involved thus eliminating the need for the use of vacuum. There are, however, two major limitations. One is the low sensitivity of the photoresists (PMMA, PGMA (poly(glycidyl methacrylate-co-ethyl acrylate)) to X rays as well as the high cost of sufficiently bright X-ray sources. The second is the mask making, which basically consists of a pattern of X-ray absorbing materials (like gold) on a substrate transparent to X-rays (Ti, Si, SiC, BE). Structures of about 30 nm are now routinely fabricated (161).

Methods based on writing with particles (electrons or ions) rather than photons accomplish the same task. Focused electron beams (electron beam lithography), beyond observing samples as in scanning electron microscopy (SEM) or transmission electron microscopy (TEM), can be used to form patterned nanostructures in an electron sensitive resist film, such as PMMA (166). Interaction of the electron beam with the resist causes local changes in its solubility, and in the case of PMMA, the electrons induce local chain scission and formation of micropores that cause the material to be soluble in a developer, such as methylisobutyl ketone and 2-propanol (164). Some of its attractive features are that no mask is needed, that precise control of the energy to a resist-coated wafer (0.0005 nm for 50 keV) is possible, the ability to register accurately over small areas of a wafer, a large depth of focus because of continuous focusing over topography. However, electrons also need to be held in vacuum and scatter in solids, limiting practical resolution to dimensions greater than 10 nm.

In contrast, ion-beam lithography has a better resolution than electron beam lithography because the secondary electrons produced by an ion beam are of lower energy and have a shorter diffusion range so that hardly any back scattering occurs. The ion-beam spot has the

smallest possible size and is reaching 8 nm. It offers direct writing and masking fabrication opportunities. Ions (H^+, He^{2+}, Ar^+) react with the substrate allowing a greater variety of surface modifications, such as patterned doping.

10.4.3.3 Soft lithography

Soft lithography is the collective name for a set of lithographic techniques: replica modeling (REM), micromolding in capillaries (MIMIC), microtransfer molding (μTM), solvent-assisted micromolding (SAMIM), near-field conformal photolithography using an elastomeric phase-shifting mask (which has been developed as an alternative to photolithography and replication technology for micro- and nanofabrication), and microcontact printing (μCP). These techniques have in common the use of a patterned elastomer as the mold/stamp/mask (Figure 10.15) to generate/transfer patterns on solid interfaces. The elastomer usually used is poly(dimethoxysiloxane) (PDMS). Soft lithography offers immediate advantages over photolithography in applications where patterning of nonplanar substrates or large area patterning are the main concerns. For an excellent review on soft lithography, see Xia *et al.* (161). μCP has also been used for the construction of microelectrode arrays.

(a) Soft lithography: microcontact printing

The technique of μCP is a routine way of fabricating chemical patterns with micrometer dimensions (161, 167, 168). Being a "dry" process, it only involves transient contact between a gold surface and an inked "stamp". No liquid drops are present that might influence the quality of the film. μCP has mainly been developed with self-assembled monolayers (SAM) of alkanethiolates on gold (169), silver (170), and copper (171). The procedure for carrying out μCP is rather simple and is shown in Figure 10.15 together with the formation of the stamp.

The technique requires stamps generated by casting PDMS against a "master" consisting of a surface having the desired pattern in low relief (this gives a low relief pattern on the surface (Figure 10.15). The master can be fabricated photolithographically in thin PMMA films supported on silicon wafers, provided the mask required for photolithography is available (167). Chrome mask generation is too expensive and slow to make this method practical for exploratory work requiring microfabrication. "Rapid prototyping", a technique for the generation of masks developed by Whitesides is an alternative. It uses high-resolution printing to make photo masks generating lines of 20–50 μm width (172). Another method that does not require the generation of conventional photo masks and is
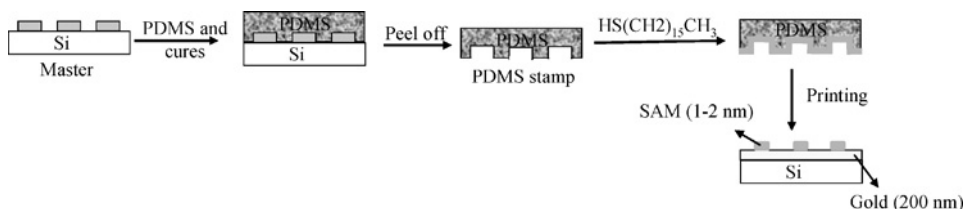

Figure 10.15 Schematic procedure for micro-contact printing. (for colour version: see colour section at the end of the book).

capable of resolution higher than rapid prototyping is laser ablation of thin polymer films (173). Whitesides has developed an inexpensive bench top technique for the fabrication of PDMS stamps using laser ablation of dye-doped thin polymer films with a low power visible laser yielding features as small as 1 μm. The PDMS stamp is then inked with an appropriate solution, often an alkanethiol, because it forms a very stable and organized monolayer on gold (174). This chemically modified stamp is brought into contact with the gold substrate as seen in Figure 10.15, and the ink molecules are transferred to those regions of the substrate that contact the stamp. The success of μCP relies on the conformal contact between the stamp and the surface of the substrate, on the rapid formation of highly ordered monolayers (<1 sec), and on the autophobicity of the SAM, which effectively blocks the reactive spreading of the ink across the surface. Another advantage of microcontact patterning is that it is a parallel method and SAMs can be formed over relatively large surfaces in a single process. It is thus a useful tool for the fabrication of microelectrode arrays. Figure 10.16 shows a variety of micropatterns on gold using μCP. Figure 10.16A shows the friction force image of a microelectrode array formed using hexadecylmercaptane ($(HS(CH_2)_{15}CH_3)$ stamped using μCP onto gold (41). The key point of SAM-based microelectrodes is that the closely packed SAM terminated with hydrophobic functional groups can efficiently block electron transfer and mass transfer between the gold substrate and the redox couple in solution.

10.4.5   Etching techniques

A number of subtractive and/or additive processes, where material is removed/added to a device in a selective manner, precede lithographic processes. One way of removing material for the construction of electrode arrays is through etching. Reactive-ion etching has
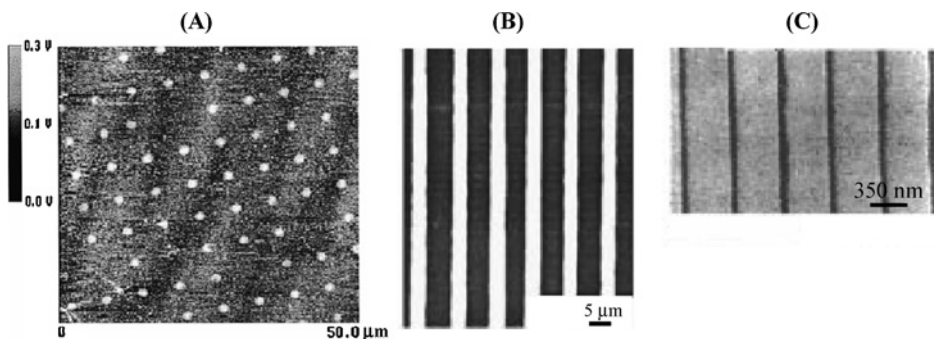
Figure 10.16   Microcontact printing (μCP): (A) friction force image of the prepared SAM-based microelectrode array 1 μm in diameter and 5 μm in pitch (41); (B) optical micrograph of lines patterned by stamping hexadecanethiol onto gold, followed by selective etching of gold. The patterns were generated by stamping hexadecanethiol onto a gold surface, followed by selective etching of the gold. Stamps used in generating these patterns were obtained via ablation through an objective (80×) and with a laser scan rate of 10 mm min^{-1}, power 10 mW. The white regions correspond to the unetched gold (167), and (C) array of 35 nm trenches fabricated in gold by μCP with hexadecanethiol (175).

been discussed. However, subtractive etching techniques range from wet etching, electro-chemical etching, photo-electrochemical etching to focused ion-beam milling, plasma etching, laser machining, ultrasonic drilling, and mechanical methods (160).

Chemical etching has been widely used for the fabrication of three-dimensional micro-electrode arrays. These kinds of electrode array configurations have been widely used to explore and assess intracortical brain activity (176). It is widely accepted that the cerebral cortex provides the easiest access to motor intent and sensory perception and is thus an attractive region for interfacing potential future devices for restoring neurological functions lost due to degenerative muscular diseases, strokes, or spinal cord injury (177). Much is still unknown about the generation of different motor behaviors, but it has been recognized that for clinical applications of such "brain-machine" interfaces, the activities of hundreds of thousands of neurons must be simultaneously sampled. A three-dimensional electrode array allows capturing neural signals from a collection of recording sites with a pre-selected spatial distribution. Two well-known approaches include the development of microelectrode arrays at the University of Utah (178, 179) and at the University of Michigan (180). Fofonoff reported the fabrication of a three-dimensional array by electrical discharge machining followed by chemical etching (181). To reduce the dimensions of the micromachined array, it was placed into a hot HCl bath heated close to its boiling point (Figure 10.17A). Electroplating with gold followed by platinum and final electrical insulation into parylene formed an array of platinum-coated electrodes (Figure 10.17B).

A rather different approach for the fabrication of three-dimensional electrode arrays is based on the use of optical imaging fiber arrays. An imaging fiber array has thousands of individual optical fibers (diameter of 3–4 μm) melted and drawn together in a coherent way. This imaging fiber can be used as a platform for the construction of a three-dimensional electrode array through chemical etching of the optical fibers. In the case of a silica fiber, the optical fiber is chemically etched in one-step procedure by dipping the fiber array into a solution of hydrofluoric acid (160) and ammonium fluoride (NH_4F) buffer (34, 182). The fiber's etch rate is dependent on the dopant concentration in the fiber and the concentration of the acid solution. In the case of the fibers used by Walt *et al.*, etching occurs at different rates between the pure SiO_2 of the fiber cladding and the GeO_2 doped SiO_2 of the core (Figure 10.17B1). The chemical reaction of SiO_2 and GeO_2 with HF acid can be summarized by reactions (10.8)–(10.10). The fluorosilicic acid (H_2SiF_6)
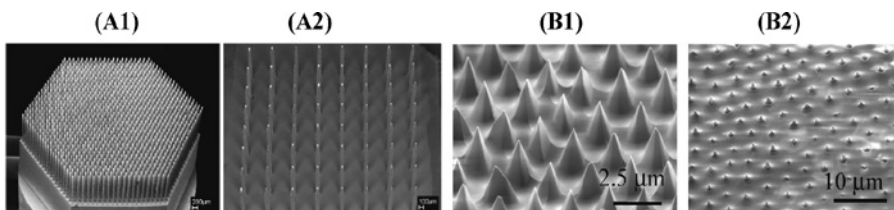
Figure 10.17   Microelectrodes array formed through chemical etching. (A1) SEM of an 1141-electrode titanium alloy electrode array, (A2) SEM image of a parylene-coated assembly of platinum-coated electrodes (181), (B1) SEM of an etched optical imaging fiber bundle, and (B2) SEM of a with gold covered and with electrophoretic paint insulated microelectrode array (with permission from reference (34)).

and the hexafluorogermanic acid (H_2GeF_6) is produced either directly (reactions (10.8a) and (10.8b)) or as outlined by reactions (10.9)–(10.11).

$$SiO_2 + 6HF \rightarrow H_2SiF_6 + 2H_2O \tag{10.8a}$$

$$GeO_2 + 6HF \rightarrow H_2GeF_6 + 2H_2O \tag{10.8b}$$

$$SiO_2 + 4HF \rightarrow SiF_4 + 2H_2O \tag{10.9a}$$

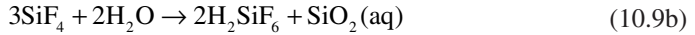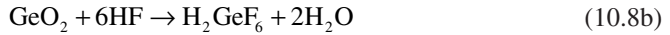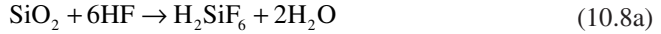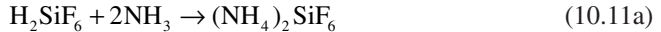$$3SiF_4 + 2H_2O \rightarrow 2H_2SiF_6 + SiO_2(aq) \tag{10.9b}$$

$$GeO_2 + 4HF \rightarrow GeF_4 + 2H_2O \tag{10.10a}$$

$$3GeF_4 + 2H_2O \rightarrow 2H_2GeF_6 + GeO_2(aq) \tag{10.10b}$$

If an ammonium fluoride buffered etching solution is used, there is a further possible dissolution step involved, which arises from the involvement of ammonic ionized from the solution (reactions (10.11a) and (10.11b)).

$$H_2SiF_6 + 2NH_3 \rightarrow (NH_4)_2SiF_6 \tag{10.11a}$$

$$H_2GeF_6 + 2NH_3 \rightarrow (NH_4)_2GeF_6 \tag{10.11b}$$

It is the difference in the solubility of the resultant $(NH_4)_2SiF_6$ and $(NH_4)_2GeF_6$, which leads to the difference in etching rates between the core and cladding. The tip cone angle is thus primarily a function of the etching solution and the GeO_2 doping level of the fiber core, while the temperature, the type, and concentration of the acid used, and the etching time are crucial for the optical and geometrical characteristics (such as cone angle and aperture diameter) of the tips formed. An ordered array of individual microelectrodes (6 µm center-to-center spacing) was fabricated by coating such a chemically etched imaging fiber bundle with gold and insulating the base of the fiber array with an electrophoretic paint. Electrophoretic paints have been shown to be useful for the fabrication of microelectrodes (183, 184). The electrophoretic paint consists mainly of two types of resins: polyacrylates and polyurethanes, where the cross-linking reaction is between the isocyanate group on the urethane resins and the hydroxyl groups in the polyacrylates. The principle mechanism of deposition is by depletion of hydrogen ions at the cathode via application of a positive DC voltage between the cathode (fiber bundle) and the anode (Cu wire). The resulting increase in pH destabilizes the cationic resin emulsion and the resin loses the colloidal condition and deposits onto the cathodic surface. Curing the fiber subsequently at 200 °C results in the shrinking of the deposited film and insures that the tip apex is not covered (Figure 10.17B2).

10.5   ELECTROCHEMICAL CHARACTERISATION OF MICROELECTRODE ARRAYS

Microelectrode arrays are generally characterized using a combination of voltammetry, SEM, and atomic force microscopy (185, 186). In addition to these techniques, other methods are reported which have been shown to be important in characterizing *in situ* the

electrochemical reactivities of ensembles of microelectrodes operating at the same potential or addressed individually.

10.5.1   Chronoamperometry and cyclic voltammetry

For a microelectrode array, chronoamperometric responses are complex and depend on the time frame of the experiment and the limiting behaviors described in section 10.3.1 (26). In the case of a regular ensemble of electrodes, the general trend of the chronoamperometric response is well known. At short times, the array behaves as individual electrodes and the response to a potential step shows planar diffusion (Cottrellian behavior with dependence of the current as $1/\sqrt{\tau}$) since no interference from overlapping diffusion occurs. At longer times, this behavior changes to a mixed regime where hemispherical diffusion prevails and this regime is finally converted again to one of planar diffusion. In this last case, the diffusion layers fully overlap and the entire array behaves as a macroelectrode whose area is equal to the total geometric surface area (see Section 10.3.1).

An analytical expression for the current was provided by Shoup and Szabo (106) for an infinite number of microdisk interfaces operating at the same potential in a hexagonal array:

$$f(\tau,\theta) = \frac{i}{4nFrDC^*} = \frac{\sqrt{\pi}}{2\sqrt{\tau}} + \frac{\pi}{4} + \left(1 - \frac{\pi}{4}\right)\exp\left[\frac{-B\theta^2(3-2\theta)}{\sqrt{\tau}}\right]$$

$$- \exp\left[-\frac{\dfrac{\sqrt{\pi}}{2}\left(\dfrac{\theta}{1-\theta}\right) + B\left(1-\dfrac{\pi}{4}\right)\theta^2(3-2\theta)}{\sqrt{\tau}}\right]\left(1 + \frac{3\sqrt{\pi}}{2\tau}\frac{\theta^3}{(1-\theta)}\right)^{-1} \qquad (10.12)$$

where τ is the dimensionless time with $\tau = 4Dt/r^2$, θ the array coverage with θ - $(2r/d)^2$, r the radius of the microdisks, d the center-to-center distance between microdisks, and B a constant equal to 0.7823. At short times, the predicted currents follow the Cottrell equation given for linear diffusion to the area of a single microdisk (i.e., πr^2), while at longer times, they converge to the Cottrell equation corresponding to linear diffusion to the total geometric area (i.e., $\pi d^2/4$). The characteristic time corresponding to a nonlinear to a linear transition from when diffusion layers overlap depends on both the size of the individual microelectrodes and their packing in the array as well as on the diffusion coefficient of redox species. This time t_c can be evaluated by (106)

$$t_c = \frac{(d/2 - r)^2}{6D} \qquad (10.13)$$

However, equation 10.13 is not always experimentally appropriate (187) and gives only a crude estimation of the transition time t_c when individual diffusion layers begin to overlap according to the packing density of the array. Similar results have been also derived from a simple analytical approach to hexagonal, square, and random arrays (21). It must be emphasized that all these approaches remain valid over a specific range of parameters

resulting from particular assumptions or approximations (see Section 10.3.1). For example, numerical simulations of chronoamperometric responses of infinite arrays (110) showed that equation 10.12 was valid only for values of θ exceeding 0.9. The electrochemical properties depend strongly on the way the microelectrodes are packed as arrays of recessed microelectrodes behave differently from arrays of inlaid electrodes in the short and medium time domains (110).

The interpretation of the response of an assembly of microelectrodes to a cyclic voltammetric waveform is more complicated than in the case of chronoamperometry. When applied to microelectrode arrays, it is mainly used in the steady-state limit. From an electroanalytical point of view, the major issue is to choose an appropriate scan rate v to ensure steady-state diffusion at the array interface. If the scan rate is not properly chosen, a peak-shaped voltammogram is observed whose characteristics can be derived only from simulations (188). Figure 10.18 shows simulated cyclic voltammograms obtained at an infinite number of microdisks ($r = 10$ μm) in a hexagonal array with d/r ranging from 3 to 100 and d ranging from 20 to 1000 μm.

Two characteristic polarization curves can be observed. In the case of high d/r ratios, a sigmoidal shape is related to the individual mipcrodisk electrode behavior (hemispherical diffusion). As in the case of low d/r ratios, a peak-shaped voltammogram is obtained corresponding to linear diffusion. For intermediate d/r ratios, a mixed diffusion
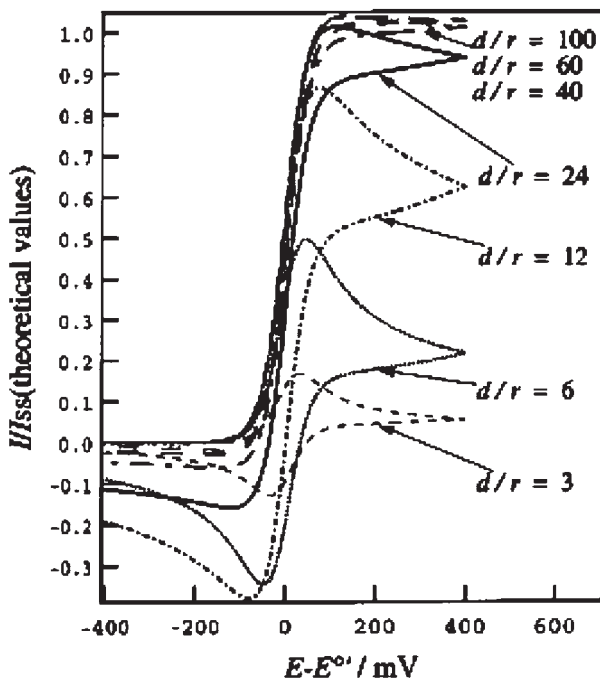

Figure 10.18 Simulated cyclic voltammograms obtained at an infinite number of microdisks in a hexagonal array having various interelectrode (center-to-center) distance, d. $d/r = 3$–100, $v = 10$ mV sec^{-1}, $r = 10$ μm, $D = 10^{-7}$ cm^2 sec^{-1} (with permission from reference (188)).

regime takes place where the current slowly increases with d/r and the peak separation widens. Moreover, the peak-to-peak separation becomes larger in the same way as when the apparent electron transfer process is lowered, even if a Nernstian system is assumed during simulation. The characteristic scan rate v from which a steady-state voltammogram is observed can be easily derived from equation 10.12 as the equivalency in voltammetry between time and scan rate is straightforward (i.e., $t_c = RT/Fv$). This behavior has been predicted by Amatore *et al.* (14) for charge transfer at partially blocked electrodes (see Section 10.3.1). The shapes and characteristics of the voltammograms can be deduced from a zone diagram (Figure 10.19), which defines four main domains where different characteristic behaviors are encountered. Vertical frontiers delimit the linear and spherical diffusion fields. From the upper side to the lower side, a distinction is made between voltammograms exhibiting either a fast electron transfer or an apparent quasi-irreversible electron transfer. This zone diagram shows clearly the strong influence of the fractional coverage or packing density of the array on the apparent standard rate constant of the electrochemical reaction. It can be easily derived for a hexagonal array of microdisk electrodes with the assumption of disk inactive sites rather than hexagonal ones (188).
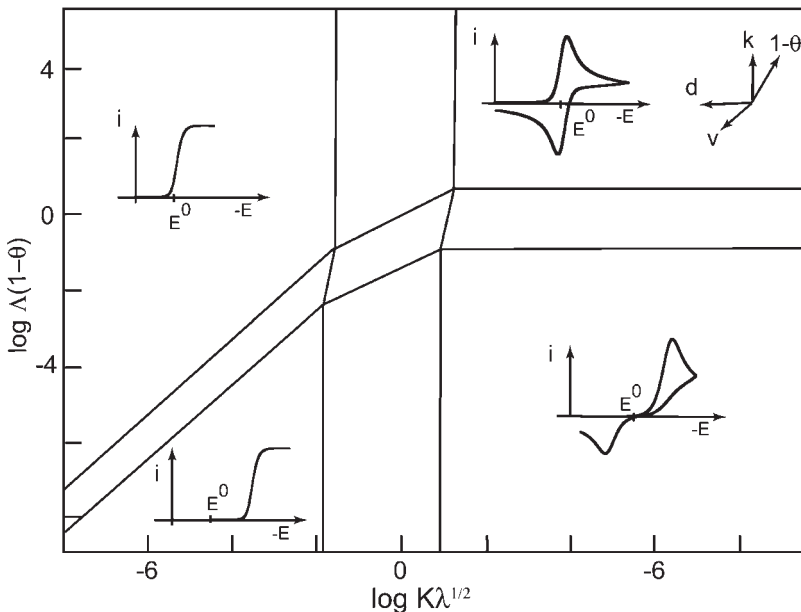
Figure 10.19   Zone diagram representing the main characteristics of cyclic voltammograms as a function of two dimensionless parameters, $K\lambda^{1/2}$ and $\Lambda(1-\theta)$ with $K\lambda^{1/2} = [(1-\theta)/\theta][(8D/d^2)\theta^{-1}(1-\theta)^{-1}/\ln[1+0.27(1-\theta)^{-1/2}]]^{1/2}t_c^{1/2}$ and $\Lambda(1-\theta) = k(t_c/D)^{1/2}(1-\theta)$. θ represents the fractional coverage of the insulating sites and is defined as $\theta = S_{ins}/(S_{ins}+S_{act})$ with S_{ins} and S_{act} the insulating and electroactive surface areas, respectively. k is the standard rate constant for the electron transfer at the active site. $t_c = RT/Fv$ with v the scan rate. Adapted from reference (14).

10.5.2 Scanning electrochemical microscopy

Scanning electrochemical microscopy (SECM) is commonly used to characterize different substrates and microelectrodes as well as to image their interfaces (189). For a more detailed discussion about SECM see Chapter 12. In comparison to conventional microscopies, this method gives valuable information regarding the conductivity, connectivity, and reactivity of microelectrode arrays (190). It can be used not only to map microelectrode arrays or track patterns but also to determine at the same time the integrity of the insulator coatings. Different SECM modes can be used depending on whether the microelectrodes in the array and the tips used for imaging the surface are reciprocally biased or unbiased. The feedback and the substrate generation/tip collection (SG/TC) modes of SECM were found to address each of these issues (190). The features of these two SECM modes have found to be particularly useful when random microelectrode arrays are being fabricated and characterized.

10.5.3 Optical microscopy

Information about the geometry, homogeneity, and morphology of array surfaces may be obtained from scanning methods, like AFM, STM, SECM, or SEM. However, these methods are not capable of giving direct evidence of the electrochemical activities of microelectrodes in arrays. Except for SECM, one way to overcome this difficulty is to detect optically the ECL initiated on each microelectrode. Indeed, by placing the microelectrode array under an optical microscope fitted with a high sensitivity CCD camera, ECL images can be acquired from the focal plane, which are directly correlated to the electrochemical activities of each microelectrode of the array (34). Furthermore, according to the mechanism of the ECL reaction involved, the size of the individual diffusion layers can be evaluated from the size of the ECL spots, which in turn, gives an estimation of the electrode dimension. The resolution achieved by this method allows the imaging of sub-micrometer electrodes.

Another way to characterize the electrochemical activity of microelectrode arrays is to map the electroactive species generated at each electrode by confocal Raman spectroscopy. Indeed, the use of confocal signal detection enables Raman spectroscopic measurements of very small sample volumes (even down to a few μm^3). Applied to a microelectrode array, it provides a statistical picture of the distribution of active sites on the array (60). As in the case of SECM, these two optical methods are particularly useful to verify if individual diffusion layers do not overlap and if the microelectrodes in the array are diffusely independent, particularly for random microelectrode arrays.

10.6 CONCLUSION AND PROSPECTS

Microelectrode arrays have been widely discussed in the literature from theoretical and practical viewpoints and these have led to a better understanding of typical characteristics encountered during their operation. Such devices offer advantages in a number of areas of

investigation. The main achievement in recent years has been the development of reliable methods for fabricating microelectrode arrays. The availability of these methods should open the field for further studies and development of novel applications in physical electrochemistry, imaging science, analytical science, and within the medical and biosensing fields.

Current research is also directed at decreasing the dimensions of the individual electrodes in the array in order to produce nanoelectrode arrays. In these nanoelectrode arrays, the critical dimension is decreased to the same order as the thickness of the electrical double layer or the molecular size of redox species, and the experimental behavior starts to deviate from extrapolations of behavior at larger electrodes. This point may be viewed as the separation point between nanoelectrodes and microelectrodes arrays (191).

REFERENCES

1. M. A. Dayton, J. C. Brown, K. J. Stutts, R. M. Wightman, *Anal. Chem.* **52**, 946 (1980).
2. R. M. Wightman, *Science* **240**, 415 (1980).
3. J. Cassidy, J. Ghoroghchian, F. Sarfarazi, J. J. Smith, S. Pons, *Electrochim. Acta* **31**, 629 (1986).
4. R. Cieslinski, N. Armstrong, *Anal. Chem.* **51**, 565 (1979).
5. O. Contamin, E. Levart, *J. Electroanal. Chem.* **136**, 259 (1982).
6. L. J. Magee, J. Osteryoung, *Anal. Chem.* **61**(18), 2124 (1989).
7. R. M. Penner, C. R. Martin, *Anal. Chem.* **59**, 2625 (1987).
8. S. G. Weber, *Anal. Chem.* **61**, 295 (1989).
9. T. Gueshi, K. Tokuda, H. Matsuda, *J. Electroanal. Chem.* **89**, 247 (1978).
10. H. Reller, E. Kirowaeisner, E. Gileadi, *J. Electroanal. Chem.* **138**(1), 65 (1982).
11. H. Reller, E. Kirowaeisner, E. Gileadi, *J. Electrochem. Soc.* **131**(3), C110 (1984).
12. H. Reller, E. Kirowaeisner, E. Gileadi, *J. Electroanal. Chem.* **161**(2), 247 (1984).
13. D. E. Weisshaar, D. E. Tallman, *Anal. Chem.* **55**, 1146 (1983).
14. C. Amatore, J. M. Saveant, D. Tessier, *J. Electroanal. Chem.* **147**(1–2), 39 (1983).
15. J. L. Anderson, K. K. Whiten, J. D. Brewster, T.-Y. Ou, W. K. Nonidez, *Anal. Chem.* **57**, 1366 (1985).
16. A. Aoki, T. Matsue, I. Uchida, *Anal. Chem.* **62**(20), 2206 (1990).
17. K. Aoki, *J. Electroanal. Chem.* **270**, 35 (1989).
18. I. F. Cheng, C. R. Martin, *Anal. Chem.* **60**, 2163 (1988).
19. I. F. Cheng, L. D. Whiteley, C. R. Martin, *Anal. Chem.* **61**(7) 762 (1989).
20. C. E. Chidsey, B. J. Feldman, C. Lundgren, R. W. Murray, *Anal. Chem.* **58**(3), 601 (1986).
21. B. J. Scharifker, in *Microelectrodes: Theory and Applications*, M. I. Montenegro, M. A. Queiros, J. L. Daschbach, Eds., NATO ASI Series Kluwer Academic Publishers: Dordrecht, 1991, Vol. 4, p. 227.
22. B. R. Scharifker, *J. Electroanal. Chem.* **240**, 61 (1988).
23. B. R. Scharifker, *J. Electroanal. Chem.* **458**(1–2), 253 (1998).
24. B. J. Seddon, H. H. Girault, M. J. Eddowes, *J. Electroanal. Chem.* **266**, 227 (1989).
25. N. Sleszynski, J. Osteryoung, M. Cartier, *Anal. Chem.* **56**(2), 130 (1984).
26. C. Amatore, in *Physical Electrochemistry*, I. Rubinstein, Ed., Marcel Dekker: New York, 1995, p. 131.
27. T. A. Postlethwaite, J. E. Hutchison, R. Murray, B. Fosset, C. Amatore, *Anal. Chem.* **68**(17), 2951 (1996).

28. G. Kindlman, R. A. Normann, A. Badi, J. Bigler, C. Keller, R. Coffey, G. M. Jones, C. R. Johnson, *BISTI 2003 Symposium, Digital Biology: The Ermging Paradigm*, www.bisti.nih.gov/2003 meeting (2003).

29. W. L. Caudill, J. O. Howell, R. M. Wightman, *Anal. Chem.* **54**, 2532 (1982).

30. P. Bindra, A. P. Brown, M. Fleischmann, D. Pletcher, *J. Electroanal. Chem.* **58**, 31 (1975).

31. P. Bindra, J. Ulstrup, *J. Electroanal. Chem.* **140**, 131 (1982).

32. E. Sabatini, I. Rubinstein, *J. Phys. Chem.* **91**, 6663 (1987).

33. E. Sabatini, I. Rubinstein, R. Maoz, J. Sagiv, *J. Electroanal. Chem.* **219**, 365 (1987).

34. S. Szunerits, J. M. Tam, L. Thouin, C. Amatore, D. R. Walt, *Anal. Chem.* **75**(17), 4382 (2003).

35. S. Szunerits, D. R. Walt, *Anal. Chem.* **74**(7), 1718 (2002).

36. S. Szunerits, D. R. Walt, *Chemphyschem* **4**(2), 186 (2003).

37. A. Chovin, P. Garrigue, P. Vinatier, N. Sojic, *Anal. Chem.* **76**(2), 357 (2004).

38. M. DeAbreu, W. C. Purdy, *Anal. Chem.* **59**(1), 204 (1987).

39. H. Ecken, S. Ingebrandt, M. Krause, D. Richter, M. Hara, A. Offenhauser, *Electrochim. Acta* **48**, 3355 (2003).

40. G. C. Fiaccabrino, M. Koudelkahep, S. Jeanneret, A. Vandenberg, N. F. Derooij, *Sens. Actuat. B Chem.* **19**(1–3), 675 (1994).

41. H. X. He, Q. G. Li, Z. Y. Zhou, H. Zhang, S. F. Y. Li, Z. F. Liu, *Langmuir* **16**(25), 9683 (2000).

42. F. Heer, W. Franks, A. Blau, S. Taschini, C. Ziegler, A. Hierlemann, H. Baltes, *Biosens. Bioelectron.* **20**, 358 (2004).

43. Y. Iwasaki, O. Niwa, M. Morita, H. Tabei, P. T. Kissinger, *Anal. Chem.* **68**(21), 3797 (1996).

44. S. P. Kounaves, W. Deng, P. R. Hallock, G. T. A. Kovacs, C. W. Storment, *Anal. Chem.* **66**(3), 418 (1994).

45. H. J. Lee, C. Beriet, H. H. Girault, *J. Electroanal. Chem.* **453**, 211 (1998).

46. J. Pei, M. L. Tercier-Waeber, J. Buffle, G. C. Fiaccabrino, M. Koudelka-Hep, *Anal. Chem.* **73**, 2273 (2001).

47. B. J. Seddon, C. F. Wang, W. F. Peng, X. J. Zhang, *J. Chem. Soc.-Faraday Trans.* **90**(4), 605 (1994).

48. C. Amatore, C. Sella, L. Thouin, *J. Phys. Chem. B* **106**(44), 11565 (2002).

49. I. B. Svir, A. I. Oleinick, R. G. Compton, *J. Electroanal. Chem.* **560**(2), 117 (2003).

50. C. Amatore, M. Belotti, Y. Chen, E. Roy, C. Sella, L. Thouin, *J. Electroanal. Chem.* **573**, 333 (2004).

51. C. Amatore, L. Thouin, J.-S. Warkocz, *Chem. Eur. J.* **5**(2), 456 (1999).

52. I. A. Arkoub, C. Amatore, C. Sella, L. Thouin, J. S. Warkocz, *J. Phys. Chem. B* **105**(37), 8694 (2001).

53. B. Fosset, C. A. Amatore, J. E. Bartelt, A. C. Michael, R. M. Wightman, *Anal. Chem.* **63**(4), 306 (1991).

54. T. V. Shea, A. J. Bard, *Anal. Chem.* **59**(17), 2101 (1987).

55. C. Amatore, A. R. Brown, *J. Am. Chem. Soc.* **118**, 1482 (1996).

56. J. E. Bartelt, M. R. Deakin, C. A. Amatore, R. M. Wightman, *Anal. Chem.* **60**, 2167 (1988).

57. H. A. O. Hill, N. A. Klein, I. S. M. Psalti, N. J. Walton, *Anal. Chem.* **61**, 2200 (1989).

58. R. G. Compton, B. A. Coles, J. J. Gooding, A. C. Fisher, T. I. Cox, *J. Phys. Chem.* **98**, 2446 (1994).

59. J. H. Thomas, S. K. Kim, P. J. Hesketh, H. B. Halsall, W. R. Heineman, *Anal. Biochem.* **328**(2), 113 (2004).

60. L. J. Yang, Y. B. Li, G. F. Erf, *Anal. Chem.* **76**(4), 1107 (2004).

61. J. Senior, A. Shah, C. Monteux, V. De Biasi, *J. Pharm. Biomed. Anal.* **24**(5–6), 843 (2001).

62. R. Kurita, H. Tabei, Z. M. Liu, T. Horiuchi, O. Niwa, *Sens. Actuat. B Chem.* **71**(1–2), 82 (2000).

63. R. M. Blanchard, A. R. Noble-Luginbuhl, R. G. Nuzzo, *Anal. Chem.* **72**(7), 1365 (2000).

64. O. Niwa, R. Kurita, Z. M. Liu, T. Horiuchi, K. Torimitsue, *Anal. Chem.* **72**(5), 949 (2000).

65. M. P. Nagale, I. Fritsch, *Anal. Chem.* **70**(14), 2902 (1998).

66. M. Morita, O. Niwa, T. Horiuchi, *Electrochim. Acta* **42**(20–22), 3177 (1997).
67. M. Morita, O. Niwa, *Nat. Rev.* **8**(2), 77 (1996).
68. S. Hoshino, O. Niwa, H. Tabei, M. Takahashi, M. Morita, *Denki Kagaku* **64**(3), 195 (1996).
69. O. Niwa, *Electroanalysis* **7**(7), 606 (1995).
70. M. Paeschke, U. Wollenberger, C. Kohler, T. Lisec, U. Schnakenberg, R. Hintsche, *Anal. Chim. Acta* **305**(1–3), 126 (1995).
71. O. Niwa, T. Horiuchi, H. Tabei, *J. Electroanal. Chem.* **367**(1–2), 265 (1994).
72. O. Niwa, M. Morita, H. Tabei, *Electroanalysis* **6**(3), 237 (1994).
73. O. Niwa, H. Tabei, *Anal. Chem.* **66**(2), 285 (1994).
74. A. J. Bard, J. A. Crayston, G. P. Kittlesen, T. V. Shea, M. S. Wrighton, *Anal. Chem.* **58**(11), 2321 (1986).
75. J. A. Alden, M. A. Feldman, E. Hill, F. Prieto, M. Oyama, B. A. Coles, R. G. Compton, P. J. Dobson, P. A. Leigh, *Anal. Chem.* **70**(9), 1707 (1998).
76. K. Aoki, M. Morita, O. Niwa, H. Tabei, *J. Electroanal. Chem.* **256**, 269 (1988).
77. K. Aoki, M. Tanaka, *J. Electroanal. Chem.* **266**, 11 (1989).
78. B. J. Feldman, R. W. Murray, *Anal. Chem.* **58**(13), 2844 (1986).
79. B. J. Feldman, R. W. Murray, *Inorg. Chem.* **26**, 1702 (1987).
80. O. Niwa, M. Morita, H. Tabei, *Anal. Chem.* **62**(5), 447 (1990).
81. O. Niwa, Y. Xu, H. B. Halsall, W. R. Heineman, *Anal. Chem.* **65**, 1559 (1993).
82. O. Niwa, M. Morita, *Anal. Chem.* **68**(2), 355 (1996).
83. L. E. Fosdick, J. L. Anderson, *Anal. Chem.* **58**(12), 2481 (1986).
84. R. Merletti, D. Farina, M. Gazzoni, *J. Electromyogr. Kinesiol.* **13**, 37 (2003).
85. T. Masuda, H. Miyano, T. Sadoyama, *Electroencephalogr. Clin. Neurophysiol.* **56**, 597 (1983).
86. S. Szunerits, P. Garrigue, J.-L. Bruneel, L. Servant, N. Sojic, *Electroanalysis* **15**, 548 (2003).
87. T. E. McKnight, A. V. Melechko, D. W. Austin, T. Sims, M. A. Guillorn, M. L. Simpson, *J. Phys. Chem. B* **108**(22), 7115 (2004).
88. S. Fletcher, in *Microelectrodes: Theory and Applications*, M. I. Montenegro, M. A. Querios, J. L. Daschbach, Eds., Kluwer: Dordrecht, 1991, p. 342.
89. S. Fletcher, M. D. Horne, *Electrochem. Commun.* **1**(10), 502 (1999).
90. P. Connolly, G. R. Moores, W. Monagham, J. Shen, S. Britland, P. Clark, *Sens. Actuat.* **B6**, 113 (1992).
91. D. W. Deer, C. W. Toblas, *J. Electrochem. Soc.* **134**, 369 (1987).
92. M. G. Sullivan, H. Utomo, P. J. Fagan, M. D. Ward, *Anal. Chem.* **71**, 4369 (1999).
93. T. Livache, H. Bazin, P. Caillat, A. Roget, *Biosens. Bioelectr.* **13**, 629 (1998).
94. C. Berloment, M.-L. Tercier, J. Buffle, G. C. Fiaccabrino, M. Koudelka-Hep, *Anal. Chim. Acta* **329**, 203 (1996).
95. Q. Bai, K. D. Wise, *Trans. Biomed. Eng.* **48**(8), 911 (2001).
96. J. J. Pancrazio, J. P. P. Bey, D. S. Cuttino, J. K. Kusel, D. A. Borkholder, K. M. Shaffer, G. T. A. Kovacs, D. A. Stenger, *Sens. Actuat.* **B53**, 179 (1998).
97. N. H. E. Weste, K. Eshraghian, *Principles of Cmos Vlsi Design*, Addison Wesley: Reading, MA, 1994.
98. L. Berdondini, P. D. van der Wal, N. F. de Rooij, A. Koudelka-Hep, *Sens. Actuat. B Chem.* **99**(2–3), 505 (2004).
99. L. E. Fosdick, J. L. Anderson, T. A. Baginski, R. C. Jaeger, *Anal. Chem.* **58**, 2750 (1986).
100. K. Aoki, J. Osteryoung, *J. Electroanal. Chem.* **125**, 315 (1981).
101. T. Gueshi, K. Tokuda, J. Matsuda, *J. Electroanal. Chem.* **101**, 29 (1979).
102. W. Thormann, P. v. d. Bosch, A. M. Bond, *Anal. Chem.* **57**(14), 2764 (1985).
103. K. Tokuda, T. Gueshi, H. Matsuda, *J. Electroanal. Chem.* **102**(1), 41 (1979).

104. E. Levart, D. Schauhmann, E. Contamin, M. Etman, *J. Electroanal. Chem.* **70**, 117 (1976).

105. J. Lindemann, R. Landsberg, *J. Electroanal. Chem.* **30**, 79 (1971).

106. D. Shoup, A. Szabo, *J. Electroanal. Chem.* **160**(1–2), 19 (1984).

107. B. A. Brookes, T. J. Davies, A. C. Fisher, R. G. Evans, S. J. Wilkins, K. Yunnus, J. D. Wadhawan, R. G. Compton, *J. Phys. Chem. B* **107**, 1616 (2003).

108. T. J. Davies, B. A. Brookes, A. C. Fisher, K. Yunnus, S. J. Wilkins, P. R. Greene, J. D. Wadhawan, R. G. Compton, *J. Phys. Chem. B* **107**, 6431 (2003).

109. A. Szabo, R. Zwanzig, *J. Electroanal. Chem.* **314**, 307 (1991).

110. C. Beriet, R. Ferrigno, H. H. Girault, *J. Electroanal. Chem.* **486**(1), 56 (2000).

111. W. E. Morf, *Anal. Chim. Acta* **330**(2–3), 139 (1996).

112. S. D. Kolev, J. H. M. Simons, W. E. Vanderlinden, *Anal. Chim. Acta* **273**(1–2), 71 (1993).

113. B. Fosset, C. Amatore, J. Bartelt, R. M. M. Wightman, *Anal. Chem.* **63**, 1403 (1991).

114. A. I. Oleinick, I. B. Svir, C. Amatore, *J. Electroanal. Chem.* **553**, 49 (2003).

115. T. Horiuchi, O. Niwa, M. Morita, *J. Electroanal. Chem.* **142**(9), L146 (1995).

116. V. P. Menon, C. R. Martin, *Anal. Chem.* **67**, 1920 (1995).

117. M. P. Nagale, I. Fritsch, *Anal. Chem.* **70**, 2908 (1998).

118. D. M. Odell, W. J. Bowyer, *Anal. Chem.* **62**(15), 1619 (1990).

119. M. Ohtani, T. Sunagawa, S. Kuwabata, H. Yoneyyama, *J. Electroanal. Chem.* **396**, 97 (1995).

120. J. L. Anderson, L. A. Coury, J. Leddy, *Anal. Chem.* **70**(12), 516R (1998).

121. O. T. Guenat, J.-F. Dufour, P. D. van der Wal, W. E. Morf, N. F. de Rooij, M. Koudelka-Hep, *Sens. Actuat. B* **105**, 65 (2005).

122. J. J. Hickman, C. Zou, D. Ofer, P. D. Harvey, M. S. Wrighton, *J. Am. Chem. Soc.* **111**, 7271 (1989).

123. S. K. Kim, P. J. Hesketh, C. Li, J. H. Thomas, H. B. Halsall, W. R. Heinemann, *Biosens. Bioelectr.* **20**, 887 (2004).

124. G. P. Kittlesen, H. S. White, M. S. Wrighton, *J. Am. Chem. Soc.* **106**, 7389 (1984).

125. C. D. Merritt, B. L. Justus, *Chem. Mater.* **15**(13), 2520 (2003).

126. E. W. Paul, A. J. Ricco, M. S. Wrighton, *J. Phys. Chem.* **89**, 1441 (1985).

127. B. J. Seddon, M. J. Eddowes, A. Firth, A. E. Owen, H. H. J. Girault, *Electrochim. Acta* **36**(5–6), 763 (1991).

128. G. Sreenivas, S. S. Ang, I. Fritsch, W. D. Brown, G. A. Gerhardt, D. J. Woodward, *Anal. Chem.* **68**(11), 1858 (1996).

129. K. D. Sternitzke, R. L. McCreery, *Anal. Chem.* **62**(13), 1339 (1990).

130. H. Suzuki, *Electroanalysis* **12**(9), 703 (2000).

131. K. Tsunozaki, Y. Einaga, T. N. Rao, A. Fujishima, *Chem. Lett.* **5**, 502 (2002).

132. H. S. White, G. P. Kittlesen, M. S. Wrighton, *J. Am. Chem. Soc.* **106**, 5375 (1984).

133. H. P. Wu, *Anal. Chem.* **65**(11), 1643 (1993).

134. H. Xiong, J. D. Guo, K. Kurihara, S. Amemiya, *Electrochem. Commun.* **6**(6), 615 (2004).

135. R. M. Wightman, D. O. Wipf, in *Electroanalytical Chemistry*, A. J. Bard, Ed., Marcel Dekker: New York, 1989, Vol. 15, p. 267.

136. A. C. Barton, S. D. Collyer, F. Davis, D. D. Gornall, K. A. Lawa, E. C. D. Lawrence, D. W. Mills, S. Myler, J. A. Pritchard, M. Thompsonc, S. P. J. Higson, *Biosens. Bioelectr.* (2004).

137. J. Schwarz, H. Kaden, U. Enseleit, *Electrochem. Commun.* **2**, 606 (2000).

138. P. J. Welford, J. Freeman, S. J. Wilkins, J. D. Wadhawan, C. E. W. Hahn, R. G. Compton, *Anal. Chem.* **73**, 6088 (2001).

139. B. K. Davis, S. G. Weber, A. P. Sylwesert, *Anal. Chem.* **62**, 1000 (1990).

140. C. R. Martin, *Science* **266**, 1961 (1994).

141. G. L. Hornay, C. J. Patrissi, C. R. Martin, *J. Phys. Chem. B* **101**, 1548 (1997).

142. W. E. Williams, N. Giordano, *Rev. Sci. Instrum.* **55**, 410 (1984).

143. R. L. Fleischer, P. B. Price, R. M. Walker, *Nuclear Tracks in Solids*, University of California Press: Berkeley, CA, 1975.
144. P. P. Ngugen, D. H. Pearson, R. J. Tonucci, K. Babcock, *J. Electrochem. Soc.* **145**, 247 (1998).
145. G. E. Possin, *Rev. Sci. Instrum.* **41**, 772 (1970).
146. K. Hiruma, M. Yazawa, T. Katsuyama, K. Ogawa, K. Haraguchi, M. Koguchi, H. Kakibayashi, *J. Appl. Phys.* **77**, 447 (1995).
147. C. A. Huber, T. E. Huber, M. Sadoqi, J. A. Lubin, S. Manalis, C. B. Prater, *Science* **263**, 800 (1994).
148. C. R. Martin, *Adv. Mater.* **3**, 457 (1991).
149. C. R. Martin, *Acc. Chem. Res.* **28**, 61 (1995).
150. Y.-L. Tai, H. Teng, *Chem. Mater.* **16**, 338 (2004).
151. J. C. Hulteen, K. B. Jirage, C. R. Martin, *J. Am. Chem. Soc.* **120**, 6603 (1998).
152. S. Valizadeh, J. M. George, P. Leisner, L. Hultman, *Electrochim. Acta* **47**(6), 865 (2001).
153. B. B. Lakshmi, C. J. Patrissi, C. R. Martin, *Chem. Mater.* **9**, 2544 (1997).
154. S. A. Miller, V. Y. Young, C. R. Martin, *J. Am. Chem. Soc.* **123**, 12335 (2001).
155. P. C. Hidberg, P. F. Nealey, W. Helbig, G. M. Whitesides, *Langmuir* **12**, 5209 (1996).
156. Z. Hou, S. Dante, N. Abbott, P. Stroeve, *Langmuir* **15**, 3011 (1999).
157. S. Metzer, R. Resch, B. E. Koel, M. E. Thompson, A. Madhukar, A. A. G. Requicha, P. Will, *Langmuir* **17**, 1713 (2001).
158. A. Vaskelis, in *Coating Technology Handbook*, D. Satas, A. A. Tracton, Eds., Marcel Dekker: New York, 2001, p. 213.
159. G. O. Marrory, J. B. Hajdu, *Electroless Plating: Fundamentals and Applications*, American Electroplates and Surface Finishing Society: Orlando, FL, 1990, p. 29.
160. M. Madou, *Fundamentals in Microfabrication*, CRC Press: Boca Raton, FL, 1997.
161. Y. Xia, J. A. Rogers, K. E. Paul, G. M. Whitesides, *Chem. Rev.* **99**, 1823 (1999).
162. M. Hibbs, R. Kunz, M. Rothschild, *Solid State Technol.* **38**, 69 (1995).
163. M. Samuelsson, M. Atmgarth, C. Nylander, *Anal. Chem.* **63**(9), 931 (1991).
164. W. M. Moreau, *Semiconductor Lithography: Principles and Materials*, Plenum: New York, 1988.
165. A. F. Revzin, K. Sirkar, A. Simonian, A. V. Pishko, *Sens. Actuat.* **B81**, 359 (2002).
166. W. Xu, J. Wong, C. C. Cheng, R. Johnson, A. Scherer, *J. Vac. Sci. Technolo. B* **13**(6), 2372 (1995).
167. B. A. Grzybowski, R. Haag, N. Bowden, G. M. Whitesides, *Anal. Chem.* **70**, 4645 (1998).
168. A. Kumar, G. M. Whitesides, *Appl. Phys. Lett.* **63**, 2002 (1993).
169. A. Kumar, H. Biebuyck, G. M. Whitesides, *Langmuir* **10**, 1495 (1994).
170. Y. Xia, E. Kim, G. M. Whitesides, *J. Electrochem. Soc.* **143**, 10790 (1996).
171. Y. Xia, E. Koim, M. Mrksich, G. M. Whitesides, *Chem. Mater.* **8**, 601 (1996).
172. D. Quin, Y. Xia, G. M. Whitesides, *Adv. Mater.* **8**, 917 (1996).
173. M. A. Roberts, J. S. Rossier, P. Bercier, H. Girault, *Anal. Chem.* **69**, 2035 (1997).
174. A. Ulman, *Chem. Rev.* **96**, 1553 (1996).
175. H. A. Bibuyck, N. B. Larsen, E. Delamarche, B. Mitchel, *IBM J. Res. Dev.* **41**, 159 (1997).
176. M. A. Nicolelis, *Nature* **409**, 403 (2001).
177. Donoghue, *Nat. Neur. Rev.* **5**, 1085 (2002).
178. K. E. Jones, P. K. Campbell, R. A. Normann, *Ann. Biomed. Eng.* **20**, 423 (1992).
179. P. J. Rousche, R. A. Normann, *IEEE Trans. Biomed. Eng.* **7**, 56 (1999).
180. A. Hoogerwerf, K. Wise, *IEEE Trans. Biomed. Eng.* **41**, 1136 (1994).
181. T. A. Fofonoff, S. M. Martel, N. G. Hatsopoulos, J. P. Donoghue, I. W. Hunter, *IEEE Trans. Biomed. Eng.* **51**, 890 (2004).
182. P. Pantano, D. R. Walt, *Rev. Sci. Instrum.* **68**(3), 1357 (1997).
183. C. J. Slevin, N. J. Gray, J. V. Macpherson, M. A. Webb, P. R. Unwin, *Electrochem. Commun.* **1**, 282 (1999).

184. J. L. Conyers, H. S. White, *Anal. Chem.* **72**, 4441 (2000).

185. M. Wittkampf, K. Cammann, M. Amrein, R. Reichelt, *Sens. Actuat. B* **40**, 19 (1997).

186. R. Feeney, J. Herdan, M. A. Nolan, S. H. Tan, V. V. Tatasov, S. P. Kounaves, *Electroanalysis* **10**, 89 (1998).

187. W. S. Baker, R. M. Crooks, *J. Phys. Chem. B* **102**, 10 041 (1998).

188. H. J. Lee, C. Beriet, R. Ferrigno, H. H. Girault, *J. Electroanal. Chem.* **502**(1–2), 138 (2001).

189. A. J. Bard, M. V. Mirkin, *Scanning Electrochemical Microscopy*, Marcel Dekker: New York, 2001.

190. C. Zoski, N. Simjee, O. Guenat, M. Doudelka-Hep, *Anal. Chem.* **76**, 62 (2004).

191. C. Zoski, *Electroanalysis* **14**, 1041 (2002).

Part Three

TECHNIQUES

This page intentionally left blank

– 11 –

Classical Experiments

Guy Denuault, Maciej Sosna, and Kirsty-Jo Williams

School of Chemistry, University of Southampton,
Southampton, SO17 1BJ, UK

11.1   INTRODUCTION

This chapter focuses on a selection of key electrochemical techniques, chosen because they constitute the majority of experiments carried out in most laboratories, including research laboratories. Some less common methods have been included purely for pedagogical reasons, e.g. double potential step since it is one of the simplest reversal techniques. *Classical experiments* are broadly defined as those commonly found on commercial instruments, namely potential steps, potential sweeps, sweep and step combinations, AC impedance, microelectrodes and rotating disc electrodes. A section on numerical simulations is included since the availability of commercial software widens access to the powers of modelling. The chapter concludes with guidelines for troubleshooting electrochemical experiments, especially voltammetric ones, with conventional and microelectrodes. Many techniques including controlled current, polarography, hydrodynamic (e.g. flow cells) and spectroelectrochemical methods were considered to be too exotic and have been left out. With Part I of this handbook providing a solid theoretical background, this chapter only covers a brief reminder of the theoretical principles for each experiment considered.

Electrochemical experiments are always conducted under diffusion-controlled mass transport. This is achieved by (1) adding a large concentration of electrolyte to suppress the migration of ions due to the electrical field between the working and counter electrodes, (2) avoiding natural convection by completing the experiment under 30 s, (3) using controlled hydrodynamics to limit the diffusion layer thickness or (4) using microelectrodes to yield a true steady-state diffusion-controlled current before the onset of natural convection. Hence, all the cases presented involve the diffusion of the reactant towards and of the product away from the electrode. Unless stated otherwise, the model system considered is the one electron reduction of O to R where both are soluble and only O is initially present in solution. The theory is initially covered for diffusion control then extended to include the effect of electron transfer kinetics. Where appropriate, the effects of coupled chemical reactions are mentioned but not developed.

Handbook of Electrochemistry
Edited by C.G. Zoski

11.2   SELECTED EXPERIMENTAL TECHNIQUES

11.2.1   Potential steps

11.2.1.1   Principles

This section presents a selection of equations used in interpreting and predicting the experimental response of a simple electrochemical reaction to a step change in potential. For complete derivations and information on more complex systems, e.g. coupled chemical reactions, the reader should consult references (1–3).

In chronoamperometry, one observes the current–time behaviour of an electrochemical system after a potential step in a still solution. Consider a system where species O is electroinactive at E_i and the potential of the electrode is stepped to E_f (Figure 11.1a), where O is reduced in a simple charge transfer reaction: $O + e^- \rightarrow R$.

E_f is chosen so that the concentration of O at the electrode surface remains zero. The current (Figure 11.1b) is only due to the diffusion of O towards the electrode as illustrated in Figure 11.1c. The theoretical expression for the evolution of the concentration profile is obtained by solving Fick's second law of diffusion with appropriate boundary conditions. To derive the solution, one often uses the Laplace transform (2). For a planar electrode:

Mass transport equation:

$$\frac{\partial C_O(x,t)}{\partial t} = D_O \frac{\partial^2 C_O(x,t)}{\partial x^2} \tag{11.2.1}$$

Initial condition:

$$C_O(x \geq 0, 0) = C_O^* \tag{11.2.2}$$

Boundary conditions:

$$C_O(\infty, t > 0) = C_O^* \tag{11.2.3}$$
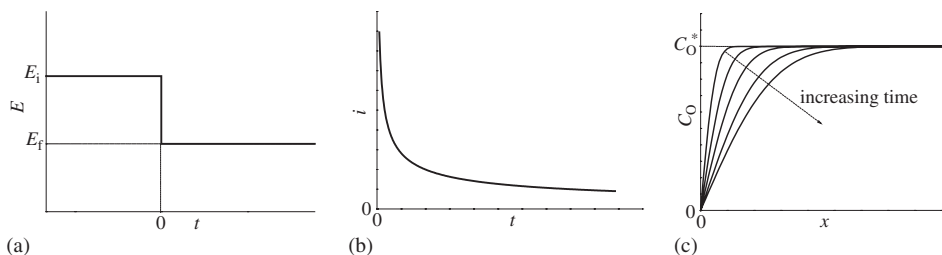
$$C_O(0, t > 0) = 0 \tag{11.2.4}$$

Figure 11.1   Potential step experiment to a planar electrode: (a) potential waveform, (b) current response and (c) concentration profile in the vicinity of the electrode.

Concentration profile:

$$C_O(x,t) = C_O^* \left[1 - \text{erfc}\left(\frac{x}{2(D_O t)^{1/2}} \right) \right] \tag{11.2.5}$$

Current definition:

$$i(t) = FAD_O \left. \frac{\partial C_O(x,t)}{\partial x} \right|_{x=0,t>0} \tag{11.2.6}$$

Current transient:

$$i(t) = \frac{FAD_O^{1/2} C_O^*}{\pi^{1/2} t^{1/2}} \tag{11.2.7}$$

For a spherical electrode:

Mass transport equation:

$$\frac{\partial C_O(r,t)}{\partial t} = D_O \left(\frac{\partial^2 C_O(r,t)}{\partial r^2} + \frac{2}{r} \frac{\partial C_O(r,t)}{\partial r} \right) \tag{11.2.8}$$

Initial condition:

$$C_O(r \geq r_0, 0) = C_O^* \tag{11.2.9}$$

Boundary conditions:

$$C_O(\infty, t > 0) = C_O^* \tag{11.2.10}$$

$$C_O(r_0, t > 0) = 0 \tag{11.2.11}$$

Concentration profile:

$$C_O(r,t) = C_O^* \left[1 - \frac{r_0}{r} \text{erfc}\left(\frac{r - r_0}{2(D_O t)^{1/2}} \right) \right] \tag{11.2.12}$$

Current definition:

$$i(t) = FAD_O \left. \frac{\partial C_O(r,t)}{\partial r} \right|_{r=r_0,t>0} \tag{11.2.13}$$

Current transient:

$$i(t) = \frac{FAD_O^{1/2} C_O^*}{\pi^{1/2} t^{1/2}} + \frac{FAD_O C_O^*}{r_0} \tag{11.2.14}$$

Equation (11.2.7) is known as the Cottrell equation (4) and a typical current transient is shown in Figure 11.1b. For spherical electrodes, the current transient (11.2.14) contains a steady-state term accounting for the effect of radial diffusion. This term will dominate at larger t when the Cottrell term tends to zero and the current reaches a steady-state value. The time required to establish the steady state is a function of the electrode radius. The smaller the electrode, the sooner the radial diffusion term becomes dominant (see Section 11.2.4 in this Chapter and Section 2.4 in Chapter 2, and Chapters 6 and 19 on Microelectrodes). To test whether the current response is controlled by diffusion, one plots i vs. $t^{-1/2}$. For both geometries, the graph should be linear but its intercept will be zero for a planar electrode and equal to the steady-state current for a spherical electrode. For planar electrodes, the current is therefore expected to decay to zero at long times. In practice, this cannot be observed because of the onset of natural convections after 30 s.

Equations (11.2.7) and (11.2.14) were derived assuming that E_f was such that the surface concentration of O was zero. The Nernst equation (11.2.15) predicts the ratio of surface concentrations of O and R in terms of the electrode potential and it is thus possible to predict the current for any value of the potential between E_i and E_f.

$$E = E^{0\prime} + \frac{RT}{F}\ln\left(\frac{C_O(0,t)}{C_R(0,t)}\right) \tag{11.2.15}$$

For planar electrodes and spherical electrodes at short times:

$$i = \frac{1}{1+\xi\theta}\times\frac{FAD_O^{1/2}C_O^*}{\pi^{1/2}t^{1/2}} \tag{11.2.16}$$

For spherical electrodes under steady-state conditions:

$$i_d = \frac{1}{1+\xi^2\theta}\times\frac{FAD_OC_O^*}{r_0} \tag{11.2.17}$$

where

$$\xi = \left(\frac{D_O}{D_R}\right)^{1/2} \tag{11.2.18}$$

$$\theta = \exp\left[\frac{F}{RT}(E-E^{0\prime})\right] \tag{11.2.19}$$

The expressions given above assumed that the electron transfer kinetics was very fast. Those given in Table 11.1 consider the case where the current is controlled by both mass transport and kinetics. Hence, the forward and reverse rates of electron transfer are taken into account.

Table 11.1

Chronoamperometric responses for kinetically limited one electron electrochemical reactions

Irreversible	Planar	$i = FAk_f C_O^* \exp\left(\dfrac{k_f^2 t}{D_O}\right) \mathrm{erfc}\left(\dfrac{k_f t^{1/2}}{D_O^{1/2}}\right)$	(11.2.20)
	Spherical	$i = FAk_f C_O^* \left[\left(1 + \dfrac{D_O}{k_f r_0}\right)\exp\left(\dfrac{k_f^2 t}{D_O}\right)\mathrm{erfc}\left(\dfrac{k_f t^{1/2}}{D_O^{1/2}}\right) - \dfrac{D_O}{k_f r_0}\right]$	(11.2.21)
Quasi-reversible	Planar	$i = FAk_f C_O^* \exp(H^2 t)\mathrm{erfc}(Ht^{1/2}), \quad \text{for } C_{R(t=0)}^* = 0$	(11.2.22)
		$i = FA(k_f C_O^* - k_b C_R^*)\exp(H^2 t)\mathrm{erfc}(Ht^{1/2}), \quad \text{for } C_{R(t=0)}^* \neq 0$	(11.2.23)
	Spherical[1]	$i = FAk_f C_O^* \left[\left(1 + \dfrac{D^{1/2}}{r_0 H'}\right)\exp(H'^2 t)\mathrm{erfc}(H't^{1/2}) - \dfrac{D^{1/2}}{r_0 H'}\right],$	
		$\text{for } C_{R(t=0)}^* = 0$	(11.2.24)
		$i = FA(k_f C_O^* - k_b C_R^*)\left[\left(1 + \dfrac{D^{1/2}}{r_0 H'}\right)\exp(H'^2 t)\mathrm{erfc}(H't^{1/2}) - \dfrac{D^{1/2}}{r_0 H'}\right],$	
		$\text{for } C_{R(t=0)}^* \neq 0$	(11.2.25)

[1]$D = D_O = D_R$.

where the forward and backward electron transfer rate constants are given by

$$k_f = k^0 \exp\left(-\frac{\alpha F(E - E^{0\prime})}{RT}\right) \tag{11.2.26}$$

$$k_b = k^0 \exp\left(\frac{(1-\alpha)F(E - E^{0\prime})}{RT}\right) \tag{11.2.27}$$

with

$$H = \frac{k_f}{D_O^{1/2}} + \frac{k_b}{D_R^{1/2}} \quad \text{and} \quad H' = \frac{k_f + k_b}{D^{1/2}} - \frac{D^{1/2}}{r_0}$$

The expression $\exp(\lambda^2)\mathrm{erfc}(\lambda)$, where $\mathrm{erfc}(\lambda)$ is the complementary error function (5), is represented by a power series of λ. Retaining only its linear terms, it reduces to $1 - 2\lambda/\pi^{1/2}$, which in turns simplifies equation (11.2.20) to

$$i = FAk_f C_O^* \left(1 - \frac{2k_f t^{1/2}}{\pi^{1/2} D_O^{1/2}}\right) \tag{11.2.28}$$

The equation predicts a linear variation of i with $t^{-1/2}$ from which the value of k_f can be derived. As $\mathrm{erfc}(\lambda)$ strongly depends on λ, k_f restricts the validity of equation (11.2.28).

In general, the larger the k_f, the shorter is the time over which equation (11.2.28) is accurate.

It is worth reiterating that all the equations given above are for mass transport by diffusion alone. Therefore, experimental responses will deviate from the predicted ones at long times because of natural convection (vibration, thermal and density gradients) or forced convection if using a rotating disc electrode. Moreover, at short times, the experiment will be affected by the charging of the double layer. The charging current i_c occurs in parallel to the faradaic current and contributes to the overall current response; see Section 11.2.6. It decays exponentially with time (equation (11.2.29)) and its magnitude depends on the solution resistance R_Ω and the double layer capacity C_d which is directly proportional to the electrode surface area. Ninety-five percent of the charging is completed in $3\tau_c$, where τ_c is the time constant for charging (equation (11.2.30)):

$$i_c = \frac{\Delta E}{R_\Omega} \exp\left(-\frac{t}{R_\Omega C_d}\right) \qquad (11.2.29)$$

$$\tau_c = R_\Omega C_d \qquad (11.2.30)$$

11.2.1.2 Double potential steps

The double potential step method (6) is included in this chapter as it underpins many other reversal techniques designed to study the stability of the product. Its principle is rather simple and it is a good stepping stone before tackling cyclic voltammetry. The potential is stepped to a value E_1 where species R is formed at a diffusion-controlled rate, and then, after a time τ, to a more anodic value E_2 where R is oxidised (Figure 11.2a).

The current response for the first step (Figure 11.2b) is treated as shown in Section 11.2.1.1. For the reverse step, however, the initial conditions have to be derived from the concentration profile of R at time τ. The calculation of the response is complex and often treated as a superposition of two signals (7–13). In the simplest case where both reactions are diffusion-controlled, the $i(t)$ relationships are:

$$i = \frac{FAD_O^{1/2}C_O^*}{\pi^{1/2}t^{1/2}}, \quad \text{for } 0 < t < \tau \qquad (11.2.7)$$
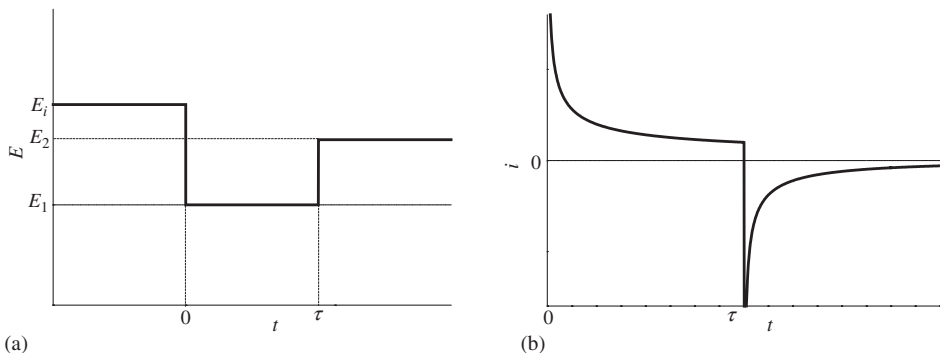

Figure 11.2   Double potential step experiment: (a) potential waveform and (b) current response.

$$i = FAD_O^{1/2}C_O^* \left\{ \frac{1}{[\pi(t-\tau)]^{1/2}} - \frac{1}{(\pi t)^{1/2}} \right\}, \quad \text{for } t > \tau \tag{11.2.31}$$

Additional theories are available for complex systems, including cases where one or both reactions are kinetically controlled (8, 12) or where a homogeneous reaction follows the electrode reaction (14).

11.2.1.3 Bulk electrolysis

Unlike most electroanalytical techniques where the amount of substance consumed or produced at the electrode is not appreciable, bulk electrolysis significantly alters the bulk concentration. This requires a large electrode surface area (A) to solution volume (V) ratio and very efficient mass transport conditions. Usually electrolysis is carried out under potentiostatic conditions by stepping the potential from a value where no faradaic current is observed to one where the reaction is mass transport-controlled. The $i(t)$ equations for a potential step apply but require corrections for the bulk concentration, C_O^*, as it evolves with time. Considering the model reaction $O + ne^- \rightarrow R$, the current transient is obtained by equating the current at a time t of the step (11.2.32) with the current indicating the rate of consumption of O (assuming 100% efficiency) (equation (11.2.33)). The evolution of the bulk concentration with time is derived (equation (11.2.34)) and using equation (11.2.32)), the corresponding current transient is given by equation (11.2.35). Integration of the current (often done in real time with an electronic integrator) yields the charge (equation (11.2.36)), where Q^0 is the charge at the end of the electrolysis (equation (11.2.37)). This is the most useful information since it provides the value of n. Q^0 may be determined from the charge transient (Figure 11.3a) or from the intercept of the straight line obtained when plotting $i(t)$ vs. $Q(t)$ (Figure 11.3b), since the current and charge transients are linearly related (equation (11.2.38)).

$$i(t) = nFAm_oC_O^*(t) \tag{11.2.32}$$

$$i(t) = -nF\left(\frac{dN_O}{dt}\right) = -nFV\left(\frac{dC_O^*(t)}{dt}\right) \tag{11.2.33}$$
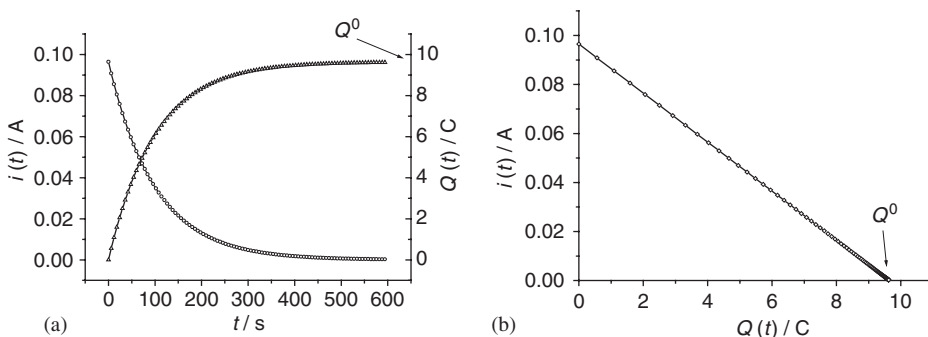

Figure 11.3 Controlled potential bulk electrolysis: (a) current and charge transients and (b) current vs. charge plot used to determine Q^0.

$$C_O^*(t) = C_O^*(0)\exp\left(-\frac{m_O A}{V}t\right) \qquad (11.2.34)$$

$$i(t) = nFAm_O C_O^*(0)\exp\left(-\frac{m_O A}{V}t\right) \qquad (11.2.35)$$

$$Q(t) = Q^0\left(1 - \exp\left(-\frac{m_O A}{V}t\right)\right) \qquad (11.2.36)$$

$$Q^0 = nFVC_O^*(0) \qquad (11.2.37)$$

$$Q(t) = nFVC_O^*(0) - \frac{V}{Am_O}i(t) \qquad (11.2.38)$$

Typical applications of bulk electrolysis include the determination of n or of the total amount of species present (e.g. by electrogravimetry), small-scale preparative electrosynthesis and electroseparation. In addition, any deviation in the linearity of $\ln(i(t))$ vs. t or $Q(t)$ vs. $i(t)$ indicates complexity in the reaction mechanism (e.g. coupled reactions).

11.2.2 Potential sweeps

11.2.2.1 Principles

In potential sweep methods, the current is recorded while the electrode potential is changed linearly with time between two values chosen as for potential step methods. The initial potential, E_1, is normally the one where there is no electrochemical activity and the final potential, E_2, is the one where the reaction is mass transport controlled. In linear sweep voltammetry, the scan stops at E_2, whereas in cyclic voltammetry, the sweep direction is reversed when the potential reaches E_2 and the potential returned to E_1. This constitutes one cycle of the cyclic voltammogram. Multiple cycles may be recorded, for example, to study film formation. Other waveforms are used to study the formation and kinetics of intermediates when studying coupled chemical reactions (Figure 11.4c).

Choosing the waveform parameters is the most important step when preparing the experiment. The starting and reversal potentials determine the driving force for electron transfer and the oxidation state of the species involved. Appropriate choice of the potentials will
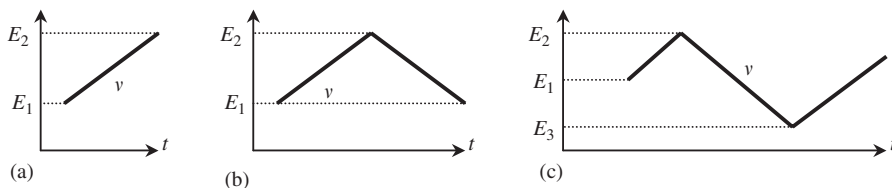

Figure 11.4   Waveforms used in linear sweep (a) and cyclic voltammetry (b and c). E_1, E_2 and E_3 are the starting and reversal potentials while v is the scan rate.

thus determine whether a species is formed or consumed, and whether the reaction is under kinetic or mass transport control. The potential scan rate sets the timescale of the experiment, e.g. with coupled homogeneous reactions, the value of v will determine whether intermediates are formed or consumed and to what extent. Typically v ranges from a few mV sec^{-1} to a few V sec^{-1}, although this upper limit can easily be extended to a few kV s^{-1} with microelectrodes; see Section 11.2.4.

Voltammetric methods produce current–voltage curves with features characteristic of the reaction mechanism and kinetic conditions. Combining this with the ease of changing the waveform parameters, cyclic voltammetry is nearly always the first technique used to study a new system. It is particularly useful for assessing reaction mechanisms, even when there are additional complications such as coupled homogeneous reactions, or surface adsorption. These techniques also provide quantitative information as will be shown below with a selection of theoretical expressions.

When first looking at a system with cyclic voltammetry, it is useful to carry out qualitative experiments. Typically, E_1, E_2, v, pH and C_O^* are varied systematically and the difference in the shape of the voltammogram is analysed. Points to note are the number of peaks present, the shape, size (peak current) and position (peak potential) of the peaks. By monitoring how each of these varies, it is possible to derive mechanistic and kinetic information.

11.2.2.2   Classical cyclic voltammetry

The cyclic voltammogram for a diffusion-controlled electron transfer reaction on an inert planar electrode is shown in Figure 11.5. Its shape derives from the evolution of the
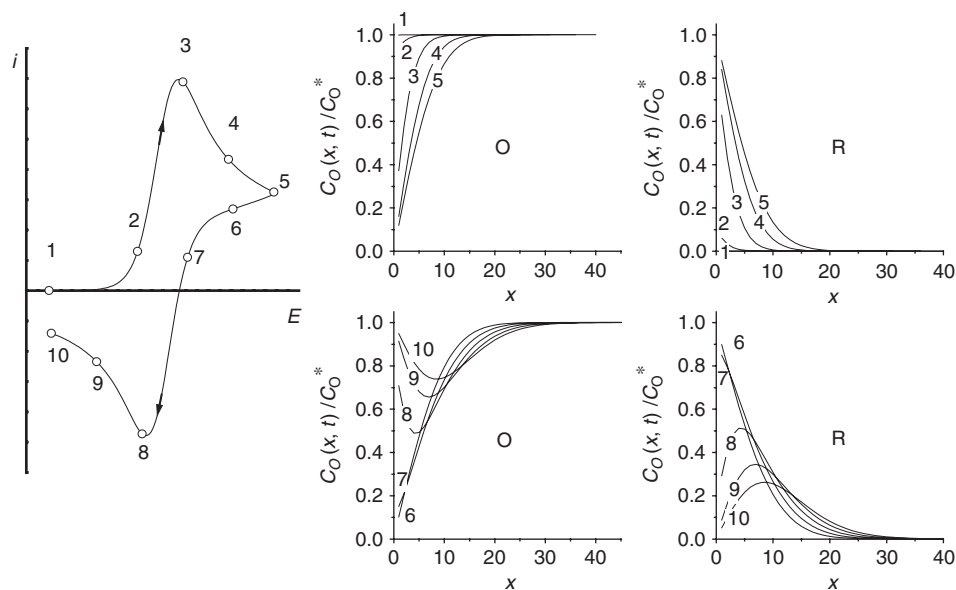

Figure 11.5   Cyclic voltammogram and corresponding O and R concentration profiles for diffusion to a planar electrode. Numbers on the concentration profiles correspond to the numbered points on the voltammogram.

concentration profiles resulting from the potential sweep and planar diffusion. Changing the electrode potential produces new surface concentrations for O and R and induces their diffusion between the bulk and the electrode. From Fick's first law of diffusion, the current is proportional to the gradient of concentration at the electrode surface. To illustrate the relationship between the concentration profiles and the current–voltage curve, selected points along the voltammogram have been linked to their corresponding concentration profile (Figure 11.5).

For points 1–7, species O is consumed at the electrode and a reduction current is observed, whereas for points 8–10, O is regenerated by oxidation of R and an oxidation current is observed. Note that the change of sign in the current is directly related to the inversion of the concentration gradient for O at the electrode surface: the gradient is positive for points 1–7 and negative for points 8–10. For additional theoretical background readers should consult Chapters 6 in reference (1), 6 in reference (2), 6 in reference (3) and 10 in reference (15).

One of the key features of the voltammogram is the peak height. For a planar diffusion-controlled case, the peak current is given by:

$$i_{\mathrm{p}} = 0.4463 \frac{n^{3/2} F^{3/2}}{R^{1/2} T^{1/2}} A D_{\mathrm{O}}^{1/2} C_{\mathrm{O}}^{*} v^{1/2} \qquad (11.2.39)$$

This equation, known as the Randles–Sevčik equation, predicts that the peak current is proportional to the square root of the sweep rate. This is analogous to the inverse square root of time dependence found with potential steps (equation (11.2.7)). Therefore, a plot of i_{p} vs. $v^{1/2}$ should be linear, pass through the origin and have a gradient from which the diffusion coefficient may be estimated. Below is a list of the diagnostic criteria used to characterise a reversible voltammogram:

$$i_{\mathrm{p}} \propto v^{1/2} \qquad (11.2.40)$$

$$E_{\mathrm{p}} \text{ is independent of } v \qquad (11.2.41)$$

$$\Delta E_{\mathrm{p}} = E_{\mathrm{pa}} - E_{\mathrm{pc}} = \frac{59}{n} \mathrm{mV} \text{ at } 298\,\mathrm{K} \qquad (11.2.42)$$

$$\left| E_{\mathrm{p}} - E_{\mathrm{p/2}} \right| = \frac{59}{n} \mathrm{mV} \text{ at } 298\,\mathrm{K} \qquad (11.2.43)$$

$$\left| \frac{i_{\mathrm{pa}}}{i_{\mathrm{pc}}} \right| = 1 \qquad (11.2.44)$$

The shape of the voltammogram changes significantly when the rate of mass transport overcomes the rate of electron transfer (Figure 11.6). When the mass transfer coefficient is comparable to the rate constant for electron transfer, the voltammogram is almost identical to the diffusion-controlled one (Figure 11.5). However, when the mass transfer coefficient is increased, i.e. at large values of v, the voltammogram becomes drawn out. The
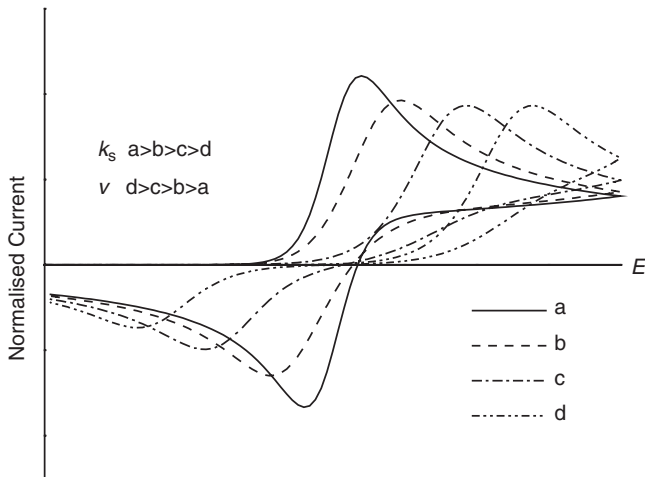
Figure 11.6   Voltammograms under kinetic control. The current scale has been normalised to illustrate either the effect of changing the sweep rate for a given electron transfer rate constant or changing the electron transfer rate constant for a given sweep rate. (a) The mass transfer coefficient is smaller than the electron transfer rate constant. (b–d) The mass transfer coefficient is increasingly larger than the electron transfer rate constant.

peaks broaden and the peak separation increases because a greater overpotential is needed to achieve the same rate of electron transfer.

As the rate of mass transport increases, the reverse peak becomes less and less pronounced. In the limit of a very slow rate of electron transfer, a case known as an irreversible system, the reverse peak disappears. Below are diagnostic criteria used to characterise an irreversible voltammogram:

$$i_{p,c} \propto v^{1/2} \tag{11.2.45}$$

$$\text{No reverse peak} \tag{11.2.46}$$

$$E_{p,c} \text{ shifts to higher overpotentials as } v \text{ increases} \tag{11.2.47}$$

$$\mid E_p - E_{p/2} \mid = \frac{48}{\alpha n} \text{mV at } 25\,^{\circ}\text{C} \tag{11.2.48}$$

11.2.2.3   Potential sweep experiments in the steady state

In cases where the mass transport conditions reach a steady state, e.g. with a microelectrode where spherical diffusion dominates (Section 11.2.4) or with a rotating disc electrode where hydrodynamic convection controls the diffusion layer thickness (Section 11.2.5), the current–voltage curve takes the form of a sigmoidal wave (Figure 11.7). The voltammogram is described by equation (11.2.49) when the kinetics are reversible. If however the
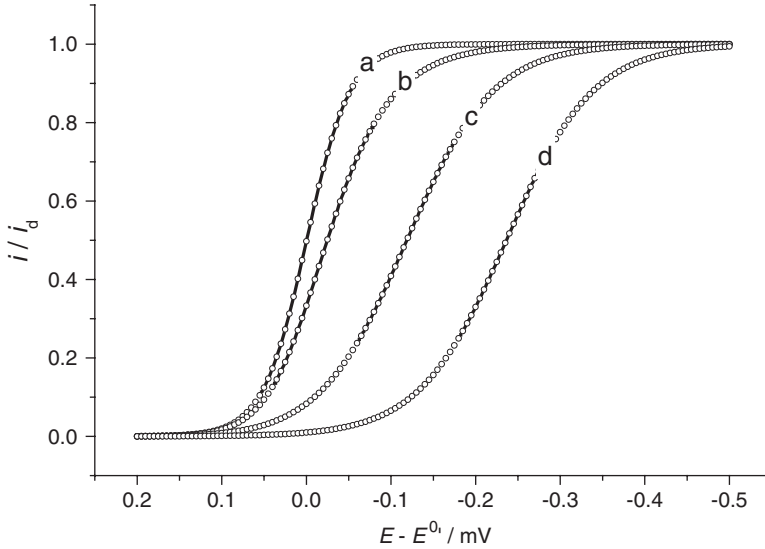
Figure 11.7   Steady-state voltammograms under different kinetic regimes: (a) reversible, (b) quasi-reversible and (c and d) totally irreversible.

kinetics of electron transfer become limiting, then the current–voltage curve is said to be quasi-reversible or even irreversible and is described by equation (11.2.50):

$$i = \frac{i_d}{1 + (D_O / D_R)\exp((F / RT)(E - E^{0'}))} \tag{11.2.49}$$

$$i = i_d \frac{k_f}{m_O + k_f + k_b(D_O / D_R)} \tag{11.2.50}$$

where k_f and k_b, respectively, the forward and reverse electron transfer rate constants, are both functions of the electrode potential as defined in equations (11.2.26) and (11.2.27). Both i_d, the mass transport-controlled limiting current, and m_O, the mass transfer coefficient for O, depend on the technique used.

When the standard rate constant for electron transfer k^0 is very small, k_f and k_b are also both very small. Moreover, k_b becomes negligible as the electrode potential is made increasingly negative to drive the reduction of O. In this case, the voltammogram is said to be totally irreversible and equation (11.2.50) reduces to equation (11.2.51). After substitution of k_f and further rearrangement, the potential is expressed in terms of the current (equation (11.2.52)):

$$i = i_d \frac{k_f}{m_O + k_f} \tag{11.2.51}$$

$$E = E^{0'} + \frac{RT}{\alpha F}\ln\left(\frac{k^0}{m_O}\right) + \frac{RT}{\alpha F}\ln\left(\frac{i_d - i}{i}\right) \tag{11.2.52}$$

Thus, a plot of the electrode potential against $\ln((i_d - i)/i)$ should be linear and yield the values of α and k^0.

The shape of the current–voltage curve is easily analysed with the Tomeš criteria:

$$\text{if } |E_{3/4} - E_{1/4}| = \frac{56.4}{n}\,\text{mV at }25\,°\text{C}, \quad \text{then the voltammogram is reversible} \qquad (11.2.53)$$

$$\text{if } |E_{3/4} - E_{1/4}| = \frac{51.4}{\alpha n}\,\text{mV at }25\,°\text{C}, \quad \text{then the voltammogram is irreversible} \qquad (11.2.54)$$

Steady-state voltammograms also reflect the mechanism and kinetics of coupled chemical reaction (16) but this is outside the scope of this chapter. For additional material, readers should consult Chapter 5 in references (2) and reference (17).

11.2.2.4 *Potential sweep experiments involving adsorbed species*

Potential sweep experiments are very sensitive to redox reactions involving adsorption of a reactant or a product. The cyclic voltammetry where both O and R are adsorbed on the electrode surface is different to that when both are in solution. This is because there is no mass transport step to consider. The typical shape of a cyclic voltammogram for an ideal Nernstian electron transfer with the Langmuir isotherm describing adsorption (only short-range repulsive interactions between the adsorbates) is shown in Figure 11.8. It consists of two symmetrical peaks, where the charges (the areas under the peaks) for oxidation and reduction are equal as all the adsorbed species undergo reduction/oxidation. The current peaks and decays to zero because there is a fixed amount of reactant present. The charged
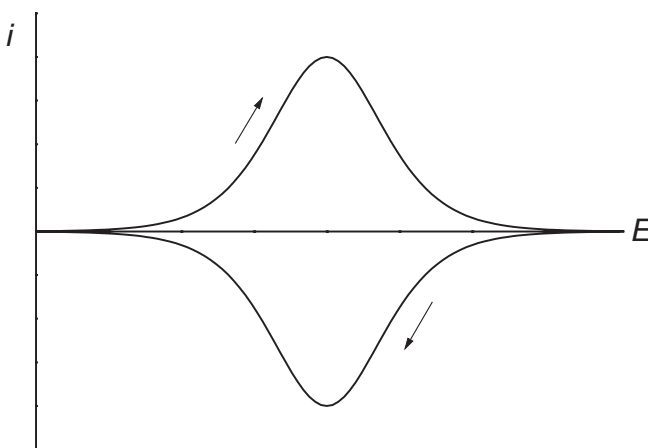

Figure 11.8 Cyclic voltammogram for a redox process with O and R adsorbed on the electrode surface.

passed must remain constant. Therefore, if the scan rate is increased, the peak current must also increase as shown by the following expression:

$$i_p = \frac{n^2 F^2}{4RT} v A \Gamma_O^*$$ (11.2.55)

where Γ_O^* is the maximum coverage for species O.

The list below shows the characteristic features of a cyclic voltammogram involving an ideal Nernstian adsorption with Langmuir isotherm:

$$\Delta E_p = 0$$ (11.2.56)

$$i_{p,a} = -i_{p,c}$$ (11.2.57)

$$Q_a = -Q_c$$ (11.2.58)

$$\Delta E_{p/2} = 3.53 \frac{RT}{nF} = \frac{90}{n} \text{mV at } 298\,\text{K}$$ (11.2.59)

The shape of the peaks is indicative of the nature of the interactions between the adsorbates and other isotherms have been used to model these interactions (18). Similarly, the position of the peaks along the potential axis is indicative of the reversibility of the electron transfer process. The larger the ΔE_p, the more irreversible is the electron transfer. For additional information on these effects, see Chapter 14 in reference (2).

Quantitatively, the voltammetric response of reactions involving adsorption is remarkably sensitive and without any special effort or experimental precautions, the voltammogram indicates the reduction or oxidation of a very small number of molecules, as low as a fraction of a monolayer. Qualitatively, the position and shape of the peaks give a signature, the voltammetric fingerprint, of the surface processes (Figure 11.9). Overall, this makes potential sweep experiments highly suited to the study of redox processes with adsorption steps.
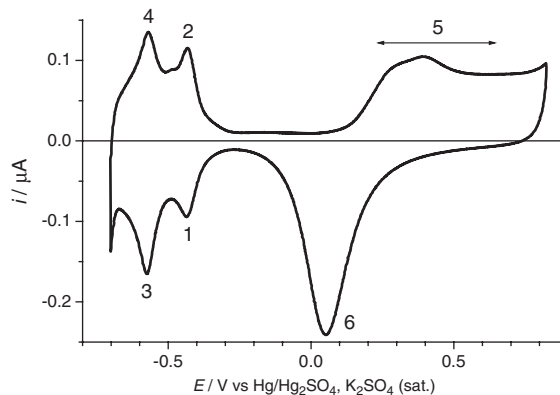

Figure 11.9 "Fingerprint" voltammogram for a high surface area Pt electrode in H_2SO_4. (1 and 2) Strong hydrogen adsorption/desorption, (3 and 4) weak hydrogen adsorption/desorption and (5 and 6) formation/reduction of Pt oxides.
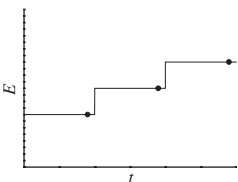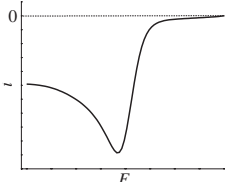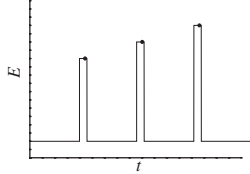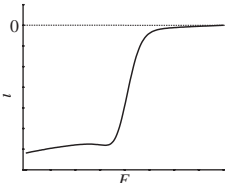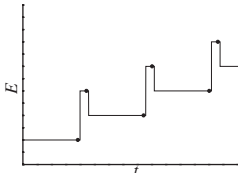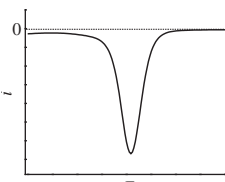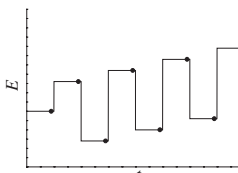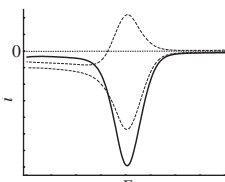
11.2.3   Combinations of sweeps and steps

11.2.3.1   *Pulse voltammetry*

Methods employing complex potential waveforms involving combinations of sweeps and steps evolved from polarography, mainly to improve detection limits. They were particularly advantageous in Dropping Mercury Electrode (DME) experiments, where a continuous charging current resulting from the drop growth is observed. The move to the Static Mercury Drop Electrode (SMDE) eliminates this requirement. Applied to stationary electrodes, pulsed voltammetric methods yield significant enhancements. The most important pulse voltammetric techniques together with key references are presented in Table 11.2.

Table 11.2

Potential waveforms and typical current responses for selected techniques

Technique	Potential waveform	Current response	References
Staircase voltammetry (SCV)			(19, 20)
Normal pulse voltammetry (NPV)			(20–23)
Differential pulse voltammetry (DPV)			(20, 22–25)
Square wave voltammetry (SWV)			(20, 24, 26–31)

The dot indicates the time when the current is sampled. The current response is that for the reduction of a reversible redox couple.

   All four methods can be considered as fixed potential techniques with the current being sampled after the potential has remained constant for sufficiently long time, typically 40 msec. Discrimination against charging current is thus achieved by sampling the current just before the end of the pulse (or the end of the step for a staircase), where the charging current is negligible compared to the faradaic component. DPV and SWV further improve the sensitivity by subtracting current values sampled at two different times. SWV combines advantages of the other three and offers significant improvements. The result is a voltammetric response akin to a Gaussian, characterised by an excellent suppression of background current and yielding improved quantitative information with a wider range of timescales.

11.2.3.2   Stripping analysis

Stripping techniques extensively described by Wang (32) are used in quantitative determination and speciation in particular of metals and metal complexes. The procedure involves a pre-electrolysis step followed by a potential sweep to strip the pre-concentrated species of interest (Figure 11.10). Depending on the nature of the analyte, different modes of stripping analysis are used. The most common is *Anodic Stripping Voltammetry* (ASV), employing an SMDE or a Mercury Film Electrode (MFE). The main application of this method is the analysis of metal ions and the pre-electrolysis step allows detection in very diluted solutions (down to 10^{-11} M). Metal cations are reduced forming an amalgam and subsequently oxidised by means of potential sweep (LSV or DPV). A typical stripping response is shown in Figure 11.10b.

   The amount of metal is calculated from the charge under the stripping peak. Using standard addition or calibration, this amount can be related to the concentration of the metal ion in the analyte. For this, all parameters—pre-concentration potential and time, stirring conditions, temperature and quantity of Hg—should remain constant throughout the calibration and be identical to those used with the sample.
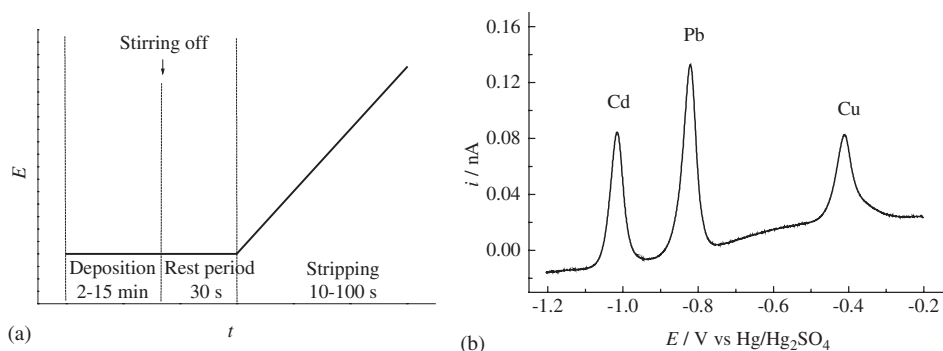

(a)

(b)

Figure 11.10   (a) Potential waveform for a typical ASV experiment and (b) anodic stripping analysis in 0.1 M NaClO$_4$ solution containing 0.2 mM Cu^{2+}, 0.25 mM Pb^{2+} and 0.25 mM Cd^{2+}. The stripping was performed by LSV at $v = 10$ mV s^{-1} on an Hg film microdisc electrode.

Potentiometric Stripping Analysis is an alternative for metal ions analysis. As with ASV, the pre-electrolysis is carried out under potential-controlled conditions. Amalgamated metals are subsequently stripped by either applying a controlled anodic current or addition of an oxidising agent to the solution (e.g. dissolved oxygen). The resulting chronopotentiogram presents stripping plateaus corresponding to the different metals. These plateaus are qualitatively identified using the Nernst equation for each $M^{n+}/M(Hg)$ couple. The quantitative analysis can be facilitated by differentiating the E vs. t curve yielding a peak-shaped response.

Cathodic Stripping Voltammetry (CSV) can be used to detect organic and inorganic compounds. An anodic potential is applied during the pre-concentration step and the compound of interest forms an insoluble salt with mercury. Stripping is carried out with a potential sweep towards negative potentials.

Adsorptive Stripping Voltammetry broadens even more the range of species that can be analysed by the stripping techniques. It often offers a significant improvement in sensitivity and selectivity of metal ions analysis. The principle of the method is the formation of surface-active metal complex which is subsequently adsorbed and undergoes reduction at the electrode surface. The electrochemical process may involve the ligand as well as the metal centre. The method is also suitable for numerous important organic compounds (polycyclic hydrocarbons, nucleic acids and drugs). For different species, either cathodic or anodic stripping can be utilised. While very useful for trace analysis, the technique has limitations for higher concentrations due to the limited number of adsorption sites at the electrode surface.

11.2.4 Microelectrodes

The practical characteristics of microelectrodes are discussed in Chapter 6 of this handbook; hence, this section is restricted to a brief theoretical background followed by a discussion of key experiments where microelectrodes have made significant improvements.

Microelectrodes are defined as electrodes having at least one dimension small enough that their properties are a function of this size (33). This characteristic dimension (radius, width or thickness depending on geometry) must be smaller than circa 50 μm, otherwise the electrode behaves like a conventional electrode. Three key electrochemical properties are significantly affected by the size of the electrode: (1) the mass transport regime, (2) the charging of the double layer and (3) the ohmic drop in solution. Only two geometries will be considered: spherical microelectrodes because of their simple theory and microdisc electrodes because they offer the best compromise between ease of fabrication, robustness and "friendly" theoretical treatment.

11.2.4.1 *The mass transport regime*

Diffusion to a microelectrode is notably different than that to a conventional electrode, including mm-size electrodes. For a simple fast electron transfer process, the application of a potential step from a value where no current flows to one where the reaction is diffusion controlled produces different diffusion regimes. At short times, the diffusion layer is very thin relative to the electrode. Diffusion to and from the electrode is planar (irrespective of
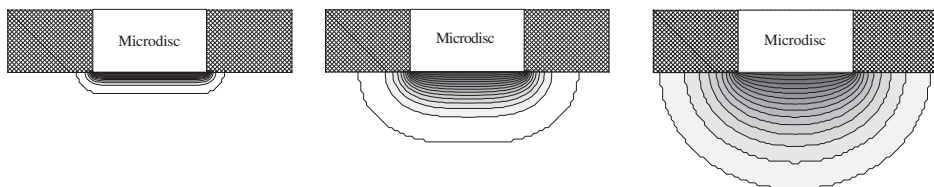
Figure 11.11   Diffusion regimes following a potential step to a microdisc electrode. From left to right: planar diffusion at short times, transition from planar to quasi-hemispherical, and then hemispherical diffusion at long times.

the electrode geometry) and the microelectrode behaves like a conventional electrode. As time increases, the diffusion layer thickness becomes comparable, and then larger than the dimensions of the electrode. The diffusion regime evolves from planar to spherical (quasi-hemispherical for a microdisc) (Figure 11.11) and yields a steady-state rate of mass transport to the electrode. So in contrast to the constant planar diffusion regime observed with large electrodes, a microelectrode shifts from planar to spherical diffusion. This, of course, depends on the characteristic dimension of the electrode. Below 50 μm, the microelectrode can fully develop its diffusion layer without influence from natural convection. Larger electrodes produce thicker diffusion layers which soon become affected by natural convection. In this case, the steady rate of mass transport observed is greater than that for diffusion alone.

11.2.4.2   Double layer charging

Because microelectrodes have a very small electroactive area, the time required to charge or discharge the double layer is very short. Hence, a great property of microelectrodes is to significantly improve the discrimination against charging current. Reliable recordings of the faradaic current can be made at times shorter than those with a conventional electrode and this has opened the application of voltammetric and chronoamperometric experiments to the sub-millisecond timescale.

11.2.4.3   Ohmic drop

Due to their small size, the faradaic current flowing to microelectrodes typically ranges from a few pA to a few nA. In contrast, the resistive drop is small because most of it occurs very close to the microelectrode (e.g. within a few radii for a spherical or microdisc electrode). This is in contrast with large electrodes where the resistive drop continually increases with distance between the working electrode and the reference electrode. Taking these two effects into account, the ohmic drop due to the passage of the current in the solution is much reduced and the distortion of voltammetric curves becomes negligible. This property enables voltammetric experiments to be conducted in poorly conducting media, such as organic solvents, and even in the absence of supporting electrolyte.

   Classical experiments performed with microelectrodes derive from the mass transport regimes and include steady-state voltammetry, fast scan cyclic voltammetry and

chronoamperometry. A key decision to make in microelectrode experiments is the choice of the timescale since this determines the diffusion regime. In the next few lines, a simple analysis based on the chronoamperometric response to a spherical electrode (equation (11.2.14)) is used to provide guidelines for the choice of timescale.

Comparing the two terms in equation (11.2.14) yields the time t_{planar} below which the response is controlled by planar diffusion and the time $t_{spherical}$ above which the response is controlled by spherical diffusion:

$$t_{planar} \ll \frac{r_0^2}{\pi D_O} \tag{11.2.60}$$

$$t_{spherical} \gg \frac{r_0^2}{\pi D_O} \tag{11.2.61}$$

Extending this analysis to all geometries, any microelectrode has therefore a characteristic diffusion time $t_{diffusion}$ given by

$$t_{diffusion} \approx \frac{(\text{characteristic dimension})^2}{D} \tag{11.2.62}$$

and the rule of thumb is that the response will be under planar diffusion if the experimental time is much less than $t_{diffusion}$ or under spherical diffusion (for a sphere, quasi-hemispherical for a microdisc and hemicylindrical for a microband) if the experimental time is greater than $t_{diffusion}$. Figure 11.12 summarises the relationship between the timescale, the corresponding diffusion field and the chronoamperometric and voltammetric responses.

Since at short times, a microelectrode behaves as a conventional electrode, all the theories developed for potential steps and potential sweeps at large electrodes are applicable. Conversely, at long times, the theories developed for steady-state techniques are applicable. However, the geometry of the electrode determines the expression for the limiting current. The most important ones are given in Table 11.3. For microbands and microcylinders, the current reaches a quasi-steady state. This is a consequence of the infinite length of the electrode relative to its characteristic dimension.

For the sphere, hemisphere and disc electrodes, the limiting current is proportional to the characteristic length. This has led to one of the classical experiments with a microdisc electrode where steady-state voltammograms are recorded for microdiscs of different radii and the limiting current is plotted against the radius of the electrodes. If the electrochemical process is diffusion controlled, the plot should be linear and yield the diffusion coefficient of the reactant. This is analogous to recording the limiting current for various rotation rates on a rotating disc electrode. However, the drawback is that one needs to fabricate different microdisc electrodes to perform this experiment.

Overall, microelectrodes offer three key advantages: (1) high rate of steady-state mass transport, (2) decreased ohmic drop distortion and (3) decreased double layer charging
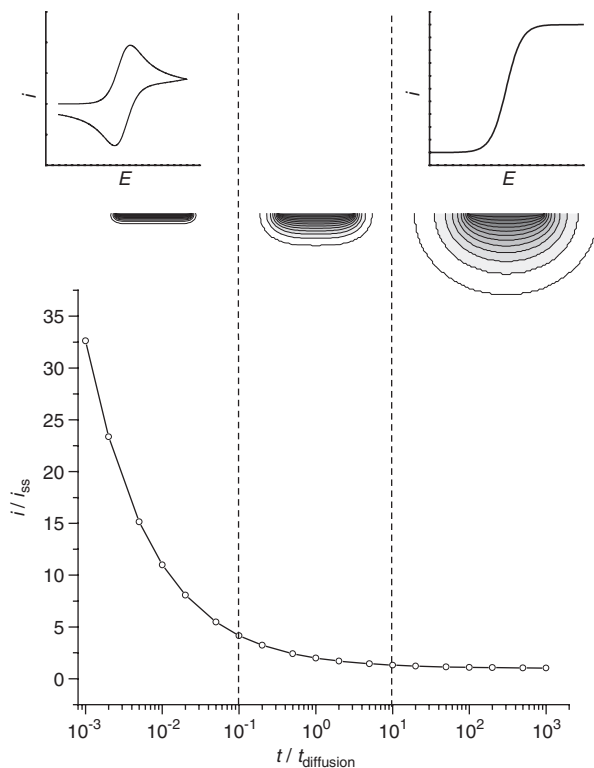
Figure 11.12   Current transient to a microdisc. The dashed lines have been arbitrarily drawn at $t_{\text{planar}} = t_{\text{diffusion}}/10$ and $t_{\text{spherical}} = 10 \times t_{\text{diffusion}}$. The grey scale contour lines, simulated concentration maps, illustrate the shape of the diffusion layer for each regime. The corresponding transient and steady-state voltammetric responses are also indicated.

Table 11.3

Expression for the limiting current at various microelectrode geometries

Geometry	Characteristic length	Steady-state current	
Sphere	r_0	$i_{ss} = 4\pi nFD_O C_O^* r_0$	(11.2.63)
Hemisphere	r_h	$i_{ss} = 2\pi nFD_O C_O^* r_h$	(11.2.64)
Disc	a	$i_{ss} = 4nFD_O C_O^* a$	(11.2.65)
Band[a]	w	$i_{ss} = \dfrac{2\pi nFD_O C_O^* l}{\ln((64D_O t)/w^2)}$	(11.2.66)
Cylinder[a]	r_c	$i_{ss} = \dfrac{4\pi nFD_O C_O^* l}{\ln((4D_O t)/r_c^2)}$	(11.2.67)

[a]l is the length of the electrode.

distortion. This has led to simpler experiments (e.g. steady state instead of transient measurements) and easier data analysis (e.g. no need to correct for ohmic drop), and enabled electroanalytical experiments on to microsecond timescale (voltammetry up to MV s^{-1}). In all the following cases, microelectrodes should be considered:

- when a high current density is obtained: namely high concentrations of reactants, short time experiments and high rate processes (electron transfer or homogeneous kinetics);
- where a steady-state measurement is desirable;
- where access to sub-millisecond timescale is required, e.g. for high rate processes (electron transfer or homogeneous kinetics);
- where electroanalytical measurements need to be performed in poorly conducting media, even in absence of supporting electrolyte.

For additional information, consult references (34–37), and Chapter 6 of this handbook.

11.2.5 Rotating disc electrodes

The rotating disc electrode (RDE) is the classical hydrodynamic electroanalytical technique used to limit the diffusion layer thickness. However, readers should also consider alternative controlled flow methods including the channel flow cell (38), the wall pipe and wall jet configurations (39). Forced convection has several advantages which include: (1) the rapid establishment of a high rate of steady-state mass transport and (2) easily and reproducibly controlled convection over a wide range of mass transfer coefficients. There are also drawbacks: (1) in many instances, the construction of electrodes and cells is not easy and (2) the theoretical treatment requires the determination of the solution flow velocity profiles (as functions of rotation rate, viscosities and densities) and of the electrochemical problem; very few cases yield exact solutions.

The RDE consists of a disc (e.g. of Pt, Ni, Cu, Au, Fe, Si, CdS, GaAs, glassy carbon and graphite) set into an insulating (PTFE) surround. The electrode is rotated about its vertical axis (Figure 11.13), typically between 400 and 10,000 rpm. The theory for the hydrodynamics at the RDE (40–42) assumes that the electrode is uniformly accessible and affords a precise and reproducible control of the convection and diffusion of reactant to the electrode. Hence, the RDE can be used to study the kinetics of interfacial processes.

The theoretical treatment yields the concentration profile of reactant towards the RDE and defines a layer with thickness δ_O where diffusion is the sole mode of mass transport (Figure 11.14)

$$\delta_O = 4.98 D_O^{1/3} v^{1/6} \omega^{-1/2} \tag{11.2.68}$$

where ω is the rotation rate in rpm.

From the concentration profile is derived an expression for the limiting current, known as the Levich equation:
ω in rpm:

$$i_l = 0.201 n F A D_O^{2/3} v^{-1/6} C_O^* \omega^{1/2} \tag{11.2.69}$$
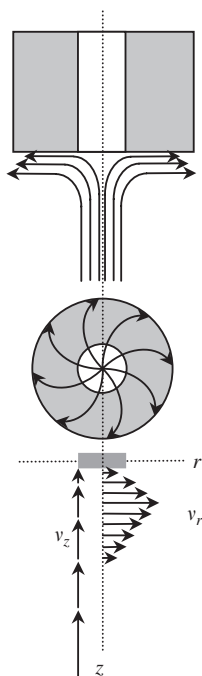
Figure 11.13   Streamlines for flow and vector representation of fluid velocities near a rotating disc electrode.
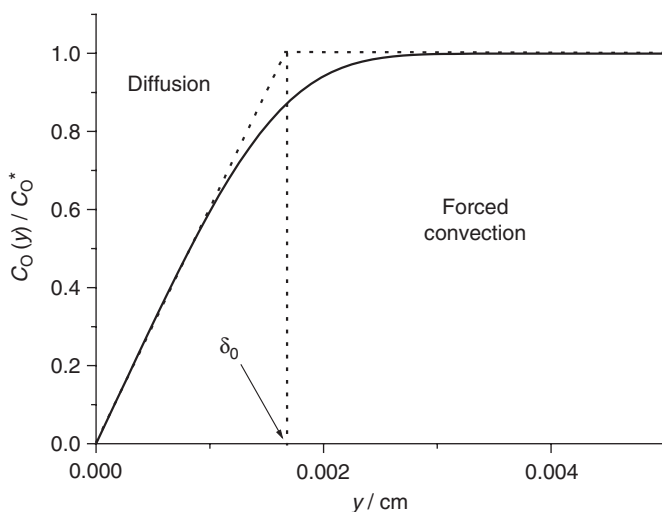

Figure 11.14   Steady-state concentration profile at the RDE, showing the well-stirred bulk where convection dominates and the thin stagnant layer at the electrode surface where diffusion dominates. δ_0 is the diffusion layer thickness. $D_O = 10^{-5}$ cm^2 s^{-1}, $v = 0.01$ cm^2 s^{-1} and $\omega = 100$ Hz.

ω in rad s^{-1}:

$$i_l = 0.621 nFAD_O^{2/3} v^{-1/6} C_O^* \omega^{1/2} \qquad (11.2.70)$$

ω in Hz:

$$i_l = 1.554 nFAD_O^{2/3} v^{-1/6} C_O^* \omega^{1/2} \qquad (11.2.71)$$

Classically, the limiting current is reached by recording a linear sweep voltammogram at a low scan rate (1–10 mV s^{-1}). Under such mass transport conditions, the current–voltage curve is a sigmoidal wave analogous to that found with a spherical microelectrode under steady-state conditions. So the same criteria apply to analyse the shape of the curve. Whereas a range of microelectrodes with different radii is needed to obtain a range of steady-state mass transfer coefficients, the RDE simply needs a range of rotation rates. Hence, the classical RDE experiment consists in recording a series of linear sweep voltammograms at a low scan rate for a range of rotation rates. The Levich equation predicts that a plot of the limiting current vs. the square root of the rotation rate should be a straight line passing through the origin with a slope determined by the number of electrons, the geometric area of the electrode, the diffusion coefficient, the bulk concentration O and the kinematic viscosity of the solution, v.

When the redox process is reversible, the shape of the wave should not depend on ω. Hence, at any potential, the current should, like the limiting current, be proportional to $\omega^{1/2}$. If the shape of the curve depends on ω, then the redox process is kinetically limited. In this case, one can measure the current at fixed potentials along the voltammogram and for each potential plot the inverse of the current vs. $\omega^{1/2}$. This is known as a Koutecký–Levich plot and follows the Koutecký–Levich equation:

$$\frac{1}{i} = \frac{1}{i_K} + \frac{1}{0.201 FAD_O^{2/3} v^{-1/6} C_O^* \omega^{1/2}} \quad \text{with } \omega \text{ in rpm} \qquad (11.2.72)$$

where i_K is the kinetically controlled current that would be obtained for $\omega^{-1/2} = 0$, i.e. for an infinite rotation speed where the mass transfer would be so efficient that the surface concentration of C_O would be equal to C_O^*. Thus, a plot of $1/i$ vs. $\omega^{-1/2}$ should be linear and extrapolation to $\omega^{-1/2} = 0$ should yield i_K. By repeating this plot for different potentials along the voltammogram, it is possible to determine the kinetic parameters k_0 and α; see Chapter 9 in reference (2).

One of the most important refinements of the RDE is the rotating ring disc electrode (RRDE) where the central disc is surrounded by an insulating ring, and then by a secondary annular working electrode. The purpose of this configuration is to perform steady-state generation–collection experiments. This is analogous to the reversal techniques, double potential steps or transient cyclic voltammetry but without the problems inherent to transient methods. Typically, the disc acts as the generator while the ring acts as the collector. The disc need not be an electrode and it is possible to study interfacial processes on the disc by electrochemically detecting the products with the ring. Interested readers should refer to reference (40). The geometry of the RRDE is critical to the quality of the results and good ring–disc assemblies are difficult to make.

11.2.6   Small amplitude perturbations and impedance methods

Most, if not all, of the classical experiments considered so far involve large amplitude per-
turbations of the electrode–solution interface. That is, in a typical voltammetric experi-
ment, the electrode is subjected to a potential ramp often spanning several hundred millivolts
(from a potential where no current flows to one where a mass transport-controlled reaction
occurs on the electrode surface) and representing several orders of magnitude in electro-
chemical driving force. As a consequence, the current–potential response is nonlinear
(Figure 11.15) and it is customary to analyse the voltammogram in terms of a few key val-
ues: E_{pa}, E_{pc}, $E_{1/4}$, $E_{1/2}$, $E_{3/4}$, i_{pa}, i_{pc} or i_l. Similarly, in chronoamperometry, the potential step
amounts to a large perturbation and the current–time response is nonlinear.

   Another methodology consists in applying small amplitude perturbations where the
steps or sweeps are sufficiently small to yield a linear current–potential relationship
(Figure 11.15). This approach is at the heart of electrochemical impedance methods.

   Electrochemical impedance experiments comprise the following steps: (1) the electro-
chemical cell is subjected to a small amplitude periodic (usually sinusoidal, although
square waves can be used) electrical perturbation (Figure 11.16); (2) its electrical response
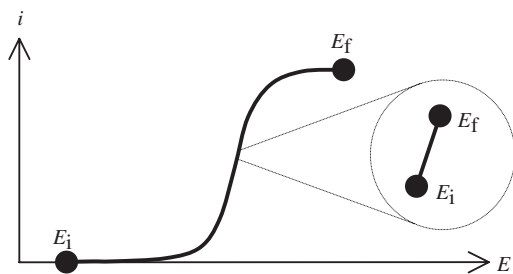

Figure 11.15   A large amplitude perturbation, here a potential sweep to a mass transport-controlled
region, yields a nonlinear current–potential relationship. In contrast, a small amplitude perturbation,
a few mV between E_i and E_f, yields a linear relationship between current and potential.
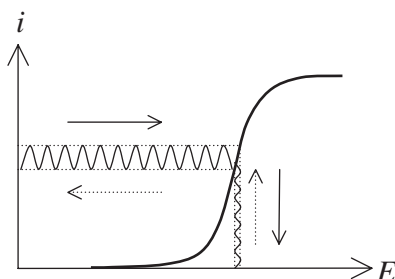
Figure 11.16   Solid arrows: an AC current is applied to the electrode and an AC potential response
is obtained. Dashed arrows: an AC potential is applied to the electrode and an AC current is obtained.
In both cases, the i–E relationship is recorded over a range of frequencies. Because of the small
amplitude used, the current is proportional to the potential and the response is also sinusoidal. The
perturbation is shown here around $E_{1/2}$ for the clarity of the drawing.

is acquired over a range of perturbation frequencies; (3) an equivalent electrical circuit is worked out; (4) components of the equivalent circuit are related to key physical or chemical characteristics of the electrochemical system.

As for conventional electrical circuits, the electrochemical impedance of the electrochemical cell is defined as

$$Z_{cell} = \frac{E_{cell}}{i_{cell}} \tag{11.2.73}$$

where E_{cell} is the voltage across the cell and i_{cell} the current circulating through the cell. Alternatively, the admittance is defined as

$$Y_{cell} = \frac{1}{Z_{cell}} = \frac{i_{cell}}{E_{cell}} \tag{11.2.74}$$

where Z is akin to a generalised resistance and has units of Ω, whereas Y is analogous to a conductance and has units of Ω^{-1} or Siemens. By definition, Z and Y are ratios of AC signals and thus each will have a phase and an amplitude. To facilitate interpretation, both are written as complex numbers in Cartesian or polar coordinates.

The experimental configuration commonly used is shown in Figure 11.17. Alternatively, one may use a low-pass filter and a lock-in amplifier to obtain the DC part, AC part and phase of the cell response.

The key step in electrochemical impedance experiments is the construction of an equivalent circuit that mimics the electrical behaviour of the cell. For this, it is necessary to consider the different ways in which the ionic charges are involved in the passage of current.

Between the electrodes, the solution behaves as an ionic conductor with a resistance, R_{Ω}, known as the ohmic solution resistance. At the electrode–solution interface, some of the ions are used to adjust the ionic atmosphere until the charge balance between the electrode surface and the solution is reached. Electrically, this is equivalent to the charge or discharge of a capacitor with capacitance C_d, known as the double layer capacitance. Simultaneously, i.e. in parallel, redox species undergo an electron transfer with the electrode; this yields the faradaic current whose magnitude reflects the rate of arrival of the reactants (the rate of mass transport) and the rate of the electron transfer process. Electrically, this is equivalent to two resistors in series: one for the kinetics of the electron
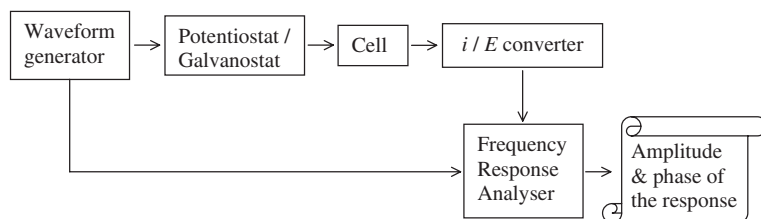
Figure 11.17   The common experimental arrangement for electrochemical impedance experiments relies on the use of a frequency response analyser to derive the Cartesian or polar coordinates of the impedance and admittance.
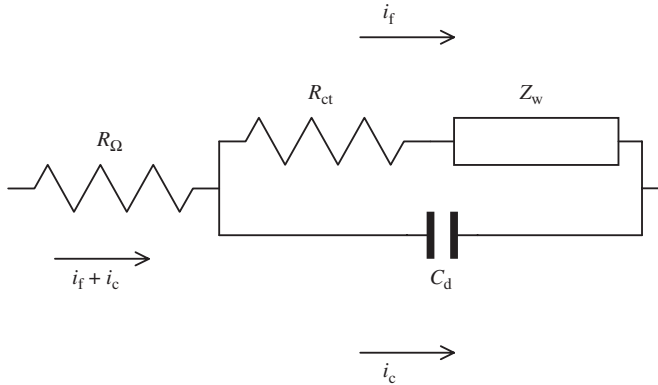
Figure 11.18   The equivalent circuit for a simple reversible electron transfer. R_Ω, the Ohmic solution resistance; R_{ct}, the charge transfer resistance; Z_w, the Warburg impedance or mass transfer resistance; C_d, the double layer capacitance; i_c, the charging current; i_f, the faradaic current.

transfer process, R_{ct}, known as the charge transfer resistance and one for the rate of mass transport, Z_w, known as the Warburg impedance. Pulling all this together, the simplest electrical equivalent circuit consists of four components connected as shown in Figure 11.18.

The solution resistance is determined by the solution conductivity and the geometry of the cell, namely the distance between the electrodes and the cross-sectional area of solution linking the electrodes. The double layer capacitance reflects the electrostatic interplay between the electrode and the electrolyte and depends on the electrode area and nature and the electrolyte ionic strength and permittivity. Together, R_{ct} and Z_w make up the faradaic impedance. R_{ct} reflects the charge transfer kinetics and can be thought of as the ratio of overpotential to current in absence of mass transfer limitation. R_{ct} goes through a maximum at the equilibrium potential; hence, it is best to perturb the electrochemical system around this value. There, the current–potential relationship can be linearised, and R_{ct} is found to be inversely related to the exchange current, i_0:

$$R_{ct} = \frac{RT}{nFi_0} \tag{11.2.75}$$

The mass transfer impedance depends on the mode of mass transport within the cell. For semi-infinite linear diffusion, Z_w is a complex number whose real and imaginary parts depend on the perturbation frequency:

$$Z_w = \sigma\omega^{-1/2} - j\sigma\omega^{-1/2} \tag{11.2.76}$$

with

$$\sigma = \frac{RT}{n^2 F^2 A \sqrt{2}} \left(\frac{1}{C_O^* D_O^{1/2}} + \frac{1}{C_R^* D_R^{1/2}} \right) \tag{11.2.77}$$

and

$$\omega = 2\pi f \tag{11.2.78}$$

Combining the impedance of the four components gives the overall impedance of the cell:

$$Z_{cell} = Z_{Re} + jZ_{Im} \tag{11.2.79}$$

with

$$Z_{Re} = R_\Omega + \frac{R_{ct} + \sigma\omega^{-1/2}}{(C_d\sigma\omega^{1/2} + 1)^2 + \omega^2 C_d^2 (R_{ct} + \sigma\omega^{-1/2})^2} \tag{11.2.80}$$

and

$$Z_{Im} = -\frac{\omega C_d (R_{ct} + \sigma\omega^{-1/2})^2 + \sigma\omega^{-1/2}(C_d\sigma\omega^{1/2} + 1)}{(C_d\sigma\omega^{1/2} + 1)^2 + \omega^2 C_d^2 (R_{ct} + \sigma\omega^{-1/2})^2} \tag{11.2.81}$$

The frequency response of the cell is represented by plotting $-Z_{Im}$ vs. Z_{Re}. This is known as a Nyquist plot (Figure 11.19). Alternatively, Bode plots ($\log(|Z|)$) and phase angle vs. $\log(\text{frequency})$ or $\log(Z_{Re})$ and $\log(Z_{Im})$ vs. $\log(\text{frequency})$) may be used.

Figure 11.19 is best understood by considering the dominant impedance for various frequency limits as shown in Table 11.4.

It is usual to extract the following information from the impedance diagram:

- R_Ω from the high frequency intercept on the real axis;
- R_{ct} from the diameter of the circle;
- C_d from the frequency at the maximum of the circle.

Increasingly complex equivalent circuits are used to model a wide range of electrochemical processes (e.g. corrosion, adsorption or porous electrodes) and to facilitate analysis, commercial impedance software includes libraries of equivalent circuits which can be

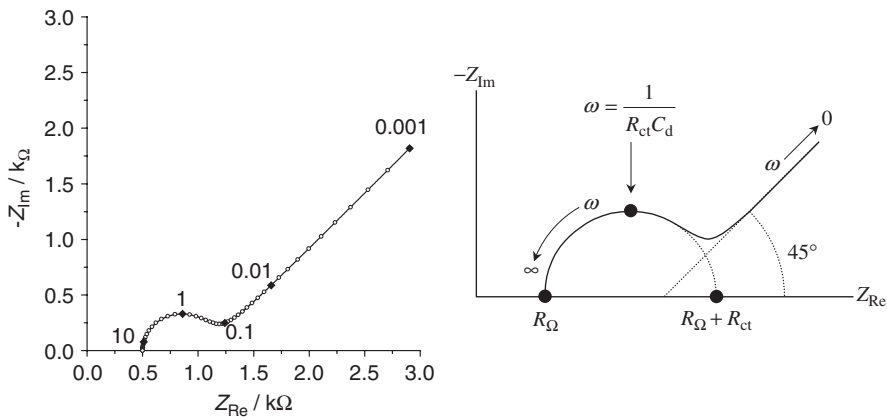**Figure 11.19** (a) Nyquist plot calculated from equations (11.2.80) and (11.2.81) with $R_\Omega = 500\ \Omega$, $R_{ct} = 600\ \Omega$, $T = 298$ K, $C_d = 2 \times 10^{-4}$ F, $n = 1$, $A = 1$ cm^2, $D_O = 7.2 \times 10^{-6}$ cm^2 s^{-1}, $D_R = 6.5 \times 10^{-6}$ cm^2 s^{-1} and $C_O = C_R = 1$ mM. Numbers by points are frequencies in Hz. (b) Key features of an impedance diagram.

Table 11.4

Impedance-frequency dependence and equivalent circuit for a typical electrochemical cell

Frequency	Equivalent circuit	Impedance diagram
$\omega \to 0$	R_Ω, R_{ct}, $Z_w \propto \omega^{-1/2}$, Z_{C_d} ∞	$-Z_{Im}$ vs Z_{Re}
$\omega \approx 1/R_{ct}C_d$	R_Ω, R_{ct}, $Z_w \to 0$, Z_{C_d}	$-Z_{Im}$ vs Z_{Re}
$\omega \to \infty$	R_Ω, R_{ct}, $Z_w = 0$, $Z_{C_d} \to 0$	$-Z_{Im}$ vs Z_{Re}

The dotted lines indicate the least resistive current path.

fitted to the experimental impedance data. However, users should resist the temptation to improve the fit by adding new components to the circuit. Instead, the values of some of the components should be backed up by other electrochemical experiments. Electrochemical impedance methods should be considered as complementary techniques to large amplitude methods. One of their main advantages is to provide a complete electrochemical response over a wide timescale. For in depth reviews and early articles, readers should consult references (1, 43–52).

11.3   SIMULATIONS

With the availability of significant desktop computing power and of electrochemical modelling software, the possibility of simulating electrochemical experiments is no longer restricted to the programming aficionados. For this reason, the present chapter covers the basic principles and applications of numerical simulations of electrode reactions. The section starts with a series of questions, continues with a consideration of simulation principles and finishes with an example.

11.3.1   Electrochemical simulations—a few questions

11.3.1.1   Why use a simulation?

(1)   To predict the electrochemical response when the problem has no known or simple analytical solution, e.g. cyclic voltammetry, microelectrodes, coupled chemical reactions, etc.

(2)   To test a proposed model against experimental results and derive experimental quantities.
(3)   To learn or teach the principles of a technique, e.g. the evolution of concentration profiles during a cyclic voltammogram.

11.3.1.2   What do they do?

Typically, an electrochemical simulation models the transport of the reactant from the bulk to the electrode surface, the transfer of electrons at the electrode/solution interface and the transport of the product away from the electrode. Depending on the complexity of the electrochemical process, the simulation may account for the rate of electron transfer kinetics, the possibility and rate of preceding or following chemical reactions, the possibility and rate of adsorption processes and even combinations of different forms of mass transport (planar or spherical diffusion, convection and migration). In other words, the simulation performs a series of actions which mimic the sequence of events thought to occur in the electrode reaction.

11.3.1.3   How is a simulation put together?

Traditionally, a simulation is constructed as follows: (1) the real world problem is analysed and cast in terms of mathematical expressions (e.g. the differential equations for mass transport and the initial and boundary conditions for what happens at the electrode surface and in the bulk); (2) the expressions are then rewritten in dimensionless form; (3) the continuous variables (typically, concentration, space and time) are discretised; (4) the differential equations and boundary conditions are discretised; (5) an algorithm is chosen and a program written in Fortran, Pascal, Basic or C; (6) the simulation is tested with conditions yielding a known solution; (7) finally, the simulation is applied to the conditions of interest.

Physical approaches not requiring the numerical solution of the differential equations have also been developed. For example, an "atomistic" model considers the cell as a domain filled with a population of particles and diffusion is simulated by the random walk of the particles within the domain (53, 54). The current is computed by counting the number of particles that reach the electrode per unit time. Convection and migration can even be included. Another model, the "box" method used in the early days of electrochemical simulation (55), divides the solution in thin slabs (boxes wherein the concentration is assumed to be uniform) and calculates the movement of species between slabs using Fick's first law of diffusion. Although more intuitive, these approaches are in fact equivalent to solving the transport equation.

11.3.1.4   How are they used?

It was common to run the simulation for a range of dimensionless parameters and produce working curves and case diagrams. The experimental data were then cast in dimensionless form and analysed by comparison with the simulated working curves. The tendency is now to move towards a direct fitting of simulated data to experimental data by adjusting the

simulation parameters and running the simulation in real time until a fit is obtained. This is made possible by the computing power available nowadays and is in contrast to conventional procedures where an analytical expression is fitted to the experimental data.

The "home-made" simulation is still required for demanding situations (e.g. voltammetry at a microdisc electrode) but for most problems, DigiSim (56–61), a commercial simulation software, and DigiElch (62), a free equivalent software, offer a much simpler alternative. An electrochemical simulator operates as a black box requiring almost no prior knowledge about numerical simulations of electrode reactions. The user may exploit it as a virtual instrument to predict a theoretical response for a given set of conditions, as an analytical tool to fit experimental results to a model and derive experimental parameters or as a learning or even a teaching tool. At the click of the mouse, the software offers an array of simulation conditions: (1) a range of electrode geometries (planar and spherical); (2) a range of mass transports (semi-infinite diffusion, finite diffusion and convection); (3) single or multiple electron transfer reactions; (4) first- and second-order-coupled chemical reactions; (5) a dynamic display of concentration profiles during cyclic voltammetry; (6) the possibility to import experimental data files for comparison and least-squares fitting with simulated data. DigiElch even includes 2D simulations for microdiscs and microband electrodes. Other free softwares are available (63, 64), including a site for online data analysis and simulations (65).

11.3.2   Basic principles of an electrochemical simulation

Although a simulator may be taken as a black box, the user will soon find that some basic knowledge of the principles of electrochemical simulations is essential. A simple simulation will now be described to highlight the fundamental principles of electrochemical modelling. For additional information, readers should consult Britz's excellent book (66) and Speiser's extensive review (67).

The following assumptions are made: (1) the electrode is planar and the reaction is a fast electron transfer; (2) only O is present in the cell initially; (3) the diffusion coefficients of O and R are identical; (4) the potential of the electrode is stepped from a value where no reaction occurs to one where the reaction is diffusion controlled; (5) the objective is to predict the current transient and the concentration profiles as a function of time. Under these conditions, the latter should be given by equation (11.2.5) and the former by equation (11.2.7). Using the following definitions:

Dimensionless concentration:

$$c = \frac{C_{\mathrm{O}}}{C_{\mathrm{O}}^*} \tag{11.3.1}$$

Dimensionless distance:

$$X = \frac{x}{\delta} \tag{11.3.2}$$

Dimensionless time:

$$T = \frac{t}{\tau} \tag{11.3.3}$$

Dimensionless current:

$$\Psi = \frac{i\delta}{nFAD_{\mathrm{O}}C_{\mathrm{O}}^{*}} \tag{11.3.4}$$

Diffusion layer thickness:

$$\delta = \sqrt{D_{\mathrm{o}}\tau} \tag{11.3.5}$$

where τ is a characteristic time of the experiment (e.g. the duration of the experiment); the transport equation (11.2.1), the initial condition (equation (11.2.2)), the boundary conditions (equations (11.2.3) and (11.2.4)) and the current (equation (11.2.6)) are recast in dimensionless form to avoid unnecessary runs of the simulation.

$$\frac{\partial c(X,T)}{\partial T} = \frac{\partial^2 c(X,T)}{\partial X^2} \tag{11.3.6}$$

$$c(X \geq 0,0) = 1 \tag{11.3.7}$$

$$c(\infty,T > 0) = 1 \tag{11.3.8}$$

$$c(0,T > 0) = 0 \tag{11.3.9}$$

$$\Psi = \left. \frac{\partial c}{\partial X} \right|_{X=0,T>0} \tag{11.3.10}$$

Using finite difference approximations (66), the discrete form of equation (11.3.6) is obtained:

$$\frac{c_i^{k+1} - c_i^k}{\Delta T} = \frac{c_{i+1}^k - 2c_i^k + c_{i-1}^k}{\Delta X^2} \tag{11.3.11}$$

where c_i^k is the discretised dimensionless concentration at location i along the profile and time k equivalent to $C_{\mathrm{O}}(x, t)$ in the usual units. Rearranging yields:

$$c_i^{k+1} = c_i^k + \frac{\Delta T}{\Delta X^2}(c_{i+1}^k - 2c_i^k + c_{i-1}^k) \tag{11.3.12}$$

or

$$c_i^{k+1} = \frac{\Delta T}{\Delta X^2}c_{i+1}^k + \left(1 - 2\frac{\Delta T}{\Delta X^2}\right)c_i^k + \frac{\Delta T}{\Delta X^2}c_{i-1}^k \tag{11.3.13}$$
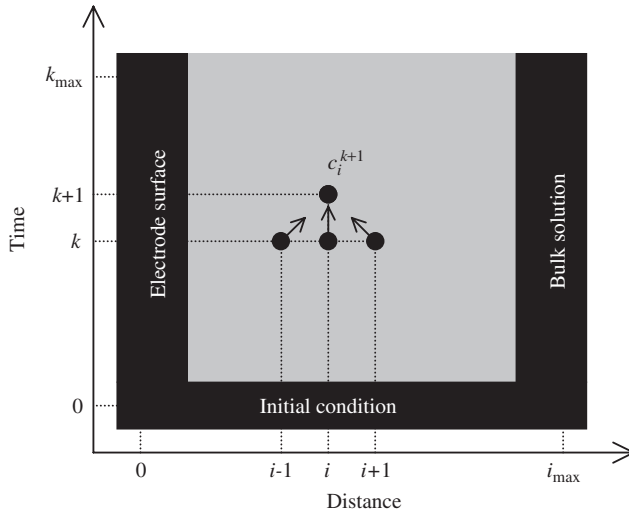
Figure 11.20   Schematic representation of the explicit finite difference algorithm. The grey region indicates unknown concentrations, whereas the black regions indicate known concentrations. Starting with $k = 0$, the unknown concentrations c_i^{k+1} are calculated from the known values of c_{i-1}^k, c_i^k and c_{i+1}^k. Iterating from $i = 1$ to i_{max-1} yields the concentration profile at $k = 1$. The procedure is repeated to compute all the concentrations profiles until k_{max}.

All the concentrations on the RHS correspond to the present and are known. Thus, it is possible to calculate the concentration in the future, c_i^{k+1}. This scheme is known as explicit finite difference or EFD and works as shown in Figure 11.20. The ratio $\Delta T/\Delta X^2$ is akin to a dimensionless or model diffusion coefficient and should be as large as possible to make the simulation efficient. However, it cannot be greater than 0.5 or the scheme becomes unstable and produces negative concentrations. In practice, a value of 0.45 is chosen. This is one of the main limitations of EFD and other more efficient algorithms are available (66). Increasing i_{max} and k_{max} improves the resolution of the discretisation and therefore the accuracy of the simulation but at the expense of computing time. With the desktop computers available nowadays, this is no longer a limitation.

The current at time k is calculated by discretising equation (11.3.10):

$$\Psi^k = \frac{c_1^k - c_0^k}{\Delta X} \tag{11.3.14}$$

Thus, equations (11.3.13) and (11.3.14) provide the means to calculate the current value and concentration profile for each time iteration. See Figure 11.21 for an example of simulation codes. With $\Delta T/\Delta X^2 = 0.45$, the scheme converges rapidly with current values accurate to 5% after 25 iterations (Figure 11.22). The algorithm is rather simple and yet very powerful. For example, to simulate the transient current for a double potential step, it is simply a matter of changing the surface concentration while the simulation

```
'   c(i) : concentration                    For i = 0 To imax + 1
' cnew(i) : new concentration                 c(i) = 1
'     cur : current                         Next i
'      dt : time increment                  c(0) = 0
'      dx : space increment                 For k = 1 To kmax
'       i : counter for space increments      cur = (c(1) - c(0)) / dx
'    imax : number of space increments        tim = k / kmax
'       k : counter for time steps         ' output tim and cur here
'    kmax : number of time steps             For i = 1 To imax
'     mdc : model diffusion coefficient        cnew(i) = c(i) + mdc * (c(i - 1) - 2
'     tim : time                                            * c(i) + c(i + 1))
Dim c(1000), cnew(1000)                       Next i
kmax = 1000                                   For i = 1 To imax
mdc = 0.45                                      c(i) = cnew(i)
dt = 1 / kmax                                  Next i
dx = Sqr(dt / mdc)                          Next k
imax = CInt(6 * Sqr(mdc * kmax))
```

Figure 11.21 Typical codes used to simulate the current transient for a diffusion-controlled reaction on a planar electrode. Written in Visual Basic as found in a spreadsheet macro. For a given time t, diffusion does not affect the concentration profile beyond a distance equal to $6\sqrt{Dt}$, hence the relationship linking i_{max} to k_{max}.
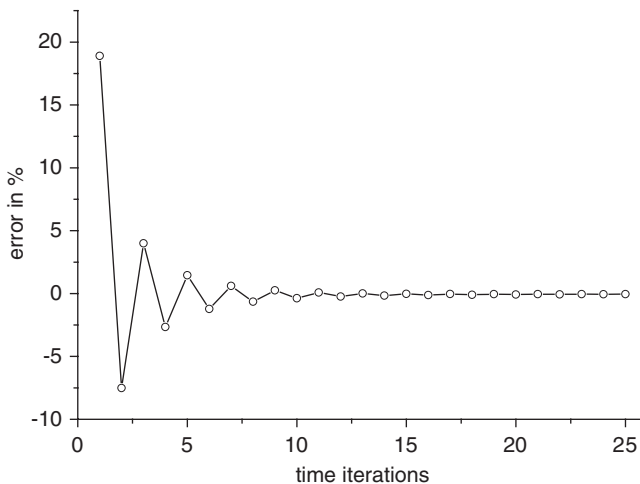

Figure 11.22 Convergence plot for the explicit finite difference algorithm.

is running. The concentration profile gradually adjusts to the new boundary condition and the current follows the characteristic feature of a double pulse experiment (Figure 11.23). Compared to the theoretical treatment, the simulation is exceedingly simple. Similarly, incorporation of potential sweep, heterogeneous or homogeneous kinetics is not difficult and the algorithm can be tailored to simulate complex electrochemical problems.

Many different numerical simulations have been reported, often more accurate and more efficient than EFD. Some include two-dimensional mass transport but they are outside the
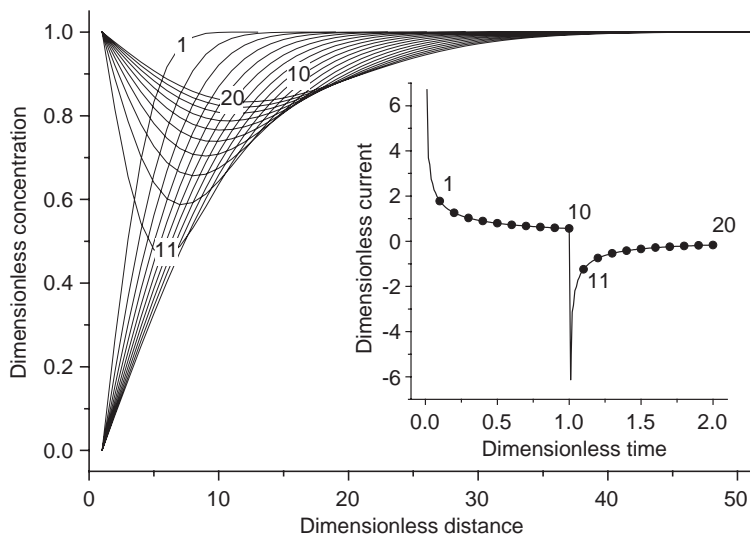
Figure 11.23 Simulated concentration profiles and current transient for a double potential step at a planar electrode under diffusion control. The profiles were taken at the times indicated by the corresponding numbers on the transient.

scope of this chapter and interested readers should consult references (55, 66, 67). The fact is that EFD remains the simplest algorithm and offers the easiest route to implementing complex mechanisms and electrochemical techniques. Since computer power is no longer an issue, EFD's inefficiency is not a concern anymore and interested readers should try to write their own simulation.

11.4 TROUBLE SHOOTING ELECTROCHEMICAL EXPERIMENTS: A CHECKLIST

11.4.1 Checking the results

Electrochemical experiments are often carried out in similar conditions and it is easy to check whether the magnitude of a result is in agreement with expectations. Table 11.5 presents a list of the parameter values typically used to check whether the experimental results obtained have the correct order of magnitude. Many incidents can occur in the course of an electrochemical experiment and the remainder of this section aims to identify the most common causes of problems, as well as how to recognize and correct them.

11.4.2 No current response

Assuming the instruments are turned on, no current indicates that the electrochemical circuit is incomplete. Check the quality of the wires and of the connections. A broken wire at

Table 11.5

Values used to check the magnitude of experimental results.

Quantity	Value	Conditions
C_d	20 μF/(cm^2 real area)	Pt electrode
D_O, D_R	10^{-5} cm^2 s^{-1}	Aqueous solution
i_l	0.4 nA/mM/(μm radius)	Microdisc electrode, $n = 1$
i_l	10 μA/(cm^2 geometric area)/mM/rpm^2	RDE, $n = 1$, aqueous solution
i_p	200 μA/(cm^2 geometric area)/mM	Voltammetry, $n = 1$, $v = 0.1$ V s^{-1}
$Q_{monolayer}$	200 μC/(cm^2 real area)	Pt electrode
R_Ω	1 Ω cm/(cm radius)$^{-1}$	Spherical electrode, 0.5 M NaCl

the back of a rusty crocodile clip is not uncommon. Ensure that the electrodes are fully immersed in the solution. Test the electrochemical circuit by replacing the electrochemical cell with a resistive dummy cell. Connect the WE connector to one end of the resistor, the CE and RE to the other side and run a potential sweep. The current–voltage plot obtained should be purely ohmic: that is, a straight line through the origin with a gradient equal to the inverse of the resistance of the dummy cell. Should this be the case, then the problem lies with the electrochemical cell. Check that the internal connections within the WE, CE or RE are intact. With microelectrodes, it is common to find that the microwire is loose and no longer in electrical contact with the main wire. If the problem is not obvious, replace each electrode in turn to identify the culprit. If the problem does not lie with the electrochemical cell, simply replace each lead/connection/equipment in turn until the problem is resolved.

11.4.3   Potential shift

First, using a DVM, check the potential difference between the WE and the RE. An unexpected potential shift in the current response is likely due to the reference electrode. If a problem with the RE is suspected, run a voltammogram with a pseudo-reference (e.g. Ag or Pt wire). To test the faulty RE, place it in an electrolyte and measure its potential against a commercial RE of the same type. The potential difference between them should be less than 5 mV and stable. Major sources of error in a RE can come from either the electrode being stored in the wrong solution or the presence of a bubble in the electrode. If in doubt, empty the solution from the electrode and replace with fresh solution. A freshly made RE needs time to equilibrate, so store it in the same solution as the internal one and check its potential against a commercial RE. After 24 h, the difference should be less than 5 mV and stable. If it is not, then dismantle the electrode and recondition it (e.g. for an SCE ensure that the internal solution is saturated in KCl). With non-aqueous solvents, it is not advised to use a RE with an aqueous internal solution; instead, use a quasi-RE with an internal redox standard, such as ferrocene.

11.4.4 Currents lower than expected

If the current–voltage curve obtained is correct in shape, but not in magnitude, then the most probable cause is the working electrode. The WE is very susceptible to fouling and requires regular cleaning. Polymers or adsorbed species can easily block the surface, so the electrode should be polished on a polishing pad covered with damp alumina powder (or diamond paste), starting with a high grain size (approximately 1 μm) and reducing down to approximately 0.05 μm, rinsing off between grain sizes. Some electrodes can also be reconditioned by potential cycling in 1 M H_2SO_4 between oxygen and hydrogen evolutions. For example, once cleaned, a Pt electrode should present its typical "fingerprint" (Figure 11.9). Other problems that affect working electrodes include a poor seal between the glass and the electrode, a poor connection between the electrode wire and the connecting wire or the electrode recessing over time (especially in cases where the electrode is much softer than the glass, e.g. carbon fibre electrodes). Diffusion-controlled currents are very sensitive to temperature changes (D increases by 1–2% $°C^{-1}$), so to enable comparison between data recorded at different times (morning vs. afternoon and summer vs. winter), any diffusion-controlled experiment should be thermostated to within 1 °C.

11.4.5 Slanted voltammogram

If the correct shape is seen, but is slanted slightly, then this implies that there is an added resistance in the circuit. The most common reason for this is a bubble inside the RE. This creates a discontinuity in the conductivity of the reference electrode filling solution. The RE should be reconditioned as mentioned above.

11.4.6 Noisy current

This is a particular problem with microelectrodes where the current is typically a few nA. The noise is likely due to the mains and appropriate shielding is required. The cell should be placed inside a grounded Faraday cage. The electrochemical circuit should consist of shielded cables (e.g. BNC) and the instruments should be grounded avoiding ground loops. If possible, battery-operated instruments (e.g. current followers) should be used. A common problem is the use of a thermostatic water bath with a pumped water circuit and a jacketed cell. The water circuit transmits the mains noise which is easily picked up by the WE by coupling through the glass walls. Any mains powered instrument, stirrer or heating mantle, should be removed from the Faraday cage or replaced with battery-operated ones.

11.4.7 Other common problems

(a) *Ohmic distortion*: Increase supporting electrolyte concentration, reposition Luggin capillary, use a microelectrode, decrease reactant concentration or use *iR* compensation.

(b) *Double layer charging*: Reduce the WE area and lower the scan rate.
(c) *Migration*: Increase supporting electrolyte concentration.
(d) *Natural convection*: Work under 30 s.
(e) *Oxygen reduction*: Purge with N_2 or better, Ar.
(f) *Electrode contamination*: Use ultra-pure water and ultra-pure reagents.
(g) *Chloride contamination*: Use SMSE instead of SCE.
(h) *Bad cell geometry*: Position CE opposite WE and ensure CE area is greater than WE area.
(i) *Poor WE geometry*: Avoid geometries with corners.
(j) *Offset and linearity*: Calibrate instruments.

REFERENCES

1. D. D. Macdonald, *Transient Techniques in Electrochemistry*, Plenum Press: New York, 1977.
2. A. J. Bard, L. R. Faulkner, *Electrochemical Methods: Fundamentals and Applications*, Wiley: New York, 2001.
3. R. Greef, R. Peat, L. M. Peter, D. Pletcher, J. Robinson, *Instrumental Methods in Electrochemistry*, Ellis Horwood: Chichester, 1985.
4. F. G. Cottrell, *Z. Phys. Chem.* **42**, 385 (1903).
5. M. Abramowitz, I. A. Stegun, *Handbook of Mathematical Functions*, Dover Publications, Inc.: New York, 1970.
6. J. Koutecky, *Collection Czech. Chem. Commun.* **21**, 433 (1956).
7. D. D. Macdonald, *Transient Techniques in Electrochemistry*, Plenum Press: New York, 1977.
8. W. M. Smit, M. D. Wijnen, *Recueil des Travaux Chimiques des Pays-Bas et de la Belgique* **79**, 5 (1960).
9. T. Kambara, *Bull. Chem. Soc. Jpn.* **27**, 529 (1954).
10. J. Koutecky, *Collection Czech. Chem. Commun.* **21**, 433 (1956).
11. G. C. Barker, *Anal. Chim. Acta* **18**, 118 (1958).
12. F. M. Kimmerle, J. Chevalet, *J. Electroanal. Chem. Interfacial Electrochem.* **21**, 237 (1969).
13. A. J. Bard, L. R. Faulkner, *Electrochemical Methods: Fundamentals and Applications*, John Wiley & Sons, Inc.: New York, 2001.
14. W. M. Schwarz, I. Shain, *J. Phys. Chem.* **69**, 30 (1965).
15. H. Girault, *Analytical and Physical Electrochemistry*, EPFL Press: Lausanne, 2004.
16. K. B. Oldham, *J. Electroanal. Chem.* **313**, 3 (1991).
17. K. B. Oldham, J. C. Myland, C. G. Zoski, A. M. Bond, *J. Electroanal. Chem.* **270**, 79 (1989).
18. E. Laviron, *J. Electroanal. Chem.* **100**, 263 (1979).
19. R. Bilewicz, K. Wikiel, R. Osteryoung, J. Osteryoung, *Anal. Chem.* **61**, 965 (1989).
20. J. Osteryoung, *Acc. Chem. Res.* **26**, 77 (1993).
21. A. M. Bond, *Modern Polarographic Methods in Analytical Chemistry*, Marcel Dekker: New York, 1980.
22. E. P. Parry, R. A. Osteryoung, *Anal. Chem.* **37**, 1634 (1965).
23. J. B. Flato, *Anal. Chem.* **44**, 75A (1972).
24. R. A. Osteryoung, J. Osteryoung, *Philos. Trans. R. Soc. Lond. A Math. Phys. Eng. Sci.* **302**, 315 (1981).
25. K. B. Oldham, E. P. Parry, *Anal. Chem.* **40**, 65 (1968).
26. J. Osteryoung, J. O'Dea, *Electroanalytical Chemistry*, A. J. Bard, Ed., Marcel Dekker: New York, 1986, Vol. 14, p. 209.

27. G. C. Barker, I. L. Jenkins, *Analyst* **77**, 685 (1952).

28. J. H. Christie, J. A. Turner, R. A. Osteryoung, *Anal. Chem.* **49**, 1899 (1977).

29. J. A. Turner, J. H. Christie, M. Vukovic, R. A. Osteryoung, *Anal. Chem.* **49**, 1904 (1977).

30. J. J. O'Dea, J. Osteryoung, R. A. Osteryoung, *Anal. Chem.* **53**, 695 (1981).

31. L. Ramaley, M. S. Krause, Jr., *Anal. Chem.* **41**, 1362 (1969).

32. J. Wang, *Stripping Analysis: Principles, Instrumentation, and Applications*, VCH: Dearfield Beach, FL, 1985.

33. M. I. Montenegro, M. A. Queirós, J. L. Daschbach, Eds., *Microelectrodes: Theory and Applications*, Kluwer Academic Publishers: Dordrecht, 1991.

34. R. M. Wightman, *Anal. Chem.* **53**, 1125A (1981).

35. M. Fleischmann, S. Pons, D. R. Rolison, P. P. Schmidt, Eds., *Ultramicroelectrodes*, Datatech Systems Inc.: Morganton, NC, 1987.

36. R. M. Wightman, D. O. Wipf, *Electroanal. Chem.* **15**, 267 (1989).

37. K. Stulik, C. Amatore, K. Holub, V. Marecek, W. Kutner, *Pure Appl. Chem.* **72**, 1483 (2000).

38. P. R. Unwin, R. G. Compton, in *Comprehensive Chemical Kinetics*, R. G. Compton, A. Hamnett, Eds., Elsevier: Amsterdam, 1989, Vol. 29, p. 173.

39. J. W. Albery, C. C. Jones, A. R. Mount, in *Comprehensive Chemical Kinetics*, R. G. Compton, A. Hamnett, Eds., Elsevier: Amsterdam, 1989, Vol. 29, p. 129.

40. W. J. Albery, M. L. Hitchman, *Ring–Disc Electrodes*, Clarendon: Oxford, 1971.

41. V. G. Levich, *Physicochemical Hydrodynamics*, Prentice-Hall: Englewood Cliffs, NJ, 1962.

42. J. Newman, in *Electroanalytical Chemistry*, A. J. Bard, Ed., Marcel Dekker: New York, 1973, Vol. 6, p. 187.

43. D. D. Macdonald, *Electrochim. Acta* **35**, 1509 (1990).

44. J. R. Macdonald, *Electrochim. Acta* **35**, 1483 (1990).

45. F. Mansfeld, *Electrochim. Acta* **35**, 1533 (1990).

46. C. Gabrielli, M. Keddam, H. Takenouti, *Electrochim. Acta* **35**, 1553 (1990).

47. I. D. Raistrick, *Electrochim. Acta* **35**, 1579 (1990).

48. R. Oltra, M. Keddam, *Electrochim. Acta* **35**, 1619 (1990).

49. J. R. Macdonald, *Electrochim. Acta* **38**, 1883 (1993).

50. D. D. Macdonald, in *Techniques for Characterization of Electrodes and Electrochemical Processes*, J. R. S. Ravi Varma, Ed., Wiley: New York, 1991, Chapter 11.

51. F. Mansfeld, W. J. Lorenz, in *Techniques for Characterization of Electrodes and Electrochemical Processes*, R. Varma, J. R. Selman, Eds., Wiley: New York, 1991, Chapter 12.

52. C. Gabrielli, in *Physical Electrochemistry Principles, Methods, and Applications*, I. Rubinstein, Ed., Marcel Dekker: New York, 1995, Chapter 6.

53. G. Nagy, Y. Sugimoto, G. Denuault, *J. Electroanal. Chem.* **433**, 167 (1997).

54. G. Nagy, G. Denuault, *J. Electroanal. Chem.* **433**, 175 (1997).

55. S. W. Feldberg, in *Electoanalytical Chemistry, A Series of Advances*, A. J. Bard, Ed., Marcel Dekker: New York, Vol. 3, 1969.

56. M. Rudolph, D. P. Reddy, S. W. Feldberg, *Anal. Chem.* **66**, A589 (1994).

57. M. Rudolph, *J. Electroanal. Chem.* **314**, 13 (1991).

58. M. Rudolph, in *Physical Electrochemistry Principles, Methods, and Applications*, I. Rubinstein, Ed., Marcel Dekker: New York, 1995, p. 81.

59. M. Rudolph, *J. Electroanal. Chem.* **338**, 85 (1992).

60. W. Luo, S. W. Feldberg, M. Rudolph, *J. Electroanal. Chem.* **368**, 109 (1994).

61. M. Rudolph, *J. Electroanal. Chem.* **375**, 89 (1994).

62. M. Rudolph, http://www.digielch.de/index.html, 2004.

63. C. Nervi, http://lem.ch.unito.it/chemistry/esp_manual.html, 1998.

64. L. Biesniasz, http://www.cyf-kr.edu.pl/~nbbienia/elsim3ad.html, 1996.
65. R. G. Compton, J. A. Alden, http://physchem.ox.ac.uk/~rgc/datan/datan.htm, 1998.
66. D. Britz, *Digital Simulation in Electrochemistry*, Springer-Verlag: Berlin, Heidelberg, 1988.
67. B. Speiser, in *Electroanalytical Chemistry, A Series of Advances*, A. J. Bard, I. Rubinstein, Eds., Marcel Dekker: New York, 1996, Vol. 19, p. 1.